



HAL
open science

Improvement of the recovery of heavy chlorinated organic compounds in saturated porous media by thermal and chemical enhancements: experimental and two-phase flow modeling approaches

Stéfan Colombano

► **To cite this version:**

Stéfan Colombano. Improvement of the recovery of heavy chlorinated organic compounds in saturated porous media by thermal and chemical enhancements: experimental and two-phase flow modeling approaches. Environmental Engineering. Université Paris-Est, 2019. English. NNT : 2019PESC2032 . tel-03167524

HAL Id: tel-03167524

<https://theses.hal.science/tel-03167524>

Submitted on 12 Mar 2021

HAL is a multi-disciplinary open access archive for the deposit and dissemination of scientific research documents, whether they are published or not. The documents may come from teaching and research institutions in France or abroad, or from public or private research centers.

L'archive ouverte pluridisciplinaire **HAL**, est destinée au dépôt et à la diffusion de documents scientifiques de niveau recherche, publiés ou non, émanant des établissements d'enseignement et de recherche français ou étrangers, des laboratoires publics ou privés.

Docteur de l'Université Paris-Est
Ecole doctorale : Sciences, Ingénierie et Environnement
Spécialité : Science et Technique de l'Environnement

Degree of Doctor of the Paris-Est University
Doctoral school: Science, Engineering and Environment
Specialty: Environmental Science and Technology

Thèse – PhD thesis

Stéfan COLOMBANO

Amélioration de la récupération des composés organochlorés lourds en milieux poreux saturés par soutiens thermiques et chimiques : approches par expérimentations et par modélisation d'écoulement diphasique

Improvement of the recovery of heavy chlorinated organic compounds in saturated porous media by thermal and chemical enhancements: experimental and two-phase flow modeling approaches

Defended on October, 14, 2019

In front of the PhD committee:

Prof. Marie-Odile SIMONNOT	Reviewer
Prof. Olivier ATTEIA	Reviewer
Dr. Hab. Dominique GUYONNET	Examiner
Dr. Hab. Edvina LAMY	Examiner
Dr. Hab. Nicolas FATIN-ROUGE	Examiner
Prof. Christophe GUIMBAUD	Examiner
Prof. Eric D. VAN HULLEBUSCH	Co-Promotor
Dr. Hab. Ioannis IGNATIADIS	Co-Promotor
Dr. Hossein DAVARZANI	Invited
Dr. David HUGUENOT	Invited

Table of Contents

List of Tables.....	ix
List of Figures	xi
List of Appendices	xxiv
Notation.....	xxv
Greek symbols.....	xxxi
Dimensionless numbers.....	xxxv
Definition of terms	xxxvi
Remerciements	xxxviii
Acknowledgments	xl
Résumé.....	xlii
Abstract	xliv
1. INTRODUCTION	2
1.1 Background	2
1.1.1 Overview on polluted sites in France	2
1.1.2 French public policy for contaminated sites and land management	3
1.1.3 Treatment of LNAPL- and DNAPL-contaminated groundwater in France.....	4
1.1.4 NAPL behaviour in porous media.....	7
1.1.5 Toxicity of chlorinated compounds.....	9
1.1.6 Classical techniques for recovering DNAPL free product.....	9
1.1.6.1 Free product recovery with groundwater extraction and skimming (Upwelling)	11
1.1.6.2 Water flooding	12
1.1.6.3 Trench systems.....	13
1.1.7 Improving DNAPL recovery.....	14
1.1.7.1 Effect of temperature on DNAPL recovery	16
1.1.7.2 Effect of adding surfactants on DNAPL recovery (surfactant flushing)	16
1.1.7.3 Using surfactant foam for DNAPL recovery	17
1.2 Thesis context and objectives	17
1.2.1 SILPHES project	18
1.2.2 Description of the site	18
1.2.3 Composition of DNAPL of the INOVYN site	20
1.3 Objectives and structure of the thesis	21

1.4	Funders	22
2.	LITTERATURE REVIEW	24
2.1	Single-phase flow in porous media	24
2.1.1	Dynamics of saturated porous media	24
2.1.2	Solubility and dissolution	25
2.1.2.1	Solubility	25
2.1.2.2	Dissolution	26
2.1.3	Volatilization	28
2.1.4	Viscosity	29
2.2	Multiphase flow in porous media	32
2.2.1	Different scales in porous media	32
2.2.2	Water and DNAPL saturations	33
2.2.3	Interfacial tension	34
2.2.4	Wettability and Contact Angle	34
2.2.5	Capillary Pressure	35
2.2.6	Drainage-imbibition and residual saturations	37
2.2.7	Relative Permeability	39
2.2.8	Capillary pressure, relative permeability – saturation relationships, and main affecting factors.....	40
2.2.9	Retention Models k_r-S_w and P_c-S_w	41
2.2.10	DNAPL trapping mechanisms	43
2.2.11	Drainage-imbibition experimental work	44
2.2.12	Dimensionless numbers related to the displacement of DNAPLs	45
2.2.12.1	Capillary number, Bond number, total trapping number	45
2.2.12.2	Mobility ratio	46
2.3	Effect of thermal enhancement on DNAPL mobility in saturated porous media	47
2.3.1	Heating technologies	47
2.3.2	Influence of temperature on dynamic viscosity	48
2.3.3	Influence of temperature on interfacial tension.....	48
2.3.4	Influence of temperature on density	48
2.3.5	Temperature effect on capillary pressure-saturation function.....	49
2.3.6	Effects of temperature on solubilization	50
2.3.7	Effects of temperature on adsorption onto solid phase	51

2.4	Effect of chemical enhancement on DNAPL mobility in saturated porous media	52
2.4.1	Surfactant injection technologies	53
2.4.2	Background on surfactants	53
2.4.3	Surfactant recovery mechanisms.....	54
2.4.4	Strategy for using surfactants: benefits, limitations and complementarity with other remediation technologies	56
2.4.5	Main surfactants used in soil remediation.....	59
2.4.6	Surfactants used to recover chlorinated compounds	60
2.4.7	Effect of surfactant on solubilization and interfacial tension of chlorinated compounds	62
2.5	Multiphase flow modeling and numerical simulation	65
2.5.1	General model of multiphase/multicomponent flow and transport in porous media	66
2.5.2	Mathematical models and formulations of two-phase immiscible flow in porous media	67
2.5.2.1	Phase pressure–saturation formulation	67
2.5.2.2	Pressure-pressure formulation	68
2.5.2.3	Flooding formulation	68
2.5.2.4	Fractional flow formulations.....	69
2.5.2.5	Two-phase mixed formulation	70
2.5.2.6	Mathematical models and formulations of two-phase immiscible flow in porous media	71
2.5.3	Commercial numerical models.....	71
2.6	Electromagnetism, resistivity and permittivity	74
2.6.1	Maxwell equations	74
2.6.2	Material behaviour with electromagnetic solicitation	74
2.6.3	Frequency dependence of the materials	76
2.6.4	Electrical resistivity and induced polarization	76
2.6.4.1	Electrical resistivity	77
2.6.4.2	Induced polarization.....	82
2.6.4.3	NAPL and electrical resistivity	83
2.6.5	Dielectric permittivity	84
2.6.5.1	Background	84
2.6.5.2	NAPL and dielectric permittivity.....	85

2.7	Other non-invasive imaging methods and optical imaging methods	87
2.7.1	Alternative methods	87
2.7.2	Optical imaging methods	87
2.7.2.1	Background	87
2.7.2.2	Light Reflected Methods	89
2.7.2.3	Light Transmitted Methods	92
3.	CHARACTERIZATION OF THE DNAPL MIXTURE	96
3.1	Materials and methods	96
3.1.1	Rheological DNAPL characterization	96
3.1.1.1	Dynamic viscosity	96
3.1.1.2	Interfacial tension and contact angle between DNAPL-water	97
3.1.1.3	Density	98
3.1.2	Solubilization	98
3.1.3	Volatilization	99
3.2	Results and discussion	99
3.2.1	Rheological DNAPL characterization	99
3.2.1.1	Dynamic viscosity	99
3.2.1.2	Interfacial tension and contact angle between DNAPL-water	101
3.2.1.3	Capillary pressure	107
3.2.1.4	Density	108
3.2.2	Solubilization	109
3.2.2.1	Quantification of chlorinated compounds in the aqueous phase	109
3.2.2.2	Effect of chemical enhancement	111
3.2.2.3	Determination of CMC_{real}	114
3.2.2.4	Effect of thermal enhancement	114
3.3	Conclusions	116
4.	EXPERIMENTS IN 1D CELLS	118
4.1	Materials and methods	118
4.1.1	Porous media characterization	118
4.1.1.1	Porosity	118
4.1.1.2	Particle-size distribution	118
4.1.1.3	Permeability and hydraulic conductivity	119
4.1.2	Drainage-imbibition experiments	119

4.1.2.1	Main objectives	119
4.1.2.2	Experimental set-up	119
4.1.2.3	Experimental procedure	121
4.1.3	Monitoring of the drainage-imbibition experiments with permittivity and electrical resistivity	123
4.1.3.1	Dielectric permittivity monitoring	123
4.1.3.2	Electrical resistivity monitoring.....	124
4.1.4	Monitoring of the drainage-imbibition experiments with image interpretation	125
4.1.4.1	Camera	125
4.1.4.2	Calibration procedure.....	125
4.1.4.3	Data analysis software	126
4.2	Results and discussion	127
4.2.1	Porous media characterization	127
4.2.1.1	Porosity	127
4.2.1.2	Particle-size distribution	127
4.2.1.3	Permeability and hydraulic conductivity	128
4.2.2	Fitting of experimental results with different parametric models for the P_c - S_w curves	131
4.2.3	Capillary pressure-water saturation curves for 0.5 and 0.1 mm glass beads ...	131
4.2.3.1	Comparison of P_c - S_w curves for 0.5 mm and 0.1 mm glass beads with membranes	131
4.2.3.2	Comparison of P_c - S_w curves for 0.5 mm and 0.1 mm glass beads without membranes	136
4.2.3.3	Permittivity monitoring.....	138
4.2.3.4	Electrical resistivity monitoring.....	144
4.2.3.5	Optical density monitoring	150
4.2.4	Capillary pressure-water saturation curves for 0.5 and 0.1 mm glass beads with chemical enhancement	152
4.2.4.1	Comparison of P_c - S_w curves for 0.1 mm and 0.5 mm glass beads with chemical enhancement	153
4.2.4.2	Permittivity monitoring.....	158
4.2.4.3	Electrical resistivity monitoring.....	161
4.2.4.4	Optical density monitoring	163

4.2.5	Capillary pressure-water saturation curves for 0.5 and 0.1 mm glass beads with thermal enhancement	163
4.2.5.1	Comparison of P_c - S_w curves for 0.1 mm and 0.5 mm glass beads with thermal enhancement.....	163
4.2.5.2	Permittivity monitoring.....	165
4.2.5.3	Electrical resistivity monitoring.....	169
4.2.5.4	Optical density monitoring	173
4.3	Conclusions	173
5.	EXPERIMENTS IN 1D COLUMNS	176
5.1	Materials and methods	176
5.2	Numerical and mathematical modeling	177
5.2.1	COMSOL Multiphysics®	177
5.2.2	Design of the model	177
5.2.3	Initial values and boundary conditions.....	178
5.2.3.1	Initial values	179
5.2.3.2	Boundary conditions	179
5.3	Results and discussion	180
5.3.1	Experiments in 1 D columns without enhancement.....	180
5.3.1.1	Experimental results and comparison with numerical simulation	180
5.3.1.2	Permittivity monitoring.....	187
5.3.1.3	Electrical resistivity monitoring.....	191
5.3.2	Experiments in 1 D columns with chemical enhancement	195
5.3.2.1	Experimental results and comparison with numerical simulation	196
5.3.2.2	Permittivity monitoring.....	197
5.3.2.3	Electrical resistivity monitoring.....	198
5.3.3	Experiments in 1 D columns with thermal enhancement.....	200
5.3.3.1	Experimental results and comparison with numerical simulation	201
5.3.3.2	Permittivity monitoring.....	202
5.3.3.3	Electrical resistivity monitoring.....	204
5.4	Conclusions	206
6.	EXPERIMENTS IN THE 2D TANK	209
6.1	Materials and methods	209
6.1.1	Drainage-imbibition experiments.....	209
6.1.1.1	Experimental set-up	209

6.1.1.2	Experimental procedure	211
6.1.2	Drainage-imbibition experiments with permittivity and electrical resistivity monitoring.....	213
6.1.2.1	Permittivity monitoring.....	213
6.1.2.2	Electrical resistivity monitoring.....	214
6.1.3	Monitoring of the drainage-imbibition experiments with image interpretation	215
6.1.3.1	Camera set-up	215
6.1.3.2	Image interpretation	215
6.2	Numerical and mathematical modeling	220
6.2.1	Design of the model	220
6.2.2	Initial values and boundary conditions.....	220
6.2.2.1	Initial values	221
6.2.2.2	Boundary conditions	221
6.3	Results and discussion	221
6.3.1	Experiments in the 2D tank without enhancement.....	221
6.3.1.1	Experimental results: comparison of numerical simulation with optical density monitoring.....	221
6.3.1.2	Permittivity monitoring.....	229
6.3.1.3	Electrical resistivity monitoring.....	233
6.3.2	Experiments in the 2D tank with chemical enhancement	239
6.3.2.1	Experimental results: comparison of numerical simulation with optical density monitoring.....	239
6.3.2.2	Permittivity monitoring.....	244
6.3.2.3	Electrical resistivity monitoring.....	246
6.3.3	Experiments in the 2D tank with thermal enhancement	249
6.3.3.1	Experimental results: comparison of numerical simulation with optical density monitoring.....	250
6.3.3.2	Permittivity monitoring.....	254
6.3.3.3	Electrical resistivity monitoring.....	257
6.3.4	Comparison of permittivities without enhancement, with chemical and thermal enhancements	260
6.3.5	Comparison of resistivities without enhancement, with chemical and thermal enhancements	261

6.3.6	Comparison of fingerings effect at the DNAPL-water interface without enhancement, with chemical and thermal enhancements	262
6.4	Technical and economical analysis	263
6.5	Conclusions	264
7.	CONCLUSIONS AND PERSPECTIVES	268
8.	REFERENCES	273

List of Tables

Table 1: Classification of main treatment techniques and methods for groundwater remediation by volume treated in 2012 (in m ³) – excluding industrial waste [ADEME and Ernst & Young (2014)]	4
Table 2: Pollution remediation techniques used for polluted groundwater by total petroleum hydrocarbons and chlorinated compounds (excluding industrial pollution) [ADEME and Ernst & Young (2014)].....	5
Table 3: IARC Classification for Chlorinated Compounds in DNAPL [IARC (2018)].....	9
Table 4: Functional role for commonly used remediation technologies in generalized sequential treatment strategy [Williamson (2014)].....	15
Table 5: Hydrogeological description of the site [Cazaux <i>et al.</i> (2014)].....	18
Table 6: Composition of the "DNAPL" by average mass [Cazaux <i>et al.</i> (2014)]	20
Table 7: Main physical and chemical characteristics of chlorinated compounds from DNAPL.....	21
Table 8: Dimensionless numbers for dissolution and dilution (adapted from [Luciano (2009)])	27
Table 9: Mass Transfer Correlations [Imhoff <i>et al.</i> (1997)]	28
Table 10: Vapor pressure and Henry's constant of certain pollutants constituting our DNAPL (at 10 °C).....	29
Table 11: Pure mixing rules with blending index for calculating the viscosity of mixtures....	30
Table 12: Mixing rules with extra-parameters and excess function for calculating the viscosity of mixtures.....	31
Table 13: Two-fluid capillary pressure and permeability models [Chen <i>et al.</i> (1999)].....	42
Table 14: Variation in solubility for various chlorinated solvents for the given temperature ranges	51
Table 15: Selection criteria for surfactant solutions [Martel <i>et al.</i> (1993)].....	59
Table 16: Representative Examples of Surfactant Flushing Field Demonstrations [Pennell <i>et al.</i> (2014)].....	61
Table 17: Comparison of TCE solubilization and IFT reduction for representative surfactants.....	62
Table 18: Comparison of PCE solubilization and IFT reduction for representative surfactants.....	63
Table 19: Characteristics of two-phase flow models (adapted from [Wang and Beckermann (1993); Chen <i>et al.</i> (2006); Bjørnara and Aker (2008)]).....	71
Table 20: Characteristics of three-phase flow models [Sleep (2003)]	72
Table 21: Characteristics of two-phase flow models and vadose zone models [Sleep (2003)].....	73
Table 22: Electrical resistivity for different geological formations and water [Telford <i>et al.</i> (1990); Guérin <i>et al.</i> (2004)]	78
Table 23: Dielectric permittivity in rocks and water at 100 MHz (adapted from [Martinez and Byrnes (2001)].....	85
Table 24: Chromatography column characteristics.....	99

Table 25: Viscosity of each compound at the site.....	100
Table 26: Mixing rules with extra-parameters and excess function for calculating the viscosity of mixtures.....	100
Table 27: DNAPL-water interfacial tension at 20 °C	101
Table 28: Names and chemical properties of the surfactants used.....	101
Table 29: DNAPL-water-glass contact angle.....	104
Table 30: DNAPL-water-glass beads contact angle.....	106
Table 31: Reduction of the capillary pressure with chemical and thermal enhancements.....	107
Table 32: Component breakdown for the UNIFAC method.....	110
Table 33: Effective aqueous solubility of the DNAPLs.....	110
Table 34: Estimation of the CMC_{real}	114
Table 35: Glass beads information.....	118
Table 36: Porosity of the glass beads and the Tavaux soil sample	127
Table 37: Empirical equation used to calculate hydraulic conductivity on the basis of the particle size distribution curve	129
Table 38: Determination of descriptive parameters for the particle size distribution curve ..	130
Table 39: Estimation of theoretical hydraulic conductivities of the Tavaux soil sample	130
Table 40: Results of drainage-imbibition experiments for 0.5 and 0.1 mm GB with membrane (average).....	133
Table 41: Calculated and measured entry pressure without enhancement.....	136
Table 42: Correction factors applied to the drainage-imbibition results to transform the values of the cells without membranes into cells with membranes.....	137
Table 43: Results of drainage-imbibition experiments for 0.5 and 0.1 mm GB with SDSB (average).....	154
Table 44: Calculated entry pressure without enhancement and with chemical enhancement.....	158
Table 45: Results of drainage-imbibition experiments for 0.5 and 0.1 mm GB with thermal enhancement (average).....	165
Table 46: Equations forming the two-phase flow model with COMSOL Multiphysics® (pressure-pressure formulations).....	178

List of Figures

Figure 1: Main pollutants encountered in contaminated sites in France [MTES (2018)].....	2
Figure 2: Pollutants treated in 2012 on groundwater remediation sites located in France [ADEME and Ernst & Young (2014)]	4
Figure 3: Variability of average costs for treatment techniques of groundwater ($\text{€}\cdot\text{m}^{-3}$) in France - excluding taxes - in 2012 [ADEME and Ernst & Young (2014)].....	6
Figure 4: Schematic representation of the behaviour of Light Non-Aqueous Phase Liquids (in the saturated zone) (adapted from [US EPA (1996a)])	7
Figure 5: Schematic representation of the behaviour of Dense Non-Aqueous Phase Liquids (in the saturated zone) (adapted from [Cohen and Mercer (1993)]).....	8
Figure 6: Average and maximum lengths of contamination plumes as a function of contaminant type [Stupp and Paus (1999)]	8
Figure 7: Schematic representation of DNAPL free product recovery (adapted from [Colombano <i>et al.</i> (2010)]).....	10
Figure 8: Schematic representation of free product recovery with groundwater extraction and skimming (upwelling) (adapted from [Villaume <i>et al.</i> (1983)])	11
Figure 9: Schematic representation of the principle of water flooding (adapted from [Colombano <i>et al.</i> (2010)]).....	12
Figure 10: Schematic representation of trench systems (adapted from [Huling and Weaver (1991); Sale and Kuhn (1988)])	14
Figure 11: Rebound assessment at source depletion sites: concentration reduction from before treatment to immediately after treatment and at end of data record (chlorinated compounds) [McGuire <i>et al.</i> (2006)]	15
Figure 12: Map of factory location and source site for study [Cazaux <i>et al.</i> (2014)]	19
Figure 13: Hydrogeological cross section and schematic representation of SILPHES project site [adapted from [Cazaux <i>et al.</i> (2014)]	19
Figure 14: Transfer of the pollutant from the storage sector to the plume area: total concentrations of chlorinated compounds in a) 1989 and b) 2009 [Cazaux <i>et al.</i> (2014)]	20
Figure 15: Organization of the different stages of the thesis	22
Figure 16: Different scales in porous media [Quintard <i>et al.</i> (2001)].....	32
Figure 17: Illustration of water and DNAPL saturation differences	33
Figure 18: Wetting in different fluids [Yuan and Lee (2013)].....	34
Figure 19: Illustration of a capillary tube immersed in a liquid [Wilson <i>et al.</i> (1990)].....	35
Figure 20: Analogy of capillary pressure at various sizes of the capillary tube ([Lu and Likos (2004)].....	36
Figure 21: Various pore radii of the pore throat in the soil pores [Bear and Cheng (2010)] ..	37
Figure 22: Drainage-imbibition curves (adapted from [Benremita (2002)])	37
Figure 23: Relative permeability curve for a DNAPL-water system [Schwille (1988)]	39
Figure 24: Relative permeabilities in a two-phase NAPL/water system (according to [Williams and Wilder (1971)]).....	40
Figure 25: Capillary pressure and relative permeability for water-wet and mixed wet conditions [Abdallah <i>et al.</i> (2007)]	41

Figure 26: Capillary trapping mechanisms – by-passing (adapted from [Chatzis <i>et al.</i> (1983)]).....	44
Figure 27: Capillary trapping mechanisms - snap-off (adapted from [Chatzis <i>et al.</i> (1983)])	44
Figure 28: Phase-diagram of multiphase domain displacement [Lenormand <i>et al.</i> (1988)]....	46
Figure 29: Schematic representation of Hot Water Flooding (adapted from [Colombano <i>et al.</i> (2010)]).....	47
Figure 30: Schematic representation of surfactant flooding (adapted from [Colombano <i>et al.</i> (2010)]).....	53
Figure 31: Influence of surfactant concentration on the IFT and solubility of NAPLs of a NAPL-water system [Pennell <i>et al.</i> (2014)].....	55
Figure 32: Displacement of PCE-DNAPL as a function of N_T [Pennell <i>et al.</i> (1996)]	56
Figure 33: Schematic pseudo-ternary diagram [Martel <i>et al.</i> (1993)].....	57
Figure 34: S_n as a function of N_{Ca} for mobilization experiments using water alone, surfactant solution, low and high ∇P foams and low ∇P foam completed by micellar solubilization [Maire <i>et al.</i> (2018)]	59
Figure 35: Aqueous solubility of a) TCE and b) PCE in different surfactant solutions at 20 °C (from [Pennell <i>et al.</i> (1996); Sabatini <i>et al.</i> (2000); Ramsburg and Pennell (2001); Taylor <i>et al.</i> (2001)]).....	64
Figure 36: IFT reduction of TCE-water and PCE-water systems with different surfactant solutions at 20°C (from [Pennell <i>et al.</i> (1996); Sabatini <i>et al.</i> (2000); Ramsburg and Pennell (2001); Taylor <i>et al.</i> (2001)])	65
Figure 37: Flow chart as a decision tool for selecting the right model type (adapted from [ADEME <i>et al.</i> (2007)])	73
Figure 38: Electric relaxation as a function of frequency (adapted from [Nicolini <i>et al.</i> (1998)]).....	76
Figure 39: Principle of electrical resistivity measurement (adapted from [Noel (2014)]).....	80
Figure 40: Distribution of the current flow in a homogeneous soil [Samouëlian <i>et al.</i> (2005)].....	80
Figure 41: Measurement of electrical resistivity: dipole-dipole arrangement (adapted from [Noel (2014)])	81
Figure 42: Electrical sounding sketch [Guérin <i>et al.</i> (2004)].....	82
Figure 43: Time domain waveform illustrations [Reynolds (2011)]	82
Figure 44: Frequency domain waveform illustrations [Revil (2012)]	82
Figure 45: Photographs of a) the DHR 3 and b) Haake Mars III rheometers	96
Figure 46: Photographs of a) the Tracker-S and b) DSA-100 tensiometers	97
Figure 47: Contact angle of digitized drop a) without and b) with the glass beads	97
Figure 48: Digitized pendant drop during the measurement of IFT.....	98
Figure 49: Variation of DNAPL and water dynamic viscosities as a function of temperature.....	100
Figure 50: DNAPL-water interfacial tension variation with different surfactant concentrations.....	102
Figure 51: Estimation of the trend curve $IFT=f([\text{surfactant}])$ and estimation of the real CMC for a) Triton X-100, b) Tween 80, c) Aerosol MA-80, d) SDBS	103
Figure 52: Variation of DNAPL-water interfacial tension as a function of temperature.....	103

Figure 53: Variation of DNAPL-water-glass contact angle with chemical enhancement at different surfactant concentrations	104
Figure 54: Variation of DNAPL-water-glass contact angle as a function of temperature	105
Figure 55: Variation of DNAPL-water-glass beads contact angle with chemical enhancement at different surfactant concentrations	106
Figure 56: Variation of DNAPL-water-glass beads contact angle as a function of temperature (compared with the variation of DNAPL-water-glass contact angle).....	107
Figure 57: a) Variation in capillary pressure and b) percentage reduction in capillary pressure with chemical and thermal enhancements.....	108
Figure 58: Variation of DNAPL and water densities as a function of temperature	109
Figure 59: Distribution of [COCs] at 20 °C	109
Figure 60: Variation of [Σ COCs] with different surfactant concentrations	111
Figure 61: Variation of IFT and [Σ COCs] with different surfactant concentrations (a) Triton X-100, b) Tween 80, c) Aerosol MA-80, d) SDBS)	112
Figure 62: Variation of [COCs] with different surfactant concentrations.....	112
Figure 63: Distribution of [COCs] a) without surfactant and with different surfactant concentrations (b) Triton X-100, c) Tween 80, d) Aerosol MA-80, e) SDBS)	113
Figure 64: Variation of [COCs] at different temperatures	115
Figure 65: Distribution of the [COCs] at a) 12 °C and b) 60 °C.....	115
Figure 66: Experimental set-up of the a) drainage and b) imbibition experiments.....	120
Figure 67: Experimental 1D cell set-up	120
Figure 68: a) Photograph and b) schematic drawing of a 1D cell.....	121
Figure 69: Global view of the entire experimental device for the 1D cells	121
Figure 70: a) Stainless and b) PVDF filters of a 1D cell.....	122
Figure 71: TDR probe	123
Figure 72: Unpolarizable copper sulphate potential electrodes	124
Figure 73: Optical calibration experiment in the flat cell: a) picture taken during the calibration experiment, b) global AOI, c) global AOI transformed into 8 bits format	126
Figure 74: Particle size distribution curves of Tavaux soil samples	127
Figure 75: Particle size distribution curve of the Tavaux soil samples.....	128
Figure 76: Determination of the permeabilities with $Q/A=f(\Delta H/\Delta L) - 1.0$ and 0.5 mm GB	128
Figure 77: Determination of the permeabilities with $Q/A=f(\Delta H/\Delta L) - 0.1-0.2$, 0.1 mm GB and Tavaux sample.....	129
Figure 78: Comparison of the experimental and theoretical a) permeability and b) hydraulic conductivity of different glass beads size and the soil sample.....	130
Figure 79: P_c-S_w curves for 0.5 mm GB with membrane (a) raw values and b) VGM fitting).....	132
Figure 80: P_c-S_w curves for 0.1 mm GB with membrane (a) raw values and b) VGM fitting).....	132
Figure 81: P_c-S_w curves for 0.1 and 0.5 mm GB with membrane (VGM fitting)	132
Figure 82: h_c as a function of P_c-S_w 0.5 mm GB/ P_c-S_w 0.1 mm GB with membrane – VGM fitting	134

Figure 83: Relative permeabilities as a function of S_w for 0.5 and 0.1 mm GB (a) drainage 1 and b) imbibition 1).....	134
Figure 84: P_c - S_w curves for 0.09, 0.1, 0.12, 0.5, 0.74 mm GB in the air/water system, comparison with 0.1, 0.5 mm for DNAPL-water system corrected by the β factor – VGM fitting	135
Figure 85: P_c air-water system/ P_c DNAPL-water system as a function of S_w	135
Figure 86: P_c - S_w curves for 0.1 and 0.5 mm GB with and without membrane – VGM fitting	137
Figure 87: P_c - S_w curves for 0.5 mm GB without membrane (a) raw and corrected values and b) VGM fitting)	138
Figure 88: P_c - S_w curves for 0.1 mm GB without membrane (a) raw and corrected values and b) VGM fitting)	138
Figure 89: Change of water saturation and permittivity as a function of time without enhancement (example of a drainage-imbibition experiment with 0.5 mm GB).....	139
Figure 90: Change of water saturation and permittivity as a function of time without enhancement (example of a drainage-imbibition experiment with 0.1 mm GB).....	139
Figure 91: Calibration curve $\varepsilon = f(S_w)$ for 0.5 mm GB with and without membrane	140
Figure 92: Calibration curve $\varepsilon = f(S_w)$ for 0.1 mm GB with and without membrane	140
Figure 93: Comparison of the permittivity values between 0.5 and 0.1 mm GB as a function of saturation	141
Figure 94: Fitting the experimental permittivity values as function of water saturation with the CRIM model (0.5 mm GB with and without membrane)	142
Figure 95: Fitting the experimental permittivity values as a function of water saturation with the CRIM model (0.1 mm GB with and without membrane)	142
Figure 96: Ratios of the experimental permittivity values/CRIM model values as a function of water saturation (for 0.1 and 0.5 mm GB with and without membrane)	143
Figure 97: Change of water saturation and permittivity (measured and estimated) as a function of drainage-imbibition cycle for 0.5 and 0.1 mm GB in 1D cells (without enhancement).....	144
Figure 98: Change of water saturation and resistivity as a function of time (example of one drainage-imbibition experiment with 0.5 mm GB)	144
Figure 99: Change of water saturation and resistivity as a function of time (example of one drainage-imbibition experiment with 0.1 mm GB)	145
Figure 100: Calibration curve $\rho_c = f(S_w)$ for 0.5 mm GB with and without membrane	145
Figure 101: Calibration curve $\rho_c = f(S_w)$ for 0.1 mm GB with and without membrane	146
Figure 102: Comparison of the resistivity values between 0.5 and 0.1 mm GB as a function of water saturation	146
Figure 103: Fitting the experimental resistivity values as a function of water saturation with the Archie's law (0.5 mm GB with and without membrane)	148
Figure 104: Fitting the experimental resistivity values as a function of water saturation with the Archie's law (0.1 mm GB with and without membrane)	148
Figure 105: Ratios of the experimental resistivity measured values/Archie's law values (for 0.1 and 0.5 mm GB with and without membrane)	148
Figure 106: Change of water saturation and resistivity (measured and estimated) as a function of drainage-imbibition cycle for 0.5 and 0.1 mm GB in 1D cells (without enhancement).....	149

Figure 107: Drainage-imbibition experiments in the flat cell (example with 0.5 mm GB)...	150
Figure 108: a) Mean grey values variations as a function of the AOI length variations (example with 0.5 mm GB) and b) variation of the AOI	151
Figure 109: Calibration curve - Optical Density = $f(S_w)$ for 0.5 and 0.1 mm GB	151
Figure 110: Drainage-imbibition experiments with optical density monitoring (0.5 mm GB)	152
Figure 111: Drainage-imbibition experiments with optical density monitoring (0.1 mm GB)	152
Figure 112: S_m and remediation yields with the four surfactants with 0.5 and 0.1 mm GB (average values at the end of imbibition 1)	153
Figure 113: P_c-S_w curves for 0.5 mm GB with SDBS (a) corrected values and b) VGM fitting).....	154
Figure 114: P_c-S_w curves for 0.1 mm GB with SDBS (a) corrected values and b) VGM fitting).....	154
Figure 115: Comparison of P_c-S_w curves for a) 0.5mm GB and b) 0.1 mm GB with and without SDBS (with VGM fitting).....	155
Figure 116: $S_n/S_{n,SDBS}$ as a function of h_c for 0.5 and 0.1 mm GB – VGM fitting.....	155
Figure 117: Comparison of a) Capillary number (N_{ca}), b) Bond number (N_B), and c) Total trapping number (N_T) for 0.5 and 0.1 mm GB	156
Figure 118: S_m as a function of N_T	157
Figure 119: P_c-S_w curves for 0.5 mm GB with SDBS addition at the beginning of drainage 1 (a) corrected values and b) VGM fitting).....	157
Figure 120: P_c-S_w curves for 0.1 mm GB with SDBS addition at the beginning of drainage 1 (a) corrected values and b) VGM fitting).....	157
Figure 121: Permittivity measurements during drainages with water and the four surfactants.....	159
Figure 122: Impact of surfactants on permittivity measurements	159
Figure 123: Water saturation and permittivity (measured and estimated) at the end of imbibition 1 for 0.5 and 0.1 mm GB in 1D cells (with and without chemical enhancement)	160
Figure 124: Differences between the measured permittivities and those estimated as a function of saturation during chemical enhancement with a) 0.5 and b) 0.1 mm GB.....	160
Figure 125: Impact of surfactants on resistivity measurements	161
Figure 126: Water saturation and resistivity (measured and estimated) at the end of imbibition 1 for 0.5 and 0.1 mm GB in 1D cells (with and without chemical enhancement).....	162
Figure 127: Differences between the measured resistivities and those estimated during chemical enhancement with a) 0.5 and b) 0.1 mm GB	162
Figure 128: Imbibition experiments with Optical Density monitoring in the flat cell (0.1 mm GB) with and without surfactant (SDBS - CMC)	163
Figure 129: P_c-S_w curves for 0.5 mm GB with thermal enhancement (a) corrected values and b) VGM fitting)	164
Figure 130: P_c-S_w curves for 0.1 mm GB with thermal enhancement (a) corrected values and b) VGM fitting).....	164

Figure 131: Comparison of P_c - S_w curves for a) 0.5 mm GB and b) 0.1 mm GB with and without thermal enhancement (with VGM fitting)	164
Figure 132: Permittivity and temperature for DNAPL with 0.5 mm GB: a) permittivity and temperature variations as a function of time and b) permittivity variation as a function of temperature.....	165
Figure 133: Permittivity and temperature for DNAPL without GB: a) permittivity and temperature variations as a function of time and b) permittivity variation as a function of temperature.....	166
Figure 134: Permittivity and temperature for water with 0.5 mm GB: a) permittivity and temperature variations as a function of time and b) permittivity variation as a function of temperature.....	166
Figure 135: Permittivity and temperature for water without GB: a) permittivity and temperature variations as a function of time and b) permittivity variation as a function of temperature.....	167
Figure 136: Comparison between the experimental permittivity values and models as a function of time (for water without GB)	167
Figure 137: Evolution of water saturation and permittivity as a function of time with thermal enhancement (example of a drainage-imbibition experiment with 0.5 mm GB).....	168
Figure 138: Evolution of water saturation and permittivity as a function of time with thermal enhancement (example of a drainage-imbibition experiment with 0.1 mm GB).....	168
Figure 139: Water saturation and permittivity (measured and estimated) at the end of imbibition 1 for 0.5 and 0.1 mm GB in 1D cells (with and without thermal enhancement)..	169
Figure 140: Resistivity and temperature for DNAPL with 0.5 mm GB: a) resistivity and temperature variations as a function of time and b) resistivity variation as a function of temperature.....	169
Figure 141: Resistivity and temperature for DNAPL without GB: a) resistivity and temperature variations as a function of time and b) resistivity variation as a function of temperature.....	170
Figure 142: Resistivity and temperature for water with 0.5 mm GB: a) resistivity and temperature variations as a function of time and b) resistivity variation as a function of temperature.....	170
Figure 143: Resistivity and temperature for water without GB: a) resistivity and temperature variations as a function of time and b) resistivity variation as a function of temperature	171
Figure 144: Resistivity variation as a function of temperature for DNAPL without GB, DNAPL+GB, water without GB, water+GB	171
Figure 145: Evolution of water saturation and resistivity as a function of time with thermal enhancement (example of a drainage-imbibition experiment with 0.5 mm GB).....	172
Figure 146: Evolution of water saturation and resistivity as a function of time with thermal enhancement (example of a drainage-imbibition experiment with 0.1 mm GB).....	172
Figure 147: Water saturation and resistivity (measured and estimated) at the end of imbibition 1 for 0.5 and 0.1 mm GB in 1D cells (with and without thermal enhancement)	173
Figure 148: Experimental 1D column set-up	176
Figure 149: Schematic drawing of 1D column	176
Figure 150: Geometry and meshing of 1D column.....	179

Figure 151: Boundary conditions for drainage and imbibition in 1D column experiments .. 179

Figure 152: Experimental function h_{pn} and h_{pw} as a function of time 180

Figure 153: Change in water saturation as a function of drainage-imbibition cycle for 0.5 and 0.1 mm GB in 1D cells and 1D columns (with and without membrane)..... 181

Figure 154: Evolution of the effective water saturation (S_{ew}) modeled during drainage with 0.5 mm GB 182

Figure 155: Comparison of experimental and modeled results for drainage in 1D column with 0.5 mm GB: a) average S_w and volume of DNAPL recovered and b) DNAPL-water interface position 182

Figure 156: Evolution of V_{DNAPL} measured/ V_{DNAPL} modeled ratios during drainage in 1D column with 0.5 mm GB 183

Figure 157: Comparison of experimental and modeled results for imbibition in 1D column with 0.5 mm GB: a) average S_w and volume of DNAPL recovered and b) DNAPL-water interface position 183

Figure 158: Evolution of V_{DNAPL} measured/ V_{DNAPL} modeled ratios during imbibition in 1D column with 0.5 mm GB 183

Figure 159: Comparison of experimental and modeled results for drainage in 1D column with 0.1 mm GB: a) average S_w and volume of DNAPL recovered and b) DNAPL-water interface position 184

Figure 160: Evolution of V_{DNAPL} measured/ V_{DNAPL} modeled ratios during drainage in 1D column with 0.1 mm GB 184

Figure 161: Comparison of experimental and modeled results for imbibition in 1D column with 0.1 mm GB: a) average S_w and volume of DNAPL recovered and b) DNAPL-water interface position 185

Figure 162: Evolution of V_{DNAPL} measured/ V_{DNAPL} modeled ratios during imbibition in 1D column with 0.1 mm GB 185

Figure 163: Comparison between modeled and measured DNAPL volume (V_{DNAPL}) for experiments with 0.5 and 0.1 mm GB..... 185

Figure 164: Comparison of the water saturation (S_w) modeled profile for different times during a) drainage and b) imbibition experiments (for 0.5 and 0.1 mm GB) 186

Figure 165: Comparison of water-DNAPL interface transitions zones modeled with 0.5 and 0.1 mm GB (drainage experiment at $t=8.24$ d) 187

Figure 166: Position of the TDR probes 187

Figure 167: Evolution of water saturation and permittivity as a function of time in 1D column (example of a drainage-imbibition experiment with 0.5 mm GB)..... 188

Figure 168: Evolution of water saturation and permittivity as a function of time in 1D column (example of a drainage-imbibition experiment with 0.1 mm GB)..... 188

Figure 169: Comparison of measured and estimated permittivity and estimated water saturation as a function of time in 1D column (for 0.5 mm)..... 189

Figure 170: Comparison of measured and estimated permittivity and modeled water saturation as a function of time in 1D column (for 0.1 mm) 189

Figure 171: Change in water saturation and permittivity (measured and estimated) as a function of drainage-imbibition cycle for 0.5 and 0.1 mm GB in 1D cells and 1D columns (without enhancement)..... 190

Figure 172: Measured permittivity/estimated permittivity ratios as a function of drainage-imbibition cycle for 0.5 and 0.1 mm GB in 1D cells and 1D columns (without enhancement)	191
Figure 173: Position of the unpolarizable potential electrodes of 1D column.....	191
Figure 174: Evolution of water saturation and resistivity as a function of time in 1D column (example of a drainage-imbibition experiment with 0.5 mm GB).....	192
Figure 175: Evolution of water saturation and resistivity as a function of time in 1D column (example of a drainage-imbibition experiment with 0.1 mm GB).....	192
Figure 176: Comparison of measured and estimated resistivity and modeled water saturation as a function of time in 1D column (for 0.5 mm)	193
Figure 177: Comparison of measured and estimated resistivity and modeled water saturation as a function of time in 1D column (for 0.1 mm GB).....	193
Figure 178: Change in water saturation and resistivity (measured and estimated) as a function of drainage-imbibition cycle for 0.5 and 0.1 mm GB in 1D cells and 1D columns (without enhancement)	194
Figure 179: Measured resistivity/estimated resistivity ratios as a function of drainage-imbibition cycle for 0.5 and 0.1 mm GB in 1D cells and 1D columns (without enhancement)	195
Figure 180: Change in water saturation as a function of drainage-imbibition cycle for 0.5 and 0.1 mm GB in 1D cells and 1D columns (with and without chemical enhancement)	196
Figure 181: Comparison of drainage-imbibition experiments for a) 0.5 and b) 0.1 mm GB with chemical enhancement (DNAPL modeled volume vs DNAPL measured volume)	196
Figure 182: Evolution of water saturation and permittivity as a function of time in 1D column with chemical enhancement (example of drainage-imbibition experiments with a) 0.5 mm GB and b) 0.1 mm GB).....	197
Figure 183: Change in water saturation and permittivity (measured and estimated) as a function of drainage-imbibition cycle for 0.5 and 0.1 mm GB in 1D cells and 1D columns (with and without chemical enhancement).....	197
Figure 184: Measured permittivity/estimated permittivity ratios as a function of drainage-imbibition cycle for 0.5 and 0.1 mm GB in 1D cells and 1D columns (with and without chemical enhancement)	198
Figure 185: Evolution of water saturation and resistivity as a function of time in 1D column with chemical enhancement (example of drainage-imbibition experiments with a) 0.5 mm GB and b) 0.1 mm GB).....	199
Figure 186: Change in water saturation and resistivity (measured and estimated) as a function of drainage-imbibition cycle for 0.5 and 0.1 mm GB in 1D cells and 1D columns (with and without chemical enhancement).....	199
Figure 187: Measured resistivity/estimated resistivity ratios as a function of drainage-imbibition cycle for 0.5 and 0.1 mm GB in 1D cells and 1D columns (with and without chemical enhancement)	200
Figure 188: Change in water saturation as a function of drainage-imbibition cycle for 0.5 and 0.1 mm GB in 1D cells and 1D columns (with and without thermal enhancement)	201
Figure 189: Comparison of drainage-imbibition experiments for a) 0.5 and b) 0.1 mm GB with thermal enhancement (DNAPL modeled volume vs DNAPL measured volume)	201

Figure 190: Evolution of water saturation and permittivity as a function of time in 1D column with thermal enhancement (example of drainage-imbibition experiments with a) 0.5 mm GB and b) 0.1 mm GB).....	202
Figure 191: Change in water saturation and permittivity (measured and estimated) as a function of drainage-imbibition cycle for 0.5 and 0.1 mm GB in 1D cells and 1D columns (with and without thermal enhancement).....	203
Figure 192: Measured permittivity/estimated permittivity ratios as a function of drainage-imbibition cycle for 0.5 and 0.1 mm GB in 1D cells and 1D columns (with and without thermal enhancement)	204
Figure 193: Evolution of water saturation and resistivity as a function of time in 1D column with thermal enhancement (example of drainage-imbibition experiments with a) 0.5 mm GB and b) 0.1 mm GB).....	204
Figure 194: Change in water saturation and resistivity (measured and estimated) as a function of drainage-imbibition cycle for 0.5 and 0.1 mm GB in 1D cells and 1D columns (with and without thermal enhancement)	205
Figure 195: Measured resistivity/estimated resistivity ratios as a function of drainage-imbibition cycle for 0.5 and 0.1 mm GB in 1D cells and 1D columns (with and without thermal enhancement)	206
Figure 196: Photograph of the 2D tank (a) general view, b) counter channel, c) thermo-regulated bath).....	209
Figure 197: Main dimensions of the 2D tank.....	210
Figure 198: Permittivity and resistivity monitoring probes on the back of the 2D tank.....	210
Figure 199: Photograph of the geophysics measurement (TDR and resistivity) tools network on the back of the 2D tank	211
Figure 200: Photograph of the pumping and injection system for the 2D tank	211
Figure 201: Principle of the injection and pumping device for water and DNAPL.....	212
Figure 202: Photograph of the drainage and pumping in the 2D tank	213
Figure 203: Position of TDR probes, unpolarizable potential electrodes and metallic rod current electrodes in the 2D tank.....	213
Figure 204: Position of TDR probes with associated detection zones for DNAPL.....	214
Figure 205: Position of unpolarizable potential and current electrodes with associated estimated detection zones for DNAPL.....	214
Figure 206: Photographical set-up with black and white reflectors.....	215
Figure 207: Scaling and orthogonalization	216
Figure 208: Estimation of the total S_n in the AOI	216
Figure 209: Change in the cone of depression and DNAPL-water interface displacement during pumping test.....	217
Figure 210: DNAPL-water interface and fitting with the Rodbar equation.....	218
Figure 211: Measuring height and radius of the cone of depression	218
Figure 212: Estimation of S_n in the cone of depression	218
Figure 213: Comparison of the estimated and measured DNAPL-water interfaces with the Rodbar equation (a) actual shape and b) flattened shape).....	219
Figure 214: Mesh scale and geometry of the 2D tank.....	220
Figure 215: Boundary conditions for imbibition in the 2D tank.....	221

Figure 216: Water saturation modeling over time during DNAPL pumping with 0.5 and 0.1 mm GB (without enhancement)	222
Figure 217: Evolution of measured and modeled volumes of DNAPL recovered for different flow rates with 0.5 and 0.1 mm GB (without enhancement)	222
Figure 218: Evolution of the S_w along a) and b) horizontal profile and c) and d) vertical profile at the center of the 2D tank with 0.5 and 0.1 mm GB (without enhancement)	223
Figure 219: Comparison of measured and modeled volumes of the DNAPL recovered in the 2D tank with 0.5 and 0.1 mm GB (without enhancement)	224
Figure 220: Comparison of measured and modeled DNAPL-water interface in the 2D tank at different times with a) and b) 0.5 mm GB and c) and d) 0.1 mm GB (without enhancement)	224
Figure 221: Comparison of measured and modeled a) radius and b) height of the cone of depression with 0.5 and 0.1 mm GB (without enhancement)	225
Figure 222: Darcy velocity fields for a) and b) wetting and c) and d) non-wetting fluids for 0.5 mm GB with a flow rate of $150 \text{ mL}\cdot\text{min}^{-1}$ (without enhancement).....	226
Figure 223: Evolution of the modeled $V_{\text{DNAPL pumped}}/V_{\text{DNAPL lateral}}$ ratios for different flow rates with a) 0.5 mm GB and b) 0.1 mm GB (without enhancement)	226
Figure 224: Comparison of estimated DNAPL volumes recovered experimentally (with image interpretation) and by modeling (after lateral V_{DNAPL} deduction) with 0.5 and 0.1 mm GB (without enhancement).....	227
Figure 225: DNAPL-water interface flattened (without enhancement).....	227
Figure 226: Statistical representation of fingerings of the DNAPL-water interface with 0.5 and 0.1 mm GB (without enhancement)	228
Figure 227: Parametrical study of the model (without enhancement)	228
Figure 228: Evolution of the permittivity in the 2D tank with 0.5 mm GB with a flow rate of $150 \text{ mL}\cdot\text{min}^{-1}$ (without enhancement)	229
Figure 229: Average water saturation, measured and estimated permittivity during the pumping experiment in the 2D tank with 0.5 mm GB with a flow rate of $150 \text{ mL}\cdot\text{min}^{-1}$ (without enhancement).....	230
Figure 230: Evolution of the permittivity in the 2D tank with 0.1 mm GB with a flow rate of $150 \text{ mL}\cdot\text{min}^{-1}$ (without enhancement)	231
Figure 231: Average water saturation, measured and estimated permittivity during the pumping experiment in the 2D tank with 0.1 mm GB with a flow rate of $150 \text{ mL}\cdot\text{min}^{-1}$ (without enhancement).....	231
Figure 232: Comparison of measured and estimated permittivity (with image interpretation) in the 2D tank for a) 0.5 and b) 0.1 mm GB (without enhancement).....	232
Figure 233: Surface plot of measured permittivity within an image with 0.5 mm GB with a flow rate of $150 \text{ mL}\cdot\text{min}^{-1}$ (without enhancement) at $t = 18 \text{ min}$	232
Figure 234: Evolution of the resistivity in the 2D tank with 0.5 mm GB with a flow rate of $150 \text{ mL}\cdot\text{min}^{-1}$ (without enhancement) – a) R1 to R20 and b) R21 to R47.....	233
Figure 235: Average water saturation, measured and estimated resistivity during the pumping experiment in the 2D tank with 0.5 mm GB with a flow rate of $150 \text{ mL}\cdot\text{min}^{-1}$ (without enhancement) – a) R1 to R20 and b) R21 to R47	234

Figure 236: Evolution of the resistivity in the 2D tank with 0.1 mm GB with a flow rate of 150 mL.min ⁻¹ (without enhancement) – a) R1 to R20 and b) R21 to R47	235
Figure 237: Average water saturation, measured and estimated resistivity during the pumping experiment in the 2D tank with 0.1 mm GB with a flow rate of 150 mL.min ⁻¹ (without enhancement) – a) R1 to R20 and b) R21 to R47	236
Figure 238: Comparison of measured and estimated resistivity (with image interpretation) in the 2D tank for a) 0.5 and b) 0.1 mm GB with a flow rate of 150 mL.min ⁻¹ (without enhancement)	237
Figure 239: Comparison of measured and estimated resistivity (with image interpretation) in the 2D tank with a flow rate of 150 mL.min ⁻¹ for a) 0.5 mm GB-rectangular detection areas, b) 0.5 mm GB-square detection areas, c) 0.1 mm GB-rectangular detection areas, d) 0.1 mm GB-square detection areas (without enhancement).....	238
Figure 240: Surface plot of measured resistivity with an image with 0.5 mm GB with a flow rate of 150 mL.min ⁻¹ (without enhancement) at t = 18 min	239
Figure 241: Evolution of measured and modeled volumes of DNAPL recovered for different flow rates with 0.5 mm GB (with chemical enhancement).....	239
Figure 242: Evolution of measured and modeled volumes of DNAPL recovered for different flow rates with 0.1 mm GB (with chemical enhancement).....	240
Figure 243: Modeled $V_{\text{DNAPL, chemical}}/V_{\text{DNAPL, reference}}$ ratios as a function of time with 0.5 and 0.1 mm GB	240
Figure 244: Evolution of the S_w along a) and b) horizontal profile and c) and d) vertical profile at the center of the 2D tank with 0.5 and 0.1 mm GB (with chemical enhancement)	241
Figure 245: Comparison of measured and modeled volumes of the DNAPL recovered in the 2D tank with 0.5 and 0.1 mm GB (with chemical enhancement)	242
Figure 246: Comparison of measured and modeled a) radius and b) height of the cone of depression with 0.5 and 0.1 mm GB (with chemical enhancement).....	242
Figure 247: Comparison of estimated DNAPL volumes recovered experimentally (with image interpretation) and by modeling (after lateral V_{DNAPL} deduction) with 0.5 and 0.1 mm GB (with chemical enhancement).....	243
Figure 248: Statistical representation of fingerings of the DNAPL-water interface with 0.5 and 0.1 mm GB (with chemical enhancement).....	243
Figure 249: Evolution of the permittivity in the 2D tank with 0.5 mm GB with a flow rate of 150 mL.min ⁻¹ (with chemical enhancement).....	244
Figure 250: Average water saturation, measured and estimated permittivity during the pumping experiment in the 2D tank with 0.5 mm GB with a flow rate of 150 mL.min ⁻¹ (with chemical enhancement)	244
Figure 251: Evolution of the permittivity in the 2D tank with 0.1 mm GB with a flow rate of 150 mL.min ⁻¹ (with chemical enhancement).....	245
Figure 252: Average water saturation, measured and estimated permittivity during the pumping experiment in the 2D tank with 0.1 mm GB with a flow rate of 150 mL.min ⁻¹ (with chemical enhancement)	245
Figure 253: Comparison of measured and estimated permittivity (with image interpretation) in the 2D tank for a) 0.5 and b) 0.1 mm GB (with chemical enhancement)	246

Figure 254: Evolution of the resistivity in the 2D tank with 0.5 mm GB with a flow rate of 150 mL.min⁻¹ (with chemical enhancement) – a) R1 to R20 and b) R21 to R47 246

Figure 255: Average water saturation, measured and estimated resistivity during the pumping experiment in the 2D tank with 0.5 mm GB with a flow rate of 150 mL.min⁻¹ (with chemical enhancement) – a) R1 to R20 and b) R21 to R47 247

Figure 256: Evolution of the resistivity in the 2D tank with 0.1 mm GB with a flow rate of 150 mL.min⁻¹ (with chemical enhancement) – a) R1 to R20 and b) R21 to R47 248

Figure 257: Average water saturation, measured and estimated resistivity during the pumping experiment in the 2D tank with 0.1 mm GB with a flow rate of 150 mL.min⁻¹ (with chemical enhancement) – a) R1 to R20 and b) R21 to R47 248

Figure 258: Comparison of measured and estimated resistivity (with image interpretation) in the 2D tank for a) 0.5 and b) 0.1 mm GB with a flow rate of 150 mL.min⁻¹ (with chemical enhancement) 249

Figure 259: Evolution of measured and modeled volumes of DNAPL recovered for different flow rates with 0.5 mm GB (with thermal enhancement) 250

Figure 260: Evolution of measured and modeled volumes of DNAPL recovered for different flow rates with 0.1 mm GB (with thermal enhancement) 250

Figure 261: Evolution of the S_w along a) and b) horizontal profile and c) and d) vertical profile at the center of the 2D tank with 0.5 and 0.1 mm GB (with thermal enhancement) .. 251

Figure 262: Comparison of measured and modeled volumes of the DNAPL recovered in the 2D tank with 0.5 and 0.1 mm GB (with thermal enhancement) 252

Figure 263: Comparison of measured and modeled a) radius and b) height of the cone of depression with 0.5 and 0.1 mm GB (with thermal enhancement) 252

Figure 264: Comparison of estimated DNAPL volumes recovered experimentally (with image interpretation) and by modeling (after lateral V_{DNAPL} deduction) with 0.5 and 0.1 mm GB (with thermal enhancement)..... 253

Figure 265: Statistical representation of fingerings of the DNAPL-water interface with 0.5 and 0.1 mm GB (with thermal enhancement) 253

Figure 266: Parametric study of the model (with thermal enhancement): a) V_{DNAPL} recovered as a function of time and b) Final V_{DNAPL} at t= 30 min 254

Figure 267: Evolution of the permittivity in the 2D tank with 0.5 mm GB with a flow rate of 150 mL.min⁻¹ (with thermal enhancement)..... 255

Figure 268: Average water saturation, measured and estimated permittivity during the pumping experiment in the 2D tank with 0.5 mm GB with a flow rate of 150 mL.min⁻¹ (with thermal enhancement) 255

Figure 269: Evolution of the permittivity in the 2D tank with 0.1 mm GB with a flow rate of 150 mL.min⁻¹ (with thermal enhancement)..... 256

Figure 270: Average water saturation, measured and estimated permittivity during the pumping experiment in the 2D tank with 0.1 mm GB with a flow rate of 150 mL.min⁻¹ (with thermal enhancement) 256

Figure 271: Comparison of measured and estimated permittivity (with image interpretation) in the 2D tank for a) 0.5 and b) 0.1 mm GB (with thermal enhancement)..... 257

Figure 272: Evolution of the resistivity in the 2D tank with 0.5 mm GB with a flow rate of 150 mL.min⁻¹ (with thermal enhancement) – a) R1 to R20 and b) R21 to R47..... 257

Figure 273: Average water saturation, resistivity measured and estimated during the pumping experiment in the 2D tank with 0.5 mm GB with a flow rate of 150 mL.min⁻¹ (with thermal enhancement) – a) R1 to R20 and b) R21 to R47 258

Figure 274: Evolution of the resistivity in the 2D tank with 0.1 mm GB with a flow rate of 150 mL.min⁻¹ (with thermal enhancement) – a) R1 to R20 and b) R21 to R47..... 258

Figure 275: Average water saturation, resistivity measured and estimated during the pumping experiment in the 2D tank with 0.1 mm GB with a flow rate of 150 mL.min⁻¹ (with thermal enhancement) – a) R1 to R20 and b) R21 to R47 259

Figure 276: Comparison of measured and estimated resistivity (with image interpretation) in the 2D tank for a) 0.5 and b) 0.1 mm GB with a flow rate of 150 mL.min⁻¹ (with thermal enhancement) 260

Figure 277: Comparison of measured permittivity in the 2D tank for 0.5 mm GB with a flow rate of 150 mL.min⁻¹ (with and without enhancements) 260

Figure 278: Comparison of measured permittivity in the 2D tank for 0.1 mm GB with a flow rate of 150 mL.min⁻¹ (with and without enhancements) 261

Figure 279: Comparison of measured resistivity in the 2D tank for 0.5 mm GB with a flow rate of 150 mL.min⁻¹ (with and without enhancements) 261

Figure 280: Comparison of measured resistivity in the 2D tank for 0.1 mm GB with a flow rate of 150 mL.min⁻¹ (with and without enhancements) 262

Figure 281: Representation of experimental results on the phase-diagram of multiphase domain displacement (adapted from [Lenormand *et al.* (1988)]) 262

Figure 282: Total financial estimate and unit costs of DNAPL free product recovery (with and without chemical enhancement) [Colombano *et al.* (2018)]..... 263

List of Appendices

Appendix 1 Characterization of the DNAPL without enhancement and with chemical/thermal enhancements A-1

Appendix 2 1D cells experiments without enhancement A-22

Appendix 3 1D cells experiments with chemical enhancement..... A-55

Appendix 4 1D cells experiments with thermal enhancement A-75

Appendix 5 1D columns experiments without enhancement..... A-82

Appendix 6 1D columns experiments with chemical enhancement A-90

Appendix 7 1D columns experiments with thermal enhancement..... A-96

Appendix 8 2D tank experiments without enhancement..... A-99

Appendix 9 2D tank experiments with chemical enhancement A-109

Appendix 10 2D tank experiments with thermal enhancement A-119

Notation

Symbols	Descriptions	Units
A	Coefficient of amplitude	Torr.s ⁻¹
a	Empirical parameter for Archie's law	-
a _a	Distance of the electrodes for the geometrical coefficient (apparent electrical resistivity)	m
A _c	Cross sectional area for the determination of $\rho_{\text{eff,c}}$	m ²
a _c	Empirical parameter for Archie's law	-
A _t	Total cross-sectional area of drained pores at negative pressure head for LTM without calibration procedure	m ²
A _{t,T}	Total cross-sectional area of all effective pores for LTM without calibration procedure	m ²
a ⁿ	Specific interfacial area between the non-wetting phase and the wetting phase	m ² .m ⁻³
B	Magnetic induction	T
b _l	Path length	cm
b _μ	Empirical constant for viscosity determination	-
C	Dissolved phase concentration	mg.L ⁻¹
C _g	Coefficient of soil gradation (particle diameter)	-
C _i	Concentration of each component in the mixtures	mg.L ⁻¹
C _{i,s}	Concentration of compound i in the solid phase	mg.kg ⁻¹
C _{i,w}	Concentration of compound i in the aqueous phase	mg.kg ⁻¹
C _{io}	Ion concentration	mol.m ⁻³
C _o	Molar concentration of the solubilized organic	mol.L ⁻¹
C _{o,sol}	Aqueous solubility of the organic	mol.L ⁻¹
C _s	Effective solubility	mg.L ⁻¹
C _{sc}	Storage coefficient	-
C _{surf}	Total molar concentration of the surfactant added	mol.L ⁻¹
C _{surf,CMC}	Molar concentration of the surfactant at the CMC	mol.L ⁻¹
C _u	Uniformity coefficient (particle diameter)	-
C _w	Concentration of dissolved substance	mole.m ⁻³
c _ε	Speed of light (velocity of electromagnetic waves) in vacuum	m.s ⁻¹
C _μ	Empirical constant for viscosity determination	-
D	Mass diffusivity	m ² .s ⁻¹
D _c	Capillary diffusion coefficient	-
D _e	Electric displacement field	C.m ⁻²
D _{i_l}	Average optical densities	-
d _{ji}	Optical density of the individual pixels	-
D _{i_l} ^o	Average optical densities for each pixel contained in the images of air-NAPL two fluid phase systems	-
D _{i_l} ^{ow}	Average optical densities contained in the image of air-water-NAPL three fluid system at i _l wavelength	-
D _{i_l} ^w	Average optical densities for each pixel contained in the images of air-water two fluid phase systems	-

Symbols	Descriptions	Units
$\begin{bmatrix} D_{i_l} \\ D_{j_l} \end{bmatrix}_{m_l n_l}$	Optical density on the mesh elements measured in both wavelength	-
$D_{k_l}^{ow}$	Average optical densities contained in the image of air-water-NAPL three fluid system at k_l wavelength	-
D_M	Diameter of a “medium” sand grain assumed as 0.05 cm	m
$D_m^{k,\alpha}$	Tensor of mechanical dispersion of component k from α phase	-
$D_o^{k,\alpha}$	Free molecular diffusion coefficient of component k from α phase	$m.s^{-2}$
D_p	Particle diameter	m
D_r	Optical density of reflected light	-
D_t	Optical density of transmitted light	-
$[D^{00}]$	Optical density for the dry sand	-
$[D^{10}]$	Optical density for the water-saturated sand	-
$[D^{01}]$	Optical density for the NAPL-saturated sand	-
D_{10}, D_{50}, D_{60}	Particle diameter such that 10%, 50%, or 60% of porous media are finer by weight	m
E_a	Energy of activation	eV
E_c	Electric field strength	$V.m^{-1}$
E_k^α	Source of k to the α phase over biotic and abiotic transformations	$kg.m^{-3}.s^{-1}$
E_μ	Empirical constant for viscosity determination	-
F	Faraday constant	$C.mol^{-1}$
f	Frequency	Hz
$F_n(x)$	Normal pore-radius distribution function (LNM)	-
F_c	Formation factor for Archie’s law	-
f_{oc}	Fraction of organic carbon in the porous medium	-
f_w	Fractional flow function of phase w	-
g	Gravitational acceleration	$m.s^{-2}$
h	Hydraulic head	m
h_c	Capillary pressure head	m
h_e	Non-wetting fluid entry pressure (m)	m
h_m	Related to the median of soil pore radius distribution function by the capillary pressure function (LNM)	m
H_{mf}	Magnetic field	$A.m^{-1}$
H_{oc}	Changes in enthalpy of phase change for sorption of the chemical to organic carbon from water	$J.mol^{-1}$
h_{pn}	Height of DNAPL from the filter at the bottom of the 1D column	m
h_{pw}	Height of water from the filter at the bottom of the 1D column	m
HS_{oc}	change of entropy of phase change for sorption of the chemical to organic carbon from water	$J.mol^{-1}.K^{-1}$
H_u	Hue, color appearance parameters	°
h_{wc}	Depth of the cone of depression of water	m
I_e	Electrical current intensity	A

Symbols	Descriptions	Units
I_{jl}^r	Intensity of the reflected light given by the individual pixel values	-
I_{jl}^0	Intensity of the light that would be reflected by an ideal white surface	-
I_k^α	Transfer of component k by phase change and diffusion throughout the α phase boundaries	$\text{kg.m}^{-3}.\text{s}^{-1}$
i_l	Wavelength	nm
I_r	Reflected luminous intensity	-
I_t	Transmitted luminous intensity	-
$I_{t,in}$	Incident light intensity	-
$I_{t,out}$	Emergent light intensity	-
$I_{t,out,S}$	Light intensity transmitted through a saturated sand	-
I_{t,out,S_w}	Light intensity transmitted at a residual saturated sand	-
I_v	Intensity of transmitted light	-
I_{vd}	Emergent light intensity for the dry sample	-
I_{vn}	Normalized light intensity for light transmitted methods	-
I_{vs}	Emergent light intensity for the saturated sample	-
I_0	Initial luminous intensity	-
J	Solute mass flux dissolution from non-wetting phase to wetting phase	$\text{mg.L}^{-1}.\text{s}^{-1}$
J_c	Conduction current density	A.m^{-2}
J_d	Displacement current density	A.m^{-2}
J_e	Total current density	A.m^{-2}
$J_{k,x}^\alpha$	Diffusive flux of component k from α phase in the x direction	$\text{kg.m}^{-2}.\text{s}^{-1}$
j_l	Wavelength	nm
j_l	Sum index for a given spectral band i	-
K	Hydraulic conductivity	m.s^{-1}
k	Intrinsic permeability	m^2
K_a	Geometrical coefficient for apparent electrical resistivity	-
k_B	Boltzmann constant	eV.K^{-1}
K_c	Mass transfer coefficient	m.s^{-1}
k_c	Reaction rate	s^{-1}
K_d	Adsorption-desorption distribution	mL.g^{-1}
K_e	Equilibrium constant (for solubility in water)	-
k_{en}	Effective permeability of the non-wetting phase	m^2
k_{ew}	Effective permeability of the wetting phase	m^2
K_H	Henry's constant	$\text{atm.m}^3.\text{mole}^{-1}$
k_{ij}	Tensor of intrinsic permeability	m^2
K_l	Lumped mass transfer term	s^{-1}
k_l	Wavelength	nm
k_{la}	Average mass transfer coefficient for the non-wetting phase / wetting phase interface	m.s^{-1}
$K_{oc,i}$	Organic carbon partitioning coefficient for compound i	L.kg^{-1}
k_r	Relative permeability	-
k_{rn}	Relative permeability of the non-wetting phase	-
$k_{r,\alpha}$	Relative permeability of each α phase	-

Symbols	Descriptions	Units
k_{rw}	Relative permeability of the wetting phase	-
k_t	Empirical parameter for light transmitted methods	-
k_{1r}	Relative permeability for the displaced phase	-
k_{2r}	Relative permeability for the displacing phase	-
L	Length of the capillary	m
l	Characteristic length	m
L_c	Length of the cylinder for the determination of $\rho_{eff,c}$	m
L_p	Stable pool length	m
L_ϵ	Waveguide length	m
m	Fitting parameter depending on the width of pore-size distribution (VGM and VGB)	-
m_c	Cementing factor for Archie's law	-
M_l	Molar absorptivity or molar absorption coefficient, number of moles per liter of absorbing solution	mol.L ⁻¹
m_l	Vertical dimension of the matrix	m
m_r	Mobility ratio	-
MWH	Molecular weight of the nonionic surfactant's hydrophilic groups	g.mol ⁻¹
MWL	Molecular weight of the nonionic surfactant's lipophilic groups	g.mol ⁻¹
n	Width of pore-size distribution (VGM and VGB)	-
N	Number of pixels contained in the Area Of Interest	-
n_a	Distance of the electrodes for the geometrical coefficient (apparent electrical resistivity)	m
n_i	Ion charge	-
n^{ERT}	Saturation exponent (Archie's law)	(-)
n_l	Horizontal dimensions of the matrix	m
n_t	Ratio of refractive indices	-
$n_{t,1}$	Refractive indice of the two media constituting the diopter	-
$n_{t,2}$	Refractive indice of the two media constituting the diopter	-
n_μ	Number of the components in the mixtures for viscosity determination	-
P	Pressure of the liquid	Pa
P_c	Capillary pressure	Pa
$P_c(L_p)$	Capillary pressure at the down dip end of the pool	Pa
P_c^{ref}	Reference capillary pressure at the reference temperature, T_{ref}	Pa
P_c^T	Capillary pressure at a given temperature T	Pa
$P_c(0)$	Capillary pressure at the up dip end of the pool	Pa
P_e	Measured entry pressure of the investigated porous media	Pa
P_e^{dim}	Dimensionless entry pressure (measured in a different porous medium)	-
P_n	Pressure of non-wetting phase	Pa
P_t	Number of pores filled with water	-
P_s	Global pressure	Pa

Symbols	Descriptions	Units
P_v	Pressure of the vapor pressure of a dissolved substance in water	atm
P_{vi}	Vapor pressure of component i in the mixing system	Pa
P_{vi}^*	Pure vapor pressure of the component i	Pa
P_{vt}	Total vapor pressure in the mixing system	Pa
P_w	Pressure of wetting phase	Pa
P_z	Medium polarization (dipolar moment per unit volume)	$C.m^{-2}$
P_α	Pressure of each α phase	Pa
Q	Flow rate	$m^3.s^{-1}$
q_n	Mass source of the non-wetting phase	$kg.m^{-3}.s^{-1}$
q_{pc}	Capillary mass source	$kg.m^{-3}.s^{-1}$
q_{ps}	Global mass source	$kg.m^{-3}.s^{-1}$
q_w	Mass source of the wetting phase	$kg.m^{-3}.s^{-1}$
q_α	Mass source of the α phase	$kg.m^{-3}.s^{-1}$
R	Ideal gas constant	$J.mol^{-1}.K^{-1}$
r	Mean radius of wetting fluid/non-wetting fluid interface	m
r_c	Radius of an electrical equipotentials hemispherical sphere (current density)	m
R_e	Electrical resistance	Ω
$r_{P,max}$	Maximum radius of membrane pores	m
r_{tube}	Radius of the capillary	m
S_a	Air saturation	-
S_{ei}	Effective solubility of the component i in the mixture	$mg.L^{-1}$
S_{ew}	Effective saturation of water saturation	-
S_i	Solubility of compound i	$mg.L^{-1}$
S_n	DNAPL (non-wetting fluid) saturation	-
S_{n_i}	Initial nonaqueous phase saturation	-
S_{rn}	Residual DNAPL (non-wetting fluid) saturation	-
S_{rw}	Residual water (wetting fluid) saturation	-
S_w	Water (wetting fluid) saturation	-
S_α	Saturation of phase α	-
T	Temperature	$^{\circ}C$
T_K	Temperature	K
t_ϵ	Travel time for the pulse to traverse the length of the embedded waveguide	s
v	Darcy velocity of fluid	$m.s^{-1}$
V_e	Electrical potential	V
v_i	Volume of the i phase	-
V_n	Volume of DNAPL	m^3
V_T	Total volume of material	m^3
V_V	Volume of void-space	m^3
v_w	Darcy velocity of the wetting fluid	$m.s^{-1}$
$v_{\alpha,x}$	Darcy velocity of phase α in the x direction	$m.s^{-1}$
u	Velocity of the fluid	$m.s^{-1}$
W	Molecular weight	$kg.mol^{-1}$
X_i	Mole fraction of component i in the mixture	-

Symbols	Descriptions	Units
$(X_i)_{org}$	Mole fraction of organic phases of each component in the mixtures	-
z	Direction of gravity	-
z_1	Distance from the column inlet	m
z_n	Distance from the water table to the DNAPL-water interface	m

Greek symbols

Symbols	Descriptions	Units
α	Fitting parameter inversely proportional to the non-wetting fluid entry pressure value (VGM and VGB)	m^{-1}
α_g	Fitting parameter inversely proportional to the non-wetting fluid entry pressure value (GDM)	m^{-1}
α_{N_T}	Angle between the direction of system flow and the horizontal direction (for N_T determination)	$^{\circ}$
α_p	Dip of the bedding below horizontal	$^{\circ}$
α_{P_e}	Empirical constant for P_e determination	-
α_t	Thermal diffusivity	$m^2.s^{-1}$
$\alpha_{c,w}$	Temperature coefficient of resistivity	$^{\circ}C^{-1}$
α_{ε}	Empirical constant related to the geometry of the grains and their spatial distribution (for relative effective permittivity)	-
α_{μ}	Empirical constant for viscosity determination	-
α'_{μ}	Empirical constant for viscosity determination	-
β	Ratio of interfacial tensions between different liquids	-
β_b	Fitting parameter proportional to the non-wetting fluid entry pressure value (BRB)	m
$\beta_{i_1}^o$	Fitting coefficients of the linear regressions for average optical densities (for DNAPL)	-
$\beta_{i_1}^w$	Fitting coefficients of the linear regressions for average optical densities (for water)	-
β_L	Fitting coefficients related to the mass transfer correlations (Lumped domain)	-
β_p	Pore shape parameter	-
β_{P_c}	Fitting parameter related to the temperature dependency of interfacial tension and contact angle	-
β_{ε}	Fitting parameter for the determination of ε_{s-w-n}	-
Υ	Constant depending on the green and blue intensity	-
γ_b	Fitting parameter characterizing the pore-size distribution (BRB)	-
$(\gamma_i)_{org}$	Activity coefficients in organic phases of each component in the mixtures	-
$\varepsilon_r = \varepsilon$	Relative effective permittivity	-
ε_{air}	Relative effective permittivity of air	-
$\varepsilon_{air\ theoretical}$	Relative effective permittivity of pure air	-
ε_n	Relative effective permittivity of NAPL	-
ε_s	Relative effective permittivity of soil particles	-
ε_{s-n}	Relative effective permittivity of the soil-NAPL mixture	-
ε_{s-w}	Relative effective permittivity of the soil-water mixture	-
ε_{s-w-n}	Relative effective permittivity of the soil-water-NAPL mixture	-
ε_w	Relative effective permittivity of water	-
$\varepsilon_{water\ theoretical}$	Relative effective permittivity of pure water	-

Symbols	Descriptions	Units
ϵ_i	Relative effective permittivity of the i phase	-
ϵ^*	Complex dielectric permittivity	$F.m^{-1}$
ϵ'	Energy transfer by displacement currents, real part of the complex dielectric permittivity ($F.m^{-1}$)	$F.m^{-1}$
ϵ''	Imaginary part of the complex dielectric permittivity (which captures the losses due to conduction and polarization)	$F.m^{-1}$
ϵ_α	Volume fraction of each α phase	-
ϵ_0	Free space permittivity	$F.m^{-1}$
ϵ_l	Numerical constant for luminous intensity	$L.mol^{-1}.cm^{-1}$
η	Fitting parameter (BCM & BCB)	-
θ	Contact angle between the fluids and the solid surface	$^\circ$
$\theta_{HA-EO-M}$	Essential oil/hydro-alcoholic solution/membrane contact angle	$^\circ$
θ_n	Volumetric fraction of the nonaqueous phase	-
θ_{n_i}	Initial volumetric fraction of the nonaqueous phase	-
θ_{rw}	Residual porosity of wetting phase	-
θ_w	Porosity of water	-
θ_{ws}	Porosity of wetting phase	-
λ	Total mobility	$Pa^{-1}.s^{-1}$
λ_B	Fitting parameter characterizing the pore-size distribution (BCM & BCB)	-
λ_c	Capillary mobility	$m^2.Pa^{-1}.s^{-1}$
$\lambda_{i_1}^o$	Slope coefficients determined during calibration for average optical densities (for DNAPL) at i_1 wavelengths	-
$\lambda_{i_1}^w$	Slope coefficients determined during calibration for average optical densities (for water) at i_1 wavelengths	-
$\lambda_{k_1}^o$	Slope coefficients determined during calibration for average optical densities (for DNAPL) at k_1 wavelength	-
$\lambda_{k_1}^w$	Slope coefficients determined during calibration for average optical densities (for water) at k_1 wavelength	-
λ_n	Mobility of the non-wetting phase	$Pa^{-1}.s^{-1}$
λ_t	Mass transfer coefficient per meter	s^{-1}
λ_s	Global mobility	$m^2.Pa^{-1}.s^{-1}$
λ_w	Mobility of the wetting phase	$Pa^{-1}.s^{-1}$
μ	Dynamic viscosity of the fluid	$Pa.s$
μ_i	Dynamic viscosity of each component of the blend	$Pa.s$
μ_{io}	Ion displacement capacity	$m^2.V^{-1}.s^{-1}$
μ_w	Dynamic viscosity of wetting phase	$Pa.s$
μ_α	Dynamic viscosity of each α phase	$Pa.s$
μ_1	Fluid dynamic viscosity for the displaced phase	$Pa.s$
μ_2	Fluid dynamic viscosity for the displacing phase	$Pa.s$
ξ	Molar density	$mol.m^{-3}$
ρ	Density of fluid	$kg.m^{-3}$
$\rho_c = \rho'_{eff,c}$	Real effective electric resistivity	$\Omega.m$
$\rho_{c,bulk}$	Real effective electrical resistivity of the bulk	$\Omega.m$
$\rho_{c,DNAPL}$	Real effective electrical resistivity of the DNAPL	$\Omega.m$

Symbols	Descriptions	Units
$\rho_{c,water}$	Real effective electrical resistivity of the water	$\Omega.m$
$\rho_{c,w}$	Real effective electrical resistivity of the fluid at temperature T	$\Omega.m$
ρ_{c,w_0}	Real effective electrical resistivity of the fluid at temperature T_0	$\Omega.m$
ρ_e	Electric charge density	$C.m^{-2}$
ρ_n	DNAPL (non-wetting phase) density	$kg.m^{-3}$
ρ_0^{ERT}	Initial resistivity (ERT-electrical resistivity tomography) of the water-saturated medium (background resistivity)	$\Omega.m$
ρ_t^{ERT}	Real-time ERT (electrical resistivity tomography) measured resistivity of partially saturated medium ($\Omega.m$)	$\Omega.m$
ρ_t	Ratio of reflected/initial luminous intensity	-
ρ_w	Water (wetting phase) density	$kg.m^{-3}$
ρ_α	Density of each α phase	$kg.m^{-3}$
$\sigma_{nw}=\sigma$	Interfacial tension between the non-wetting phase and wetting phase	$N.m^{-1}$
σ_{aw}	Interfacial tension between the air phase and wetting phase	$N.m^{-1}$
σ_b	Width of soil pore radius distribution function (LNM)	-
$\sigma_c = \sigma'_{c,eff}$	Real effective electrical conductivity	$S.m^{-1}$
σ_c^*	Electrical conductivity	$S.m^{-1}$
σ'_c	Ohmic conductivity	$S.m^{-1}$
σ''_c	Dissipation due to the finite rate of displacement of charge carriers and to the various losses due to dispersion (chemical reactions or heat loss)	$S.m^{-1}$
σ_{H-EO}	Interfacial tension between the essential oil and the hydro-alcoholic solution	$N.m^{-1}$
σ_{ns}	Interfacial tension between the non-wetting phase and the solid surface	$N.m^{-1}$
$\sigma_{c,bulk}$	Real effective electrical conductivity of the bulk	$S.m^{-1}$
$\sigma_{c, DNAPL}$	Real effective electrical conductivity of DNAPL	$S.m^{-1}$
$\sigma_{c,w}$	Real effective electrical conductivity of water	$S.m^{-1}$
σ_{ws}	Interfacial tension between the wetting phase and the solid surface	$N.m^{-1}$
τ	Tortuosity	-
τ_l	Transmittance	-
τ_{sw}	Light transmission factors of sand-water interface	-
τ_{sa}	Light transmission factors of sand-air interface	-
τ_t	Light transmission factor	-
τ_α	Second rank tensor of phase tortuosity coefficients	-
ν	Kinematic viscosity	$m^2.s^{-1}$
ν_ϵ	Function of the propagation velocity	$m.s^{-1}$
ν_i	Kinematic viscosity of each component of the blend	$m^2.s^{-1}$
ν_{io}	Speed of ion I	$m.s^{-1}$
\emptyset	Porosity	-
ω_{cf}	Circular frequency	$rad.s^{-1}$
$\bar{\omega}_k^\alpha$	Mass fraction of component k in α phase (-)	-

Symbols	Descriptions	Units
Ω	Ratio of total cross-sectional area of drained pores at negative pressure head/total cross-sectional area of all effective pores	-

Dimensionless numbers

Gr	Grashof number
HLB	Hydrophilic-Lipophilic Balance
Le	Lewis number
MSR	Molar Solubilization Ratio
N_B	Bond number
N_{ca}	Capillary number
N_T	Total trapping number
Pe	Péclet number
Sc	Schmidt number
Sc_a^i	Aqueous-phase Schmidt number for species i
Sh'	Sherwood number
Sh_a^i	Aqueous-phase Sherwood number for species i
$Sh_a^{i,m}$	Modified aqueous-phase Sherwood number for species i
St	Stanton number
Re	Reynolds number
Re_a	Aqueous-phase Reynolds number
ω_D	Damkohler number

Definition of terms

ACCI	Aromatic Carbon-Chloride Group
ADEME	Agence de l'Environnement et de la Maitrise de l'Energie
AOI	Area Of Interest
BC	Brooks-Corey
BR	Brutseart
BRB	Brutsaert Burdine
BTEX	Monoaromatic compounds (Benzene, Toluene, Ethylbenzene and Xylenes)
BRGM	Bureau de Recherches Géologiques et Minières
CCD	Charge Couple Device
CPER	Contrat de Plan État-Région
CNRS	Centre National de la Recherche Scientifique
CHC	Chlorinated HydroCarbon
COC	Chlorinated Organic Compounds
CVOC	Chlorinated Volatile Organic Compounds
D3E	Direction Eau Environnement Ecotechnologie
DNAPL	Dense Non Aqueous Phase Liquid
EPIC	Etablissement Public à Caractère Industriel et Commercial
GD	Gardner
GDM	Gardner – Mualem
HCB	HexaChloroBenzene
HCBD	HexaChloroButaDiene
HCEa	HexaChloroEthane
IARC	International Agency for Research on Cancer
IFT	InterFacial Tension
LCE	Laboratoire de Chimie de l'Environnement
LD	Lognormal Distribution
LDM	Lognormal Distribution Mualem
LNAPL	Light Non-Aqueous Phase Liquid
LRM	Light Reflected Method
LTM	Light Transmitted Method
MAHYTEC	MAtériaux HYdrogène TEChnologie
MEEM	Ministère de l'Environnement, de l'Énergie et de la Mer
MESR	Ministère de l'Enseignement Supérieur et de la Recherche
MIAM	Multispectral Image Analysis Method
MP	Management Plan
MQA	Media Quality Assessment
MTES	Ministère de la Transition Ecologique et Solidaire
MRI	Magnetic Resonance Imaging
NAPL	Non-Aqueous Phase Liquid
NIEHS	National Institute of Environmental Health Sciences
PAH	Polycyclic Aromatic Hydrocarbons
PCE	PerChloroEthylene
PeCB	PentaChloroBenzene
PITT	Partitioning Interwell Tracer Test
PSO	Projet Stratégique Opérationnel
PVC	PolyVinyl Chloride

PVDF	PolyVinylidene Fluoride
RGB	Red Green Blue
RDI	Research Development and Innovation
REV	Representative Elementary Volume
SDBS	Sodium Dodecyl Benzene Sulfonate
SIAM	Simplified Image Analysis Method
SILPHES	Solutions Innovantes de Lutte contre les Produits Halogénés dans les Eaux Souterraines
SSE	Sum of Squared Errors
TCA	1,1,1-TriChloroethAne
TCM	Carbon tetrachloride
TCE	TriChloroEthylene
TPH	Total Petroleum Hydrocarbons
UNIFAC	Universal Functional Activity Coefficient
UTINAM	Univers Transport Interfaces Nanostructures Atmosphère et environnement Molécules
VOHC	Volatile OrganoHalogen Compounds
VG	van Genuchten
VGM	van Genuchten – Mualem

Remerciements

Tout d'abord, je souhaite remercier le BRGM, mon employeur, et l'ADEME (via le projet SILPHES) pour le financement de cette thèse.

Je voudrais exprimer ma gratitude à mes deux co-directeurs de thèse, Eric D. van Hullebusch, professeur à l'Université Paris Diderot, et Ioannis Ignatiadis, expert scientifique, chef de projet senior au BRGM (HDR), pour la confiance, la liberté et l'aide appréciable qu'ils m'ont accordées. Je suis ravi d'avoir travaillé en leur compagnie.

Les rapporteurs, Marie-Odile Simonnot et Olivier Atteia, les examinateurs, Dominique Guyonnet, Edvina Lamy, Nicolas Fatin-Rouge et Christophe Guimbaud, ainsi que les membres du jury invités, Hossein Davarzani et David Huguenot, me font l'honneur d'évaluer ce travail. Je les en remercie.

Je voudrais aussi remercier mes encadrants de thèse : Hossein Davarzani, chef de projet au BRGM, David Huguenot, Maître de Conférences à l'Université Paris-Est Marne-la-Vallée, et Dominique Guyonnet, Directeur de programme scientifique au BRGM (HDR), pour leur soutien, leurs encouragements et la relecture du manuscrit.

Je tiens à exprimer toute ma reconnaissance à Nathalie Dörfliger et Francis Garrido pour m'avoir accordé un budget afin de réaliser ma thèse sur des fonds propres D3E/3SP (dans le cadre du projet SILPHES). Sans cette aide, cette thèse n'aurait pas été possible. Je tiens à remercier aussi Hubert Leprond, qui m'a permis, lors de ma dernière année de thèse, d'avoir un planning un peu plus allégé.

De manière plus particulière, je tiens à présenter mes plus sincères remerciements à Hossein Davarzani pour son aide indéfectible et continue tout au long de ma thèse. Ses conseils judicieux, notamment pour la modélisation, ont été extrêmement précieux.

Je tiens à remercier grandement Jacques Deparis qui a extrait les données brutes de suivis de résistances et de permittivités et qui m'a aussi promulgué des conseils judicieux pour leurs interprétations.

Fabien Lion, en réalisant une macro, m'a permis d'éviter d'extraire et traiter les images une à une. Je le remercie vivement de m'avoir aidé pour cette automatisation qui m'a fait gagner beaucoup de temps. Je tiens aussi à remercier Stéphane Gaboreau pour les discussions enrichissantes que nous avons eues sur l'interprétation d'images.

Je tiens à remercier Romain Rodrigues, dont son travail sur les mesures de solubilités de produit pur, réalisé dans le cadre de sa thèse au cours du projet SILPHES, m'a été d'une très grande utilité. Un grand merci aussi pour son aide pour la partie expérimentale relative aux solubilités.

Je tiens à adresser mes remerciements à Florence Rouyer (du Laboratoire Navier- UPEM) pour m'avoir permis d'utiliser le tensiomètre de son laboratoire. Sans son aide et ses conseils, les premières mesures de tensions interfaciales et d'angles de contact n'auraient pas été possibles.

Je tiens, par ailleurs, à remercier les collègues qui m'ont encouragé et soutenu de différentes manières au cours de ce projet : Clément Zornig, Philippe Bataillard et Stéphanie Betelu. Un

grand merci aussi à Michaëlle Didier pour sa patience et son aide au quotidien. J'adresse également mes remerciements aux autres collègues de 3SP pour leur sympathie permanente et leur petit mot sur l'évolution de ma thèse.

Mes remerciements vont aussi aux stagiaires et apprentis pour leur contribution au projet SILPHES (dont une partie des résultats expérimentaux a servi à ma thèse). Ils ont contribué, chacun à leur manière, à une partie cette thèse: Benjamin Douche, Sagyn Omirbekov, Damien Jacob, Remy Marchal, Guilong Bao, Cécile Lejars, Anna Barone, Marc Déon, Akzhol Azhimbay, Emilie Nodot et Lynda Cheref. Je tiens aussi à remercier deux thésards de Bioxyval, Nicolas Philippe et Ali Irvani, pour les échanges constructifs. J'adresse également mes remerciements à Pierre Galle qui m'a aidé lors du démarrage de la partie expérimentale de ma thèse.

J'adresse aussi mes remerciements à Karen McMillan Tkaczyk pour sa très précieuse aide en anglais. J'ai grandement apprécié son professionnalisme et ses compétences.

Je tiens à remercier également tous les partenaires du projet SILPHES. Mes remerciements vont à Guillaume Masselot (de l'ADEME) pour son suivi du projet SILPHES dans son ensemble. L'ambiance de ce projet lors des comités de pilotage et sur le terrain était « rafraichissante ». Dans ma carrière, il y aura eu un avant et un après SILPHES tant d'un point de vue humain que professionnel. Vivement les autres projets avec les mêmes partenaires ! Je tiens à remercier plus particulièrement mon ami, David Cazaux, pour son soutien et tous les échanges qui nous avons eu sur ma thèse, SILPHES, les sols pollués et d'autres sujets malicieux. Merci aussi David pour les analyses de la phase dissoute faites à INOVYN. Merci également à Alain Dumestre et Antoine Joubert pour les échanges professionnels, leurs soutiens et leurs espiègleries. Merci enfin à Nicolas Fatin-Rouge, Benoit Paris, Julien Maire et Quentin Giraud pour leurs encouragements et les échanges constructifs.

Mes remerciements vont également à mes amis qui m'ont soutenu et encouragé pendant cette thèse : Xavier, Gaëtan, Mylène, David, Florian, Jérôme, Sabrina, Stéphane, Virginie, Pascal, Gerald, Boris, Pascale, Mickaël, Valérie, Yamina, Sylvain, Marie, Daphnée.

Je tiens à remercier ma famille qui m'a encouragé durant ses années : Anne-Sophie, Jules, Lison, David, Sophie, Elvire, Jean, Marise, Mikaël, Cécile, Louis, Danièle, Pierre-Marcel, Sarah, Anna, Renée, Serge, Françoise, Camille, Julien.

J'adresse une pensée spéciale à ma mère, Claude, qui m'a soutenu tout au long de cette thèse. Merci pour son soutien et tout ce qu'elle a fait pour moi depuis mon enfance.

Un grand merci à Yann, mon frère jumeau (*moun jumeu*), qui a fait plus que me soutenir pendant cette thèse. Il m'a conseillé lors des premières prises de vue au laboratoire. Il m'a également mis en relation avec Stéphane Rivière, photographe professionnel, qui m'a prodigué des cours de photos en lumière artificielle. Sans son aide et son professionnalisme, les prises de vue sans reflet auraient été impossibles. Stéphane et Yann, un grand merci pour votre aide.

Enfin, mes derniers remerciements vont à Claire, mon épouse, qui m'a soutenu tout au long de cette thèse. Son aide, sa bienveillance et ses encouragements m'ont aidé à aller jusqu'au bout de ma thèse.

Acknowledgments

First, I thank BRGM, my employer, and ADEME (in the SILPHES project) for financing this PhD project.

I want to express my gratitude to the two co-Directors of my PhD, Eric D. van Hullebusch, Professor at Université Paris Diderot, and Ioannis Ignatiadis, a scientific expert, Senior Project Leader at BRGM (Dr. Hab.), for their confidence in me and the freedom and considerable help that they have given me. I am delighted to have worked alongside them.

The reporters, Marie-Odile Simonnot and Olivier Atteia, examiners, Dominique Guyonnet, Edvina Lamy, Nicolas Fatin-Rouge and Christophe Guimbaud, and invited members of the jury, Hossein Davarzani and David Huguenot, are honoring me in evaluating my work. Thank you.

I also want to thank my PhD supervisors: Hossein Davarzani, BRGM Project Leader, David Huguenot, Senior Professor at Université Paris-Est Marne-la-Vallée, and Dominique Guyonnet, Director of the Scientific Program at BRGM (Dr. Hab.), for their support and encouragement and for reviewing the manuscript.

I am so thankful to Nathalie Dörfliger and Francis Garrido for having given me a budget to achieve my PhD from the D3E/3SP budget (as part of the SILPHES project). Without this help, this PhD would not have been possible. I also thank Hubert Leprond, who let me have a slightly lighter load during the final year of my PhD.

More particularly, I send my sincere thanks to Hossein Davarzani for his unfailing and continuous help throughout my PhD. His judicious advice, in particular for the modeling, was extremely valuable.

I am so thankful to Jacques Deparis, who extracted the raw data for resistance and permittivity monitoring and who also gave me precious advice about how to interpret them.

Fabien Lion made a macro that meant I did not have to extract and process the images one by one. I thank him deeply for having helped me with this time-saving automation. I also thank Stéphane Gaboreau for our productive discussions on image interpretation.

I thank Romain Rodrigues, whose work on solubility measurements on pure products, done as part of his PhD during the SILPHES project, was very useful to me. I also thank him for his help in the experimental section on solubilities.

I also thank Florence Rouyer (at the Laboratoire Navier-UPEM) for letting me use the tensiometer in her laboratory. Without her help and advice, the first measurements of interfacial tensions and contact angles would not have been possible.

I also thank the colleagues who have encouraged and supported me in different ways during this project: Clément Zornig, Philippe Bataillard and Stéphanie Betelu. Thank you also to Michaëlle Didier for her daily patience and help. I also thank the other 3SP staff for their never-ending sympathy and for asking how my PhD was going.

Thank you also to the interns and apprentices who contributed to the SILPHES project (of which a portion of the experimental results was used for my PhD). They each contributed in their own way to a portion of this PhD: Benjamin Douche, Sagyn Omirbekov, Damien Jacob, Remy Marchal, Guilong Bao, Cécile Lejars, Anna Barone, Marc Déon, Akzhol Azhimbay, Emilie Nodot and Lynda Cheref. Thank you also to the Bioxyval PhD students, Nicolas Philippe and Ali Iravani, for constructive discussions. I thank Pierre Galle, who helped me as I was starting the experimental section of my PhD.

Thank you to Karen McMillan Tkaczyk for her very precious help with English. I greatly appreciated her professionalism and skills.

Thank you to all of the partners in the SILPHES project and to Guillaume Masselot (at ADEME) in particular for his management of the entire SILPHES project. This project's ambiance during steering committee and on the field was refreshing. My career will have been marked by before and after SILPHES from both the professional and personal standpoints. Here's to other projects with the same partners! More specifically I thank my friend, David Cazaux, for his support and all the discussions we have had about my PhD, SILPHES, polluted soils and other mischievous subjects. Thank you also David for the dissolved phase analyses done at INOVYN. Thanks also to Alain Dumestre and Antoine Joubert for professional discussions, support and shenanigans. Finally thank you to Nicolas Fatin-Rouge, Benoit Paris, Julien Maire and Quentin Giraud for their encouragement and constructive discussions.

I also thank my friends who have supported and encouraged me during this PhD: Xavier, Gaëtan, Mylène, David, Florian, Jérôme, Sabrina, Stéphane, Virginie, Pascal, Gerald, Boris, Pascale, Mickaël, Valérie, Yamina, Sylvain, Marie, Daphnée.

Thank you to my family for encouraging me during these years: Anne-Sophie, Jules, Lison, David, Sophie, Elvire, Jean, Marise, Mikaël, Cécile, Louis, Danièle, Pierre-Marcel, Sarah, Anna, Renée, Serge, Françoise, Camille, Julien.

I send a special thought to my mother, Claude, who has supported me all the way through. Thank you for supporting me and for everything you have done for me since my childhood.

Big thanks to my twin brother Yann (*moun jumeu*), who has been more than supportive during this PhD. He advised me during the first photo takes in the laboratory. He also put me in touch with Stéphane Rivière, professional photographer, who gave me photography lessons on artificial light. Without his help and professionalism, photos without reflections would have been impossible. Stéphane and Yann, thank you so much for your help.

Finally, my last thanks go to Claire, my wife, who has supported me throughout this PhD. Her help, caring and encouragement helped me to keep going to the end of this PhD.

Résumé

La pollution des eaux souterraines par des composés organochlorés constitue un problème majeur. En effet, ces polluants, particulièrement toxiques, dégradent durablement les sols et les eaux souterraines. Leur dispersion (par solubilisation et volatilisation) à partir des sources de pollution peut générer des panaches de contamination importants.

La récupération de ces composés sous forme de produit pur (DNAPL) est principalement basée sur les techniques de pompage/traitement. Pour autant, cette technique est lente et ne permet pas de récupérer le DNAPL de manière efficace. Une quantité de DNAPL reste piégée dans le sol sous forme de saturation résiduelle (S_{rn}).

L'objectif de cette thèse est d'améliorer le rendement et la vitesse de récupération du DNAPL en utilisant les soutiens chimiques et thermiques au cours du pompage. L'augmentation de la température vise à diminuer la viscosité du DNAPL (et donc à augmenter sa mobilité) alors que l'ajout de surfactant vise à diminuer les forces capillaires qui piègent le DNAPL. Des expérimentations à l'échelle du laboratoire (basées notamment sur des suivis de permittivités, résistivités électriques et densités optiques) et une modélisation multiphasique ont été réalisées afin de pouvoir quantifier les effets de ces soutiens.

Le chauffage du DNAPL, réalisé jusqu'à 50 °C (afin d'éviter la volatilisation), diminue la viscosité par un facteur 2. L'ajout d'un surfactant, le Sodium Dodecyl Benzene Sulfonate-SDBS, à sa Concentration Micellaire Critique (afin d'éviter la solubilisation du DNAPL) diminue la tension interfaciale par un facteur 12.

Les essais de drainage-imbibition ont été réalisés dans des cellules 1D afin d'obtenir les courbes de rétention du système diphasique (pression capillaire en fonction de la saturation en eau). Les diminutions des S_{rn} obtenues avec le SDBS sont de 28% pour les billes de verre (BV) de 0,5 mm de diamètre et 46% pour les BV de 0,1 mm. Aucune amélioration significative du rendement épuratoire a été obtenue avec le chauffage. Les courbes ont été calées avec le modèle de van Genuchten - Mualem dans le but de fournir les données pour la modélisation.

Les expériences de drainage-imbibition ont été réalisées dans des colonnes 1D pour caractériser les écoulements diphasiques (notamment le déplacement de l'interface DNAPL-eau en fonction des pressions appliquées). Le modèle d'écoulement diphasique a été réalisé avec la formulation de pression-pression (à l'aide de COMSOL Multiphysics®). La modélisation des volumes récupérés et du déplacement de l'interface sont en accord avec les résultats expérimentaux. Les rendements épuratoires avec les soutiens chimiques et thermiques étaient du même ordre de grandeur que pour les cellules 1D.

Des essais de pompage ont été effectués dans un bac 2D à différents débits avec les BV de 0,5 mm et 0,1 mm. Les expériences ont également été réalisées avec et sans soutien. Les modélisations ont été comparées à l'interprétation d'images (basée sur l'étalonnage de la densité optique). Les valeurs expérimentales sont en adéquation avec les valeurs modélisées. Les rapports $V_{DNAPL, chimique} / V_{DNAPL, référence}$ pour des débits lents et élevés, étaient en moyenne respectivement de 2,90 et 1,40 pour les BV de 0,5 mm et, de 1,37 et 1,18 pour les BV de 0,1 mm. Le chauffage n'a aucun effet bénéfique sur la récupération du DNAPL.

Les mesures indirectes des saturations en eau (S_w) pour les expériences 1D ou 2D aboutissent aux résultats suivants: i. les permittivités mesurées sont très proches des valeurs modélisées avec le modèle de CRIM ; ii. les modélisations des résistivités électriques avec la loi d'Archie sont moins probantes ; iii. les densités optiques permettent d'estimer S_w avec précision. A l'échelle terrain, la combinaison des suivis avec la résistivité électrique (qui permet d'avoir une vision intégrative) et la permittivité (qui fournit des données précises mais spatialement limitées), permettrait de mieux quantifier les S_m .

Mots clés : DNAPL, modélisation d'écoulement diphasique, expérimentation, surfactant, composés organochlorés, saturation résiduelle

Abstract

Groundwater pollution by chlorinated organic compounds is a major problem. Actually, these particularly toxic pollutants, permanently degrade soil and groundwater quality. Their dispersion (by solubilization and volatilization) from the pollution source zone can generate large contaminants plumes.

Chlorinated organic compounds are recovered as pure product (Dense Non-Aqueous Phase Liquids-DNAPL) mainly using pump/treat technologies. However, these technologies are time-consuming and do not recover the pure product in an efficient way. A significant amount of DNAPL remains trapped in soil as residual saturation (S_m).

The objective of this PhD project was to enhance DNAPL recovery rate and yield using chemical and thermal enhancements during the pumping process. Temperature increases aimed to reduce the viscosity of DNAPL (and therefore to increase its mobility) while the addition of surfactant aimed to reduce the capillary forces that trap the DNAPL. Experiments at the laboratory scale (based on monitoring of permittivities, electrical resistivities and optical densities) and two-phase flow modeling were performed to quantify the effects of these enhancements.

Heating the DNAPL up to 50 °C (to avoid volatilization) decreases the viscosity by a factor of two. The addition of surfactant, Sodium Dodecyl Benzene Sulfonate-SDBS, at its Critical Micelle Concentration (to prevent DNAPL solubilization) decreases interfacial tensions by a factor of 12.

Drainage-imbibition experiments were carried out in 1D cells to obtain the retention curves of the two-phase system (capillary pressure as a function of water saturation). The decreases of S_m obtained with SDBS were 28% for 0.5 mm glass beads (GB) diameter and 46% for 0.1 mm GB. We reported no significant improvement in the remediation yield with thermal enhancement. The curves were fitted with the van Genuchten – Mualem model to generate data for modeling.

Drainage-imbibition experiments were carried out in 1D columns to characterize two-phase flow (and in particular the displacement of the DNAPL-water interface according to the pressures applied). The two-phase flow model used a pressure-pressure formulation (using COMSOL Multiphysics®). The modeling of recovered volumes and the displacement of the interface agreed with the experimental results. The remediation yields with chemical and thermal enhancements were of the same order of magnitude as those reported in 1D cells.

For 2D tank experiments, pumping was performed at different flow rates with 0.5 mm and 0.1 mm GB. The experiments were also performed with and without enhancement. Models were compared with image interpretation (based on the optical density calibration). Comparing experimental and modeled values shows that the model fitted well with the experiments. The $V_{DNAPL,chemical}/V_{DNAPL,reference}$ ratios were for low and high flow rates on average respectively 2.90 and 1.40 for 0.5 mm GB and 1.37 and 1.18 for 0.1 mm GB. Thermal enhancement had no beneficial effect on DNAPL recovery rate or yield.

Indirect measurements of water saturations (S_w) for 1D or 2D experiments yielded the following results: i. the measured permittivities were very similar to the values modeled with the CRIM model; ii. modeling of electrical resistivities with Archie's Law was less accurate; iii. optical

densities allow accurate S_w estimation. At field scale, the combination of monitoring both electrical resistivities (which provide a global picture) and permittivities (which provide precise but spatially limited data), is expected to provide S_m data.

Keywords: DNAPL, two-phase flow modeling, experimentation, surfactant, chlorinated compounds, residual saturation

A mon père, Marcel

A moun paire, Marcel

*Aurii talamen aimat que sigue encà aquí per partià aquéu moumen embé èu ;
mà tamben per proufità de lu siéu counsèu, de la siéu benevoulença, e de lou siéu umour ;
per proufità de èu.*

1. INTRODUCTION

1. INTRODUCTION

This thesis is part of the SILPHES project, which aims, in particular, to develop and validate new *in situ* remediation technologies.

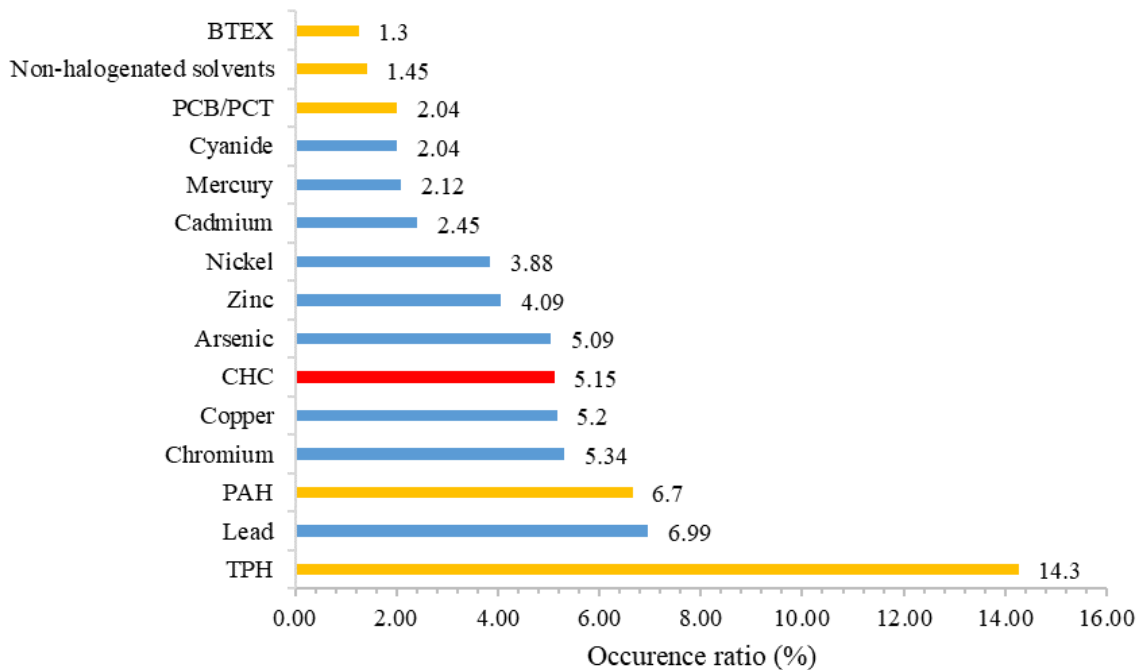
This introduction describes the situation for polluted sites in France and for French public policy for contaminated sites and land management. It moves on to introduce chlorinated compounds in porous media and existing techniques for recovering these compounds.

This chapter concludes with a presentation of the thesis and the SILPHES project.

1.1 Background

1.1.1 Overview on polluted sites in France

Figure 1 shows the main pollutants encountered in polluted sites and soils in France.



BTEX: monoaromatic compounds (benzene, toluene, ethylbenzene and xylene); PCB/PCT: Polychlorinated biphenyls and Polychlorinated terphenyls; CHC: chlorinated hydrocarbon; PAH: Polycyclic aromatic hydrocarbons; TPH: Total petroleum hydrocarbons

Figure 1: Main pollutants encountered in contaminated sites in France [MTES (2018)]

Chlorinated Organic Compounds (COC) represent 5% of the pollution load reported. The total organic pollution load represents 30% of the total pollution load reported. However, because of their toxicity and their potential mobility in different environmental compartments, organic pollutants (including COC) represent a large share of soil remediation market in France.

The Basol database [MTES (2018)] shows that:

- 17% of sites monitored by the French government are contaminated by chlorinated solvents (Volatile OrganoHalogen Compounds - VOHC);
- 31% of groundwater monitoring programs are conducted due to the presence of VOHC;
- 36% of the water resources used for drinking water supply are not exploited due to contamination by VOHC.

1.1.2 French public policy for contaminated sites and land management

In 2007, a national methodology was developed for managing polluted sites and soils. It was revised in 2017 [MEEM (2017a); MEEM (2017b); MEEM (2017c)]. It uses the following principles: precaution, proportionality, specificity, and transparency. In accordance with that methodology, sites are managed on a case by case basis.

The risk assessment approach implemented for a polluted site is based on: i. its uses (occupation type); ii. their fate and transport (pollutant behaviour); iii. the maximum allowable concentrations based on regulatory guideline values, and iv. the human health quantitative risk assessment. To calculate remediation thresholds, this risk analysis is correlated with the natural geochemical background values and the technical-economic feasibility analysis.

The methodology uses the three following tools: a conceptual site model, a media quality assessment, and a management plan.

Conceptual Site Model

The conceptual model establishes a factual summary of the state of the soil at the site to assist in understanding relations between pollution sources, pathways and what is being protected (populations, natural resources, etc.). The conceptual model is based on diagnoses made in different soil compartments (groundwater, soils, gases etc). It is updated according to the results of the diagnoses.

Media Quality Assessment (MQA)

The Media Quality Assessment is based on study of the conceptual model and is carried out when the uses of the site are already fixed, to ensure that the state of the site is compatible with the latter.

The results of the diagnostics are compared with the different maximum allowable concentrations provided by the methodology for the existing situations: regulatory guideline values and human health quantitative risk assessment.

The goal is to distinguish sites that do not need specific action from those where simple action (*i.e.* soil excavation) will be sufficient and those that need a management plan.

Management Plan (MP)

A management plan is established when site uses can be chosen, or when compatibility between the uses determined and the actual current state of the soil cannot be made compatible by simple measures. This is an orientation document studying different scenarios for managing the pollution. It includes definitions of the pollution sources, rehabilitation goals, cost-benefit analyses and financial demonstrations. At least two management scenarios must be shown, validated if necessary by feasibility and processing studies. For scenarios that do not lead to complete elimination of the sources, a residual risk analysis should be included. The

management plan also includes monitoring and testing measures that will be used to ensure that the measures taken during the remediation phase are effective.

Remediation technology is the last step of the methodology. It has two phases: the design plan for the remediation phase and monitoring of the work done to determine the remediation efficiency.

1.1.3 Treatment of LNAPL- and DNAPL-contaminated groundwater in France

ADEME (The French Environmental Protection Agency) has recently published a report indicating the cost and implementation frequency of various remediation techniques [ADEME and Ernst & Young (2014)]. This report is based on a questionnaire sent to soil remediation professionals (research and operations consultancies). *Figure 2* displays the type of pollutants treated in groundwater remediation sites in France in 2012. It also shows that organic compounds, which can be present as LNAPL or DNAPL, represent the majority of the pollution encountered in these sites (53%).

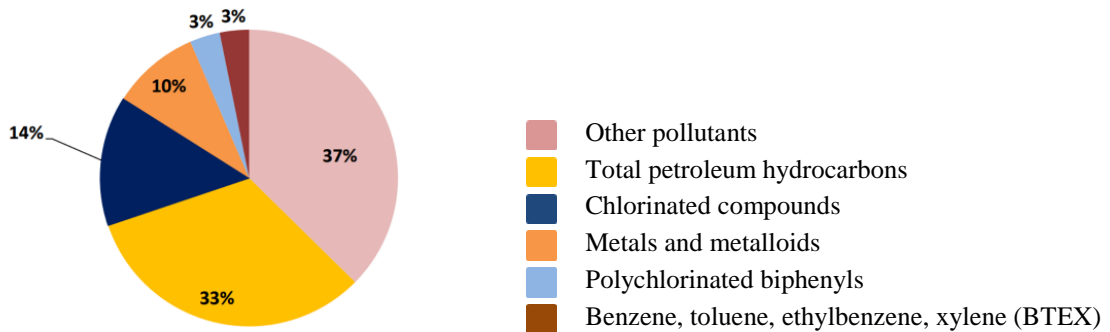


Figure 2: Pollutants treated in 2012 on groundwater remediation sites located in France [ADEME and Ernst & Young (2014)]

This study also reports the different types of groundwater treatment approaches implemented in France in 2012 (Table 1).

Table 1: Classification of main treatment techniques and methods for groundwater remediation by volume treated in 2012 (in m³) – excluding industrial waste [ADEME and Ernst & Young (2014)]

Technique	Type	Volumes (m ³ in place)	Level of use (%)
Pump and treat	On site	1,287,800	49.00
Sparging - Biosparging	<i>In situ</i>	486,800	19.00
Slurping	<i>In situ</i>	327,000	13.00
Free product recovery with skimming	On site	322,200	12.00
Bioaugmentation/Biostimulation	<i>In situ</i>	105,300	4.00
Oxidation/Reduction	<i>In situ</i>	76,000	3.00
Permeable reactive barrier	<i>In situ</i>	1,900	0.07
	Total	2,607,000	

More specifically, Table 2 shows the share of different remediation techniques for the removal TPH and chlorinated compounds.

Table 2: Pollution remediation techniques used for polluted groundwater by total petroleum hydrocarbons and chlorinated compounds (excluding industrial pollution) [ADEME and Ernst & Young (2014)]

Technique	Volumes (m ³ in place)	
	Total petroleum hydrocarbons	Chlorinated compounds
Free product recovery with skimming	273,200	-
Pump and treat	246,300	164,200
Slurping	151,400	83,400
Sparging – Biosparging	132,300	28,700
Bioaugmentation/Biostimulation	37,100	23,800
Oxidation/Reduction	-	68,900

Regarding TPH, we can see that free product recovery with the skimming approach is the most applied technique (33%), ahead of pump and treat and slurping (30 and 18%, respectively). Therefore, the extraction techniques are the most frequent processes for recovering TPH (80%). This is logical because these techniques focus on the recovery of free product, which is the first step of the treatment. With the exception of pump and treat, which deals both with the free product and the dissolved phase, techniques applied to treat less concentrated pollution (on residual saturation or the dissolved phase), represent only 20% of the total treatments market and consist, essentially, of sparging/biosparging treatments.

For chlorinated compounds, extractive techniques (*i.e.* pump and treat and slurping) also represent the majority of treatment techniques implemented (67%). Treatments on the less concentrated phases are mainly handled by chemical techniques (such as oxidation and reduction) (19%). Other techniques (*i.e.* bioaugmentation/biostimulation and sparging/biosparging) represent only 14% of treatments.

Note that a decade ago, chemical treatments that are effective for residual saturation of chlorinated compounds (oxidation/reduction) were much less implemented. Changes in remediation practices occurred because the classic pumping/skimming approach was demonstrated to be technically and economically inefficient (because of the very long treatment duration and very poor remediation yield).

Thermal and chemical enhancements of saturated zones are not (or are rarely) used at full scale for the remediation of areas contaminated with TPH or chlorinated compounds. Feedback from different working groups at the French Ministry of the Environment indicates that most product pumping tests only consist of simple pumping without considering any potential hydraulic enhancement (hydraulic loops, upwelling, etc.). Therefore, there is room for improvement for those willing to implement pumping of pure products at full scale.

Figure 3 shows the remediation costs for groundwater in France in 2012.

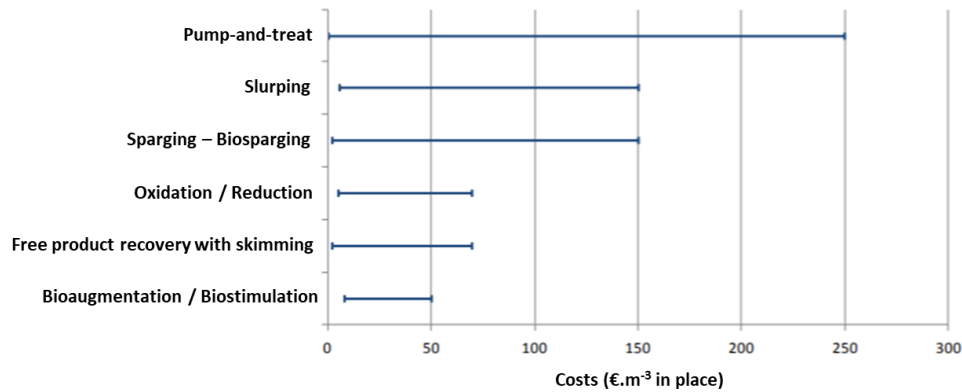


Figure 3: Variability of average costs for treatment techniques of groundwater (€/m³) in France - excluding taxes - in 2012 [ADEME and Ernst & Young (2014)]

There is no fixed cost for a remediation technique. The cost always varies according to site characteristics (hydraulic conductivity, depth of water table, volume, etc.). Generally, cost ranges are very broad for groundwater remediation techniques because they are directly related to the groundwater's characteristics. Therefore, cost analysis must be conservative.

One of the major problems in the field of contaminated sites and soils is the limited accountability regarding the feasibility and treatability tests performed for the selection of the best remediation techniques and the low number of contaminated sites that have detailed multiphase modeling. This means that implementing simple pumping without integrating any enhancements leaves recovery rates and yields as they were, unoptimized.

ADEME has published guidelines on feasibility studies and multiphase modeling [ADEME (2009)]. Also a more recent guide has been published to improve treatability and feasibility (in particular with enhancement techniques) [ADEME *et al.* (2018)]. Moreover, in 2007, the French Ministry of the Environment developed a methodology for managing polluted sites and soils; this was revised in 2017 [MEEM (2017c)]. This methodology highlights the need to perform extensive monitoring, as well as feasibility and treatability tests, before implementing costly remediation full-scale operations [MEEM (2017a); MEEM (2017b)].

Based on field experience feedback, it has become obvious that too many sites have been remediated without necessarily having a clear idea of the extent of the pollution source (in particular, for chlorinated compounds). This leads to inefficient pump and treat operations lasting for years. To deal with this issue, new regulatory guidelines requiring accurate pollution source monitoring are needed. Research and development efforts are currently underway nationally to improve the accuracy of monitoring methodologies at contaminated sites and soils, by considering soil gas monitoring by passive samplers, dynamic extraction tests, phytoscreening, geophysics, and environmental forensics.

Finally, for more than a decade, combined research and development projects (partnerships between remediation companies, polluted site owners and research institutes) have been ongoing to improve and innovate in the field of on-site remediation. These projects are mainly financed by ADEME, the "Agence Nationale de la Recherche" (French National Research Agency), and regional governmental bodies.

1.1.4 NAPL behaviour in porous media

Non-Aqueous Phase Liquids (NAPLs) are liquid organic contaminants that are poorly soluble in water. When present as free products, they move into soils and groundwater as oily liquids. They can be divided into two classes [Mercer and Cohen (1990); Lemièrè *et al.* (2008)]:

- Light NAPLs (LNAPLs) are lighter than water and therefore float on the top of the water table. LNAPLs include various classes of chemical compounds including monoaromatic compounds (such as benzene and toluene), fuels, oils, lubricants, crude oil, and cyclohexane.
- Dense NAPLs (DNAPLs) are heavier than water. If the mass of contaminant is sufficient, DNAPLs sink throughout the saturated zone to accumulate at the bottom of the aquifer where their movement is dictated by gravity and heterogeneity; *e.g.* the topography of the subsurface geological formations (involving layers and fractures characteristics) and groundwater flow direction. DNAPLs include creosotes, chlorinated compounds, polycyclic aromatic hydrocarbons, and coal tar.

These contaminants exist simultaneously in several phases (free product, dissolved phase and gaseous phase). The fundamental NAPL dissolved phase transport mechanisms are the same as those of miscible contaminants (*i.e.* convection, dispersion, diffusion etc.). Thereby, the global transport mechanism depends on the behaviour laws of each phase [Mercer and Cohen (1990); Pankow and Cherry (1996)]. Therefore, this is a particularly complex situation, where NAPL contamination leads to the formation of mixed contaminated phases (water, NAPL, air), each phase has its own physical characteristics (density, viscosity, etc.). Each moving phase conveys the contaminants that can pass from one phase to another (by dissolution, vaporization or condensation) and can interact with the surrounding solid phases (*i.e.* sorption-desorption) [Mercer and Cohen (1990); Cohen and Mercer (1993); Huling and Weaver (1996)].

The contaminant bulk forms a liquid phase distinct from water phase; NAPL fraction may be soluble and can dissolve in water (two-phase NAPL/water system). In the unsaturated zone, another phase exists as the gas phase (three-phase NAPL/water/gas system) (Figure 4 and Figure 5) [Pinder and Abriola (1986); Feenstra and Cherry (1988)].

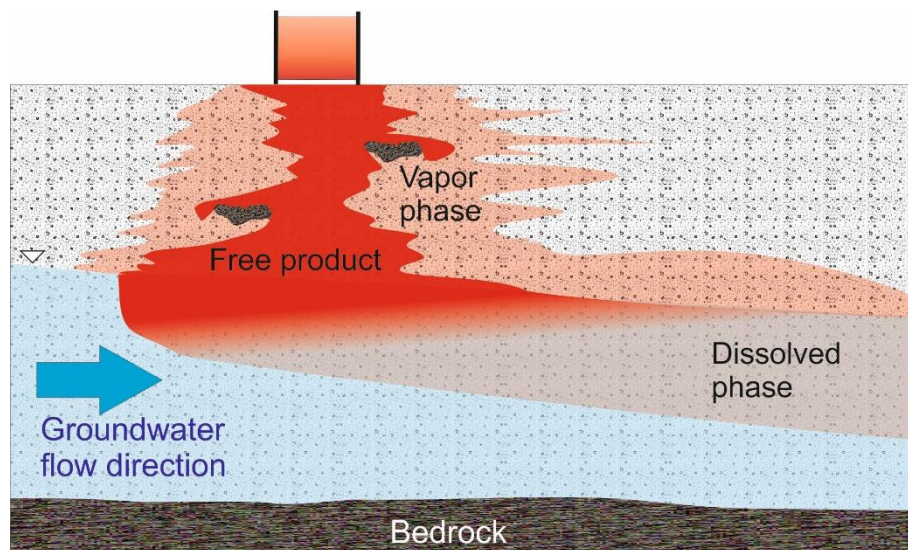


Figure 4: Schematic representation of the behaviour of Light Non-Aqueous Phase Liquids (in the saturated zone) (adapted from [US EPA (1996a)])

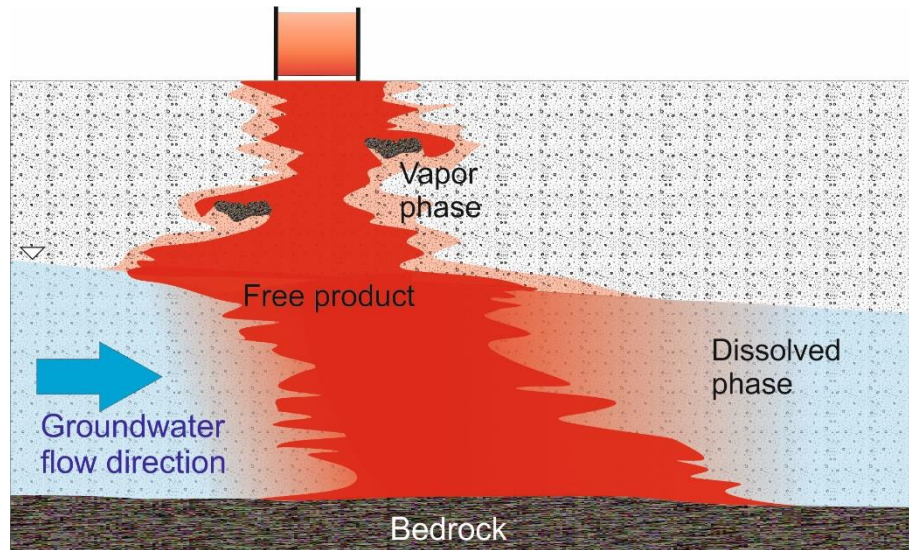
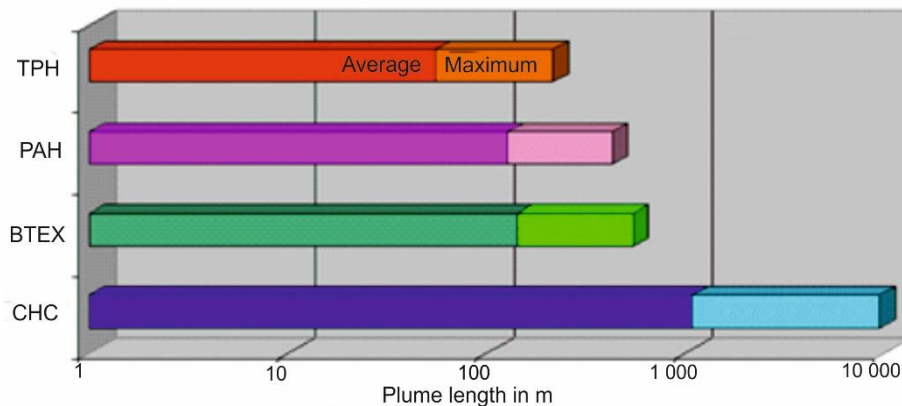


Figure 5: Schematic representation of the behaviour of Dense Non-Aqueous Phase Liquids (in the saturated zone) (adapted from [Cohen and Mercer (1993)])

Figure 6 shows the average and maximum dimensions of contamination plumes as a function of contaminant type. Stupp and Paus (1999) have highlighted that the largest plumes are related to volatile chlorinated compounds.



TPH: Total petroleum hydrocarbons; PAH: Polycyclic aromatic hydrocarbons; BTEX: monoaromatic compounds (benzene, toluene, ethylbenzene and xylene); CHC: chlorinated hydrocarbon

Figure 6: Average and maximum lengths of contamination plumes as a function of contaminant type [Stupp and Paus (1999)]

Field studies conducted by McGuire *et al.* (2006) and Falta *et al.* (2005a and 2005b) clearly showed that decreasing contaminant quantity at the source (via *e.g.* excavation or pump and treat) reduces contaminants concentrations in groundwater. However, these studies and others reported that the reduction of contaminants in groundwater is closely related to the source architecture, in particular, how the DNAPL source is distributed and shaped in the subsurface [Sale (2001); Stroo *et al.* (2003); Falta *et al.* (2005a); Falta *et al.* (2005b); McDade *et al.* (2005); Newell and Adamson (2005); McGuire *et al.* (2006); Huang *et al.* (2015)]. McGuire *et al.* (2006) concluded that even when there is no detailed understanding of the source architecture, the concentration in groundwater will be reduced, in a rather short time, and be proportional to the contaminant mass drop at the source. Moreover, the studies mentioned above showed that treating these contamination sources has a significant impact on the DNAPL release period as

well as on contaminant concentrations in the plume, and on how far the plume spreads. Similar observations were reported for LNAPL [Huntley and Beckett (2002)].

1.1.5 Toxicity of chlorinated compounds

Organochlorine pollutants are compounds that contain carbon, chlorine, and hydrogen atoms. Their chlorine-carbon bonds are very strong, which means that they do not break down easily. They are highly insoluble in water but are attracted to fats. Since they resist metabolism and are readily stored in fatty tissue of any animal ingesting them, they accumulate in animals in higher trophic levels. Organochlorine insecticides are among the oldest, most toxic, and most environmentally destructive synthetic pesticides. First introduced in the 1940s and 1950s, these chemicals were used extensively in agriculture, forestry, and in-home pest control until most of them were banned in the 1970s and 1980s. They target the central nervous system, and many of them are suspected to be carcinogenic [NIEHS (2015)]. Most chlorinated compounds are very harmful for human health.

The International Agency for Research on Cancer (IARC) Working Groups classify agents, mixtures and exposures into one of five categories.

- Group 1: The agent is carcinogenic to humans.
- Group 2A: The agent is probably carcinogenic to humans.
- Group 2B: The agent is possibly carcinogenic to humans.
- Group 3: The agent is not classifiable as to its carcinogenicity to humans.
- Group 4: The agent is probably not carcinogenic to humans.

Table 3 shows various organochlorinated compounds (COC) present in DNAPL as a function of the IARC groups.

Table 3: IARC Classification for Chlorinated Compounds in DNAPL [IARC (2018)]

Group 1	Group 2A	Group 2B	Group 3
Vinylchloride	Perchloroethylene	Chloroform	Chloroethane
Trichloroethylene	Trichloropropane	Dichloroethane	Chloromethane
		Dichloromethane	Hexachlorobutadiene
		Hexachlorobenzene	
		Hexachloroethane	
		Trichloromethane	
		Tetrachloroethane	
		Carbon tetrachloride	

1.1.6 Classical techniques for recovering DNAPL free product

Techniques for recovering LNAPL in pure phase (free product) are easier than those implemented for recovering DNAPL. LNAPL float on the top of the water table, which ease the localization and remediation of the contamination (even though specific skills are necessary to get the best results at lowest cost).

The random distribution of DNAPLs (depending on soil permeabilities and associated variations in the required threshold pressure intake) makes free products migrate downward by fingering until they are totally blocked at the impermeable substratum (if the volume of DNAPL is high enough).

Initially, free product is recovered via vertical or horizontal wells or trenches (by specific pumping approaches using specific skimmers) (Figure 7) [ITRC (2004)]. This technique can prevent mobile DNAPLs from migrating and allow the recovery of most of the contaminants, but without an enhanced thermal or chemical technique, it cannot reach concentrations below residual saturations. However, this step will significantly improve the total remediation efficiency (in particular, for pumping and treating the dissolved phase) [Huling and Weaver (1996); Kueper and Gerhard (2014)]. Pumping can be performed until the DNAPL recovery rates fall.

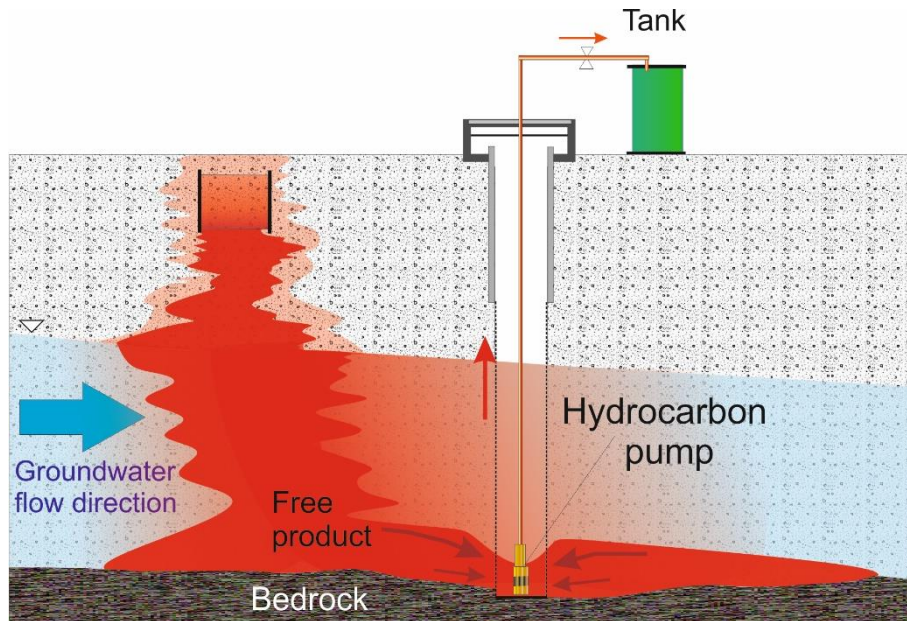


Figure 7: Schematic representation of DNAPL free product recovery (adapted from [Colombano *et al.* (2010)])

The best configuration for recovering pure DNAPL combines the following: i. a DNAPL continuum trapped in a small shallow depression (whose substratum is impermeable); ii. a permeable aquifer [Cohen and Mercer (1993)].

If there is a lot of DNAPL and the stakes are significant (for example a drinking water supply close to the site), dynamic pumping operations are started for the contaminated groundwater (dissolved phase with water pumps) and DNAPL (with hydrocarbon pumps), once the DNAPL recovery kinetics decrease significantly. The pumps are placed in the same recovery wells as skimmers or in adjacent wells. This complementary operation creates a hydraulic confinement and increases pure DNAPL recovery [Schmidtke *et al.* (1992); Huling and Weaver (1996); Sale and Applegate (1997); Kueper and Gerhard (2014)].

Recovery well diameters do not influence total DNAPL recovery but they increase pumping flow rates; indeed, small well diameters reduce the DNAPL-water mixture. Wells equipped with strainers only above the portion affected by the pure DNAPL can recover a maximum of products by limiting water intrusion [Schmidtke *et al.* (1992)].

Varied pumping techniques such as upwelling, water flooding and trench systems can be implemented with the aim of improving the recovery of pure product [Connor *et al.* (1989)]. These different approaches must be optimized by performing feasibility/treatability tests and *ad hoc* modeling to secure the remediation of the sites when possible.

1.1.6.1 Free product recovery with groundwater extraction and skimming (Upwelling)

The upwelling technique consists in pumping the water above the DNAPL recovery zone. The cone of depression created by pumping the groundwater will raise the level of the DNAPL-water interface [Villaume *et al.* (1983); Wisniewski *et al.* (1985); Ferry and Dougherty (1986); Cazaux *et al.* (2014)]. The process involves specific hydrocarbon pumps and dedicated water pumps. These are placed in the same recovery wells or in two separate wells (Figure 8).

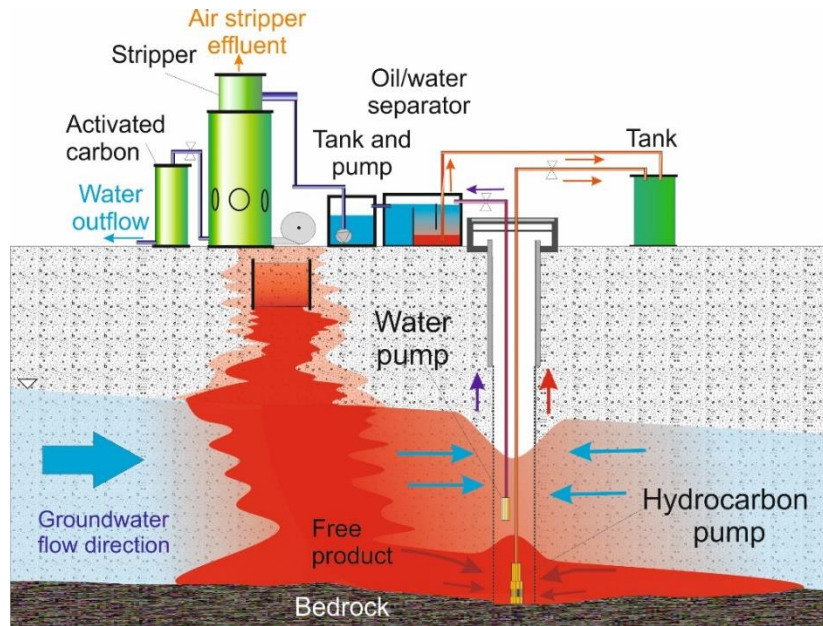


Figure 8: Schematic representation of free product recovery with groundwater extraction and skimming (upwelling) (adapted from [Villaume *et al.* (1983)])

This technique can significantly increase the DNAPL recovery yield in the wells. Recovery flow rates two to three times higher than for classic pumping have been reported for dimethyl phthalate [Wisniewski *et al.* (1985)]. However the water pumping rate must be determined very carefully: if it is too high, the flow rate will create emulsions; if it is too low, the flow rate will not result in any upwelling.

The level of the DNAPL-water interface is estimated from the depth of the cone of depression, using the modified Ghyben-Herzberg equation (Eq. 1):

$$z_n = \left(\frac{\rho_w}{\rho_n - \rho_w} \right) h_{wc} \quad \text{Eq. 1}$$

where:

z_n : distance from the water table to the DNAPL-water interface (m)

h_{wc} : depth of the cone of depression of water (m)

ρ_w : water density ($\text{kg}\cdot\text{m}^{-3}$)

ρ_n : DNAPL density ($\text{kg}\cdot\text{m}^{-3}$)

1.1.6.2 Water flooding

Water flooding (or hydraulic displacement or dual phase extraction) takes into account the fact that, under certain conditions, hydraulic gradients can cause the DNAPL pool to migrate [Craig (1971); Willhite (1986); Gerhard *et al.* (2001); Alexandra *et al.* (2012)].

The process comprises specific oleophilic skimmers and dedicated water pumps allocated to groundwater pumping (just above the DNAPL-water interface). These are placed in the same recovery well or in two separate wells (Figure 9).

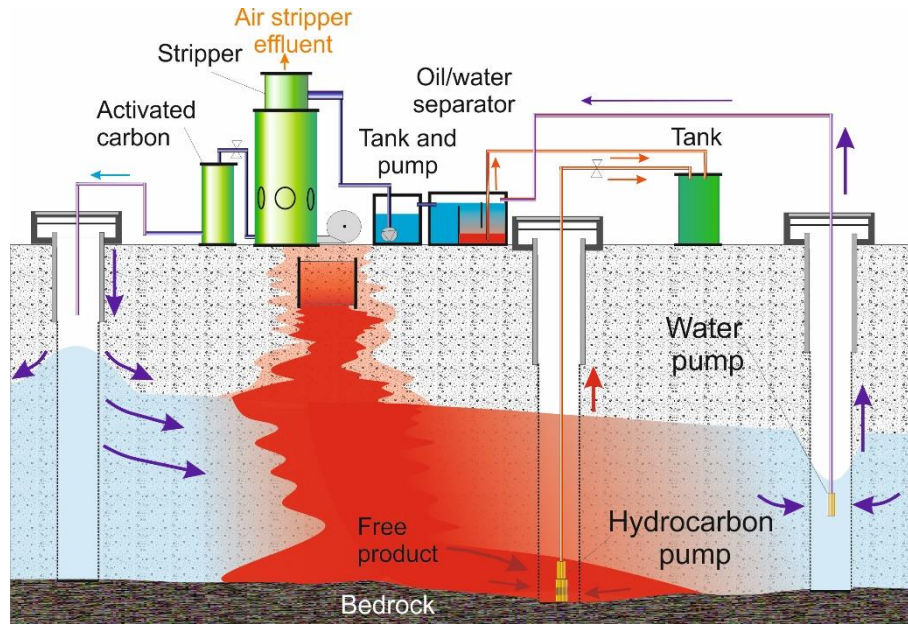


Figure 9: Schematic representation of the principle of water flooding (adapted from [Colombano *et al.* (2010)])

Two methods are implemented to obtain a first estimate of the necessary pumping characteristics.

a) A DNAPL pool located on an impermeable substratum has the following characteristics: capillary pressure increases with the pool's internal depth; but capillary pressures are identical at the edges of the pool. When a hydraulic gradient is applied everywhere in the pool, the capillary pressures are higher in the downstream zone than in the upstream zone of the pool. Therefore, these differences can cause the DNAPL pool to migrate. According to Kueper and Gerhard (2014), the DNAPL will migrate if the left-hand side of Eq. 2 is greater than the right-hand side as follows [Kueper and Gerhard (2014)]:

$$\frac{\Delta\rho}{\rho_w} L_p \sin\alpha_p + \Delta h > \frac{P_c(L_p) - P_c(0)}{\rho_w g} \quad \text{Eq. 2}$$

where:

$\Delta\rho$: difference between the DNAPL density, ρ_n , and water density, ρ_w ($\text{kg}\cdot\text{m}^{-3}$)

L_p : stable pool length (m)

α_p : dip of the bedding below horizontal ($^\circ$)

Δh : difference in hydraulic head between the up dip end of the pool and the down dip end of the pool ($h(0)-h(L)$) (m)

$P_c(L_p)$: capillary pressure at the down dip end of the pool (Pa)

$P_c(0)$: capillary pressure at the up dip end of the pool (Pa)

g : gravitational acceleration ($m.s^{-2}$)

b) Another approach is based on the fact that the DNAPL is mobilized when the interfacial tension (IFT) between the wetting (water) and non-wetting (DNAPL) phases decreases. The drop of IFT coupled with the change of viscosity in the non-wetting phase allows the capillary pressure (which keeps the DNAPL in the pores) to be overcome [Pennell *et al.* (2014)]. Pennell *et al.* (1996) used a method to estimate DNAPL mobilization in the porous medium [Pennell *et al.* (1996)]. This method uses three numbers: the capillary number (N_{ca}), the Bond number (N_B) and the total trapping number, N_T (see section 2.2.12).

Pressure differences, sometimes even small ones, can favor DNAPL migration [Kueper *et al.* (2008)]. Once the water is pumped and treated, it can then be injected again into the upstream of the treatment zone to increase the hydraulic gradients.

Moreover, in some cases water flooding allows significant recovery of DNAPL. For instance, with chlorinated compounds, Alexandra *et al.* (2012) demonstrated that the ganglia-to-pool ratio (*i.e.* a reduction in the pool fraction) could vary from 0.1 to 0.3 or even 0.7 (depending on the type of DNAPL, the degree of heterogeneity of the soil, and the applied hydraulic gradient) [Alexandra *et al.* (2012)].

If the free product in a recovery well is pumped too quickly, that can break the free product continuum, and stop the migration and recovery of this free product [Pennell *et al.* (2014)]. To resume recovery, the threshold pressure must be exceeded, which means that new recovery wells must be installed or higher hydraulic pressures imposed upstream. Once the water is pumped and treated, it can then be reinjected upstream of the treatment zone to increase the hydraulic gradients.

This technique increases DNAPL dissolution by: i. forming ganglia (with higher DNAPL-water contact surface than the initial surface); ii. changing the phase equilibria due to contact between DNAPL and uncontaminated water [Miller *et al.* (1990); Imhoff *et al.* (1993); Nambi and Powers (2003); Grant and Gerhard (2007a); Grant and Gerhard (2007b)].

1.1.6.3 Trench systems

Trenches, backfilled with gravel pack, have been used successfully to recover DNAPL. As shown in Figure 10, pumping systems can be passive (without water pumping but only with a hydrocarbon pump) or active (skimmers associated with water pumping).

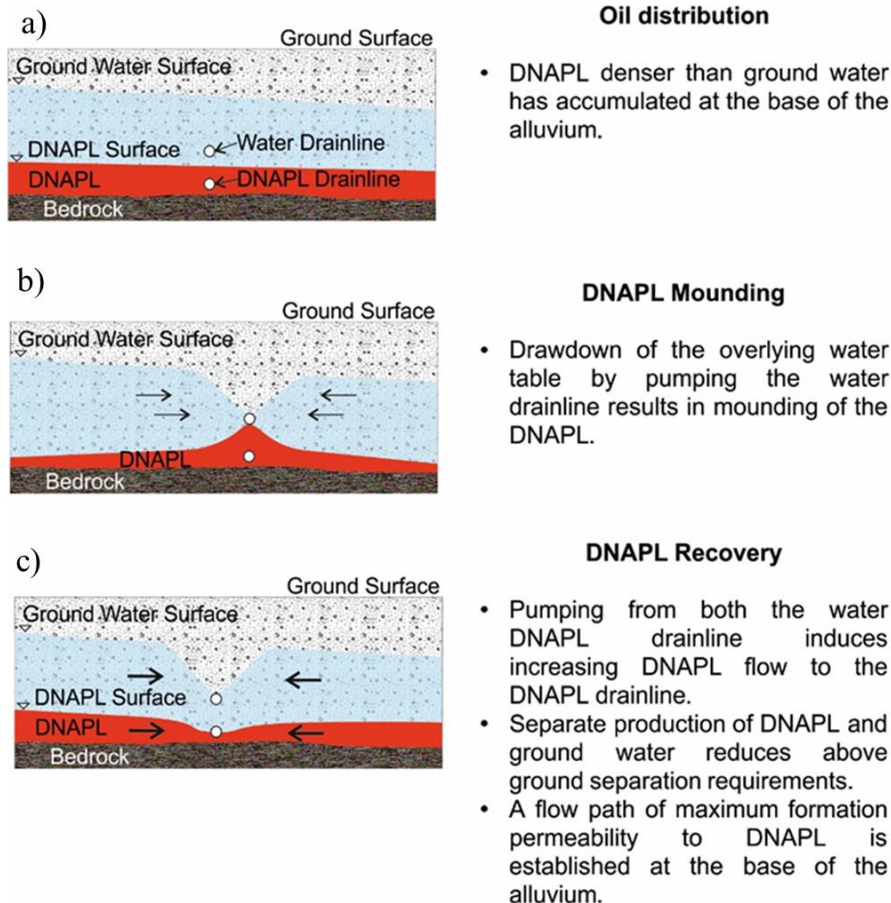


Figure 10: Schematic representation of trench systems (adapted from [Huling and Weaver (1991); Sale and Kuhn (1988)])

This system is preferably used when the aquifer is shallow. Directional drilling or specific excavations with *ad hoc* support can be implemented if the depths are greater. Groundwater can be pumped to increase DNAPL recovery levels [Sale and Kuhn (1988); Huling and Weaver (1996)]. This pumping can be used for both upwelling and water flooding.

1.1.7 Improving DNAPL recovery

The pumping operations for free product are performed by pump and treat operations. Usually, these operations are long (*e.g.* often more than 30 years or chlorinated solvents) [Harkness and Konzuk (2014)]. They are not very effective in the long term because of the slow release from the residual saturation and the low remediation yield [Mackay and Cherry (1989); Travis and Doty (1990); Berglund and Cvetkovic (1995); Pankow and Cherry (1996)].

This is why, more and more frequently, new technologies are implemented to enhance these remediation operations, which are costly in the long term [US EPA (2003); Williamson (2014)]. In particular, various enhanced technologies have been designed to reduce the residual mass of contaminants. The technologies used to recover chlorinated compounds are presented in Table 4. For other DNAPL (mainly polycyclic aromatic hydrocarbons, heavy chlorinated compounds, coal tars and creosotes), the enhanced techniques are almost identical (with the exception of *in situ* chemical reduction techniques, *in situ* air sparging, *in situ* bioremediation and air sparging, which are less suitable, considering the product characteristics).

Table 4: Functional role for commonly used remediation technologies in generalized sequential treatment strategy [Williamson (2014)]

Mobile DNAPL Extraction Technologies	Source Zone Primary Treatment Technologies	Source Zone Polishing Technologies
Hydraulic displacement	Excavation	<i>In situ</i> chemical oxidation
<i>In situ</i> thermal treatment	<i>In situ</i> thermal treatment	<i>In situ</i> bioremediation
Surfactant-enhanced extraction	Surfactant/co-solvent flushing	<i>In situ</i> chemical reduction
	<i>In situ</i> chemical oxidation	<i>In situ</i> air sparging
	<i>In situ</i> bioremediation	Natural attenuation
	<i>In situ</i> chemical reduction	
	Soil mixing with ZVI* or other reagent	
	<i>In situ</i> air sparging	

*: ZVI: Zero Valent Iron

A study conducted by McGuire *et al.* (2006) on 59 sites contaminated by chlorinated compounds in the US compared the treatment duration and remediation yield of groundwater remediation techniques (Figure 11). The techniques examined were: *in situ* biological reduction, *in situ* thermal desorption and washing with surfactants. The average remediation yield values for these techniques were found to be: 95% (biological reduction), 97% (thermal desorption) and 95% (surfactant and co-solvent). In addition, the treatment durations were remarkably shorter than with the classic pump and treat approach (2 to 21 months versus several decades).

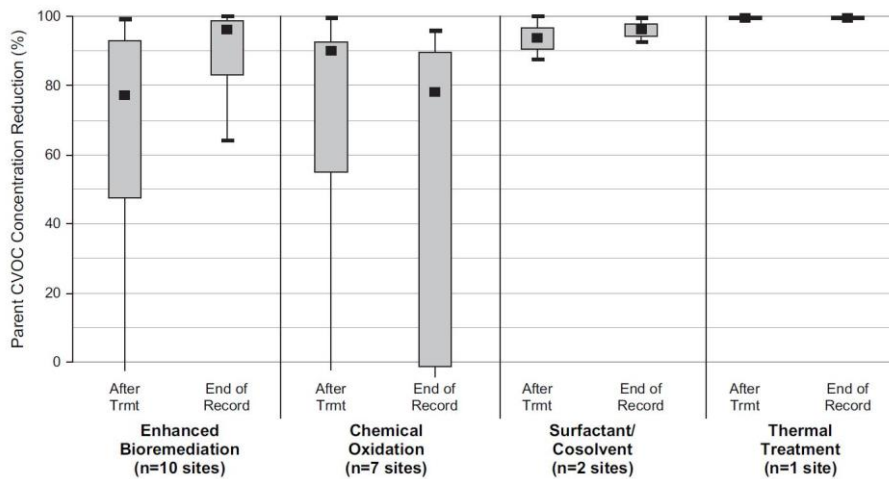


Figure 11: Rebound assessment at source depletion sites: concentration reduction from before treatment to immediately after treatment and at end of data record (chlorinated compounds) [McGuire *et al.* (2006)]

Performance for these extraction enhanced techniques (desorption and washing) is explained in particular by their ability to considerably reduce the quantity of pure products present in the pores (by reducing the interfacial tension, desorbing the contaminants for the solid matrix and reducing the viscosity). Indeed, releasing a source of pure product (mass flow) will depend not only on the groundwater characteristics and the primary physical and chemical characteristics of the DNAPL, but also on the characteristics of each source: i. its magnitudes (in particular, the area of the DNAPL-water interface); ii. the Ganglia-to-pool mass ratio; iii. how the pores

are connected (allowing water to pass), and iv. residual saturations [Miller *et al.* (1990); Imhoff *et al.* (1993); Nambi and Powers (2003); Falta *et al.* (2005b); Falta *et al.* (2005a); Grant and Gerhard (2007a); Grant and Gerhard (2007b); Carey and McBean (2010a); Carey and McBean (2010b); Alexandra *et al.* (2012)].

1.1.7.1 Effect of temperature on DNAPL recovery

Thermal methods have been implemented successfully with DNAPL. Considering the example of coal tar, increasing temperature can remobilize the residual coal tar by decreasing the following: density, interfacial tension with water, contact angle with water on a solid medium, and viscosity [Huling and Weaver (1996); Heron *et al.* (1998a); U.S. Army Corps of Engineers (2014)]. Specifically, coal tar's viscosity is very sensitive to temperature as it can vary by one to two orders of magnitude when the temperature is increased from 20 °C to 70 °C [Baker *et al.* (2006); Brown *et al.* (2006); Birak and Miller (2009); Philippe *et al.* (2017)].

A few cases of thermally-enhanced coal-tar pumping have been reported in the literature, in relation with field testing [McLaren *et al.* (2009)]. These authors studied thermal enhancement as a sustainable alternative technique. The coal tars were heated to 30 °C, which reduced their kinematic viscosity by almost one order of magnitude (100 cSt to 10 cSt). Globally, 22 m³ of coal tar was recovered in six months of pumping, with a 30% reduction in costs compared to classic pump and treat methods.

Thermal enhancement can lead to high treatment yields (90%), particularly interesting for highly-contaminated areas with low permeabilities that are not well suited for treatment using flushing methods [Suchomel *et al.* (2014)].

1.1.7.2 Effect of adding surfactants on DNAPL recovery (surfactant flushing)

The recovery mechanisms during surfactant flushing include two main stages: (1) decreasing interfacial tension (IFT) and increasing contaminant solubility (NAPLs) (2) mobilizing the residual contamination (see section 2.4.3) [Pennell *et al.* (2014)].

a) Decreasing IFT and increasing contaminant solubility:

At low concentrations, surfactant molecules will mainly accumulate at solid-liquid or liquid-liquid interfaces (NAPL-water interface in our case, where a pure phase exists). Surfactant molecules will gradually cover the NAPL-water interface as surfactant concentration increases.

Increasing surfactant concentration will reduce IFT until all NAPL-water interfaces are covered. At this stage, increasing surfactant concentrations will no longer reduce the IFT: the surfactant molecules will agglomerate together (formation of surfactant micelles) and will increase the solubility of the NAPL (present in the dissolved phase). This concentration is called the Critical Micelle Concentration (CMC) [Rosen and Kunjappu (2012); Vishnyakov *et al.* (2013); Pennell *et al.* (2014)].

In general, interfacial tension decreases with increasing temperature (*e.g.* $5.5 \times 10^{-5} \text{ N.m}^{-1} \cdot \text{°C}^{-1}$ for crude oil-water systems) and can also be influenced by pH, the addition of surfactants, and other substances in the solution [Schowalter (1979)]. The capillary pressure is directly related to the interfacial tension in the DNAPL-water system [Mercer and Cohen (1990)]. The interfacial tension in a DNAPL-water system varies between zero for completely miscible

liquids and $72 \times 10^{-3} \text{ N.m}^{-1}$ for absolutely immiscible liquids ($72 \times 10^{-3} \text{ N.m}^{-1}$ is the surface tension of water/air at 25 °C) [Lyman *et al.* (1982)].

b) Mobilizing residual contamination:

Surfactants are used to reduce the IFT to: i. recover maximum pure products (DNAPLs) and ii. decrease residual saturations.

DNAPL is displaced when the reduced IFT coupled with the change of non-wetting phase viscosity overcomes the capillary pressure. Therefore, the optimal surfactant concentration that improves the recovery yield (and thus reduces residual saturation) should be chosen.

Surfactants have the effect of solubilizing and reducing IFT for the TCE-water and PCE-water system. Aerosol-MA-80, Tween 80, Triton X-100 and SDBS have been reported to be effective in IFT reduction for TCE and PCE. IFT, after addition of these surfactants, may be less than 1 mN.m^{-1} , corresponding to decreases of more than 90% [Dwarakanath *et al.* (1999); Sabatini *et al.* (2000); Taylor *et al.* (2001); Childs *et al.* (2004); Suchomel *et al.* (2007); Harendra and Vipulanandan (2011)].

Field experiments report recovery yields for pure chlorinated solvents ranging from 60 to 70% [Rao *et al.* (1997); Holzmer *et al.* (2000); Jawitz *et al.* (2000); Brooks *et al.* (2004); Soga *et al.* (2004)] or even more than 90% [Londergan *et al.* (2001); Abriola *et al.* (2005); Ramsburg *et al.* (2005); Pennell *et al.* (2014)].

1.1.7.3 Using surfactant foam for DNAPL recovery

Surfactant foam technology has been investigated to remove NAPLs from contaminated soils [Peters *et al.* (1994); Kilbane *et al.* (1997); Rothmel *et al.* (1998); Jeong *et al.* (2000)]. Foams enhance the flooding efficiency of surfactant flushing even in a heterogeneous porous medium, resulting in higher removal efficiencies [Jeong *et al.* (2000); Wang and Mulligan (2004)].

Recent laboratory studies on surfactant foam technology for *in situ* removal of chlorinated DNAPLs have shown that this technique could be a promising line of research [Maire *et al.* (2015); Maire *et al.* (2016)]:

- High foam stability for $C_{\text{surfactant}} = 0.05\%$ was maintained in the presence of DNAPL.
- Strong foams (finely textured foams) removed more than 95% of DNAPL for a surfactant dose of 10 g per kg of DNAPL recovered.
- No DNAPL fragmentation or enhanced dissolution ($<0.5 \text{ g.L}^{-1}$) were observed.

1.2 Thesis context and objectives

This PhD thesis is part of the SILPHES project ("Solutions Innovantes de Lutte contre les Produits Halogénés dans les Eaux Souterraines": Innovative Solutions for the recovery of Halogenated products from Groundwater). SILPHES is financially supported by ADEME (the French Agency for Environment and Energy Management) and extends over 4 years as part of Future Investments ("Investissements d'Avenir") funding scheme.

1.2.1 SILPHES project

SILPHES began in 2013 and ended in 2018. The following partners were involved in the project consortium:

- Owner of the polluted sites and project coordinator: INOVYN,
- Remediation companies: SERPOL and REMEA,
- Environmental engineering consulting companies: INTERA
- Renewable energy storage company: MAHYTEC,
- Franche-Comté University - National Center for Scientific Research: Laboratoire (CNRS): Chrono-Environnement and Laboratoire UTINAM,
- French Geological Survey (BRGM).

The main objective of the SILPHES project was to combine characterization tools and techniques for the remediation of groundwater contaminated by organochlorine compounds. The various complementary techniques that were implemented in this project give it an innovative structural setup where projects are offshoots of a central core principle:

- The development and validation of pollution characterization techniques for "source zones" (very concentrated areas from which pollution emanates) and "plume zones" (extension of pollution from the source area) to optimize the design and management of pollution control units;
- The development and validation of new *in situ* remediation technologies;
- The development of new decision support tools for future projects.

1.2.2 Description of the site

The project took place at the INOVYN plant in Tavaux (Bourgogne-Franche-Comté, France).

The Tavaux site is a large chloroalkali chemical plant. It extends over 300 hectares. The site's hydrogeological characteristics are reported in Table 5 (from top to bottom):

Table 5: Hydrogeological description of the site [Cazaux *et al.* (2014)]

Thickness	Lithology	Hydraulic conductivity ($m.s^{-1}$)
2 to 4 m	Modern fine alluvium: superficial clays and loams	10^{-7} to 10^{-9}
5 to 10 m	Quaternary old alluvium (more or less clayey sands and gravel stones alluvial deposits)	10^{-2} to 10^{-4}
From a depth of 10 to 12 m	Marls	10^{-9}

The plant held a landfill from 1964 to 1986 where production waste was dumped (in particular, liquid waste) (Figure 12). This landfill was built with a clayed landfill barrier. However, a pollution was discovered in 1987 while monitoring groundwater quality. The different monitoring campaigns have shown that there are about 30,000 metric tons of chlorinated compounds present in the form of free product in the underlying water table. The free product accumulated right above the substratum.

From the early 1980s to 2007, a historical DNAPL pool of several hectares was physically confined, and its migration was monitored (Figure 13). After DNAPL migration from the landfill, a steady-state plume formed within a shallow water-table sandy aquifer located above

a clayey unit at 10 meters deep. DNAPL thicknesses of 0.20 m to 1.50 m have been observed following the morphology of the substratum [Cazaux *et al.* (2014)]. DNAPL migration has been controlled by two water-pumping wells for the past thirty years. This has caused a water depression and inverse gradient in the area. The average flow rate of the hydraulic confinement is $40 \text{ m}^3 \cdot \text{h}^{-1}$.

Currently the free product extends over several hectares by creating pollution source areas consisting of around 20,000 tons of pure DNAPL and a 15 km impacted plume zones (Figure 14). It has been monitored since 1970. Recovery wells helped to limit expansion of the pure product and the pollution plume.

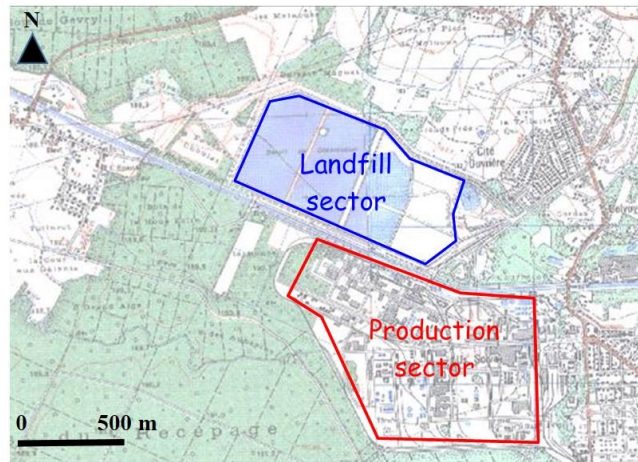


Figure 12: Map of factory location and source site for study [Cazaux *et al.* (2014)]

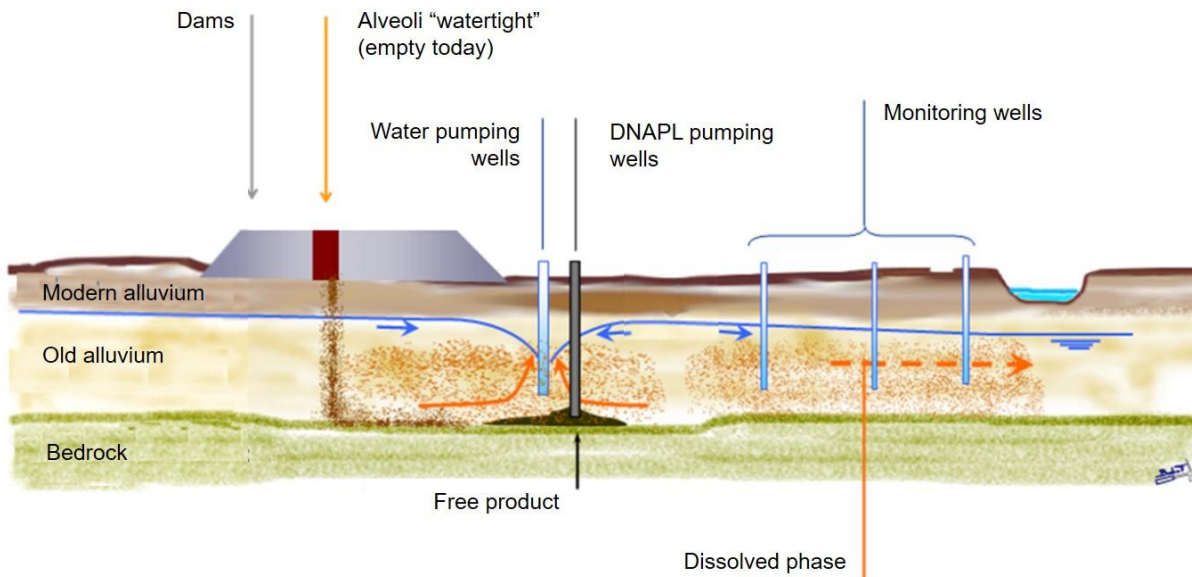


Figure 13: Hydrogeological cross section and schematic representation of SILPHES project site [adapted from [Cazaux *et al.* (2014)]]

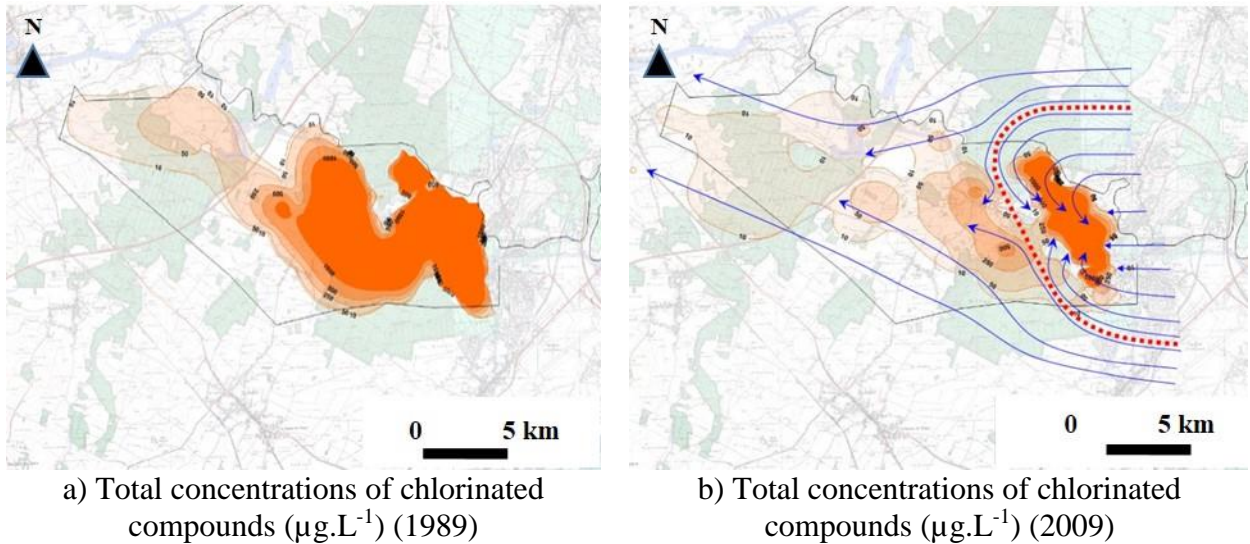


Figure 14: Transfer of the pollutant from the storage sector to the plume area: total concentrations of chlorinated compounds in a) 1989 and b) 2009 [Cazaux *et al.* (2014)]

1.2.3 Composition of DNAPL of the INOVYN site

Most of the phase is composed of heavy chlorinated compounds: hexachlorobutadiene, hexachloroethane, and hexachlorobenzene. Other lighter substances are also present in the pure phase, such as tri- and tetrachlorobenzenes, trichloropropane (1,2,3), tetrachloroethanes (1,1,1,2 and 1,1,2,2), pentachlorobutane, and pentachloroethane. These compounds are lighter and more soluble; they disperse and form the contamination “plume” with other light chlorinated compounds such as di and tri-chloroethylene, di and tri-chloroethane, or di and tri-chloropropane (Table 6).

Table 6: Composition of the "DNAPL" by average mass [Cazaux *et al.* (2014)]

Compounds	Chemical formula	Percent (%) (w/w)
Hexachlorobutadiene (HCBd)	C_4Cl_6	52 – 58
Hexachloroethane (HCEa)	C_2Cl_6	12 – 16
Perchloroethylene (PCE)	C_2Cl_4	7 – 9
Pentachlorobenzene (PeCB)	C_6HCl_5	4
Carbon tetrachloride (TCM)	CCl_4	3 – 5
Trichloroethylene (TCE)	C_2HCl_3	2
Hexachlorobenzene (HCB)	C_6Cl_6	1
Others	-	5 – 19

The main physical and chemical characteristics of the chlorinated compounds from DNAPL are presented in Table 7.

Table 7: Main physical and chemical characteristics of chlorinated compounds from DNAPL

DNAPL	Molecular formula	Amount (%) (w/w)	Density (kg.m ⁻³)	Solubility in water(mg.L ⁻¹)	Viscosity (cP)	Surface tension (mN.m ⁻¹)	Interfacial tension (H ₂ O) (mN.m ⁻¹)
Hexachlorobutadiene	(C ₄ Cl ₆)	52-58%	1675.53 (15 °C) [1]	2–2.55 (20 °C) [2]	2.446(37.8 °C) [1]	35.5 (30 °C) [3]	
			1550 (20 °C) [2]	3.2 (20 °C) [5]	9.22 (15 °C) [6]	36 (20 °C) [4]	N/A
			1680 (20 °C) [5]	4 (20 °C) [6]	3.68 (21 °C) [6]	31.4 (20 °C) [6]	
			1680 (20 °C) [6]		2.40 (50 °C) [6]		
Hexachloroethane	(C ₂ Cl ₆)	12-16%	1821 [1]	50 (22 °C) [1]		42.8 [1]	
			2090 (20 °C) [2]	50 (25 °C) [2]	N/A	42.9 ± 3.0 [3] pred.	N/A
			2091 (25 °C) [3] exp.	8.152 (25 °C) [3] pred.			
			2094 (20 °C) [3] exp.	50 (22 °C) [4]			
Perchloroethylene	(C ₂ Cl ₄)	7-9%	1619.45(23.8 °C) [1]	160 (20 °C) [1]	0.848 (23.8 °C) [1]	31.3 (20 °C) [1]	44.4 (25 °C) [1]
			1623(20 °C) [2]	150 (20 °C) [3]	0.880 (20 °C) [3]	32.2 (20 °C) [3]	
			1623(20 °C) [3]	150 (25 °C) [4]	0.880 (20 °C) [4]	32.1 (20 °C) [4]	
			1623(20 °C) [4]				
Pentachlorobenzene	(C ₆ HCl ₅)	4%	1800 [1]	0.56 (20 °C) [2]		45.1 [4]	
			1834 (20 °C) [2]	1.677 (25 °C) [3]			
Carbon tetrachloride	(CCl ₄)	3%	1587.10 (23.8 °C) [1]	800 (25 °C) [1]	0.922 (23.8 °C) [1]	27 (20 °C) [1]	45 (20 °C) [1]
			1594.7 (20 °C) [2]	800 (25 °C) [2]	1.35 (20 °C) [2]	26.7 (20 °C) [2]	
Trichloroethylene	(C ₂ HCl ₃)	2%	1454 (23.8 °C) [1]	1100 (25 °C) [1]	0.562 (23.8 °C) [1]	29.3 (20 °C) [1]	34.5 (24 °C) [1]
			1464.2 (20 °C) [2]	1100 (25 °C) [2]	0.58 (20 °C) [5]	26.4 (20 °C) [5]	
			1465 (20 °C) [3]	1000 (25 °C) [3]			
			1465 (20 °C) [5]	1100 (25 °C) [4]			
				1070 (20 °C) [5]			
Hexachlorobenzene	(C ₆ Cl ₆)	1%	1570 (23.6 °C) [1]	0.035 [1]	N/A	47.3 ± 3.0 [3] pred.	N/A
				0.284 (25 °C) [2]			

[1]: [Abdallah *et al.* (2007)]; [2]: [Adamskii *et al.* (2003)]; [3]: [Adamson and Gast (1997)]; [4]: [Anderson (1986)]; [5]: [Antontsev (1972)]; [6]: [Ataie-Ashtiani and Raeesi-Ardekani (2010)]

1.3 Objectives and structure of the thesis

The main objective of this thesis was to study the impact of thermal enhancement (increasing the temperature) and chemical enhancement (by addition of surfactants) on the recovery of chlorinated compounds in a saturated porous media.

To achieve this, the effect of temperature and surfactant on multiphase flow of chlorinated compounds in saturated porous media was considered. Here, the DNAPL was considered as a pure and immiscible free phase product. Understanding these multi-phase phenomena coupling with thermal and chemical enhancements have been investigated by performing a joint experimental and modeling approach.

This doctoral thesis project fully focused on laboratory experiments and modeling of two-phase (water/DNAPL) flow in porous media, using the COMSOL Multiphysics® software. The thesis can be divided into three main parts:

1. Experimental determination of INOVYN DNAPL parameters such as viscosity, density, wettability and also the properties of the porous media used such as residual saturation, porosity permeability, and retention curve (using an experimental 1D cell setup) as a function of temperature and surfactant concentrations;

2. Experimental investigation of enhanced DNAPL recovery using 1D columns and also 2D tank laboratory-scale setups;
3. Numerical simulation of enhanced DNAPL recovery in laboratory scale (1D columns and 2D tank). The modeling approach simulates the flow of chlorinated organic compounds in contaminated soil. This was performed in experimental 1D cells, 1D columns and a 2D tank. The numerical simulation results were compared with the results of laboratory experiments. Also, there was a parametric investigation of enhancement on recovery processes.

Firstly, the characteristics of the DNAPLs were studied (chapter 3). Secondly, how the DNAPL and water behaved in porous media were characterized in 1D cells (chapter 4). Thirdly a series of drainage-imbibition experiments in 1D columns was performed (chapter 5) and finally, 2D tank pumping experiments were carried out (chapter 6). The experiments were performed with images and permittivity and resistivity monitorings.

The structure of the thesis is shown in Figure 15.

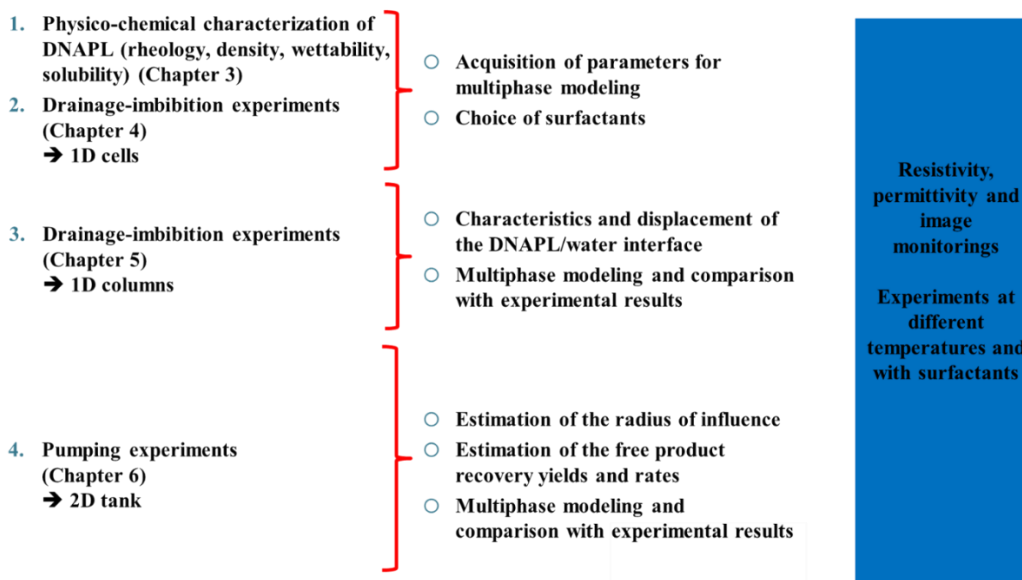


Figure 15: Organization of the different stages of the thesis

1.4 Funders

This research was carried out as part of the SILPHES project funded by ADEME (French Environment and Energy Management Agency) as part of Future Investments ("Investissements d'Avenir") funding scheme. The author acknowledges the BRGM/D3E division for its financial support during this thesis as part of specific internal project and the MULTISCALEXPER PSO3 project. I gratefully acknowledge the financial support provided to the PIVOTS project by the Centre – Val de Loire region (ARD 2020 program and CPER 2015-2020) and the French Ministry of Higher Education and Research (CPER 2015-2020 and public service subsidy to BRGM). This operation is co-funded by the European Union. Europe is committed to the Centre-Val de Loire region with the European Regional Development Fund.

2. LITERATURE REVIEW

2. LITTERATURE REVIEW

This section provides a literature review regarding the following aspects:

- Single-phase and two-phase flow in porous media,
- Thermal and chemical enhancements,
- Two-phase flow modeling,
- Monitoring methodologies: electrical resistivity, induced polarization, non-invasive imaging methods.

2.1 Single-phase flow in porous media

2.1.1 Dynamics of saturated porous media

Descriptions of how a fluid flows in a porous medium are based on various physical laws, according to the observation scale. At the microscopic scale, fluid flow is usually controlled by capillary forces, flow rate, gravity, and fluid viscosity [Rose and Channapragada (1960)]. Poiseuille (1838) developed a model that describes how fluid flows in a capillary tube (Eq. 3).

$$Q = - \frac{\pi}{8\mu} r_{\text{tube}}^4 \frac{\Delta P}{L} \quad \text{Eq. 3}$$

where:

- Q: flow rate ($\text{m}^3 \cdot \text{s}^{-1}$)
- r_{tube} : radius of the capillary (m)
- L: length of the capillary (m)
- P: driving pressure of the fluid (Pa)
- μ : dynamic viscosity of the fluid (Pa.s)

In a single-phase flow system, we can use Darcy's law using the following equation (Eq. 4):

$$v = - \frac{k}{\mu} (\nabla P - \rho g) \quad \text{Eq. 4}$$

where:

- v: Darcy velocity of fluid ($\text{m} \cdot \text{s}^{-1}$)
- ρ : density of fluid ($\text{kg} \cdot \text{m}^{-3}$)
- ∇P : pressure gradient (Pa)
- k: intrinsic permeability (m^2)

For a water single-phase flow in porous media, we often use hydraulic conductivity, K, to characterize the facility where water circulates in the porous medium (Eq. 5).

$$K = - \frac{k\rho g}{\mu} \quad \text{Eq. 5}$$

where:

- K: hydraulic conductivity ($\text{m} \cdot \text{s}^{-1}$)

The intrinsic permeability can be estimated from Carman–Kozeny equation, derived from Poiseuille law, connects the medium's permeability to the geometric properties of this medium (Eq. 6 combined with Eq. 7). This equation is only valid if the particles composing the medium are spherical and uniform.

$$k = \frac{\emptyset^3 D_p^3}{72(1 - \emptyset)^2 \tau} \quad \text{Eq. 6}$$

$$\phi = \frac{V_V}{V_T} \quad \text{Eq. 7}$$

where:

- k: permeability (μm^2)
- D_p : particle diameter (m)
- ϕ : porosity (-)
- V_V : volume of void-space (m^3)
- V_T : total volume of material (m^3)
- τ : tortuosity (-)

2.1.2 Solubility and dissolution

2.1.2.1 Solubility

Solubility is the maximum concentration of a substance that will dissolve in pure solvent (*e.g.* water) at a particular temperature [Rogers and Stovall (2000)].

Normally NAPLs are composed of multiple components, therefore, the aqueous solubility of a component of the mixture can be estimated by multiplying its mole fraction by its pure aqueous solubility [Banerjee (1984); Feenstra *et al.* (1991); Mackay *et al.* (1991)]. If the DNAPL has just a single component, its pure phase solubility can be used to estimate their effective aqueous solubility. For DNAPLs with multiple components the effective solubility can be estimated by the following equation (Eq. 8) [Shiu *et al.* (1988); Feenstra *et al.* (1991); Newell and Ross (1992)].

$$S_{ei} = X_i S_i \quad \text{Eq. 8}$$

where:

- S_{ei} : effective solubility of the component *i* in the mixture (mg.L^{-1})
- X_i : mole fraction of component *i* in the mixture (-)
- S_i : solubility of compound *i* (mg.L^{-1})

Note that in a DNAPL mixture, there are always some unknown or almost insoluble substances. The presence of these substances reduces the mole fraction of the components and therefore the effective solubility. The above relationship is approximate and can be only used for ideal mixtures [Cohen and Mercer (1993)].

The effective solubility can be also estimated by using partition coefficients. For example, some researchers show many regression equations that estimate the aqueous solubility with coefficients K_{ow} (octanol and water) and K_{oc} (organic carbon and water) [Lyman *et al.* (1982); Kenaga and Goring (1980)]. K_{ow} is defined as the ratio between the phase dissolved in *n*-octanol and the phase dissolved in water. This coefficient represents the relative polarity of the liquid. K_{oc} is defined as the ratio between the phases adsorbed to the organic substance in soil and the phase dissolved in groundwater [Cohen and Mercer (1993)]. Various factors can affect solubility, for example, temperature, the reaction between the dissolved substance, and salinity [Cohen and Mercer (1993)]. Some work shows that the effective solubility of most organic substances increases with temperature but this relationship varies according to the aqueous system [Lyman *et al.* (1982)]. Some authors have also proposed that the aqueous solubility of most organic substances generally decreases with the addition of salts [Rossi and Thomas (1981)]. Here to estimate the effective aqueous solubility of our DNAPLs, we used a method based on activity coefficient that was developed by Banerjee (Eq. 9) [Banerjee (1984)].

$$C_i = (x_i)_{org} (\gamma_i)_{org} S_i \quad \text{Eq. 9}$$

where:

C_i : concentration of each component in the mixtures (mg.L^{-1})

$(x_i)_{\text{org}}$: mole fraction of organic phases of each component in the mixtures (-)

$(\gamma_i)_{\text{org}}$: activity coefficients in organic phases of each component in the mixtures (-)

The activity coefficients can be calculated by the Universal Functional Activity Coefficient (UNIFAC) method. The UNIFAC method calculates the activity coefficients of each chemical groups (*e.g.* C=C) and brings together all of these different groups to derive the activity coefficients of one component.

2.1.2.2 Dissolution

In regard to the aqueous solubility of NAPLs, some laboratory dissolution experiments [Anderson (1988); Schville (1988)] showed that the concentrations of NAPLs in water are approximately equal to their aqueous solubility values when water flowing rates are 10-100 cm.d^{-1} through NAPL-polluted sands. Some field measurements reported that the organic compounds found in groundwater are usually at values of less than ten percent of their solubility limits [Mackay *et al.* (1985)]. The difference between field and laboratory results is probably due to the heterogeneity of field conditions (*e.g.* the groundwater flow is not uniform and the DNAPL distribution is complex) [Mackay *et al.* (1985); Feenstra and Cherry (1988); Powers *et al.* (1991)]. Some studies also show that the dissolution of NAPLs may be limited when groundwater flow velocities are high, because the NAPLs in this case do not have enough time to dissolve in the groundwater [Powers *et al.* (1994a)]. For some special NAPLs, for example some halogenated solvents, even when their groundwater concentration is low, the chemical and hydrodynamic processes of these solvents can create large plumes of groundwater which can strongly influence groundwater quality [Cohen and Mercer (1993)].

Mass transfer across the DNAPL-water interface is commonly described using:

- a conventional single-boundary layer. In this model, the mass transfer from the DNAPL to the aqueous phase is the result of the difference in chemical potential that occurs entirely in one phase or in the other [Hunt *et al.* (1988); Miller *et al.* (1990); Powers *et al.* (1992); Imhoff *et al.* (1993); Grant (2005)];
- a dual-boundary layer model. In this model the chemical potential difference is apportioned between the phases [Brusseau *et al.* (1992)].

For the conventional single boundary layer, the solute mass flux from the DNAPL is a function of concentration gradient and interfacial area DNAPL-water (Eq. 10) [Miller *et al.* (1990)].

$$J = k_{la} a^n (C_s - C) \quad \text{Eq. 10}$$

where:

J : solute mass flux dissolution from non-wetting phase to wetting phase ($\text{mg.L}^{-1}.\text{s}^{-1}$)

k_{la} : average mass transfer coefficient for the non-wetting phase/wetting phase interface (m.s^{-1})

a^n : specific interfacial area between the non-wetting phase and the wetting phase ($\text{m}^2.\text{m}^{-3}$)

C_s : effective solubility (mg.L^{-1})

C : dissolved phase concentration (mg.L^{-1})

Several methods have been developed to determinate the specific interfacial area. However, these methods are complex, so much research has focused on solutions combining k_{la} and a^n into a lumped mass transfer term (K_l). This is justified by the fact that mass transfer near the

DNAPL-water interface is the result of advective and diffusive processes (and also chemical kinetics) (Eq. 11) [Miller *et al.* (1990); Grant and Gerhard (2004); Grant (2005)].

$$J = K_1(C_s - C) \quad \text{Eq. 11}$$

where:

K_1 : lumped mass transfer term (s^{-1})

The value of K_1 is determined from laboratory measurements [Miller *et al.* (1990); Imhoff *et al.* (1993); Nambi and Powers (2003); Grant (2005)].

There are different methods for evaluating convective mass-transfer coefficients: i. dimensional analysis coupled with experiments; ii. analogy between momentum, energy, and mass transfer; iii. exact laminar boundary-layer analysis; iv. approximate boundary-layer analysis [Eckert and Drake (1987)].

Various dimensionless numbers exist to explain the dissolution and dilution phenomena (Table 8).

Table 8: Dimensionless numbers for dissolution and dilution (adapted from [Luciano (2009)])

Sherwood number modified	$Sh' = \frac{\lambda_t l^2}{D}$	Eq. 12	Dimensionless concentration gradient at the surface
Sherwood number	$Sh' = \frac{K_c l}{D}$	Eq. 13	Dimensionless concentration gradient at the surface
Stanton number	$St = \frac{K_c}{u}$	Eq. 14	Modified Nusselt number
Schmidt number	$Sc = \frac{v}{D} = \frac{\mu}{\rho D}$	Eq. 15	Ratio of the momentum and mass diffusivities
Lewis number	$Le = \frac{\alpha}{D}$	Eq. 16	Ratio of thermal and mass diffusivities
Reynolds number	$Re = \frac{lu}{v}$	Eq. 17	Ratio of the inertial and viscous forces
Grashof number	$Gr = \frac{l^3 g \Delta \rho / \rho}{v^2}$	Eq. 18	Ratio of the buoyancy to viscous forces
Péclet number	$Pe = \frac{lu}{D}$	Eq. 19	Ratio of the convective to diffusive mass transport
Damkohler number	$\omega_D = \frac{k_c l^2}{D}$	Eq. 20	Ratio of the reaction timescale to the diffusion time scale

where:

λ_t : mass transfer coefficient per meter (s^{-1})

l : characteristic length (m)

u : velocity of the fluid ($m \cdot s^{-1}$)

v : kinematic viscosity ($m^2 \cdot s^{-1}$)

α_t : thermal diffusivity ($m^2 \cdot s^{-1}$)

D : mass diffusivity ($m^2 \cdot s^{-1}$)

K_c : mass transfer coefficient ($m \cdot s^{-1}$)

k_c : reaction rate (s^{-1})

Empirical Models for Nonaqueous-Aqueous Phase Mass Transfer are presented in Table 9.

Table 9: Mass Transfer Correlations [Imhoff *et al.* (1997)]

Model type	Formulation	Reference
Lumped domain	$Sh_a^i = 12(\phi - \theta_n)Re_a^{0.75}\theta_n^{0.60}Sc_a^{i 0.5}$ Eq. 21	[Miller <i>et al.</i> (1990)]
Lumped domain	$Sh_a^i = 4.13Re_a^{0.598} \left(\frac{D_{50}}{D_M}\right)^{0.673} C_u^{0.369} \left(\frac{\theta_n}{\theta_{n_i}}\right)^{\beta_L}$ $\beta_L = 0.518 + 0.114 \left(\frac{D_{50}}{D_M}\right) + 0.10C_u$ Eq. 22	[Powers <i>et al.</i> (1994a)]
Lumped domain	$Sh_a^i = 340\theta_n^{0.87}Re_a^{0.71} \left(\frac{z}{D_{50}}\right)^{-0.31}$ (a) Eq. 23	[Imhoff <i>et al.</i> (1993)], model 4
Sphere	$Sh_a^i = 70.5 Re_a^{1/3} \theta_n^{4/9} S_{n_i}^{5/9} \phi^{-2/3} \left(\frac{D_{50}}{D_{n_i}}\right)^{5/3}$ (b) Eq. 24	[Geller and Hunt (1993)]
Multiple sphere	$Sh_d^{i,m} = 36.8 Re_a^{0.654}$ Eq. 25	[Powers <i>et al.</i> (1994b)]

(a): $z_1/D_{50} = 7$ for conditions without dissolution fingering [Imhoff and Miller (1996)]

(b): [Imhoff *et al.* (1994)]

where:

Sh_a^i : aqueous-phase Sherwood number for species $i = (K_a^i D_{50}^2) / D_a^i$ (-)

θ_n : volumetric fraction of the nonaqueous phase (-)

Re_a : aqueous-phase Reynolds number = $(D_{50}v_a) / \nu_a$ (-)

Sc_a^i : aqueous-phase Schmidt number for species $i = \nu_a / D_a^i$ (-)

D_M : diameter of a “medium” sand grain assumed as 0.05 cm (m)

D_{10}, D_{50}, D_{60} : particle diameter such that 10%, 50%, or 60% of porous media are finer by weight (m)

C_u : uniformity coefficient = D_{60} / D_{10} (-)

θ_{n_i} : initial volumetric fraction of the nonaqueous phase (-)

$Sh_a^{i,m}$: modified aqueous-phase Sherwood number for species $i = (K_a^i D_{50}) / D_a^i$ (-)

z_1 : distance from the column inlet (m)

S_{n_i} : initial nonaqueous phase saturation (-)

2.1.3 Volatilization

In the porous medium, volatilization means the transfer of gaseous substances from their aqueous (solubilized) or solid phase (adsorbed). Various factors influence the rate of volatilization, including the concentration of substance in the medium, the water saturation of medium, the properties of the aquifer (temperature, porosity, presence of organic matters) and so on [Lyman *et al.* (1982)]. Volatilization is greater in the non-saturated zone than in saturated zone. Some experimental work shows that as water saturation increases in a porous medium volatilization of substances decreases [Acher *et al.* (1989)]. The adsorption of volatile organic compounds (such as PCE or other chlorinated compounds) on organic matter reduces volatilization. On the other hand, increasing the temperature and air circulation of the porous medium can increase volatilization [Zytner *et al.* (1989)].

Several laws are used to estimate the volatilization of the NAPL in the porous medium. Raoult's law and Henry's law are the most frequently used [Cohen and Mercer (1993)]. Henry's law can estimate the vapor pressure of a dissolved substance in water using a constant, the Henry's law constant. It can be described as follows (Eq. 26):

$$P_v = K_H C_w \quad \text{Eq. 26}$$

where:

- P_v : pressure of the vapor pressure of a dissolved substance in water (atm)
- K_H : Henry's constant ($\text{atm}\cdot\text{m}^3\cdot\text{mole}^{-1}$)
- C_w : concentration of dissolved substance ($\text{mole}\cdot\text{m}^{-3}$)

Vapor pressures and Henry's constants of the pollutants constituting our DNAPL are shown in the following table (Table 10).

Table 10: Vapor pressure and Henry's constant of certain pollutants constituting our DNAPL (at 10 °C)

DNAPL	Vapor pressure (mm Hg)	Henry's constant ($\text{atm}\cdot\text{m}^3\cdot\text{mole}^{-1}$)	Reference
Carbon tetrachloride	90	3.02×10^{-2}	[Cohen and Mercer (1993)]
Hexachlorobutadiene	0.150	2.60×10^{-2}	[Cohen and Mercer (1993)]

Normally when the value of Henry's constant increases the chemical's volatilization capacity also increases. For our DNAPLs the Henry's constants of the most important components are not very high, so one can say that our DNAPL has low volatility. However, Henry's law considers the vapor pressure of a pure substance. Our DNAPLs contain several compounds and to estimate the volatilization of a mixed system we can use the Raoult's law. Raoult's law developed from Henry's law by adding the mole fraction of each component in the system (Eq. 27 and Eq. 28):

$$P_{vi} = X_i P'_{vi} \quad \text{Eq. 27}$$

$$P_{vt} = \sum P_{vi} \quad \text{Eq. 28}$$

where:

- P_{vi} : vapor pressure of component i in the mixing system (Pa)
- P'_{vi} : pure vapor pressure of the component i (Pa)
- P_{vt} : total vapor pressure in the mixing system (Pa)

In regard to vapor transport in a porous medium, several authors have proposed models. The main mechanism in these models is macroscopic diffusion [Zytner *et al.* (1989); Baehr and Corapcioglu (1987); Jury *et al.* (1990); Sleep and Sykes. (1989); Falta *et al.* (1989); Brusseau (1991)]. The dense vapor in the non-saturated zone usually will sink below the water table, and how it migrates into the saturated zone will be influenced by medium's heterogeneities [Cohen and Mercer (1993)].

2.1.4 Viscosity

A fluid's viscosity is a measure of its resistance to flow. Viscosity is an important parameter for DNAPL recovery remediation. It helps to determine the exact flow rate of pure phase recovery. Viscosity can be defined in two different ways: dynamic viscosity (absolute viscosity), μ , and kinematic viscosity, ν (Eq. 29):

$$\nu = \frac{\mu}{\rho} \quad \text{Eq. 29}$$

where:

- ν : kinematic viscosity ($\text{m}^2\cdot\text{s}^{-1}$)
- μ : dynamic viscosity (Pa.s)
- ρ : density ($\text{kg}\cdot\text{m}^{-3}$)

Most fluids have a constant viscosity; these fluids are named Newtonian. Pressure has very little influence on the Newtonian fluid (except when the pressure is extremely high). Viscosity tends to decrease as temperature increases; for example, water's viscosity changes from 1.002 cP to 0.403 cP if the temperature increases from 20 to 70 °C [Kestin *et al.* (1978)].

There are various ways of estimating the viscosity of a mixture of compounds. This estimation depends on additive properties (*e.g.* dilution rate of the components, viscosities, densities, fraction of components, different densities, impurity content and temperature) [Centeno *et al.* (2011)].

There are some mixing rules and models which can be used to predict the viscosity of mixtures with different components. Arrhenius (1887) was the first person to propose the rules to estimate the viscosity of mixtures [Arrhenius (1887)]. Bingham was one of the first who looked at the theoretical and experimental bases together to predict the viscosity of binary mixtures [Bingham (1914)]. Kendall and Monroe proposed an equation based on the fractions of components which had a good estimation with the measured viscosities [Kendall and Monroe (1917)]. Some other authors have used more complex equations with parameters calculated from experimental measurements to predict the viscosities [Walther (1931); Cragoe (1933); Ishikawa (1958); Lobe (1973); Twu and Bulls (1981); Miadonye *et al.* (2000)]. For the heavy oil and liquid hydrocarbons, various expressions have also been used to predict their viscosities [Mehrotra (1990); Mehrotra (1991); Mehrotra *et al.* (1996)].

Table 11 and Table 12 show the various models for estimating viscosities for mixtures with different components (respectively for pure mixing rules and for mixing rules with additional parameters and excess functions).

Table 11: Pure mixing rules with blending index for calculating the viscosity of mixtures

Author	Equation	Reference
Arrhenius	$\log\mu = X_a \log\mu_a + X_b \log\mu_b + \dots$ Eq. 30	[Arrhenius (1887)]
Bingham	$\frac{1}{\mu} = \frac{X_a}{\mu_a} + \frac{X_b}{\mu_b} + \dots$ Eq. 31	[Bingham (1914)]
Kendall and Monroe	$\mu^{1/3} = X_a \mu_a^{1/3} + X_b \mu_b^{1/3} + \dots$ Eq. 32	[Kendall and Monroe (1917)]
Refutas	$VBI_i = 10.975 + 14.534 \ln[\ln(v_i + 0.8)]$ Eq. 33	[Baird (1989)]
	$VBI_B = X_a VBI_a + X_b VBI_b + \dots$ Eq. 34	
	$v = e^{e^{\left(\frac{VBI_B - 10.975}{14.534}\right)}} - 0.8$ Eq. 35	
Chevron	$VBI_i = \frac{\log v_i}{3 + \log v_i}$ Eq. 36	[Riazi (2005)]
	$VBI_B = \sum_{i=1}^n X_i VBI_i$ Eq. 37	
	$v = 10^{\left(\frac{3VBI_B}{1 - VBI_B}\right)}$ Eq. 38	

where:

VBI_i : viscosity blending index component (-)

μ_i : dynamic viscosity of each component of the blend (Pa.s)

X_i : mass fraction of each component of the blend (-)

v_i : kinematic viscosity of each component of the blend (mm²/s)

Table 12: Mixing rules with extra-parameters and excess function for calculating the viscosity of mixtures

Author	Equation	Reference
Walther	$\log[\log(v + C_\mu)] = X_a \log[\log(v_a + C_\mu)] + X_b \log[\log(v_b + C_\mu)]$	Eq. 39 [Walther (1931)]
Lederer	$\ln \mu = X'_a \ln \mu_a + X'_b \ln \mu_b$	Eq. 40
	$X'_a = \frac{\alpha_\mu X_a}{\alpha_\mu X_a + X_b}$	Eq. 41
	$X'_b = 1 - X'_a$	Eq. 42
	$\frac{\mu}{\mu_b} - 1 = [\alpha_\mu \ln(\frac{\mu_a}{\mu_b})] X_a$	Eq. 43
Shu	$\alpha'_\mu = \frac{17.04 \Delta \rho^{0.5237} \rho_a^{3.2745} \rho_b^{1.6316}}{\ln(\frac{\mu_a}{\mu_b})}$	Eq. 44 [Shu (1984)]
Grunberg and Nissan	$\ln \mu = X_a \ln \mu_a + X_b \ln \mu_b + X_a X_b G_{ab}$	Eq. 45 [Grunberg and Nissan (1949)]
Power	$\mu = (X_a \mu_a^{n_\mu} + X_b \mu_b^{n_\mu} + \dots)^{1/n_\mu}$	Eq. 46 [Centeno <i>et al.</i> (2011)]
Twu and Bulls	$\ln[\ln(v + 0.7)] = X \ln T_K + b_\mu$	Eq. 47 [Twu and Bulls (1981)]
Reik	$v_i = \frac{X_i v_{i0}}{\gamma_i^{1/3}}$	Eq. 48 [Reik (1955)]
Ratcliff and Khan	$(\ln v)^{id} = \sum X_i \ln v_i$	Eq. 49
	$(\ln v)^{real} = \sum X_i \ln v_i \pm (\ln v)^{E_\mu}$	Eq. 50 [Ratcliff and Khan (1971)]

where:

v_i : kinematic viscosity of each component of the blend ($\text{mm}^2 \cdot \text{s}^{-1}$)

C_μ : empirical constant for viscosity determination (-)

α_μ : empirical constant for viscosity determination (-)

α'_μ : empirical constant for viscosity determination (-)

n_μ : number of the components in the mixtures (-)

b_μ : empirical constant for viscosity determination (-)

T_K : temperature (K)

γ_i : activity coefficient (-)

E_μ : empirical constant for viscosity determination (-)

The pure mixing rules [Eq. 30 to Eq. 32 in Table 11] use the viscosity of each component and their volume or weight fractions (*e.g.* Arrhenius equation, Bingham equation, and Kendall and Monroe equation) [Arrhenius (1887); Bingham (1914); Kendall and Monroe (1917)]. Some mixing rules with a viscosity blending index can be used to predict mixing viscosities. The most commonly used methods are the Refutas index method and the Chevron method [Baird (1989); Riazi (2005)]. The equations of these methods (Eq. 33 to Eq. 38) are also presented in Table 11.

Several authors have developed the traditional mixing rules by adding in extra parameters (which are normally obtained by mathematical estimation) (Table 12, Eq. 39 to Eq. 50). Walther developed an equation that calculates an extra parameter by regression analysis [Walther (1931)]. Lederer and Shu added an expression to the Arrhenius equation to estimate the fraction of components [Lederer (1933); Shu (1984)]. The Grunberg-Nissan equation has also modified Arrhenius by using an empirical parameter [Grunberg and Nissan (1949)]. Power modified Kendall and Monroe's equation by using an exponent in its estimation [Centeno *et al.* (2011)]. Twu and Bulls took account of the influence of temperature in their equation [Twu and Bulls (1981)]. Reik developed the fictitious method which requires the activity coefficients of the components in the system [Reik (1955)]. Ratcliff and Khan modified the Arrhenius equation by an excess function to take account of the deviation between ideal mixing and real mixing [Ratcliff and Khan (1971)].

2.2 Multiphase flow in porous media

2.2.1 Different scales in porous media

In the saturated zone, porous media contain pores that are usually filled with a fluid. Porous media are intricate systems where various phenomena influence fluid flow. When the medium has multiphase flow, the system is even more complex. To better understand flow in porous medium, the scale concept needs to be understood. Understanding flow dynamics in porous media requires observation at three different scales: the pore scale (microns), the Darcy scale (centimeters to meters) and the large scale (kilometers) (Figure 16) [Quintard *et al.* (2001)].

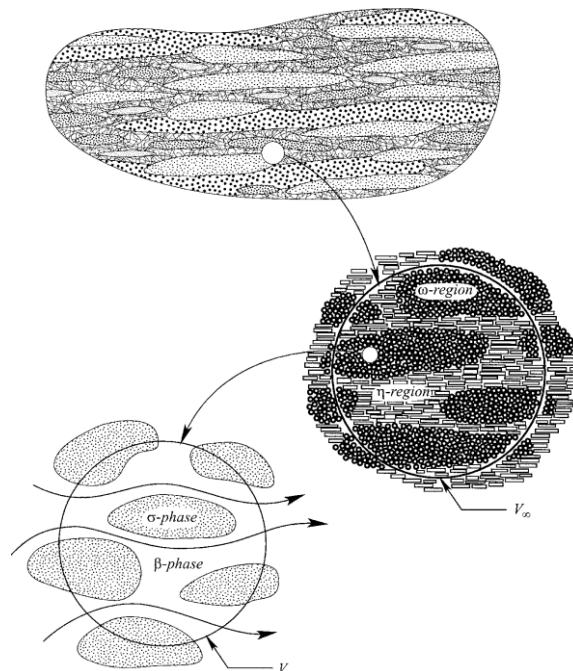


Figure 16: Different scales in porous media [Quintard *et al.* (2001)]

At pore scale (or microscopic scale), the characteristic values are the average pore diameter or the grain diameter in the medium. In the case of a single phase, flow theory is described by the Navier-Stokes equations. Two-phase flow situations are more complex; since the pores do not have equal access to phase flow and some phases may be trapped or disconnected within the media [Mercer and Cohen (1990)]. The Darcy scale (or macroscopic scale) is based on the

existence of an average pore volume. At this scale, we can define the medium's average characteristics, for example, porosity, permeability, and saturation. At the same time, heterogeneity at the microscopic scale is negligible because average pore volume is considered as an average value. In practice, a representative elementary volume (REV) containing many pores is used in order to get a macroscopic description representing the effective behaviour of the porous medium [Whitaker (1999)]. The large scale describes large media volume. At this kilometer-scale, the medium volume is so large that heterogeneity at macroscopic scale becomes more significant [Nsir (2009)].

Multiphase flow consists of three critical forces: 1) gravity or buoyancy forces (related to the density differences of the fluids); 2) viscous dynamic forces (related to phase viscosities and pressure gradients); and, 3) capillary forces (related to the adhesive forces between fluid pairs and the porous media) [Rose and Channapragada (1960)]. Each force by itself can change fluid flow and transport.

Studying phase interactions at the pore scale is important to understand the mechanisms of fluid flow but predicting migration at such a fine scale is generally considered to be impractical [Grant (2005)]. To use the process more practically, the continuum concept provides pore scale to local scale using a theoretical framework [Reeves and Celia (1996)].

2.2.2 Water and DNAPL saturations

In our case of two-phase flow (water-DNAPL), the volume of void space, V_v , is filled with either water or DNAPL. The proportions of DNAPL or water present, called water and DNAPL saturation (respectively S_w and S_n), can be calculated as follows (Eq. 51 to Eq. 53):

$$S_w = \frac{V_w}{V_v} \quad \text{Eq. 51}$$

$$S_n = \frac{V_n}{V_v} \quad \text{Eq. 52}$$

$$S_w + S_n = 1 \quad \text{Eq. 53}$$

where:

S_w : water (wetting fluid) saturation (-)

S_n : DNAPL saturation (-)

V_v : volume of void-space (m^3)

V_w : volume of water (m^3)

V_n : volume of DNAPL (m^3)

Figure 17 illustrates saturation differences in porous media.

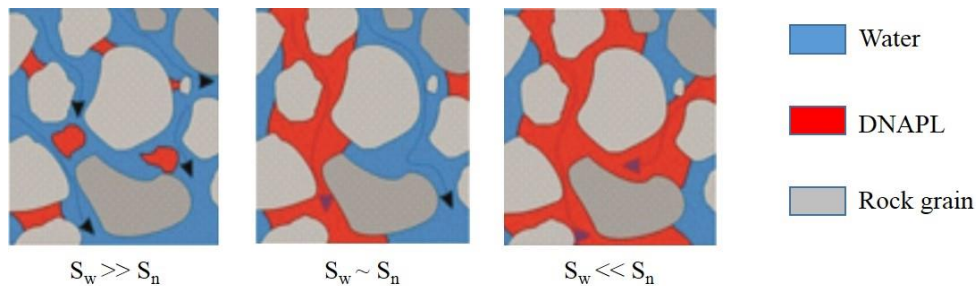


Figure 17: Illustration of water and DNAPL saturation differences

2.2.3 Interfacial tension

When a system presents two immiscible phases it has a contact surface between the two phases; in this area the various molecules interact. This contact zone between two fluids can be called an interface. The tension between a liquid and its vapor is named surface tension. Normally, when a liquid has a high surface tension it can produce a large residual saturation in the porous medium [Mercer and Cohen (1990)]. For a two-immiscible liquid system (*e.g.* DNAPL-water), the tension existing in the contact zone is called interfacial tension. It is the energy per unit of the interface formed between two immiscible liquids (N.m^{-1}).

In general, interfacial tension decreases with increasing temperature (*e.g.* $5.5 \times 10^{-5} (\text{N.m}^{-1}) \text{ } ^\circ\text{C}^{-1}$ for the crude oil-water systems) and can also be influenced by pH, the addition of surfactants and the substances in solution [Schowalter (1979)]. The interfacial tension in the DNAPL-water system is directly related to the capillary pressure in the interface [Mercer and Cohen (1990)]. The interfacial tension with water systems vary between zero for completely miscible liquids and $72 \times 10^{-3} \text{ N.m}^{-1}$ for absolutely immiscible liquids ($72 \times 10^{-3} \text{ N.m}^{-1}$ is the surface tension of air-water at $25 \text{ } ^\circ\text{C}$) [Lyman *et al.* (1982)].

2.2.4 Wettability and Contact Angle

Wettability describes the extent to which a fluid adheres to the surface of a solid in a system composed of at least two fluids. The solid has a greater affinity for the fluid that has the smallest interaction energy at the interface. This “preferred” fluid is called the wetting fluid. The other fluid, with the higher interaction energy at the interface, is called the non-wetting fluid [Abdallah *et al.* (2007); Yuan and Lee (2013)]. Generally, for DNAPL-water systems, the DNAPL is considered as the non-wetting fluid and water as the wetting fluid. Wettability can be described and measured by the contact angle (θ) between the fluids and the solid surface [Hiemenz and Rajagopalan (1997)].

Figure 18 shows wetting of different fluids. Fluids with a low contact angle ($< 90^\circ$) have high wettability. Those with a high contact angle ($> 90^\circ$) have low wettability.

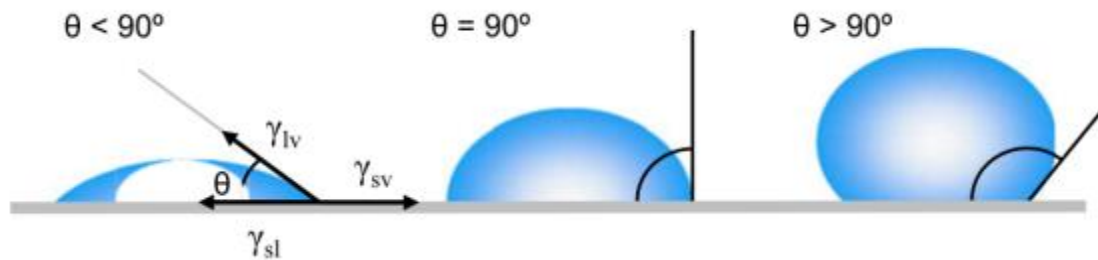


Figure 18: Wetting in different fluids [Yuan and Lee (2013)]

For a two-phase incompressible fluid system, such as DNAPL and water, the contact angle between the fluids and the solid surface can be described by the Laplace-Young equation as below (Eq. 54) as reported by [Nsir (2009)]:

$$\cos\theta = \frac{\sigma_{ns} - \sigma_{ws}}{\sigma_{nw}} \quad \text{Eq. 54}$$

where:

θ : contact angle between the fluids and the solid surface ($^\circ$)

σ_{ns} : interfacial tension between the non-wetting phase and the solid surface (N.m^{-1})

σ_{ws} : interfacial tension between the wetting phase and the solid surface (N.m^{-1})

σ_{nw} : interfacial tension between the non-wetting phase and wetting phase (N.m^{-1})

The above equations show that the interfacial tension has an important influence on the wettability and contact angle. Wettability in the DNAPL-water system can be affected by several factors, for example, the medium's environmental characteristics (*e.g.* salt concentrations [Kueper *et al.* (2003)]), the presence of surfactants, and the medium's saturation history [Mercer and Cohen (1990)]. Wettability generally increases (the contact angle decreases) in DNAPL phases as surfactants are added [Mercer and Cohen (1990)]. Villaume (1985) showed that the contact angle is smaller when DNAPLs are spread in a non-contaminated environment than in a medium already contaminated with DNAPLs as reported by Villaume [Villaume (1985)].

Wettability is not set over time, so for former pollution sites and in areas extremely saturated with DNAPL, we observe that water can only be present in a very low saturation and so the DNAPL becomes wetting (weathering). Moreover, depending on the nature of the soil, which is by definition heterogeneous, we see that the DNAPL can be wetting and non-wetting [Abdallah *et al.* (2007)].

2.2.5 Capillary Pressure

In porous media, capillary pressure is an important parameter because it controls fluid flow. In systems with two immiscible fluids, when the system is stable, there is an interface between the wetting and non-wetting phases within the pores. Pressure affecting this interface is called capillary pressure. The capillary pressure can be defined as the difference between the pressures of the wetting and non-wetting fluids [Wilson *et al.* (1990)]. Figure 19 shows the interface between two phases; this interface is curved by the effect of a pressure discontinuity, where the non-wetting phase pressure is greater than the wetting phase pressure.

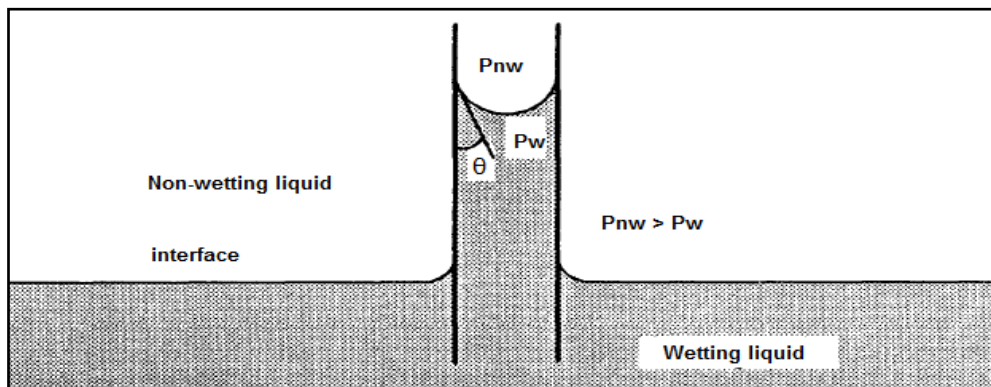


Figure 19: Illustration of a capillary tube immersed in a liquid [Wilson *et al.* (1990)]

As mentioned previously for a DNAPL-water system, the DNAPL is generally regarded as the non-wetting fluid and the water is regarded as the wetting fluid. Since the DNAPL pressure is greater than that of water, the capillary pressure can be defined as follows (Eq. 55):

$$P_c = P_n - P_w \quad \text{Eq. 55}$$

where:

P_c : capillary pressure (Pa)

P_n : pressure of non-wetting fluid (Pa)

P_w : pressure of the wetting fluid (Pa)

By combining the capillary pressure with the Laplace-Young equation (Eq. 54), we obtain the relationship between the capillary pressure, the pore contact angle and the radius of the capillary tube [Bear (1979)], as follows (Eq. 56):

$$P_c = \frac{2\sigma\cos\theta}{r} \quad \text{Eq. 56}$$

where:

P_c : capillary pressure (Pa)

$\sigma = \sigma_{nw}$: interfacial tension ($\text{mN}\cdot\text{m}^{-1}$)

θ : pore contact angle ($^\circ$)

r : mean radius of interface (cm), $r=r_{\text{tube}}/\cos\theta$

From Eq. 55 and Eq. 56, it is clear that the capillary pressure decreases as the interfacial tension decreases and as the contact angle increases. For a non-wetting fluid (such as the DNAPLs) to enter into a water-saturated zone a minimum pressure is required to overcome the resistance of the capillary pressure (*i.e.* entry pressure) [Schwille (1988)].

Therefore, P_c depends on the diameter of the tubes holding the liquids. *Figure 20* illustrates this phenomenon. In porous media, P_c depends greatly on the radii of the pore throats that correspond to the actual space between the glass beads (*Figure 21*). Therefore, P_c can vary locally.

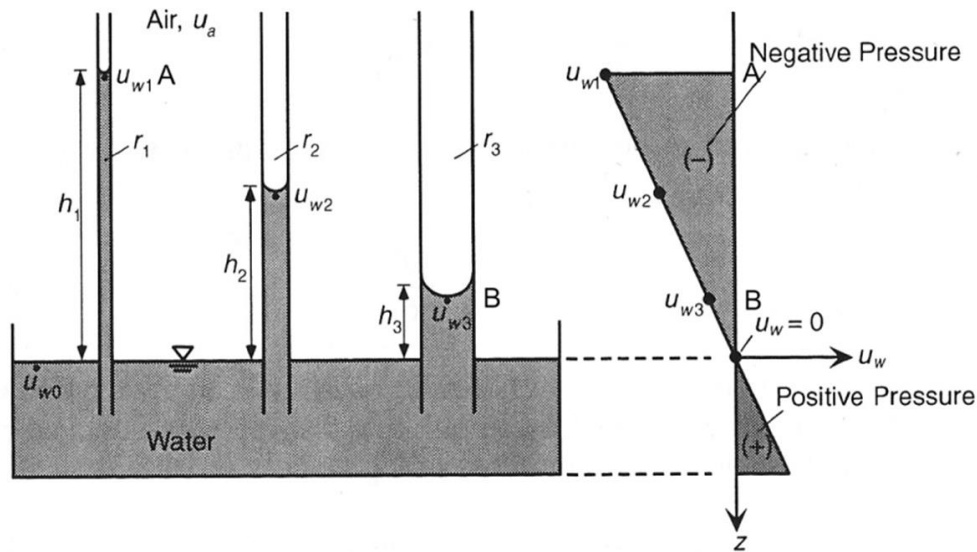


Figure 20: Analogy of capillary pressure at various sizes of the capillary tube ([Lu and Likos (2004)]

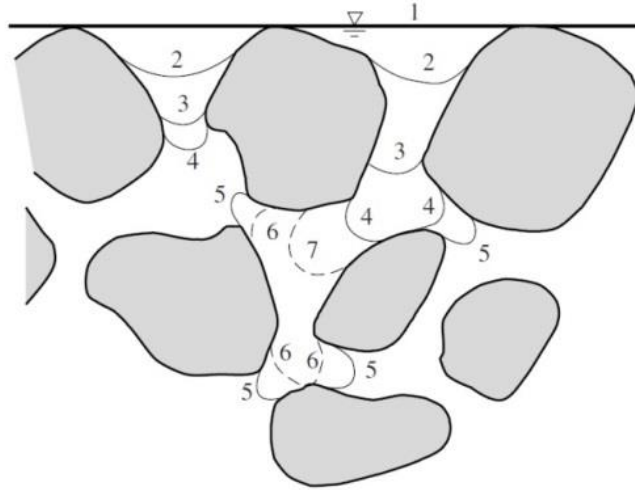


Figure 21: Various pore radii of the pore throat in the soil pores [Bear and Cheng (2010)]

Changes in the fluid-fluid interface depend on increasing or decreasing the phase pressure. Small pressure changes will cause a movement or deformation at the interface and contact angle. This phenomenon is described as ‘interface pinning’ [Braun and Holland (1994)].

2.2.6 Drainage-imbibition and residual saturations

The residual saturation is the volume of liquid that cannot be recovered from a porous medium by applying a pressure gradient. Decreasing residual saturation is one of the most important challenges in soil remediation engineering. The residual saturation of non-wetting fluids can be measured in the laboratory by drainage-imbibition experiments. Various researchers have defined residual saturation based on drainage-imbibition experiment curves [Bear (1972); Dullien (1992); Fetter (1994); Freeze and McWhorter (1997); Pickell *et al.* (1966)]. Figure 22 is an example of a drainage-imbibition curve.

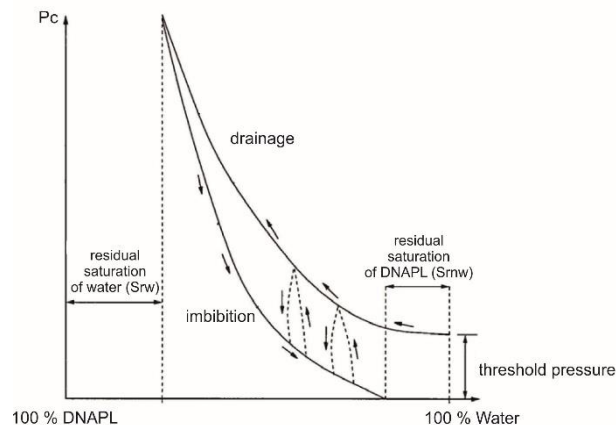


Figure 22: Drainage-imbibition curves (adapted from [Benremita (2002)])

For a drainage-imbibition experiment, when the capillary pressure is increased ($P_c = P_n - P_w$), drainage starts, and water saturation begins to decrease (from 100%). Water saturation continues to decrease until no more water can exit the porous medium system; the water left in the medium is called "irreducible water saturation" (S_{rw} or residual water saturation). If the capillary pressure is decreased, imbibition starts and DNAPL saturation begins to decrease (from $(1 - S_{rw})$). By reducing the capillary pressure, DNAPL saturation continues to decrease

until a certain point at which no more DNAPL can exit the system. This DNAPL saturation in the system is called "residual DNAPL saturation" (S_m). The threshold pressure is the minimum force required to overcome the resistance of the capillary pressure (entry pressure) of a porous medium.

The imbibition and drainage P_c - S_w curves do not overlap. This hysteresis in P_c - S_w behaviour occurs because pore drainage and pore imbibition are distinct [Beliaev and Hassanizadeh (2001); Gerhard and Kueper (2003a); Gerhard and Kueper (2003b); Grant (2005)]. During the imbibition process, the DNAPL is displaced; at the same time, some DNAPL is trapped (snap-off or by-passing trapping) and is difficult to displace (see section 2.2.10).

Nowadays many aquifer treatment technologies and research activities exists, like pump and treat, thermal treatment, chemical reactions, and injection of surfactants or foam. The main goal of all these technologies is to decrease the residual NAPL saturation as much as possible.

The main factors that affect residual saturation are same as for capillary pressure: the relative permeability-saturation factors discussed in the previous section. It is also known that residual saturation increases with decreasing grain size and permeability [Schwille (1988); Wilson *et al.* (1990); Hoag and Marley (1986); Zytner *et al.* (1993); Boley and Overcamp (1998); Gerhard (2002); Grant (2005); Pickell *et al.* (1966); Bear (1972); Dullien (1992); Fetter (1994); Freeze and McWhorter (1997)].

Entry pressure

The Leverett function (1941) proposed the following equation (Eq. 57) [Leverett (1941)]:

$$P_e^{\text{dim}} = \frac{P_e}{\sigma} \left[\frac{k}{\phi} \right]^{\alpha_{P_e}} \quad \text{Eq. 57}$$

where:

- P_e^{dim} : dimensionless entry pressure (measured in a different porous medium) (-)
- P_e : measured entry pressure of the investigated porous media (Pa)
- $\sigma = \sigma_{\text{NW}}$: Interfacial tension between the non-wetting phase and wetting phase ($\text{N}\cdot\text{m}^{-1}$)
- α_{P_e} : Empirical constant for P_e determination, often set to 0.5 (-)

Kueper and Frind (1991) found a value of 0.65 for α and 0.186 for P_e^{dim} for a set of PCE-water capillary pressure curves measured using samples of sand with K varying between 4.3×10^{-3} and $1.2 \times 10^{-2} \text{ cm}\cdot\text{s}^{-1}$ [Kueper and Frind (1991a)].

Dupuy *et al.* (2011) presented an equation, derived from the Young-Laplace equation, to determine the entry pressure (Eq. 58) [Dupuy *et al.* (2011)]:

$$\Delta P_c = \frac{2\beta_p \sigma_{\text{HA-EO}} \cos\theta_{\text{HA-EO-M}}}{r_{p,\text{max}}} \quad \text{Eq. 58}$$

where:

- ΔP_c : breakthrough pressure, threshold above which the non-wetting liquid passes through the membrane (Pa)
- $\sigma_{\text{HA-EO}}$: interfacial tension between the essential oil and the hydro-alcoholic solution ($\text{mN}\cdot\text{m}^{-1}$)
- β_p : pore shape parameter ($\beta_p = 1$ for cylindrical pores and $0 < \beta < 1$ for non-cylindrical pores)
- $\theta_{\text{HA-EO-M}}$: essential oil/hydro-alcoholic solution/membrane contact angle ($^\circ$)
- $r_{p,\text{max}}$: maximum radius of membrane pores (m)

2.2.7 Relative Permeability

When several fluids are present in a porous medium, they compete to fill the pore space. Because of this competition, the mobility of all fluids in the system will be reduced. The concept of relative permeability explains this decrease. It is the ratio between the effective permeability of fluid in the system and its "single" phase permeability. The relative permeability varies from 0 to 1 (Eq. 59 and Eq. 60) [Brooks and Corey (1964); Cohen and Mercer (1993)].

$$k_{ew} = k_{rw}k \quad \text{Eq. 59}$$

$$k_{en} = k_{rn}k \quad \text{Eq. 60}$$

where:

k_{ew} : effective permeability of the wetting phase (m^2)

k_{en} : effective permeability of the non-wetting phase (m^2)

k_{rw} : relative permeability of the wetting phase (-)

k_{rn} : relative permeability of the non-wetting phase (-)

k : intrinsic permeability (m^2)

Several studies showed that the relative permeability of a fluid can be defined as a function of its saturation in the porous medium [Luckner *et al.* (1989); Mualem (1976)]. Schwille (1988) proposed the relative permeability curve shown in Figure 23, for a DNAPL-water system [Schwille (1988)]:

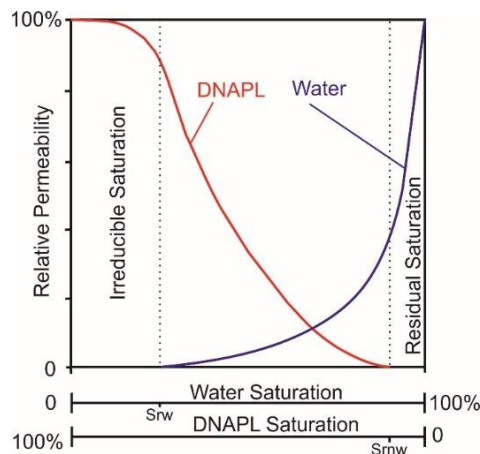


Figure 23: Relative permeability curve for a DNAPL-water system [Schwille (1988)]

From the relative permeability curve, we see that the relative permeability of DNAPL is normally greater than that of water at the same saturation and that when the relative permeability of DNAPL decreases, the relative permeability of water increases.

The principle of multiphase flow and relative permeability is illustrated in Figure 24. A phase's permeability depends in particular on how much the porosity is saturated by the other phase. The domain saturated in both NAPL and water, where both the NAPL and water phases are mobile, is called "funicular saturation state" [Williams and Wilder (1971)]. Beyond a certain level of water saturation, the NAPL phase is no longer continuous. The NAPL phase is then trapped in the residual state in the form of droplets that are dispersed in the insular saturation state, whereas the water phase remains mobile [Bear (1972); Mercer and Cohen (1990); Cohen and Mercer (1993); Huling and Weaver (1996)].

When NAPL saturation exceeds 70-80%, water is immobile and only the NAPL phase migrates to the "pendular saturation state" [Cohen and Mercer (1993)]. Therefore, above the residual saturation, the organic phase is mobile while below that saturation, it is immobile.

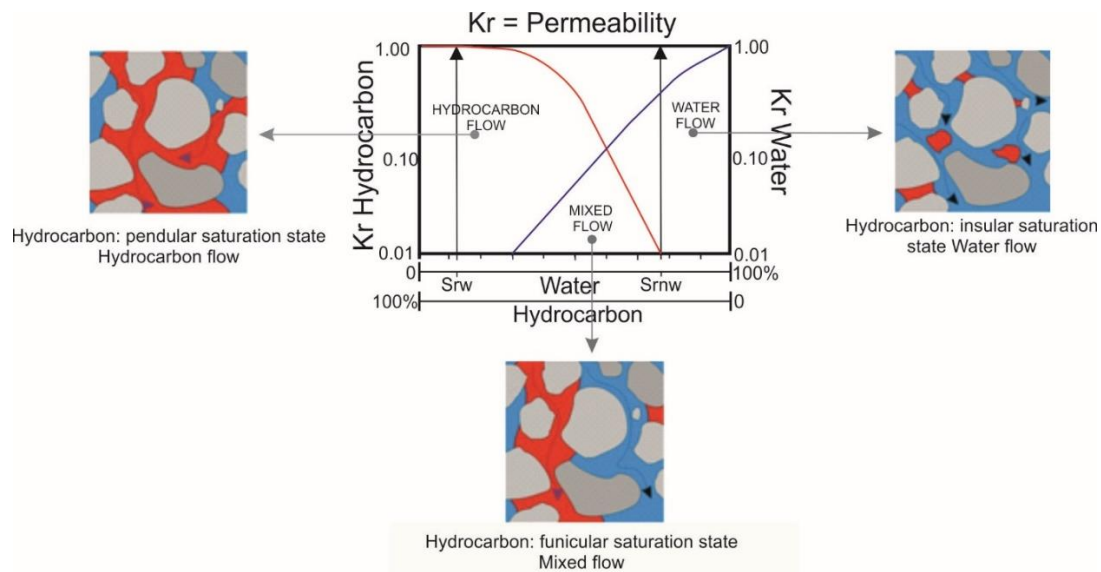


Figure 24: Relative permeabilities in a two-phase NAPL/water system (according to [Williams and Wilder (1971)])

2.2.8 Capillary pressure, relative permeability – saturation relationships, and main affecting factors

As considered in the previous section, wettability, saturation and capillary pressure are basically pore scale phenomena. If a medium is homogeneous, its capillary pressure also can be clearly defined at local scale. This means that capillary pressure at the pore scale is typically the same as at the local scale and can be equated to the difference between pressures averaged over REV [Morrow (1976); Melrose and Brandner (1974)]. However, it can be problematic to measure experimentally, when the capillary pressure is close to the residual saturation. In this case, capillary pressures are always determined to be zero [Hassanizadeh and Gray (1993)]. Also, during experiments, interaction between fluids is apparent; this kind of problem can only be considered on the pore scale. The determination of capillary pressure – saturation relationships needs several drainage–imbibition experiments. The main affecting factors for this process are pore size distribution, wettability, and interfacial tension. There is also a problem of heterogeneity, dead tails, dual porosity and fractures in porous media which can affect capillary pressure – saturation relationships. Lowry and Miller (1995) have analyzed the influence of pore size distribution on drainage-imbibition curves. They have shown that the influence of the imbibition curve was much higher than drainage [Lowry and Miller (1995)]. Wettability has much more effect on capillary pressure – saturation relationships [Morrow (1976)].

The main factors affecting wettability are as follows: i. fluid-fluid pair combination [Powers *et al.* (1996)]; ii. solid phase mineralogy [Anderson (1986)]; iii. surface roughness [Morrow (1975)]; pH [Lord *et al.* (2000)]; iv. the presence of organic acids and bases [Dubey and Doe (1993)]; v. exposure to coal tar [Powers *et al.* (1996); Villaume (1985)]; vi. exposure to synthetic gasoline [Powers and Tamblin (1995)]; vii. temperature [She and Sleep (1998)]; viii. uncovering to surface active solutes [Gaudin and Decker (1967); Jennings (1975)]; and finally, ix. phase pressure [Grant (2005)]. All these factors can change wettability; for porous media materials we have to consider them very mindfully.

One of the main parameters of multiphase flow is relative fluid permeability, which affects mobility in each phase. This means that relative permeability should be considered as well as other phenomena. Factors which affect the relative permeability, K_r , are: i. pore properties; ii. intrinsic permeability; iii. wettability; iv. interfacial tension; v. viscosity ratio [Demond and Roberts (1987)]. Demond and Roberts (1987) found that non-wetting fluid tends to flow in larger pores while wetting fluid flows in smaller pores; consequently pore-size distribution must affect relative permeability. They concluded that, in general, relative permeability is not a function of intrinsic permeability and even small interfacial tension will significantly change the shape of relative permeability curves [Demond and Roberts (1987)]. Viscosity only influences relative permeability at low intrinsic permeability [Larson *et al.* (1981)]. Abdallah *et al.* (2007) examined wettability and performed several experiments and compared by each factor [Abdallah *et al.* (2007)].

As one can see in Figure 25, there is also a considerable difference between water-wet and mixed-wet media. In mixed media water becomes more mobile (non-wetting) and that affects the relative permeability and the capillary pressure curve.

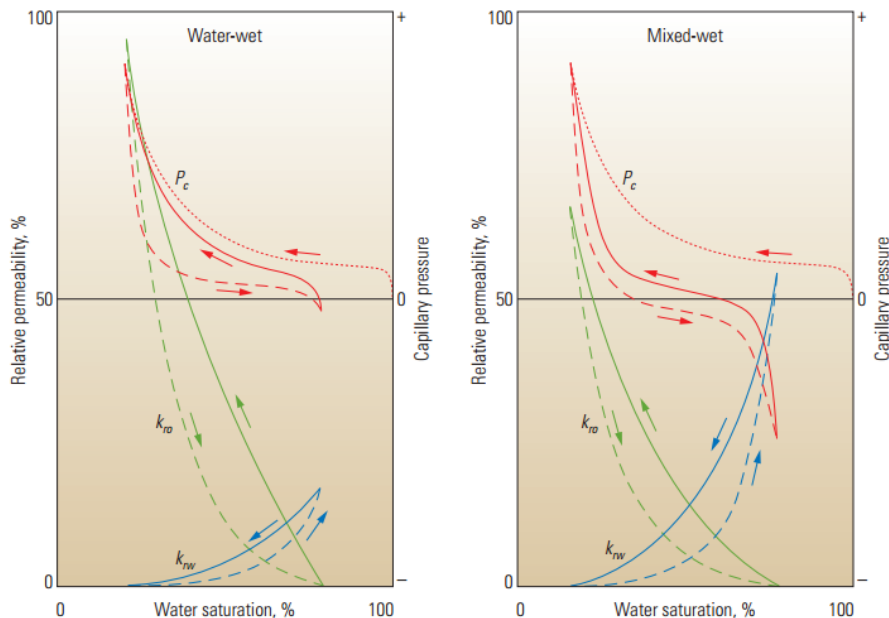


Figure 25: Capillary pressure and relative permeability for water-wet and mixed wet conditions [Abdallah *et al.* (2007)]

2.2.9 Retention Models k_r - S_w and P_c - S_w

Many researchers have used empirical relationships and experimental data-fitting by mathematical functions to obtain P_c - S_w and k_r - S_w curves (*e.g.* [van Genuchten (1980)] and [Brooks and Corey (1964)]). Numerical models generally use a van Genuchten-based (VG) or a Brooks-Corey-based (BC) constituent model. These constituent models are integrated with extensions of the relative permeability functions proposed by either [Burdine (1953)] or [Mualem (1976)]. In reservoir engineering, a commonly used expression is the Brooks-Corey and Burdine relationship. Aquifer treatment and remediation also use van Genuchten-Mualem relationships. Brooks-Corey-Mualem, van Genuchten-Burdine, and van Genuchten-Mualem relationships have been used successfully [O'Carroll *et al.* (2004)]. Seven different parametric models for capillary pressure – saturation and relative permeability functions are displayed in

Table 13 [Chen *et al.* (1999)]. All the models were tested by multi-step outflow-based experiments of DNAPL migration in porous media. Chen *et al.* (1999) discussed and concluded that the van Genuchten-Mualem (VGM), lognormal distribution-Mualem (LDM), Brutsaert-Burdine (BRB) and Gardner-Mualem (GDM) models successfully characterized two-fluid experimental data [Chen *et al.* (1999)].

Table 13: Two-fluid capillary pressure and permeability models [Chen *et al.* (1999)]

Models	Parameters	Capillary pressure Function	Permeability Function	Eq.
VGM & VGB (van Genuchten-Mualem/Burdine) [1], [2] and [3]	θ_{ws} θ_{rw} k α n	$S_{ew} = \frac{1}{[1 + (\alpha h_c)^n]^m}$ Eq. 61	(a) VGM: ($m=1-1/n$) $k_{rw} = S_{ew}^{0.5} \left[1 - \left(1 - S_{ew}^{\frac{1}{m}} \right)^{m-2} \right]$ Eq. 63	Eq. 62
			$k_{rn} = (1 - S_{ew})^{0.5} \left[1 - S_{ew}^{\frac{1}{m}} \right]^{2m}$ Eq. 64	Eq. 63
			(b) VGB: ($m=1-2/n$) $k_{rw} = S_{ew}^2 \left[1 - \left(1 - S_{ew}^{\frac{1}{m}} \right)^m \right]$ Eq. 66	Eq. 65
			$k_{rn} = (1 - S_{ew})^2 \left[1 - S_{ew}^{\frac{1}{m}} \right]^m$ Eq. 67	Eq. 66
				Eq. 67
BCM & BCB (Brook and Corey-Mualem/Burdine) [3] and [4]	θ_{ws} θ_{rw} k h_c λ η	$S_{ew} = \left(\frac{h_e}{h_c} \right)^\lambda$ Eq. 68	(c) BCM: $k_{rw} = S_{ew}^{\eta+2+2/\lambda}$ Eq. 69	Eq. 69
			$k_{rn} = (1 - S_{ew})^\eta \left[1 - S_{ew}^{1+1/\lambda} \right]^2$ Eq. 70	Eq. 70
			(4) BCB: ($m=1-1/n$) $k_{rw} = S_{ew}^{3+2/\lambda}$ Eq. 72	Eq. 71
			$k_{rn} = (1 - S_{ew})^2 \left[1 - S_{ew}^{1+2/\lambda} \right]$ Eq. 73	Eq. 72
LNM (Lognormal Distribution-Mualem) [5] and [1]	θ_{ws} θ_{rw} k h_m σ_b η	$S_{ew} = F_n \left[\frac{\ln \left(\frac{h_m}{h_c} \right)}{\sigma_b} \right]$ Eq. 74	$k_{rw} = S_{ew}^\eta \{ F_n [F_n^{-1}(S_{ew}) + \sigma_b] \}^2$ Eq. 75	Eq. 75
			$k_{rn} = (1 - S_{ew})^\eta \{ 1 - F_n [F_n^{-1}(S_{ew}) + \sigma_b] \}^2$ Eq. 76	Eq. 76
			$F_n(x) = \frac{1}{\sqrt{2\pi}} \int_{-\infty}^x \exp \left(-\frac{x^2}{2} \right) dx$ Eq. 77	Eq. 77
			$= \frac{1}{2} \operatorname{erfc} \left(\frac{x}{\sqrt{2}} \right)$ Eq. 78	Eq. 78
BRB (Brutsaert-Burdine) [2] and [6]	θ_{ws}, θ_{rw} k β_b, γ_b	$S_{ew} = \frac{\beta_b}{\beta_b + h_c^{\gamma_b}}$ Eq. 79	$k_{rw} = S_{ew}^2 [1 - (1 - S_{ew})^{1-2/\gamma_b}]$ Eq. 80	Eq. 80
			$k_{rn} = (1 - S_{ew})^{3-2/\gamma_b}$ Eq. 81	Eq. 81
GDM (Gardner-Mualem) [1] and [7]	θ_{ws}, θ_{rw} k α_g	$S_{ew} = \left(1 + \frac{1}{2} \alpha_g h_c \right) e^{-\frac{1}{2} \alpha_g h_c}$ Eq. 82	$k_{rw} = e^{-\alpha_g h_c}$ Eq. 83	Eq. 83
			$k_{rn} = \left(1 - e^{-\frac{1}{2} \alpha_g h_c} \right)^2$ Eq. 84	Eq. 84

[1]: [Mualem (1976); van Genuchten (1980)]; [2]: [Burdine (1953)]; [3]: [Luckner *et al.* (1989)]; [4]: [Brooks and Corey (1964)]; [5]: [Kosugi (1994); Kosugi (1996)]; [6]: [Brutsaert (1967)]; [7]: [Gardner (1958)]

where:

θ_{ws} : porosity of wetting phase, measured value (-)

θ_{rw} : residual porosity of wetting phase (-)

S_{ew} : effective saturation (-)

h_c : capillary pressure head (m)

VGM and VGB:

α : fitting parameter inversely proportional to the non-wetting fluid entry pressure value (m^{-1})

n : width of pore-size distribution (-)

BCM & BCB:

h_e : non-wetting fluid entry pressure (m)

η : fitting parameter (-)

λ_B : fitting parameter characterizing the pore-size distribution (-)

LNM:

$F_n(x)$: normal pore-radius distribution function (-)

h_m : related to the median of soil pore radius distribution function by the capillary pressure function (m)

σ_b : width of soil pore radius distribution function (-)

BRB:

β_b : fitting parameter proportional to the non-wetting fluid entry pressure value (m)

γ_b fitting parameter characterizing the pore-size distribution (-)

GDM:

α_g : fitting parameter inversely proportional to the non-wetting fluid entry pressure value (m^{-1})

S_{ew} is calculated as follows (Eq. 85):

$$S_{ew} = \frac{S_w - S_{rw}}{1 - S_{rw}} = \frac{\theta_w - \theta_{rw}}{\theta_{ws} - \theta_{rw}} \quad \text{Eq. 85}$$

where:

θ_w : porosity of water (-)

S_{ew} : effective saturation (-)

S_w : water saturation in the porous medium (-)

S_{rw} : residual water saturation in the porous medium (-)

The van Genuchten capillary pressure-saturation function is one of the most commonly used models in water environments, because it usually fits very well with experimental data [Liu *et al.* (1998)].

2.2.10 DNAPL trapping mechanisms

The DNAPL residual saturation, S_m , is due to various trapping phenomena: viscous fingering, capillary instability, by-passing, and surface trapping. If the DNAPL is non-wetting, no surface trapping phenomena take place [Anderson (1987); Homsy (1987); Chatzis *et al.* (1983); Lenormand *et al.* (1988); Powers *et al.* (1992)].

Viscous fingering is related to displacement instability. It depends on fluid densities, viscosities, directions, and velocities. Displacement instability is caused by DNAPL pools that were not flushed out by the displacement fluid being left behind the migration front (*continuum* rupture) [Lenormand *et al.* (1988)].

Capillary instability and by-passing trappings are related to capillary trapping mechanisms. Capillary instability occurs in high aspect ratio pores where the pore body is much larger than the pore throat resulting in a single droplets of residual DNAPL (snap-off trapping) (Figure 26). By-passing trapping occurs when wetting fluid flow disconnects the non-wetting fluid, causing DNAPL ganglia to be trapped in clusters of large pores surrounded by smaller pores (see Figure 27) [Anderson (1987); Homsy (1987); Chatzis *et al.* (1988); Powers *et al.* (1992)].

Thus, S_m tends to increase with increasing pore aspects ratios and pore size distribution.

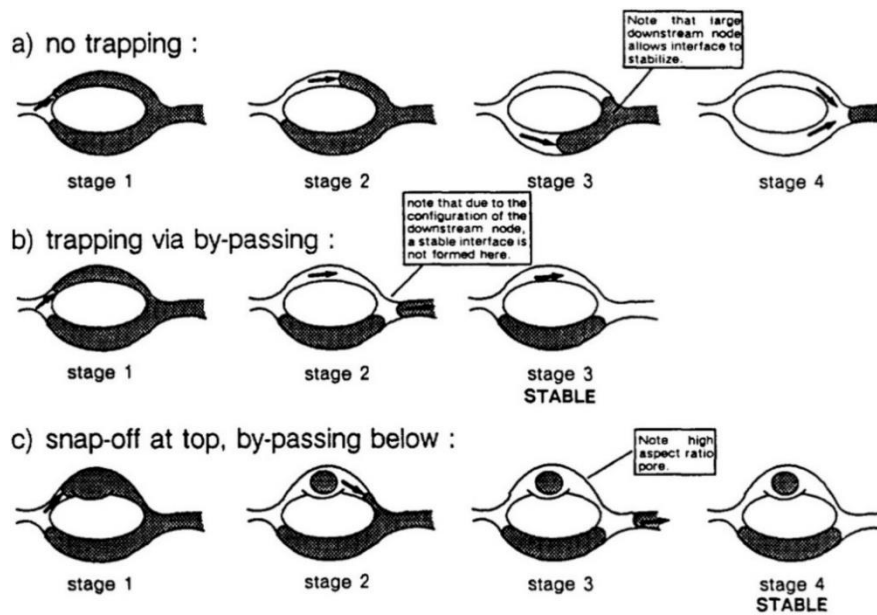


Figure 26: Capillary trapping mechanisms – by-passing (adapted from [Chatzis *et al.* (1983)])

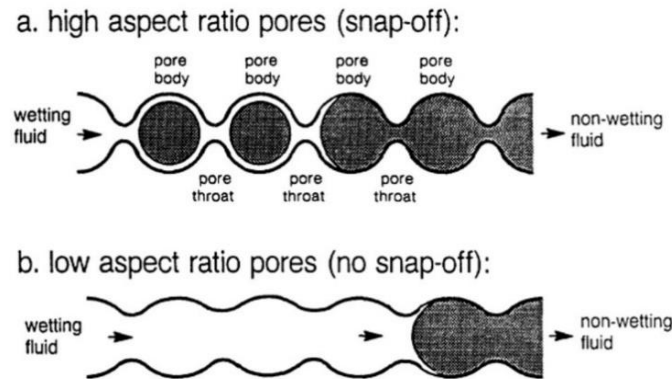


Figure 27: Capillary trapping mechanisms - snap-off (adapted from [Chatzis *et al.* (1983)])

2.2.11 Drainage-imbibition experimental work

Various researchers have experimentally investigated the migration behaviour of non-wetting fluids. Most of the environmental researchers did their investigations on a laboratory or small field scale and generally employed an ideal porous medium consisting of homogeneous blocks of sand (*e.g.* [Kueper *et al.* (1989); Illangasekare *et al.* (1995a); Hofstee *et al.* (1998); Rathfelder *et al.* (2003); O'Carroll *et al.* (2004)]. This approach helps to simplify the numerical model validation, which needs the parameters of the fluid (density, viscosity, wettability) and the porous media. Also, it considers how to describe the way the non-wetting fluid migrates. In

numerical models, it is difficult to examine heterogeneity of processes and also those with laboratory experiments. To build a numerical model and to use it, it is important to know the parameters of all the fluids and porous media.

That is why laboratory scale experiments have been investigated using known porous media parameters. This allows easy identification of the impact of the other factors on two-phase flow (*e.g.* thermal and chemical enhancement effects). For instance, Kueper and Frind (1992) conducted laboratory scale experiments to validate a model versus the visual observation of non-wetting fluid migration [Kueper and Frind (1992)]. Rathfelder *et al.* (2003) investigated the influence of surfactant on the interfacial tension [Rathfelder *et al.* (2003)]. Illangasekare *et al.* (1995a) used a dual-gamma attenuation system to measure very accurate non-wetting phase saturations [Illangasekare *et al.* (1995a)]. Hofstee *et al.* (1998) used visual inspection, photography and video recording to monitor the infiltration of perchloroethylene in water-saturated porous media [Hofstee *et al.* (1998)]. Saturation measurements by mass and volume balance were also widely used [Schwille (1988); Liu *et al.* (1998)]. A light transmission image capture and analysis was also successfully employed in one-dimensional porous media experiments [Gerhard and Kueper (2003b)], and there was no significant limit to saturation measurement.

2.2.12 Dimensionless numbers related to the displacement of DNAPLs

2.2.12.1 Capillary number, Bond number, total trapping number

The drop in IFT coupled with the change of viscosity in the non-wetting phase overcomes the capillary pressure (which keeps the DNAPL in the pores) [Pennell *et al.* (2014)]. Pennell *et al.* (1996) used a method to estimate NAPL mobilization in the porous medium [Pennell *et al.* (1996)]. This method uses two types of numbers: the capillary number (N_{ca}) and the Bond number (N_B). The capillary number can be expressed as (Eq. 86):

$$N_{ca} = \frac{v_w \mu_w}{\sigma \cos \theta} \quad \text{Eq. 86}$$

where:

v_w : Darcy's velocity of the wetting phase (upward direction is considered positive) (m.s^{-1})
 μ_w : dynamic viscosity of wetting phase (Pa.s)

The Bond number, N_B , is a function of gravitational forces and capillary pressure (Eq. 87):

$$N_B = \frac{g k k_{rw} \Delta \rho}{\sigma \cos \theta} \quad \text{Eq. 87}$$

where:

$\Delta \rho$: difference of densities between the wetting and non-wetting phase ($= \rho_w - \rho_n$) (kg.m^{-3})

If we combine the two numbers, one can obtain the total trapping number, N_T (Eq. 88):

$$N_T = \sqrt{N_{ca}^2 + 2N_{ca}N_B \sin \alpha_{N_T} + N_B^2} \quad \text{Eq. 88}$$

where:

α_{N_T} : angle between the direction of system flow and the horizontal direction ($^\circ$)

Pennell *et al.* (1996) ran several experiments with PerChloroEthylene (PCE) in columns (packed with quartz sand). They showed that for the PCE-water system the N_T is equal to 2×10^{-5} (at this value, the PCE stored in the pores start to move); when the N_T is over 1×10^{-4}

almost all of the PCE is removed [Pennell *et al.* (1996)]. Many experimental data show that as the N_{ca} is increased, the residual saturations are decreased [Lake (1989); Sheng (2015)].

2.2.12.2 Mobility ratio

Shear forces, which depend on the viscosity contrast between wetting and non-wetting liquids, cannot be neglected for viscous liquids such as coal tar, motor oil, and some crude oils [Ng *et al.* (1978)]. In this case, using the mobility ratio is proposed (m_r) [Dullien (1992)] (Eq. 89).

$$m_r = \frac{k_{2r}\mu_1}{k_{1r}\mu_2} \quad \text{Eq. 89}$$

where:

- m_r : mobility ratio (-)
- k_{1r} : relative permeability for the displaced phase (-)
- k_{2r} : relative permeability for the displacing phase (-)
- μ_1 : fluid dynamic viscosity for the displaced phase (Pa.s)
- μ_2 : fluid dynamic viscosity for the displacing phase (Pa.s)

Viscous fingering tends to reduce with increased temperature; this phenomenon is related to the fact that, given the reduced NAPL viscosity, the ratio of the mobility of the displacing fluid to the displaced fluid is lower [Lenormand *et al.* (1988); Munson *et al.* (2009)].

Lenormand *et al.* (1988) have shown three multiphase domain displacements corresponding to a different "basic" mechanism where only one kind of force is acting (the two others being negligible at the scale of the network) [Lenormand *et al.* (1988)]:

- Stable displacement: the principal force is due to the viscosity of the injected fluid (capillary effects and pressure drop in the displaced fluid are negligible)
- Viscous fingering: the principal force is due to the viscosity of the displaced fluid (capillary effects and pressure drop in the displacing fluid are negligible)
- Capillary fingering: at low N_{ca} the viscous forces are negligible in both fluids and the principal force is due to capillarity.

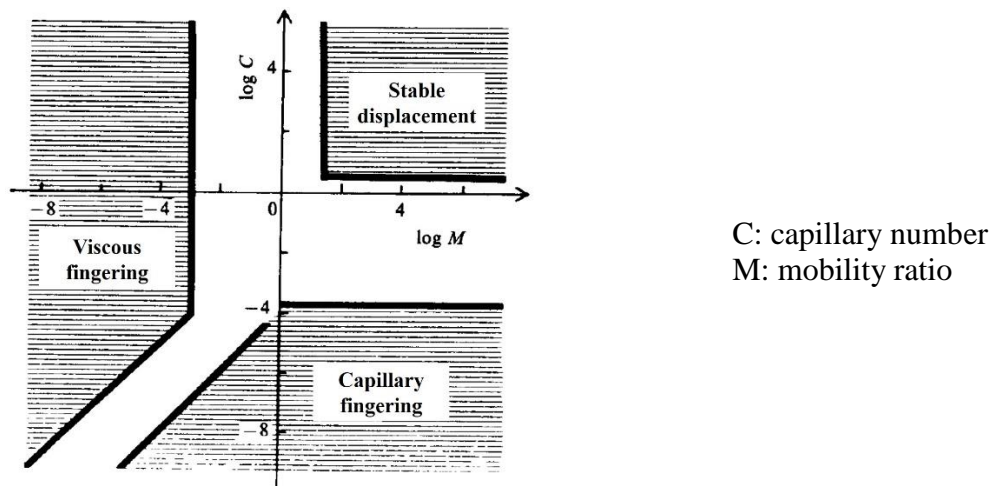


Figure 28: Phase-diagram of multiphase domain displacement [Lenormand *et al.* (1988)]

2.3 Effect of thermal enhancement on DNAPL mobility in saturated porous media

2.3.1 Heating technologies

Various technologies exist for injecting heat into soils, the most commonly used being the hot water flooding approach.

Hot water flooding was first developed and used by the oil industry to increase crude oil recovery [Burger *et al.* (1984); Edmondson (1965); Fournier (1965)]. It was later used in the field of contaminated sites and soils remediation. Many large-scale applications have been reported in this domain [Fulton *et al.* (1991); US EPA (2000)], yet this technique cannot be directly transferred to the domains of contaminated sites and soils [Dokla (1981); Fournier (1965); Goodyear *et al.* (1996); Okasha *et al.* (1998)]. This technique is similar to free product recovery with groundwater extraction (for LNAPL) or water flooding (for DNAPL) (see section 1.1.6); the difference lies in the fact that the hydraulic gradient applied to increase NAPL recovery is generated by injecting hot water. This hot water injection reduces interfacial tension and viscosity of the NAPL, leading to their enhanced mobility [Kingston *et al.* (2014)].

Figure 29 illustrates a schematic representation of hot water flooding.

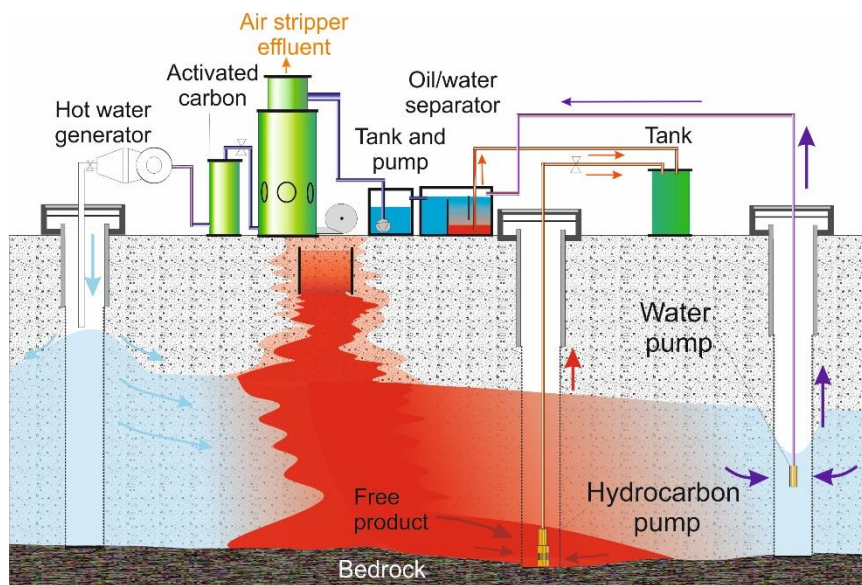


Figure 29: Schematic representation of Hot Water Flooding (adapted from [Colombano *et al.* (2010)])

Other heat injection technologies derived from treatments of the unsaturated zone can also be adapted to heating the saturated zone.

- Thermal Conduction Heating (TCH), also called *In Situ* Thermal Desorption (ISTD), consists in heating the underground by conduction and simultaneously applying negative pressure,
- Steam-Enhanced Extraction (SEE) consists in injecting vapor to extract organic compounds,
- RadioFrequency Heating (RFH) consists in injecting electromagnetic waves in the microwave frequency range into the soil,

- Electrical Resistance Heating (ERH) heats the soil by passing a flow of alternating electric current through the soil matrix placed between an electrode network (hexagonal or triangular arrays). The resistance provided by the porous media increases the temperature.

2.3.2 Influence of temperature on dynamic viscosity

Significant reductions in water and NAPL viscosities have been reported when temperature increases (*e.g.* [Edmondson (1965); Sleep and Ma (1997); Villaume *et al.* (1983)]).

Typically, chlorinated solvents are more fluid than water (viscosity less than 10^{-3} Pa.s⁻¹). In addition, under the effect of temperature, when a liquid expands, the interactions between the molecules fall and viscosity falls. The viscosity of a chlorinated solvent is generally reduced by 1% per degree Celsius [Davis (1997)]. The study by Sleep and Ma (1997) on measuring PCE viscosity as a function of temperature observed this significant viscosity reduction with increasing temperature [Sleep and Ma (1997)]. They found a relationship that connects the dynamic viscosity of PCE with temperature as (Eq. 90):

$$\ln\mu_{\text{PCE}} = -4.723 + \frac{1.890 \times 10^3}{T_K} - \frac{2.035 \times 10^5}{T_K^2} \quad \text{Eq. 90}$$

where:

μ_{PCE} : dynamic viscosity of PCE (cP)

Consequently, Chlorinated Volatile Organic Compounds (CVOCs) mobility (in a free liquid phase) will be particularly improved when the ground temperature rises after a thermal treatment.

2.3.3 Influence of temperature on interfacial tension

In soils, the free product phase can be immobilized by the soil's capillary forces. Reduced interfacial tension could then lead to the remobilization of trapped free product. The study by Sleep and Ma (1997) demonstrated a slight reduction in the PCE/water system's interfacial tension with increasing temperature (0.042 mJ.m⁻².°C⁻¹). From these results, they proposed the following linear relationship (Eq. 91) to predict the PCE surface tension behaviour for temperature between 20 and 90 °C [Sleep and Ma (1997)]:

$$\sigma_{\text{PCE}} = 45.808 - 0.042T \quad \text{Eq. 91}$$

where:

σ_{PCE} : Interfacial tension of PCE-water (mJ.m⁻²)

These results confirm Imhoff *et al.*'s (1997) study showing a slight reduction (7%) of the surface tension between the PCE and water on a temperature range varying from 5 to 40 °C.

2.3.4 Influence of temperature on density

The density of CVOCs is a function of molar mass [Lemière *et al.* (2008)]. During the experiment performed by Sleep and Ma (1997), PCE density was measured as a function of temperature. It showed that PCE density falls when temperature rises. The equation that predicts how density behaves as a function of temperature given by Sleep and Ma (1997) is as follows (Eq. 92):

$$\rho_{\text{PCE}} = 1.6294 - 6.6655 \times 10^{-4}T - 4.9643 \times 10^{-6}T^2 \quad \text{Eq. 92}$$

where:

ρ_{PCE} : PCE density ($\text{g}\cdot\text{cm}^{-3}$)

This density decrease is too small to significantly increase recovery efficacy during a thermal treatment [Sleep and Ma (1997)]. However, according to Davis (1997), a temperature increase of 100 °C causes a 10% density reduction. The density of water decreases by about 4% when temperature rises from 0 to 100 °C. Even though these changes are small, it can influence contaminant migration.

2.3.5 Temperature effect on capillary pressure-saturation function

Many studies showed that the volume of entrapped non-wetting phase decreases with increasing temperature, as do interfacial tension and contact-angle temperature-dependent variables [Adamson and Gast (1997); Grant and Salehzadeh (1996); Hopmans and Dane (1986); Poston *et al.* (1970); Sinnokrot *et al.* (1971)]. Hopmans and Dane (1986) found that entrapped air volume decreases with increasing temperature [Hopmans and Dane (1986)].

The impact of temperature variations on capillary pressure-saturation relationships has been also studied from both the experimental and theoretical point of view [Davis (1994); Grant (2003); Grant and Salehzadeh (1996); O'Carroll and Sleep (2007); She and Sleep (1998)]. Grant and Salehzadeh (1996) have developed a formula that calculates the capillary pressure at a given temperature (Eq. 93) [Grant and Salehzadeh (1996)]:

$$P_c^T = P_c^{\text{ref}} \left(\frac{\beta_{P_c} + T}{\beta_{P_c} + T_{\text{ref}}} \right) \quad \text{Eq. 93}$$

where:

P_c^T : capillary pressure at a given temperature T (Pa)

P_c^{ref} : reference capillary pressure at the reference temperature T_{ref} (Pa)

T: temperature at which P_c^T is desired (°C)

β_{P_c} : fitting parameter related to the temperature dependency of interfacial tension and contact angle (-)

Recent studies conclude that the capillary pressure-temperature relationship and the β_{P_c} fitting parameter are not only related to changes in interfacial tension with temperature. It has been suggested to also consider how contact angles change with temperature to improve the use of Eq. 93 [Bachmann *et al.* (2002); She and Sleep (1998)].

Poston *et al.* (1970) investigated the temperature dependence of the contact angle. They measured the contact angle of oil in a temperature range of 25-88 °C in an oil-water-glass system and concluded that contact angles decreased slightly with increasing temperature [Poston *et al.* (1970)]. Likewise, they concluded that increasing the temperature led to a very small change in the contact angle [Bradford and Leij (1996); Davis (1994)]. Dokla (1981) also showed that for mixtures of crude oil-water-sand systems, the contact angles increased from 64° (at 30 °C) to 76° (at 70 °C) [Dokla (1981)].

In almost all types of porous media (sand, soil or glass beads), studies on air-water systems showed that residual water saturation decreases as temperature increases [Liu and Dane (1993)]. However, Davis (1994) showed increasing irreducible water saturations in air-water and hydrocarbon-water systems in the range of 10-30 °C [Davis (1994)]. Other researchers showed that in organic-water systems the residual water saturation increases and the residual organic

saturation decreases when temperature increases [Davis (1994); Poston *et al.* (1970); She and Sleep (1998); Sinnokrot *et al.* (1971)]. In a porous medium consisting of 3 mm glass beads the water residual saturation (S_{rw}) varied by over 8-8.5% when interfacial tension ranged between 22 and 71.2 mN.m⁻¹ [Morrow (1970)].

She and Sleep (1998) found that increasing temperature decreased residual PCE, but the irreducible water value increased when the temperature increased [She and Sleep (1998)]. They concluded that not only the interfacial tension and the contact angle influence the capillary pressure–saturation curve but also that viscosity may change the displacement process, which will affect the capillary pressure.

These residual saturations can be estimated using the concept of total trapping number (N_T) developed by Pennell *et al.* (1997), from the combination of capillary number (N_{Ca}) and bond number (N_B) [Pennell *et al.* (1996)]. N_B accounts for gravity and capillary forces whereas N_{Ca} accounts for viscous and capillary forces [Kingston *et al.* (2014)]. As a first approach, N_T can be used to estimate the impacts of variations in this data as a function of temperature [Kingston *et al.* (2014)]. According to the experiments of Sleep and Ma (1997) on heating PCE in a saturated porous medium (90 °C), the mobilization of trapped, pure PCE did not increase. Indeed, increasing temperature reduced interfacial tension but also, and more significantly, it reduced water viscosity [Sleep and Ma (1997)].

Chevalier and Fonte (2000) developed correlation models between the residual saturation and soil and fluid properties from the experimental data: model for S_{rn} independent of N_{Ca} (Eq. 94), dependent on N_{Ca} (Eq. 95) and as a function of N_T (Eq. 96). The experiments used different types of sand and SOLTROL® (isoparaffinic solvents) as LNAPL [Chevalier and Fonte (2000)].

$$S_{rn} = -11.59 \left(\frac{C_u N_B}{C_g} \right)^2 + 0.182 \quad \text{For } N_{Ca} < 2 \times 10^{-6} \quad \text{Eq. 94}$$

$$S_{rn} = -10.58 \left(\frac{C_u N_B}{C_g} \right)^2 + 0.1274 N_{Ca}^{-0.03} \quad \text{For } 2 \times 10^{-6} < N_{Ca} < 4.13 \times 10^{-5} \quad \text{Eq. 95}$$

$$S_{rn} = 0.0371 C_u^{-0.1118} C_g^{0.1071} N_T - 0.1417 \quad \text{For all conditions} \quad \text{Eq. 96}$$

where:

S_{rn} : residual saturation of non-wetting fluid (-)

C_g : coefficient of soil gradation; $C_g = \frac{D_{30}^2}{D_{60} D_{10}}$ (-)

2.3.6 Effects of temperature on solubilization

CVOCs have low water solubility [Lemière *et al.* (2008)]. The effects of temperature on CVOCs solubility must be known in order to predict how CVOCs will distribute during a thermal remediation process.

It has been demonstrated several times for common CVOCs, PCE and TCE, that solubility increases exponentially with temperature [Heron *et al.* (2006); Knauss *et al.* (2000)], but some authors have observed a minimum solubility for temperatures ranging from 20 °C to 40 °C [Imhoff *et al.* (1997)]. The influence of temperature on compound solubility is a function of the chemical structure of the chlorinated contaminant under consideration. Table 14 shows the solubility variation for various chlorinated solvents for a given temperature ranges. Generally, the same effects are observed with higher temperature and higher chlorinated solvent solubility.

Table 14: Variation in solubility for various chlorinated solvents for the given temperature ranges

Contaminant	Temperature range	Solubility variation	Source
Dichloromethane	0 – 36 °C	< 15%	[Stephenson (1992)]
1,2-Dichloroethane	0 – 82 °C	+ 30%	[Stephenson (1992)]
TCE	9 – 71 °C	+ 15%	[Heron <i>et al.</i> (1998b)]
	21 – 117 °C For the interval: 21 – 75 °C	+ 270% + 30%	[Knauss <i>et al.</i> (2000)]
PCE	30 – 87 °C	+ 60%	[Sleep and Ma (1997)]
	22 – 161 °C For the interval: 22 – 75 °C	+ 1207% + 63%	[Knauss <i>et al.</i> (2000)]
	0 - 92 °C	+ 90%	[Stephenson (1992)]
2-Chloroethyl Ether	0 - 92 °C	+ 30%	[Stephenson (1992)]

Even if a temperature increase improves CVOC solubility, this would not significantly improve the efficacy of a thermal treatment [Imhoff *et al.*, 1997]. However, the CVOC dissolution rate increases by a factor of five for temperatures ranging from 10 to 60 °C [Imhoff *et al.* (1997)].

Knauss *et al.* (2000) have established equations that control PCE and TCE solubilities as a function of temperature (Eq. 97 and Eq. 98).

$$R \ln K_e(\text{TCE}) = [-2.64(\pm 0.32) \times 10^3] + \frac{[1.19(\pm 0.15) \times 10^5]}{T_K} + [3.87(\pm 0.47) \times 10^2] \ln T_K \quad \text{Eq. 97}$$

$$R \ln K_e(\text{PCE}) = [-2.41(\pm 0.26) \times 10^3] + \frac{[1.06(\pm 0.14) \times 10^5]}{T_K} + [3.50(\pm 0.37) \times 10^2] \ln T_K \quad \text{Eq. 98}$$

where:

$$K_e: \text{equilibrium constant: } K_e(\text{TCE}) = \frac{[\text{TCE}_{\text{aq}}]}{[\text{TCE}_{\text{liq}}]} \text{ and } K_e(\text{PCE}) = \frac{[\text{PCE}_{\text{aq}}]}{[\text{PCE}_{\text{liq}}]}$$

$$R: \text{ideal gas constant, } R = 8.314 \text{ J} \cdot \text{mol}^{-1} \cdot \text{K}^{-1}$$

Sleep and Ma (1997) have also established an equation that connects the solubility variations of PCE with temperature (Eq. 99):

$$C_{\text{PCE}} = 0.02098T^2 - 0.788T + 168.0 \quad \text{Eq. 99}$$

where:

$$C_{\text{PCE}}: \text{solubility of PCE in water (mg} \cdot \text{L}^{-1}\text{)}$$

2.3.7 Effects of temperature on adsorption onto solid phase

Adsorption involves the attachment of molecules present in a fluid on a solid surface. Adsorption is a mechanism that affects the transport of compounds in aqueous phase. The soil–water distribution coefficient, K_d , characterizes the adsorption capacity of a dissolving substance i on a solid substrate at equilibrium (for linear sorption) (Eq. 100).

$$K_d = \frac{C_{i,s}}{C_{i,w}} \quad \text{Eq. 100}$$

where:

K_d : soil–water distribution coefficient ($L.kg^{-1}$)

$C_{i,s}$: concentration of compound i in the solid phase ($mg.kg^{-1}$)

$C_{i,w}$: concentration of compound i in the aqueous phase ($mg.L^{-1}$)

Various models are used to characterize the adsorption of organic compounds on solid surfaces, such as the nonlinear model (Langmuir, Freundlich and Langmuir-Hinshelwood isotherm models). Generally, the organic carbon-water partition, K_{oc} , is more often used to better determinate the adsorption capacity on organic matter (Eq. 101):

$$K_d = f_{oc}K_{oc,i} \quad \text{Eq. 101}$$

where:

f_{oc} : fraction of organic carbon in the porous medium (-)

$K_{oc,i}$: organic carbon partitioning coefficient for compound i ($L.kg^{-1}$)

The equation accounts only for the adsorption on the organic matter. The effect of temperature on K_{OC} can be described by the van't Hoff equation [Schwarzenbach *et al.* (2003); Panagopoulos *et al.* (2017)] (Eq. 102):

$$\ln K_{oc} = \frac{-\Delta H_{oc}}{RT_K} + \frac{+\Delta HS_{oc}}{R} \quad \text{Eq. 102}$$

where:

ΔH_{oc} : changes in enthalpy of phase change for sorption of the chemical to organic carbon from water ($J.mol^{-1}$)

ΔHS_{oc} : change of entropy of phase change for sorption of the chemical to organic carbon from water ($J.mol^{-1}.K^{-1}$)

In general, this is an exothermic process and, as such, the amount of molecules sorbed decreases as temperature increases [Delle Site (2001)]. Heron *et al.* (1996) demonstrated theoretically that, based on sorption heat, CVOCs adsorption from the aqueous phase into soils should decrease by a factor of about 2.2 when the temperature increases from 20 to 90 °C. Sleep and McClure (2001) demonstrated that K_{oc} of PCE decreased from approximately 820 to 490 $cm^3.g^{-1}$ between 22 and 92 °C [Sleep and McClure (2001)]. However, the effect of temperature on desorption remains specific to the type of soil and the degree of water saturation in this soil. Heron *et al.* (1998b) have shown that the adsorption coefficient for TCE in saturated conditions decreases by ca. 50% from 20 to 90 °C and by a factor of 10 in unsaturated conditions with the same temperature range.

2.4 Effect of chemical enhancement on DNAPL mobility in saturated porous media

Because of DNAPL's high density, low solubility and high interfacial tension, free product recovery with groundwater extraction and skimming is not effective for mass removal: typical recovery rates do not exceed 60% even at their highest [ITRC (2002)]. Adding surfactants improves the performance of PT [Pennell *et al.* (2014); Mao *et al.* (2015)].

There are different types of chemical enhancement [Atteia *et al.* (2013); Pennell *et al.* (2014)]:

- Surfactant: decrease interfacial tension
- Solubilisation: increases the solubility in water but do not modify the behaviour of the organic phase,

- Cosolvent: transforms a diphasic system (NAPL-water) into a single-phase system,
- Polymers: increases viscosity in high permeability areas (and thus increase the flushing of low permeability areas),
- Foams: increase viscosity in high permeability areas leading to homogeneous displacement fronts.

2.4.1 Surfactant injection technologies

Technologies for DNAPL recovery with chemical enhancement are similar to those used for DNAPL recovery (water flooding) (see section 1.1.6.1). The difference lies in adding surfactants. This technology is also called Surfactant-Enhanced Aquifer Remediation (SEAR) or flushing or surfactant flooding.

The surfactant injection is carried out upstream or surrounding the zone to be treated (via injection wells). The free product and the aqueous phase are pumped at the heart of the pollution or downstream immediately via recovery wells (Figure 30). The remediation can be applied either laterally or centrifugally [NAVFAC (2002)]. A less used also application exists: Vertical Circulation Well Flow (VCW) [US EPA (1996b)].

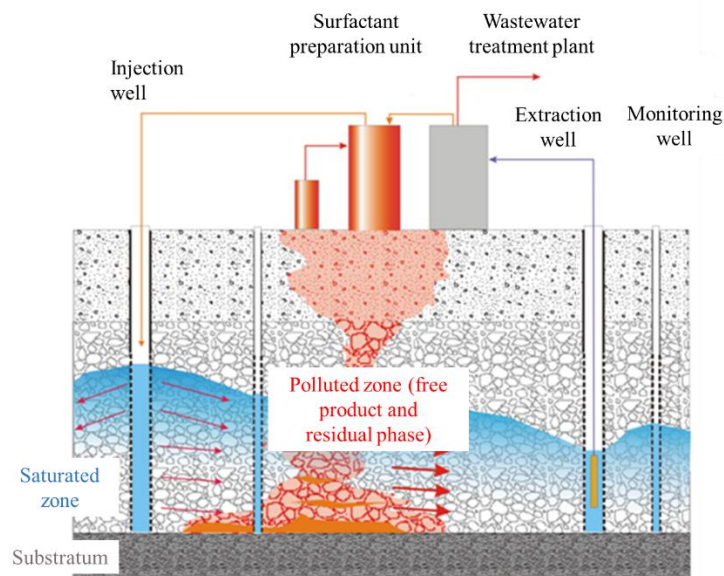


Figure 30: Schematic representation of surfactant flooding (adapted from [Colombano et al. (2010)])

The liquids pumped are then sent to a wastewater treatment plant before being discharged into the environment or into the wastewater or rainwater sewer networks.

2.4.2 Background on surfactants

Surfactants are organic compounds composed of hydrophobic and hydrophilic parts (amphiphilic compounds). Surfactants are either ionic or nonionic. Ionic surfactants can also be classified into cationic, anionic and zwitterionic surfactants. Zwitterionic surfactants have both a positive and a negative charge. Nonionic surfactants have no charge.

The hydrophobic groups are mainly alkyl or alkylaryl hydrocarbon groups, but fluoroalkyl, silaalkyl, thiaalkyl and oxaalkyl groups are also possible. The hydrophilic groups depends on the category of surfactants [Lowe *et al.* (1999); Farn (2008)]:

- Cationic surfactants: primary, secondary, tertiary quaternary ammonium salts,
- Anionic surfactants: alkylbenzene sulfonates, lauryl sulfate, di-alkyl sulfosuccinate, lignosulfonates, phosphate esters, carboxylates,
- Zwitterionic surfactants: amine oxide, betaine, aminocarboxylate,
- Nonionic: polyethylene (ethoxylate), polyglucose, acetylenic, mono and diethanolamine.

When surfactants are present in a water-soil system, they may be adsorbed on the surface of soil particles. Normally, hydrophilic parts of surfactant tend to bind to the aqueous phase of the system and the lipophilic parts tend to bind to hydrophobic substance (*e.g.* DNAPLs) or soil particles [Pennell *et al.* (2014); Mao *et al.* (2015)]. Surfactants can reduce the interfacial tension and therefore increase the wetting properties of a non-wetting compound [Myers (1999); Mao *et al.* (2015)]. In the aqueous phase, the surfactants are aggregated in the form of micelles [Rosen and Kunjappu (2012)].

2.4.3 Surfactant recovery mechanisms

The recovery mechanisms during surfactant flushing have two principal features: (1) decreasing IFT and increasing pollutant (NAPL) solubility (2) mobilizing residual pollutions [Laha *et al.* (2009); Vishnyakov *et al.* (2013); Rosen and Kunjappu (2012); Pennell *et al.* (2014)].

a) Decreasing the IFT and increasing the solubility:

At low concentrations, surfactant molecules will mainly accumulate at the interface of solid-liquid or liquid-liquid (NAPL-water interface in our case, where a free phase exists). The surfactant molecules will gradually cover the NAPL-water interface as their concentration increases.

Increasing concentrations of surfactants will reduce the IFT until all NAPL-water interfaces are covered. At this stage, increasing surfactant concentrations will no longer reduce the IFT: the surfactant molecules will agglomerate (form surfactant micelles) and will increase the solubility of the NAPL (present in the dissolved phase). This concentration is called the Critical Micelle Concentration (CMC) [Rosen and Kunjappu (2012); Vishnyakov *et al.* (2013); Pennell *et al.* (2014)]. The CMC of a surfactant depends on its structure, on the system's temperature and ionic strength, and on whether any organic additives are present in the solution [Laha *et al.* (2009)].

The influence of surfactant concentrations on the IFT and solubility of the NAPLs in the NAPL-water system are presented in Figure 31.

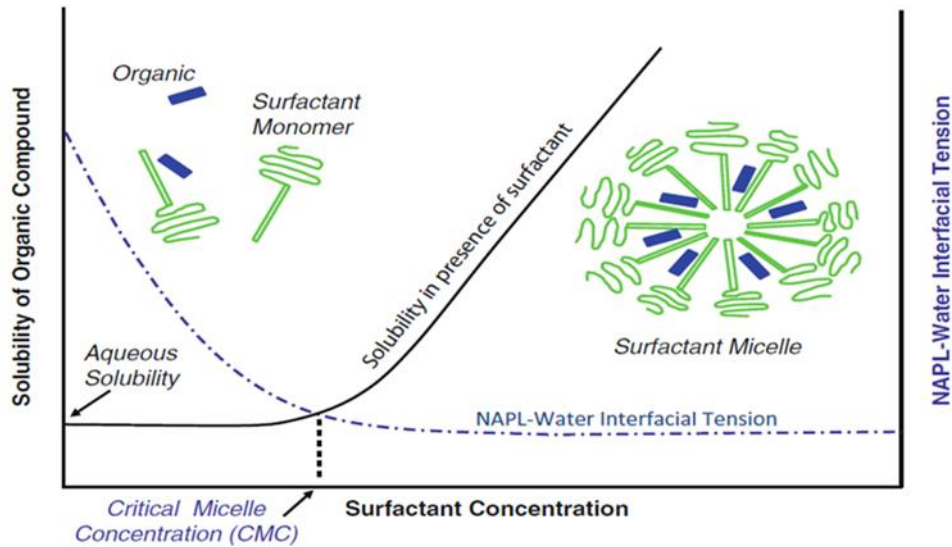


Figure 31: Influence of surfactant concentration on the IFT and solubility of NAPLs of a NAPL-water system [Pennell *et al.* (2014)]

The solubilization capacity of a surfactant for a particular NAPL can be quantified by the Molar Solubilization Ratio (MSR). The MSR is a ratio of the moles of organic solubilized to the moles of surfactant in micellar form (Eq. 103) [Edwards *et al.* (1991)]:

$$\text{MSR} = \frac{C_o - C_{o,\text{sol}}}{C_{\text{surf}} - C_{\text{surf,CMC}}} \quad \text{Eq. 103}$$

where:

MSR: Molar Solubilization Ratio (-)

C_o : molar concentration of the solubilized organic (mol.L^{-1})

$C_{o,\text{sol}}$: aqueous solubility of the organic (mol.L^{-1})

C_{surf} : total molar concentration of the surfactant added (mol.L^{-1})

$C_{\text{surf,CMC}}$: molar concentration of the surfactant at the CMC (mol.L^{-1})

How surfactants perform depends on their working environmental conditions. For example, the temperature and salinity of the system influences their effectiveness. When the temperature increases, the reaction between the hydrophilic component of a nonionic surfactant and water decreases. For ionic surfactants, when the salinity of the system increases, the reaction between the hydrophilic component and water also decreases [Rosen and Kunjappu (2012)].

Nonionic surfactants can be characterized by the hydrophilic-lipophilic balance (HLB). Griffin (1949) has defined the HLB by the following equation (Eq. 104) [Griffin (1949)]:

$$\text{HLB} = 20 * \frac{MW_H}{MW_H + MW_L} \quad \text{Eq. 104}$$

where:

HLB: hydrophilic-lipophilic balance (g.mol^{-1})

MW_H : molecular weight of the nonionic surfactant's hydrophilic groups (g.mol^{-1})

MW_L : molecular weight of the nonionic surfactant's lipophilic groups (g.mol^{-1})

For subsurface remediation applications, nonionic surfactants with HLBs between 12 and 15 are typically selected because they readily dissolve in water and do not strongly partition into organic liquids. This index was developed for nonionic surfactants. Its validity for ionic surfactants is not really established [Rosen and Kunjappu (2012); Pennell *et al.* (2014)].

The surfactant can modify the properties of surfaces (of the soil particles) by neutralizing surface charges and/or by reversing wettability. Surfactants with an HLB value between 7 and 9 are particularly suitable for use as a wetting agent [Tadros (2005)].

When the interfacial tension between two fluids is close to 1 mN.m^{-1} , the separation between the two fluids is not so clear and there is a fine emulsion of one phase in the other phase. Four main types of equilibrium systems may result:

- Winsor Type I: oil-in-water microemulsion coexists with the excess oil
- Winsor Type II: water-in-oil microemulsion coexists with excess water
- Winsor Type III: free organic and aqueous phases are in equilibrium with a third solubilized phase containing the three components
- Winsor Type IV: system contains no free organic or aqueous layers and the three components are mutually solubilized

Surfactants with an HLB value between 3 and 6, and between 8 and 18, will be respectively efficient to form water-in-oil emulsions, and oil-in-water emulsions [Tadros (2005)]. It is possible to observe a change in the type of microemulsion (from a Winsor type I to a Winsor type II via a Winsor type III) when salinity increases for anionic surfactants or when the temperature increases for nonionic surfactants [Rosen and Kunjappu (2012); Pennell *et al.* (2014)].

b) Mobilization of the residual pollutions:

The mechanism for displacing NAPLs in a porous medium has already been discussed in section 2.2.12. In our study, we used surfactants to reduce the IFT in order: i. to displace maximum pure products (DNAPLs) and, ii. to decrease residual saturations.

Mobilization starts when the sum of viscous and buoyancy forces exceeds the capillary forces of the contaminated medium [Pennell *et al.* (1996); Rosen and Kunjappu (2012)].

2.4.4 Strategy for using surfactants: benefits, limitations and complementarity with other remediation technologies

Using surfactants reduces IFT, N_T and therefore S_n . Figure 32 presents the benefits of adding surfactants to S_n values.

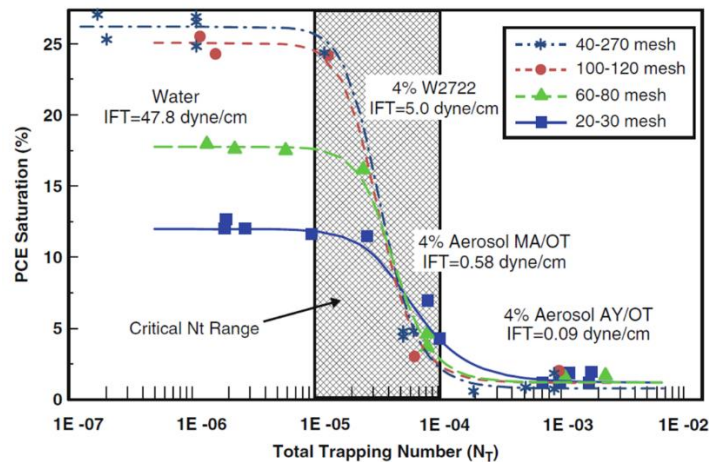


Figure 32: Displacement of PCE-DNAPL as a function of N_T [Pennell *et al.* (1996)]

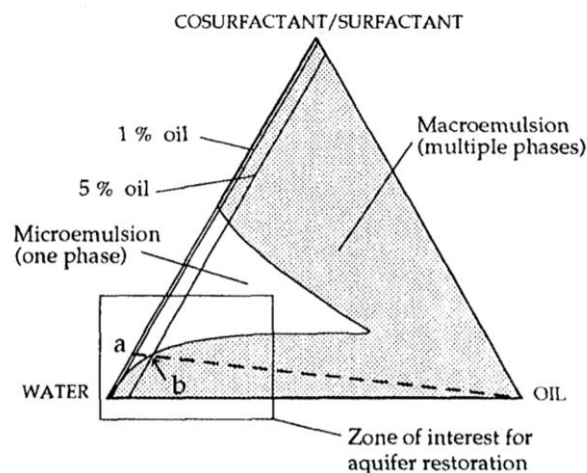
Different DNAPL recovery strategies can be used depending on surfactant concentrations [Paria (2008); Rosen and Kunjappu (2012); Maire *et al.* (2018)]:

- $C_{\text{surf}} < \text{CMC}$: mobilization of the residual phase,
- $C_{\text{surf}} \sim \text{CMC}$: emulsification (microemulsion),
- $C_{\text{surf}} > \text{CMC}$: dissolution of contaminants into micelles that arises when C_{surf} exceeds the CMC-value in pores mobilization.

The volumes and concentrations of surfactants must not only consider this concentration in relation to the CMC, but they must also include losses related to adsorption, precipitation, biodegradation and dilution (at the front). In addition, the minimum contact time must be integrated into the design [Martel *et al.* (1993); ITRC (2013); Pennell *et al.* (2014)].

The advantage of mobilization lies in the fact that it requires a limited amount of surfactants. The DNAPL remediation efficiencies and recovery times are significantly improved. The disadvantages are mainly related to uncontrolled transfer of DNAPL to deeper areas of the aquifer not included in the pumping system or to less permeable zones. Therefore, this treatment must be based on a thorough knowledge of the polluted area and on an *ad hoc* modeling work. In addition, it is recommended to use this treatment only in the case of a shallow aquifer with limited heterogeneity [Rathfelder *et al.* (2003); Abriola *et al.* (2005); Ramsburg *et al.* (2005); Robert *et al.* (2006)]. The amounts of surfactants used are about maximum 5% v/v. Under optimal conditions, the treatment can be carried out with very low volumes of surfactant solution, of the order of 2 to 3 pore volumes [ITRC (2013)].

Emulsification can generate microemulsions smaller than 100 nm, which is smaller than the diameter of most pores in permeable to semi-permeable alluvial contexts. Microemulsions can therefore move relatively easily; the capillary trapping mechanisms (by-passing or snap-off) are thus limited. Therefore more DNAPL is recovered than by mobilization alone. However, it should be noted that the generation of the emulsion requires substantial laboratory work (based on a specific phase diagram – see Figure 33). Moreover, this emulsion often requires a large input of inorganic salts [Martel *et al.* (1993); Szafranski *et al.* (1998)]. Finally, since the amount of surfactants does not exceed 15 to 30% (surfactant/COC), the uncontrolled transfer of DNAPL problems mentioned above must be taken into account [Szafranski *et al.* (1998); Oostrom *et al.* (1999)].



a: minimum C_{surf} required for the extraction of oil saturated solution containing b% oil

Figure 33: Schematic pseudo-ternary diagram [Martel *et al.* (1993)]

The dissolution of DNAPL into micelles by adding surfactants alone is not very effective for several reasons. First, since the ability to solubilize with surfactant is limited (compared to solvents), this technique requires a very large amount of surfactants [Pennell *et al.* (1996); Rosen and Kunjappu (2012)]. Secondly, the quantities of wastewater generated are very large and can *de facto* generate prohibitive costs [Sabatini *et al.* (1998)]. If this option is chosen, a surfactant with a high MSR must be selected. It is often customary to improve the process through the use of a co-solvent (often an alcohol with 1 to 3 carbon atoms) [Saint-Pierre *et al.* (2004)]. The process can be further enhanced by adding a solvent to the surfactant and the alcohol (in the case of viscous compounds) [Martel *et al.* (1998a)].

The limitations of SEAR are as for most *in situ* treatments [Hyman and Dupont (2001); Rosen and Kunjappu (2012); ITRC (2013)]:

- low permeability soils that oppose the liquid injection,
- fractured or anisotropic soils, in which it is difficult to ensure a homogeneous circulation of fluids

In unfavorable cases, the technical limits can be postponed in two ways: addition of a polymer solution and injection of surfactants in the form of foam (foam flushing).

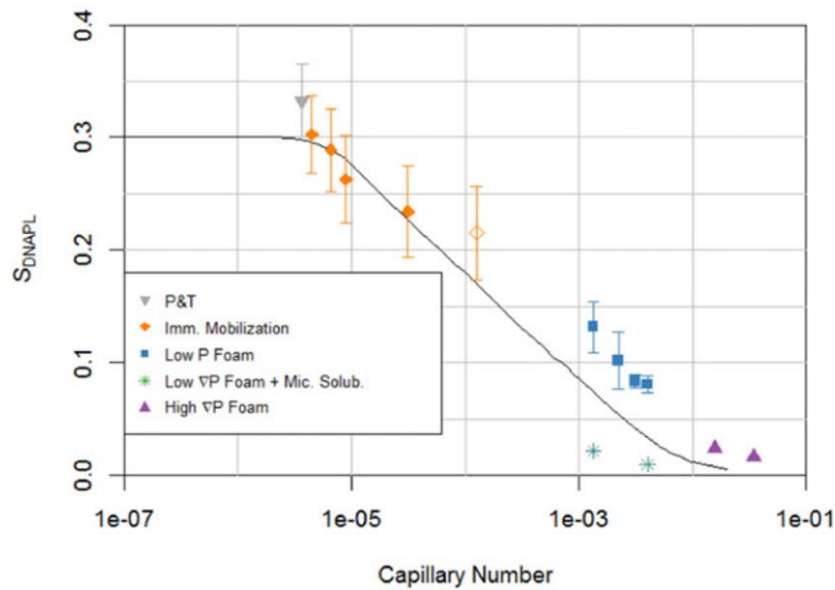
The addition of polymers during the injection of surfactants makes it possible to change the dynamic viscosity of the surfactant or the groundwater, which improves the homogeneity of the injection (front flattening). The initial injection reduces the preferential flow of the surfactant, the posterior injection moves the surfactant by plug effect. Sometimes the polymer additions can be made both before and after the injection of surfactants (or at the same time) [Dwarakanath *et al.* (1999); Giese and Powers (2002); Martel *et al.* (2004); Robert *et al.* (2006); Atteia *et al.* (2013)]. Xanthan, which is soluble at the temperatures of the groundwater and has noticeable shear thinning behaviour, is often used as a polymer [Martel *et al.* (1998b)].

Foam consists of a mass of small bubbles that are formed when gas and a liquid are mixed together. In most foams, the volume of gas is large, with thin films of liquid separating the regions of gas (gas bubbles separated by liquid lamellae). In porous media, lamellae must stretch to go through pores or break, opposing resistance to gas flow. This gives a high apparent viscosity to the foam and produces the same effects as for the polymers: i. the injection of the foam is homogeneous (front flattening); ii. foam penetrates not only into large pores but also into smaller pores [Bertin *et al.* (1998); Atteia *et al.* (2013); Maire *et al.* (2018)]. Foams can enhance mobility control of the surfactant solution by lowering the relative permeability of the coarse layers due to the presence of air [Falls *et al.* (1989)].

Foam (water/surfactant mixture with air) can be prepared in different ways: created by coinjection or successive injection of gas and water/surfactant. Foam can be prepared on-site or *in situ*. The choice of surfactants (concentrations) and the mode of injection make it possible to form strong or weak foams. Foam is defined as “strong” if gas bubbles occupy all the pore space, and “weak” if gas channels exist [Schramm (1994); Rossen (1996)]. It is therefore possible to create: i. different pressure gradients; ii. varying foam lifetimes (and therefore different radii of action) [Hirasaki *et al.* (1997); Rosen and Kunjappu (2012); Longpré-Girard *et al.* (2016)].

Regarding the recovery of DNAPL, interesting progress has been made in recent years. It has been demonstrated in the laboratory that the injection of foam could be very effective to

mobilize DNAPL, with varying foam injection pressures and with successions of foam injection and surfactants in liquid form [Maire *et al.* (2015); Maire and Fatin-Rouge (2017)]. Figure 34 presents the results of these studies.



Curve: theoretical data ([Lake (1989)])

Figure 34: S_n as a function of N_{Ca} for mobilization experiments using water alone, surfactant solution, low and high ∇P foams and low ∇P foam completed by micellar solubilization [Maire *et al.* (2018)]

The pumped groundwater must be treated, which sometimes limits the implementation of this technique for economic reasons. Mobilization, emulsification and foam flushing generate much less wastewater and are less expensive than dissolution. These techniques have their place as a support technique for conventional PT [Hyman and Dupont (2001); ITRC (2013); Mao *et al.* (2015)]. How to reuse surfactants and to reduce treatment costs of pumped water is the subject of substantial research [Mousset *et al.* (2014); Trellu *et al.* (2017)].

Surfactants are also used to convey reducing agents such as zero-valent iron and consequently lead to increase remediation yields [Cho and Park (2006); Harendra and Vipulanandan (2011); Zhang *et al.* (2011)].

2.4.5 Main surfactants used in soil remediation

The main parameters to consider for the selection of surfactants are presented in Table 15.

Table 15: Selection criteria for surfactant solutions [Martel *et al.* (1993)]

Performance	Effects	Impacts
Formation of oil-in-water microemulsions	Low sensitivity to water hardness	Low toxicity
Water solubility	Low clay dispersion	High biodegradability
Low interfacial tension	Low adsorption on soil	Safe to handle
Recoverable or treatable	Low foaming power	
Analyzable		
Low cost		

The most commonly used ionic surfactants for soil flushing are Sodium Dodecyl Sulfate (SDS), Sodium Dodecyl Benzene Sulfonate (SDBS), for anionic surfactants, and CetylTriethyl Ammonium Bromide (CTAB) for cationic surfactants [Margesin and Schinner (1999); Mao *et al.* (2015)].

Cationic surfactants tend to adsorb to negatively charged soil particles, which reduces the amount of product available for remediation (unlike anionic surfactants) [Wagner *et al.* (1994); Taylor *et al.* (2001); Paria (2008)]. Moreover, cationic surfactants are usually more toxic [Ivankovic and Hrenovic (2010)]. This is why most of the studies and experiments with soil flushing are carried out with anionic surfactants [Mao *et al.* (2015)].

At pilot scales, ionic surfactants are useful for the remediation of some pollutants: TCB, NAPLs, and BTEX. However, soil flushing remediation at industrial scales is limited [Strbak (2000); Ranjan *et al.* (2006); Giannis *et al.* (2007); Lee *et al.* (2007)].

Nonionic surfactants are hard to ionize in aqueous solution [Rosen and Kunjappu (2012)]. Nonionic surfactants can more easily exhibit micellization than ionic surfactants because the molecules need less energy to overcome the electrostatic reaction [Douroumis and Fahr (2013)]. Nonionic surfactants have low CMC, very good solubilization capacity, and also low toxicity, so nonionic surfactants are widely used for soil remediation [Zheng *et al.* (2012)]. The most commonly used nonionic surfactants for soil surfactant flushing are Triton X-100 (PEO (9.5) isooctylphenol), Tween 80 (PEO (20) sorbitan monooleate) and Brij-35 (PEO(23) dodecyl ether) [Mulligan and Eftekhari (2003); Torres *et al.* (2012); Rios *et al.* (2013)].

Besides the two types of surfactant discussed above, some studies have also used bio-surfactants to enhance the remediation of hydrocarbon pollutions [Zhang and Miller (1992)]. Bio-surfactants are surfactants produced from plant, animal, or bacterial sources [Muthusamy *et al.* (2008); Pacwa-Plociniczak *et al.* (2011)]. Compared with the chemical surfactants described, bio-surfactants are more difficult to produce and the quantities produced are often too low for field-scale application [Pennell *et al.* (2014)].

2.4.6 Surfactants used to recover chlorinated compounds

Nonionic surfactants are effective for the remediation of chlorinated solvents such as tetrachloroethylene (PCE) and trichloroethylene (TCE) because of their ability to reduce the IFT and increase pollutant solubility [Taylor *et al.* (2001); Zhong *et al.* (2003); Zhao *et al.* (2006); Suchomel *et al.* (2007); Harendra and Vipulanandan (2011)].

Table 16 presents a selection of SEAR [Pennell *et al.* (2014)].

Table 16: Representative Examples of Surfactant Flushing Field Demonstrations [Pennell *et al.* (2014)]

Field Site	Surfactant Formulation	NAPL	Amount Recovered (Estimated Recovery) ^a	References
Dover AFB, DE	3.3% Aerosol® MA + 3.3% isopropanol + 0.4% CaCl ₂	PCE	46 L (68%)	[Childs <i>et al.</i> (2006)]
Bachman Road Oscoda, MI	6% Tween® 80	PCE	19 L (90%)	[Abriola <i>et al.</i> (2005); Ramsburg <i>et al.</i> (2005)]
Alameda Point, CA	5% Dowfax® 8390 + 2% Aerosol® MA + 3% NaCl + 1% CaCl ₂	TCA, TCE, DCA, DCE	325 kg (97%)	[Hasegawa <i>et al.</i> (2000)]
Camp Lejeune, Marine Corps Base, NC	4% Alfoterra® 145-4PO sulfate + 16 % propanol + 0.2% CaCl ₂	PCE	288 L (72%)	[Delshad <i>et al.</i> (2000); Holzmer <i>et al.</i> (2000)]
Hill AFB OU1, UT	3% Brij® 97 + 2.5% pentanol	Jet fuel, chlorinated solvents	396 L (72%)	[Jawitz <i>et al.</i> (2001)]
Hill AFB OU1 (Cell 5), UT	2.2% Aerosol® OT + 2.1% Tween® 80 + 0.4% CaCl ₂	Jet fuel, chlorinated solvents	14.4 kg (43%)	[Knox <i>et al.</i> (1997)]
Hill AFB OU1 (Cell 6), UT	4.3% Dowfax® 8390	Jet fuel, chlorinated solvents	1.5 kg (85-95%)	[Knox <i>et al.</i> (1997)]
Hill AFB OU2, UT	3.5% Aerosol® MA + 1% NaCl + air injection (foam)	TCE, TCE, PCE, CT	68.8 L (93%)	[Hirasaki <i>et al.</i> (1997); Szafranski <i>et al.</i> (1998); Meinardus <i>et al.</i> (2002)]
Hill AFB OU2, UT	7.6% Aerosol® MA + 4.5% isopropanol + 0.7% NaCl	TCE, TCE, PCE, CT	363 L (98%)	[Londergan <i>et al.</i> (2001)]
Coast Guard Station, Traverse City, MI	3.6% Dowfax® 8390	PCE, Jet Fuel	3.3 g PCE + 47 kg TH	[Knox <i>et al.</i> (1997)]
Thouin Sand Quarry, Quebec, Canada	9.2% butanol + 9.2% Hostapur® SAS 60 + 13.2% toluene + 13.2% d-limonene	TCE, PCE, waste oil	532 kg (86%)	[Martel <i>et al.</i> (1998c)]
Canadian Forces Base Borden, Ontario, Canada	2% 1:1 Rexophos® 25/97 + Alkasurf® NP10	PCE	67 L (69%)	[Fountain <i>et al.</i> (1996)]

2.4.7 Effect of surfactant on solubilization and interfacial tension of chlorinated compounds

According to the literature review, the most studied chlorinated compounds are PCE and TCE. For our DNAPL, the percentages of TCE and PCE are only about 15% (w/w). There are almost no studies on the compounds found most in our DNAPLs (HCB and HCA). The results of the literature review are presented in Table 17 and Table 18.

Table 17: Comparison of TCE solubilization and IFT reduction for representative surfactants

Surfactant	Chemical name	Class	CMC (mg.L ⁻¹)	HLB	Solubility (mg.L ⁻¹)	IFT (mN.m ⁻¹)	Reference
Tween 80 (Uniquema)	PEO (20) sorbitan monooleate	Non-ionic	35	15	85800 (5 wt% surfactant)	10.4	[Suchomel <i>et al.</i> (2007)]
Aerosol MA-80 (Cytec)	Sodium dihexyl sulfosuccinate	Anionic	1200	NR	46724 (5 wt% surfactant)	0.2	[Dwarakanath <i>et al.</i> (1999)]
Aerosol MA-80 (Uniquema) + cosolvent (1:2.5)	Sodium dihexyl sulfosuccinate	Anionic	582	NR	39100 (3.3 wt% surfactant)	0.19	[Suchomel <i>et al.</i> (2007)]
Tween 80 (Aldrich) + cosolvent (1:1)	PEO (20) sorbitan monooleate	Nonionic	15	NR	59200 (4 wt% surfactant)	10	[Zhong <i>et al.</i> (2003)]
T-MAZ-60	PEO (20) sorbitan monostearate	Nonionic	26	14.9	14700 (6.5 wt% surfactant)	NR	[Shiau <i>et al.</i> (1994)]
Triton X-100 (Sigma Chemical Company) + SDBS (Tokyo Kasei Kogyo Co) (1:3)	PEO (9.5) isoctylphenol/ Sodium dodecyl benzene sulfonate	Non-ionic/ anionic	164.7/ 963.2	NR	7900 (1 wt% surfactant)	NR	[Zhao <i>et al.</i> (2006)]

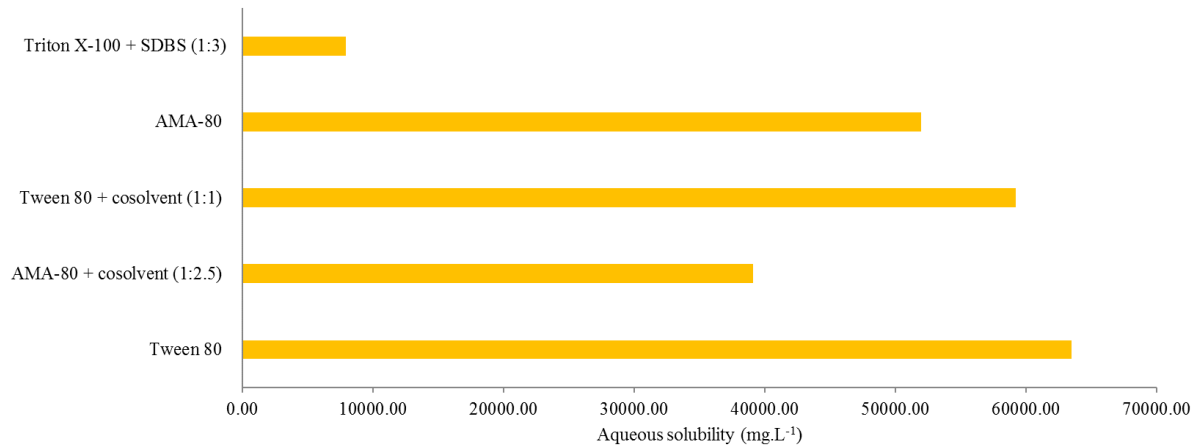
The results show that all of the representative surfactants have the effect of solubilizing and reducing IFT for the TCE-water and PCE-water system. For TCE, Aerosol-MA-80 (5 wt%) has good capacity to reduce the IFT of the TCE-water system. The IFT of the TCE-water system decreases from 35.2 to 0.2 mN.m⁻¹ [Dwarakanath *et al.* (1999)]. Tween 80 (5 wt%) can also reduce the IFT of the TCE-water system from 35.2 to 10.4 mN.m⁻¹ [Suchomel *et al.* (2007)]. For PCE, Aerosol family surfactants have very good capacity to reduce the system's IFT, from for example 47.8 to less than 0.01 mN.m⁻¹ [Dwarakanath *et al.* (1999); Sabatini *et al.* (2000); Childs *et al.* (2004)]. Triton X-100 and Tween 80 are also effective at decreasing the system's IFT [Taylor *et al.* (2001); Harendra and Vipulanandan (2011)].

Table 18: Comparison of PCE solubilization and IFT reduction for representative surfactants

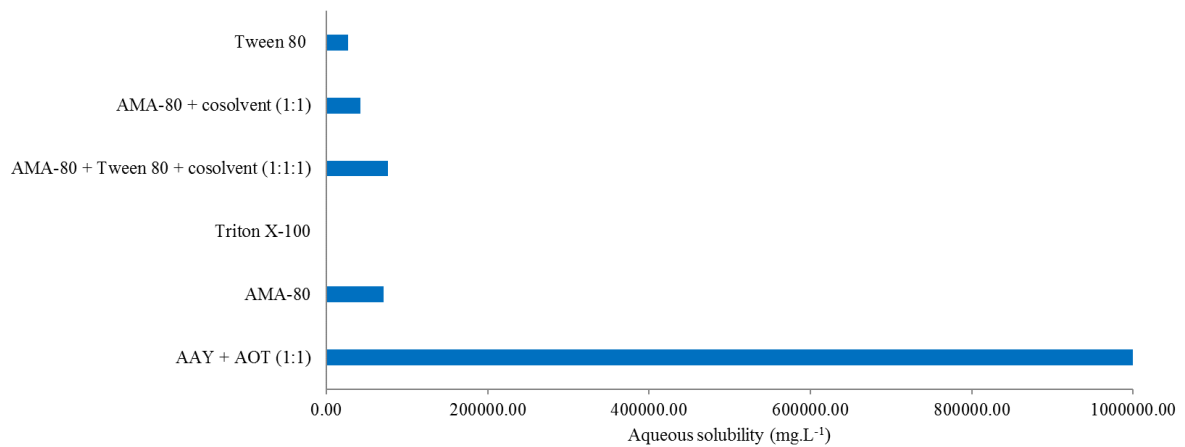
Surfactant	Chemical name	Class	CMC (mg.L ⁻¹)	HLB	Solubility (mg.L ⁻¹)	IFT (mN.m ⁻¹)	Reference
Aerosol-AY + Aerosol-OT (Cytec) (1:1)	Sodium diamyl sulfosuccinate/Sodium dioctyl sulfosuccinate	Anionic/anionic	NR	NR	1000000 (4 wt% surfactant)	0.01	[Dwarakanath <i>et al.</i> (1999)]
T-MAZ-60	PEO (20) sorbitan monostearate	Nonionic	26	14.9	16900 (2 wt% surfactant)	NR	[Shiau <i>et al.</i> (1994)]
Aerosol MA-80 (80% active Cytec)	Sodium dihexyl sulfosuccinate	Anionic	582	NR	71000 (2 wt% surfactant)	0.05	[Sabatini <i>et al.</i> (2000)]
Triton X-100 (Sigma-Aldrich)	PEO (9.5) isooctylphenol	Nonionic	130	13.5	1250 (1 wt% surfactant)	7	[Harendra and Vipulanandan (2011)]
Aerosol MA-80 (Cytec) + Tween 80 (Uniquema) + cosolvent (1:1:1)	Sodium dihexyl sulfosuccinate/PEO (20) sorbitan monooleate	Anionic/nonionic	582/15	NR	76000 (5 wt% surfactant)	0.05	[Childs <i>et al.</i> (2004)]
Tween 80(Tween 80 (ICI Surfactants)	PEO (20) sorbitan monooleate	Nonionic	15	15	26880 (4 wt% surfactant)	5.38	[Taylor <i>et al.</i> (2001)]
Aerosol MA-80 + cosolvent (1:1)	Sodium dihexyl sulfosuccinate	Anionic	582	NR	42000 (3.3 wt% surfactant)	0.1	[Childs <i>et al.</i> (2006)]

Figure 35 shows the comparison of how these surfactants enhance the aqueous solubility of TCE. All of these surfactants have increased the solubility of TCE in the aqueous phase (the aqueous solubility of TCE without enhancement is 1100 mg.L⁻¹). Regarding PCE, Figure 35 shows that Aerosol AY and Aerosol OT can dissolve an enormous quantity of PCE (the aqueous solubility of PCE is 150 mg.L⁻¹) and Triton X-100 dissolves least quantity of PCE.

a) Aqueous solubility of TCE



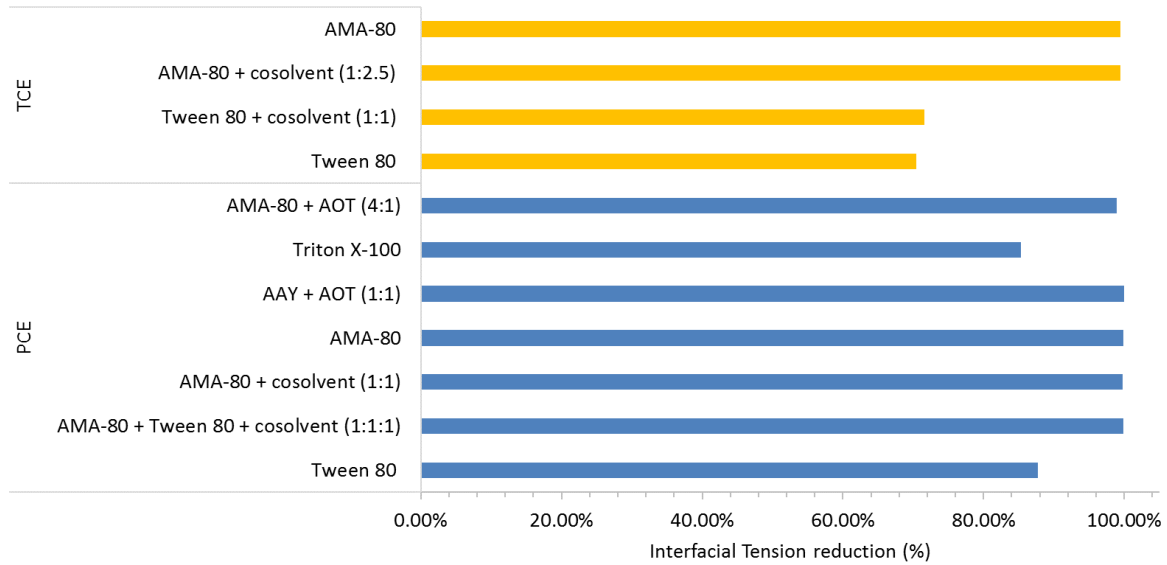
b) Aqueous solubility of PCE



AMA-80: Aerosol MA-80, AMA-80 + cosolvent: Aerosol MA-80 + isopropanol, Tween 80 + cosolvent: Tween 80 + isopropanol, AMA-80 + AOT: Aerosol MA-80 + Aerosol OT, AMA-80 + Tween 80 + cosolvent: Aerosol MA-80 + Tween 80 + isopropanol, AAY + AOT: Aerosol AY + Aerosol OT

Figure 35: Aqueous solubility of a) TCE and b) PCE in different surfactant solutions at 20 °C (from [Pennell et al. (1996); Sabatini et al. (2000); Ramsburg and Pennell (2001); Taylor et al. (2001)])

Figure 36 shows the IFT reduction of TCE-water and PCE-water systems with the same surfactants. The results shows that all of these surfactants can reduce more than 70% of the IFT in the TCE-water system. Aerosol MA-80 is more effective than Tween 80. All of these surfactants can also reduce the IFT of the PCE-water system by more than 85%. The effectiveness of these surfactants in reducing IFT is: Aerosol family > Tween 80 > Triton X-100.



AMA-80: Aerosol MA-80, AMA-80 + cosolvent: Aerosol MA-80 + isopropanol, Tween 80 + cosolvent: Tween 80 + isopropanol, AMA-80 + AOT: Aerosol MA-80 + Aerosol OT, AMA-80 + Tween 80 + cosolvent: Aerosol MA-80 + Tween 80 + isopropanol, AAY + AOT: Aerosol AY + Aerosol OT

Figure 36: IFT reduction of TCE-water and PCE-water systems with different surfactant solutions at 20°C (from [Pennell et al. (1996); Sabatini et al. (2000); Ramsburg and Pennell (2001); Taylor et al. (2001)])

Rodrigues *et al.* (2017) have shown that the presence of Triton X-100, Tween 80, and SDBS at concentrations above their respective CMC linearly enhanced the apparent solubility of HCB and HCA, in agreement with the increase number of micelles in which they can partition [Rodrigues *et al.* (2017)].

2.5 Multiphase flow modeling and numerical simulation

Numerical modeling is widely used in the NAPL remediation industry, to optimize costs and to improve predictive capability in terms of remediation performance and residual risks. In the past, numerical simulation has helped to model recovery processes in the oil industry. Prediction and simulation in reservoir engineering is often performed via the Buckley-Leverett analytical solution, which has helped to solve problems in the secondary recovery stage by water flooding in oil recovery projects. Most NAPL soil remediation technologies and related technologies, such as chemical and thermal treatment, derive from the oil recovery applications. Concerns regarding environmental issues only started to appear during the second half of the 20th century, which provided the impetus to develop new technologies for environmental applications.

The continuum concept considers fluids and the solid phase as continuous and averages the fluid flow by volume at the subsurface, becoming a representative elementary volume (REV) [Bear (1972)]. It is a minimal volume of porous medium, starting from which the averaged intensive parameters become stable and no longer depend on the size of the medium. The REV is considered to be at the centimeter scale for properties such as porosity, permeability, and saturation. It means that on this scale Darcy's law is considered to be valid [Bear (1972)].

Most numerical modeling studies have been developed with the continuum approach, by focusing on applying local-scale equations parameters. In traditional models, the required constituent relationships for two-phase flow are pressure-saturation and relative permeability-

saturation functions [Kueper and Frind (1992)]. Two-phase flow also provides further coupling of two equations through the phase saturations [Reeves and Celia (1996)]. In the next section, we review these constituent relationships.

2.5.1 General model of multiphase/multicomponent flow and transport in porous media

The local-scale governing equations for multiphase and multicomponent flow in porous media were derived by considering the averaging over the pore scale. This means that all physical and chemical procedures need to consider pore scale phenomena. The mass balance equation for component k in phase α is derived as (Eq. 105) [Huyakorn and Pinder (1983); Miller *et al.* (1998); Crichlow (1977); Bear (1972)]:

$$\frac{\partial}{\partial t}(\varepsilon_{\alpha}\rho_{\alpha}\bar{\omega}_{k}^{\alpha}) + \frac{\partial}{\partial x}(\varepsilon_{\alpha}\rho_{\alpha}\bar{\omega}_{k}^{\alpha}v_{\alpha,x}) - \frac{\partial}{\partial x}J_{k,x}^{\alpha} = I_{k}^{\alpha} + E_{k}^{\alpha} \quad \text{Eq. 105}$$

where:

- ε_{α} : volume fraction of each α phase (-)
- ρ_{α} : density of each α phase (kg.m^{-3})
- $\bar{\omega}_{k}^{\alpha}$: mass fraction of component k in α phase (-)
- $v_{\alpha,x}$: Darcy velocity of phase α in the x direction (m.s^{-1})
- $J_{k,x}^{\alpha}$: diffusive flux of component k from α phase in the x direction ($\text{kg.m}^{-2}.\text{s}^{-1}$)
- I_{k}^{α} : transfer of component k by phase change and diffusion throughout the α phase boundaries ($\text{kg.m}^{-3}.\text{s}^{-1}$)
- E_{k}^{α} : source of k to the α phase over biotic and abiotic transformations ($\text{kg.m}^{-3}.\text{s}^{-1}$)

The Darcy velocity in the direction x can be written as follows (Eq. 106):

$$v_{\alpha,x} = -\frac{k k_{r,\alpha}}{\varepsilon_{\alpha}\mu_{\alpha}} \left[\frac{\partial P_{\alpha}}{\partial x} + \rho_{\alpha}g \frac{\partial z}{\partial x} \right] \quad \text{Eq. 106}$$

where:

- P_{α} : pressure of each α phase (Pa)
- z : direction of gravity
- μ_{α} : dynamic viscosity of each α phase (Pa.s)
- k : tensor of intrinsic permeability (m^2)
- $k_{r,\alpha}$: relative permeability of each α phase (-)

Eq. 105 is derived from the fact that the mass fractions of the components, within a given phase, all add up to one. Also, the fractional phase volumes add up to one and the mass of a given component is conserved among the phases [Kueper and Frind (1992)]. Diffusive flux term of k component in α , J_{k}^{α} , was also represented by [Kueper and Frind (1992)] by assuming that hydrodynamic dispersion is Fickian in nature (Eq. 107):

$$J_{k}^{\alpha} = -\varepsilon_{\alpha}(\tau_{\alpha}D_{o}^{k,\alpha} + D_{m}^{k,\alpha}) \frac{\partial(\rho_{\alpha}\bar{\omega}_{k}^{\alpha})}{\partial x} \quad \text{Eq. 107}$$

where:

- τ_{α} : second rank tensor of phase tortuosity coefficients (-)
- $D_{o}^{k,\alpha}$: free molecular diffusion coefficient of component k from α phase (m.s^{-2})
- $D_{m}^{k,\alpha}$: tensor of mechanical dispersion of component k from α phase (-)

2.5.2 Mathematical models and formulations of two-phase immiscible flow in porous media

In reservoir simulations, especially in the oil industry, flow in two or more fluid phases is interesting, especially during the process of flooding within a porous medium. In this case, we consider two-phase flow as having fluids that are immiscible and no mass transfer between the phases [Chen *et al.* (2006)].

As mentioned above, Eq. 105 is the general mass balance equation of multiphase, multicomponent flow. However, depending on phase, component and porous media behaviour, and considering certain assumptions, it can be simplified. In multiphase modeling, we can assume that component breakdown and transformation does not substantially affect phase flow [Grant (2005)]. This assumption is valid for low-solubility DNAPLs, and also accounts for relatively short migration times [Kueper and Frind (1992)].

By assuming that fluids and porous media are incompressible (non-deformable), that flow is laminar, that DNAPL is non-soluble, and disregarding source or sink terms, mass balance continuity equations for wetting (subscript "w") and non-wetting (subscript "n") phases can be written as (Eq. 108 and Eq. 109) [Bear (1972)]:

$$\emptyset \frac{\partial(\rho_w S_w)}{\partial t} - \nabla \cdot \left[\rho_w \frac{\mathbf{k}_{ij} k_{r,w}}{\mu_w} (\nabla P_w - \rho_w \mathbf{g} \nabla z) \right] = q_w \quad \text{Eq. 108}$$

$$\emptyset \frac{\partial(\rho_n S_n)}{\partial t} - \nabla \cdot \left[\rho_n \frac{\mathbf{k}_{ij} k_{r,n}}{\mu_n} (\nabla P_n - \rho_n \mathbf{g} \nabla z) \right] = q_n \quad \text{Eq. 109}$$

where:

\mathbf{k}_{ij} : tensor of intrinsic permeability (m^2)

q_w : mass source of the wetting phase ($\text{kg} \cdot \text{m}^{-3} \cdot \text{s}^{-1}$)

q_n : mass source flow rate of the non-wetting phase ($\text{kg} \cdot \text{m}^{-3} \cdot \text{s}^{-1}$)

Phase pressures are linked through capillary pressure as follows (Eq. 110):

$$P_c(S_w) = P_n - P_w \quad \text{Eq. 110}$$

and the sum of the phase saturations is equal to one (Eq. 111):

$$S_w + S_n = 1 \quad \text{Eq. 111}$$

Now the equations are totally closed, with four unknowns and four equations. Eq. 108 to Eq. 111 give closed forms of the governing equations for two-phase immiscible flow in porous media.

There are many two-phase flow formulations in porous media. Here we have mentioned several formulations: phase pressure-saturation formulation, pressure-pressure formulation, flooding formulation, fractional flow formulation and two-phase mixed formulation. For convenience and depending on variables, Eq. 108 to Eq. 111 can be used to extract different formulations and primary variables.

2.5.2.1 Phase pressure–saturation formulation

This formulation is valid if saturation can be expressed as a function of capillary pressure. Later, we can reformulate it, in terms of the pressure of one phase and the saturation of another phase. Therefore, there are two main formulations [Bastian (1999)]:

1. The dependent variables are wetting phase pressure and non-wetting phase saturation (Eq. 112):

$$\left. \begin{aligned}
 -\emptyset \frac{\partial(\rho_w S_n)}{\partial t} - \nabla \cdot \rho_w [\mathbf{k}_{ij} \lambda_w (\nabla P_w - \rho_w \mathbf{g} \nabla z)] &= q_w \\
 -\emptyset \frac{\partial(\rho_n S_n)}{\partial t} - \nabla \cdot \rho_n [\mathbf{k}_{ij} \lambda_n (\nabla P_w + \nabla P_c - \rho_n \mathbf{g} \nabla z)] &= q_n \\
 \nabla P_c &= \frac{dP_c}{dS_n} \nabla S_n \\
 \lambda_w &= \frac{k_{r,w}}{\mu_w}; \lambda_n = \frac{k_{r,n}}{\mu_n}
 \end{aligned} \right\} S_n - P_w \quad \text{Eq. 112}$$

2. Dependent variables are wetting phase saturation and non-wetting phase pressure (Eq. 113):

$$\left. \begin{aligned}
 -\emptyset \frac{\partial(\rho_w S_w)}{\partial t} - \nabla \cdot \rho_w [\mathbf{k}_{ij} \lambda_w (\nabla P_n - \nabla P_c - \rho_w \mathbf{g} \nabla z)] &= q_w \\
 -\emptyset \frac{\partial(\rho_n S_w)}{\partial t} - \nabla \cdot \rho_n [\mathbf{k}_{ij} \lambda_n (\nabla P_n - \rho_n \mathbf{g} \nabla z)] &= q_n \\
 \nabla P_c &= \frac{dP_c}{dS_w} \nabla S_w
 \end{aligned} \right\} S_w - P_n \quad \text{Eq. 113}$$

where:

λ_w : mobility of the wetting phase ($\text{Pa}^{-1} \cdot \text{s}^{-1}$)

λ_n : mobility of the non-wetting phase ($\text{Pa}^{-1} \cdot \text{s}^{-1}$)

2.5.2.2 Pressure-pressure formulation

The dependent variables that are solved for wetting phase pressure and non-wetting phase pressure are one of the working models in the COMSOL Multiphysics® model library [COMSOL Multiphysics (2012)]. There was a convergence problem when the model was 100% saturated with water. In addition, Ataie-Ashtiani and Raeesi-Ardekani (2010) observed that the selection of the pressure-based formulation did not converge when the organic liquids were initially absent from a domain [Ataie-Ashtiani and Raeesi-Ardekani (2010)]. However, if the Brooks–Corey capillary pressure equation was used, with the assumption of $P_c = P_e$, the problem would converge to an acceptable solution (Eq. 114).

$$\left. \begin{aligned}
 C_{sc} \rho_w \left[\frac{\partial P_n}{\partial t} - \frac{\partial P_w}{\partial t} \right] - \nabla \cdot \rho_w [\mathbf{k}_{ij} \lambda_w (\nabla P_w - \rho_w \mathbf{g} \nabla z)] &= q_w \\
 -C_{sc} \rho_n \left[\frac{\partial P_n}{\partial t} - \frac{\partial P_w}{\partial t} \right] - \nabla \cdot \rho_n [\mathbf{k}_{ij} \lambda_n (\nabla P_n - \rho_n \mathbf{g} \nabla z)] &= q_n \\
 C_{sc} &= -\emptyset \frac{\partial S_w}{\partial P_c}
 \end{aligned} \right\} P_w - P_n \quad \text{Eq. 114}$$

where:

C_{sc} : storage coefficient (-)

2.5.2.3 Flooding formulation

This name came from flooding problem and it was traditionally used for flooding processes. The dependent variables are: a global pressure P_s and the capillary pressure P_c (Eq. 115) [Bjørnará and Aker (2008)]:

$$\left. \begin{aligned}
 \frac{\partial}{\partial x} \left(\lambda_s \frac{\partial P_s}{\partial x} + \lambda_c \frac{\partial P_c}{\partial x} \right) + \frac{\partial}{\partial y} \left(\lambda_s \frac{\partial P_s}{\partial y} + \lambda_c \frac{\partial P_c}{\partial y} \right) &= q_{ps} \\
 -2C_{sc} \frac{\partial P_c}{\partial t} + \frac{\partial}{\partial x} \left(\lambda_s \frac{\partial P_c}{\partial x} + \lambda_c \frac{\partial P_s}{\partial x} \right) + \frac{\partial}{\partial y} \left(\lambda_s \frac{\partial P_c}{\partial y} + \lambda_c \frac{\partial P_s}{\partial y} \right) &= q_{pc} \\
 C_{sc} &= -\phi \frac{\partial S_w}{\partial P_c} \\
 \lambda_c &= \frac{1}{2} \left(\frac{k_{r,n}}{\mu_n} - \frac{k_{r,w}}{\mu_w} \right) \mathbf{k}_{ij} \\
 \lambda_s &= \frac{1}{2} \left(\frac{k_{r,n}}{\mu_n} - \frac{k_{r,w}}{\mu_w} \right) \mathbf{k}_{ij}
 \end{aligned} \right\} P_c - P_s \quad \text{Eq. 115}$$

where:

- P_s : global pressure (Pa)
- q_{ps} : global mass source ($\text{kg.m}^{-3}.\text{s}^{-1}$)
- q_{pc} : capillary mass source ($\text{kg.m}^{-3}.\text{s}^{-1}$)
- λ_c : capillary mobility ($\text{m}^2.\text{Pa}^{-1}.\text{s}^{-1}$)
- λ_s : global mobility ($\text{m}^2.\text{Pa}^{-1}.\text{s}^{-1}$)

2.5.2.4 Fractional flow formulations

Fractional flow was traditionally developed in the petroleum engineering literature, and it has been known as equations that describe two-phase flow in petroleum reservoirs. The system of equations can be written in terms of a global pressure and saturation of one phase ([Antontsev (1972); Chavent and Jaffre (1986); Chen and Ewing (1997)]). The fractional flow approach considers the multiphase flow problem as a total fluid flow of a single phase, and then describes each phase as fractions of the total flow. This approach consists of two equations; the global pressure equation and the saturation equation. The first pressure equation can be found by adding the mass balances and doing some numerical manipulation for total phase; the second saturation equation is found by subtracting the mass balances and doing some numerical manipulation for one phase (Eq. 116) [Bjørnarå and Aker (2008)]:

$$\begin{aligned}
 \nabla \cdot \mathbf{v} &= q_n + q_w \\
 \phi \frac{\partial S_\alpha}{\partial t} + \nabla \cdot \mathbf{v}_\alpha &= q_\alpha
 \end{aligned} \quad \text{Eq. 116}$$

where:

- q_α : mass source of the α phase ($\text{kg.m}^{-3}.\text{s}^{-1}$)
- S_α : saturation of α phase (-)

Chen *et al.* (2006) illustrated many types of fractional flow formulations and compared them for realistic two-phase flow in petroleum reservoirs as below (Eq. 117 to Eq. 119) [Chen *et al.* (2006)]:

Phase formulation (P_n - S_w)

$$\begin{aligned}
 \mathbf{v} &= -\mathbf{k}_{ij} [\lambda(S_w) \nabla P_n - \lambda_w(S_w) \nabla P_c] - (\lambda_w \rho_w + \lambda_n \rho_n) \mathbf{g} \nabla z \\
 \phi \frac{\partial S_w}{\partial t} + \nabla \cdot \left\{ \mathbf{k}_{ij} f_w(S_w) \lambda_n(S_w) \left[\frac{dP_c}{dS_n} \nabla S_w + (\rho_0 - \rho_w) \mathbf{g} \nabla z \right] + f_w(S_w) \cdot \mathbf{v} \right\} &= q_w \\
 \lambda &= \lambda_w + \lambda_n \\
 f_w &= \frac{\lambda_w}{\lambda}
 \end{aligned} \quad \text{Eq. 117}$$

where:

λ : total mobility ($\text{m}^2 \cdot \text{Pa}^{-1} \cdot \text{s}^{-1}$)

f_w : fractional flow function of phase w (-)

Weighted formulation

This formulation is smoother than the phase formulation, and it can work even if one of the phases disappears [Chen *et al.* (2006)]

$$P = S_w P_w + S_n P_n$$

$$v = -\mathbf{k}_{ij} \{ \lambda(S_w) \nabla P - [S_w \lambda(S_w) - \lambda_w(S_w)] \nabla P_c + \lambda(S_w) P_c \nabla S_w - (\lambda_w \rho_w + \lambda_n \rho_n) \mathbf{g} \nabla z \} \quad \text{Eq. 118}$$

Global formulation

$$P = P_n - \int^S \left(f_w \frac{dP_c}{dS_w} \right) (\xi) d\xi$$

$$v = -\mathbf{k}_{ij} \{ \lambda(S_w) \nabla P - [\lambda_w \rho_w + \lambda_n \rho_n] \mathbf{g} \nabla z \} \quad \text{Eq. 119}$$

where:

ξ : molar density = $\frac{\rho}{W}$ ($\text{mol} \cdot \text{m}^{-3}$)

W: molecular weight ($\text{kg} \cdot \text{mol}^{-1}$)

Chen and al. (2006) have shown that the numerical results obtained using the phase and global formulations match well in terms of production rates, characterization curves, and water cuts. Numerical comparisons between three formulations led to the conclusion that results for the global and phase formulations are very close. However, when matched, the weighted formulation was rather different from reservoir data relative to the global and phase formulation. When the capillary effect is neglected, three formulations gave same the results [Chen *et al.* (2006)]. In this case, the saturation equation becomes the familiar Buckley-Leverett equation.

2.5.2.5 Two-phase mixed formulation

The mixture model has been derived from classical two-phase flow model (Eq. 108 to Eq. 111), without any approximation [Wang and Beckermann (1993)] as

Conservation of mass

$$\emptyset \frac{\partial \rho}{\partial t} + \nabla \cdot \rho \mathbf{u} = 0 \quad \text{Eq. 120}$$

In Eq. 120, it is clear that ρ is total density and \mathbf{u} velocity of fluid mixture, which are equal to:

$$\rho = S_w \rho_w + S_n \rho_n \quad \text{Eq. 121}$$

Conservation of momentum

$$v = -\mathbf{k}_{ij} (S_w \lambda_w + S_n \lambda_n) \cdot [\nabla p - \rho_K(S_w) \mathbf{g} \nabla z] \quad \text{Eq. 122}$$

$$\emptyset \frac{\partial (S_w \rho_w)}{\partial t} + \nabla \cdot (S_w \rho_w \mathbf{u}) = \nabla \cdot D_c \nabla \cdot (S_w \rho_w) - \nabla \cdot \left[m(S_w) \frac{\rho_n K \Delta \rho}{\mu_n} \mathbf{g} \nabla z \right] \quad \text{Eq. 123}$$

where:

D_c : capillary diffusion coefficient (-)

Eq. 123 is a direct manifestation of the liquid phase of mass balance. The right hand side of the equation is a combination of the capillarity-induced diffusive flux and the gravity-induced migration flux, where $D_c(S_w)$ is the so called diffusion coefficient, *i.e.* [Wang and Beckermann (1993)]:

$$D_c(S_w) = \frac{\rho_n K}{\mu_n} \lambda(1 - \lambda) \cdot \left(- \frac{dP_c}{dS_w} \right) \quad \text{Eq. 124}$$

and $m(S_w)$, expressed as

$$m(S_w) = k_{r,n}(S_w) \lambda(S_w) \quad \text{Eq. 125}$$

is termed the hindrance function for phase migration and eventual separation. The kinetic mixture density that is depends on relative mobility of each phase.

$$\rho_K(S_w) = \rho_w \lambda_w + \rho_n \lambda_n \quad \text{Eq. 126}$$

To close the equation system, we need unity of all saturation.

$$S_w + S_n = 1 \quad \text{Eq. 127}$$

2.5.2.6 Mathematical models and formulations of two-phase immiscible flow in porous media

The pros and cons of each formulation are listed in Table 19. However, it was hard to judge them without verifying them ourselves.

Table 19: Characteristics of two-phase flow models (adapted from [Wang and Beckermann (1993); Chen *et al.* (2006); Bjørnarå and Aker (2008)])

#	Two-phase immiscible flow models	Dependent variables	Comments
1	Phase pressure–saturation formulation	$P_w S_n$ or $P_n S_w$	Very sensitive to time step, mesh and boundary conditions. Convergence problem.
2	Pressure-pressure formulation	$P_w P_n$	Saturation was implemented depending on two pressures. Boundary conditions should be selected by saturation change.
3	Flooding formulation	$P_s P_c$	Close to pressure-pressure formulation. Needs more investigation for full understanding.
4	Fractional flow formulations	$P_s S_n$ or $P_s S_w$	One of the most investigated formulations. Easy to implement; simulation time is shorter than pressure formulations.
4.1	Phase formulation	$P_n S_w$	All three models come from fractional flow, with different pressure and saturation formulations. As discussed before, the matching results weighted formulation was more irregular than global and phase formulations. Also, weighted formulation requires a denser mesh and is very sensitive to this [Bjørnarå and Aker (2008)].
4.2	Weighted formulation	$P=P_w \times S_w + P_n \times S_n S_w$	
4.3	Global formulation	$P_s S_w$	
5	Two-phase mixed formulation	$P_s S_w$	Very similar formulation to the fractional flow model.

2.5.3 Commercial numerical models

Several commercial numerical software packages can simulate multiphase flow phenomena in porous media.

These models are used to properly design remediation processes. Before installing treatment units, it is appropriate to:

- Make sure that the contaminant sources (pure product) are clearly defined,
- Acquire data on the groundwater quality (permeability, transmissivity, etc.),
- Perform feasibility and treatability tests.

A brief description of some of these models is presented in Table 20 and Table 21.

Table 20: Characteristics of three-phase flow models [Sleep (2003)]

Numerical models	Description	Selected references
T2VOC	3D model, three-phase single component transport; it includes phase partition, mass transfer, reactive aspects (convective transport, diffusion, adsorption and biodegradation of a simple model - Non-sequential reactions)	[Falta <i>et al.</i> (1995)]
TOUGH2	3D model, three-phase multicomponent multi-species transport; it includes phase partition, mass transfer, reactive aspects (convective transport, diffusion, adsorption and biodegradation of a simple model - Non-sequential reactions)	[Pruess (1991)]
TMVOC	Module for Tough 2: 3D model, three-phase flow with multi-species transport; it includes phase partition, mass transfer, reactive aspects (convective transport, diffusion, adsorption and biodegradation of a simple model - Non-sequential reactions)	[Pruess <i>et al.</i> (1999)]
MOFAT	2D model, three-phase flow with multi-species transport	[Katyal <i>et al.</i> (1991)]
STOMP	3D model, three-phase flow with multi-species transport (including heat and transport model "dual porosity")	[Lenhard <i>et al.</i> (1995)]
NAPL	3D model, three-phase flow with the transport of a single chemical species (includes mass transport in dynamic conditions) k-D-P sub-model with hysteresis. Dissolution and volatilization are accounted for using mass transfer sub-models.	[Guarnaccia <i>et al.</i> (1997)]
FEHM	3D model, three-phase flow with multi-species transport (including heat and transport model "dual porosity")	[Zyvoloski <i>et al.</i> (1995)] [Dash <i>et al.</i> (1997)]
MAGNUS	3D model, three-phase flow with transport for only one chemical species	[Huyakorn <i>et al.</i> (1994)]
MUFTE	3D model, three-phase flow with transport for only one chemical specie	[Helmig <i>et al.</i> (1994)]
NUFT	3D model, three-phase flow with multi-species transport (includes heat transport model "dual porosity" and ability to simulate "system injection" systems)	[Nitao (1996)]
COMP-FLOW	3D model, three-phase flow with multi-species transport (including "dual porosity" model and ability to work with fractured systems)	[White and Oostrom (1996)]
COMP-SIM	3D model, three-phase flow multi-species transport (includes heat transport model "dual porosity" and biodegradation)	[Unger <i>et al.</i> (1995)] [Sleep and Sykes (1993)]
UTCHEM	3D model, three-phase flow with multi-species transport (includes mass transport in dynamic conditions, different models and the reactive surfactant effect)	[Pope <i>et al.</i> (1999)]

Table 21: Characteristics of two-phase flow models and vadose zone models [Sleep (2003)]

Numerical models	Description	Selected references
CHAIN_2D	2D flow model in the unsaturated zone, with multi-species transport and sequential decay	[Simunek and van Genuchten (1994)]
HBGC123D + FEMWATER	3D flow model in the saturated zone with multi-species transport (including heat transport, biogeochemical reactions and model "dual porosity")	[Yeh <i>et al.</i> (1998)]
3DMURF + 3DMURT	3D flow model in the unsaturated zone, with transport of a single chemical species ("dual porosity" model)	[Gwo <i>et al.</i> (1995)]
R-UNSAT	1D model (vertical) or 2D (radial configuration) flow in the unsaturated zone, including multi-species transportation (diffusion in the liquid and vapor) with schematic of the NAPL source and sequential decay	[Lahvis and Baehr (1997)]
SUTRA Model	2D flow in a variable saturation system with transport of a single chemical species	[Voss (1984)]
VLEACH	1D flow model in the unsaturated with transport of a single chemical species and its diffusion in the vapor phase	[Turin (1990)]
VS2DI	2D model of flow in a variable saturation system with transport of a single chemical species or heat	[Lappala <i>et al.</i> (1987)]

A methodology for how to choose the model type, depending on the objectives and available data, is presented in Figure 37.

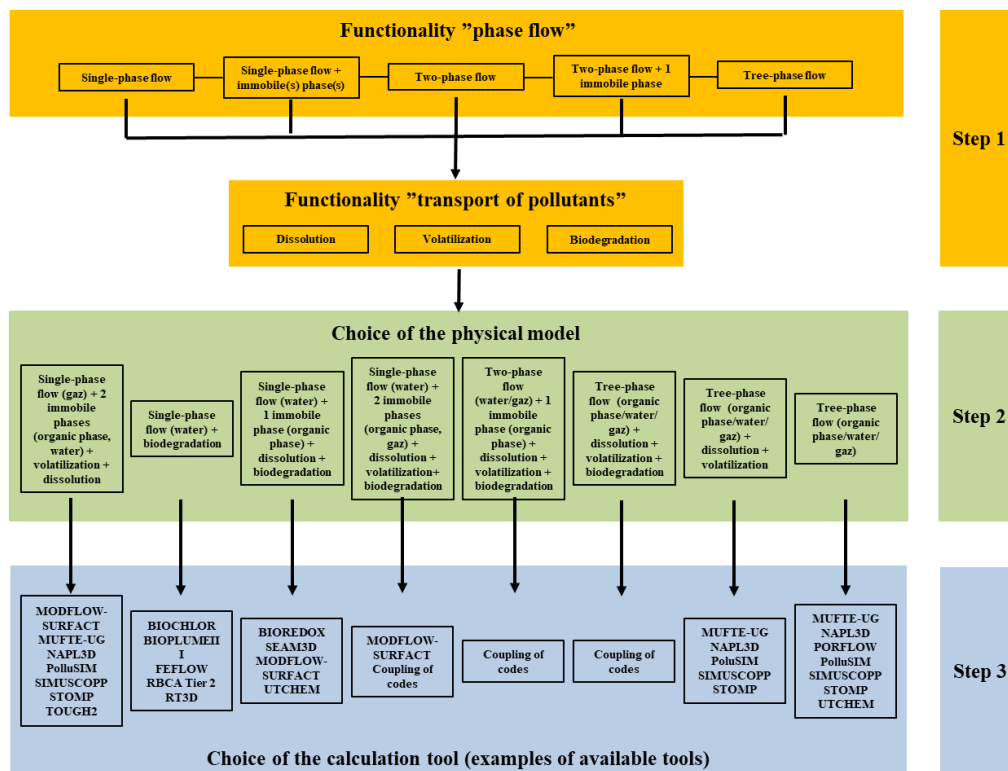


Figure 37: Flow chart as a decision tool for selecting the right model type (adapted from [ADEME *et al.* (2007)])

2.6 Electromagnetism, resistivity and permittivity

2.6.1 Maxwell equations

An electromagnetic field is defined as a set of four vectors: the electric field, the magnetic field, the electric displacement field and the magnetic induction. The principle of electromagnetic wave propagation is based on Maxwell's theory of equations, grouped as follows (Eq. 128 to Eq. 131) [Maxwell (1878)].

$$\nabla \vec{E}_c = \frac{\partial \vec{B}}{\partial t} \quad (\text{Maxwell-Faraday Law}) \quad \text{Eq. 128}$$

$$\vec{H}_{mf} = \vec{J}_c + \frac{\partial \vec{D}_e}{\partial t} \quad (\text{Maxwell-Ampere Law}) \quad \text{Eq. 129}$$

$$\nabla \vec{D}_e = \rho_e \quad (\text{Gauss's law - electric induction}) \quad \text{Eq. 130}$$

$$\nabla \vec{B} = 0 \quad (\text{Gauss's law - magnetic induction}) \quad \text{Eq. 131}$$

where:

\vec{E}_c : electric field (V.m⁻¹)

\vec{B} : magnetic induction (T)

\vec{H}_{mf} : magnetic field (A.m⁻¹)

\vec{J}_c : electrical conduction current density (A.m⁻²)

\vec{D}_e : electric displacement field (C.m⁻²)

ρ_e : electric charge density (C.m⁻²)

In general, the transmission of energy takes place mainly in a conduction current diffusion mode for frequencies below 10 MHz. Above this frequency, the energy transmission takes place mainly in a displacement current propagation mode. It should be noted that the more conductive the medium, the higher the energy losses (the mode of propagation of the energy will be mainly diffusive) [Reynolds (2011)].

2.6.2 Material behaviour with electromagnetic sollicitation

The intrinsic conductive and capacitive properties of materials can be represented by complex electrical conductivity, complex resistivity, or complex permittivity. Electrical conductivity is the ability of a material to support the flow of an electrical current (S.m⁻¹). Conductivity is the inverse of resistivity (Ω.m). Permittivity is the material's ability to store charge from an applied electrical field without conducting electricity (F.m⁻¹) [Reynolds (2011); Revil (2012)].

The general introductory equations for electric phenomena in rocks are shown below [Ruffet (1993); Comparon (2005); Reynolds (2011)].

The total current density, J_e , can be described as follows:

$$J_e = J_c + J_d \quad \text{Eq. 132}$$

where:

J_e : total current density (A.m⁻²)

J_d : displacement current density (A.m⁻²)

J_c , conduction current density, is related by Ohm's law to the electric field (in a linear manner):

$$J_c = \sigma_c^* E_c = (\sigma_c' + i\sigma_c'') E_c \quad \text{Eq. 133}$$

where:

E_c : electric field strength ($V.m^{-1}$)

σ_c^* : electrical conductivity ($S.m^{-1}$)

σ_c' : Ohmic conductivity ($S.m^{-1}$)

σ_c'' : dissipation due to the finite rate of displacement of charge carriers and to the various losses due to dispersion (chemical reactions or heat loss) ($S.m^{-1}$)

J_d is the displacement current density, which is the partial derivative of the electric displacement field (D_e). In the time domain and in the frequency domain, respectively, the equation is as follows:

$$J_d = \frac{dD_e}{dt} \quad \text{Eq. 134}$$

$$J_d = i\omega_{cf}D_e \quad \text{Eq. 135}$$

where:

i^2 : imaginary unit, $i^2 = -1$

ω_{cf} : circular frequency; $\omega = 2\pi f$ ($rad.s^{-1}$)

f : frequency (Hz)

The electric displacement field is proportional to the electric field, E_c , via the following constituent relationship (see chapter 2.6.5):

$$D_e = \varepsilon^*E_c = \varepsilon_0E_c + P_z \quad \text{Eq. 136}$$

where:

ε^* : complex dielectric permittivity ($F.m^{-1}$)

P_z : medium polarization (dipolar moment per unit volume) ($C.m^{-2}$)

ε_0 : free space permittivity ($8.85 \times 10^{-12} F.m^{-1}$)

$$J_d = i\omega_{cf}\varepsilon^*E_c \quad \text{Eq. 137}$$

Dielectric permittivity, ε^* , is also presented as a complex number:

$$\varepsilon^* = \varepsilon' + i\varepsilon'' \quad \text{Eq. 138}$$

where:

ε' : energy transfer by displacement currents, real part of the complex dielectric permittivity ($F.m^{-1}$)

ε'' : imaginary part of the complex dielectric permittivity (which captures the losses due to conduction and polarization) ($F.m^{-1}$)

Finally, as the total current density, J_e , is the sum of the conduction current density and the displacement current density:

$$J_e = (\sigma_c^* + i\omega_{cf}\varepsilon^*)E_c = \left[(\sigma_c' + i\omega_{cf}\varepsilon'') + i\omega_{cf} \left(\varepsilon' + \frac{\sigma_c''}{\omega_{cf}} \right) \right] E_c \quad \text{Eq. 139}$$

The conduction and displacement currents cannot be distinguished. As a result, the imaginary part of the permittivity plays the role of conductivity, and the imaginary part of the conductivity plays the role of permittivity. Experimentally, it is no longer possible to distinguish the contributions σ' and ε'' on the one hand, and σ'' and ε' on the other hand. The concepts of permittivity effective (ε_{eff}) and effective conductivity (σ_{eff}) can be defined as follows (Eq. 140 and Eq. 141) [Deparis (2007)]:

$$\sigma'_{c,eff} = \sigma_c' + i\omega_{cf}\varepsilon'' \quad \text{Eq. 140}$$

$$\varepsilon'_{eff} = \varepsilon' + \frac{\sigma_c''}{\omega_{cf}} \quad \text{Eq. 141}$$

where:

$$\sigma'_{c,eff}: \text{real effective electrical conductivity (S.m}^{-1}\text{)}$$

$$\epsilon'_{eff}: \text{real effective dielectric permittivity (F.m}^{-1}\text{)}$$

The resistivity and permittivity measured during our experiments only consider the real part of the equation. The imaginary part of the permittivity was not measured. The imaginary part of the resistivity was measured but were not interpreted.

2.6.3 Frequency dependence of the materials

The permittivity and the resistivity present differences of behavior according to the frequency of solicitation of the matter. These phenomena are called polarization and superimpose themselves. The main phenomena are [Telford *et al.* (1990); Nicolini *et al.* (1998)]:

- electronic or atomic polarization,
- ionic polarization,
- dipolar or orientation polarization,
- interface or space charge polarization.

These different phenomena are characterized by more or less important relaxation times. Figure 38 shows electric relaxation as a function of frequency.

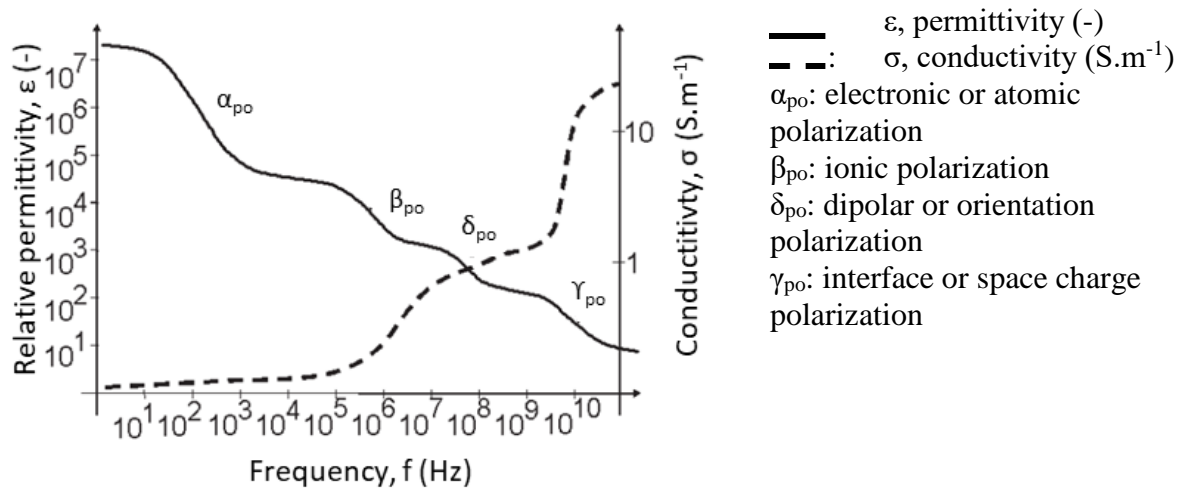


Figure 38: Electric relaxation as a function of frequency (adapted from [Nicolini *et al.* (1998)])

In the case of complex resistivity measurement, some authors describe, for frequencies below 1 MHz, 5 polarization mechanisms: Maxwell-Wagner polarization, polarization of the Stern layer, polarization of the diffuse layer, membrane polarization, and electrode polarization [Kemna *et al.* (2012); Revil (2012)].

2.6.4 Electrical resistivity and induced polarization

Artificially generated electric currents are supplied to the soil and the resulting potential differences are measured.

2.6.4.1 Electrical resistivity

Electrical resistivity surveys aim to determine the resistivity distribution of the surrounding soil volume [Telford *et al.* (1990); Samouëlian *et al.* (2005)].

The electrical resistance is defined by Ohm's law (Eq. 142):

$$R_e = \frac{\Delta V_e}{I_e} \quad \text{Eq. 142}$$

where:

R_e : electrical resistance (Ω)

ΔV_e : electrical potential difference (V)

I_e : electrical current intensity (A)

Ohm's law applies in the vast majority of geophysical cases unless high current densities (J) occur, in which case the linearity of the law may break down [Reynolds (2011)].

Electrical resistivity quantifies how strongly a material opposes the flow of electric current. The resistivity of an isotropic and homogeneous cylinder, with unit length and radius, is given by (Eq. 143):

$$\rho'_{\text{eff},c} = \frac{R_e A_c}{L_c} \quad \text{Eq. 143}$$

where:

$\rho'_{\text{eff},c}$: real effective electric resistivity ($\Omega \cdot \text{m}$)

A_c : cross sectional area (m^2)

L_c : length of the cylinder (m)

The reciprocal of electrical resistivity is electrical conductivity, σ_c ($\text{S} \cdot \text{m}^{-1}$) (Eq. 144).

$$\sigma'_{\text{eff},c} = \sigma_c = \frac{1}{\rho'_{\text{eff},c}} = \frac{1}{\rho_c} \quad \text{Eq. 144}$$

In this thesis, later, for the sake of simplification, $\sigma'_{\text{eff},c}$ will be called σ_c . and $\rho'_{\text{eff},c}$ will be called ρ_c .

Resistivity varies enormously in geological formations. It may range from 1 $\Omega \cdot \text{m}$ for saturated clays in water and very conducting at $10^6 \Omega \cdot \text{m}$ for naturally isolating magmatic rocks (Table 22).

Table 22: Electrical resistivity for different geological formations and water [Telford *et al.* (1990); Guérin *et al.* (2004)]

Formation/media	Electrical resistivity range ($\Omega.m$)
Water	
Sea water	0.1–0.3
Salted water	0.3–0.9
Brackish water	0.9–5
Leachate	0.9–5
Fresh water	5–80
Groundwater (fresh)	10-100
Sedimentary rocks and soils	
Sandstone	$8-4 \times 10^3$
Shale	$20-2 \times 10^3$
Limestone	$50-4 \times 10^2$
Wet sand	20–150
Dry sand	$250-4 \times 10^3$
Clay	1-100
Alluvium	10-800
Igneous and metamorphic rocks	
Granite	$5 \times 10^3-10^6$
Basalt	10^3-10^6
Slate	$6 \times 10^2-4 \times 10^7$
Marble	$10^2-2.5 \times 10^8$
Quartzite	$10^2-2 \times 10^8$

a) Parameters that affect electrical resistivity

Electrical resistivity measured in the porous medium depends on many parameters. As a first approach, as the Table 22 shows, most materials encountered in soils and subsoils have high resistivity (with the exception of a few metallic minerals). Also, soil resistivity is largely dependent on porosity, water saturation and pore fluid conductivity (it is in this case electrolytic conduction).

The presence of clay greatly influences the electric response. Surfaces of layers of clay are negatively charged. So all materials that contain a certain quantity of clay have a higher electrical conductivity than when it is absent [Vinegar and Waxman (1984)].

The pore water contains ions; it can *de facto* drive the electrical current. The ions are displaced under the effect of an external electric field, which creates the electrical current. The higher the ion content in solution in the water pore, the higher the electric charge. The electrical conductivity of a solution depends on two factors: the quantity of ions and also ion displacement (Eq. 145 and Eq. 146) [Telford *et al.* (1990)]:

$$v_{io} = \mu_{io} E_c \quad \text{Eq. 145}$$

where:

v_{io} : speed of ion I ($m.s^{-1}$)

μ_{io} : ion displacement capacity ($m^2.V^{-1}.s^{-1}$)

If we consider a pore water with several types of ions, the conductivity is the sum of the contribution from each ion (Kohlrausch's Law) (Eq. 146):

$$\sigma_{c,w} = F \sum_i C_{i0} |n_i| \mu_{i0} \quad \text{Eq. 146}$$

where:

$\sigma_{c,w}$: real effective electrical conductivity of water (S.m^{-1})

C_{i0} : ion concentration (mol.m^{-3})

n_i : ion charge (-)

F: Faraday constant ($F=9.65 \times 10^4 \text{ C.mol}^{-1}$)

The temperature also influences ionic mobility considerably, and de facto electrical resistivity [Dakhnov (1962); Grellier *et al.* (2008)]. Accordingly, between the temperatures of 0-200 °C, Dakhnov (1962) established the following relationship (for ionic fluids) (Eq. 147):

$$\rho_{c,w} = \frac{\rho_{c,w_0}}{1 + \alpha_{c,w}(T - T_0)} \quad \text{Eq. 147}$$

where:

$\rho_{c,w}$: electrical resistivity of the fluid at temperature T ($\Omega.m$)

ρ_{c,w_0} : resistivity of the fluid at temperature T_0 ($\Omega.m$)

$\alpha_{c,w}$: temperature coefficient of resistivity; $\alpha_{c,w} \approx 0.023 \text{ } ^\circ\text{C}^{-1}$ for $T_0 = 23 \text{ } ^\circ\text{C}$, and $0.025 \text{ } ^\circ\text{C}^{-1}$ for $T_0 = 0 \text{ } ^\circ\text{C}$

Of course, the higher the water saturation, the higher the electrical conductivity. In the same way, the higher then porosity (connected), the higher the electrical conductivity [Telford *et al.* (1990); Hersir and Árnason (2009)].

b) Archie's law

In the case of electrolytical conduction, the water pore is the key point to consider in approaching electrical conductivity in groundwater. It has been observed for many cases that resistivity of water-bearing rocks varies approximately with the inverse square of the porosity. Archie's law describes how resistivity depends on porosity if ionic conduction in the pore fluid dominates other conduction mechanisms in the rocks [Archie (1942)] (Eq. 148).

$$\rho_c = \rho_{c,w} a_c \phi^{-m_c} \quad \text{Eq. 148}$$

where:

a_c : empirical parameter, varies from <1 for intergranular porosity to > 1 for joint porosity, usually around 1 (-)

m_c : cementing factor, an empirical parameter, varies from 1.2 for unconsolidated sediments to 3.5 for crystalline rocks, usually around 2 (-)

Parameters related to rock are often grouped in the term of formation factor F_c (Eq. 149):

$$F_c = a_c \phi^{-m_c} \quad \text{Eq. 149}$$

where:

F_c : formation factor (-)

Archie's law seems to be a good approximation when the conductivity is dominated by the saturating fluid, which corresponds to a large part of non-consolidated porous media with a low clay content [Árnason *et al.* (2000)]. Parameters a and m can be determined precisely in a laboratory.

Models similar to Archie's law have been developed in the case of soils containing clay (taking into account the surface conduction) [Waxman and Smits (1968); de Lima and Sharma (1990); Revil *et al.* (1998)].

c) Basic principles of the experimental set-up

Classical measurement of electrical resistivity (time domain) consists in injecting a current via two current electrodes and in recording the resulting potential difference via two potential electrodes. Figure 39 shows this device (points A and B: current electrode; points M and N: potential electrodes). These four points form a quadripole.

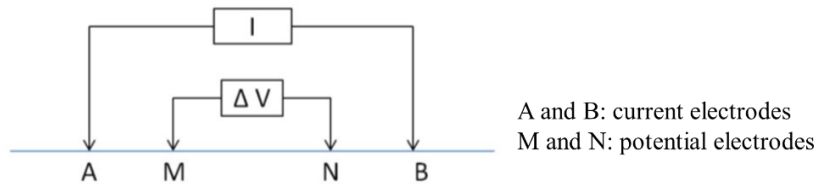


Figure 39: Principle of electrical resistivity measurement (adapted from [Noel (2014)])

In a completely homogeneous and isotropic medium, electrical equipotentials are hemispherical when the currents are on the soil surface (Figure 40) [Kearey *et al.* (2002); Samouëlian *et al.* (2005)].

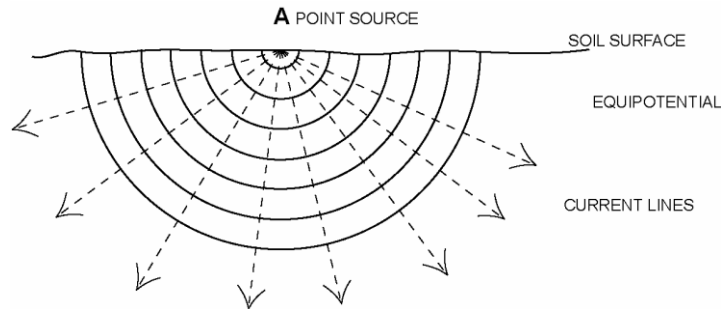


Figure 40: Distribution of the current flow in a homogeneous soil [Samouëlian *et al.* (2005)]

Therefore current density, J_e , propagates in all directions evenly; it can be determined as follows (Eq. 150):

$$J_e = \frac{I_e}{2\pi r_c^2} \quad \text{Eq. 150}$$

where:

$2\pi r_c^2$: surface of a hemispherical sphere of radius r_c (m^2)

Potential (V_e) can be calculated (Eq. 151):

$$V_e = \frac{\rho_c I_e}{2\pi r_c} \quad \text{Eq. 151}$$

If we refer to Ohm's law (Eq. 142) applied to the quadripole, we can deduce the potential difference, ΔV , measured between electrodes M and N (Eq. 152) [Samouëlian *et al.* (2005)]:

$$\Delta V_e = \frac{\rho_c I_e}{2\pi} \left[\frac{1}{AM} - \frac{1}{BM} - \frac{1}{AN} + \frac{1}{BN} \right] \quad \text{Eq. 152}$$

where:

AM, BM, AN, BN: distance A-M, B-M, A-N, B-N (m)

From this we can calculate the apparent electrical resistivity, ρ_c , with the following equation (Eq. 153):

$$\rho_c = \left[\frac{2\pi}{\frac{1}{AM} - \frac{1}{BM} - \frac{1}{AN} + \frac{1}{BN}} \right] \frac{\Delta V_e}{I_e} = K_g \frac{\Delta V_e}{I_e} \quad \text{Eq. 153}$$

where:

K_g : geometrical coefficient (that depends on the arrangement of the four electrodes A,B, M and N) (m)

Different arrangements exist for the four electrodes A, B, M and N: Wenner, Wenner-Schlumberger, dipole-dipole [Ward and Sill (1982)]. In our study, the electrodes configuration used are Wenner for the 1D cells, Wenner-Schlumberger 1D columns, and Wenner or equatorial dipole-dipole for the 2D tank, which are a commonly used array in similar laboratory tank experiments (Figure 41) [Wang *et al.* (2010); Power *et al.* (2014); Orlando and Renzi (2015); Deng *et al.* (2017)].

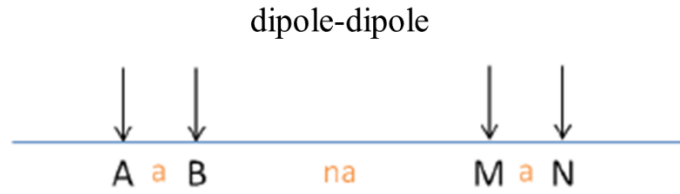


Figure 41: Measurement of electrical resistivity: dipole-dipole arrangement (adapted from [Noel (2014)])

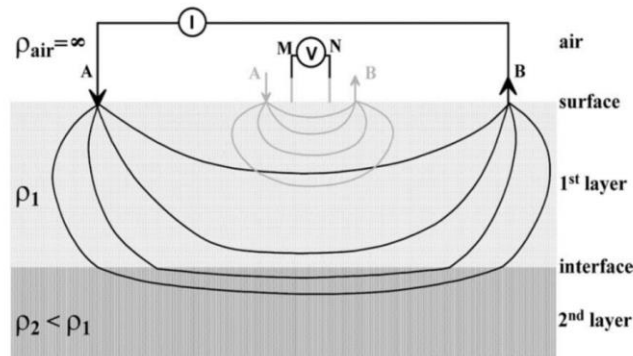
In the dipole-dipole arrangement case, the geometrical coefficient is equivalent to (Eq. 154):

$$K_a = \pi n_a (n_a + 1) (n_a + 2) a_a \quad \text{Eq. 154}$$

where:

a_a and n_a : distance A-M, B-M, A-N, B-N (m)

When the medium is homogeneous (*i.e.* in the case of our experiments with homogeneous glass beads), the measured electrical resistivity is the real electrical resistivity. Therefore, it can be interpreted directly. However, in the natural medium, this configuration is rather rare. Therefore we have to account for the fact that the electrodes are not perfectly aligned and that the electric signals encounter materials with very different properties. The wave propagations become substantially modified. Figure 42 shows a medium composed of two homogeneous layers (the first with resistivity ρ_1 , the second more conductive, with resistivity ρ_2). The current lines deviate at the boundary between the two layers. In this heterogeneous example, we have to use an inversion to obtain a quantitative measurement.



Grey lines: current lines for a small quadrupole; black lines: current lines for the biggest quadrupole; A and B: current electrodes; M and N: potential electrodes

Figure 42: Electrical sounding sketch [Guérin et al. (2004)]

2.6.4.2 Induced polarization

Induced polarization (IP) means a material's capacity to act as a capacitor, *i.e.* its capacity to charge when a current is applied and to discharge when the current is stopped. Two types of induced polarization can be measured [Reynolds (2011); Kemna et al. (2012)]:

- Time Domain Induced Polarization (TDIP) consists of measuring the voltage decay after stopping the transmitted current (Figure 43),
- Frequency Domain Induced Polarization (FDIP) consists of measuring a phase shift of the received voltage waveform relative to the transmitted waveform (Figure 44).

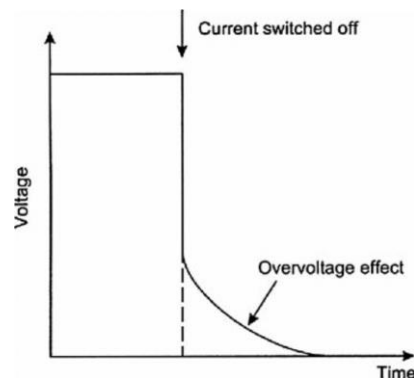


Figure 43: Time domain waveform illustrations [Reynolds (2011)]

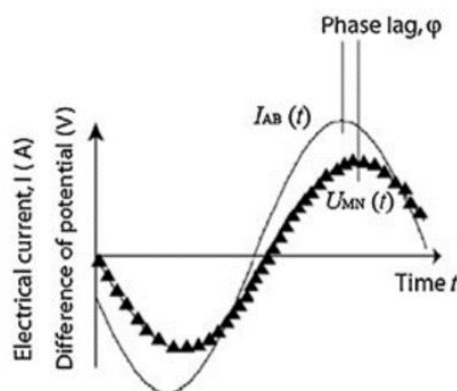


Figure 44: Frequency domain waveform illustrations [Revil (2012)]

For this thesis, only real resistivity will be studied.

2.6.4.3 NAPL and electrical resistivity

Electrical Resistivity Tomography (ERT) in underground water is based essentially on the electrical properties of water. Low changes in said electric properties of water have a substantial impact on measured apparent resistivity in the entire aquifer studied.

Therefore, electrical resistivity monitoring showed soil water content, saline water intrusion, and tracer tests [Revil *et al.* (2011); Lehtikoinen *et al.* (2009); de Franco *et al.* (2009); Perri *et al.* (2012)].

Geophysical research used to characterize hydrocarbon spill sites mainly relies on the electric properties of hydrocarbons because their presence may change some of the medium's physical properties, which can be captured by electric measurements and more particularly electrical resistivity measurements (classic and complex). These pollutants have high electrical resistivity and low dielectric constant, which respectively reduces and increases with changing degradation, as does electric chargeability, *i.e.* a capacity to polarize, which is significant and depends on their degradation state [Brown *et al.* (2003); Brown *et al.* (2004); Schmutz *et al.* (2010); Smallwood (2012)]. Since the early 2000s, geophysical methods have been the subject of intensive research to study environmental problems associated with hydrocarbons and to determine geophysical pollution/signal interaction. For example, Sauck (2000) interpreted his electrical resistivity measurements in monitoring wells in a LNAPL plume by considering a geo-electric model sensitive to various biogeochemical processes [Sauck (2000)]. Haridy *et al.* (2004) estimated LNAPL and water saturation in columns of sand water TDR (Time Domain Reflectometry) probes sensitive to resistivity and the dielectric constants of different phases in the medium [Haridy *et al.* (2004)]. What is more, several electrical resistivity monitoring experiments were conducted to follow biogeochemical remediation in sites polluted by chlorinated solvents and refined hydrocarbon [Nyquist *et al.* (1999); Power *et al.* (2014); Noel *et al.* (2016)].

Recent studies have also shown that the polarization caused would allow us to better characterize the organic pollution plume than classic electrical resistivity because we can measure chargeability too [Orozco *et al.* (2012); Ntarlagiannis *et al.* (2016)]. Power *et al.* (2014, 2015) and Deng *et al.* (2017) have shown the value of using laboratory tomography measurements for electrical resistivity (classic) combined if possible with imaging techniques to improve the interpretation of reverse resistivity measurements on sites polluted by NAPL composed of materials with varying permeabilities [Power *et al.* (2014); Power *et al.* (2015); Deng *et al.* (2017)].

Research has been undertaken specifically to connect DNAPL saturation and electrical resistivities. Resistivity is described by the sum of a bulk conductivity term and a surface conductivity term (both terms are saturation-dependent) [Revil (2012)]. Usually for sands, clean sands, and clean sandstones, surface conductivity is very low and can be neglected [Deng *et al.* (2017)]. Therefore, we can write the second Archie's law as follows (Eq. 155) [Archie (1942)]:

$$S_n = 1 - \left(\frac{\rho_{c,0}^{ERT}}{\rho_{c,t}^{ERT}} \right)^{\frac{1}{n^{ERT}}} \quad \text{Eq. 155}$$

where:

- $\rho_{c,0}^{ERT}$: initial resistivity (ERT-electrical resistivity tomography) of the water-saturated medium (background resistivity) ($\Omega.m$)
- $\rho_{c,t}^{ERT}$: real-time ERT measured resistivity of partially saturated medium ($\Omega.m$)
- n^{ERT} : saturation exponent (-)

The value for n is often estimated as being close to two for clean sand (without clay) [Archie (1942); Hearst *et al.* (2000); Monego *et al.* (2010)]. For two-phase system (water/air), Ulrich and Slater (2004) calculated a saturation exponent, n , that ranged between 1.1 and 2.7 [Ulrich and Slater (2004)].

Longeron *et al.* (1989) have demonstrated in drainage-imbibition experiments in a two-phase system (oil/air) that $n = 2.08$ [Longeron *et al.* (1989)]. Several authors have successfully interpreted experiments in a two-phase (DNAPL-water) system using the hypothesis that $n = 2$ [Chambers *et al.* (2004); Power *et al.* (2014); Deng *et al.* (2017)].

2.6.5 Dielectric permittivity

2.6.5.1 Background

Dielectric permittivity, ϵ^* , is a physical property which characterizes the degree of electrical polarization of a material under the influence of an external electric field, E_c (Eq. 139). The complex dielectric permittivity consists of two parts, a real and an imaginary part (Eq. 156) [Ledieu *et al.* (1986)]:

$$\epsilon^* = \epsilon' + i \left[\epsilon'' + \frac{\sigma_c''}{\omega_{cf}\epsilon_0} \right] \quad \text{Eq. 156}$$

At the highest effective frequency of the TDR Probes (200 MHz to 1.5 GHz) ϵ^* is considered to represent the real part only ϵ' [Heimovaara *et al.* (1994)]. The TDR probe used in our experiments operates at 70 MHz (see section 4.1.3).

The relative effective permittivity, ϵ_r , is defined as the ratio of the real effective dielectric permittivity, ϵ'_{eff} , and the free space permittivity, ϵ_0 (Eq. 159):

$$\epsilon_r = \frac{\epsilon'_{eff}}{\epsilon_0} \quad \text{Eq. 157}$$

where:

- $\epsilon_r = \epsilon$: relative effective permittivity (-)

In this thesis, later, all dielectric permittivity values are expressed relatively. In addition, for the sake of simplification, ϵ_r will be called ϵ .

TDR have been used since the 1970s and early 1980s to measure the apparent dielectric constant in soils [Topp *et al.* (1980)]. The principle rests on the difference between the dielectric constant of water (80), non-magnetic soil minerals (4-8), and air (1) [von Hippel (1954); Martinez and Byrnes (2001); Comegna *et al.* (2013)]. The difference in dielectric constants for the three elements (water, air, soil) is such that the permittivity value for wet soils depends closely on water saturation [Fellner-Feldegg (1969); Topp *et al.* (1980); Dalton *et al.* (1984)]. Topp *et al.*, 1980, showed that it was possible to connect the dielectric constant measured in soil with S_w using a calibration curve whose validity has been demonstrated for most nonorganic soils [Topp

et al. (1980)]. Subsequent studies have shown that TDR signals could be related to bulk electrical conductivity, σ_a (This parameter could depend on ion concentrations.) [Dalton *et al.* (1984)].

In geology, the permittivity is lowest for igneous rock. It is ten times higher for clays (Table 23).

Table 23: Dielectric permittivity in rocks and water at 100 MHz (adapted from [Martinez and Byrnes (2001)])

Formation/media	Dielectric permittivity (-)
Pure water	80
Clay	5 - 40
Sand (dry to saturated)	3 - 30
Shale	5 - 15
Limestone	7 - 8
Igneous rock	4 - 6
Air	1

The TDR instrument sends a high-frequency (20 kHz to 1.5 GHz) electromagnetic step pulse through a transmission line of known length L , and the pulse is reflected back at the end of the line. From the travel time of the pulse analysis, the soil's bulk dielectric constant is computed [Topp *et al.* (1980); Persson and Berndtsson (2002)]. The dielectric constant can be estimated as (Eq. 158):

$$\epsilon_r = \epsilon = \left(\frac{c_\epsilon}{v_\epsilon}\right)^2 = \left(\frac{c_\epsilon t_\epsilon}{2L_\epsilon}\right)^2 \quad \text{Eq. 158}$$

where:

- c_ϵ : speed of light (velocity of electromagnetic waves) in vacuum ($c_\epsilon = 3 \times 10^8 \text{ m.s}^{-1}$)
- v_ϵ : function of the propagation velocity, $v_\epsilon = 2L_\epsilon/t_\epsilon \text{ (m.s}^{-1}\text{)}$
- L_ϵ : waveguide length (m)
- t_ϵ : travel time for the pulse to traverse the length of the embedded waveguide (down and back: $2L$) (s)

2.6.5.2 NAPL and dielectric permittivity

One of the most used physical models of dielectric permittivity describes soil as a mixture of particles, water and air, called the Complex Refractive Index Model (CRIM). It is presented in Eq. 159 [Birchak *et al.* (1974); Roth *et al.* (1990); Endres and Knight (1992)]:

$$\epsilon = \left[\sum_{i=1}^N v_i \epsilon_i^{\alpha_\epsilon} \right]^{1/\alpha_\epsilon} \quad \text{Eq. 159}$$

where:

- ϵ : relative effective permittivity of the mixture (-)
- ϵ_i : relative effective permittivity of the i phase (-)
- v_i : volume of the i phase (-)
- α_ϵ : empirical constant related to the geometry of the grains and their spatial distribution (-)

For mixtures of soil saturated with water, the CRIM equation is as follows (Eq. 160):

$$\varepsilon_{s-w} = \left[(1 - \emptyset) \varepsilon_s^{\alpha_\varepsilon} + \emptyset S_w \varepsilon_w^{\alpha_\varepsilon} + \emptyset (1 - S_w) \varepsilon_a^{\alpha_\varepsilon} \right]^{\frac{1}{\alpha_\varepsilon}} \quad \text{Eq. 160}$$

where:

- ε_{s-w} : relative effective permittivity of the soil-water mixture (-)
- ε_s : relative effective permittivity of soil particles (-)
- ε_w : relative effective permittivity of water (-)
- ε_a : relative effective permittivity of air (-)

For mixtures of soil saturated with NAPL, the CRIM equation becomes (Eq. 161):

$$\varepsilon_{s-n} = \left[(1 - \emptyset) \varepsilon_s^{\alpha_\varepsilon} + \emptyset S_n \varepsilon_n^{\alpha_\varepsilon} + \emptyset (1 - S_n) \varepsilon_a^{\alpha_\varepsilon} \right]^{\frac{1}{\alpha_\varepsilon}} \quad \text{Eq. 161}$$

where:

- ε_{s-n} : relative effective permittivity of the soil-NAPL mixture (-)
- ε_n : relative effective permittivity of NAPL (-)

Combining the equations above (Eq. 160 et Eq. 161) leads to the following formulations (Eq. 162 et Eq. 163) [Comegna *et al.* (2013)]:

$$\varepsilon_{s-w-n} = \left[\beta_\varepsilon \varepsilon_n^{\alpha_\varepsilon} + (1 - \beta_\varepsilon) \varepsilon_{s-w}^{\alpha_\varepsilon} \right]^{\frac{1}{\alpha_\varepsilon}} \quad \text{Eq. 162}$$

$$\text{with } \beta_\varepsilon = \frac{S_n}{S_n + S_w} \quad \text{Eq. 163}$$

where:

- ε_{s-w-n} : relative effective permittivity of the soil-water-NAPL mixture (-)
- β_ε : fitting parameter for the determination of ε_{s-w-n} (-)

The empirical constant, α_ε , related to the geometry of the grains and their spatial distribution, can be estimated for homogeneous and isotropic soils as being 0.5 [Alharti *et al.* (1986); Gueguen and Palciauskas (1994); Huisman *et al.* (2003); Mavko *et al.* (2009); Coppola *et al.* (2013)]. However we know that α_ε can vary significantly in a soil-water-air system (from 0.46 to 0.67) and in a soil-water-bound water-air system (from 0.39 to 0.81) [Dobson *et al.* (1985); Roth *et al.* (1990); Jacobsen and Schjønning (1995); Ajo-Franklin *et al.* (2004)].

For a three-phase mineral/water/NAPL mixture and using the hypothesis that α_ε is 0.5, the CRIM formula can be written as follows (Eq. 164) [Ajo-Franklin *et al.* (2004)]:

$$\varepsilon = \left[\emptyset (S_w \sqrt{\varepsilon_w} + S_n \sqrt{\varepsilon_n}) + (1 - \emptyset) \sqrt{\varepsilon_s} \right]^2 \quad \text{Eq. 164}$$

Very good correlations between the CRIM model and experimental measurements have been obtained to describe dielectric properties in the unsaturated zone (air-water in porous media) [Knight (2001)] and soil-water-NAPL mixtures [Francisca and Montoro (2012)].

In the 1990s, studies were undertaken to connect the S_n in NAPL in saturated soils to the ε measured by TDR probes [Redman *et al.* (1991); Redman and DeRyck (1994); Kueper *et al.* (1993); Brewster *et al.* (1995)]. PCE samples spiked at controlled saturations were monitored by TDR. This showed good correlation, so it led to mixing models to estimate S_n in saturated porous media [Redman and DeRyck (1994)]. For the vadose zone, it is impossible to measure S_n using only ε if S_w is unknown [Redman and DeRyck (1994)].

Ajo-Franklin *et al.* (2004) have also obtained correlations greater than 97% using the CRIM model with TCE in the saturated zone [Ajo-Franklin *et al.* (2004)].

Finally, Persson and Berndtsson (2002) demonstrated that the mixing model used led to errors up to 0.05 in saturated sand polluted by sunflower seed oil, synthetic motor oil and paraffin [Persson and Berndtsson (2002)]. To overcome this error, Persson and Berndtsson coupled TDR probes with de conductivity measurements.

2.7 Other non-invasive imaging methods and optical imaging methods

Four methods are currently used: X-ray, gamma radiation, magnetic resonance imaging (MRI) and optical imaging [Werth *et al.* (2010)].

2.7.1 Alternative methods

X-ray has a high-resolution acquisition and can measure fluid saturations in three-dimensional (3D) laboratory experiments. But this method is suited for relatively small sample size (maximum a few cm) and takes much time to record a complete 3D scan (10 to 30 minutes) [Brusseau *et al.* (2008); Schnaart and Brusseau (2005)]. The sample saturation profile can also be changed during image acquisition.

Gamma radiation can work with a relatively wide scale (from cm to several meters). Another advantage is accurate data. This method is quite difficult to design but becomes easy to maintain. Its disadvantages include the long counting time (observed 45 seconds or more) for accurate determination ($\sim 1 \text{ cm}^2$). This method measured conditions close to or at equilibrium state. The calibration procedure needed for high data acquisition takes a long time [Illangasekare *et al.* (1995b); Jalbert *et al.* (2003); Brusseau *et al.* (2000); Ostrom *et al.* (1999)].

MRI can directly plot 1D, 2D and 3D imaging of processes occurring in porous media. This method is original because the MRI signal is generated directly from fluids or solid phases. MRI has excellent accuracy (up to $10 \mu\text{m}$) with fast imaging acquisition that allows monitoring under dynamic conditions. This method is sensitive to the presence of ferromagnetic materials. The main disadvantage is that a magnetic resonance scanner is very expensive and complex to maintain [Zhang *et al.* (2007); Caprihan and Fukushima (1990); Chu *et al.* (2004); Dijk *et al.* (1999); Johns and Gladden (1999)].

Optical imaging acquisition is cheaper than the other methods mentioned above. This technique is also the easiest option for visualizing fluid saturation, flows, and solute transport in a two-dimensional (2D) laboratory porous medium [Werth *et al.* (2010)].

For these reasons we wanted to review the literature in this area to understand and study many techniques and to establish our own technique to upgrade optical imaging analysis.

2.7.2 Optical imaging methods

2.7.2.1 Background

Cameras are the central instrument for acquiring the optical data. Early work was based on silver photographs that were scanned to digitize the information [Schincariol and Schwartz (1990)]. Nowadays all work uses a digital camera. Basically, the diaphragm and shutter of a digital camera let the correct quantity of light strike a CCD sensor (Charge Couple Device) to capture the image. The CCD sensor is the main image acquisition component. A CCD sensor

is a small plate piece placed inside the camera body. The CCD sensor is composed of several capacitors (pixels) which converted light information into electronic information. A pixel is the elementary part containing information on the three intensity lights: red, green and blue. A picture is composed of many pixels and the higher the pixel density, the better the resolution.

The Beer Lambert law is fundamental in the optical imaging analysis field. The power of a beam striking a block with absorbing properties (perpendicular to the surface) decreases because of the absorption. This law can be mathematically expressed [Skoog *et al.* (2007)] as (Eq. 165):

$$\log_{10} \left(\frac{I_t}{I_0} \right) = \varepsilon_l b_l M_l = D_t \quad \text{Eq. 165}$$

where:

I_0 : initial luminous intensity (-)

I_t : transmitted luminous intensity (-)

ε_l : numerical constant ($\text{L} \cdot \text{mol}^{-1} \cdot \text{cm}^{-1}$)

b_l : path length (cm)

M_l : molar absorptivity or molar absorption coefficient, number of moles per liter of absorbing solution ($\text{mol} \cdot \text{L}^{-1}$)

D_t : optical density of transmitted light (-)

The light transmitted through a photograph is defined as transmittance, τ , and can be expressed as (Eq. 166):

$$\tau_l = \frac{I_t}{I_0} \quad \text{Eq. 166}$$

where:

τ_l : transmittance (-)

RAW files are equivalent to photographic films, and the pixel value is equivalent to the transmitted light (I_t) [Flores *et al.* (2011)].

The optical density of transmitted light, D_t , is commonly defined as (Eq. 167):

$$D_t = -\log_{10}(\tau) \quad \text{Eq. 167}$$

The optical density of reflected light, D_r , can be defined as (Eq. 168 and Eq. 169):

$$D_r = -\log_{10}(\rho_t) \quad \text{Eq. 168}$$

$$\rho_t = \frac{I_r}{I_0} \quad \text{Eq. 169}$$

where:

D_r : optical density of reflected light (-)

ρ_t : ratio of reflected/initial luminous intensity (-)

I_r : reflected luminous intensity (-)

I_0 : initial luminous intensity (-)

However, due to its simplicity, the Beer-Lambert law is accurate only if the following conditions are met: i. the absorbing medium is homogeneous; ii. the light source is monochromatic; iii. scattering and reflection must not occur [Skoog *et al.* (2007)].

Currently, two kinds of optical imaging methods emerge in the research field, the Light Reflection Methods (LRM) and Light Transmission Methods (LTM) [Alazaiza *et al.* (2016)].

2.7.2.2 Light Reflected Methods

Several authors used reflected light to quantify fluid saturation inside a two-dimensional laboratory tank. The following is a non-exhaustive review but we focus on the main articles and the newest emergent alternative light reflected methods.

a) Primary work

Schincariol and Schwartz (1990) and Schincariol *et al.* (1993) published the first studies that correlated the reflected optical image with dyed NaCl concentration during miscible experiments. This method used a protocol based on the following eight steps [Schincariol and Schwartz (1990)] and [Schincariol *et al.* (1993)]:

- Scanning the negative: The negatives, from silver camera, were converted to 12-bit digital files, which means pixel values varied between 0 and 4095. The pixel value corresponds to the transmittance τ [Schincariol *et al.* (1993)].
- Computing an optical density curve: This involves using a greyscale card to assess the quality of pixel grey value recorded. They plotted the average transmittance value versus a known optical density value.
- Rotating and transforming the image to standard sized matrix (800×555): To ensure optimal photograph analysis, all photographs must have the same "Area of Interest", *i.e.* a region where the analysis will be performed. For this reason, they removed some detail, such as the flow tank or peripheral equipment. Then, they applied an algorithm [Cornhill *et al.* (1990)] to rotate and to translate the picture.
- Median smoothing on a 3×3 window: Median smoothing was applied on the whole matrix by averaging pixels contained in a 3 pixel \times 3 pixel window, to decrease the noise in the image.
- Subtraction of a background image: The lighting was not uniform over the whole picture. For this reason, appropriate image subtraction was necessary to correct this uneven lighting.
- Median smoothing on a 3×3 window: A second median smoothing was performed.
- Computing optical density vs. concentration standard curve: They obtained this calibration curve in which known concentrations were photographed.
- Using a standard curve to convert optical density values on scanned images to concentration: With the previous linear relationship all pixels from the matrix (800×555) values were converted into concentration values.

The authors obtained a maximum error of approximately $\pm 7-10\%$. This error could be due to the background subtraction and other correction techniques [Schincariol *et al.* (1993)].

b) Multispectral Image Analysis Method

Kechavarzi *et al.* (2000), developed a LRM based on the Schincariol *et al.* (1993) methods to quantify the fluid saturations of a three phase system (Air-Water-NAPL). They developed the MIAM (Multispectral Image Analysis Method) to quantify the residual saturation of Soltrol 220® (Phillips Petroleum).

Their study was composed of two parts. On the one hand, they established a link between the amounts of reflected light and fluid saturation in a cylindrical sample and, on the other hand,

they measured the fluid saturations in a two-dimensional laboratory tank. We focused on the second part because it is similar to our case.

It is important to define the Average Optical Density (AOD) as the following expression (Eq. 170):

$$D_{i_1} = \frac{1}{N} \sum_{j_1=1}^N d_{j_1 i_1} = \frac{1}{N} \sum_{j_1=1}^N \left[-\log_{10} \left(\frac{I_{j_1 i_1}^r}{I_{j_1 i_1}^0} \right) \right] \quad \text{Eq. 170}$$

where:

D_{i_1} : average optical densities (-)

N : number of pixels contained in the AOI (Area Of Interest) (-)

j_1 : sum index for a given spectral band i (-)

$d_{j_1 i_1}$: optical density of the individual pixels (-)

$I_{j_1 i_1}^r$: intensity of the reflected light given by the individual pixel values (-)

$I_{j_1 i_1}^0$: intensity of the light that would be reflected by an ideal white surface (-), $I_{j_1}^0$ was measured for every pixel of the nominal $I_{j_1}^0$ white patch of the Kodak® grey scale for each spectral band; $I_{j_1}^0$ was on average close to 4095.

This AOD notion involves discretization of the picture. The measurement method consists of computing in each mesh (or element) to quantify the fluid saturations.

Firstly they have established a clear linear relationship between AOD versus both water saturations and NAPL saturations as (Eq. 171 and Eq. 172):

$$D_{i_1}^w = \lambda_{i_1}^w S_w + \beta_{i_1}^w \quad \text{Eq. 171}$$

$$D_{i_1}^o = \lambda_{i_1}^o S_n + \beta_{i_1}^o \quad \text{Eq. 172}$$

where:

$D_{i_1}^w$: average optical densities for each pixel contained in the images of air-water two fluid phase systems (-)

$D_{i_1}^o$: average optical densities for each pixel contained in the images of air-NAPL two fluid phase systems (-)

$\lambda_{i_1}^w, \lambda_{i_1}^o, \beta_{i_1}^w$ and $\beta_{i_1}^o$: fitting coefficients of the linear regressions (-)

Next, they performed the spill experiment. They computed in each element the following equations to quantify the fluid saturations (Eq. 173 to Eq. 175):

$$S_{w2} = \frac{\lambda_{i_1}^o (D_{k_{12}}^{ow} - D_{k_{11}}^{ow}) - \lambda_{k_1}^o (D_{i_{12}}^{ow} - D_{i_{11}}^{ow})}{\lambda_{i_1}^o \lambda_{k_1}^w - \lambda_{k_1}^o \lambda_{i_1}^w} + S_{w1} \quad \text{Eq. 173}$$

$$S_{n2} = \frac{\lambda_{k_1}^w (D_{i_{12}}^{ow} - D_{i_{11}}^{ow}) - \lambda_{i_1}^w (D_{k_{12}}^{ow} - D_{k_{11}}^{ow})}{\lambda_{i_1}^o \lambda_{k_1}^w - \lambda_{k_1}^o \lambda_{i_1}^w} \quad \text{Eq. 174}$$

$$S_a = 1 - S_w - S_n \quad \text{Eq. 175}$$

where:

Indexes k_1 and i_1 : wavelength (nm)

Indexes 1 and 2: reference to the previous and current pictures, respectively

$D_{k_1}^{ow}$ and $D_{i_1}^{ow}$: average optical densities contained in the image of air-water-NAPL three fluid system at k_1 and i_1 wavelengths (-)

$\lambda_{k_1}^o$ and $\lambda_{k_1}^w$: slope coefficients determined during calibration (-)

This method involves a multispectral band because it is necessary to solve the previous set of equations (Eq. 173 and Eq. 174) to determine the fluid saturations. With high contrast between two spectral bands (determined by transmittance spectrum analysis), the system has enough unknown variables for enough equations.

c) Simplified Image Analysis Method

Flores *et al.*, (2011) provided another imaging analysis method because MIAM [Kechavarzi *et al.* (2000)] requires a heavy calibration procedure that consumes much time and materials [Flores *et al.* (2011); Alazaiza *et al.* (2016)]. For this reason, Flores *et al.*, (2011) developed SIAM (Simplified Image Analysis Method). This method is based on a simplified calibration procedure (3 samples) to avoid the heavy calibration procedure (47 samples) from MIAM. They quantified the residual saturation of LNAPL Sudan III dyed with brilliant blue FCF.

This method is also based on the Beer-Lambert laws. SIAM involves different band-pass filters (wavelengths are 450 nm and 640 nm). This method is summarized below.

The calibration was used with three column samples:

- $S_w = 0\%$; $S_n = 0\%$
- $S_w = 0\%$; $S_n = 100\%$
- $S_w = 100\%$; $S_n = 0\%$; for each calibration set, 2 photographs were taken at 450 nm and 640 nm.

The experiment was carried out using photographs monitoring at the 2 band pass filters. Post-processing pictures were on the Area of Interest (AOI) were discretized by 490 elements (matrix size is 70×7).

First, they calculated the optical densities acquired during the calibration process $[D_i^{00}]_{m_1 n_1}$; $[D_{i_1}^{10}]_{m_1 n_1}$; $[D_{i_1}^{01}]_{m_1 n_1}$; $[D_{j_1}^{00}]_{m_1 n_1}$; $[D_{j_1}^{10}]_j$ and $[D_{j_1}^{01}]_{m_1 n_1}$

where:

$[D^{00}]$, $[D^{10}]$ and $[D^{01}]$: optical density respectively for the dry sand, water-saturated sand, and NAPL-saturated sand, respectively at i_1 and j_1 the wavelength (-)

m_1 : vertical dimension of the matrix (m)

n_1 : horizontal dimensions of the matrix (m)

Then they solved the following set of equations to find S_w and S_n (Eq. 176):

$$\begin{bmatrix} D_{i_1} \\ D_{j_1} \end{bmatrix}_{nm} = \begin{bmatrix} (D_{i_1}^{10} - D_{i_1}^{00})S_w + (D_{i_1}^{01} - D_{i_1}^{00})S_n + D_{i_1}^{00} \\ (D_{j_1}^{10} - D_{j_1}^{00})S_w + (D_{j_1}^{01} - D_{j_1}^{00})S_n + D_{j_1}^{00} \end{bmatrix}_{mn} \quad \text{Eq. 176}$$

where:

$\begin{bmatrix} D_{i_1} \\ D_{j_1} \end{bmatrix}_{m_1 n_1}$: optical density on the mesh elements measured in both wavelength (-)

d) DNAPL counting cell method

The methods discussed above are based on the same idea. They used a calibration procedure to correlate cell intensity versus fluid saturation. Luciano *et al.* (2010) developed another way of analyzing the fluid saturations. Their method does not involve a calibration procedure or correlation cell. They counted, cell by cell, the frequency of DNAPL pixels detected inside the

cell. Cell size (15×15 pixels) was as large as the REV and pixel size was as large as grain size [Luciano *et al.* (2010)]. For those reasons, the ratio between pixels detected as DNAPL divided by total cell area gave an estimation of the fluid saturation. Of course, before counting those DNAPL pixels there was a pre-treatment procedure to detect the DNAPL pixels (summarized below).

Images were acquired and an AOI was determined. The AOI remained constant during the whole experiment. The AOI was converted into RGB 48 format to choose the best color filter. Choosing a color filter was necessary to increase the contrast between DNAPL and porous media. Once the best color contrast was chosen, then the AOI was converted to grey scale (8-bits format). An intensity pixel interval was defined as DNAPL (equal to 0) and applied to the whole AOI. The rest of the pixels (outside the interval) were defined as background (equal to 255). The image was transformed into a binary image (1=DNAPL and 0=background).

They discretized the AOI in its entirety to obtain a grid. Each cell was defined as 15 × 15 pixels. Then, they computed, with a Fortran program, the frequency of DNAPL in the cell. This DNAPL frequency represented the DNAPL cell saturation.

2.7.2.3 Light Transmitted Methods

a) Primary work on water saturation quantification

Hoar (1981) was the first to develop a Light Transmitted Method (LTM) to quantify water saturation in a sand field experimental chamber [Bob *et al.* (2008)]. In 1994, Tidwell and Glass improved this method by determining the water saturation of a two-phase experiment [Tidwell and Glass, 1994]. They correlated the number of pores filled with water to water saturation (S_w). One more step was performed with the elimination of calibration curve and K (from the Hao work) becoming an empirical parameter.

This LTM uses Fresnel's law to define the transmission (Eq. 177 and Eq. 178):

$$\tau_t = \frac{I_{t,out}}{I_{t,in}} = \frac{4n_t}{(n_t + 1)^2} \quad \text{Eq. 177}$$

$$n_t = \frac{n_{t,1}}{n_{t,2}} \quad \text{Eq. 178}$$

where:

τ_t : light transmission factor (-)

$I_{t,out}$: emergent light intensity (-)

$I_{t,in}$: incident light intensity (-)

n_t : ratio of refractive indices (-)

$n_{t,1}$ and $n_{t,2}$: refractive indices of the two media constituting the dioptr (-)

If each individual pore is either full or empty of water, then the intensity of transmitted light, I_v , is given by Eq. 179 [Tidwell and Glass (1994)]:

$$I_v = I_{vd} \left(\frac{\tau_{sw}}{\tau_{sa}} \right)^{2P_t} \quad \text{Eq. 179}$$

where:

I_v : intensity of transmitted light (-)

I_{vd} : emergent light intensity for the dry sample (-)

P_t : number of pores filled with water (-)

τ_{sw} : light transmission factors of sand-water interface (-)

τ_{sa} : light transmission factors of sand-air interface (-)

Water saturation can be computed by Eq. 180:

$$S_w = \frac{\ln[I_{vn}[(\tau_{sw}/\tau_{sa})^{2k_t} - 1] + 1]}{2k_t \ln[\tau_{sw}/\tau_{sa}]} \quad \text{Eq. 180}$$

where:

k_t : empirical parameter (-)

I_{vn} : normalized light intensity, $I_{vn} = \frac{I_v - I_{vd}}{I_{vs} - I_{vd}}$ (-)

I_{vs} : emergent light intensity for the saturated sample (-)

b) LTM without calibration procedure

Niemet and Selker (2001) improved the last work of Tidwell and Glass (1994) by eliminating the need for estimating the empirical parameter k or for a calibration procedure. They developed several models, but the best fit was obtained by the model introduced below. The model considers a wetting medium with a pore size distribution.

The fluid saturation, S_w , is computed from the numerical integration of the following equation (Eq. 181):

$$S_w = 1 - \frac{\int_0^\Omega \frac{d\Omega}{h}}{\int_0^1 \frac{d\Omega}{h}} \quad \text{Eq. 181}$$

where:

Ω : proportional to $\frac{A_t}{A_{t,T}} = \frac{\ln(I_{t,out}/I_{t,out,S})}{\ln(I_{t,out,S_w}/I_{t,out,S})}$

A_t : total cross-sectional area of drained pores at negative pressure head (m²)

$A_{t,T}$: total cross-sectional area of all effective pores (m²)

$I_{t,out,S}$: light intensity transmitted through a saturated sand (-)

I_{t,out,S_w} : light intensity transmitted at a residual saturated sand (-)

c) Imaging method based on hue

Saturation near walls can be different from that inside porous media. For this reason, Darnault *et al.*, 1998 developed a method to assess the fluid saturation in a two-phase fluid system [Darnault *et al.* (1998)]. The main concept is to use hue (color appearance parameters) instead of RGB (Red Green Blue) to calibrate and compute the fluid saturation.

A fundamental difference between their method and the previous study was using HIS (Hue-Intensity-Saturation) rather than the classic RGB format. Hue describes the pure color, intensity corresponds to the grey value and saturation is the degree of color diluted with white. They applied the HIS format to analyze the images, especially, the hue information. To use HIS, they converted RGB format into hue with the following equation (Eq. 182) [Wilson (1988)].

$$H_u = 255 \left[\frac{1}{360} \left[\gamma - \arctan \left(\frac{2R - G - B}{\sqrt{3} (G - B)} \right) \right] \right] \quad \text{Eq. 182}$$

where:

H_u : hue, color appearance parameters (°)

R: red

G: green

B: blue

Y: constant depending on the green and blue intensity, $Y=90$ for $G \geq B$ or $Y=270$ for $G < B$ (-)

This equation shows that hue is a better way to measure blue intensity than RGB format because each RGB component is affected [Darnault *et al.* (1998)].

The experimental protocol involved placing a light in front of and behind an experimental chamber. A calibration chamber was built to generate the hue vs. saturation fluid calibration. They processed with 6 different water saturations (0%, 20%, 40%, 60%, 80%, and 100%) to obtain the calibration curve (hue vs. S_w). The hue value was measured from a horizontal line 100 pixels long. The hue mean was calculated from a histogram of number of pixels vs. hue for the different water saturations. Two experiments were performed: the first to test the effectiveness of data acquisition for a simple water infiltration into an oil-saturated soil, the second to show the method for unstable fingered flow.

While the calibration experiment was performed, the oil-saturated soil looked yellow, the water saturated soil looked blue and oil-water-saturated soil looked green. However, the color was not perfectly distributed into the cell, due to oil and water ganglia formation. Each RGB format pixel was transformed into HIS. HIS has pieces of data: hue, intensity and saturation. The authors were not correlating intensity or saturation to water saturation. The calibration experiment showed that the mean hue value varied with water-saturation in the soil. A linear regression is provided with a good fit ($R^2 = 97.8\%$).

With this linear relationship between hue value and water saturation, they computed on AOI as large as 14,400 pixels surrounding a spill area to determine S_w . This linear regression fits for this experimental setup. A new calibration process must be performed for any new calibration.

The results with LTM were conclusive. The first flow infiltration experiment was monitoring; the amount of water was calculated with LTM. 19.85 mL of water was estimated by LTM for 20 mL of water injected. For the second experiment, the water content estimated with LTM was compared with X-ray measured. For the highest water content area, LTM estimated 0.26 – 0.28 $\text{cm}^3 \cdot \text{cm}^{-3}$ and X-ray estimated 0.265 $\text{cm}^3 \cdot \text{cm}^{-3}$.

3. CHARACTERIZATION OF THE DNAPL MIXTURE

3. CHARACTERIZATION OF THE DNAPL MIXTURE

In this section, we present and discuss our results for the rheological properties of the DNAPL mixture, such as dynamic viscosity, interfacial tension, contact angle, and density. These were measured at various temperatures and with different surfactants. The effects of chemical and thermal enhancements on DNAPL solubilization were also considered. The main results of this chapter were published in a peer reviewed journal [Colombano *et al.* (2019)].

3.1 Materials and methods

3.1.1 Rheological DNAPL characterization

The DNAPL used for the experiments were sampled at the Tavaux site (June 25, 2014). Since then, it has been stored in a cold room (at 4 °C).

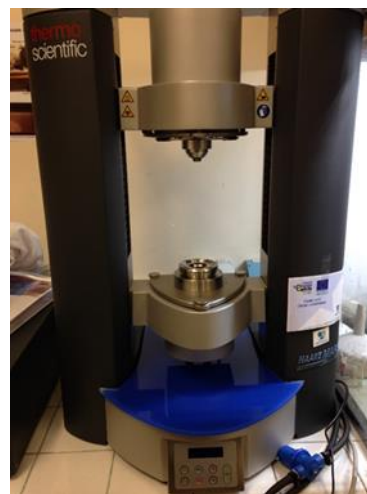
The water used for all experiments was BRGM tap water degassed using an ultrasound tank (VWR Ultrasonic Cleaner - USC500D: 60 °C, 45 Hz, 60 min). This degassing is necessary because we use the same water for all experiments (including experiments in 1D cells, 1D columns and 2D tank). It is often observed that nucleation can occur in a porous medium during drainage or imbibition when the liquid's pressure is lower than the saturation vapor pressure [Daïan (2013)].

3.1.1.1 *Dynamic viscosity*

Viscosity was measured with the Discovery Hybrid Rheometer - DHR 3 (TA Instruments) in Rheonaova Laboratory (Grenoble, France) and then at BRGM with the Haake Mars III rheometer - Thermo Fischer Scientific. The DNAPL sample was placed on the lower plane and then compressed with the top plane. The amount of product was adjusted using a syringe. Flow curves were obtained for the different samples using a measuring method based on the speed levels at constant shear rate. Shear stress and viscosity were raised once the flow was established. Measurements were made at atmospheric pressure at 10, 15, 20, 30, 45 and 60 °C. Temperature was controlled by the Peltier effect. The temperature precision was 0.5 °C. Figure 45 shows the DHR 3 and Haake Mars III rheometers.



a) DHR 3 rheometer



b) Haake Mars III rheometer

Figure 45: Photographs of a) the DHR 3 and b) Haake Mars III rheometers

Viscosity measurements were performed in triplicate.

3.1.1.2 Interfacial tension and contact angle between DNAPL-water

The IFT and contact angle between the DNAPL and water were measured with the Tracker-S tensiometer (Teclis Scientific) in Navier laboratory (Champs-sur-Marne, France) and then at BRGM with the Drop Shape Analyser tensiometer DSA-100 (Krüss).

The Tracker-S and the DSA-100 are automated drop tensiometers that can measure variations in IFT over time. The instrument can also be used to measure the contact angle between a liquid and solid. Using optional lenses, the accuracy of IFT measurement can be increased to $0.1 \text{ mN}\cdot\text{m}^{-1}$. Figure 46 shows Tracker-S and DSA-10.

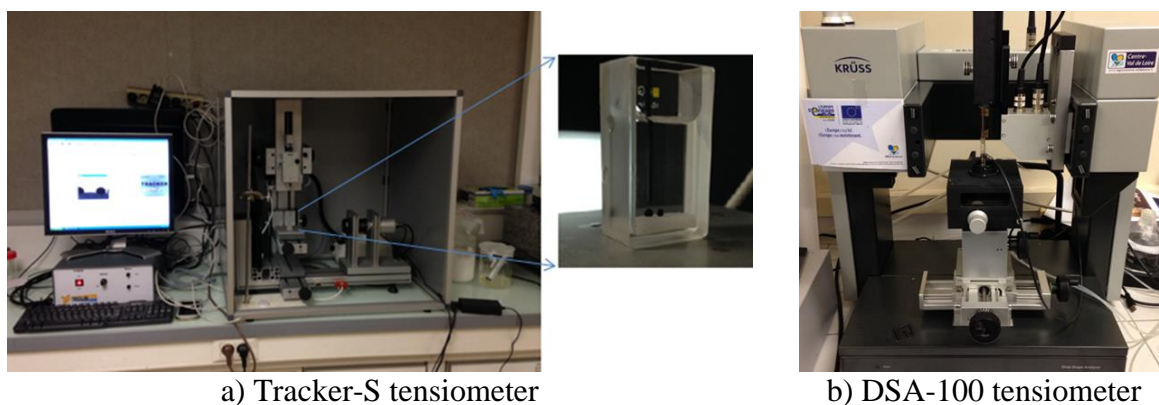


Figure 46: Photographs of a) the Tracker-S and b) DSA-100 tensiometers

The IFT and contact angle for DNAPL-water were measured at different temperatures (10 to 60 °C) and with surfactants at different concentrations. The temperature was stabilized with a thermostatically-controlled water bath. All of the measurements were carried out in triplicate.

The DNAPL contact angle for each temperature was first evaluated without the use of 0.5 mm glass beads and then with them (Figure 47). Contact angle measurements were not very accurate; variations of several degrees were often observed.

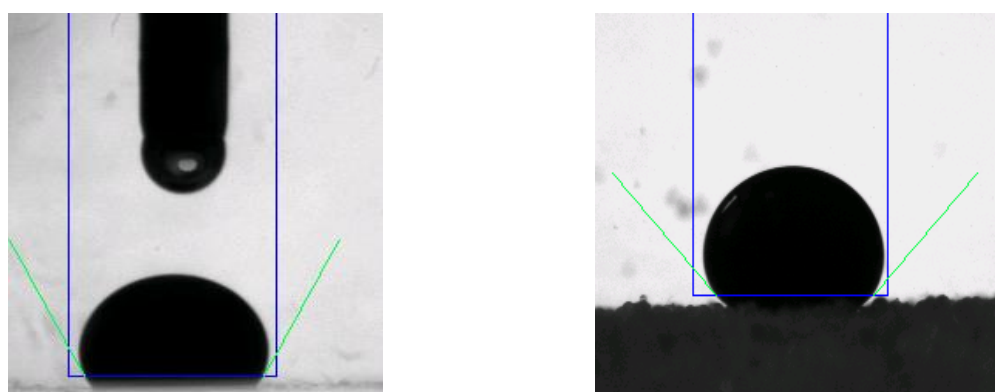


Figure 47: Contact angle of digitized drop a) without and b) with the glass beads

We used the pendant drop technique to determine interfacial tensions from the shapes of drops. This technique can measure the interfacial tension of fluid-fluid interfaces with an accuracy of $\pm 0.1 \text{ mN.m}^{-1}$ from enhancement by video-image digitization and curve-fitting the drop edge coordinates to the Young-Laplace equation (Figure 48).



Figure 48: Digitized pendant drop during the measurement of IFT

The interfacial tension of a fluid-fluid interface is determined by using a video-enhanced pendant drop tensiometer. Based on the Young-Laplace equation, it is possible to calculate the IFT, σ , g from digitized picture data (see Eq. 183).

$$\sigma = \frac{\Delta\rho g R_0^2}{\beta_p} \quad \text{Eq. 183}$$

where:

σ : interfacial tension (mN.m^{-1})

$\Delta\rho$: mass density difference between the drop and the surrounding medium (kg.m^{-3})

g : acceleration of gravity (m.s^{-2})

R_0 : radius of curvature at the drop apex ($^\circ$)

β_p : shape factor, negative for pendant drops

3.1.1.3 Density

Product densities were measured by weighing three different 100 mL flasks. Then, at each temperature, the product was weighed in the closed vial, adjusting the volume needed to fill the flask. Measurements were performed in triplicate.

3.1.2 Solubilization

Solubility measurements were made on the DNAPL using the experimental protocol developed by Rodrigues *et al.* (2017).

Isothermal solubility values were measured by the saturation shake-flask method at 5 constant temperatures in the range from 10 to 60 °C. An excess of DNAPL was added to 25 mL zero-headspace vials filled with degassed water. The vials were sealed with PTFE-lined septa and aluminum caps. Vials were stirred for 24 hours (until partition equilibrium was reached). Temperature was maintained constant ($T \pm 0.2 \text{ }^\circ\text{C}$) during stirring using a thermostatically controlled enclosure. Vials were then centrifuged at 5,000 rpm for 2 hours, at constant temperature ($T \pm 0.5 \text{ }^\circ\text{C}$), to separate the two phases. Finally, an aliquot of the supernatant was collected and sampled for analysis. Three replicates were performed for each temperature.

The same protocol was applied for solubilization experiments in the presence of surfactants. Four surfactant concentrations were studied, according to their respective CMC value, from $0.25 \times \text{CMC}$ to $8 \times \text{CMC}$. All measurements were performed in triplicate at 20°C .

COC concentrations were analyzed by gas chromatography with flame ionization detector (Varian 3800) and head space injection (Agilent 7697A). The column characteristics (Agilent; CP-SIL 5 CB) are reported in Table 24.

Table 24: Chromatography column characteristics

Column	Semi-capillary
Tube	Fused silica
Length	50 m
Internal diameter	0.53 mm
Film thickness	5 μm
Active phase	Polydimethylsiloxane
Carrier gas	Helium

The analyses were conducted by INOVYN at the Tavaux site.

3.1.3 Volatilization

All the experiments were conducted with water on the DNAPL. The volatilization phenomena can therefore be considered as minor. A PID measurement (Photoionization Detector, miniRAE3000, light 10.6 eV) above experimental devices demonstrated that the contents were below the detection limits ($\text{DL}=0.1$ ppm). Measurements with colorimetric Dräger tubes were also taken above the aqueous phase. The contents measured were below the detection limit (20 and 7 ppm for TCE and PCE, respectively).

3.2 Results and discussion

3.2.1 Rheological DNAPL characterization

3.2.1.1 *Dynamic viscosity*

The results for DNAPL dynamic viscosity measurements are presented in Figure 49 (and in Appendix 1.1).

Figure 49 shows that the measurements were reliable (standard deviation less than 0.15 mPa.s). Typically, chlorinated solvents are more fluid than water (viscosity less than 1 mPa.s) [Sleep and Ma (1997)]. In our case, the dynamic viscosity was much higher (5 mPa.s at a classical groundwater temperature).

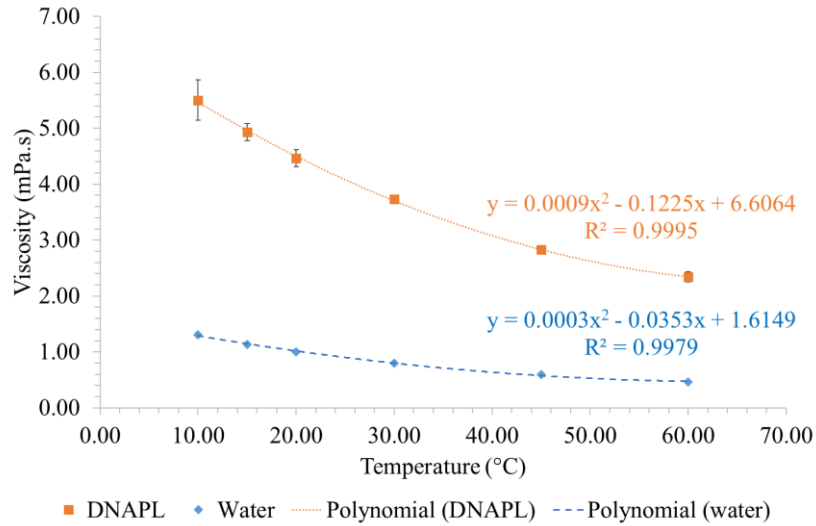


Figure 49: Variation of DNAPL and water dynamic viscosities as a function of temperature

The viscosity of each compound in our DNAPLs and the estimates of global DNAPL viscosity (from equations Table 11 - Eq. 30 to Eq. 38) are presented in Table 25 and Table 26.

Table 25: Viscosity of each compound at the site

Compound	Dynamic viscosity (Pa.s at 25 °C)	Reference
Hexachlorobutadiene (HCBd)	2.70×10^{-3}	[Lucius <i>et al.</i> (1992)]
Hexachloroethane (HCEa)	2.26×10^{-3}	[Lucius <i>et al.</i> (1992)]
Perchloroethylene (PCE)	8.06×10^{-4}	[Yaws (2015)]
Pentachlorobenzene (PeCB)	7.08×10^{-4}	[Yaws (2015)]
Carbon tetrachloride	9.04×10^{-4}	[Yaws (2015)]
Trichloroethylene (TCE)	5.46×10^{-4}	[Yaws (2015)]
Hexachlorobenzene (HCB)	4.86×10^{-4}	[Yaws (2015)]

Table 26: Mixing rules with extra-parameters and excess function for calculating the viscosity of mixtures

Equation	Estimated dynamic viscosity (Pa.s) in 25 °C
Arrhenius	1.91×10^{-3}
Refutas	1.62×10^{-3}
Bingham	1.60×10^{-3}
Kendall and Monroe	2.00×10^{-3}
Power	2.53×10^{-3}
Chevron	1.69×10^{-3}

The results show that the Power's equation gives the results closest to the measured viscosity (4.47×10^{-3} Pa.s at 20 °C). However, there is also an obvious difference between the estimated and measured results. That difference may be due to the complexity of the multi-component system because the estimated methods used do not consider the reactions between the DNAPL components. Additionally, our DNAPLs had about 10% w/w of the unknown substances and these unknown substances were not considered in the calculation.

The viscosity of a chlorinated solvent is generally reduced by 1% per degree Celsius [Davis (1997)]. The dynamic viscosity of the DNAPL fell by 57% when the temperature rose from 10 to 60 °C. The change in dynamic viscosity as a function of temperature fits a second order polynomial curve.

For water, the reduction in dynamic viscosity was 54% for the same temperatures. We therefore saw that the DNAPL viscosity was slightly closer to that of water at 60 °C. The μ_w/μ_{nw} ratio ranged from 0.23 to 0.19 for respective temperatures of 10 °C and 60 °C. This 15% reduction in viscosity ratios should have slightly improved DNAPL mobility.

3.2.1.2 Interfacial tension and contact angle between DNAPL-water

a) Interfacial tensions

Table 27 shows DNAPL-water interfacial tensions measured at 20 °C.

Table 27: DNAPL-water interfacial tension at 20 °C

Tests	Interfacial tension (mN.m ⁻¹)
Test 1	11.22
Test 2	11.11
Test 3	11.13
Average	11.15
Standard deviation	0.05

The interfacial tension was lower than that of pure TCE or PCE in distilled water (respectively 36.9 and 45.9 mN.m⁻¹) [Andersson *et al.* (2014)]. However, it is still high.

The interfacial tension measurements and contact angles were measured, on the basis of the literature review, with four surfactants (Tween 80, Triton X-100, Aerosol MA-80, SDBS) whose characteristics are shown in Table 28.

Table 28: Names and chemical properties of the surfactants used

Commercial name	Formula and chemical name	Type	MW (g.mol ⁻¹)	CMC ^{theoretical} (mmol.l ⁻¹)
Triton X-100	C ₈ H ₁₇ C ₆ H ₄ (OCH ₂ CH ₂) _x OH POE(9,5) isooctylphenol 4-(1,1,3,3-Tetramethylbutyl)phenyl- polyethylene glycol	Nonionic	602.80– 646.86	0.22–0.24
Tween 80	C ₆₄ H ₁₂₄ O ₂₆ (x)-sorbitan mono-9-octadecenoate poly(oxy-1,2-ethanediyl)	Nonionic	1309.67	0.012
Aerosol MA-80	C ₁₆ H ₂₉ NaO ₇ S Sodium 1,4-dicyclohexyl sulphonatosuccinate	Anionic	522.72	1.5
SDBS	C ₁₂ H ₂₅ C ₆ H ₄ SO ₃ Na Sodium dodecyl benzene sulfonate	Anionic	348.48	1.5

All surfactants were provided by Sigma Aldrich (laboratory grade) apart from the Aerosol MA-80, from Cytec.

Figure 50 shows the results for interfacial tension measurements (See also Appendix 1.2).

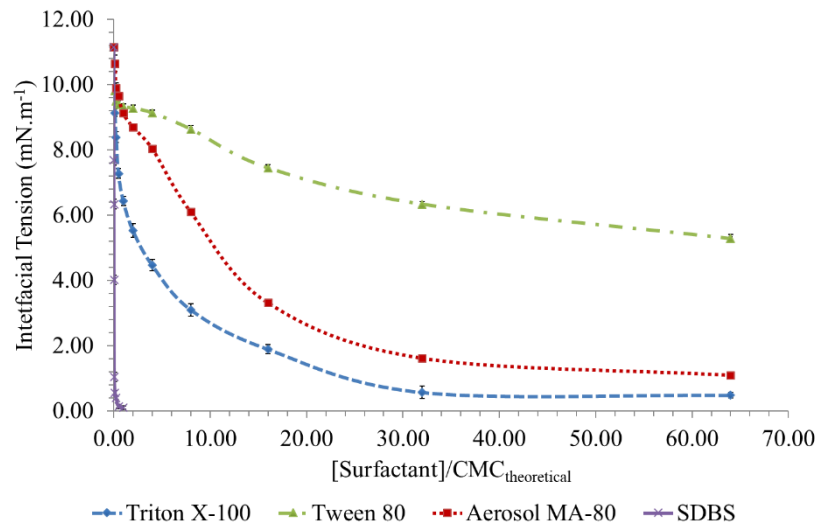


Figure 50: DNAPL-water interfacial tension variation with different surfactant concentrations

The results for reduced interfacial tensions with added surfactants are very contrasting. We saw three trends: one moderate effect (Tween 80), one substantial effect for relatively high CMC (Triton X-100 and Aerosol MA-80) and one very substantially beneficial effect for low surfactant concentrations (SDBS).

In more detail, we saw that the reduction in interfacial tension for Tween 80 was 52% for the concentration of $64 \times \text{CMC}$ ($\sigma_{\text{final}} = 5.28 \text{ mN.m}^{-1}$). As for Triton X-100 and Aerosol MA-80, the reductions were respectively 96% and 90% for the concentration of $64 \times \text{CMC}$ ($\sigma_{\text{final}} = 0.48 \text{ mN.m}^{-1}$ and 1.10 mN.m^{-1}). Finally, SDBS seems to be the most advantageous surfactant because it can reduce the interfacial tension by 99% at a surfactant concentration of CMC ($\sigma_{\text{final}} = 0.10 \text{ mN.m}^{-1}$).

From this, we concluded that the two anionic surfactants reduce interfacial tensions substantially, and that SDBS can even do this at low surfactant concentrations. Nonionic surfactants display less clear trends as Tween 80 is not very effective but Triton X-100 is effective at high concentrations.

Figure 51 shows trend curves from which we determine the CMC_{real} of the surfactants that correspond to the $\text{IFT} = f([\text{surfactant}])$ and $[\Sigma\text{COC}] = f([\text{surfactants}])$ curves' inflexion points.

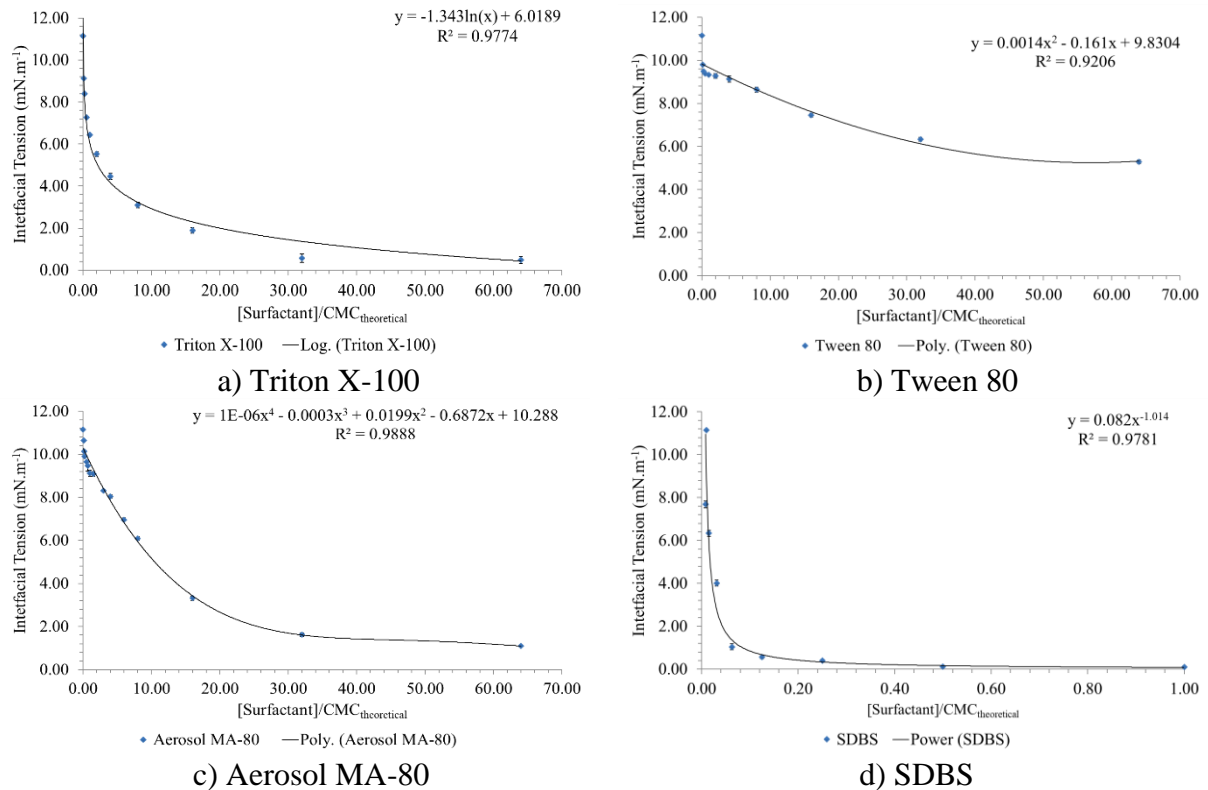


Figure 51: Estimation of the trend curve $IFT=f([surfactant])$ and estimation of the real CMC for a) Triton X-100, b) Tween 80, c) Aerosol MA-80, d) SDBS

The IFT curves, with different shapes, follow different trend curve equations (logarithmic, polynomial, power equations). These results show that the measurements are reproducible and a good fit (maximum standard deviation is less than $0.21 \text{ mN}\cdot\text{m}^{-1}$).

Figure 52 shows the results of DNAPL-water IFT measurements at different temperatures (See Appendix 1.3 for more details).

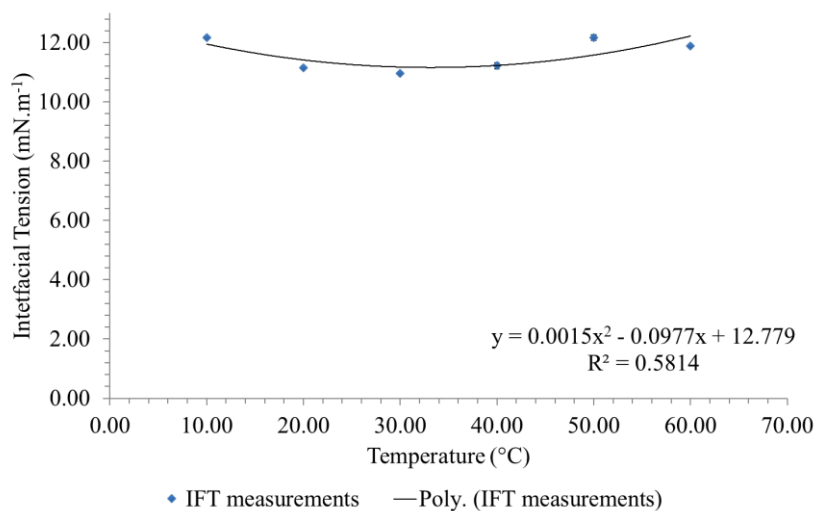


Figure 52: Variation of DNAPL-water interfacial tension as a function of temperature

Figure 52 shows that the thermal enhancement has only limited influence on IFT. This parameter falls by 2.3% between 10 and 60 °C (respectively 12.17 to 11.89 mN.m⁻¹). We see a slight inflexion in the curve for temperatures between 20 and 40 °C.

b) DNAPL-water-glass contact angles

Measuring the contact angles is more difficult because of the determination of the triple point (contact point between the DNAPL, water and glass) as the bubble being squashed. It is also difficult to position the DNAPL bubble on the glass. However, the standard deviations obtained are acceptable (<5.29°).

The measurements for contact angles without surfactant, displayed in Table 29, show that as expected, our DNAPL was particularly non-wetting. The orders of magnitude measured were closer to those reported in the literature (*e.g.* 129° for TCE in pure water) [Orphius and Kibbey (2005)].

Table 29: DNAPL-water-glass contact angle

Tests	Contact angle (°)
Test 1	124.00
Test 2	116.00
Test 3	118.00
Average	119.33
Standard deviation	4.16

Figure 53 and Appendix 1.4 show contact angles DNAPL-water-glass with chemical enhancement. Standard deviations for contact angle measurements were higher than those for interfacial tension; however, they are acceptable (standard deviation less than 5.29 °).

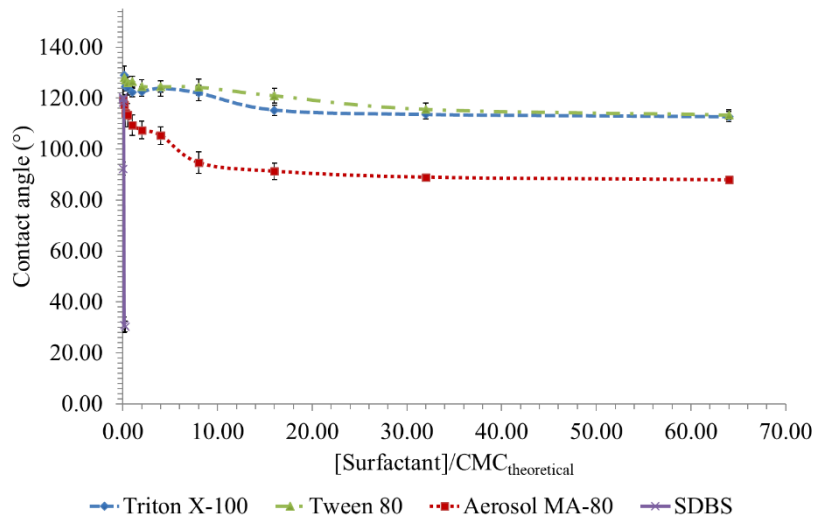


Figure 53: Variation of DNAPL-water-glass contact angle with chemical enhancement at different surfactant concentrations

The decreases in contact angles are consistent with research work in this topic [Amirpour *et al.* (2015)]. The contact angle was significantly reduced by adding SDBS; it reached 30.33° (*i.e.* a 75% drop) for SDBS concentrations clearly lower than the CMC; therefore, DNAPL became wetting since the angle is less than 90°. Regarding the other anionic surfactant, adding Aerosol

MA-80 reduced the contact angle by 23% for a concentration equivalent to $16 \times \text{CMC}$ ($\theta_{\text{final}} = 91.33^\circ$). The two nonionic surfactants gave similar curves. Triton X-100 and Tween 80 only reduced the contact angles by respectively 5.6 and 4.9% ($\theta_{\text{final}} = 112.70$ and 113.50°), respectively. We observed a rebound effect for the contact angles for the four surfactants.

These results only partially match the measurements made with interfacial tensions. The following pattern is demonstrated: $\text{SDBS} \gg \text{Triton X-100} > \text{Aerosol MA-80} \gg \text{Tween 80}$. This difference may be due to the glass, because the contact angle measurement depends not only on DNAPL-water interactions but also on how these liquids interact with the glass in the cell.

The results for DNAPL-water-glass contact angles measurements are in Figure 54 (and in Appendix 1.5).

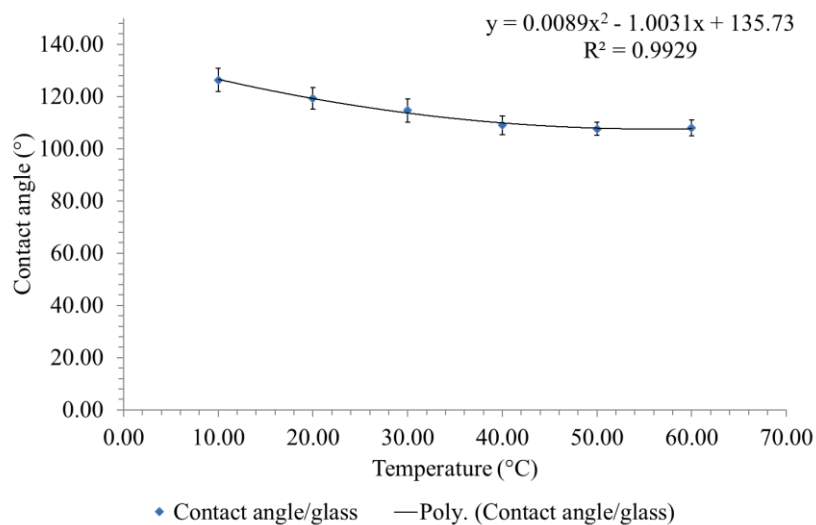


Figure 54: Variation of DNAPL-water-glass contact angle as a function of temperature

The temperature increase reduced the contact angle moderately: in changing the temperature from 10 to 60 °C, the contact angle went from 126.33 to 108.00° (*i.e.* a 14% reduction). These results are consistent with the literature [Sleep and Ma (1997)]. The increase does not seem to be linear and a plateau was reached at 50 °C.

c) DNAPL-water-glass beads contact angles

The contact angle depends greatly on the nature of the solid onto which the measurements are made. Therefore, the same glass beads as those used in drainage-imbibition (1D cells and 1D columns) and pumping (2D tank) experiments were used for performing the contact angles measurements. However, these measurements with glass beads are difficult because it is quite difficult to find the triple points with non-planar surfaces.

Contact angle measurements with glass beads, displayed in Table 30, show that the DNAPL is particularly non-wetting. The standard deviations are correct ($< 3.06^\circ$) and show representative results.

Table 30: DNAPL-water-glass beads contact angle

Tests	Contact angle (°)
Test 1	134.00
Test 2	130.00
Test 3	128.00
Average	130.67
Standard deviation	3.06

The results for the contact angle measurements with surfactants are in Figure 55 (and in Appendix 1.6).

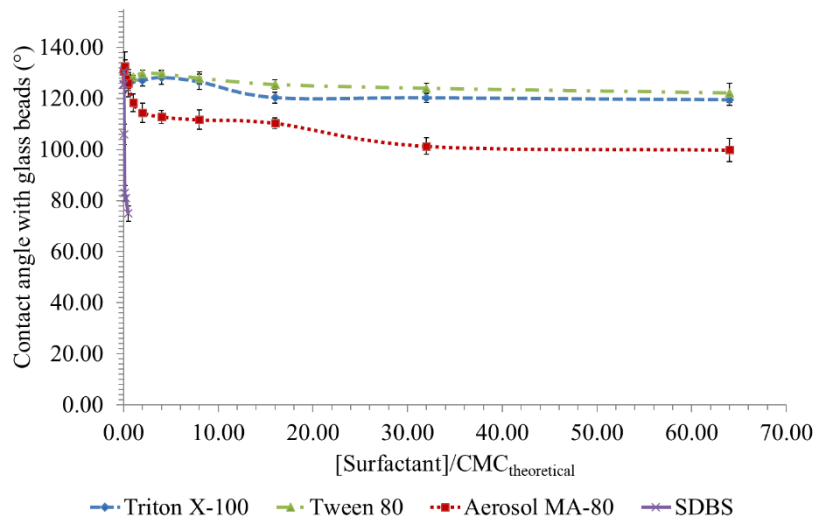


Figure 55: Variation of DNAPL-water-glass beads contact angle with chemical enhancement at different surfactant concentrations

The results for DNAPL-water-glass beads contact angle measurements show similarities with those obtained for DNAPL-water-glass. After adding surfactants, the contact angle decreases, in increasing order, are: SDBS >> Aerosol MA-80 > Triton X-100 >> Tween 80. Generally, these contact angles are slightly higher than those measured without glass beads. This difference in contact angles with surface roughness (glass vs. glass beads) agrees with the observations of Abdallah *et al.* (2007) [Abdallah *et al.* (2007)].

The contact angle decreases are respectively 6 and 9% for Tween 80 and Triton X-100 (*i.e.* 122.17 and 119.50°), and 15% for Aerosol MA-80 (*i.e.* 110.33°). For SDBS, the contact angle reaches 38° (the DNAPL mixture therefore becomes wetting).

Figure 56 shows the effect of increased temperature on DNAPL-water-glass bead contact angle (Also see Appendix 1.7).

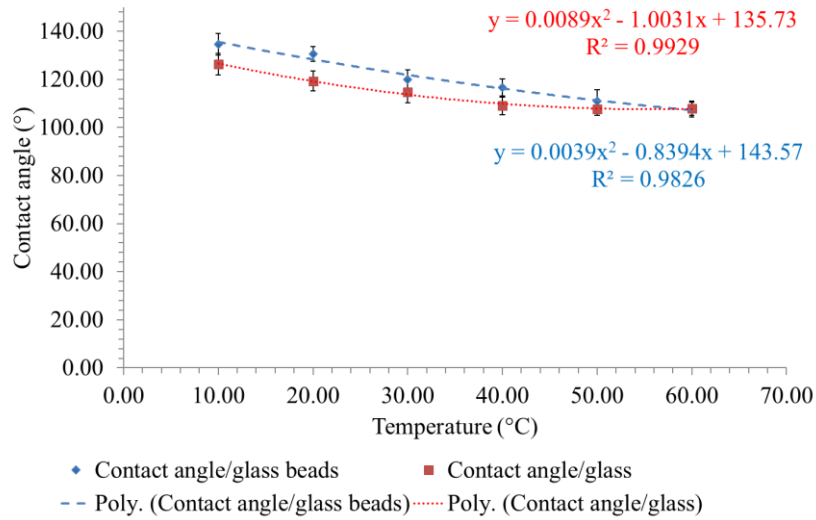


Figure 56: Variation of DNAPL-water-glass beads contact angle as a function of temperature (compared with the variation of DNAPL-water-glass contact angle)

For temperatures between 10 and 30 °C, the slopes of both straight lines (with and without glass beads) are almost parallel. For temperatures above 30 °C, one can see that the measured contact angle values are more affected when the glass beads are present. When the temperature increases from 10 to 60 °C, the contact angle decreases from 134.67 to 107.33° (*i.e.* a 20% reduction). At 60 °C the contact angles are the same with and without glass beads.

3.2.1.3 Capillary pressure

On the basis of these results, we can estimate the effect of chemical and thermal enhancements on capillary pressure, P_c , taking as a first hypothesis, DNAPL and water being placed in a tube (pore throat) whose radius is a circle sized by the space between the glass beads (in our case, 0.1 mm and 0.5 mm). This is obviously a first approach because the pore throat radii vary as a function of the actual space between the glass beads (*Figure 21*). Table 31 shows the calculations for estimations of P_c for two types of glass bead packing: cubic and rhombohedral ordered packing arrangements (see Eq. 56).

Table 31: Reduction of the capillary pressure with chemical and thermal enhancements

Parameters	Without surfactant		Triton X-100		Tween 80		Aerosol MA-80		SDBS		Thermal enhancement	
IFT (mN.m ⁻¹)	11.15	11.15	3.10	3.10	6.33	6.33	3.32	3.32	0.56	0.56	11.89	11.89
Contact angle (°)	49.33	49.33	58.00	58.00	64.33	64.33	88.67	88.67	87.70	87.70	72.00	72.00
Cubic ordered packing arrangements												
Glass bead radius (mm)	0.05	0.25	0.05	0.25	0.05	0.25	0.05	0.25	0.05	0.25	0.05	0.25
Radius pore throat, max (mm) ¹	0.02	0.10	0.02	0.10	0.02	0.10	0.02	0.10	0.02	0.10	0.02	0.10
P_c , min (Pa)	701.90	140.38	158.66	31.73	264.96	52.99	7.45	1.49	2.17	0.43	354.86	70.97
Rhombohedral ordered packing arrangements												
Glass bead radius (mm)	0.05	0.25	0.05	0.25	0.05	0.25	0.05	0.25	0.05	0.25	0.05	0.25
Radius pore throat, min (mm) ²	0.01	0.04	0.01	0.04	0.01	0.04	0.01	0.04	0.01	0.04	0.01	0.04
P_c , max (Pa)	1887.83	377.57	426.73	85.35	712.63	142.53	20.05	4.01	5.84	1.17	954.45	190.89

1: $R_{\text{pore throat}} = R_{\text{glass beads}} \times (1.4142 - 1)$; 2: $R_{\text{pore throat}} = 0.154 \times R_{\text{glass beads}}$

We see that for a single type of glass bead, the capillary pressure is much higher for the rhombohedral ordered packing arrangement than for a cubic arrangement (increase of a factor of 2.6). Reducing bead diameter also significantly increases capillary pressure; we see an increase of a factor of 5 of P_c for 0.1 mm to 0.5 mm beads.

Figure 57 shows the reduction in capillary pressures as a function of the chemical and thermal enhancements. The percentage reductions for each hypothesis (*i.e.* type of surfactant and thermal enhancement), as can be seen in Table 31, are logically identical (regardless of the glass bead radius and radius pore throat); thus, only one capillary pressure reduction is presented for each surfactant and for thermal enhancement.

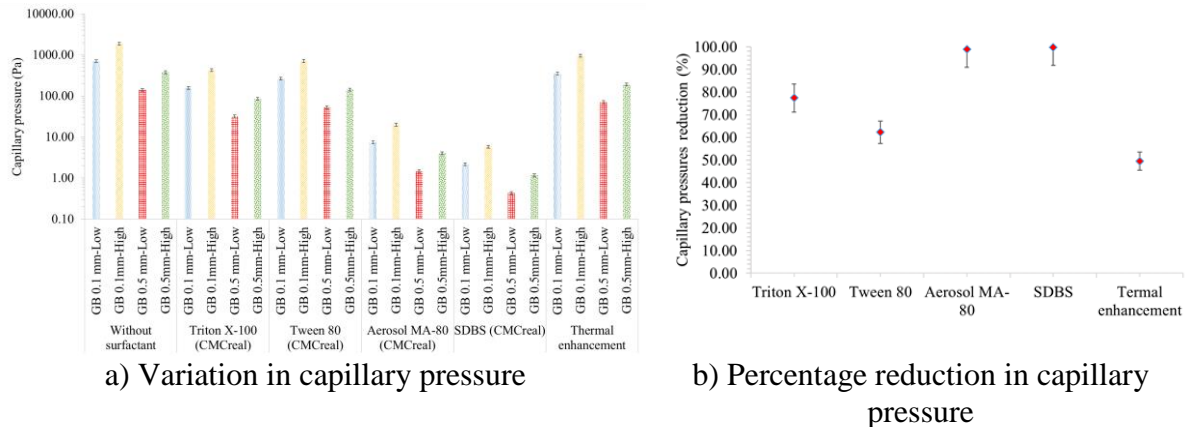


Figure 57: a) Variation in capillary pressure and b) percentage reduction in capillary pressure with chemical and thermal enhancements

We see that the nonionic surfactants reduce P_c less than the anionic surfactants. Triton X-100 and Tween 80 only reduce the capillary pressure by 77.3% and 62.5% respectively, yet, the anionic surfactants reduce the capillary pressure much more (respectively, 98.9% and 99.7% for Aerosol MA-80 and SDBS).

Thermal enhancement only has a moderate effect on P_c (49.4% reduction). Thermal enhancement especially affects DNAPL viscosity.

3.2.1.4 Density

Figure 58 shows the results for density as a function of temperature (See Appendix 1.8 for more details). Result reproducibility was satisfactory (standard deviation less than $5.63 \text{ kg}\cdot\text{m}^{-3}$).

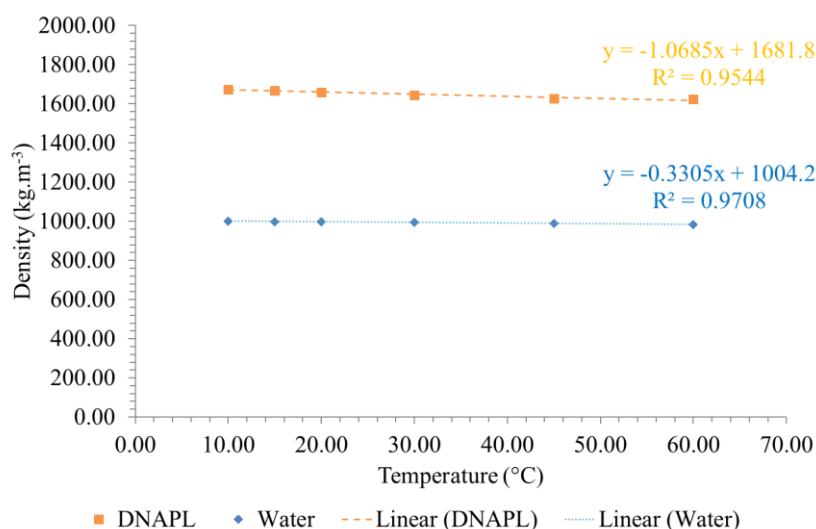


Figure 58: Variation of DNAPL and water densities as a function of temperature

The DNAPL was denser (1.66 kg.L^{-1} at $20 \text{ }^{\circ}\text{C}$) than classical chlorinated solvents like TCE and PCE (respective densities at $20 \text{ }^{\circ}\text{C}$: 1.46 and 1.62 kg.L^{-1}).

PCE density variations as a function of temperature are moderate; we see a reduction of 0.1 kg.L^{-1} over a temperature increase from 20 to $90 \text{ }^{\circ}\text{C}$ [Sleep and Ma (1997)]. The DNAPL at the Tavaux site also had a moderate density reduction as a function of temperature; the density fell by 0.05 kg.L^{-1} for temperatures ranging from 10 to $60 \text{ }^{\circ}\text{C}$ (*i.e.* a reduction of 3%).

3.2.2 Solubilization

3.2.2.1 Quantification of chlorinated compounds in the aqueous phase

The sum of the chlorinated compounds quantified and solubilized from DNAPL is of the order of 44 mg.L^{-1} (with a standard deviation of 5.2 mg.L^{-1}). Figure 59 shows the chlorinated compounds in the aqueous phase (See Appendix 1.9 for details).

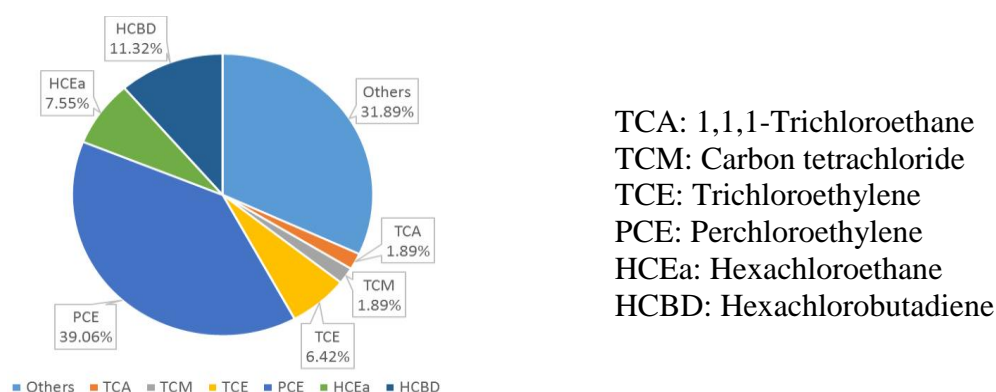


Figure 59: Distribution of [COCs] at $20 \text{ }^{\circ}\text{C}$

Note that a large percentage of the pollutants could be detected but could not be quantified (32%).

The UNIFAC method (UNIQUAC Functional-group Activity Coefficients) is a semi-empirical system for the prediction of non-electrolyte activity in non-ideal mixtures. UNIFAC uses the functional groups present on the molecules that make up the liquid mixture to calculate activity

coefficients [Fredenslund *et al.* (1975)]. Table 32 shows how the DNAPL compounds are broken down with the UNIFAC method.

Table 32: Component breakdown for the UNIFAC method

Composants	CH3	CH=C	C=C	ACH	CH2Cl	CCl3	CCl4	ACCl	Cl(C=C)
HCBD			2						6
HCA						2			
PCE			1						4
PeCB				1				5	
CLM4							1		
TCE		1							3
HCB								6	
TCA	1					1			
PCA					1	1			

The activity coefficients were calculated by a BASIC program. The parameters for the interaction energy between the ACCl group (aromatic carbon-chloride group) and the Cl(C=C) group were not available and were considered to be 0 in the calculation. We used the following equation to calculate the effective aqueous solubility of the COC in the mixed organic phase [Banerjee (1984)] (Eq. 184).

$$\frac{C_i}{S_i} = (x_i)_{\text{org}}(y_i)_{\text{org}} \quad \text{Eq. 184}$$

where:

C_i : equilibrium molar concentration of the compound i in the organic mixture (mg.L^{-1})

S_i : solubility of the compound i in the aqueous phase (mg.L^{-1})

$(x_i)_{\text{org}}$: mole fraction of the compound i in the organic phase (-)

$(y_i)_{\text{org}}$: activity coefficient of the compound i in the organic phase (-)

The estimation of the solubilities based on the Banerjee equation and the UNIFAC method are presented in Table 33.

Table 33: Effective aqueous solubility of the DNAPLs

Compounds	Molar percentage (%)	Activity coefficient (-)	Solubility in water with pure organic phase (mg.L^{-1})	Effective aqueous solubility with mixed organic phase (mg.L^{-1})	Solubility measured (mg.L^{-1})
HCBD	49%	0.94	3.23	1.50	3.75
HCEa	15%	0.80	77.1	9.23	3.33
PCE	12%	0.91	215	23.59	15.75
PeCB	4%	1.64	3.5	0.22	undetected
TCM	5%	0.54	701	18.51	2.75
TCE	4%	0.89	1417	51.08	2.83
HCB	1%	2.12	0.01	0.00	undetected

The reported results are very close to the concentrations measured analytically, with the exception of TCM (TetraChloroMethane), whose values are overestimated by a factor of 6. From this we consider that the sample preparation method and analytical method are appropriate.

HCBD and HCEa are the pollutants present at the highest levels in the free product (52 to 58% and 12 to 16% w/w, respectively). PCE ranks third in the free product (7 to 9% w/w). However, due to its higher solubility, PCE is the chlorinated compound with the highest presence in the aqueous phase (39% w/w). HCBD and HCEa are less soluble, and only represent 11 and 8% respectively of the chlorinated compounds detected. The other quantified compounds, although present in low quantity in the free product (<5% w/w), are among the most soluble chlorinated compounds: TCE (6% w/w), TCM (2% w/w) and TCA (2% w/w).

3.2.2.2 Effect of chemical enhancement

Figure 60 shows how solubilities vary as a function of surfactant concentrations (see Appendix 1.9 for more details).

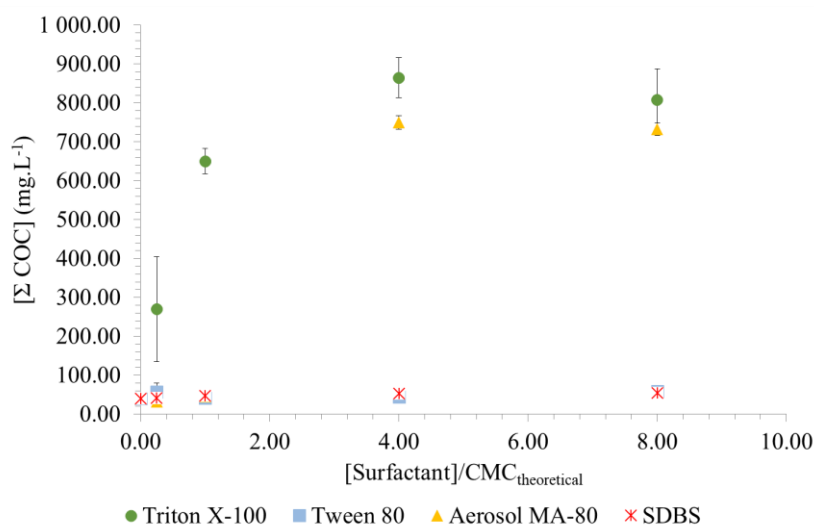


Figure 60: Variation of $[\Sigma \text{COCs}]$ with different surfactant concentrations

As a reminder, the reduction efficiencies for IFT after adding surfactants were (for the same $[\text{Surfactants}]/\text{CMC}_{\text{theoretical}}$ ratios): Tween 80 \ll Aerosol MA-80 $<$ Triton X-100 \ll SDBS. Concerning solubility reductions, adding surfactants produced very mixed results. The two nonionic surfactants generated a global solubility increase ($\Sigma[\text{COC}]$) of a factor of 20 for Triton X-100 (for a concentration of $8 \times \text{CMC}_{\text{theoretical}}$) whereas it was only 1.45 for Tween 80 for the same concentration ratio.

The results obtained for the anionic surfactants did not show a common trend either. The addition of MA-80 aerosol at $8 \times \text{CMC}$ increased the solubilization rate by a factor of 18; but only by a factor of 1.3 for SDBS with the same CMC ratios.

Normally, as surfactant concentration increases, the volume of core micelles increases, leading to a linear increase in the apparent solubility [Pennell *et al.* (2014)]. A linear change in apparent solubility has also been demonstrated for surfactant concentrations greater than their CMC for several chlorinated compounds (*e.g.* PCE, TCE, HCBD and HCEa) [Rodrigues *et al.* (2017); Harendra and Vipulanandan (2011); Kommalapati *et al.* (1997); Jafvert (1994)].

The results show that it is not easy to determine this linear curve or to determine the CMC on the basis of the $\text{IFT} = f([\text{surfactants}])$ and $[\Sigma \text{COC}] = f([\text{surfactants}])$ curves' inflection points (Figure 61).

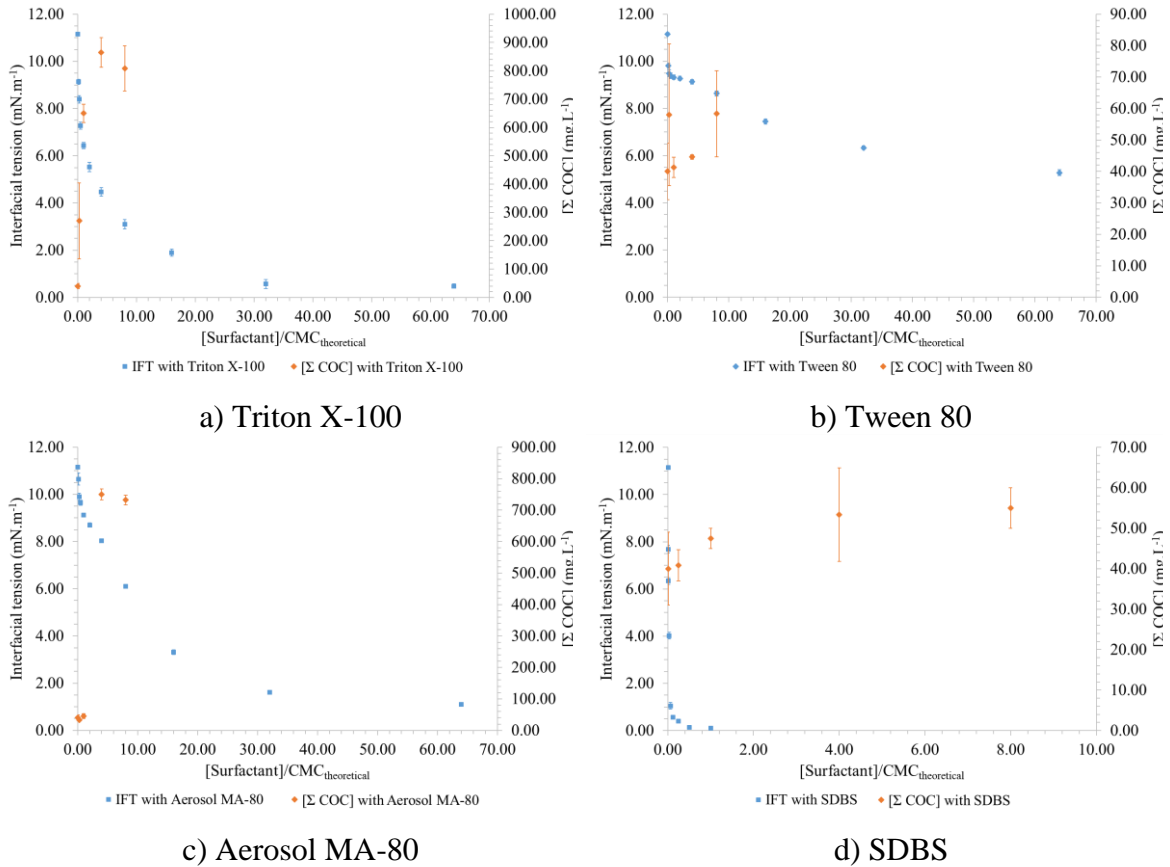


Figure 61: Variation of IFT and $[\Sigma\text{COCs}]$ with different surfactant concentrations (a) Triton X-100, b) Tween 80, c) Aerosol MA-80, d) SDBS)

This probably comes from the fact that, in contrast with studies reporting monopollutants, we have a mixture of pollutants that interacts differently with surfactants. Figure 62 shows that the surfactants increase the apparent solubilities of some COC whereas they have no effect on others.

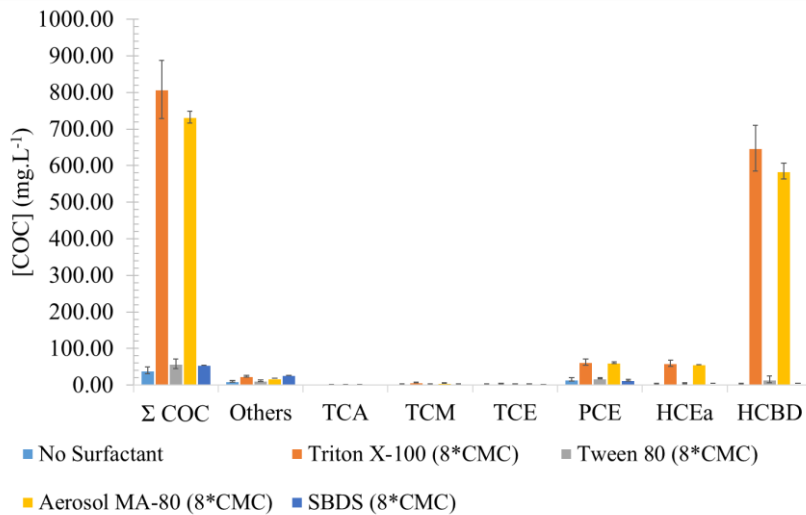


Figure 62: Variation of $[\text{COCs}]$ with different surfactant concentrations

Figure 62 shows that $[\Sigma\text{COCs}]$ depend greatly on surfactants increasing the solubility of HCBD. At concentrations of $8\times\text{CMC}$ Triton X-100 and Aerosol MA-80 considerably increase

the solubility of the HCBd *de facto* the solubility of the COCs. Figure 63 displays the distribution of each [COCs] according to different surfactant concentrations.

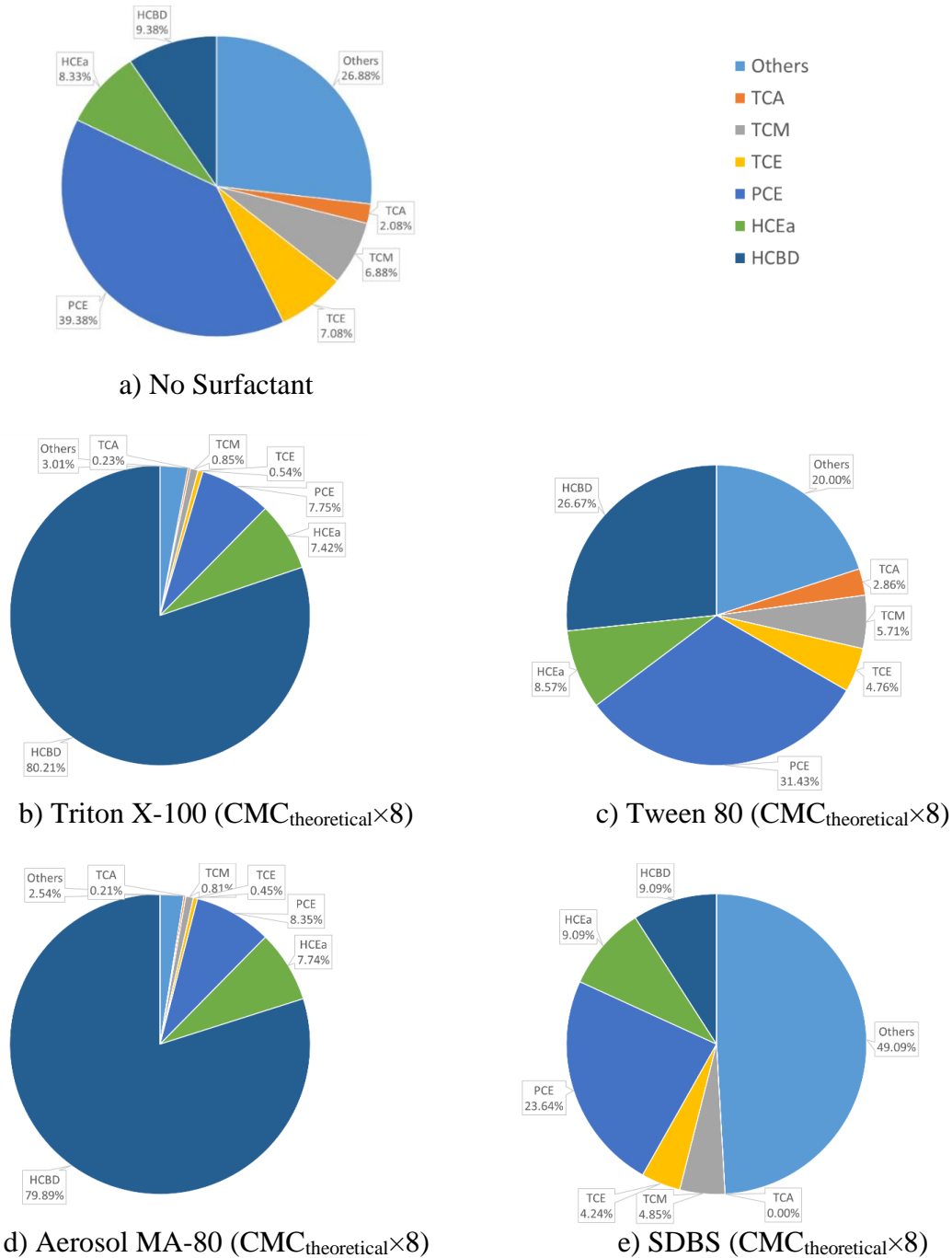


Figure 63: Distribution of [COCs] a) without surfactant and with different surfactant concentrations (b) Triton X-100, c) Tween 80, d) Aerosol MA-80, e) SDBS)

The results show that the final chemical signatures of the COCs vary considerably as a function of the type of surfactant.

Therefore, for surfactant concentrations of $8 \times CMC$, adding Triton X-100 led to a mixture in the aqueous phase essentially composed of HCBd (80%), and in a lesser degree of HCEa and PCE (respectively 7.4 and 7.7%). We should note that non-quantifiable COCs (called “others”) only represent 3%. Adding Aerosol MA-80 led to a very similar COC distribution: HCBd

(79%), HCEa (7.7%) and PCE (8.3%); “other” compounds only represented 2.5%. Also, for concentrations of 8×CMC, Aerosol MA-80 and Triton X-100 increased the apparent solubility by the same order of magnitude and generated a very similar chemical signature for COCs. The difference between the two surfactants came from the fact that solubilization is quantifiable at 0.25×CMC for Triton X-100 whereas it was only quantifiable at 4×CMC for Aerosol MA-80.

Tween 80 only had a very limited effect on apparent solubility (increase by a factor of 1.45). This increase was essentially due to the solubilization of HCBd, which represented 27% of the quantifiable soluble phase. The rest of the solubilized COC ratios were hardly affected by Tween 80. The effects of adding Tween 80 were quantifiable for low CMC (from 0.25×CMC).

Regarding SDBS, the increase in apparent solubility was significant at a concentration of 1×CMC. This was only moderate and was essentially related to an increase in non-quantifiable COCs (others) whose ratio went from 27 to 49%.

Solubilization studies on HCBd and HCEa (as monopollutant) have demonstrated that Triton X-100 and Tween 80 showed similar performances regarding micelle concentration in solution, higher than those obtained by using SDBS [Rodrigues *et al.* (2017)]. These results, obtained using the same experimental protocol, lead to different conclusions. Cosolubility phenomena explain these differences.

Since we have a mixture of COCs, it is not possible to determine the Weight Solubilization Ratio (WSR), which represents the ratio of the number of moles of solubilized COCs to the number of moles of surfactants in the micellar form [Edwards *et al.* (1991); Irvine and Sikdar (1997)].

3.2.2.3 Determination of CMC_{real}

On the basis of experiments conducted with IFT and solubilizations, one can estimate the CMC_{real} .

Figure 61 shows trend curves from which we determine the CMC_{real} of the surfactants that correspond to the $IFT=f([\text{surfactant}])$ and $[\Sigma COC]=f([\text{surfactants}])$ curves' inflection points.

The inflection points determined on the basis of these curves, corresponding to CMC_{real} , are reported in Table 34.

Table 34: Estimation of the CMC_{real}

Commercial name	$CMC_{theoretical}$ (mmol.L ⁻¹)	$CMC_{theoretical}$ (mg.L ⁻¹)	MW (g.mol ⁻¹)	CMC_{real} (×CMC)	CMC_{real} (mg.L ⁻¹)
Triton X-100	0.24	150	625	8×CMC	1200.00
Tween 80	0.012	15.72	1310	32×CMC	503.04
Aerosol MA-80	1.5	727.5	388	16×CMC	11640.00
SDBS	1.5	522.72	348.48	0.11×CMC	65.34

3.2.2.4 Effect of thermal enhancement

Figure 64 shows how solubilities varied as a function of temperature (See Appendix 1.10).

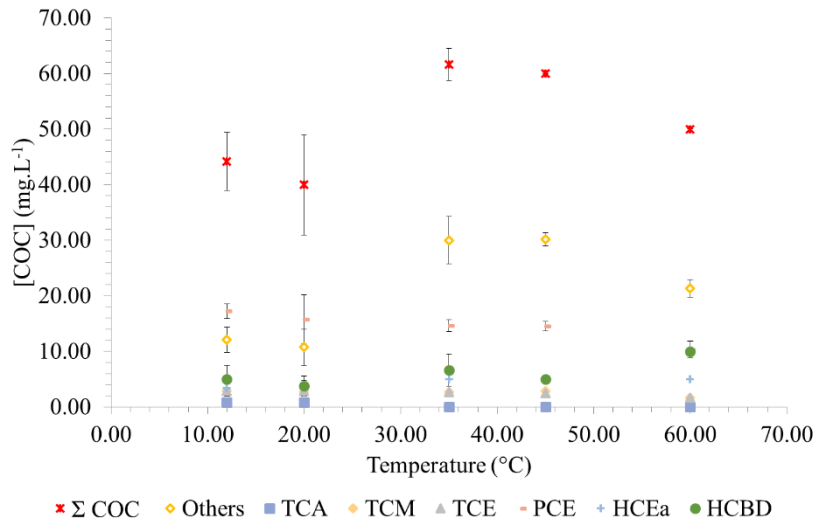


Figure 64: Variation of [COCs] at different temperatures

The standard deviations were sometimes quite high (maximum 9 mg.L⁻¹). We see that the COC solubility was low at 20 °C (40.00 mg.L⁻¹). Increasing the temperature by 12 °C (temperature of the groundwater) to 60 °C increased the solubility by 13% (44.16 versus 50.00 mg.L⁻¹), which is still low.

It was demonstrated that the solubility of chloroethanes and chloroethenes slightly reduced up to a temperature of between 20 and 40 °C, then increased exponentially beyond [Horvath (1982); Chen *et al.* (2012); Knauss *et al.* (2000); Wright *et al.* (1992)]. For chlorobenzenes, solubility increased as a function of temperature between 5 and 55 °C, with the exception of the least chlorinated compounds (chlorobenzene, 1,2- and 1,3-dichlorobenzene), where a similar trend to chloroethenes was observed [Oleszek-Kudlak *et al.* (2004)]. Regarding HCBd and HCEa, the lowest solubility was obtained for temperatures between 20 and 25 °C [Rodrigues *et al.* (2017)].

The [ΣCOC]=f(T) curve shows minimal solubilization at 20 °C (40.00 mg.L⁻¹), then maximal solubilization at 35 °C (61.66 mg.L⁻¹), then intermediate solubilization at 60 °C (50 mg.L⁻¹). This trend curve is totally different than that reported in the literature for mono-pollutants.

Figure 65 shows how [COCs] were distributed at 12 and 60 °C.

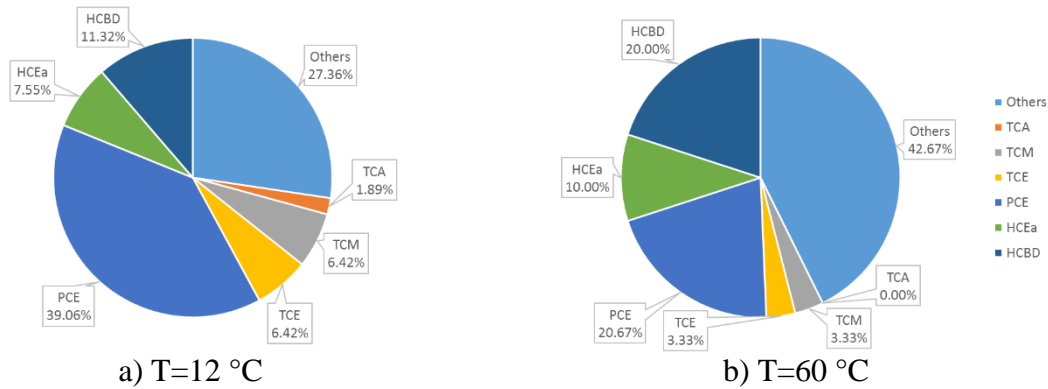


Figure 65: Distribution of the [COCs] at a) 12 °C and b) 60 °C

The results show that the chemical signatures of the COCs vary considerably as a function of temperature. Also for temperatures of 12 and 60 °C, the $[\Sigma\text{COC}]$ were similar (13% difference) but the chemical signature was totally different. The percentage of other COC increased by a factor of 1.8 and became the most concentrated compounds (43%), by contrast the percentage of PCE fell by a factor of 0.6. The percentages of HCEa and HCBd increased by a relatively high amount (from 7.5 to 10% for HCEa and 11 to 20% for HCBd).

This change in COC distribution in the dissolved phase and the cosolubility phenomena could explain why the $[\text{COC}]=f(T)$ curve no longer corresponds to that obtained in the literature with mono-pollutant compounds.

3.3 Conclusions

This study has shown that the DNAPL has moderate dynamic viscosity (4.47 mPa.s at 20 °C). However, it has been reported to be much higher than that of classic COC. The interfacial tension of the DNAPL mixture was relatively high (10.96 mN.m⁻¹ at 20 °C), the contact angle shows that our DNAPL mixture was particularly non-wetting (119.33°). The DNAPL had high density (1.66 kg.L⁻¹) at 20 °C.

The temperature increase greatly reduced its viscosity (54%) and therefore could be expected to significantly increase DNAPL mobility. The interfacial tension and density were slightly changed by thermal enhancement.

Adding surfactants reduced interfacial tensions with contrasting results. We observed three main trends: one moderate effect for Tween 80 (52% drop), one substantial effect for relatively high CMC with Triton X-100 and Aerosol MA-80 (respective drops of 96 and 90%) and one very substantially beneficial effect for low surfactant concentrations with SDBS (99% drop).

As for COC in the aqueous phase, the total concentrations were 44 mg.L⁻¹ (at 20 °C), which is less than what could be expected with light chlorinated monopollutants. Adding surfactants dramatically changed the chemical signatures of the dissolved COCs. The two nonionic surfactants generated a global solubility increase ($\Sigma[\text{COC}]$) of a factor of 20 for Triton X-100 (for a concentration of $8 \times \text{CMC}_{\text{theoretical}}$) whereas it was only 1.45 for Tween 80 for the same concentration ratio. Moreover, adding Aerosol MA-80 at $8 \times \text{CMC}$ increased solubilization by a factor of 18; yet only by a factor of 1.3 for SDBS at the same CMC ratios.

The experiments have shown that on the basis of interfacial tensions essentially (but also concentrations) the surfactants' real CMCs were: Triton X-100 = 1200.00 mg.L⁻¹, Tween 80 = 503.04 mg.L⁻¹, Aerosol MA-80 = 11640.00 mg.L⁻¹, SDBS = 65.34 mg.L⁻¹.

4. EXPERIMENTS IN 1D CELLS

4. EXPERIMENTS IN 1D CELLS

The drainage-imbibition experiments were performed in 1D cells: i. To determine the relative parameters for a two-phase flow system (required for multiphase flow modeling); ii. To calibrate measurements for permittivity, electrical resistivity and image data processing; iii. To evaluate how effectively chemical and thermal enhancements could affect DNAPL recovery yields. The main results of this chapter were published in a peer reviewed journal [Colombano *et al.* (2019)].

These experiments were performed by using glass beads with different diameters, whose hydrodynamic characteristics are close to those reported for Tavaux site.

4.1 Materials and methods

The glass beads were packed in cells using the following protocol: the glass beads were arranged in the cell in successive 2 cm layers. After each GB addition, vibrations were applied to the side of the cell to compact the porous medium. To ensure that they were reproducible, the weights of the beads put in the cell and the porosity of the medium were measured prior to performing every experiment.

The water used for all the experiments was the same as that described for the previous experiments (Chapter 3).

4.1.1 Porous media characterization

The experiments are carried out with different diameters of glass beads (1.0, 0.5, 0.1-0.2, and 0.1 mm) (Table 35).

Table 35: Glass beads information

Glass beads size (mm)	Tolerance(mm)	Company
1	± 0.2	Next Advance
0.5	± 0.1	Next Advance
0.1-0.2	± 0.02	Next Advance
0.1	± 0.02	Next Advance

4.1.1.1 Porosity

The porosities of the porous medium (glass beads and site soil sample) have been calculated by volume balance while the column was filled with water.

4.1.1.2 Particle-size distribution

The Tavaux soil samples were sampled from the site between 11.9 m and 13.3 m deep. The geological soil characteristics were the same as those of the DNAPL pollution source. First of all the largest gravels with a diameter higher than 8 mm were removed in order to work with a more homogeneous soil. A series of sieves (from 8 mm to 0.02 mm) with decreasing mesh size was used. The sieving process took place under a continuous water flow, which separated small grains stuck to big grains.

The sieve analysis proceeded as follows:

- Record the weight of the soil samples
- Assemble the clean sieves in descending order of mesh size (8 mm at top and 0.02 mm at bottom). Place the pan below 0.02 mm.
- Use the mechanical shaker to shake the sieves for at least 10 minutes.
- Remove the stack then dry, weigh and record the weight of each sieve with its retained soil. Finally, record the weight of the bottom pan containing the fine soil that passed through the last sieve.

Particle size distributions were determined at BRGM and also at INOVYN and Remea.

4.1.1.3 Permeability and hydraulic conductivity

The hydraulic conductivity was calculated by changing the hydrostatic height of two reservoirs located on each side of a 1D column filled with different packaging materials and by measuring the volumetric variations of the water in the reservoirs as a function of time.

4.1.2 Drainage-imbibition experiments

4.1.2.1 Main objectives

The main objective of the experimental studies was to characterize the soil parameters in two-phase flow conditions (DNAPL and water) and under different conditions (thermal or chemical enhancement).

To do so, the laboratory work was dedicated to drainage-imbibition experimental series in cells that were used to build the capillary pressure-saturation curves in both static and dynamic flow conditions. The curves, which were afterwards calibrated using the Van Genuchten model (the most appropriate, as shown in section 4.2.2), produce key parameters such as the irreducible water saturation (S_{rw}), the residual pollutant saturation (S_m), the entry pressure, and the calibration parameters α and n which characterize the capillary forces and the heterogeneity of the porous medium, respectively.

The 1D columns used in the same conditions mainly provide a better overview of the migration front, which is required for calibrating the multiphase flow model (see chapter 5).

4.1.2.2 Experimental set-up

The experiments consisted of conducting drainages and imbibitions for two non-miscible liquids (NAPL and water) in a porous medium exerting pressures at the lower and upper parts of the column. A schematic introduction of the experimental set-up is shown in Figure 66.



a) Drainage 1: DNAPL injection (black)

b) Imbibition 1: water injection (blue)

Figure 66: Experimental set-up of the a) drainage and b) imbibition experiments

The set-up consisted in a main porous media cell with an internal diameter of 5.8 cm and a height of 5.56 cm. Figure 67 shows this in more detail. This cell contained glass beads, which were meant to mimic an ideal porous medium.

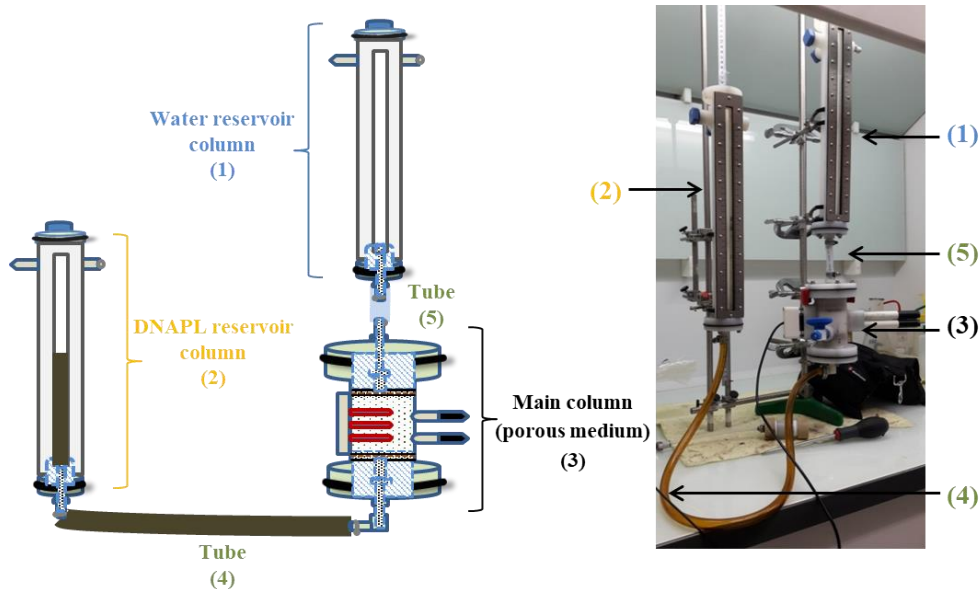


Figure 67: Experimental 1D cell set-up

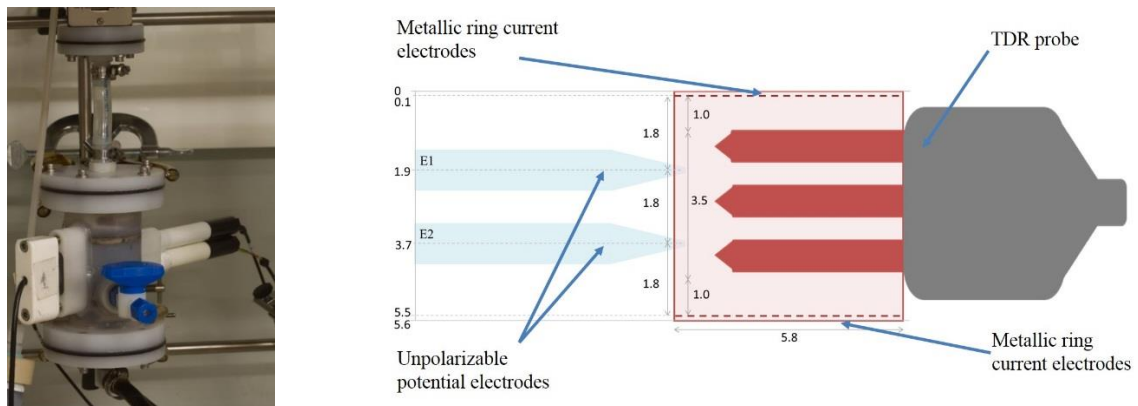
The ratio between the particle diameter and the inner diameter of the cell was less than 0.1, so the wall effects could be confidently neglected.

On both sides, the main column was connected via two tubes to two graduated “reservoir” columns (3.5 cm internal diameter and 41.8 cm high). These reservoirs stored the fluids and produced an appropriated pressure head. The one on the left contained DNAPL, and the one on the right contained water.

All three columns were made of PolyVinylidene Fluoride (PVDF), a thermoplastic material, and were designed by the SCODIP Company in Orleans, France. PVDF has much better chemical and abrasion resistance than other thermoplastic materials, especially against halogens (chlorine, bromine), and strong acids (organic solvents and oils in particular). PVDF has a working temperature range between -40 to 120 °C. PVDF is also extremely sustainable under mechanical stress, even at the lowest temperatures. PVDF also has very low gas permeability. The columns were connected by thermo-scientific Nalgene 8001-1014 | 180 metric clear PolyVinyl Chloride (PVC) tube with 1 cm internal diameter.

To prevent any risk related to product evaporation, and to prevent odor spreading inside the laboratory workplace, the whole set-up was installed under extractor hoods.

The experimental set-up was also constantly monitored by geophysics probes (potential and current electrodes to measure the resistivity) and time domain reflectometry probes to measure the permittivity. Figure 68 shows a photograph and a schematic drawing of a 1D cell. Figure 69 shows a global view of the entire experimental device.



a) Photograph of a 1D cell

b) Schematic drawing of a 1D cell

Figure 68: a) Photograph and b) schematic drawing of a 1D cell



Figure 69: Global view of the entire experimental device for the 1D cells

4.1.2.3 Experimental procedure

For the experiment described in this section, several scenarios were tested. Mainly two sizes of glass beads were used: 0.1 and 0.5 mm.

The experiment was mostly carried out at ambient temperature (20 °C) but also at 50 °C. Water was sometimes replaced by a solution of water and several types of surfactants.

Initially, the main cell only contained the glass beads to replicate the porous medium. Two stainless and PVDF filters were placed at the top and the bottom of the sample to hold the glass beads in place (Figure 70).

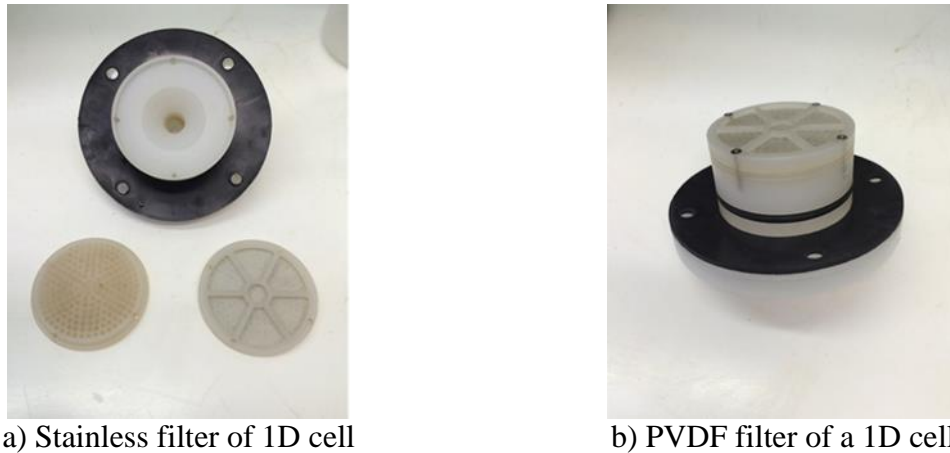


Figure 70: a) Stainless and b) PVDF filters of a 1D cell

Next, through a tap placed on the side of the cell, water was slowly poured into the column to saturate the porous medium (blue tap in Figure 68a). The low flow rate of the injection was important to ensure that no air bubbles got trapped inside the column (otherwise, it would not be a two-phase flow any more). After the column was entirely saturated, the water started to fill the water reservoir column (the one located just above the porous medium) and the water level became readable.

The other reservoir column (on the left, DNAPL reservoir) was filled with DNAPL. The amount of pollutant was precisely determined to reach equilibrium with the water at the bottom entrance of the main column. Note that the DNAPL was injected from the bottom to avoid any gravity-driven flow instability (fingering).

Firstly, the respective heights of the water and DNAPL in both reservoir columns were noted. Then the experiments could start.

The first step was water drainage. The DNAPL reservoir column, initially at a low level, was progressively moved up (2 centimeters at each step) with a stabilization time of 3 hours. Each height incrementation made the hydrostatic pressure increase, and at some point, once the entry pressure was reached, the DNAPL penetrated the porous medium while the water was drained out of it. The levels were noted at each step. The volume of water extracted from the column was calculated. The water saturation was deducted based on the values of extracted water volume, porosity and the column dimensions. In parallel, the capillary pressure, P_c was determined using the equation below (Eq. 185). Point by point, the P_c - S_w curve was built.

$$P_c = P_n - P_w = (\rho_n - \rho_w)h_c g \quad \text{Eq. 185}$$

where:

h_c : capillary pressure head (m)

The drainage was complete when the levels of water and DNAPL became constant even with new pressure increases. This means that the water reached its irreducible saturation level. Right after that, the DNAPL reservoir column (located at its highest point) was moved down in order to realize the imbibition. The process was the same and ultimately reaches the residual pollutant saturation. The drainage-imbibition cycle was completed one to three times in a row. This removed some uncertainties in the results. The total duration of a single drainage-imbibition cycle was about 2 weeks.

The drainage-imbibition experiments were conducted with hydrophilic membranes (Omnipore™ membrane filter-5.00 μm) placed just above the porous medium and the hydrophobic membranes (Miltex™ membranes filter-5.00 μm) placed just below the porous medium to maintain the liquids in the porous medium. Drainage-imbibition experiments with addition of surfactants could not be conducted with these membranes. Consequently, the experiments were run without the membrane; a correction factor was applied to be able to compare the experiments with and without membranes.

4.1.3 Monitoring of the drainage-imbibition experiments with permittivity and electrical resistivity

The 1D cells were equipped with sensors measuring electrical resistivity as well as permittivity (Figure 68).

4.1.3.1 Dielectric permittivity monitoring

Dielectric permittivities were monitored using Time Domain Reflectometry-TDR probes (Decagon Devices 5TE 40567). As well as permittivity (-), these probes monitor volumetric water content-VWC ($\text{m}^3 \cdot \text{m}^{-3}$), temperature ($^{\circ}\text{C}$), and bulk electrical conductivity-EC ($\text{dS} \cdot \text{m}^{-1}$). These probes were connected to a Campbell Scientific CR1000 (4M) data logger. These probes were only used to acquire temperature and permittivity data. The other parameters were not considered to be useful for our experiments. Figure 71 shows the TDR probe.

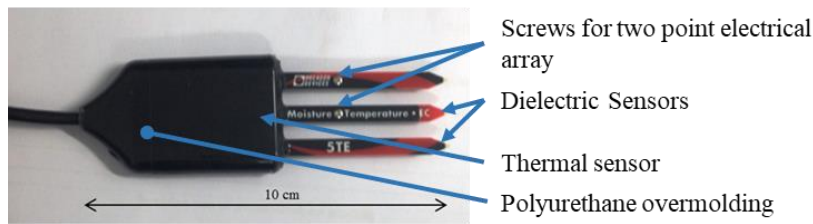


Figure 71: TDR probe

This TDR probe works using 70 MHz frequency. The acquisition frequency was 2 signals per minute.

The permittivity values were corrected relative to the reference value measured in air and in water using the following formula (Eq. 186):

$$\epsilon_{\text{corrected}} = \frac{\epsilon_{\text{water theoretical}}(\epsilon_{\text{measured}} - \epsilon_{\text{air}})}{(\epsilon_{\text{w}} - \epsilon_{\text{air}})} + \epsilon_{\text{air theoretical}} \quad \text{Eq. 186}$$

where:

- $\epsilon_{\text{water theoretical}}$: relative effective permittivity of pure water ($\epsilon_{\text{water theoretical}} = 80$)
- $\epsilon_{\text{measured}} = \epsilon$: relative effective permittivity of medium measured with the TDR probe during the experiments (-)
- ϵ_{air} : relative effective permittivity of air measured at the beginning of the experiment (-)
- ϵ_{w} : relative effective permittivity of tap water measured at the beginning of the experiment (-)
- $\epsilon_{\text{air theoretical}}$: relative effective permittivity of pure air ($\epsilon_{\text{air theoretical}} = 1$)

For the sake of simplification, $\epsilon_{\text{corrected}}$ will be called ϵ . The DNAPL detection area is limited to about 2 mm around the area formed by the 2 TDR probe branches (this distance was determined experimentally). This corresponds to 71% of the height of the 1D cell.

4.1.3.2 Electrical resistivity monitoring

Electrical resistivity was monitored using unpolarizable potential electrodes, metallic current electrodes, resistivity meter, and data acquisition software.

To limit electrode polarization phenomena, which can add noise to the measurements for induced polarization, potential electrodes must be unpolarizable [Dahlin (2000)]. For laboratory experiments, we use Cu/CuSO₄ electrodes and the method developed by Mainault [Mainault *et al.* (2004)]. These electrodes were made using the methodology described by Noël (2014): milli-Q water (ultrapure water) 72.2%, CuSO₄ 26% and Gelatin 1.7% were mixed and heated (≈ 80 °C) for 45 minutes using a shaking heating plate [Noel (2014)]. These electrodes are unpolarizable, *i.e.* they do not polarize the ground and the electrode action on the potential measured can be considered as negligible (Figure 72).

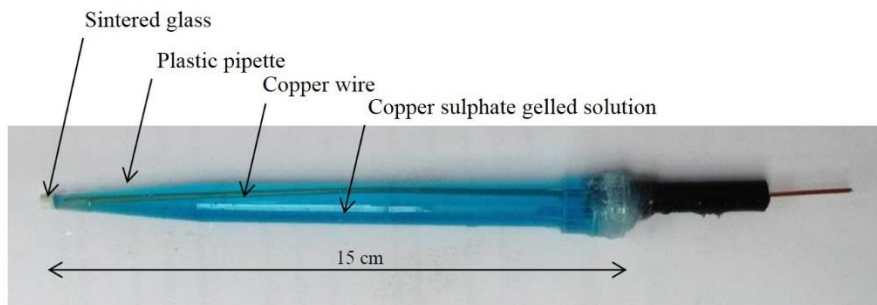


Figure 72: Unpolarizable copper sulphate potential electrodes

The metallic current electrodes are made of nickel-cobalt alloy named MP35N. The resistivity meter used was SIP LAB IV and data acquisition software was Comsys Sp. Resistivity was measured at 1.4 Hz. This frequency was chosen because it is close to that used in the field [Chambers *et al.* (2004); Constable and Srnka (2007); Han *et al.* (2015); Deparis *et al.* (2019)]. The electrodes configuration used is Wenner for the 1D cells.

The values measured were resistance values, R_e , which were transformed into apparent electrical resistivity values, ρ_c , using the geometric coefficient, K_g , (Eq. 187 and Eq. 188):

$$K_g = \frac{R_0}{R_e} \quad \text{Eq. 187}$$

$$\rho_c = R_e K_g \quad \text{Eq. 188}$$

where:

K_g : geometric coefficient (m)

$R_0 = \rho_{c,t=0}$: initial estimated resistance value ($\Omega \cdot m$)

The conductivity of the tap water, measured at the beginning of each experiment, made it possible to determine R_0 and to calculate K_g . The value of K_g was then used throughout the experiment to transform R_e into ρ_c .

The detection area for resistivity measurements of DNAPL was determined experimentally. It is limited to around 2 mm around the area formed by the two potential electrodes. This area is in the central part of the 1D cell; it corresponds only to a height of 3.9 cm.

4.1.4 Monitoring of the drainage-imbibition experiments with image interpretation

In the previous review of optical imaging method (see section 2.7.2), two kinds of method were described: LTM and LRM. Both of them are suited for our work but the experimental tank ordered by SILPHES project had an opaque wall that was not allowing light transmission. This was the reason why LRM was adopted.

4.1.4.1 Camera

The digital camera used in this study was the Nikon® D810 with NIKKOR LENS 105 (Nikon®). This digital camera has a high resolution of 34 Mega Pixels.

The image resolution calculated from Fiji (an open source image processing package based on ImageJ) for this experiments, depending on the image size [pixels×pixels] and the distance between camera and object of interest, was $0.003 \text{ mm}^2 \cdot \text{pixel}^{-1}$.

The camera had the following set up: Aperture = 1/200 s, ISO = 100 and the shutter = f/16. This set up remained the same during all experiments. We use the Capture One® software to take photograph without touching the camera. All pictures were acquired on RAW format (.raw) to save the full data information (in contrast to other format such as JPEG which is known to lose data information).

4.1.4.2 Calibration procedure

Calibration experimental set-up

We conducted the drainage-imbibition experiments in the same way as with 1D cells but this time with a flat Hele-Shaw cell (to prevent light reflection). The dimensions of this cell are as follows: height 5.00 cm; width: 5.00 cm; thickness: 2.00 cm.

The calibration cell was made by Scodip. This cell was made of PVDF like the previous columns to ensure high chemical resistance to the pure pollutant. The cell was composed of two transparent glass faces to allow photographing. The experiments were performed in a dark room and the source light was provided by two 2×300 W floodlights (Broncolor®). The camera was always placed in the same position, for all experiments. A color scale was placed beside the cell to calibrate the differences, even tiny ones, between the lighting for the various experiments.

Mean grey value calculation

We defined a global Area Of Interest (AOI) to obtain the mean grey value necessary to associate with the water saturation (Figure 73). Then, we converted each picture into 8 bit format. Finally, the mean grey values were calculated using Fiji (see section 4.1.4.3), for different AOI centered in the middle of the picture.



a) Picture taken during the calibration experiment. The yellow frame describes the global AOI

b) Global AOI (1740×1740 pixels)

c) Global AOI transformed into 8 bits format (1740×1740 pixels)

Figure 73: Optical calibration experiment in the flat cell: a) picture taken during the calibration experiment, b) global AOI, c) global AOI transformed into 8 bits format

4.1.4.3 Data analysis software

All pictures were analyzed with ImageJ 2, currently named Fiji. Fiji is an open source project developed by contributors around the world but especially by Curtis Rueden, Mark Hiner and the ImageJ team (UW-Madison, LOCI). This software is widely used in the scientific research field.

We selected Fiji because it is easy to apply a threshold that depends on pixel intensity value. The threshold depends on the calibration curve fluid saturation versus intensity. With Fiji we can determine the area associated to the threshold. With this information (DNAPL saturation and its own area), we can compute the DNAPL volumes present on the picture with the following expression (Eq. 189).

$$V_{\text{DNAPL}} = S_{\text{DNAPL}} A_{\text{DNAPL}} l \quad \text{Eq. 189}$$

where:

V_{DNAPL} : volume of DNAPL for a given saturation (m^3)

S_{DNAPL} : DNAPL saturation for a given threshold on Fiji

A_{DNAPL} : area associated of the given saturation (m^2)

l : length between the front wall and the back wall of the tank (m)

The image data analysis was performed according to the next main steps

1. Convert the picture into 8 bit format to obtain 256 shades of grey,
2. Set up the scale,
3. Set up the I_0 from the Eq. 168, which was equal to the white on the grey scale,
4. Define the AOI,
5. Set up the contrast to optimize the black pixels,
6. Compute the layers of DNAPL saturation present on the AOI that depend on the linear relation found with the calibration experiment, using an algorithm,
7. Gather all the layers into one image to draw the map of saturations.

4.2 Results and discussion

4.2.1 Porous media characterization

4.2.1.1 Porosity

The goal of these experiments was to determine hydrological and physical parameters of the soils. First, the hydrodynamic of porous media was characterized.

The porosities of the porous medium (glass beads and site soil sample) have been calculated by volume balance. All calculations have been provided by water volume (Table 36).

Table 36: Porosity of the glass beads and the Tavaux soil sample

Parameters	Glass beads or soil diameter (mm)				
	1.0	0.5	0.1-0.2	0.1	Soil (0.08-8)
Porosity (-)	0.372	0.373	0.354	0.378	0.391
Number of sample	2	26	3	26	2
Standard deviation (-)	0.0274	0.00165	0.0242	0.00138	0.0282

The porosities of very homogeneous glass bead samples (1.0, 0.5, 0.1 mm GB) are very similar ($\phi=0.37$), in accordance with orthorhombic and hexagonal grain packing. Less calibrated glass beads (0.1-0.2 mm GB) logically have lower porosity ($\phi=0.35$) [Ouchiyama and Tanaka (1984)]. The Tavaux soil sample, although less homogeneous (Figure 75), has quite high porosity ($\phi=0.39$). This is likely related to the fact that the grain shapes are more angular and irregular.

4.2.1.2 Particle-size distribution

The particle-size distributions, determined for different sample types (Tests 1 to 4), are displayed on Figure 74.

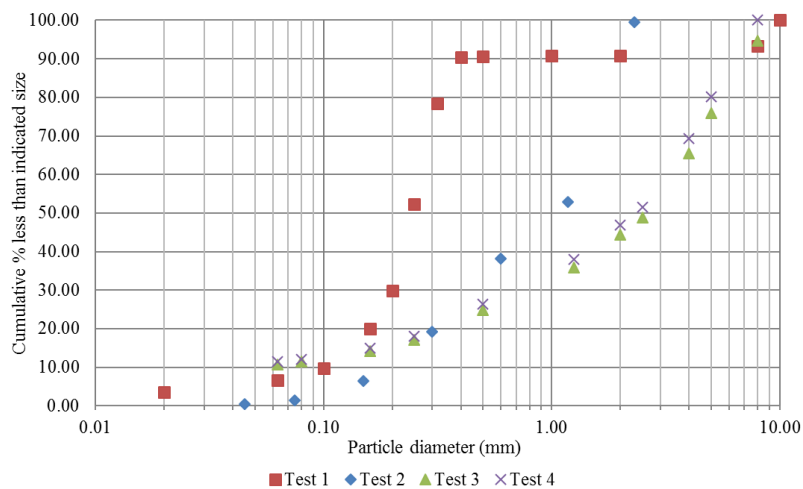


Figure 74: Particle size distribution curves of Tavaux soil samples

We saw widely varying results, typical of alluvial zones. We considered that the sample that most closely approached the soil lithology at the pollution source is test 2 (whose particle-size distributions were run by INOVYN using the same protocol as that described before). The particle-size distribution curve for this sample is shown in Figure 75.

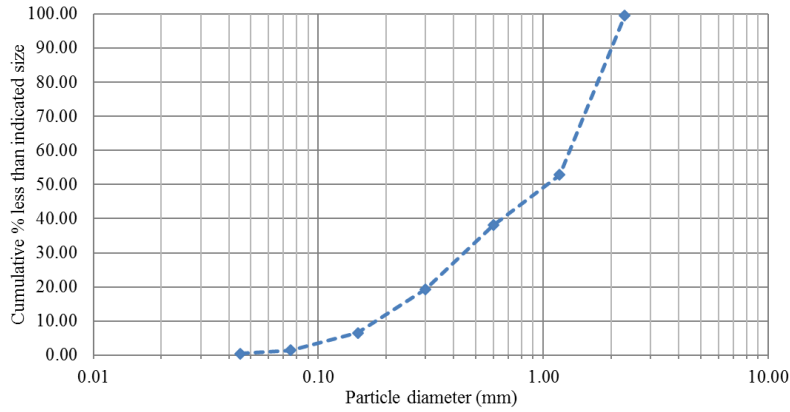


Figure 75: Particle size distribution curve of the Tavaux soil samples

The main soil grain sizes varied between 0.6 mm and 2.3 mm, which represented about 62% of the total mass of the soil samples. 20% of the total masses of soil samples had grain sizes smaller than 0.30 mm. The D_{50} was 1.0 mm.

The uniformity coefficient, C_u , at 7.07, shows uneven distribution.

4.2.1.3 Permeability and hydraulic conductivity

Permeability tests have been conducted using 1D cells and 1D columns with glass beads with different diameters (1, 0.5, 0.1-0.2 and 0.1 mm) and with the Tavaux soil sample. The experimental results are shown in Figure 76 and Figure 77 (Also see Appendix 2.1).

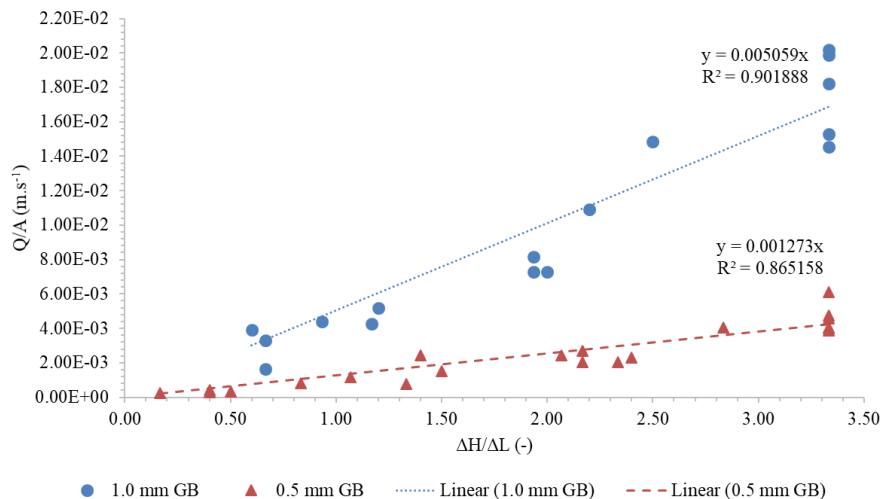


Figure 76: Determination of the permeabilities with $Q/A=f(\Delta H/\Delta L) - 1.0$ and 0.5 mm GB

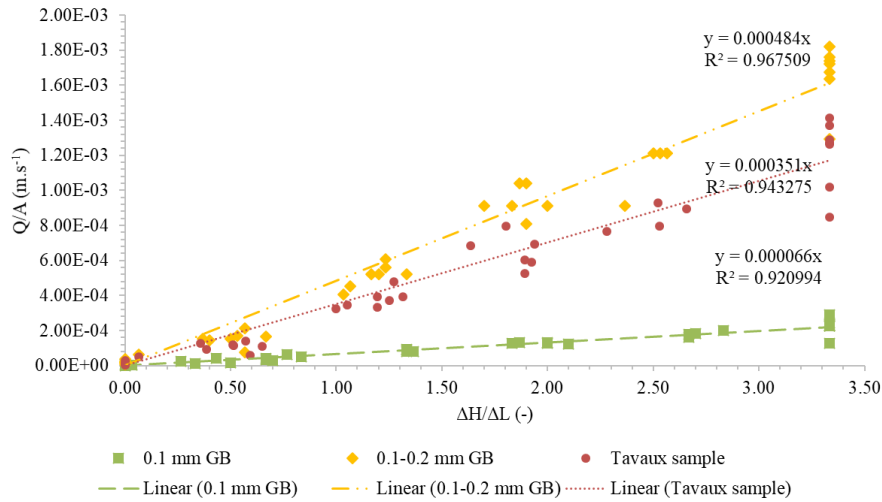


Figure 77: Determination of the permeabilities with $Q/A=f(\Delta H/\Delta L)$ – 0.1-0.2, 0.1 mm GB and Tavaux sample

The hydraulic conductivities (K) and permeabilities (k) can be deduced from the line's slope via the Darcy equation (Eq. 4, section 2.1). Next, we compared the experimental results to the theoretical permeabilities, calculated with the Carman-Kozeny equation (Eq. 6) that can, in the case of perfectly spherical glass beads, be described as follows (Eq. 190) [Bear (1972)]:

$$k = \frac{\phi^3 D_p^3}{180(1 - \phi)^2} \quad \text{Eq. 190}$$

where:

D_p : particle diameter (m)

Regarding the Tavaux soil sample, the theoretical hydraulic conductivity can be determined on the basis of the grain size distribution (Figure 75) and the following empirical equations (Table 37, Eq. 191 to Eq. 193):

Table 37: Empirical equation used to calculate hydraulic conductivity on the basis of the particle size distribution curve

Hazen equations	$K = 1.16(D_{10})^2 [0.70 + 0.03T]$ Applications range: Uniform and unstable sand $C_u \leq 5$; $0.1 \text{ mm} \leq D_{10} \leq 3 \text{ mm}$	Eq. 191
Beyer equation (extension of the Hazen equation for less uniform sand)	$K = \left[0.45 \log \left(\frac{500}{C_u} \right) \right] (D_{10})^2$ Applications range: Uniform sand to medium uniform sand $0.06 \text{ mm} \leq D_{10} \leq 6 \text{ mm}$; $1 \leq C_u \leq 20$	Eq. 192
Sauerbrei Equation	$K = 2.436 \frac{\phi^3}{(1 - \phi)^2} D_{17}^2$ Applications range: Sand and clayey sand $D_{10} \leq 0.5 \text{ mm}$	Eq. 193

where:

K: hydraulic conductivity (cm.s^{-1})

D_{10} : diameter larger than the diameters of 10% of the soil grains, 10th percentile (mm)

D_{17} : diameter larger than the diameters of 17% of the soil grains, 17th percentile (mm)

C_u : uniformity coefficient, $C_u = \frac{D_{60}}{D_{10}}$ (-)

T: temperature (°C); at 5 °C, $K=(D_{10})^2$

From the particle size distribution curve we determine the necessary parameters for the above equations (Table 38).

Table 38: Determination of descriptive parameters for the particle size distribution curve

Parameters	Value
D_5 (mm)	0.15
D_{10} (mm)	0.19
D_{60} (mm)	1.35
C_u	7.073
n *	0.323
e **	0.478

*: $n = 0.255(1 + 0.83C_u)$; **: $e = \frac{n}{1-n}$

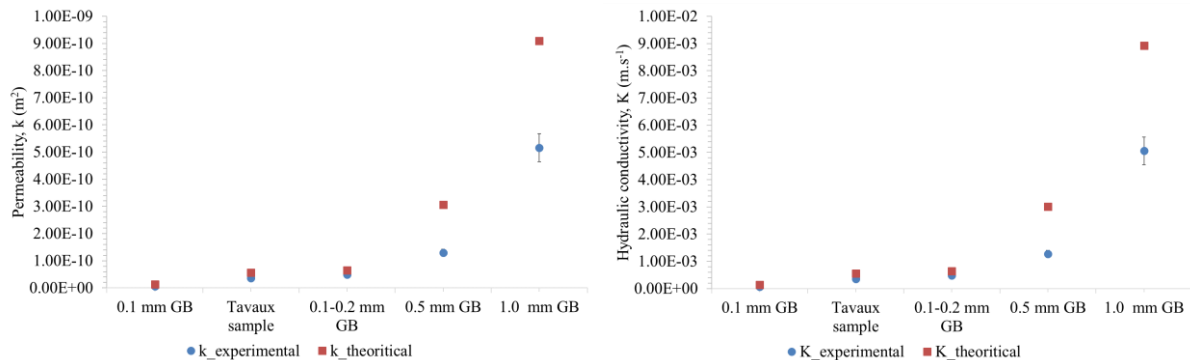
In light of this data, only the Beyer and Sauerbrei equations are applicable to our soil. The estimations of the hydraulic conductivities are reported in Table 39.

Table 39: Estimation of theoretical hydraulic conductivities of the Tavaux soil sample

Method	Hydraulic conductivity ($m.s^{-1}$)
Hazen	3.65×10^{-4}
Beyer	3.04×10^{-4}
Sauerbrei	1.12×10^{-4}

We can consider that $K_{theoretical}$ is between 3.04 and $1.12 \times 10^{-4} m.s^{-1}$. We can use the average of the results from the Beyer and Sauerbrei equations, *i.e.* $2.08 \times 10^{-4} m.s^{-1}$.

From Figure 78, we compared the permeabilities and hydraulic conductivities of the porous materials studied. The experimental results matched the theoretical data, validating our experimental setup. The orders of magnitude were the same. The differences could be due to the use of GB with different packing as well as reading errors for water levels during rapid increases and drops.



a) Permeability, k (m^2)

b) Hydraulic conductivity, K ($m.s^{-1}$)

Figure 78: Comparison of the experimental and theoretical a) permeability and b) hydraulic conductivity of different glass beads size and the soil sample

The Tavaux soil sample was very close to the 0.1-0.2 mm GB from a hydraulic point of view. Furthermore, 0.1-0.2 mm GB were slightly less homogeneous than 0.1 and 0.5 mm GB (whose diameter variability is lower). Also, for better reproducibility, the remaining experiments were based only on 0.1 and 0.5 mm GB.

The permeabilities taken into account in the rest of the thesis are:

- $1.30 \times 10^{-10} \text{ m}^2$ for 0.5 mm GB
- $6.73 \times 10^{-12} \text{ m}^2$ for 0.1 mm GB.

4.2.2 Fitting of experimental results with different parametric models for the P_c - S_w curves

The experimental data were fit to the van Genuchten-Mualem (VGM) capillary pressure-saturation function (Eq. 61 to Eq. 64) using the solver provided in Excel by minimizing the Sum of Squared Errors (SSE) (Eq. 194) [Liu *et al.* (1998); Wraith and Or (1998); Van Geel and Roy (2002)].

$$R^2 = 1 - \frac{\text{SSE}}{N\sigma_S^2} \quad \text{Eq. 194}$$

where:

R^2 : coefficient of determination

σ_S^2 : variance of the measurements on the independent variable S

N: number of data points

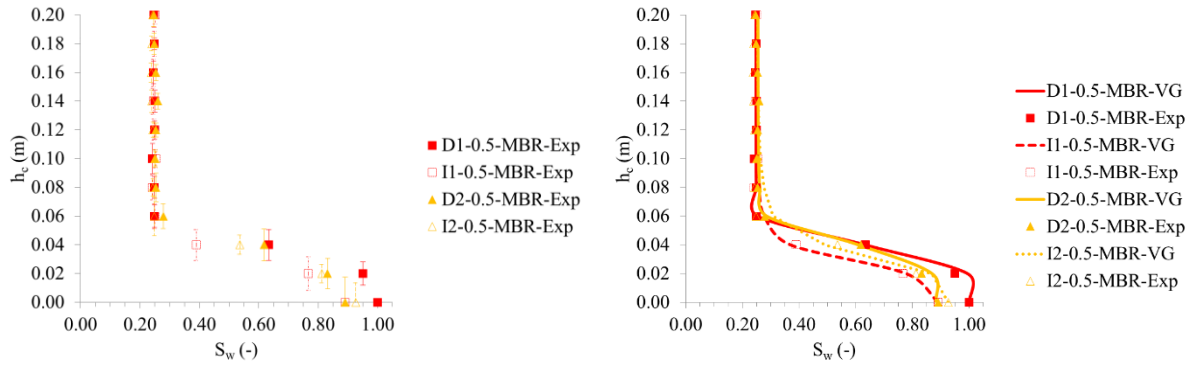
The closer the R^2 value is to 1, the more accurately the function fits the experimental data [Brown (2001); Ramli (2014)]. Fitting experiments with the Brook and Corey-Mualem/Burdine (BCM & BCB), Lognormal Distribution-Mualem (LNM), Brutsaert-Burdine (BRB), Gardner-Mualem (GDM) models were also tested but the fits were not as good (Eq. 61 to Eq. 84). For example, for drainage 1 with 0.5 mm GB, the SSE with VGM is 0.0056 while it is for the other models: 0.1001 (BCM & BCB), 0.0232 (LNM), 0.0061 (BRB), 0.0124 (GDM).

4.2.3 Capillary pressure-water saturation curves for 0.5 and 0.1 mm glass beads

First, we obtained and compared the P_c - S_w curves for 0.5 and 0.1 mm GB, with membrane then without membrane. A correction factor was determined so that the two types of experiments could be compared. Then, we compared the experiments without enhancement with the experiments with chemical and thermal enhancements.

4.2.3.1 Comparison of P_c - S_w curves for 0.5 mm and 0.1 mm glass beads with membranes

In total, 5 experiments were conducted with 0.5 mm GB. Many experiments were not conducted because of damaged membranes or leaks in the periphery of membranes. Figure 79 shows the average of the experimental results for the P_c - S_w curves fitted using the VGM model (Also see Appendix 2.2).



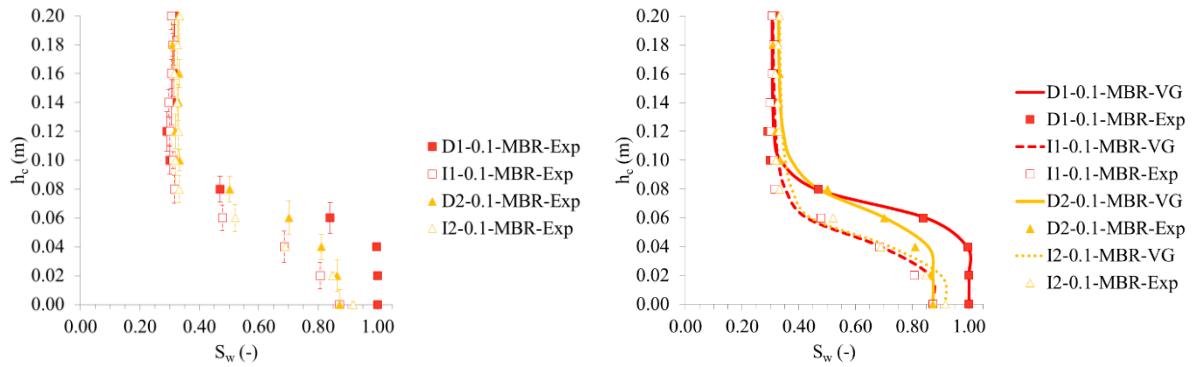
D1: drainage 1; I1: imbibition 1; D2: drainage 2; I2: imbibition 2; MBR: with membrane; VG: VGM value; Exp: experimental value

a) Raw values

b) VGM fitting

Figure 79: P_c - S_w curves for 0.5 mm GB with membrane (a) raw values and b) VGM fitting)

Six experiments were conducted using 0.1 mm GB. Figure 80 shows the average of the experimental results for the P_c - S_w curves fitted using the VGM model.



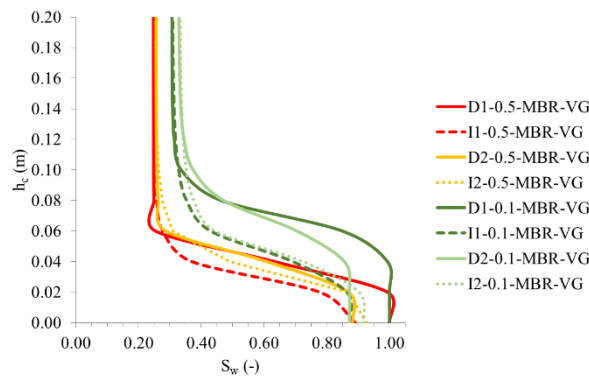
D1: drainage 1; I1: imbibition 1; D2: drainage 2; I2: imbibition 2; MBR: with membrane; VG: VGM value; Exp: experimental value

a) Raw values

b) VGM fitting

Figure 80: P_c - S_w curves for 0.1 mm GB with membrane (a) raw values and b) VGM fitting)

From Figure 81 we compared P_c - S_w curves for 0.5 and 0.1 mm GB. Table 40 shows the results of these experiments and the VGM fitting parameters.



D1: drainage 1; I1: imbibition 1; D2: drainage 2; I2: imbibition 2; MBR: with membrane; VG: VGM value

Figure 81: P_c - S_w curves for 0.1 and 0.5 mm GB with membrane (VGM fitting)

Table 40: Results of drainage-imbibition experiments for 0.5 and 0.1 mm GB with membrane (average)

Parameters	Drainage 1 D1	Imbibition 1 I1	Drainage 2 D2	Imbibition 2 I2
0.5 mm GB				
α (m^{-1})	26.06	38.36	26.69	30.84
n (-)	15.35	5.15	11.18	10.38
SSE	0.0038	0.0025	0.0039	0.0148
S_{rn} (-)	0.000	0.109	0.109	0.074
S_{rw} (-)	0.248	0.248	0.256	0.256
0.1 mm GB				
α (m^{-1})	14.72	23.29	15.25	23.85
n (-)	9.49	16.98	7.08	18.05
SSE	0.0056	0.0214	0.0141	0.0361
S_{rn} (-)	0.000	0.127	0.127	0.082
S_{rw} (-)	0.309	0.309	0.328	0.328

The SSE were low ($SSE < 0.0014$), which demonstrates that the VGM model can be used to describe the experimental results. The experiment mainly focused on residual DNAPL saturation and irreducible water saturation. It is clear from the graph that the parameters differ slightly for each size of glass bead. For 0.5 mm GB, S_{rn} was approximately 10.9% (vs. 12.7% for 0.1 mm GB). According to the results, S_{rw} was around 24.8% for 0.5 mm GB and 30.9% for 0.1 mm GB. This is explained by capillary forces as the mean radius of the porous medium is higher for 0.5 mm GB, where the influence of capillary forces is less. Therefore, during drainage, less DNAPL can be incorporated into a porous medium with 0.5 mm GB and during imbibition, higher amount of DNAPL trapped in the porous media could be extracted for 0.5 mm GB (S_m was 23.0% more than for 0.1 mm GB after the drainage and, S_m was 16.0% more than for 0.1 mm GB after the imbibition). The curve has lower amplitude in terms of S_w for 0.1 mm GB. The results are in agreement with the data reported in the literature [Mualem (1976); van Genuchten (1980); Gerhard and Kueper (2003a)].

We see that α , characteristic of the reverse of the suction effects, was higher for the 0.5 mm GB. This is expected, because as stated, capillary effects are higher for the 0.1 mm GB. The slope of the median portion of the curves is relatively flat, which demonstrates that the GB are indeed homogeneous [Ouchiyama and Tanaka (1984); Likos and Jaafar (2013); Chapuis *et al.* (2015); Chiapponi (2017)]. The interpretation of n values variations is more complicated. Indeed, the sensitivity tests carried out have shown that for high α values and n values greater than 4 (in a homogeneous medium), as in our case, the variations of n have small impact on the shape of the retention curve (See Appendix 2.6).

Figure 82 shows that the impact of grain size on capillary pressure is not the same for all saturation ranges. We found an optimal point where this impact becomes more important. The P_c - S_w ratios for 0.5 mm GB/ P_c - S_w for 0.1 mm GB as a function of h_c , shows that at constant h_c (therefore constant P_c), S_w were in most cases higher for the 0.1 mm GB. This is logical because the experiment began with drainage (a cell full of water) and capillary forces, higher with 0.1 mm GB, limit fluid displacement. We see that for h_c greater than 0.11 m, the cell contained 20% more water (for both drainage and imbibition). For h_c of between 0.03 and 0.11 mm, the ratio increased up to 1:4. Finally, for h_c below 0.03 m, the ratio fell to $h_c=0$, a value greater than 1, which corresponds to higher S_m for 0.1 mm GB.

We also see that the effects of hysteresis were higher for the 0.1 mm GB, which matches the literature [Gerhard and Kueper (2003a)].

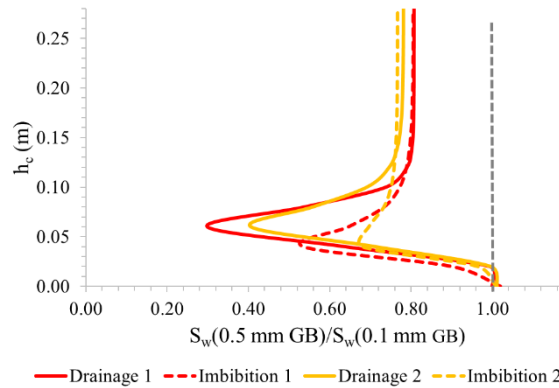
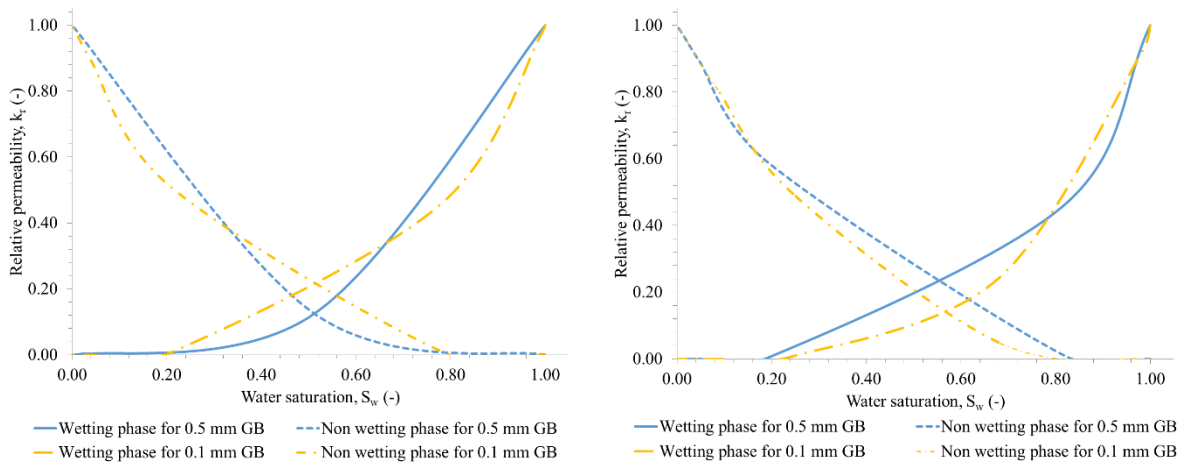


Figure 82: h_c as a function of P_c-S_w 0.5 mm GB/ P_c-S_w 0.1 mm GB with membrane – VGM fitting

a) Relative permeabilities

The curves of relative permeabilities as a function of S_w were plotted using calculated VGM parameter, n (Eq. 63 and Eq. 64). Figure 83 shows curves $k_{rw}=f(S_w)$ and $k_{rn}=f(S_w)$ for drainage 1 and imbibition 1.



a) Drainage 1

b) Imbibition 1

Figure 83: Relative permeabilities as a function of S_w for 0.5 and 0.1 mm GB (a) drainage 1 and b) imbibition 1)

Generally, k_r were much higher for the 0.5 mm GB, which is in agreement with the fact that n is higher for 0.5 mm GB (ans so the capillary forces are lower).

b) Comparison of P_c-S_w curves with P_c-S_w curves from drainage-imbibition experiments with GB with identical diameters in an air-water system

Surface tension measurements between the water used for the experiments and air were run in triplicate. The experimental protocol was the same as the one described in section 3.1.1. The results were as follows: $\sigma_{(aw)}=70.76 \pm 1.09 \text{ mN.m}^{-1}$. This value is consistent with the values

found in the literature [Nagata *et al.* (2016)]. The capillary pressure curve for DNAPL-water system ($P_{c(nw)}$) can be estimated from a known capillary pressure curve for air/water system ($P_{c(aw)}$) from the correction factor, β , as follows (Eq. 195):

$$\beta = \frac{P_{c(aw)}}{P_{c(nw)}} = \frac{\sigma_{(aw)}}{\sigma_{(nw)}} = \frac{70.76}{11.15} = 6.34 \quad \text{Eq. 195}$$

where:

- β : correlation factor (-)
- $P_{c(aw)}$: air/water capillary pressure (Pa)
- $P_{c(nw)}$: DNAPL-water capillary pressure (Pa)
- $\sigma_{(aw)}$: air/water surface tension ($\text{mN}\cdot\text{m}^{-1}$)
- $\sigma_{(nw)}$: DNAPL-water interfacial tension ($\text{mN}\cdot\text{m}^{-1}$)

Drainage experiments conducted on homogeneous GB with diameters around 0.1-0.5 mm in an air-water system are shown in Figure 84 and compared with 0.1 and 0.5 mm for DNAPL-water system corrected by the β factor (*i.e.* $P_{c(nw)}$ multiplied by 6.34) [Chiapponi (2017); Sweijen *et al.* (2017); Cao *et al.* (2018)].

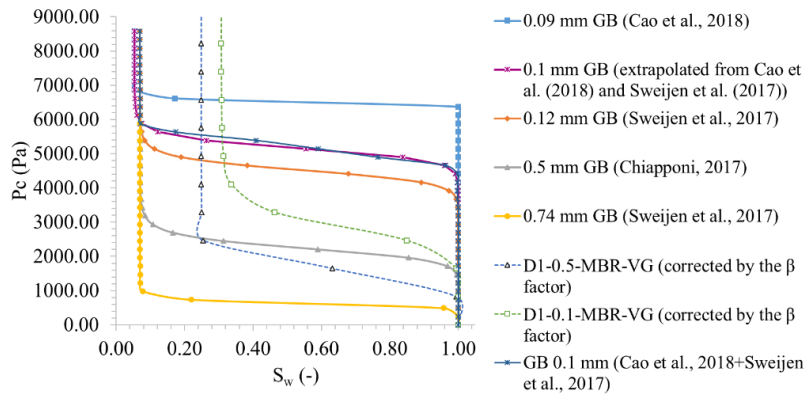


Figure 84: P_c - S_w curves for 0.09, 0.1, 0.12, 0.5, 0.74 mm GB in the air/water system, comparison with 0.1, 0.5 mm for DNAPL-water system corrected by the β factor – VGM fitting

We noted that the P_c - S_w curves obtained during our experiments has a similar shape as the literature (obtained with GB of identical diameters). The differences can be attributed to heterogeneities in packing and GB diameter. The S_{rw} were higher for the DNAPL-water system. Figure 85 shows $P_{c(aw)}/P_{c(nw)}$ as a function of S_w . $P_{c(aw)}$ comes from Chiapponi (2017), Cao *et al.* (2018) and Sweijen *et al.* (2017), for 0.5 mm GB and 0.1 mm GB, respectively.

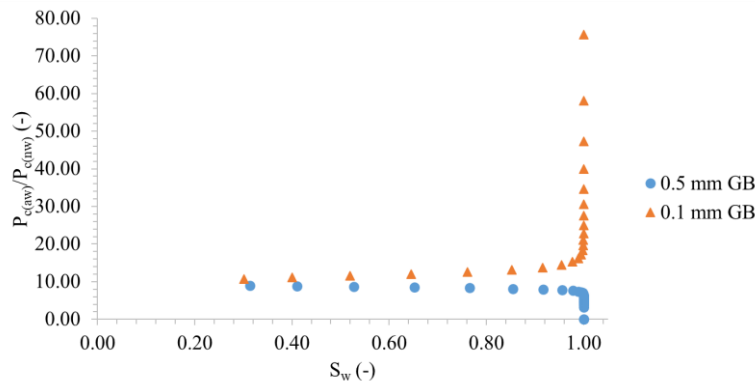


Figure 85: P_c air-water system/ P_c DNAPL-water system as a function of S_w

We see that this ratio was almost linear up to $S_w = 0.8$. For S_w between S_{rw} and $S_w=0.8$, the ratio was 9.1 on average for 0.5 mm GB. For the same interval, this ratio was of the order of 11.3 for 0.1 mm GB. Then the ratios diverged totally for 0.5 mm GB and 0.1 mm GB. For S_w less than 0.8, estimated ratios were 1.45 (for 0.5 mm GB) and 1.78 (for 0.5 mm GB) times higher than the theoretical ratio ($\sigma_{c(nw)}/\sigma_{c(nw)} = 6.34$). The order of magnitude is consistent with the experimental data. The differences can be attributed to the fact that: i. this ratio is global and theoretical; ii. the capillary pressures vary greatly (depending on the pore radii); iii. and the difference in experimental protocols [Bear and Cheng (2010)].

c) Entry pressure

The threshold pressure or entry pressure can be deduced from P_c - S_w curves (Figure 22); it can also be calculated on the basis of the following formula (Eq. 196) [Leverett (1941)]:

$$P_e^{\text{dim}} = \frac{P_e}{\sigma} \left[\frac{k}{\phi} \right]^{\alpha_{P_e}} \quad \text{Eq. 196}$$

where:

P_e^{dim} : dimensionless entry pressure (-)

P_e : measured entry pressure (Pa)

α_{P_e} : exponent (-)

The exponent, α_{P_e} , is often set to 0.5 [Kueper and Gerhard (2014)]. Kueper and Frind (1991) found P_e^{dim} to be 0.186 for a set of PCE–water P_c curves measured using samples of sand with hydraulic conductivity varying from 4.3×10^{-3} to 1.2×10^{-2} cm.s⁻¹ [Kueper and Frind (1991b)]. These hypotheses were considered, as a first approach, to calculate the entry pressures. These results were compared to entry pressures measured from drainage 1 of P_c - S_w curves (Table 41).

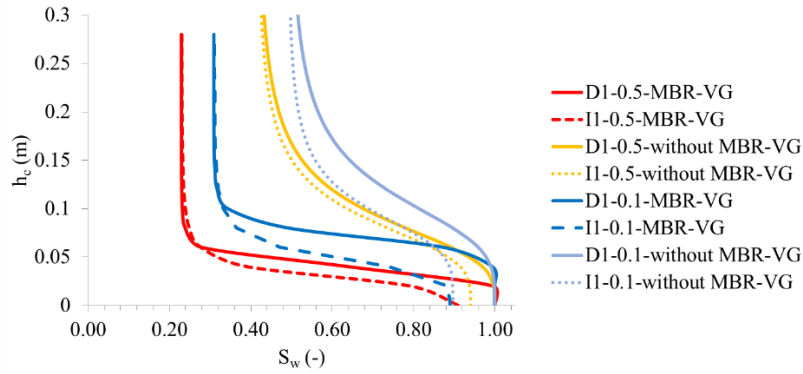
Table 41: Calculated and measured entry pressure without enhancement

Glass beads	Calculated entry pressure		Measured entry pressure
	Entry Pressure (Pa)	h_c (mm)	h_c (mm)
0.1 mm GB	473.91	73.11	60.00
0.5 mm GB	94.78	14.62	12.00

The data reported in Table 41 shows that the results match moderately the calculations (20% difference for 0.1 mm GB and 0.5 mm GB). Logically, we observed that P_e was five times higher for the 0.1 mm GB than for the 0.5 mm GB.

4.2.3.2 Comparison of P_c - S_w curves for 0.5 mm and 0.1 mm glass beads without membranes

Drainage-imbibition experiments were conducted without membranes with the goal of being able to run these experiments with surfactants (which cannot pass through the hydrophobic membranes or the hydrophilic membranes). Moreover, working without a membrane leads to fewer uncertainties, related to them being installed and pierced. To do this, 6 and 11 experiments were conducted with the 0.5 mm GB and the 0.1 mm GB, respectively. Figure 86 shows experimental results (averages) compared with the results of the experiments with the membranes (Also see Appendix 2.3).



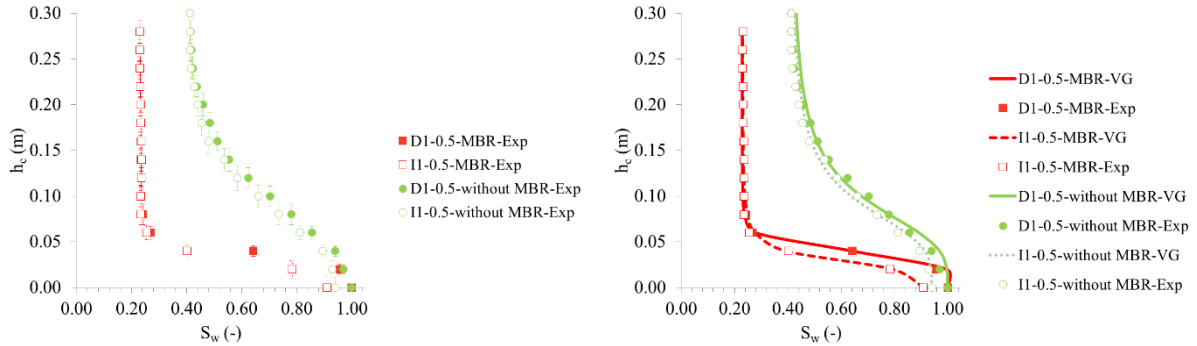
D1: drainage 1; I1: imbibition 1; MBR: with membrane; without MBR: without membrane; VG: VGM value
 Figure 86: P_c - S_w curves for 0.1 and 0.5 mm GB with and without membrane – VGM fitting

It is obvious that the absence of membrane influences the results for the P_c - S_w curves tremendously. The curves are more spread out in height; this is because the volumes measured comprise not only the porous medium ($V_{\text{between membrane}}=55.00$ mL) but also the parts above and below the porous media ($V_{\text{filters}}=29.90$ mL), which skew the porosities in the medium. Moreover, S_{rw} and S_m are different than those measured with the membranes; this is due to the porous medium in the bottom and top portion of the cells is highly influenced by the filters (which have “infinite” permeability). So these filters act as drains and boost the spill of liquids in this “drainage area” [Schwille (1988)]. Note that this drainage area, as we see discussed later, is very restricted (around 1 cm) (see sections 4.2.3.3 and 4.2.3.4). Therefore correction factors were used to “transform” the results for the cells without membranes into cells with membranes (Table 42).

Table 42: Correction factors applied to the drainage-imbibition results to transform the values of the cells without membranes into cells with membranes

h_c (m)	Correction factors			
	0.5 mm GB		0.1 mm GB	
	Drainage	Imbibition	Drainage	Imbibition
0	1.000	1.043	1.000	1.032
0.01	1.003	1.084	0.996	1.049
0.02	1.019	1.210	0.993	1.099
0.03	1.192	1.503	0.980	1.168
0.04	1.482	2.296	0.967	1.185
0.05	2.932	3.441	1.0244	1.275
0.06	3.319	3.277	1.0464	1.703
0.08	3.149	2.966	1.815	2.567
0.1	2.838	2.668	2.655	2.279
0.12	2.516	2.355	2.497	2.088
0.14	2.237	2.165	2.3250	1.942
0.16	2.069	1.938	2.135	1.794
0.18	1.955	1.834	1.904	1.672
0.2	1.858	1.779	1.849	1.607
0.22	1.766	1.731	1.719	1.609
0.24	1.710	1.676	1.665	1.609
0.26	1.684	1.663	1.609	1.609
0.28	1.668	1.663	1.609	1.609

Figure 87 shows the average of the experimental results P_c - S_w curves without membrane (raw values and corrected values to obtain "real" values comparable to experiments with membrane) for 0.5 mm GB and the curves fitted using the VGM model.



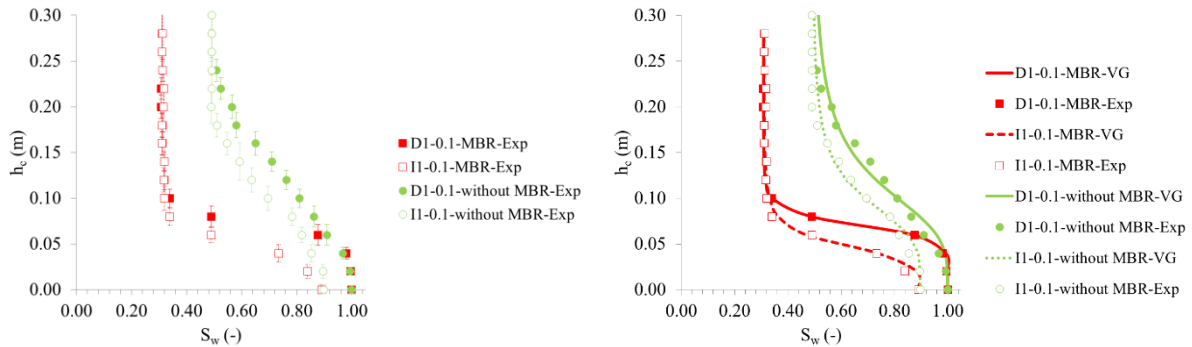
D1: drainage 1; I1: imbibition 1; MBR: with membrane (corrected values); without MBR: without membrane (raw values); VG: VGM value; Exp: experimental value

a) Raw and corrected values

b) VGM fitting

Figure 87: P_c - S_w curves for 0.5 mm GB without membrane (a) raw and corrected values and b) VGM fitting)

Figure 88 shows the average of the experimental results P_c - S_w curves without membrane (raw value and corrected values) for 0.1 mm GB and the curves fitted using the VGM model.



D1: drainage 1; I1: imbibition 1; MBR: with membrane (corrected values); without MBR: without membrane (raw values); VG: VGM value; Exp: experimental value

a) Raw and corrected values

b) VGM fitting

Figure 88: P_c - S_w curves for 0.1 mm GB without membrane (a) raw and corrected values and b) VGM fitting)

4.2.3.3 Permittivity monitoring

Figure 89 shows changes in permittivity, ϵ (corrected relative to the reference value of air and water measured at the beginning of the experiment, see Eq. 186) and in S_w (estimated from volume balance) as a function of time during a drainage-imbibition experiment conducted with 0.5 mm GB. Appendices 2.4 and 2.5 show all the drainage-imbibition experiments for 0.1 and 0.5 mm GB with permittivity and resistivity monitoring.

We see how the change in ϵ follows change in S_w . Given the respective dielectric properties for water and DNAPL (water having higher ϵ values than DNAPL – see section 2.6.5), it is logical that the higher the water content, the higher the permittivity.

The DNAPL detection area is limited to about 2 mm around the area formed by the 2 TDR probe branches (see section 4.1.3.1). ϵ changed as follows: at the start of the experiment $\epsilon = 29.45$ (porous medium filled with water) then fell to 10.4 (minimum S_w at the end of drainage 1, for $S_w=0.25$), then rose to 26.8 at the end of imbibition ($S_w=0.95$). Between the start of drainage 1 and the start of drainage 2, we saw hysteresis (5% lower S_w for 9% lower ϵ). In addition, variations in ϵ were extremely fast (almost vertical curves), which supports the fact that the capillary fringe was very sharp.

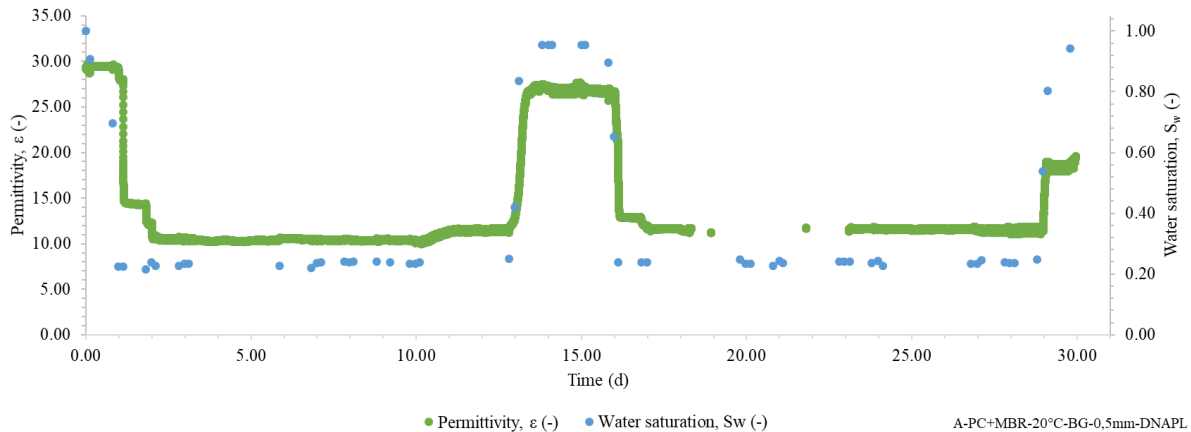


Figure 89: Change of water saturation and permittivity as a function of time without enhancement (example of a drainage-imbibition experiment with 0.5 mm GB)

Figure 90 shows how ϵ and S_w changed as a function of time during the drainage-imbibition experiments conducted with 0.1 mm GB. We see the same overall trends as for the 0.1 mm GB. Furthermore, the variations in S_w are lower (the values corresponding to S_{rn} and S_{rw} are closer).

At the start of the experiment, $\epsilon = 34.21$ (porous medium filled with water), then it fell to 19.68 (minimum S_w at the end of drainage 1, for $S_w=0.35$) and rose to 29.22 at the end of imbibition ($S_w=0.90$). Between the start of drainage 1 and the start of drainage 2, we saw hysteresis (10% lower S_w for 15% lower ϵ). Finally, the ϵ variations for 0.1 mm GB case were slower than with the 0.5 mm GB (less steep curve slope), which supports the fact that the capillary fringe was thicker (the saturation variations were slower).

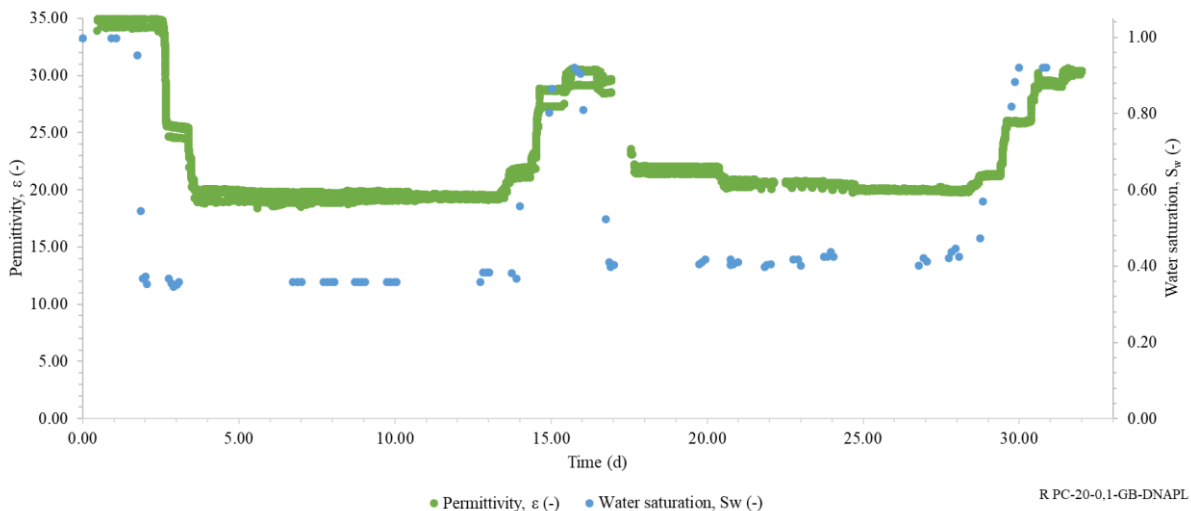


Figure 90: Change of water saturation and permittivity as a function of time without enhancement (example of a drainage-imbibition experiment with 0.1 mm GB)

Permittivity calibration curves were plotted as a function of water saturation on the basis of this data for 0.5 mm GB with and without membranes (Figure 91). Moreover, experiments with DNAPL alone in 0.5 mm GB were undertaken to determine the points corresponding to $S_w = 0\%$.

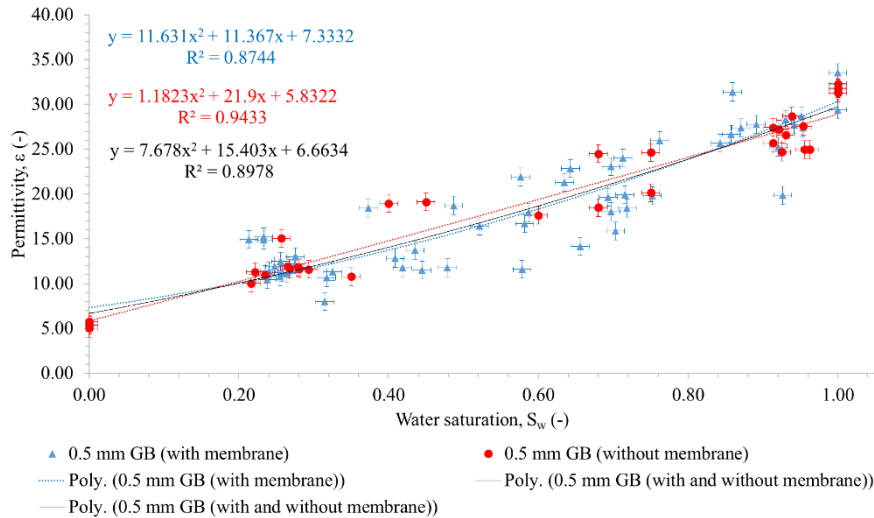


Figure 91: Calibration curve $\epsilon = f(S_w)$ for 0.5 mm GB with and without membrane

Permittivity can therefore be connected to water saturation by a polynomial function (2nd degree) that is pretty similar to a close function. The correlation factor for all data is satisfactory ($R^2 = 0.90$). We saw that for 0.5 mm GB, whether or not membranes were used, had no influence on the water saturation estimated by the TDR probes. This is explained by the TDR probe being located in the center of the 1D cell and the “drainage area” being limited to a fairly limited area around the perimeter.

The same calibration curves ($\epsilon=f(S_w)$) were plotted for 0.1 mm GB with and without membranes (Figure 92).

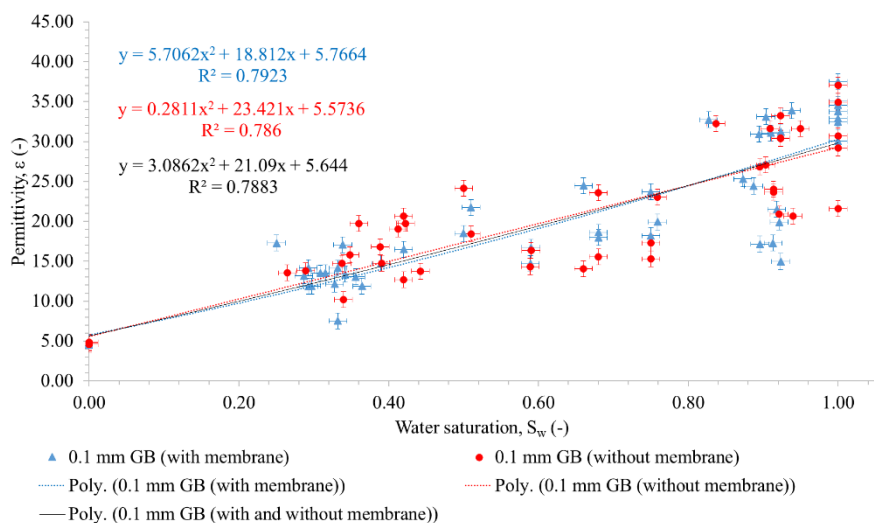


Figure 92: Calibration curve $\epsilon = f(S_w)$ for 0.1 mm GB with and without membrane

Permittivity can therefore be connected to water saturation by a polynomial relationship (2nd degree). We also saw that for 0.1 mm GB, whether or not membranes were used had no

influence on the water saturation estimated by the TDR probes. The scatter plot is more dispersed for the 0.5 mm GB than for the 0.1 mm GB; logically, R^2 is lower for the 0.1 mm GB ($R^2 = 0.79$ vs 0.90 for 0.5 mm GB). Repeatability is lower for experiments with 0.1 mm GB than with 0.5 mm GB.

Figure 93 compares the permittivity values of 0.5 and 0.1 mm GB.

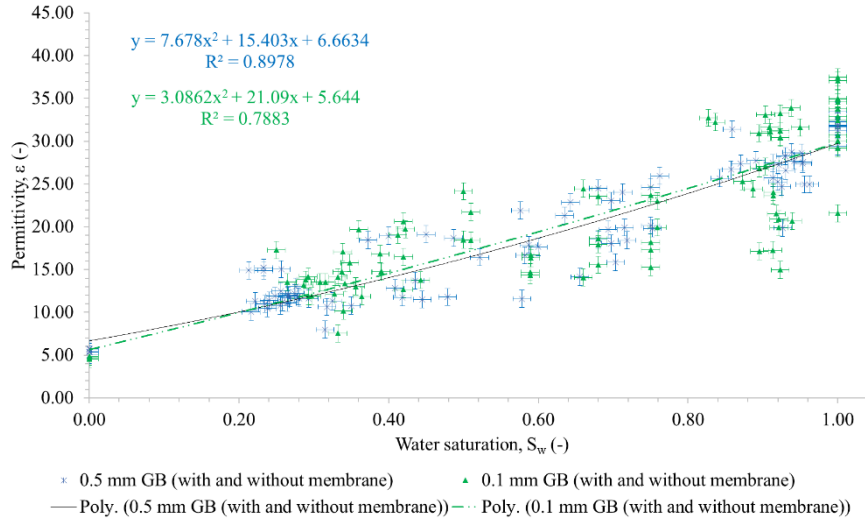


Figure 93: Comparison of the permittivity values between 0.5 and 0.1 mm GB as a function of saturation

The graph shows that the results were very similar for 0.5 and 0.1 mm GB. The calibration curves are very similar: the ratios of polynomial curves for 0.5 mm GB/polynomial curves for 0.1 mm GB vary between 0.97 and 1.20. For homogeneous porous media, grain size has little influence on permittivity. These results are consistent with research topics on permittivities in a water-air system. These small differences can be attributed to the less regular glass beads, the spherical shape of glass beads and the pore connectivity [Robinson and Friedman (2001); Robinson and Friedman (2002); Robinson *et al.* (2005); Brovelli and Cassiani (2010)].

Experimental data was fitted to the CRIM model (see Eq. 190, section 2.6.5.2). The following values were used:

$$\emptyset = 0.38 \text{ (experimental values),}$$

$$\epsilon_w = 80 \text{ (experimental value),}$$

$$\epsilon_n = 3.11 \text{ (experimental value for 100\% DNAPL),}$$

$$\epsilon_m = 7.5 \text{ (literature review for glass beads [von Hippel (1954); Robinson and Friedman (2002)]).}$$

The results of the measures/estimation comparison are shown in Figure 94 and Figure 95. Two hypotheses were considered: $\alpha_\epsilon = 0.5$, as a first approach as stated in literature review (see section 2.6.5.2) and α fitted to the experimental data (with the least-square method).

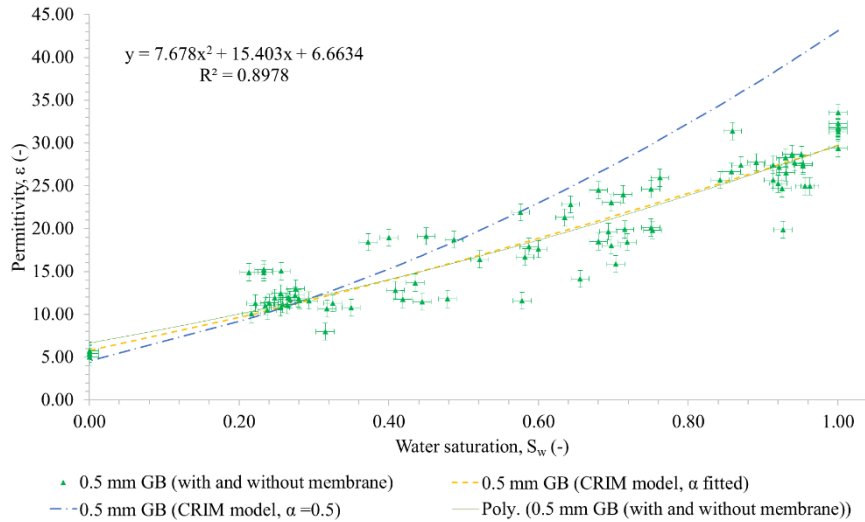


Figure 94: Fitting the experimental permittivity values as function of water saturation with the CRIM model (0.5 mm GB with and without membrane)

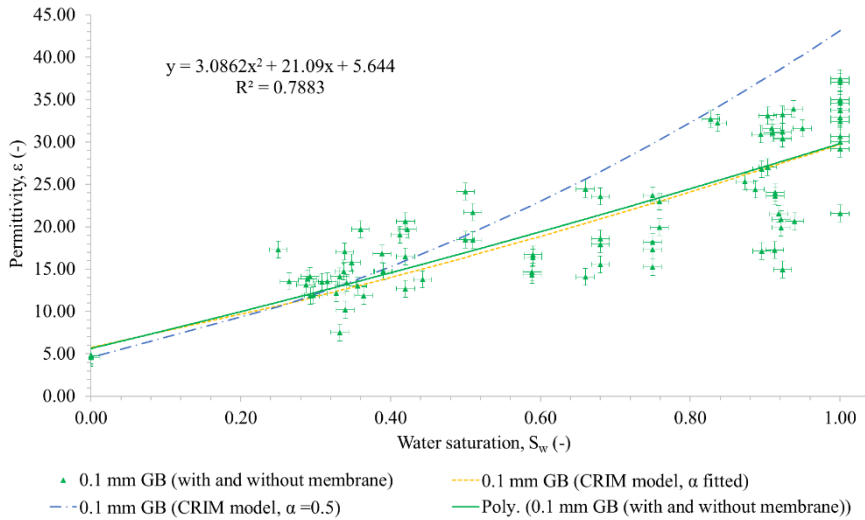


Figure 95: Fitting the experimental permittivity values as a function of water saturation with the CRIM model (0.1 mm GB with and without membrane)

We see that $\alpha_\epsilon = 0.5$ (as stated in literature review) is not suitable for our experiments. The α_ϵ values calculated by the least-square method, are respectively 0.70 and 0.75 for 0.5 mm and 0.1 mm GB (with respective R^2 of 0.89 and 0.78). Therefore, for our experiments the CRIM model can be applied using the following equations (Eq. 197 to Eq. 198):

$$\text{For 0.5 mm GB} \quad \epsilon' = \left[\phi (S_w \epsilon'_w)^{0.7} + S_n \epsilon'_n \right] + (1 - \phi) \epsilon'_m \quad \text{Eq. 197}$$

$$\text{For 0.1 mm GB} \quad \epsilon' = \left[\phi (S_w \epsilon'_w)^{0.75} + S_n \epsilon'_n \right] + (1 - \phi) \epsilon'_m \quad \text{Eq. 198}$$

Figure 96 shows the comparison of experiments results and estimated values as the $\epsilon_{\text{measured}}/\epsilon_{\text{estimated}}$ ratio for 0.5 and 0.1 mm GB.

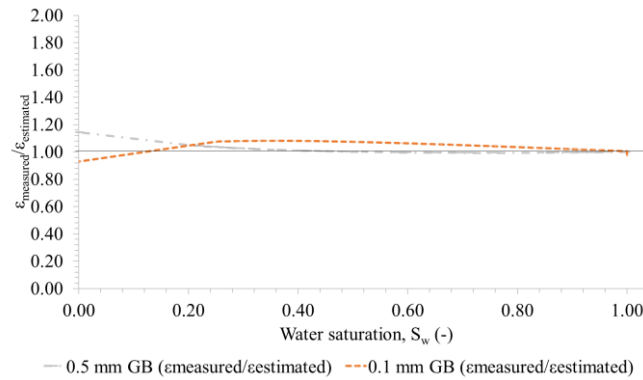


Figure 96: Ratios of the experimental permittivity values/CRIM model values as a function of water saturation (for 0.1 and 0.5 mm GB with and without membrane)

The graph shows that the CRIM model fits well relative to our experiments, for higher saturations than S_{rw} (less than 8% difference). The CRIM model fits better for 0.5 mm GB. For lower water saturation, the ratios increased. The estimated values were overestimated by a factor of 1.14 for 0.5 mm GB and were underestimated by a factor of 0.92 for 0.1 mm GB. Persson and Berndtsson (2002) obtained a better fitting by introducing an extra degree of freedom in the mixing equations [Persson and Berndtsson (2002)].

Figure 97 illustrates permittivity variations as a function of different drainage-imbibition cycles. The drainage-imbibition experiments can be correlated with permittivities. Furthermore, from the end of the second cycle (end of imbibition 2), the correlation no longer holds. This is probably because the DNAPL and water ganglions that remain trapped during the experiments impact the dielectric responses.

Some authors have shown that the CRIM model (based on the relative permittivity of free water, air (or non-wetting fluid) and solids) may not be suitable in all situations, especially in the transition phases (when S_w are between S_{rm} and S_{rw}). These authors have proposed to take into account a 4th constituent, the bound water. Indeed, the dielectric constant of bound water is very different from free water (it is due to the electrical bonds limiting the freedom of polarization of water molecules) [Dasberg and Hopmans (1992); Capparelli *et al.* (2018)]. An equation derived from the CRIM model incorporating the bound water has been proposed [Dobson *et al.* (1985); Dirksen and Dasberg (1993)]. We did not quantify the bound water.

Capparelli *et al.* (2018) carried out monitoring of S_w variations with TDR probes in unsaturated soils. They showed, like our experimental results, a difference between the values estimated with the CRIM model and the experimental values. The experimental results were compared to the classical CRIM model but also to the four-phase dielectric mixing model (with bound water), and the classical CRIM model with a variable exponent. The best results were obtained with the three-phase dielectric mixing model with a variable exponent (α_ϵ) [Capparelli *et al.* (2018)].

It should also be noted that the permittivity measurement remains local while the water saturation measurement is global. Furthermore, for the first drainage-imbibition cycle, the correlation is demonstrated.

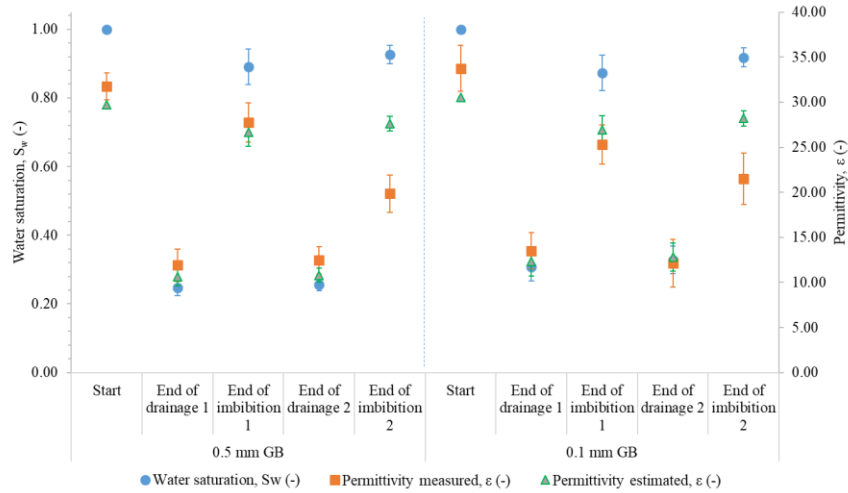


Figure 97: Change of water saturation and permittivity (measured and estimated) as a function of drainage-imbibition cycle for 0.5 and 0.1 mm GB in 1D cells (without enhancement)

4.2.3.4 Electrical resistivity monitoring

Figure 98 shows the change in resistivity at 1.4 Hz, ρ_c , and S_w as a function of time during a drainage-imbibition experiment conducted with 0.5 mm GB. We see that resistivity varied as a function of drainage and imbibition cycles. Since DNAPL has much higher resistivity than water (see section 2.6.4.1), logically during drainages, resistivity increased greatly and inversely, and during imbibition, it fell significantly. We saw a time offset between variations in S_w and electric responses (which was not the case with permittivity measurements, see section 4.2.3.3). This is because the detection area for resistivity measurements was limited to the central part of the 1D cell; it corresponded only to a height of 3.9 cm (see section 4.1.3.2).

At the start of the experiment, $\rho_c = 120 \Omega.m$ (for $S_w=1$). At the end of drainage 1, $S_w = 0.2$, which corresponded to $\rho_c = 9239 \Omega.m$. Next, at the end of drainage 2, $S_w = 0.24$ and ρ_c reached $7520 \Omega.m$. Therefore, we can see the effects of hysteresis with resistivity monitoring. Like with permittivity monitoring, we see that resistivity varied quickly with time (the curves were almost vertical), which demonstrated that the capillary fringe was sharp.

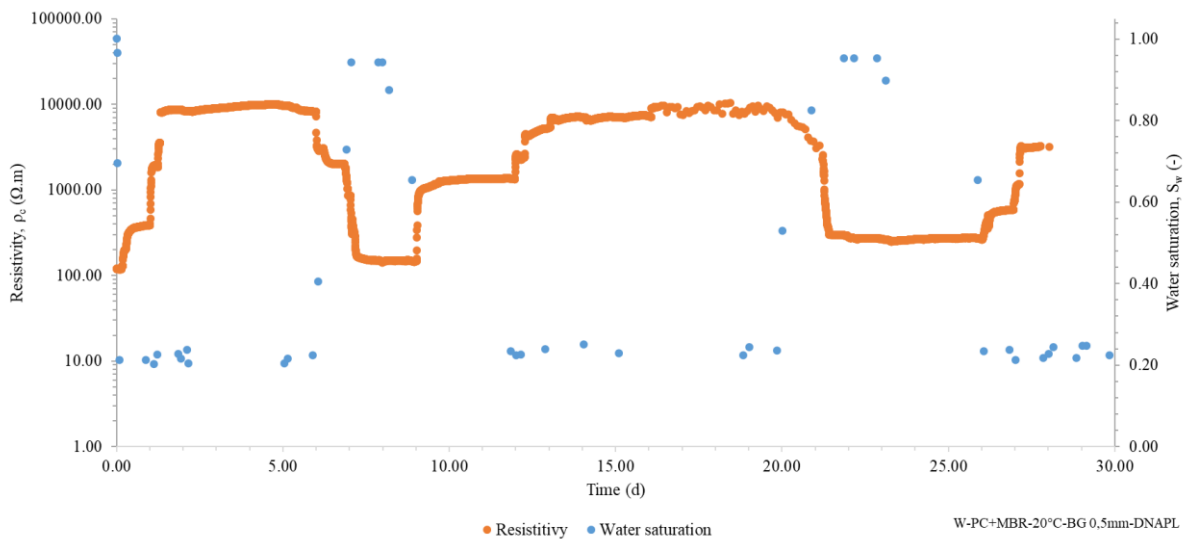


Figure 98: Change of water saturation and resistivity as a function of time (example of one drainage-imbibition experiment with 0.5 mm GB)

Figure 99 shows the change in ρ_c and S_w as a function of time during a drainage-imbibition experiment conducted with 0.1 mm GB. We see the same variations as those described in the previous paragraph. Generally resistivity variations were slower (this is related to a more spread out capillary fringe for 0.1 mm GB). Moreover, the effects of hysteresis are more important for the 0.1 mm GB than for the 0.5 mm GB (6.2% for 0.1 mm GB vs 3.2% for 0.5 mm GB). At the end of drainage 2, $S_w = 0.31$ (with $\rho_c = 25257 \Omega.m$), whereas at the end of drainage 1, $S_w = 0.28$ ($\rho_c = 90600 \Omega.m$).

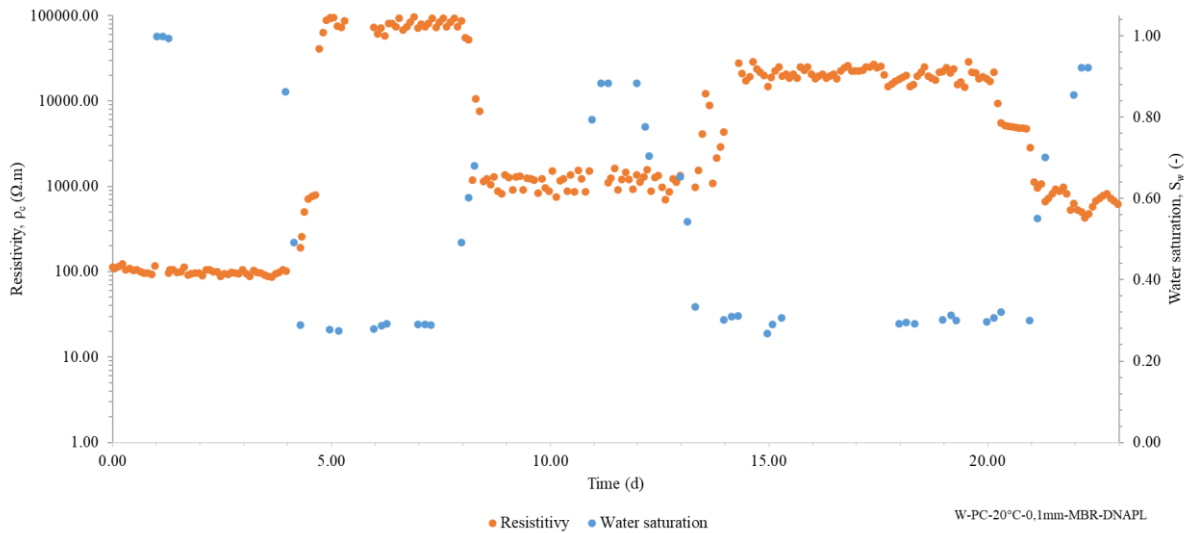


Figure 99: Change of water saturation and resistivity as a function of time (example of one drainage-imbibition experiment with 0.1 mm GB)

Calibration curves ($\rho_c=f(S_w)$) were plotted for 0.5 mm GB with and without membranes (Figure 100). Moreover, experiments with DNAPL alone in 0.5 mm GB were undertaken to determine the points corresponding to $S_w = 0\%$.

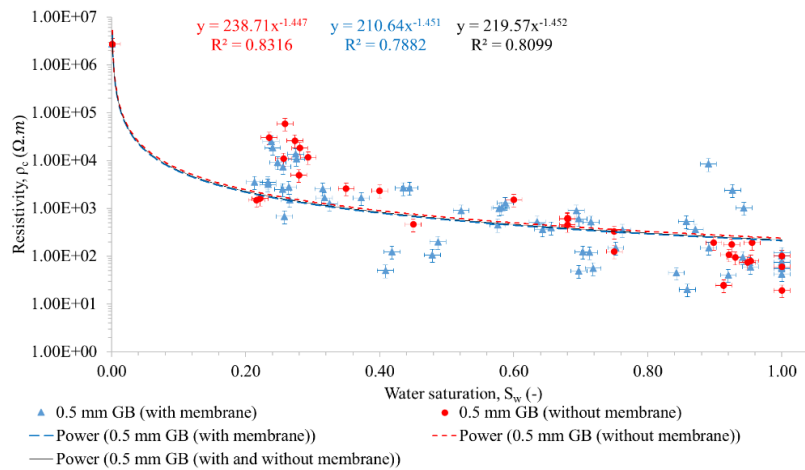


Figure 100: Calibration curve $\rho_c = f(S_w)$ for 0.5 mm GB with and without membrane

The resistivity results were more dispersed than the permittivity results. Moreover, many technical problems for connections and registrations (solved during the experiments) mean that we have less data than with the TDR probes. Whether or not to use membranes has no influence on resistivity results, which confirmed our hypothesis that the drainage area is limited to a quite limited peripheral area (see section 4.2.3.3).

Resistivity may be correlated to water saturation via a power relationship. The correlation factor for fitting all data together is satisfactory ($R^2 = 0.81$).

The same calibration curves ($\rho_c=f(S_w)$) were plotted for 0.1 mm GB with and without membranes (Figure 101).

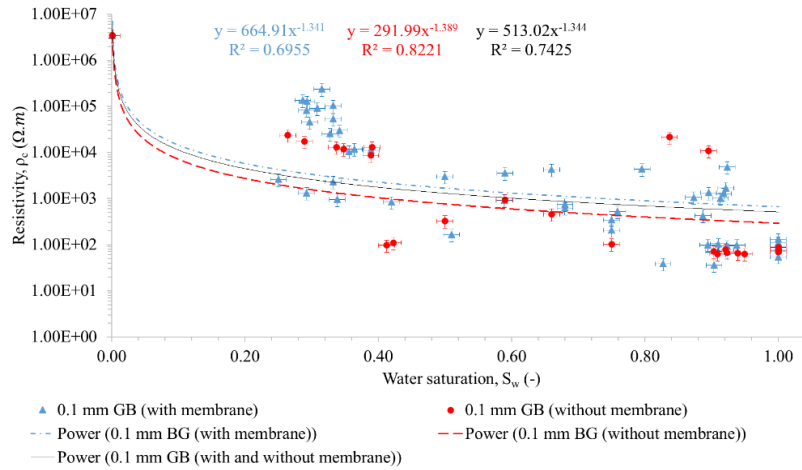


Figure 101: Calibration curve $\rho_c = f(S_w)$ for 0.1 mm GB with and without membrane

The membranes used had no influence on resistivities. The results were even more disparate with the 0.1 mm GB than with the 0.5 mm GB. Furthermore, resistivity can be connected to S_w via a power law; the correlation factor is average ($R^2 = 0.74$).

Figure 102 compares the resistivity values of 0.5 and 0.1 mm GB.

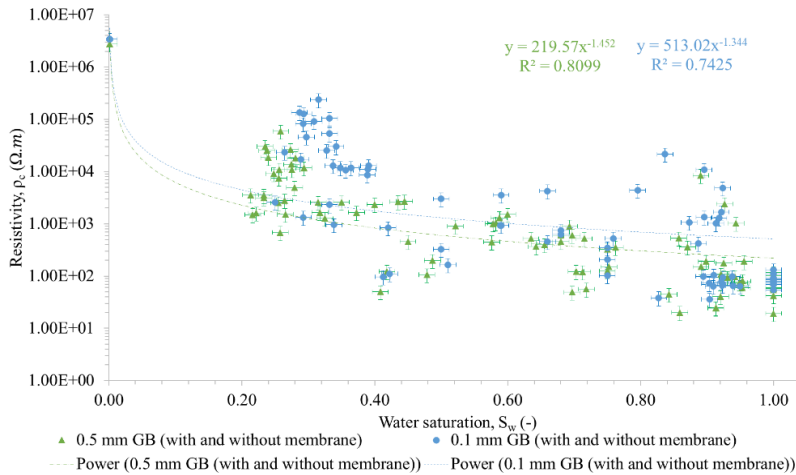


Figure 102: Comparison of the resistivity values between 0.5 and 0.1 mm GB as a function of water saturation

We see that the results were not similar for 0.5 and 0.1 mm GB: trend curves look the same but are shifted. For homogeneous beads, and for identical S_w , the resistivity was higher for the 0.1 mm GB. This is explained by the connected porosity being lower for the 0.1 mm GB.

The mathematical fitting to Archie's law (see section 2.6.4.1) was done in several steps based on work done by Glover (2010), on the basis of a two-phase system, neglecting the conductivity of glass beads, which is very low ($\sigma_{c,GB}=10^{-20}$ S.m⁻¹) (Eq. 199 to Eq. 202) [Glover (2010)].

$$\sigma_{c,bulk} = \sigma_{c,DNAPL}[\phi(1 - S_w)]^{m_1} + \sigma_{c,water}[\phi(S_w)]^{m_2} \quad \text{Eq. 199}$$

$$\left(-\frac{\phi_1^2}{2}\right)m_2^2 + \left(\phi_1 + \frac{\phi_1^2}{2}\right)m_2 - \phi_1^{m_1} = 0 \quad \text{Eq. 200}$$

$$m_2 = \frac{-\left(\phi_1 + \frac{\phi_1^2}{2}\right) \pm \left[\left(\phi_1 + \frac{\phi_1^2}{2}\right)^2 - 4\left(-\frac{\phi_1^2}{2}\right)(-\phi_1^{m_1})\right]^{\frac{1}{2}}}{-\phi_1^2} \quad \text{Eq. 201}$$

$$m_2 = \frac{-(4\phi_1 + 2\phi_1^2) \pm (4\phi_1^2 + 4\phi_1^3 + \phi_1^4 - 8\phi_1^2\phi_1^{m_1})^{\frac{1}{2}}}{-4\phi_1^2} \quad \text{Eq. 202}$$

where:

$\sigma_{c,bulk}$: real effective electrical conductivity of the bulk (S.m⁻¹)

$\sigma_{c,DNAPL}$: real effective electrical conductivity of DNAPL (S.m⁻¹)

m_1 : cementation exponent of DNAPL phase

$\sigma_{c,water}$: real effective electrical conductivity of water (S.m⁻¹)

m_2 : cementation exponent of water phase

$\phi_1 = \phi(1 - S_w)$

$\phi_2 = \phi(S_w)$

On the basis of the equations below, and by applying the least-square method, we found the following equations (Eq. 203 to Eq. 206):

$$\text{for 0.5 mm GB} \quad \sigma_{c,bulk} = \sigma_{c,DNAPL}[\phi(1 - S_w)]^{1.752} + \sigma_{c,water}[\phi(S_w)]^{1.9} \quad \text{Eq. 203}$$

$$\text{for 0.1 mm GB} \quad \sigma_{c,bulk} = \sigma_{c,DNAPL}[\phi(1 - S_w)]^{1.678} + \sigma_{c,water}[\phi(S_w)]^{2.4} \quad \text{Eq. 204}$$

i.e.

$$\text{for 0.5 mm GB} \quad \rho_{c,bulk} = \frac{1}{\sigma_{c,DNAPL}[\phi(1 - S_w)]^{1.752} + \sigma_{c,water}[\phi(S_w)]^{1.9}} \quad \text{Eq. 205}$$

$$\text{for 0.1 mm GB} \quad \rho_{c,bulk} = \frac{1}{\sigma_{c,DNAPL}[\phi(1 - S_w)]^{1.678} + \sigma_{c,water}[\phi(S_w)]^{2.4}} \quad \text{Eq. 206}$$

where:

$\rho_{c,bulk}$: real effective electrical resistivity of the bulk ($\Omega.m$)

$\rho_{c,DNAPL}$: real effective electrical resistivity of DNAPL ($\Omega.m$)

The conductivity values for DNAPL and water were taken into account to fit the model:

$\sigma_{c,DNAPL}$: 3.1807×10^{-8} S.m⁻¹

$\sigma_{c,water}$: 0.04 S.m⁻¹

Figure 103 and Figure 104 show the results of fittings relative to Archie's Law.

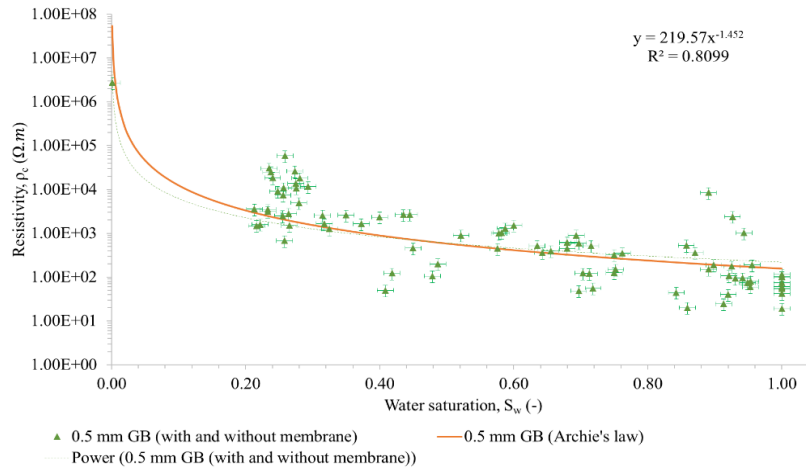


Figure 103: Fitting the experimental resistivity values as a function of water saturation with the Archie's law (0.5 mm GB with and without membrane)

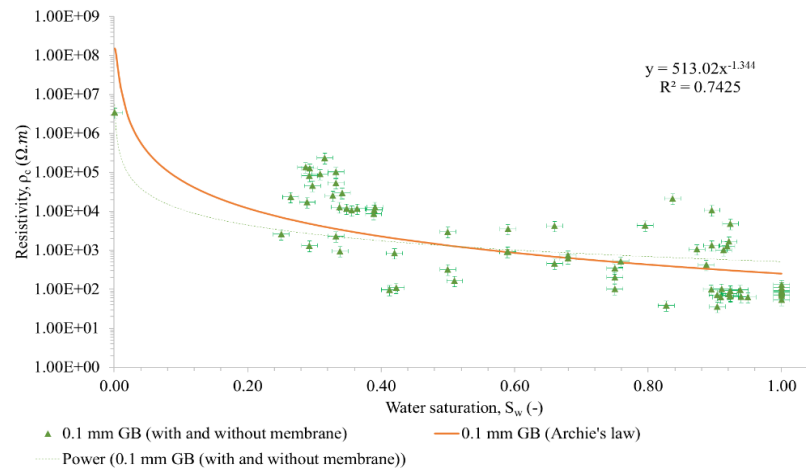


Figure 104: Fitting the experimental resistivity values as a function of water saturation with the Archie's law (0.1 mm GB with and without membrane)

The R^2 for these methods were 0.81 and 0.76 respectively for 0.5 and 0.1 mm GB, which is relatively good and demonstrates that Archie's law reasonably predicts our experimental data. Figure 105 compares experimental results and estimated values as the $\rho_{c,measured}/\rho_{c,estimated}$ ratio for 0.5 and 0.1 mm GB.

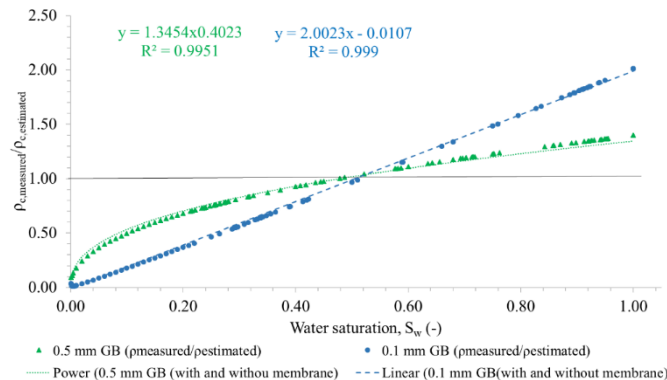


Figure 105: Ratios of the experimental resistivity measured values/Archie's law values (for 0.1 and 0.5 mm GB with and without membrane)

This graph shows that the $\rho_{c,measured}/\rho_{c,estimated}$ ratios depend on the S_w . We note that the Archie's model overestimates the measurements for S_w lower than 0.5 and underestimates the measurements for S_w greater than 0.5. For the 0.5 mm GB, these ratios vary between 0.1 and 1.4. However, it is possible to estimate the S_w accurately since this ratio follows a power law with a high correlation factor ($R^2 = 0.99$). For the 0.1 mm GB, this ratio varies between 0.04 and 2. Here again, it is possible to accurately estimate the S_w since the ratios follow a linear relation ($R^2 = 0.99$). The ratios $\rho_{c,measured}/\rho_{c,estimated}$ are respectively for S_{rw} and S_m of 0.73 and 1.33 for 0.5 mm GB whereas they are 0.6 and 1.78 for 0.1 mm GB.

Figure 106 illustrates the resistivity variations (measured and estimated) as a function of different drainage-imbibition cycles. A correction factor was used so as to approach the values shown in the 1D cells as closely as possible (Figure 105). The correction factors are as follows (Eq. 207 and Eq. 208):

$$\text{for 0.5 mm GB} \quad \frac{\rho_{c,measured}}{\rho_{c,estimated}} = 1.3454S_w^{0.4023} \quad \text{Eq. 207}$$

$$\text{for 0.1 mm GB} \quad \frac{\rho_{c,measured}}{\rho_{c,estimated}} = 2.0023S_w - 0.0107 \quad \text{Eq. 208}$$

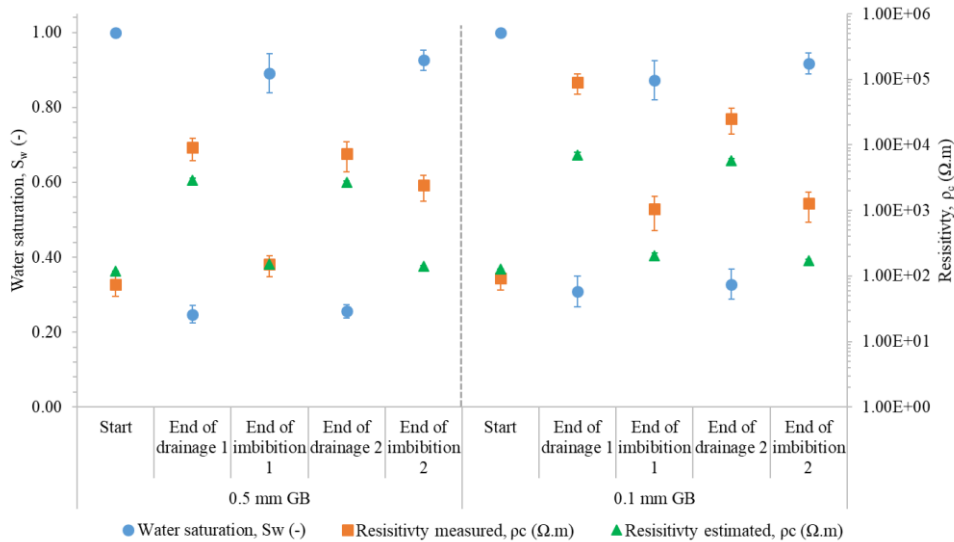


Figure 106: Change of water saturation and resistivity (measured and estimated) as a function of drainage-imbibition cycle for 0.5 and 0.1 mm GB in 1D cells (without enhancement)

We see that estimated data for resistivity correlates less well with the experimental data than for permittivity. The model overestimated the values at the start and under-estimates the values in most other cases. For the 0.5 mm GB, the average measured resistivity/estimated resistivity ratios were 0.64 for $S_w=100\%$ (start), 3.14 at the end of the drainage 1 and 0.99 at the end of the imbibition 1. For the 0.1 mm GB, these ratios were 0.72 at the start, 12.84 at the end of drainage 1 and 5.22 at the end of imbibition 1. As for permittivity, it should be noted that the resistivity measurement remains local while the water saturation measurement is global.

These resistivity overestimations have been discussed by some authors. Byun *et al.* (2019) demonstrated that, in a porous medium with water and gas, that taking into account a suitable cementation factor that does consider the saturation condition would allow better modeling of resistivity with Archie's law [Byun *et al.* (2019)].

Other authors also demonstrated that at a pore scale, the resistivity indexes did not generally obey Archie's Law in the non-homogeneous zones (for example with a transition zone constituted of values close to S_m and S_{rw}). Therefore we can over or underestimate resistivity depending on the thickness of the water films around grains of sand or glass beads [Li *et al.* (2015)]. These water films play a role not only on the pore space connectivity but also on resistivity [Bernabé *et al.* (2011); Li *et al.* (2015); Bernabé *et al.* (2016)].

Finally, it has been demonstrated that many other parameters could be taken into account at different scales in electrical conductivity models in porous media: tortuosity, pore size distribution, pore-conductance distributions, interconnectivity, universal power law of percolation [Glover (2010); Cai *et al.* (2017); Ghanbarian and Sahimi (2017)].

The ratios estimated in Figure 105 must therefore be qualified.

4.2.3.5 Optical density monitoring

Drainage-imbibition experiments have been carried out in the flat Hele-Shaw cell. Figure 107 shows an experiment with 0.5 mm GB.

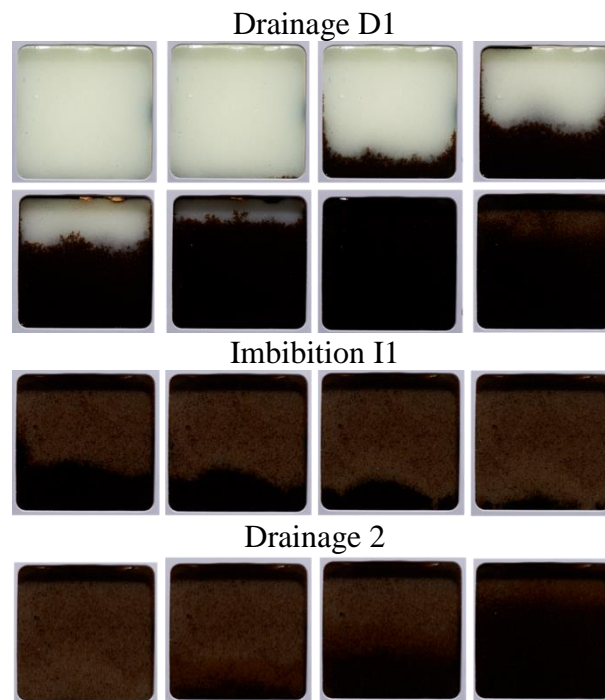
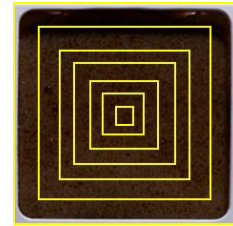
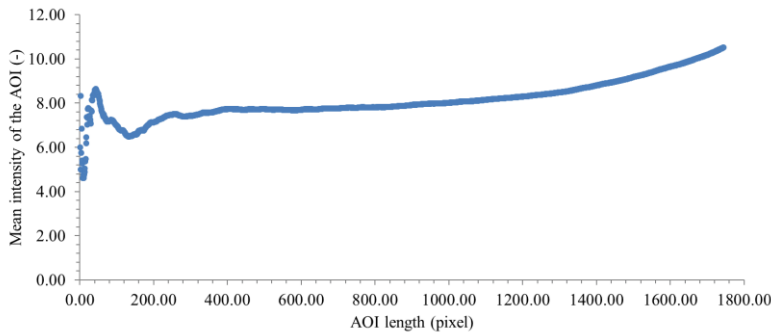


Figure 107: Drainage-imbibition experiments in the flat cell (example with 0.5 mm GB)

The pollutant was dark brown-black. Note that during drainage 1, the migration front was relatively sharp (which corresponded to curve $P_c = f(S_w)$ for D1 with a relatively horizontal plateau – Figure 81). At the end of drainage 1, the cell was filled with DNAPL but filling was not totally homogeneous (with wall effects). During imbibition 1, the migration front was more diffuse, which is logical in light of the $P_c = f(S_w)$ curve for I1, which shows a less horizontal pseudo plateau. During drainage 2, the migration front was even broader. DNAPL migrated more easily because the DNAPL ganglions present created continuums more easily; the entry pressure was very low. The more diffuse migration front also corresponded to the $P_c=f(S_w)$ curve in I1.

Figure 108 describes the variations of mean grey values for an increasing AOI that began at the center of the picture, as detailed below (Figure 108(b)). The AOI variation was due to the length increasing that increases the number of pixels contained inside the AOI. This curve was calculated with a Fiji macro. This macro was necessary because we wanted to associate a mean grey value with S_w but as we see in Figure 108 (a), the grey value was sensitive to the quantity of pixels inside the AOI selected. However, for AOI between 500 pixels and 1000 pixels the mean grey values computed are stabilized. That means we needed between 2.5×10^5 and 1.0×10^6 pixels. We chose this interval length to compute all mean grey values for the calibration curve.



a) Mean grey values variations as a function of the AOI length variations

b) Variation of the AOI

Figure 108: a) Mean grey values variations as a function of the AOI length variations (example with 0.5 mm GB) and b) variation of the AOI

Based on the experiment and AOI length described above, we have produced the calibration curve (Figure 109).

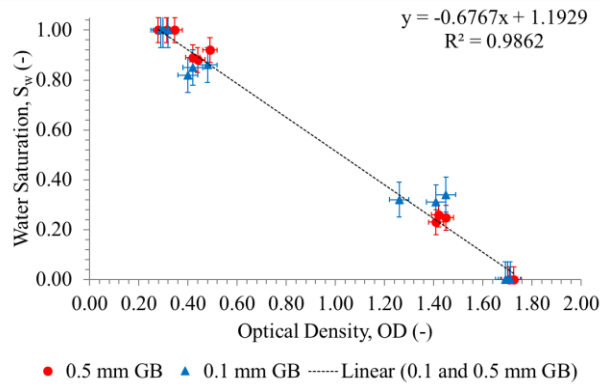


Figure 109: Calibration curve - Optical Density = $f(S_w)$ for 0.5 and 0.1 mm GB

The calibration curve could only be made for the points corresponding to $S_w=1$, $S_w=0$, S_{rn} and S_{rw} . The curve showed good correlation ($R^2 = 0.98$). The size of the glass beads did not influence the calibration curve. We saw no differences in Optical Density (OD) measured for $S_w = 1$ and $S_w = 0$. S_{rn} (with respective means of 0.24 and 0.32 for 0.5 and 0.1 mm GB) and S_{rw} (with respective means of 0.89 and 0.84 for 0.5 and 0.1 mm GB) were very close to those measured with circular 1D cells (less than 3% difference). Variations in S_{rn} and S_{rw} follow a linear regression which is in agreement with the literature [Watson *et al.* (2019)].

Figure 110 and Figure 111 show drainage-imbibition experiments with OD monitoring for 0.5 and 0.1 mm GB. The images have been converted into 8 bit format (grey) then were transformed, via the calibration curve, into S_n values (see scale color).

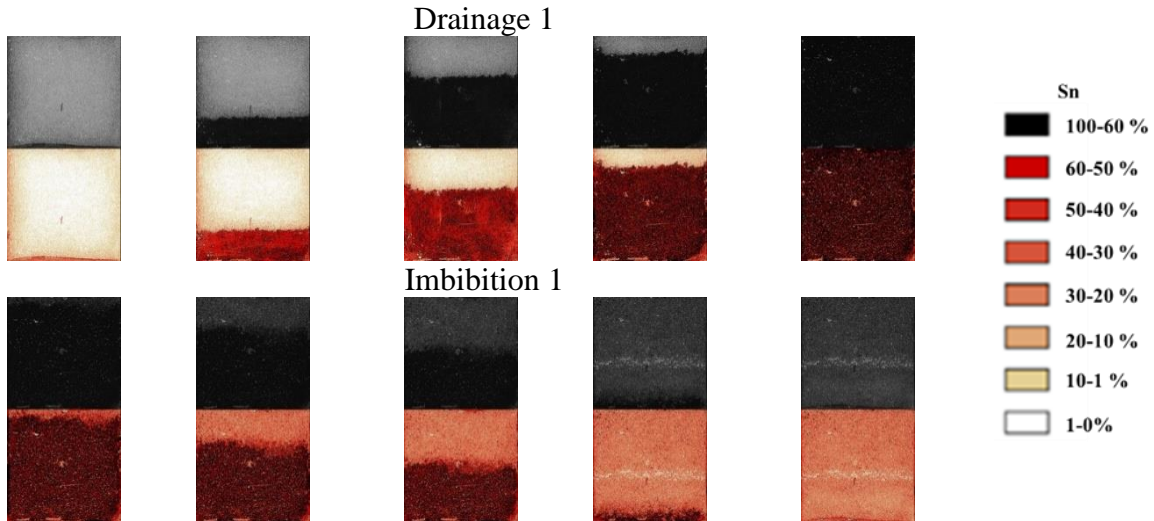


Figure 110: Drainage-imbibition experiments with optical density monitoring (0.5 mm GB)

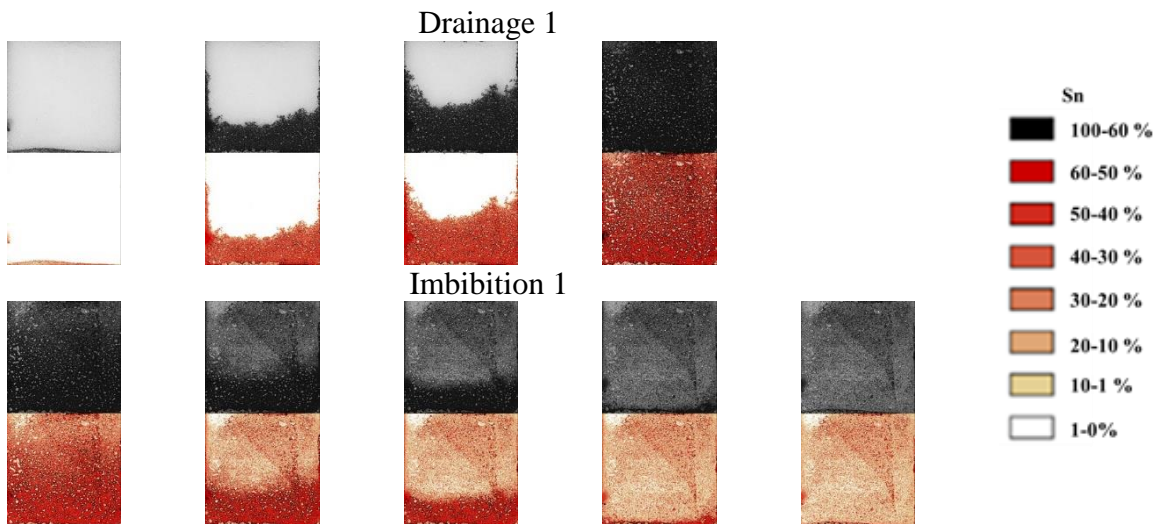


Figure 111: Drainage-imbibition experiments with optical density monitoring (0.1 mm GB)

The results show much larger fingering for the 0.1 mm GB (for drainage and imbibition). The wall effect was more important for 0.1 mm GB compared to 0.5 mm GB. During imbibition, the migration front was much sharper for the 0.5 mm GB (which corresponds to $P_c=f(S_w)$ curves with flatter II for 0.5 mm GB than for the 0.1 mm GB). It was also easy to see that at the end of drainage the black was denser for the 0.5 mm GB (which is logical because S_{rw} is lower). Finally, the OD different between the white beads at the start of drainage and the end of imbibition was more marked for the 0.1 mm GB (which should be considered in relation with a higher S_m for the 0.1 mm GB than for the 0.5 mm GB).

Note that the linear OD correlation does not depend on the different drainage-imbibition cycles (by contrast with permittivities).

4.2.4 Capillary pressure-water saturation curves for 0.5 and 0.1 mm glass beads with chemical enhancement

Drainage-imbibition experiments were conducted with surfactants to test the effect of chemical enhancement (with CMC).

4.2.4.1 Comparison of P_c - S_w curves for 0.1 mm and 0.5 mm glass beads with chemical enhancement

The surfactants were added at the end of drainage 1 in order to start with the same S_{rw} as for the experiments without surfactant.

Regarding the 0.5 mm GB, in total, eight experiments were conducted with permittivity and geophysical monitoring: three with SDBS, two with Aerosol MA-80, two with Triton X-100, one with Tween 80 (Also see Appendix 3.1). Regarding the 0.1 mm GB, in total, six experiments were conducted with permittivity and geophysical monitoring: two with SDBS, two with Aerosol MA-80, one with Triton X-100, one with Tween 80. The S_{rn} at the end of imbibition 1 (and the remediation yields) are shown in Figure 112. The remediation yield was calculated as follows (Eq. 209):

$$\text{Remediation yield} = 100 - 100 \left(\frac{S_{rn, \text{chemical enhancement}}}{S_{rn, \text{without enhancement}}} \right) \quad \text{Eq. 209}$$

where:

$S_{rn, \text{with enhancement}}$: residual saturation of non-wetting with enhancement (-)

$S_{rn, \text{without enhancement}}$: residual saturation of non-wetting without enhancement (-)



Figure 112: S_{rn} and remediation yields with the four surfactants with 0.5 and 0.1 mm GB (average values at the end of imbibition 1)

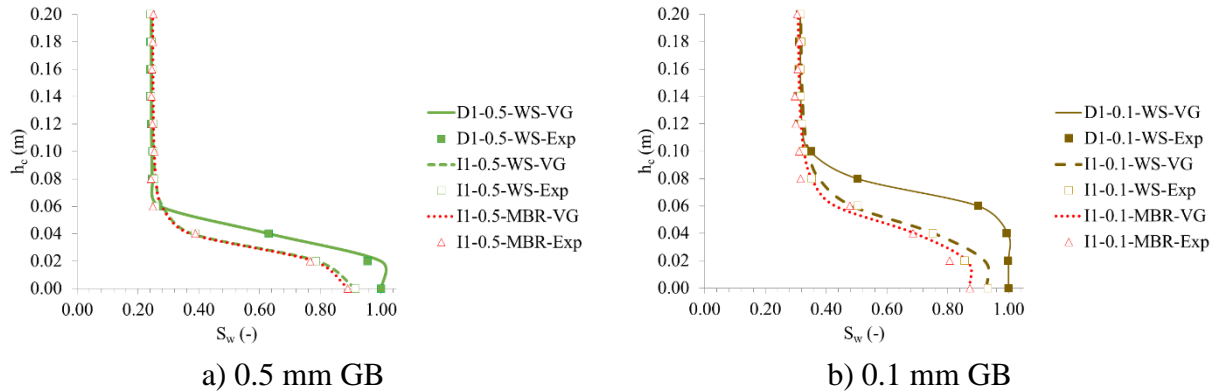
Adding SDBS reduces the highest IFT. Logically, for 0.5 mm GB the best remediation yield was obtained with SDBS (27.6% *i.e.* $S_{rn}=0.079$). Aerosol MA-80 and Triton X-100 had similar remediation yields (24.0 and 22.5% respectively, *i.e.* $S_{rn}=0.083$ and 0.085). Tween 80 had a nearly nil remediation yield ($S_{rn}=0.11$).

Concerning 0.1 mm GB, the best remediation yield was with SDBS (46.3% *i.e.* $S_{rn}=0.068$). Here Aerosol MA-80 performed better than Triton X-100: the remediation yields were respectively 35.56 and 38.1% ($S_{rn}=0.082$ et 0.078). Tween 80 had a remediation yield of 7.0% ($S_{rn}=0.118$).

The remediation yields were higher than those observed with the 0.5 mm GB. This is because the capillary forces are higher for 0.1 mm GB and the effect of the surfactants, whose purpose is to reduce the IFT, is improved.

The SSE are low ($SSE < 0.0032$), which demonstrates that the VGM model can be used to describe the experimental results. This data are integrated into the two-phase model (see sections 5 and 6).

In both cases (0.5 and 0.1 mm GB), the drainage curves with and without surfactant were very similar, which demonstrates that the experiments were reproducible. At the end of drainage, adding surfactant influences the slope of the line, which is slightly more horizontal, which demonstrates that the capillary effects and therefore the capillary fringes were lower (Figure 115).



D1: drainage 1; I1: imbibition 1; WS: with surfactant (SDBS); MBR: without surfactant; VG: VGM value; Exp: experimental value

Figure 115: Comparison of P_c - S_w curves for a) 0.5mm GB and b) 0.1 mm GB with and without SDBS (with VGM fitting)

As demonstrated by Shen *et al.* (2010), the addition of surfactant influences the interfacial tensions, the P_c - S_w curves and therefore the relative permeabilities [Shen *et al.* (2010)].

Figure 116 shows how SDBS affects S_n as a function of h_c .

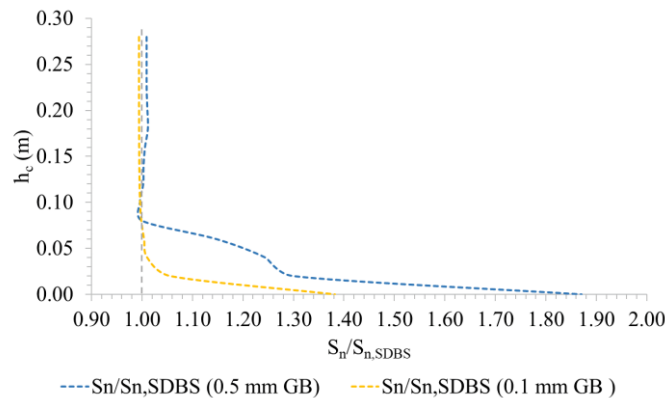


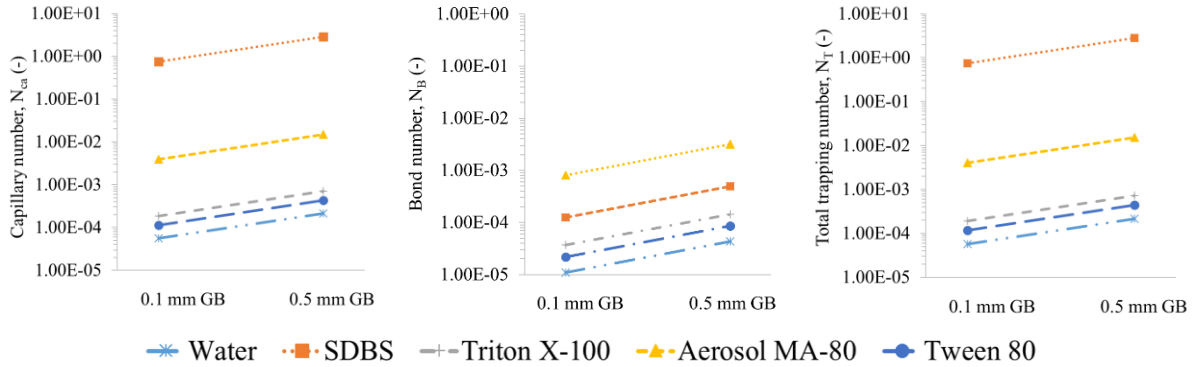
Figure 116: $S_n/S_{n,SDBS}$ as a function of h_c for 0.5 and 0.1 mm GB – VGM fitting

The $S_n/S_{n,SDBS}$ ratios close to 1 (but not equal to 1) for high h_c are related to the fact that the averages of S_{rw} were slightly different for experiments with and without surfactants. This minimal difference must not obscure the lower sections of the curves, from which we can learn much. We see the effect of the surfactant from the two-thirds of the imbibition ($h_c = 0.08$ m) for the 0.1 mm GB whereas we can only see it later for the 0.5 mm GB. We also see that the effect of surfactants is much more pronounced for 0.1 mm GB for the rest of the imbibition

whereas it is moderate for the 0.5 mm GB and becomes truly visible at the end of the ($h_c=0.03$ mm).

a) Dimensional numbers

Capillary number (N_{ca}), Bond number (N_B), and Total trapping number (N_T) were calculated using Eq. 86 tot Eq. 88 on the bases of experimental data and rheological data (Figure 117).



a) Capillary number, N_{ca} b) Bond number, N_B c) Total trapping number, N_T
 Figure 117: Comparison of a) Capillary number (N_{ca}), b) Bond number (N_B), and c) Total trapping number (N_T) for 0.5 and 0.1 mm GB

As expected, increasing the grain size, increases all three numbers. N_T depends on about 80% N_{ca} . The viscosity forces therefore predominated over gravitational forces. Globally, the capillary forces predominated over other forces. Adding surfactants increases N_{ca} and consequently N_T . Increasing N_{ca} decreases the residual saturations [Lake (1989); Pennell *et al.* (1996); Sheng (2015)].

Figure 32 connects S_m (from PCE) to N_T (See section 2.4.4). During experiments that produced this figure, Pennell *et al.* (1996) observed that in 1D columns, when the value of N_T is less than $\sim 2 \times 10^{-5}$, entrapped residual DNAPL was not expected to be mobilized, while partial or complete mobilization was expected when the value exceeded 1×10^{-4} [Pennell *et al.* (1996)]. In our case, N_T systematically exceeded 1×10^{-4} . With the addition of a surfactant, N_T was significantly higher, meaning that the mobilization of residual DNAPL is even more favored.

Figure 118 illustrates the variations in S_m as a function of N_T . Therefore we are on the right of the curve shown for PCE by Pennell *et al.* (1996). Beyond a certain point the residual saturation does not fall any more (apart from with solubilization). The results of our experiments show that for N_T values greater than 10^{-3} , the S_m hardly decreases any more (even if the correlations are not very good relative to a logarithmic relationship: $R^2 = 0.556$ and 0.565 , respectively for 0.5 and 0.1 mm GB).

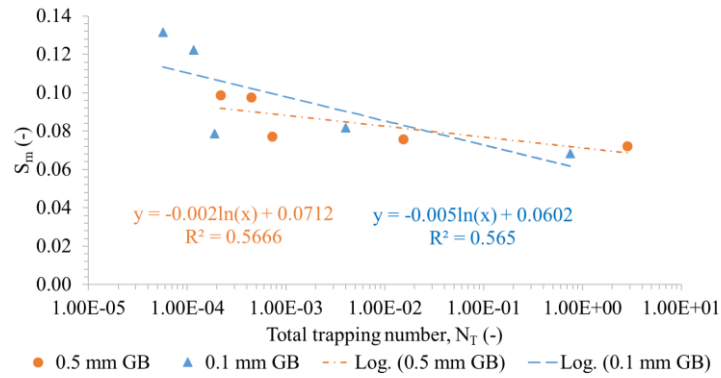
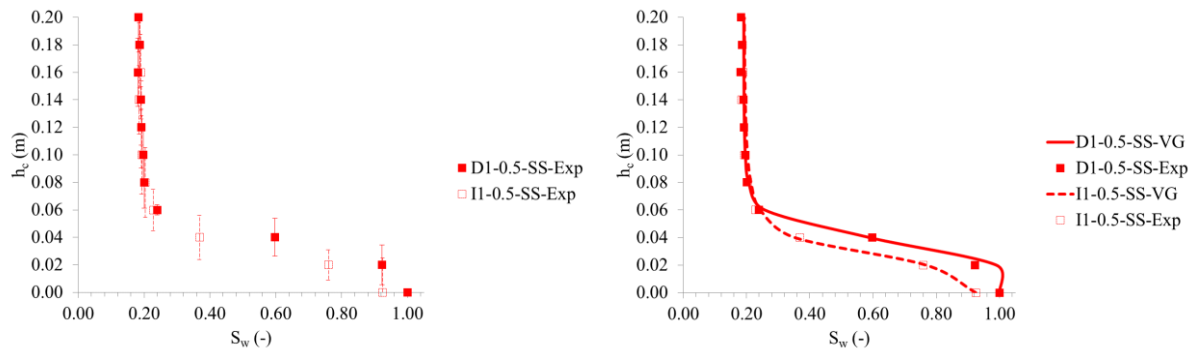


Figure 118: S_m as a function of N_T

b) Addition of surfactants from start of drainage 1

Experiments were conducted by adding the surfactant as the start of drainage 1. These experiments have not been studied systematically by permittivity and resistivity. Figure 119 and Figure 120 show the experimental results on 0.1 and 0.5 mm GB with SDBS (at the CMC) added from the start of drainage 1 (these experiments were conducted in triplicate).

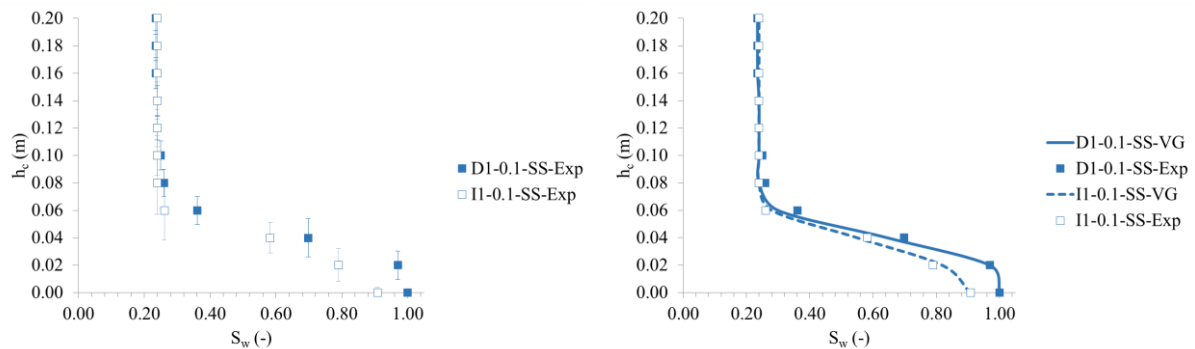


D1: drainage 1; I1: imbibition 1; SS: with surfactant (SDBS) at the beginning of drainage 1; Exp.: experimental value; VG: VGM value

a) Corrected values

b) VGM fitting

Figure 119: P_c - S_w curves for 0.5 mm GB with SDBS addition at the beginning of drainage 1 (a) corrected values and b) VGM fitting)



D1: drainage 1; I1: imbibition 1; SS: with surfactant (SDBS) at the beginning of drainage 1; Exp.: experimental value; VG: VGM value

a) Corrected values

b) VGM fitting

Figure 120: P_c - S_w curves for 0.1 mm GB with SDBS addition at the beginning of drainage 1 (a) corrected values and b) VGM fitting)

We see that threshold entry pressures, h_c , were much lower when we started the drainage by adding SDBS: they were estimated experimentally at 20 mm maximum for 0.5 mm GB and at 2 mm for 0.1 mm GB. As a reminder, they were estimated experimentally at 12 and 60 mm respectively with 0.5 and 0.1 mm GB (see section 4.2.3.1-Table 41).

The slopes of the intermediate parts of the curves were flatter during drainage 1 for the 0.5 mm GB but especially for the 0.1 mm GB if we injected SDBS from the start of drainage 1. This is explained by lower capillary effects.

The S_{rw} were also much lower: for the 0.5 mm GB (0.192 ± 0.030 with SDBS as soon as drainage 1 starts versus 0.248 ± 0.0019 without SDBS in drainage 1) and, for the 0.1 mm GB (0.239 ± 0.0018 with SDBS from the start of drainage 1 versus 0.309 ± 0.0129 without SDBS in drainage 1).

Regarding the S_m for the 0.5 mm GB, there was no notable change when we added the SDBS before or after drainage 1 (respectively 0.075 ± 0.015 and 0.079 ± 0.013). However for the 0.1 mm GB, the S_m were respectively 0.068 ± 0.014 (for the addition of SDBS at the end of drainage 1) and 0.092 ± 0.0039 (for the addition of SDBS at the start of drainage 1). Therefore, the surfactant was less effective if it is added from the start. This is presumably due to the fact that more DNAPL was incorporated in small pores during imbibition and that it is then more difficult to displace.

c) Entry pressure calculation

We calculated entry pressures for the different surfactants on the basis of Eq. 196 (Table 44).

Table 44: Calculated entry pressure without enhancement and with chemical enhancement

Enhancement	Glass beads	Entry Pressure (Pa)	h_c (mm)
Without surfactant	0.1 mm GB	473.91	73.11
	0.5 mm GB	94.78	14.62
SDBS	0.1 mm GB	23.81	3.67
	0.5 mm GB	4.76	0.73
Aerosol MA-80	0.1 mm GB	140.94	21.74
	0.5 mm GB	28.19	4.35
Triton X-100	0.1 mm GB	131.73	20.32
	0.5 mm GB	26.35	4.06
Tween 80	0.1 mm GB	269.15	41.52
	0.5 mm GB	53.83	8.30

The threshold entry pressure reductions generated by the addition of surfactants are indeed important. Accordingly, the percentage reductions are: 95% (SDBS), 70% (Aerosol MA-80), 72% (Triton X-100) et 43% (Tween 80).

4.2.4.2 Permittivity monitoring

Experiments with chemical enhancement were also monitored with TDR probes (Also see Appendix 3.2). First, we determined whether adding surfactant had an effect on permittivity measurements.

Estimation of the influence of surfactants on permittivity measurements

A specific experiment was conducted with a 1D cell with the following successive drainages:

- Water without GB,
- 0.5 mm GB + water,
- 0.5 mm GB + SDBS (CMC) and water wash,
- 0.5 mm GB + Aerosol MA-80 (CMC) and tap water wash,
- 0.5 mm GB + Triton X-100 (CMC) and tap water wash,
- 0.5 mm GB + Tween 80 (CMC) and tap water wash.

The results of these experiments are shown in Figure 121 and Figure 122.

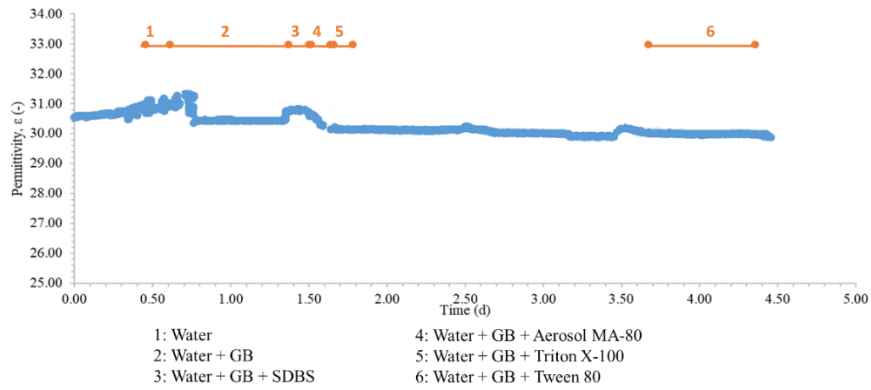


Figure 121: Permittivity measurements during drainages with water and the four surfactants

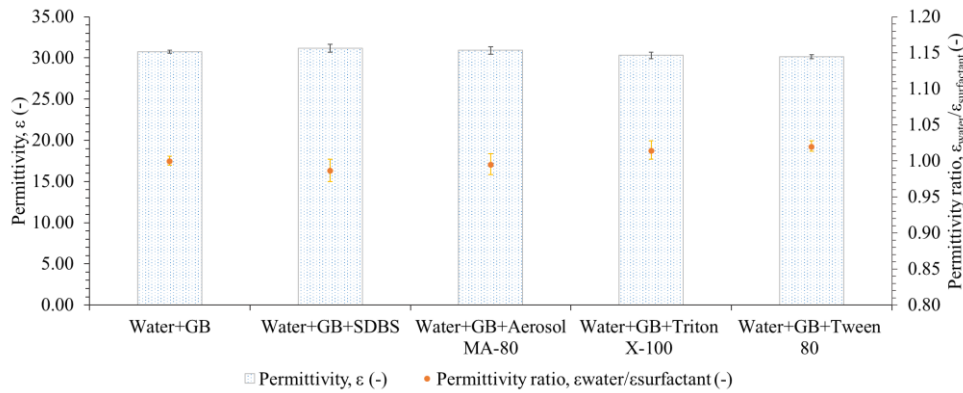


Figure 122: Impact of surfactants on permittivity measurements

Relative to the response considered as the white test (water + GB), the mean permittivities measured were respectively impacted by +1.4% (SDBS), +0.5% (Aerosol MA-80), -1.6% (Triton X-100), -2.1% (Tween 80). We found that the permittivity was slightly increased for nonionic surfactants and slightly decreased for anionic surfactants. The deviation can therefore be considered as negligible.

Drainage–imbibition experiments with permittivity monitoring

Regarding the 0.5 mm GB, in total, five experiments were conducted with SDBS, three with Aerosol MA-80, three with Triton X-100, two with Tween 80. As for 0.1 mm GB, four experiments were conducted with SDBS, three with Aerosol MA-80, three with Triton X-100, two with Tween 80 (Also see Appendix 3.1).

Figure 123 shows the averages of S_{rn} with permittivity averages corresponding to the experiments with and without surfactants (with the 0.1 and 0.5 mm GB). We only took the experiments that were followed with TDR probes.

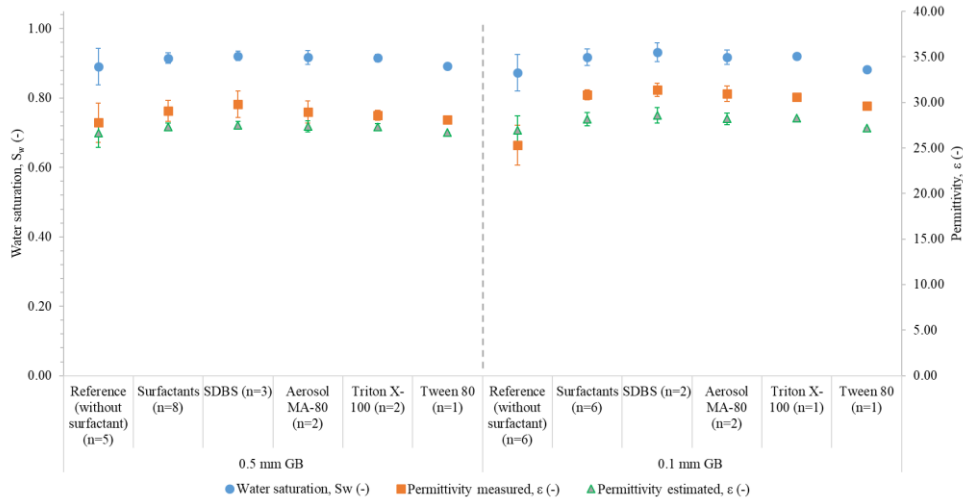
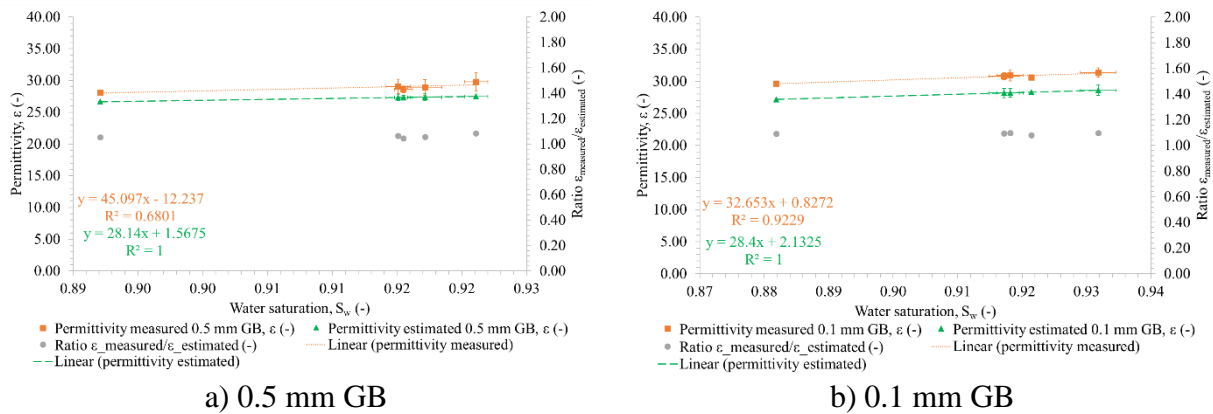


Figure 123: Water saturation and permittivity (measured and estimated) at the end of imbibition 1 for 0.5 and 0.1 mm GB in 1D cells (with and without chemical enhancement)

Even though the standard deviations sometimes overlap, we see that from the permittivity measurements we can clearly discern the trends for the recovery yields given above. Accordingly, the average permittivities for 0.5 and 0.1 mm GB without surfactants were respectively 27.77 and 25.32 (for S_w at the end of imbibition of 0.89 and 0.87). With the surfactants, the average permittivities for 0.5 mm GB and 0.1 mm GB were respectively 29.07 and 30.81 (for S_w at the end of imbibition of 0.915 and 0.917). We can also clearly distinguish the permittivities variations that match the different remediation yields as a function of the surfactants: for the 0.5 mm GB, the final permittivities, in increasing order: $\rho_{c,SDBS} > \rho_{c,Aerosol MA-80} > \rho_{c,Triton X-100} > \rho_{c,Tween 80}$.

We also see that the estimations with the CRIM model under-estimate the residual saturations in the presence of surfactants (which is not the case in the absence of surfactants). Figure 124 displays this overestimation very clearly.



a) 0.5 mm GB

b) 0.1 mm GB

Figure 124: Differences between the measured permittivities and those estimated as a function of saturation during chemical enhancement with a) 0.5 and b) 0.1 mm GB

Figure 124 only takes into account the experiments conducted with chemical enhancement. We see that the lower the residual saturation (therefore the higher the S_w) the greater the difference between measured and permittivities estimated. This increase is slight: the slope of the $S_w=f(\epsilon_{\text{measured}}/\epsilon_{\text{estimated}})$ line is almost horizontal (grey points in above figures). That means that the error value is constant. The averages of the overestimation ratios are 1.06 ± 0.02 (for the 0.5 mm GB) and 1.09 ± 0.01 (for the 0.1 mm GB).

It is therefore possible to estimate the S_m with TDR probes by applying the CRIM model and to compare remediation rate and yield between the different surfactants.

4.2.4.3 Electrical resistivity monitoring

Experiments with chemical enhancement were also monitored with resistivity (Also see Appendix 3.2). We will determine first whether adding surfactant has any influence on resistivity measurements.

Estimation of the influence of surfactants on resistivity measurements

The experiments mentioned in chapter 4.2.4.2 were also monitored for resistivity (Figure 125).

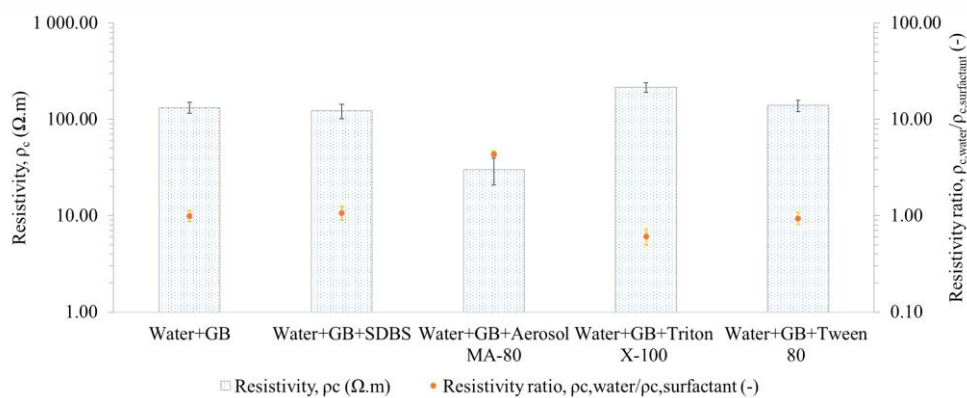


Figure 125: Impact of surfactants on resistivity measurements

The experiments show that adding surfactants generated a greater impact on resistivity measurements than on permittivity measurements. Therefore, for mean reference values of $132 \pm 17 \Omega.m$, the mean values measured for nonionic surfactants were respectively $123 \pm 21 \Omega.m$ for SDBS and $30 \pm 9 \Omega.m$ for Aerosol MA-80 (*i.e.* a factor of 0.92 and 0.22). Conversely, adding anionic surfactants increased resistivity: $216 \pm 25 \Omega.m$ for Triton X-100 and $140 \pm 19 \Omega.m$ for Tween 80, *i.e.* respective increases of a factor of 1.62 and 1.05.

These relative deviations were only moderate though, in comparison with the resistivity of the DNAPL and glass beads ($\rho_{c,DNAPL} = 2730063$ and $3413632 \Omega.m$ respectively for 0.5 and 0.1 mm GB) and also high sensitivity and low precision of the geophysical measurements in very low frequency. These deviations can therefore be considered as being negligible.

Monitoring drainage–imbibition experiments with resistivity monitoring

Figure 126 shows the averages of S_m with resistivity averages corresponding to the experiments with and without surfactants (with the 0.1 and 0.5 mm GB). We only took into account the experiments that were followed by geophysics.

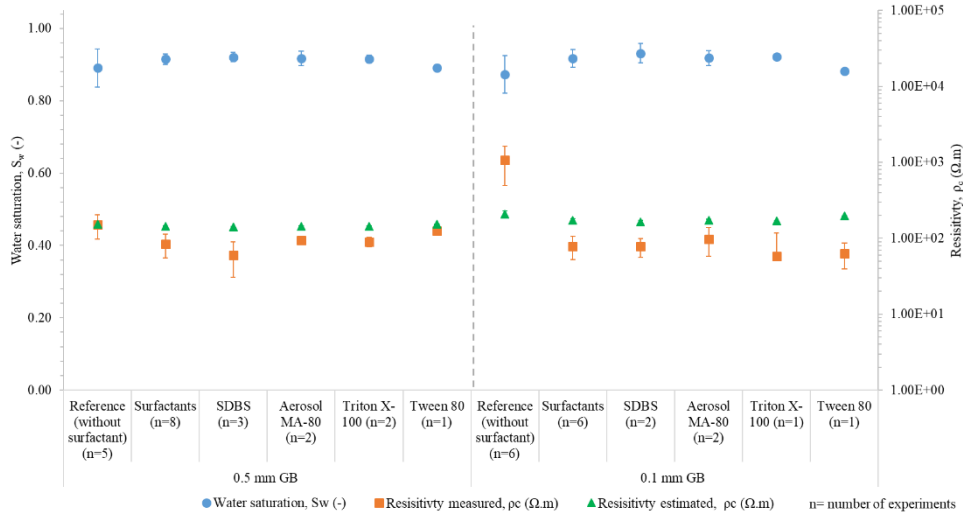


Figure 126: Water saturation and resistivity (measured and estimated) at the end of imbibition 1 for 0.5 and 0.1 mm GB in 1D cells (with and without chemical enhancement)

We see that the residual saturations can be approached by the resistivity measurements. The correlations are less clear than with the permittivities. Reduction trends for S_{rn} can be seen from the resistivity measurements. Therefore, for example, for the 0.5 mm GB, the resistivities at the end of the imbibition with and without surfactant are respectively 150 and 84 $\Omega.m$ (for S_{rn} of 0.109 and 0.085). For 0.1 mm GB, the differences are greater: 1061 $\Omega.m$ (without surfactants with $S_{rn}=0.131$) vs. 79 $\Omega.m$ (with surfactant with $S_{rn}=0.082$). The standard deviation is quite high for imbibition without surfactant.

The differences between the values estimated with Archie’s Law and the resistivities measured are substantial. At the end of the imbibition, the estimated values are always greater than the measured values apart from for the reference (without surfactant) for the 0.1 mm GB. Figure 127 shows the ratios for estimations and resistivity measurements.

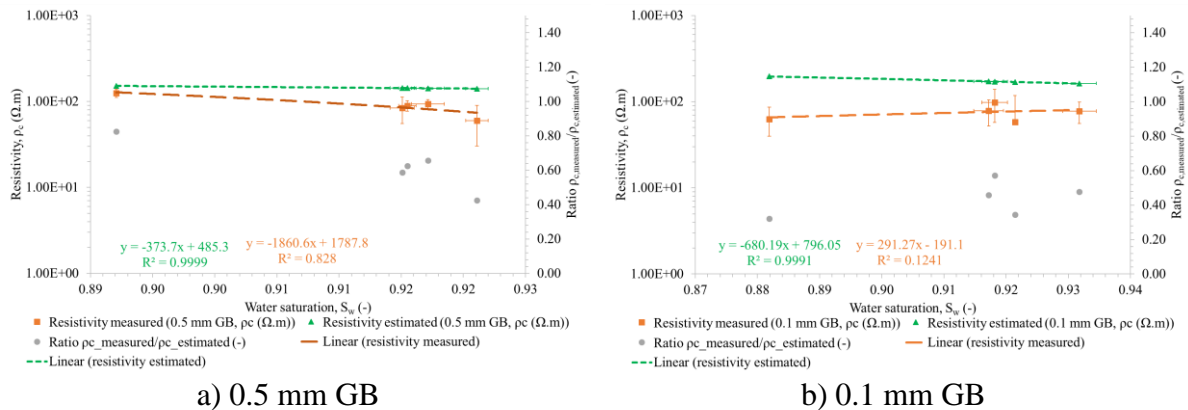


Figure 127: Differences between the measured resistivities and those estimated during chemical enhancement with a) 0.5 and b) 0.1 mm GB

The $\rho_{c,measured}/\rho_{c,estimated}$ ratios are on average 0.63 ± 0.16 for the 0.5 mm GB and 0.43 ± 0.12 for the 0.1 mm GB. This shows two opposite trends, for increasing S_w ; the ratios fall for the 0.5 mm GB and rise for the 0.1 mm GB. This can be related to the high data standard deviations.

This shows that we can estimate S_m from electrical resistivity monitoring. Archie's Law gives us a semi-quantitative approach to the experiments.

4.2.4.4 Optical density monitoring

Drainage-imbibition experiments were conducted with optical density monitoring.

Estimation of the influence of surfactants on optical density measurements

Experiments with and without surfactant were conducted in the flat Hele-Shaw cell. The variations in OD measured by replacing water with surfactants (at their CMC) were less than 0.05%. These variations are therefore considered as being insignificant.

Drainage-imbibition experiments with optical density monitoring

Drainage-imbibition experiments were conducted in the flat cell with SDBS to check whether the results acquired with the 1D cells were confirmed. Figure 128 shows the results of an experiment with 0.1 mm GB.

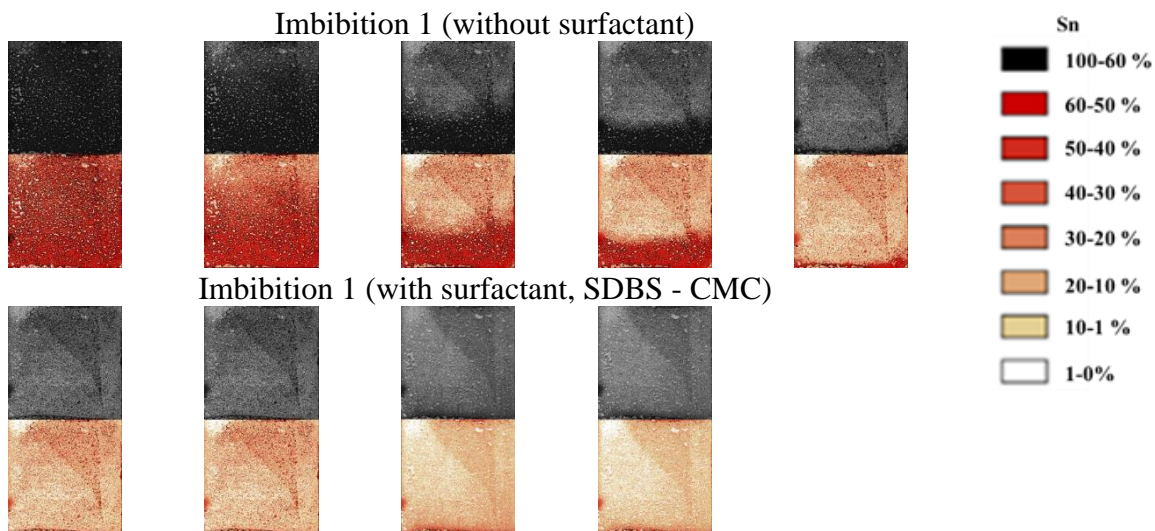


Figure 128: Imbibition experiments with Optical Density monitoring in the flat cell (0.1 mm GB) with and without surfactant (SDBS - CMC)

The experimental images for the drainage-imbibition experiments with SDBS were interpreted using the procedures described in sections 4.1.4.2 and 4.1.4.3.

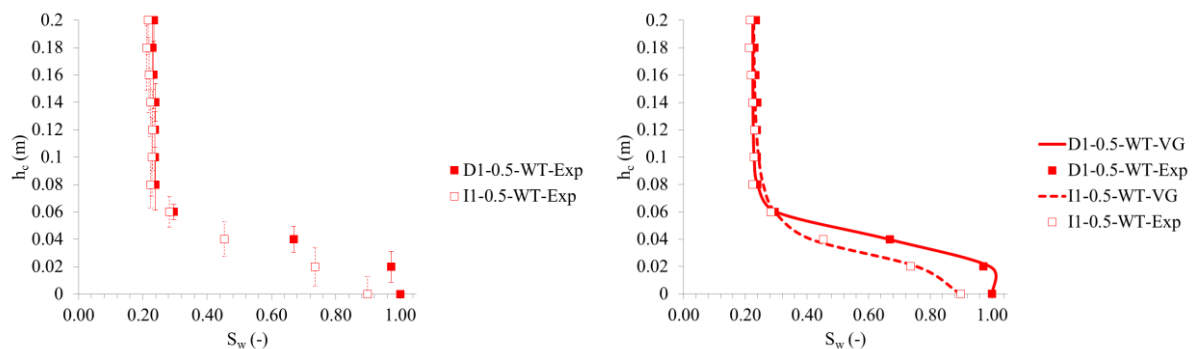
The three experiments with 0.5 and 0.1 mm GB reduced the respective S_m by $26.36 \pm 2.4\%$ and $44.72 \pm 2.3\%$. These results demonstrate that OD monitoring is reproducible and reliable.

4.2.5 Capillary pressure-water saturation curves for 0.5 and 0.1 mm glass beads with thermal enhancement

4.2.5.1 Comparison of P_c - S_w curves for 0.1 mm and 0.5 mm glass beads with thermal enhancement

Heating at 50 °C was carried out at the end of drainage 1 in order to start with the same S_{rw} as for the experiments without enhancement. Drainage-imbibition experiments with 0.5 mm GB

and 0.1 mm GB were done in triplicate. Only two experiments out of three were also monitored for permittivity and conductivity. Figure 129 and *Figure 130* show the average of the P_c - S_w curves for 0.5 mm GB and 0.1 mm GB with thermal enhancement.

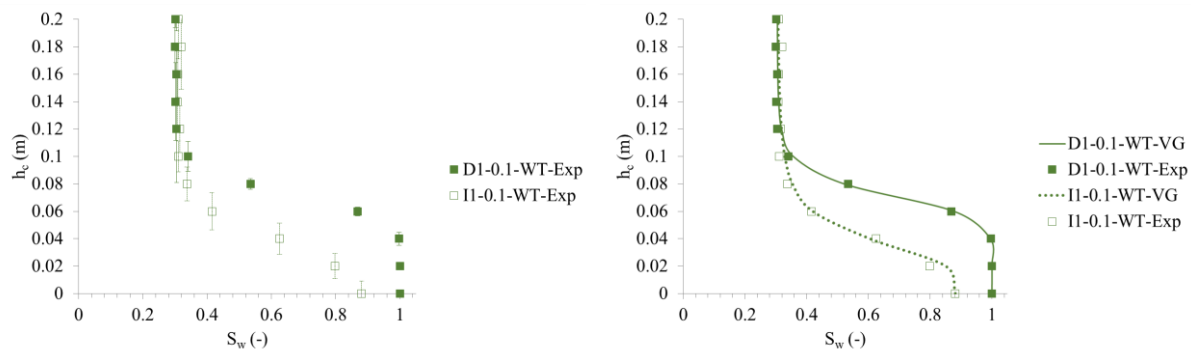


D1: drainage 1; I1: imbibition 1; WT: thermal enhancement; VG: VGM value; Exp: experimental value

a) Corrected values

b) VGM fitting

Figure 129: P_c - S_w curves for 0.5 mm GB with thermal enhancement (a) corrected values and b) VGM fitting)



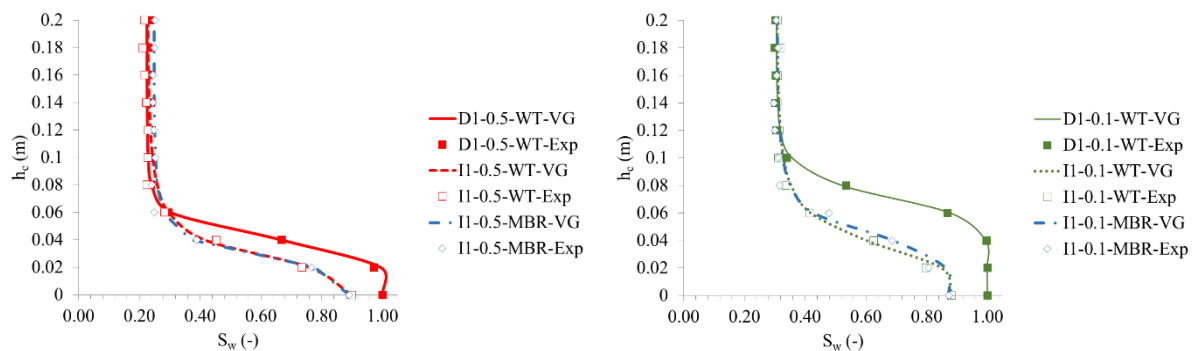
D1: drainage 1; I1: imbibition 1; WT: thermal enhancement; VG: VGM value; Exp: experimental value

a) Corrected values

b) VGM fitting

Figure 130: P_c - S_w curves for 0.1 mm GB with thermal enhancement (a) corrected values and b) VGM fitting)

Figure 131 compares the experiments with and without thermal enhancement (from imbibition 1).



D1: drainage 1; I1: imbibition 1; WT: thermal enhancement; MBR: without surfactant; VG: VGM value; Exp: experimental value

a) 0.5 mm GB

b) 0.1 mm GB

Figure 131: Comparison of P_c - S_w curves for a) 0.5 mm GB and b) 0.1 mm GB with and without thermal enhancement (with VGM fitting)

We see that the two curves for imbibition 1 are superimposed for 0.5 mm GB. Therefore, thermal enhancement had no effect on S_m or on the shape of the P_c-S_w curve during imbibition 1. The thermal enhancement only affected the viscosity (see section 3.2.1.1).

We see that the curves for imbibition 1 with 0.1 mm GB with and without thermal enhancement are very similar. But starting from $h_c < 0.04$ m we see a slightly higher quantity of DNAPL extracted (for constant h_c). This is still negligible ($< 5\%$). In addition, we see a slight reduction in S_m with thermal enhancement (0.123 vs. 0.127); this drop can be considered as being negligible. Table 45 shows the results of these experiments (average) and the VGM fitting parameters.

Table 45: Results of drainage-imbibition experiments for 0.5 and 0.1 mm GB with thermal enhancement (average)

Parameters	0.5 mm GB		0.1 mm GB	
	Drainage 1 (D1)	Imbibition 1 (I1)	Drainage 1 (D1)	Imbibition 1 (I1)
α (m^{-1})	24.76	38.31	14.10	26.97
n (-)	16.70	4.84	8.40	4.16
SSE	0.0011	0.0047	0.00082	0.00393
S_m (-)	0.000	0.101	0.00	0.123
S_{rw} (-)	0.225	0.225	0.305	0.305

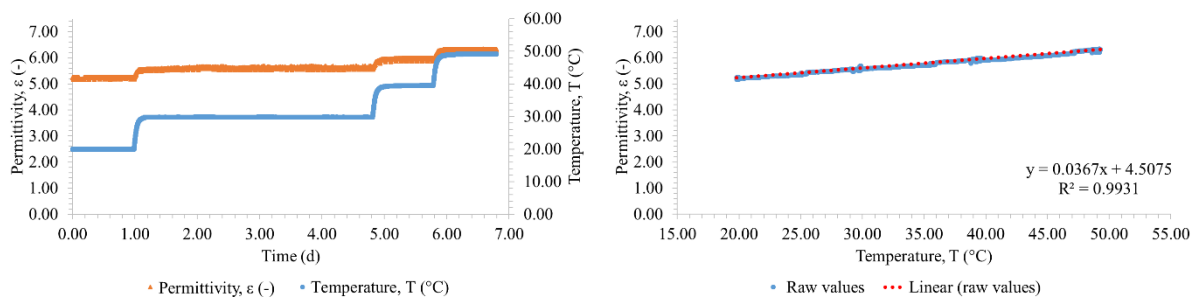
The SSE are low ($SSE < 0.0047$), which demonstrates that the VGM model can be used to describe the experimental results. We see that α and n are close to those calculated without surfactants.

4.2.5.2 Permittivity monitoring

Detailed results of the thermal enhancement experiments are in Appendices 4.1 and 4.2.

Estimation of the influence of temperature on permittivity measurements

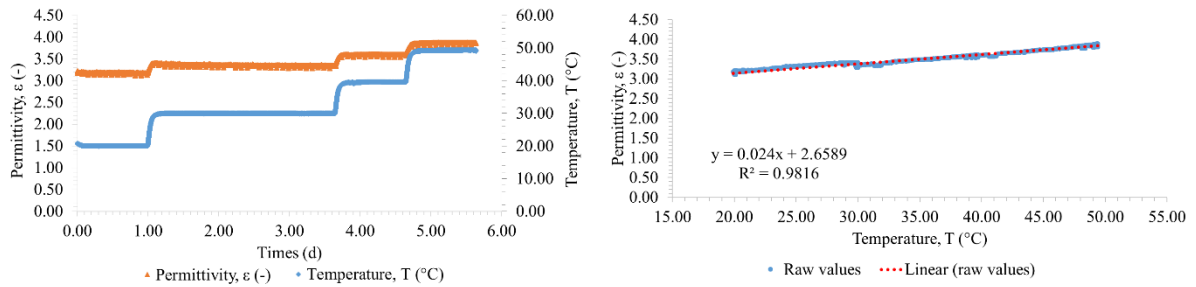
Experiments were conducted to estimate the influence of temperature on measured permittivities. The results for the 1D cell experiments are shown for DNAPL+GB in *Figure 132* and for DNAPL without GB in *Figure 133*.



a) Permittivity and temperature variations as a function of time

b) Permittivity variation as a function of temperature

Figure 132: Permittivity and temperature for DNAPL with 0.5 mm GB: a) permittivity and temperature variations as a function of time and b) permittivity variation as a function of temperature



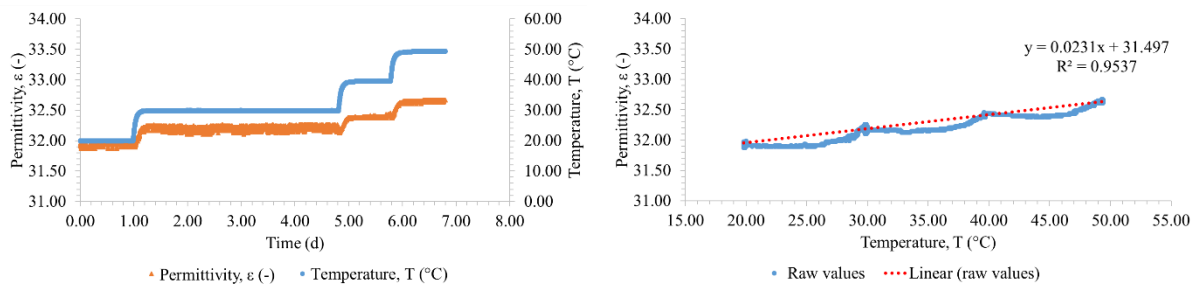
a) Permittivity and temperature variations as a function of time b) Permittivity variation as a function of temperature

Figure 133: Permittivity and temperature for DNAPL without GB: a) permittivity and temperature variations as a function of time and b) permittivity variation as a function of temperature

We see that permittivity measurements were influenced by temperature variations. Increasing the temperature from 20 to 50 °C caused an average permittivity increase for DNAPL with GB of 19.0% (from 5.45 to 6.49) and for DNAPL without GB of 19.0% (from 3.22 to 3.85). A linear relationship predicts the change in permittivity as a function of temperature very well ($R^2 = 0.99$ and 0.98 respectively for DNAPL without GB and DNAPL + GB). The slopes of the two lines are very similar. Variations in $\epsilon_{\text{DNAPL+GB}}$ as a function of temperature, estimated by the slope of lines for *Figure 132*, is $+ 0.03445 \text{ m}^3 \cdot \text{m}^{-3} \cdot \text{°C}^{-1}$.

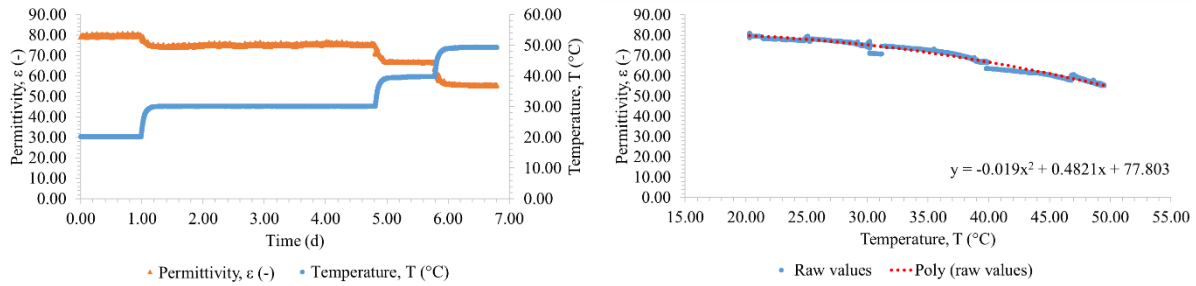
The results from different authors show that the permittivity of light chlorinated solvents falls slightly as temperature rises. A linear relation has also been established for these but with coefficients varying between -0.0034 and $-0.0506 \text{ m}^3 \cdot \text{m}^{-3} \cdot \text{°C}^{-1}$ [Morgan and Lowry (1930); Loon *et al.* (1967); Nath and Narain (1982); Nath (1995); Corradini *et al.* (1996); Ajo-Franklin *et al.* (2006)]. In our case, the DNAPL is essentially composed of a mixture of heavy chlorinated compounds, which may explain this different behavior.

The results for 1D cell experiments are shown for water +GB in *Figure 134* and, for water without GB in *Figure 135*.



a) Permittivity and temperature variations as a function of time b) Permittivity variation as a function of temperature

Figure 134: Permittivity and temperature for water with 0.5 mm GB: a) permittivity and temperature variations as a function of time and b) permittivity variation as a function of temperature



a) Permittivity and temperature variations as a function of time b) Permittivity variation as a function of temperature

Figure 135: Permittivity and temperature for water without GB: a) permittivity and temperature variations as a function of time and b) permittivity variation as a function of temperature

Regarding how permittivity varies for water without GB as a function of temperature, we saw ϵ fall substantially (79.08 to 55.4 for 20 and 50 °C respectively). The trend curve fits a second order polynomial curve. How pure water’s permittivity varies as a function of temperature has been described as follows (Eq. 210) [Weast (1986)]:

$$\epsilon'_{r,w} = 78.54[1 - 4.58 \times 10^{-3}(T - 25) + 1.19 \times 10^{-5}(T - 25)^2 - 2.8 \times 10^{-8}(T - 25)^3] \quad \text{Eq. 210}$$

where:

T: temperature (°C)

On the basis of data obtained with water used in our experiments, we can adapt the parameters in this equation (Eq. 211):

$$\epsilon'_{r,w} = 78.04[1 - 1.05 \times 10^{-2}(T - 25) + 1.19 \times 10^{-5}(T - 25)^2 - 2.8 \times 10^{-8}(T - 25)^3] \quad \text{Eq. 211}$$

Figure 136 compares results with adapted Weast’s formulation and measurements obtained during the experiments.

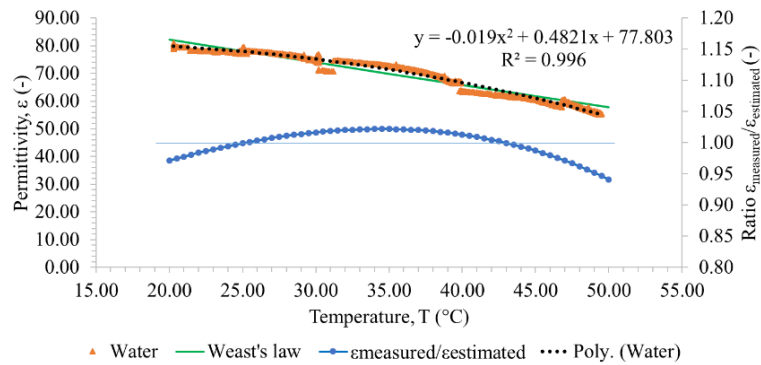


Figure 136: Comparison between the experimental permittivity values and models as a function of time (for water without GB)

The results, compared with adapted Weast’s law, demonstrate that the values we obtained are correct (the differences between the values are less than $\pm 5\%$). This validates our experimental setup and the corresponding experimental protocol. Permittivities for water with GB decrease linearly as temperature rises ($R^2=0.95$), whereas they increase without GB. Several authors have shown that depending on the type of soil or materials used, a water-saturated medium’s permittivity could whether rise or fall in a linear manner within a range of absolute values of

$\Delta\varepsilon/\Delta T$ less than $0.0007 \text{ m}^3 \cdot \text{m}^{-3} \cdot ^\circ\text{C}^{-1}$ (for pure water) [Persson and Berndtsson (1998); Logsdon (2000); Logsdon (2005); Seyfried and Grant (2007)]. The values we obtained with water + GB correspond to the slope of the line in *Figure 134b*, that is to say $0.023 \text{ m}^3 \cdot \text{m}^{-3} \cdot ^\circ\text{C}^{-1}$.

The variations in $\varepsilon_{\text{DNAPL+GB}}$ and $\varepsilon_{\text{water+GB}}$ as a function of temperature have been quantified and will be used as correction factors for the results of the drainage-imbibition experiments with 1D cells, 1D columns and the 2D tank.

Drainage–imbibition experiments with permittivity monitoring

In total, two drainage-imbibition experiments were conducted with the 0.5 mm and 0.1 mm GB. Since the results were similar, it was not necessary to triplicate our experiments (see Appendices 4.1 and 4.2 for full details). *Figure 137* and *Figure 138* show how ε and S_w change as a function of time during the drainage-imbibition experiments with thermal enhancement.

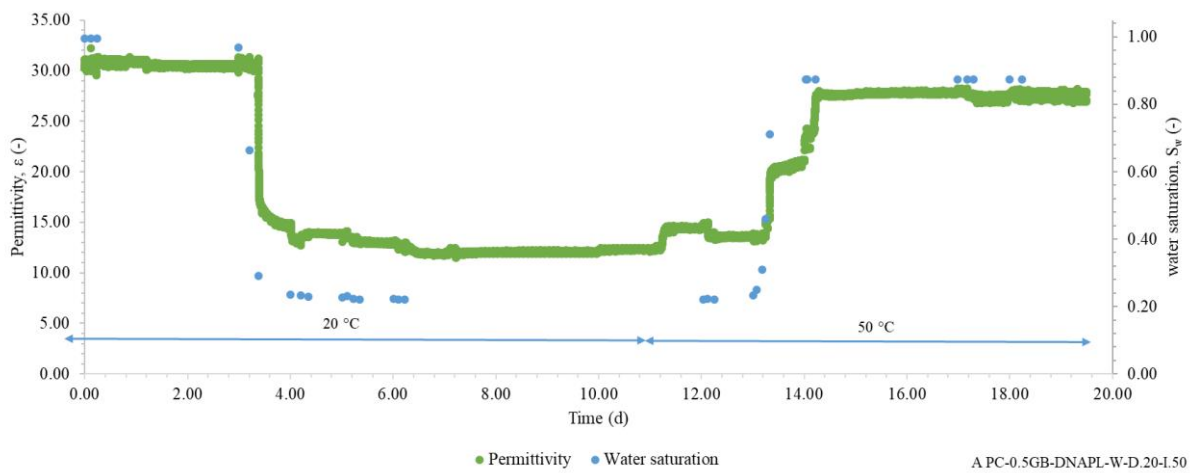


Figure 137: Evolution of water saturation and permittivity as a function of time with thermal enhancement (example of a drainage-imbibition experiment with 0.5 mm GB)

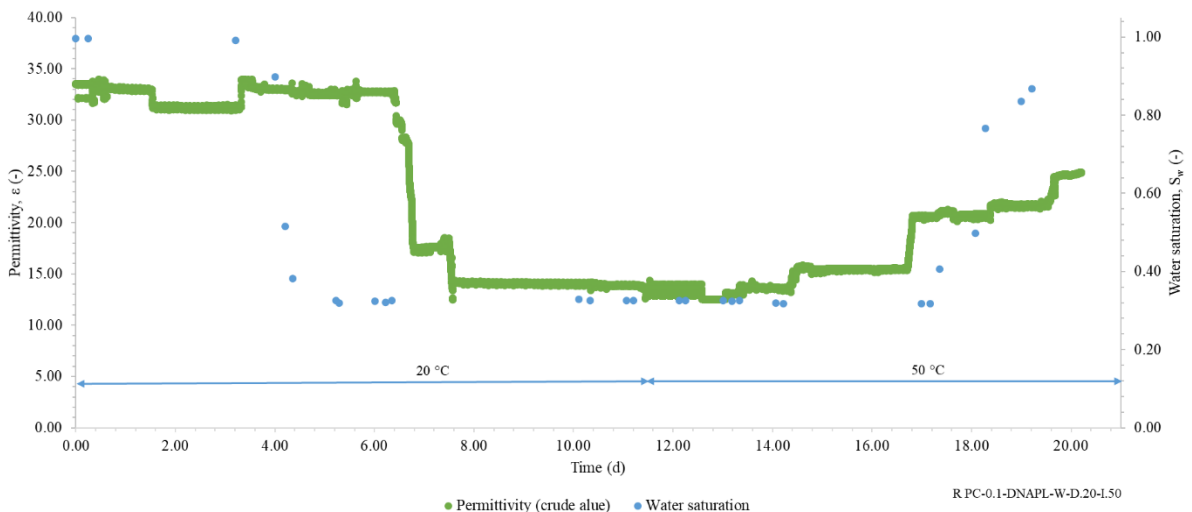


Figure 138: Evolution of water saturation and permittivity as a function of time with thermal enhancement (example of a drainage-imbibition experiment with 0.1 mm GB)

The S_m were only slightly influenced by the thermal enhancement (0.101 vs. 0.109 for 0.5 mm GB and 0.123 vs. 0.127 for 0.1 mm GB). Overall, the slopes of the ε curves during the DNAPL

rise (imbibition) are steeper than without thermal enhancement. This proves a flatter migration front, related to lower viscosity differences (between water and DNAPL). It is difficult to quantify with only having monitored permittivities, but we looked at this in more detail with the 2D tank (see section 6.3.3). Figure 139 illustrates permittivity variations as a function of drainage (at 20 °C) and imbibition (at 50 °C) cycle with thermal enhancement.

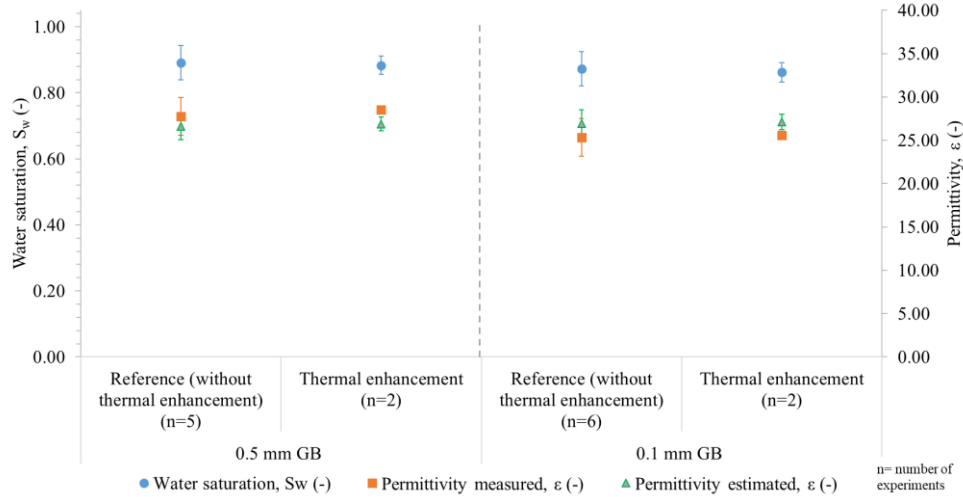


Figure 139: Water saturation and permittivity (measured and estimated) at the end of imbibition 1 for 0.5 and 0.1 mm GB in 1D cells (with and without thermal enhancement)

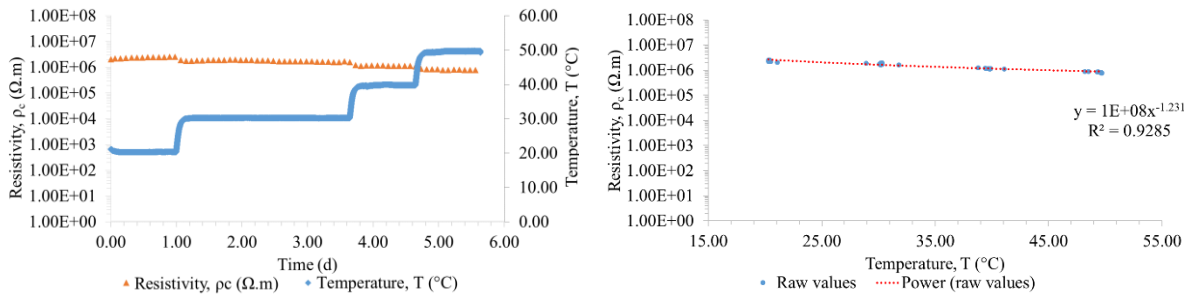
There is a good agreement between predicted and measured permittivity values. We see that $\epsilon_{\text{estimated}}$ (considering value changes related to increasing temperature on ϵ_{water} and ϵ_{DNAPL}) are closed to the measured values.

4.2.5.3 Electrical resistivity monitoring

Detailed results of the thermal enhancement experiments are in Appendices 4.1 and 4.2.

Estimation of the influence of temperature on resistivity measurements

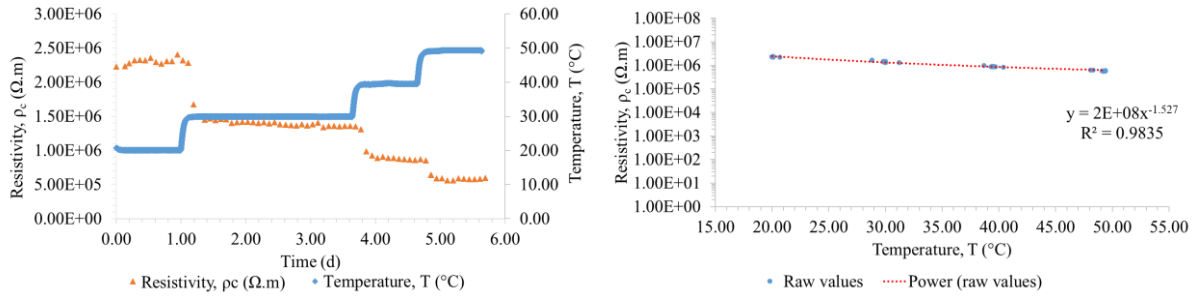
Experiments were conducted to estimate the influence of temperature on measured resistivities. The results for the 1D cell experiments are shown for DNAPL+GB in Figure 140 and for DNAPL without GB in Figure 141.



a) Resistivity and temperature variations as a function of time

b) Resistivity variation as a function of temperature

Figure 140: Resistivity and temperature for DNAPL with 0.5 mm GB: a) resistivity and temperature variations as a function of time and b) resistivity variation as a function of temperature

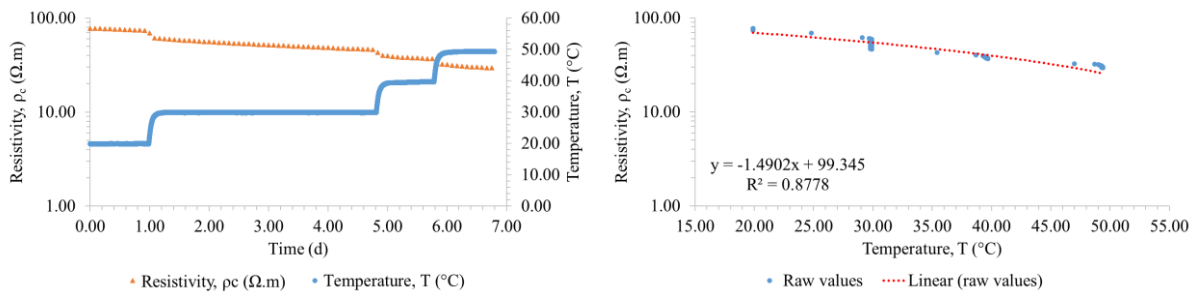


a) Resistivity and temperature variations as a function of time b) Resistivity variation as a function of temperature

Figure 141: Resistivity and temperature for DNAPL without GB: a) resistivity and temperature variations as a function of time and b) resistivity variation as a function of temperature

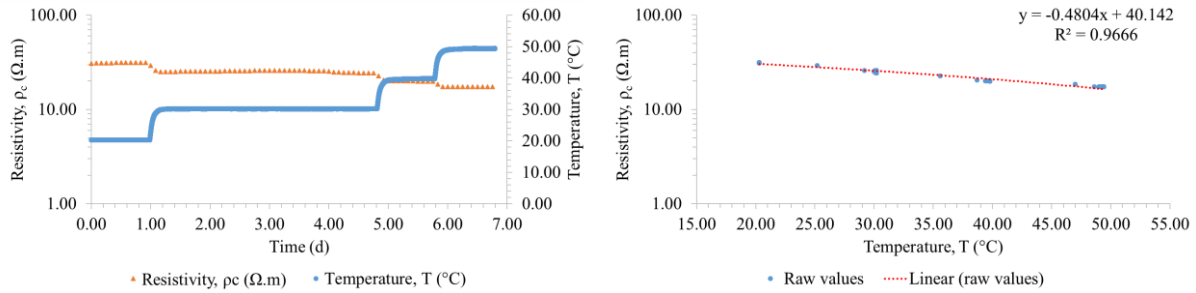
Logically, given the high electrical resistance of the GB, the resistivity values were globally higher with GB than without. The results show that increasing the temperature generated varying resistivity reductions. We also found that the resistivity of DNAPL alone at 50 °C only represented 25.3% of the resistivity at 20 °C (5.88×10^5 vs. $2.32 \times 10^6 \Omega.m$, respectively at 50 and 20 °C). The resistivity of DNAPL+GB at 50 °C was only an average of 30.3% of the value at 20 °C (2.23×10^6 vs. $7.79 \times 10^6 \Omega.m$, respectively at 50 and 20 °C). Given that the temperature hugely influences ionic mobility, and consequently electrical resistivity, the higher variation of resistivity with temperature in without GB case can be explained by increasing the liquid volume in the medium [Dakhnov (1962); Grellier *et al.* (2008)].

The results of resistivity variation with temperature for 1D cell experiments are shown for water+GB case in Figure 142 and for only water case in Figure 143.



a) Resistivity and temperature variations as a function of time b) Resistivity variation as a function of temperature

Figure 142: Resistivity and temperature for water with 0.5 mm GB: a) resistivity and temperature variations as a function of time and b) resistivity variation as a function of temperature



a) Resistivity and temperature variations as a function of time b) Resistivity variation as a function of temperature

Figure 143: Resistivity and temperature for water without GB: a) resistivity and temperature variations as a function of time and b) resistivity variation as a function of temperature

As regards water, the resistivity values were very low compared to those of DNAPL. At 20 $^{\circ}C$, resistivity values were logically higher with GB than without: 76 $\Omega.m$ (water+GB) and 31 $\Omega.m$ (water without GB). We saw less of a drop in resistivity without GB than with GB: the resistivities at 50 $^{\circ}C$ were respectively 17 (*i.e.* 57% of the value at 20 $^{\circ}C$) and of 30 $\Omega.m$ (*i.e.* 40% of the value at 20 $^{\circ}C$).

The decrease in water resistivity according to the temperature increase was due to the increased ionic mobility. This decrease was of the same order of magnitude as that described in the literature [Hayashi (2004); Light *et al.* (2005)]. The larger volume of water in the case of experiments without GB explains the less significant decrease in resistivity.

This change contradicts the DNAPL resistivity results; however, this contradiction can be ignored because the differences in resistivity between DNAPL and water are such that the influence of water's resistivity can be discarded (when DNAPL and water are present as a mixture).

Figure 144 compares $(\rho_{c,0}/\rho_c)-1=f(T-T_0)$ graphs for DNAPL without GB, DNAPL+GB, water+GB and water without GB. The slopes of the lines determine the values of the coefficient α_c for the Dahhnov equation (Eq. 147).

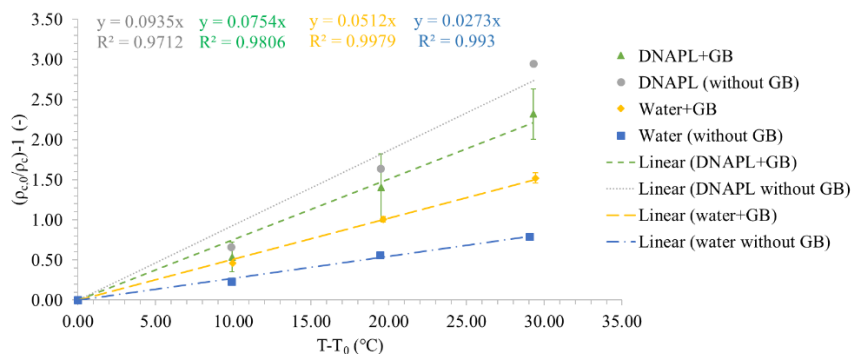


Figure 144: Resistivity variation as a function of temperature for DNAPL without GB, DNAPL+GB, water without GB, water+GB

We see clear linear relations and that the correlation factors are satisfactory ($R^2 < 0.9712$). The values are 0.0935, 0.0754, 0.0512, 0.0273 $\Omega.m.\Omega^{-1}.m^{-1}.^{\circ}C^{-1}$ respectively for DNAPL,

DNAPL+GB, water+GB and water. These values are used to correct the resistivities during thermal enhancement.

Drainage–imbibition experiments with resistivity monitoring

Figure 145 and Figure 146 show how ρ_c and S_w change as a function of time during the drainage-imbibition experiments with thermal enhancement.

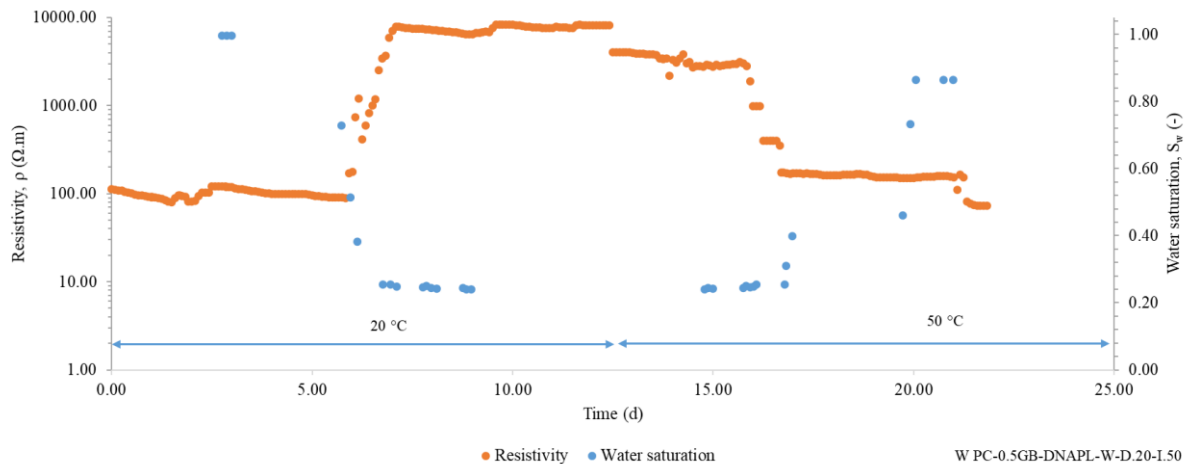


Figure 145: Evolution of water saturation and resistivity as a function of time with thermal enhancement (example of a drainage-imbibition experiment with 0.5 mm GB)

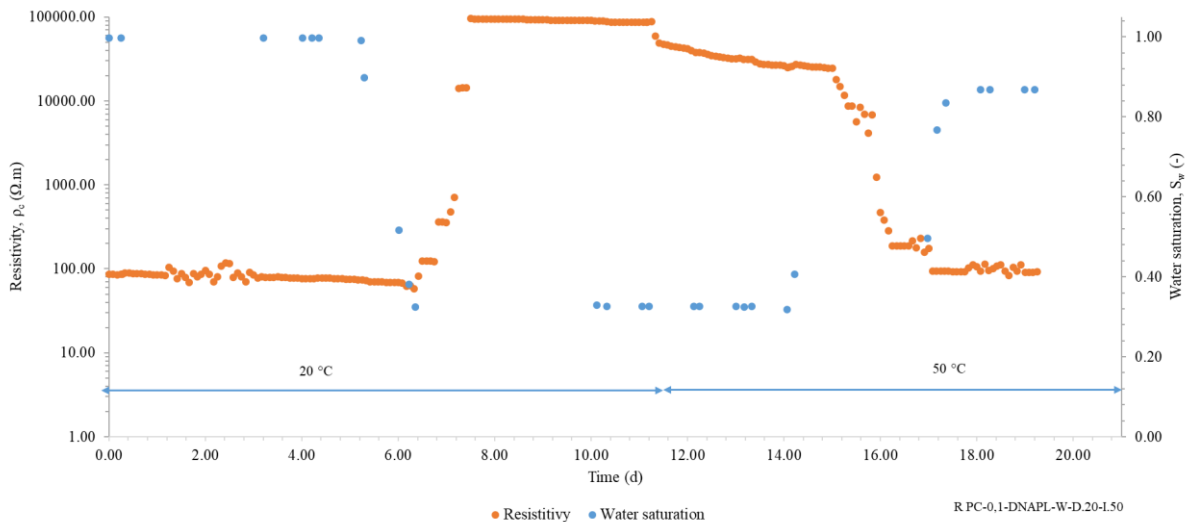


Figure 146: Evolution of water saturation and resistivity as a function of time with thermal enhancement (example of a drainage-imbibition experiment with 0.1 mm GB)

S_m were only slightly influenced by thermal enhancement (see section 4.2.5.1). We did see a substantial difference in the $\rho_{c,measured}$ from the moment when the temperature was increased. Also, from the 12th day (*i.e.* at the end of drainage 1 when the temperature was increased from 20 to 50 °C), the $\rho_{c,measured}$ decreased significantly. This is logical, given the variations observed for $\rho_{c,water}$ and $\rho_{c,DNAPL}$ with temperature increases.

Figure 147 illustrates resistivity variations as a function of drainage (at 20 °C) and imbibition (at 50 °C) cycle with thermal enhancement.

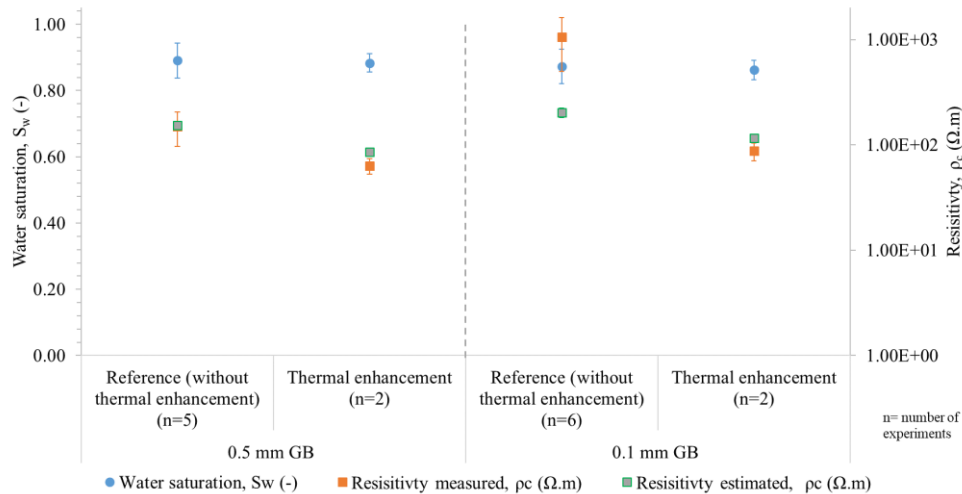


Figure 147: Water saturation and resistivity (measured and estimated) at the end of imbibition 1 for 0.5 and 0.1 mm GB in 1D cells (with and without thermal enhancement)

As we saw, the residual saturations were almost identical with and without thermal enhancement. We did see that $\rho_{c,measured}$ at the end of imbibition 1 were lower than for the thermal enhancement experiments: 63 $\Omega.m$ (vs. 150 $\Omega.m$ without thermal enhancement) for the 0.5 mm GB and 87 $\Omega.m$ (vs. 1061 $\Omega.m$ without thermal enhancement) for the 0.1 mm GB.

Taking the corrected values for $\rho_{c,water}$ and $\rho_{c,DNAPL}$ at 50 °C and taking the S_w that are equivalent to the references (without thermal enhancement) at the end of imbibition 1, the $\rho_{c,estimated}$ were respectively 84 $\Omega.m$ for 0.5 mm GB (vs. 152 $\Omega.m$ at 20 °C) and 112 $\Omega.m$ for 0.1 mm GB (vs. 203 $\Omega.m$ at 20 °C). In theory, the $\rho_{c,measured}$ should therefore reduce by 45% in both cases.

The measured values were therefore lower than those estimated (taking account of the value changes related to the temperature increase for $\rho_{c,water}$ and $\rho_{c,DNAPL}$); a $\rho_{c,measured}/\rho_{c,estimated}$ ratio of 0.74 was observed for the 0.5 mm GB and of 0.76 for the 0.1 mm GB.

4.2.5.4 Optical density monitoring

Drainage-imbibition experiments were performed with thermal enhancement. The flat cell filled with 0.1 and 0.5 mm GB and DNAPL was photographed at 20 and 50 °C. Interpreting the photographs according to the procedures described in sections 4.1.4.2 and 4.1.4.3 shows that the temperature has absolutely no influence on the OD of the DNAPL.

It should be noted that the DNAPL/water interface displacement was faster, which is logical given the viscosity decreases.

4.3 Conclusions

The drainage-imbibition experiments were performed with 0.1 and 0.5 mm glass beads that correspond to hydrogeological properties similar to the Tavaux site.

The experimental data fit well to the van Genuchten-Mualem (VGM) capillary pressure-saturation function. We acquired α and n as well as the residual and irreducible saturations with the aim of comparing the different experiments and using them in multiphase flow modeling (see chapters 5 and 6).

Four different surfactants (*i.e.* SDBS, Aerosol MA-80, Triton X-100 and Tween 80 assayed at their CMC) were tested with the objective of determining which one would generate the best recovery efficiencies. For the 0.5 mm GB, the best remediation yield was obtained with SDBS (27.6% *i.e.* $S_m=0.079$). For the 0.1 mm GB, SDBS also gives the best remediation yield (46.3% *i.e.* $S_m=0.068$).

Experiments with thermal enhancement were also conducted at 50 °C, however, no significant improvement in the remediation yield has been reported.

The drainage-imbibition experiments were monitored by electrical resistivity, permittivity and optical density. The goal was to confirm whether the residual saturations could be estimated indirectly to use these monitoring methods when performing experiments with 1D columns and 2D tank set-up described in chapters 5 and 6, respectively.

Regarding the permittivity measurements, the estimation of residual saturations fits well with the CRIM model in most cases (less than 8% difference between estimations and measurements). For water saturations below 20%, the estimation results are less accurate (the estimated values were overestimated by a factor of 1.14 for 0.5 mm GB and were overestimated by a factor of 0.92 for 0.1 mm GB). The experiments with surfactants and thermal enhancement show that the reductions in residual saturations can also be quantified with permittivity measurements.

Archie's Law was adopted to model resistivity variations as a function of residual saturation variations. The estimated electrical resistivity data correlated less well with the measurements than for permittivity. For the 0.5 mm GB, the average measured resistivity/estimated resistivity ratios were 3.14 at the end of the drainage and 0.99 at the end of the imbibition. For the 0.1 mm GB, these ratios were 12.84 at the end of drainage and 5.22 at the end of imbibition. The monitoring for experiments with surfactants and thermal enhancements shows that the reduction in residual saturations can also be quantified with resistivity.

Regardless of whether permittivity or resistivity measurements were used, we successfully monitored saturation variations and quantified residual saturations considering the correction factors (*i.e.* measured values/estimated values) that were quantified as a function of water saturation.

The optical density experiments show that residual saturations can be estimated accurately ($R^2= 0.98$) even with surfactants and thermal enhancement. The relation OD as a function of S_w demonstrated is linearly correlated.

5. EXPERIMENTS IN 1D COLUMNS

5. EXPERIMENTS IN 1D COLUMNS

The drainage-imbibition experiments were carried out in 1D columns: i. To characterize two-phase flow (and in particular the displacement of the DNAPL-water interface according to the pressures applied); ii. To validate the two-phase flow model; iii. To compare the modeled water saturations with the permittivity and resistivity measurements along the column over time; iv. To assess how chemical and thermal enhancements affect on recovery yields.

5.1 Materials and methods

The experiments were carried out with 0.1 and 0.5 mm GB. The drainage-imbibition experiments were carried out using the same experimental protocol as for the 1D small cells. The experiments were also conducted with a chemical enhancement (SDBS added to the CMC at the end of drainage 1) and a thermal enhancement (temperature increased up to 50 °C at the end of drainage 1). The column characteristics were identical to those described for the 1D cells, with the following differences (Figure 148 and Figure 149):

- height: 25.50 cm,
- 3 TRD probes,
- 6 unpolarizable potential electrodes (electrodes configuration: Wenner-Schlumberger).

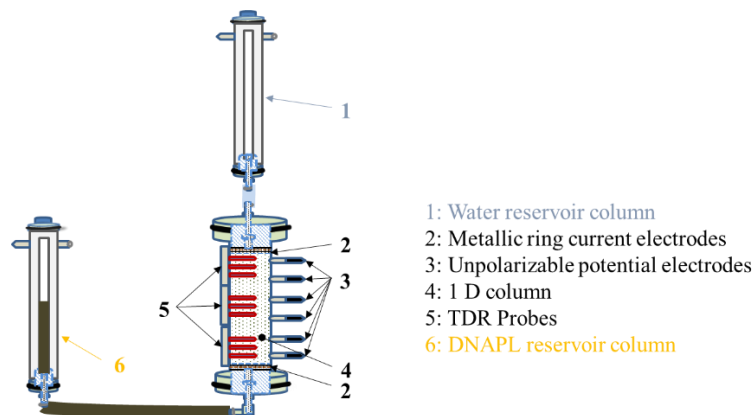


Figure 148: Experimental 1D column set-up

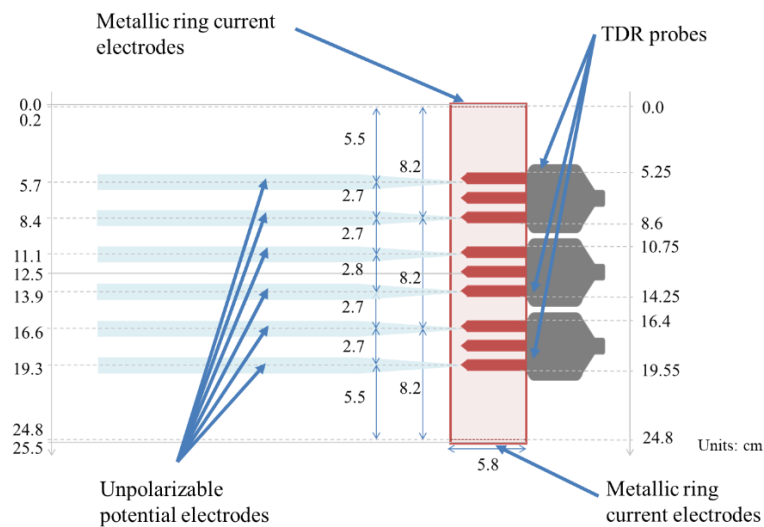


Figure 149: Schematic drawing of 1D column

No experiments were performed with optical densities in the 1D columns. That feature has been incorporated into 2D tank experiments (see chapter 6).

5.2 Numerical and mathematical modeling

The results presented in this chapter only relate to model two-phase flow using Generalized Darcy's law with non-wetting pressure-wetting pressure formulations.

5.2.1 COMSOL Multiphysics®

All equations were solved using COMSOL Multiphysics®. COMSOL Multiphysics® is a numerical simulation tool for 1, 2, and 3-dimensional cases that solves any type of simple or coupled partial differential equations using the finite element method. COMSOL Multiphysics® has the following main characteristics:

- A graphical interface defines the computing environment,
- A modeling process facilitates at all levels: definitions of geometry, mesh, physical optimization of parameters and visualization of results,
- A library of models where the models can be used or modified in many areas of physics (fluid mechanics, electromagnetic, electronics, even deformation of materials, hydraulics, thermal geophysics, or porous media), depending on the modules available in the license used.

Users can choose the appropriate method to solve a problem from an equations database that is already integrated and implemented in COMSOL Multiphysics®. Depending on the equations, it is possible to change geometry, initial and boundary conditions, and type of numerical solver to solve matrix systems. In this study, the predefined single-phase Darcy law in Fluid and Subsurface flow section were used for each phase and modified to include capillary pressure [Davarzani *et al.* (2014)]. The main modeling steps in COMSOL Multiphysics® are as below:

- Define the geometry,
- Choose the suitable physics or equations,
- Select the time dependency of the process (stationary, time dependent, etc.),
- Select the domain geometry characteristics,
- Define the boundary conditions,
- Select suitable domain mesh and time with time step,
- “Study” the process,
- Postprocess the results.

5.2.2 Design of the model

In pressure-pressure formulations, there are two Darcy law equations for wetting (w) and non-wetting (n) phases. Water saturation was estimated by capillary pressure, which was defined by the pressure difference between two phases. The capillary pressure function and relative permeability function used were based on VGM equations. Table 46 shows the equations that form the mathematical model.

Table 46: Equations forming the two-phase flow model with COMSOL Multiphysics®
 (pressure-pressure formulations)

Pressure-pressure formulation	
$C_{sc}\rho_w \left[\frac{\partial P_n}{\partial t} - \frac{\partial P_w}{\partial t} \right] - \nabla \cdot \rho_w [\mathbf{k}_{ij} \lambda_w (\nabla P_w - \rho_w \mathbf{g} \nabla z)] = q_w$	
$-C_{sc}\rho_n \left[\frac{\partial P_n}{\partial t} - \frac{\partial P_w}{\partial t} \right] - \nabla \cdot \rho_n [\mathbf{k}_{ij} \lambda_n (\nabla P_n - \rho_n \mathbf{g} \nabla z)] = q_n$	Eq. 114
$C_{sc} = -\phi \frac{\partial S_w}{\partial P_c}$	
$\lambda_w = \frac{k_{rw}}{\mu_w}$	
$\lambda_n = \frac{k_{rn}}{\mu_n}$	Eq. 112
$P_c(S_w) = P_n - P_w$	Eq. 110
$S_w + S_n = 1$	Eq. 111
Capillary pressure function	
$S_{ew} = \frac{1}{[1 + (\alpha h_c)^n]^m}$	Eq. 61
$S_{ew} = \frac{S_w - S_{rw}}{1 - S_{rw}} = \frac{\theta_w - \theta_{rw}}{\theta_{ws} - \theta_{rw}}$	Eq. 85
$S_w = S_{ew}(1 - S_{rw} - S_{rn}) + S_{rw}$	Eq. 212
Relative permeabilities function (VGM)	
$m = 1 - \frac{1}{n}$	Eq. 62
$k_{rw} = S_{ew}^{0.5} \left[1 - \left(1 - S_{ew}^{\frac{1}{m}} \right)^m \right]^2$	Eq. 63
$k_{rn} = (1 - S_{ew})^{0.5} \left(1 - S_{ew}^{\frac{1}{m}} \right)^{2m}$	Eq. 64

The experimental results considered for the modeling were based on:

- the sink and source terms are considered to be equal to zero (no reaction): $q_w = 0$ and $q_n = 0$,
- the drainage-imbibition experiments for 0.5 and 0.1 mm GB (α , n , S_m and S_{rw}): without enhancement (see Table 40, p. 133), with SDBS (see Table 43, p. 154) and with thermal enhancement (see Table 45, p. 165),
- the measured rheological parameters:
 - water and DNAPL dynamic viscosity (see Figure 49, p. 100),
 - water and DNAPL density (see Figure 58, p. 109).

5.2.3 Initial values and boundary conditions

After drawing the column geometry, selecting the equations and defining the variables, the next step was to choose the same initial and boundary conditions as in 1D column experiments. The geometry used in the simulation is drawn directly into the COMSOL Multiphysics® software with the same scale as in the 1D column experiment. The most important factor in explaining flow is to represent the experiment as accurately as possible. This is dependent on the boundary conditions.

A screen shot of the geometry and meshes of the 1D column is shown in Figure 150. The number of meshes was adapted in a way that there were no changes in results (8908 triangular meshes).

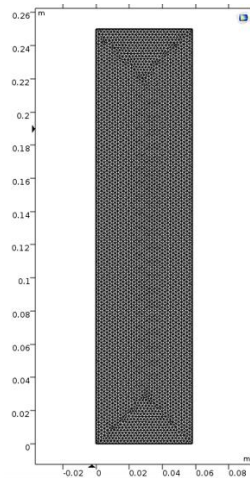


Figure 150: Geometry and meshing of 1D column

5.2.3.1 Initial values

The initial condition is the system state at the beginning of a time dependent solution. This means the value of the variable is assumed to be known at any point of the system at the initial time ($t=0$).

The initial conditions are set from the height of DNAPL, h_{pn} (m), and the height of water, h_{pw} (m), from the filter at the bottom of the 1D column. The initial conditions vary according to whether one models drainage or imbibition process:

- Drainage: $P_w = \rho_w g h_{pw}$ and $P_n = 0$ with $h_{pw} = 0.379$ m
- Imbibition: $P_w = 0$ and $P_n = \rho_n g h_{pn}$ with $h_{pn} = 0.23$ m

5.2.3.2 Boundary conditions

Figure 151 shows the boundary conditions for drainage and imbibition in 1D column experiments.

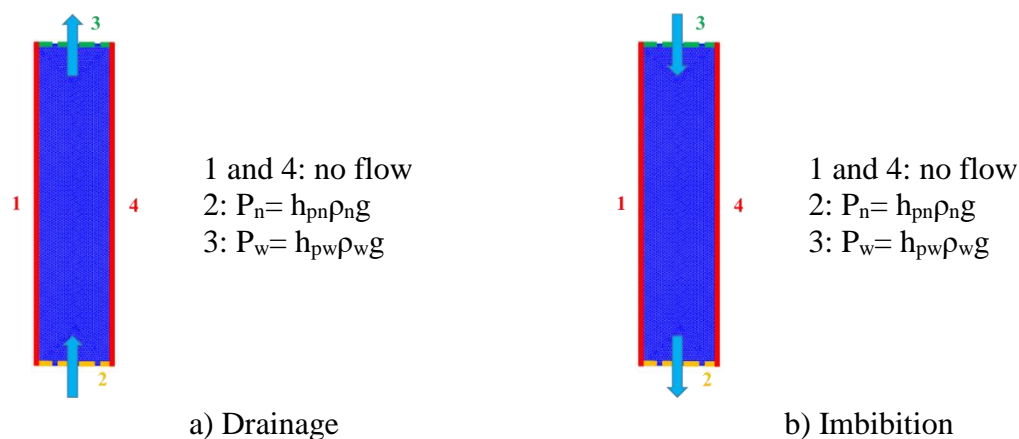


Figure 151: Boundary conditions for drainage and imbibition in 1D column experiments

Pressure head (h_{pn} and h_{pw}) variations depend: i. on height variations in the DNAPL reservoir column; ii. on the height of the DNAPL/air interface in the DNAPL reservoir column; iii. on the height of the water/air interface in the water reservoir column.

The functions $h_{pn}=f(t)$ and $h_{pw}=f(t)$, presented in Figure 152, give an example of the variations of the DNAPL and water pressure heights versus time applied in experiments for drainage with 0.5 mm GB.

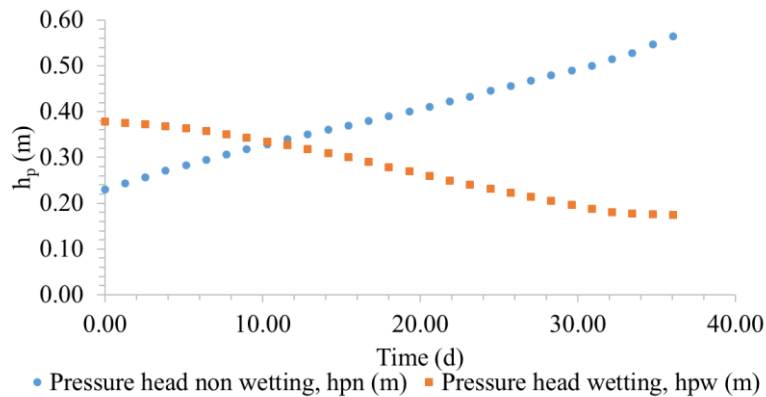


Figure 152: Experimental function h_{pn} and h_{pw} as a function of time

These measurements were performed for every experiment to impose P_n and P_w at the boundary conditions (*i.e.* 0.5 mm GB, 0.1 mm GB, without enhancement, with thermal enhancement, with chemical enhancement).

5.3 Results and discussion

5.3.1 Experiments in 1 D columns without enhancement

The drainage-imbibition experiments were conducted with 0.5 and 0.1 mm GB without enhancement. We modeled drainages and imbibitions and monitored their permittivity and electrical resistivity.

5.3.1.1 Experimental results and comparison with numerical simulation

Several drainage-imbibition experiments were performed with 1D columns:

- 3 experiments with 0.5 mm GB with membrane (of which 2 were monitored for permittivity and resistivity),
- 3 experiments with 0.5 mm GB without membrane (the 3 experiments were monitored for permittivity and resistivity),
- 3 experiments with 0.1 mm GB without membrane (of which were 2 monitored for permittivity and resistivity).

The results for water saturations at the end of drainages (S_{rw}) and imbibitions ($1-S_m$) are displayed in Figure 153.

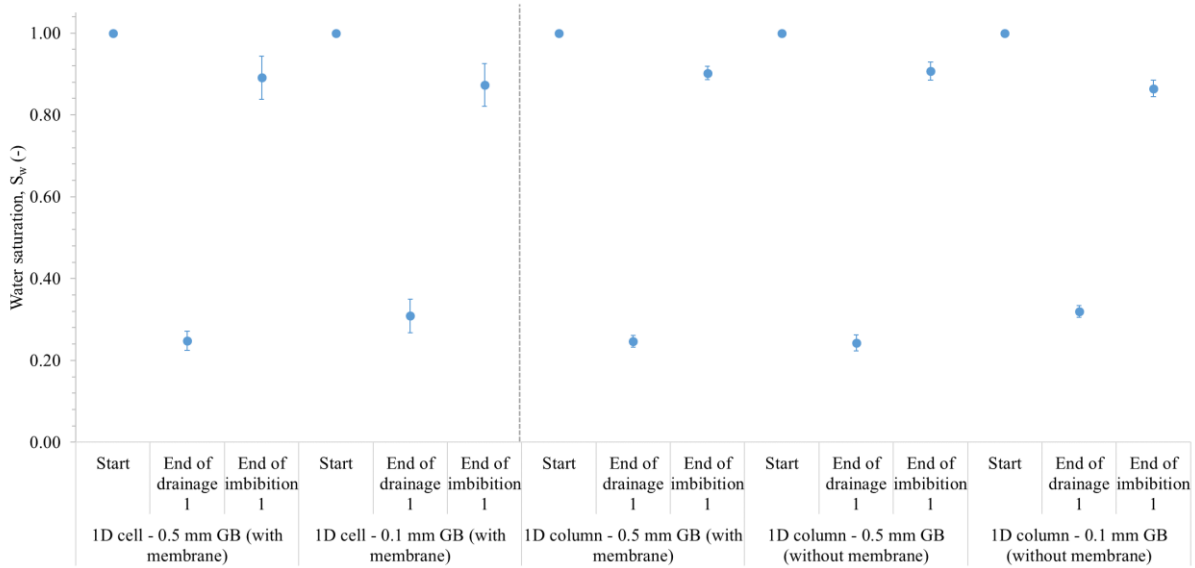


Figure 153: Change in water saturation as a function of drainage-imbibition cycle for 0.5 and 0.1 mm GB in 1D cells and 1D columns (with and without membrane)

One can see that the results for the experiments in 1D cells with a membrane were similar to those performed without membrane. As for the 0.5 mm GB, the S_w at the end of drainage and imbibition were respectively: 0.248 ± 0.023 and 0.891 ± 0.052 for 1D cells with membrane, 0.242 ± 0.014 and 0.902 ± 0.016 for 1D columns with membrane, and 0.243 ± 0.019 and 0.906 ± 0.022 for 1D columns without membrane. These results confirm that the drainage area close to the filters is very thin (see section 4.2.3.2). The effects of this drainage area are very limited on 1D columns, which are 0.25 m high.

From the experiments performed with 0.1 mm GB in 1D cells and 1D columns, we could also compare S_w . The S_w at the end of drainages and imbibitions were respectively: 0.309 ± 0.05 and 0.873 ± 0.052 for 1D cells and 0.319 ± 0.014 and 0.865 ± 0.020 for 1D columns. The results are therefore similar as well.

This shows that: i. the experiments in 1D cells and 1D columns are reliable; ii. The experiments in 1D columns do not need a membrane to generate correct S_{rw} and S_m values.

We compared the drainage-imbibition experimental results with modeling for the 0.5 and 0.1 mm GB.

a) Drainage-imbibition with 0.5 mm GB: comparison of experimental and modeled results

This section focused on a experiment with 0.5 mm GB without membrane allowing to compare modeling and the experimental results.

The results for modeling S_{e_w} over time during drainage are shown in Figure 154.

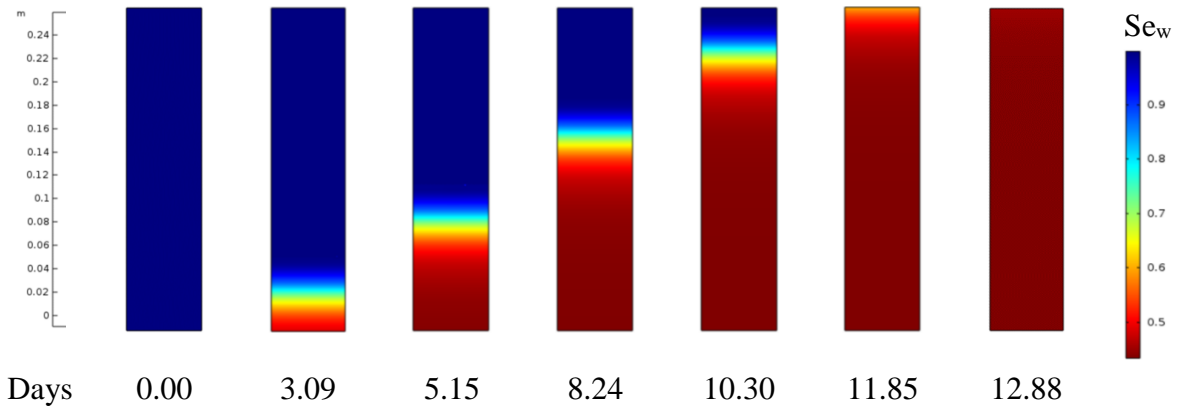


Figure 154: Evolution of the effective water saturation (S_{e_w}) modeled during drainage with 0.5 mm GB

The comparison of experimental and modeled results is based on: i. a global approach, with varied averaged S_w over the column surface (model) and DNAPL recovery volumes in 1D columns (measures of DNAPL volumes in reservoir); ii. a more detailed approach with variations in DNAPL-water interface displacement (Figure 155).

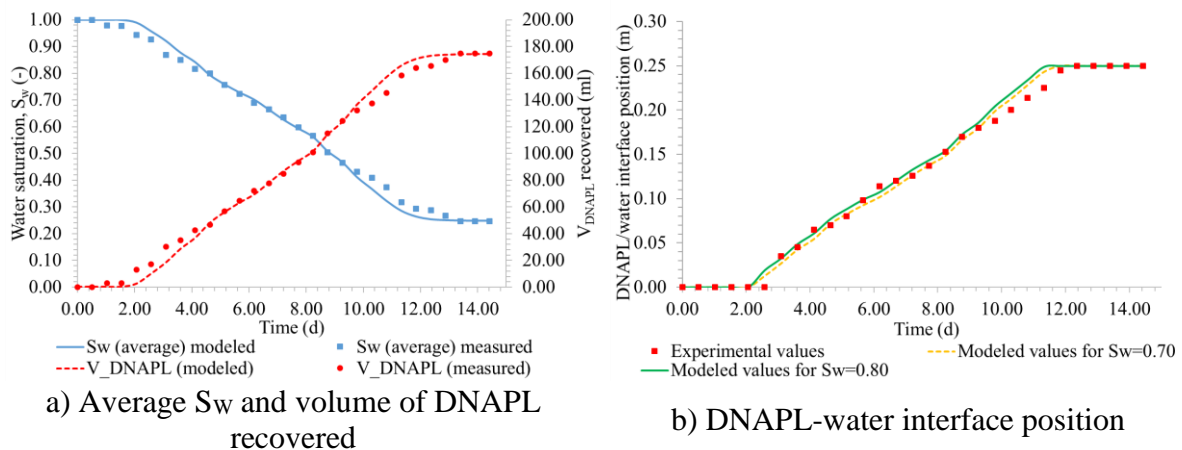


Figure 155: Comparison of experimental and modeled results for drainage in 1D column with 0.5 mm GB: a) average S_w and volume of DNAPL recovered and b) DNAPL-water interface position

The modeled volumes of DNAPL, V_{DNAPL} , were calculated as follows (Eq. 213):

$$V_{DNAPL} = V_{column} \phi (1 - S_w) \quad \text{Eq. 213}$$

From Figure 155, the differences between the modeled and experimental results are not significant. The ratios between the measured and modeled DNAPL volumes were, from the fourth day, on average about 0.98 (Figure 156). Between the first and fourth days, this ratio was higher, up to 12. This is related to the fact, at the beginning, that the volumes are small and that a small volume difference causes proportionally high variations.

As for the DNAPL-water interface migration front, we have used two hypotheses: the migration front is visible from $S_w=0.7$ and $S_w=0.8$. We see that the modeled migration front is superimposed correctly on the measured value in our experimental conditions.

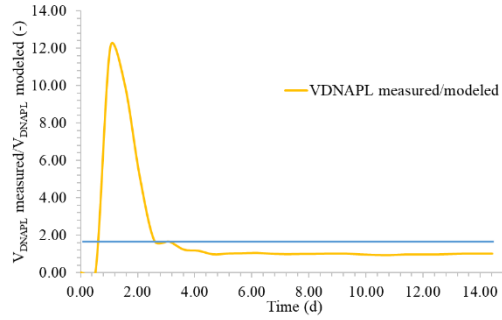


Figure 156: Evolution of $V_{DNAPL} \text{ measured}/V_{DNAPL} \text{ modeled}$ ratios during drainage in 1D column with 0.5 mm GB

The compared experimental and modeled results for imbibition are shown in Figure 157.

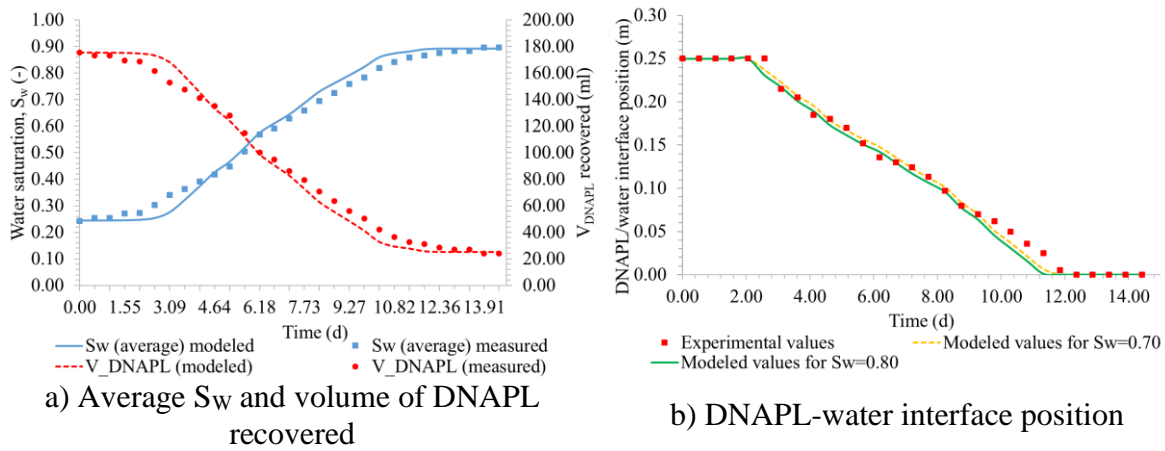


Figure 157: Comparison of experimental and modeled results for imbibition in 1D column with 0.5 mm GB: a) average S_w and volume of DNAPL recovered and b) DNAPL-water interface position

The modeling results with pressure-pressure formulation are similar to the experimental results for both DNAPL volumes recovered and the migration front displacement. Figure 158 shows how the $V_{DNAPL} \text{ measured}/V_{DNAPL} \text{ modeled}$ ratio changes and displays that the models do reproduce the experimental results reasonably well (the ratios vary between 0.90 and 1.28).

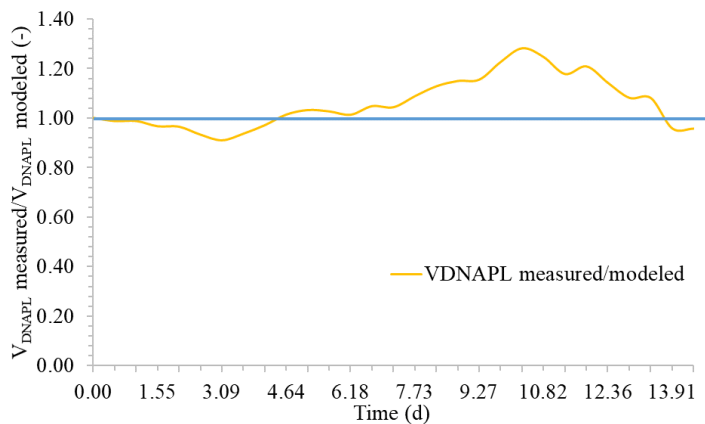


Figure 158: Evolution of $V_{DNAPL} \text{ measured}/V_{DNAPL} \text{ modeled}$ ratios during imbibition in 1D column with 0.5 mm GB

b) Drainage-imbibition with 0.1 mm GB: comparison of experimental and modeled results

An example of a drainage-imbibition experiment with 0.1 mm GB is discussed below.

Figure 159 shows how S_w and V_{DNAPL} change during drainage with 0.1 mm GB and DNAPL-water interface displacement.

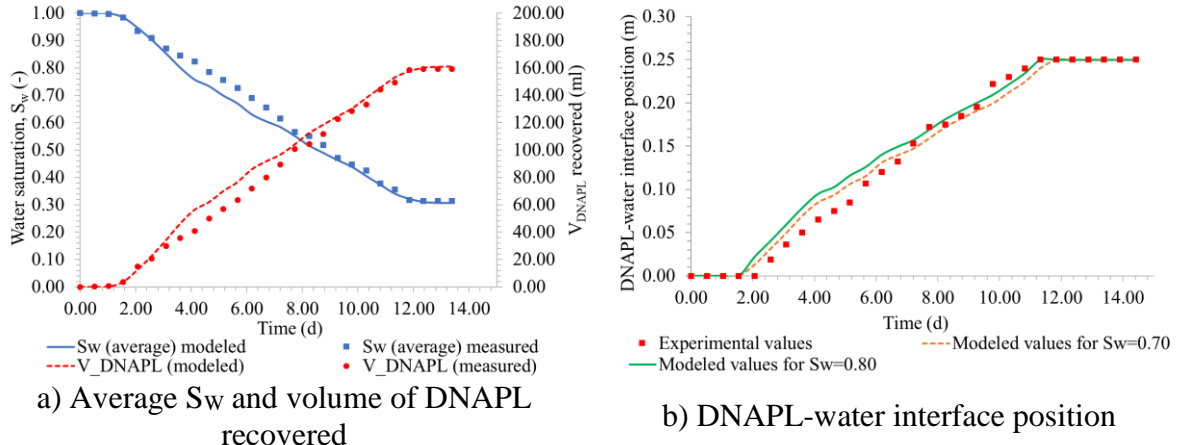


Figure 159: Comparison of experimental and modeled results for drainage in 1D column with 0.1 mm GB: a) average S_w and volume of DNAPL recovered and b) DNAPL-water interface position

The modeling results match the experimental results. The V_{DNAPL} measured/ V_{DNAPL} modeled ratio varies between 0.83 and 1.06 from the fifth day (Figure 160). Before the fifth day, the ratio was higher. This was also explained by the volumes being small and a small measurement difference causing high variation in the ratios.

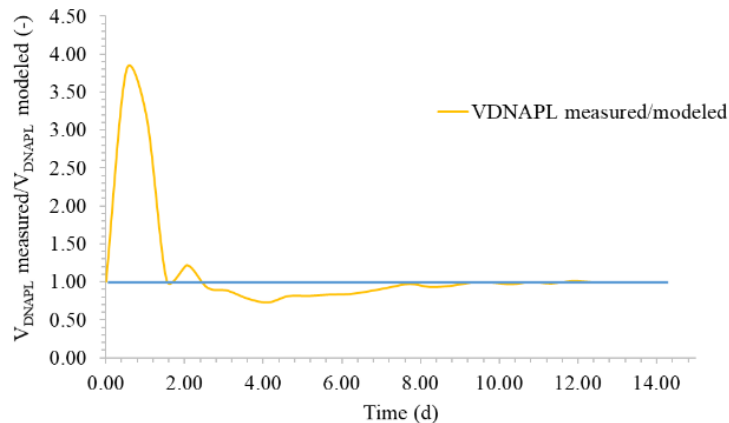


Figure 160: Evolution of V_{DNAPL} measured/ V_{DNAPL} modeled ratios during drainage in 1D column with 0.1 mm GB

Figure 161a) shows how S_w and V_{DNAPL} changed during the imbibition with 0.1 mm GB; Figure 161b) illustrates the DNAPL-water interface displacement (measured and modeled).

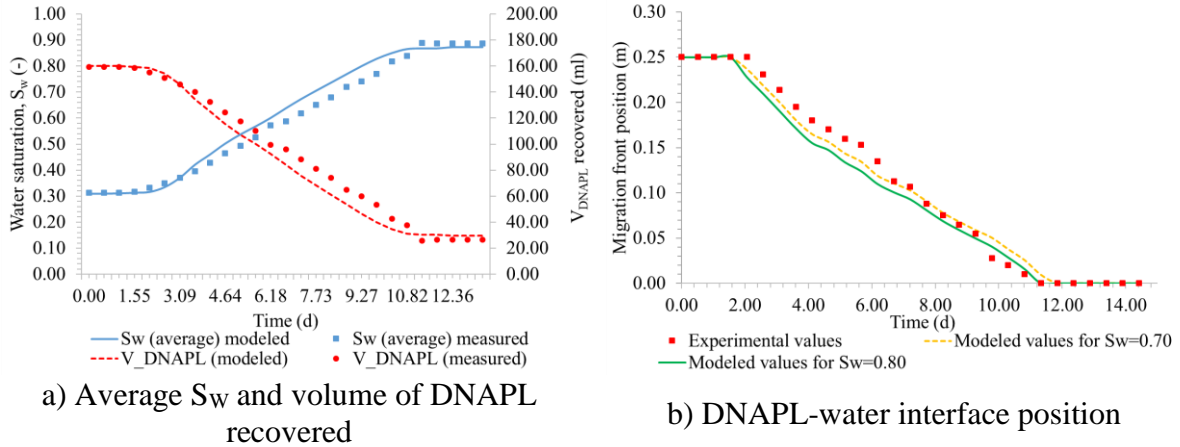


Figure 161: Comparison of experimental and modeled results for imbibition in 1D column with 0.1 mm GB: a) average S_w and volume of DNAPL recovered and b) DNAPL-water interface position

We see that the model fits the experimental results very well for both V_{DNAPL} and DNAPL-water interface. At the start of imbibition, the modeled and measured values were almost superimposable. When the DNAPL volume was smaller (from Day 7), the variations in the V_{DNAPL} measured/ V_{DNAPL} modeled ratio tended to increase (from 0.84 to 1.33) (Figure 162).

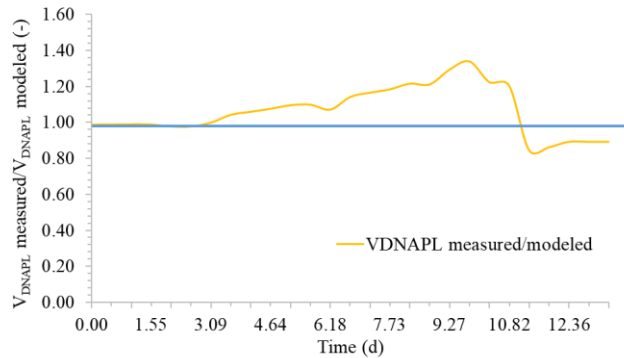


Figure 162: Evolution of V_{DNAPL} measured/ V_{DNAPL} modeled ratios during imbibition in 1D column with 0.1 mm GB

c) Comparison of drainage-imbibition experiments with 0.5 and 0.1 mm GB

Figure 163 shows drainage-imbibition results (measured and modeled) for 0.5 and 0.1 mm GB.

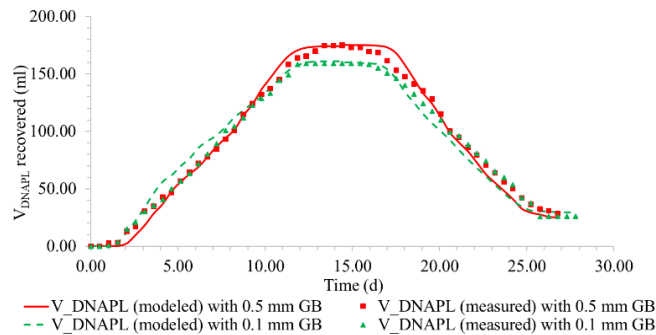


Figure 163: Comparison between modeled and measured DNAPL volume (V_{DNAPL}) for experiments with 0.5 and 0.1 mm GB

We see in Figure 163 that the volume of DNAPL added to the 1D column at the end of drainage with 0.1 mm GB was lower than with the 0.5 mm GB (respectively 161.13 mL modeled vs 174.48 mL, *i.e.* 8.9% more).

Moreover, on the same date (*i.e.* at equivalent P_c), there was little difference between the DNAPL volumes recovered during drainage and imbibition. This was related to the fact that we waited 3 hours between each P_c variation. This stabilization period was necessary to reach fluid equilibrium and to collect representative data for permittivity and resistivity. During the experiments, the stabilization periods for the DNAPL-water interface were much higher for the 0.1 mm GB than for the 0.5 mm GB. This aspect will be further discussed in the section dealing with experiments with the 2D tank (Chapter 6).

At the end of imbibition, we clearly distinguished lower recovered DNAPL volumes for 0.1 mm GB than for 0.5 mm GB. The remaining volumes in the 1D column were respectively 29.47 mL (for modeled DNAPL) vs 25.12 mL (*i.e.* 14.8% difference). This difference of recovery is related to differences in S_{m} .

Distance from column bottom (for drainage) and distance from column top (for the imbibition) as a function of S_w show the thickness of the DNAPL-water boundaries and especially the transition zones (Figure 164).

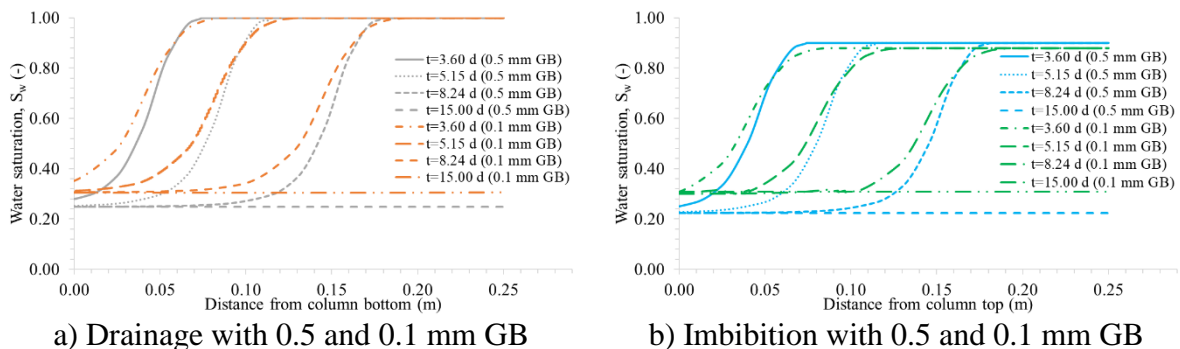


Figure 164: Comparison of the water saturation (S_w) modeled profile for different times during a) drainage and b) imbibition experiments (for 0.5 and 0.1 mm GB)

We see that the DNAPL-water interface transition is more diffuse for the 0.1 mm GB than for the 0.5 mm GB. This can be explained by the capillary effect being more important for 0.1 mm GB than the 0.5 mm ones. This corroborates the observations made with the 1D cell experiments (See section 4.2.3). Therefore, if we consider $S_w = 0.7$ and 0.8 , the water saturation profile differences during the drainage at $t = 8.24$ d are: 4.26 mm (for 0.5 mm GB) and 7.25 mm (for 0.1 mm GB), which corresponds to an increase of 78.4%. Figure 165 illustrates this phenomenon.

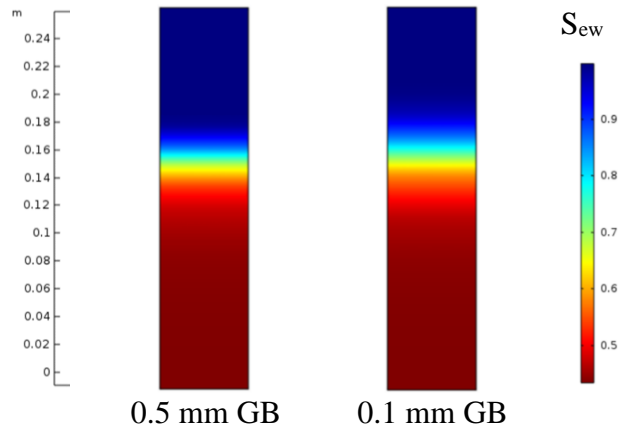


Figure 165: Comparison of water-DNAPL interface transitions zones modeled with 0.5 and 0.1 mm GB (drainage experiment at $t=8.24$ d)

The comparison between experimental and modeled recovered DNAPL volumes shows that the model predicts the experimental data well.

5.3.1.2 Permittivity monitoring

Permittivities values were monitored at three points: TDR T (top), TDR M (medium) and TDR B (bottom) (Figure 166).

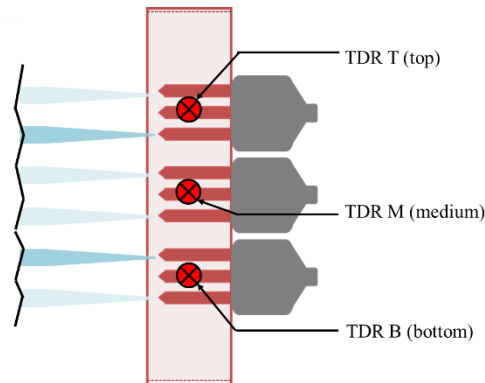


Figure 166: Position of the TDR probes

a) Drainage-imbibition with 0.5 mm GB

Figure 167 shows changes in permittivity, ϵ (corrected relative to the reference value of air and water measured at the beginning of the experiment, see Eq. 186) and in S_w (estimated from volume balance) as a function of time during a drainage-imbibition experiment conducted with 0.5 mm GB.

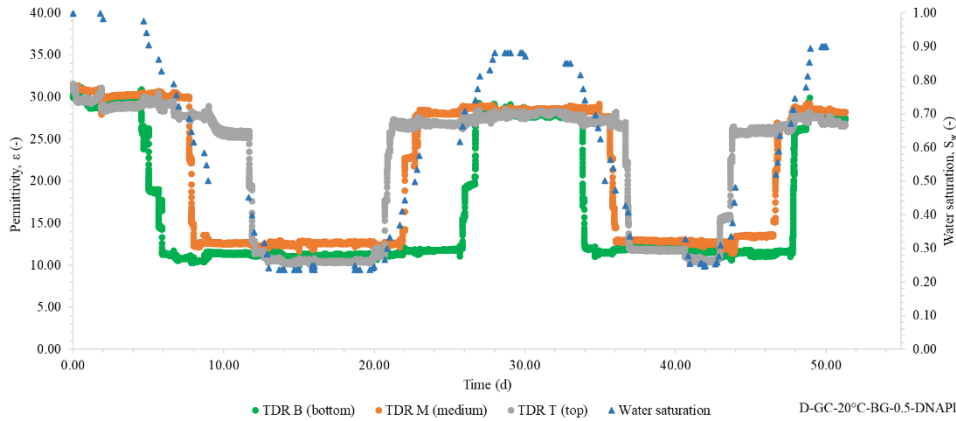


Figure 167: Evolution of water saturation and permittivity as a function of time in 1D column (example of a drainage-imbibition experiment with 0.5 mm GB)

During drainage variations in S_w were accurately detected by TDR B, then M and then H (high), and the reverse for imbibition. Therefore, the migration front was detected successively by each of the TDR probes. The ϵ measured by each of the TDR probes at the end of drainage ($\epsilon \sim 11.92$) and imbibition ($\epsilon \sim 27.77$) were relatively similar. The slopes of the curves $\epsilon = f(t)$ were almost vertical, which means very sharp DNAPL/water boundaries.

b) Drainage-imbibition with 0.1 mm GB

Figure 168 shows changes in ϵ and in S_w as a function of time during a drainage-imbibition experiment conducted with 0.1 mm GB.

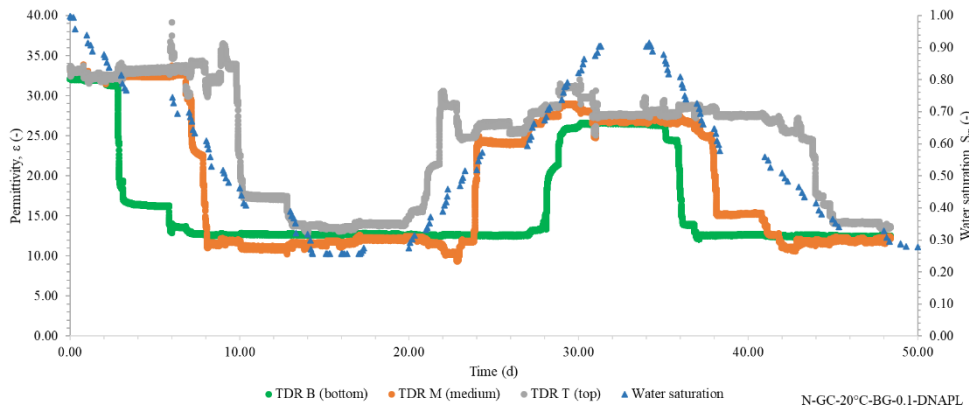


Figure 168: Evolution of water saturation and permittivity as a function of time in 1D column (example of a drainage-imbibition experiment with 0.1 mm GB)

Globally, the same variations as for the 0.5 mm GB are reported with the exception of the curve slopes $\epsilon = f(t)$ and measured ϵ by each of the TDR probes at the end of drainage and imbibition.

As expected, the slope of the curves $\epsilon = f(t)$ is less steep for the 0.1 mm GB, which demonstrates a more spread out migration front. The ϵ measured by each of the TDR probes were relatively similar but different than those acquired with the 0.5 mm GB; the permittivities measured were in average 13.65 at the end of drainage and 25.55 at the end of imbibition.

c) Comparison of drainage-imbibition with 0.5 and 0.1 mm GB

Figure 169 and Figure 170 compare measured permittivity, estimated permittivity, and modeled water saturation as a function of time for 0.5 and 0.1 mm GB, respectively. Where we examine only drainage; imbibition showed the same results. The estimated permittivity was calculated from S_w (calculated from numerical model) and Eq. 197 for 0.5 mm GB, and Eq. 198 for 0.1 mm GB (CRIM model).

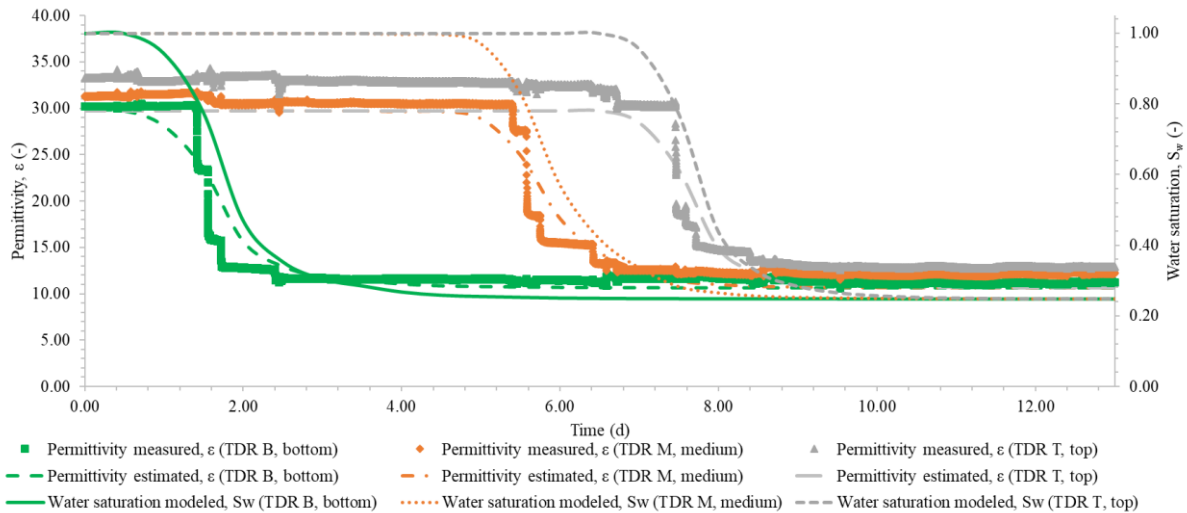


Figure 169: Comparison of measured and estimated permittivity and estimated water saturation as a function of time in 1D column (for 0.5 mm)

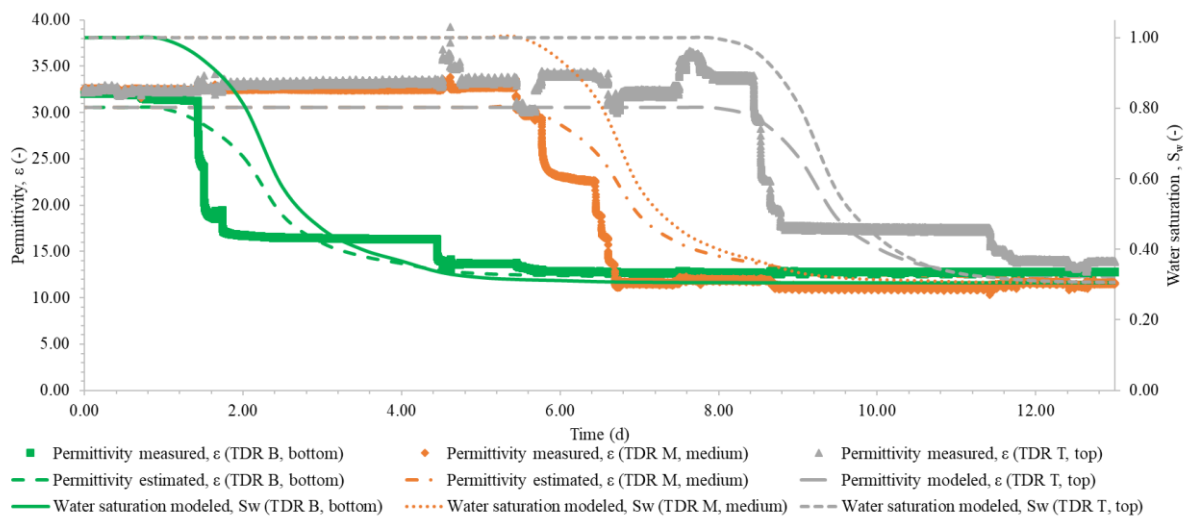


Figure 170: Comparison of measured and estimated permittivity and modeled water saturation as a function of time in 1D column (for 0.1 mm)

Values for $\epsilon_{\text{measured}}$ were similar to $\epsilon_{\text{estimated}}$: $\epsilon_{\text{estimated}}$ at the end of drainage were on average 10.63 (vs $\epsilon_{\text{measured}} = 11.09$) for 0.5 mm GB and 12.31 (vs $\epsilon_{\text{measured}} = 12.78$). This matches the results from the modeling output data (see section 4.2.3.3). However the variations in $\epsilon_{\text{measured}}$ are sharper than variations in $\epsilon_{\text{estimated}}$.

The permittivity drop for 0.1 mm GB occurred slightly earlier than the one for the 0.5 mm GB. This is due to: i. the DNAPL-water interface being more spread out for the 0.1 mm GB and;

ii.: the $\epsilon_{\text{measured}}$ changing as the DNAPL migration front approached within 2 mm of the TDR probes (see section 4.2.3.3).

The results for average water saturation and permittivity as a function of different drainage-imbibition cycles are shown in Figure 171.

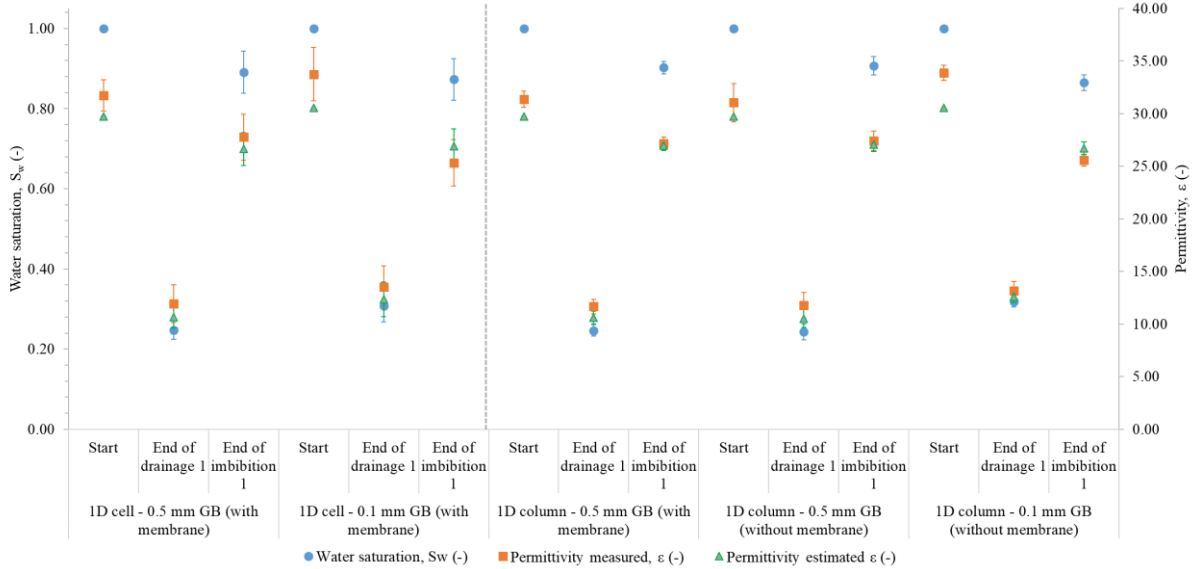


Figure 171: Change in water saturation and permittivity (measured and estimated) as a function of drainage-imbibition cycle for 0.5 and 0.1 mm GB in 1D cells and 1D columns (without enhancement)

The measured permittivities match the measured S_w . As for the 0.5 mm GB, the average permittivity measured at the end of drainages and imbibitions were respectively: 11.92 ± 1.80 and 27.77 ± 2.17 for 1D cells with membrane, 11.66 ± 0.71 and 27.16 ± 0.64 for 1D columns with membrane and, 11.78 ± 1.22 and 27.42 ± 0.92 for 1D columns without membrane.

For the 0.1 mm GB, the measured permittivities also matched the measured S_w . The ϵ measured at the end of the drainages and imbibitions were respectively: 13.52 ± 1.99 and 25.32 ± 2.19 for 1D cells with membrane and 13.17 ± 0.85 and 25.58 ± 0.55 for 1D columns without membrane.

The 1D columns have lower permittivity and water saturation standard deviations than the 1D cells. This is probably related to the fact that the volumes are higher and local heterogeneity is abated.

The estimated permittivities match the measured permittivities (Figure 172).

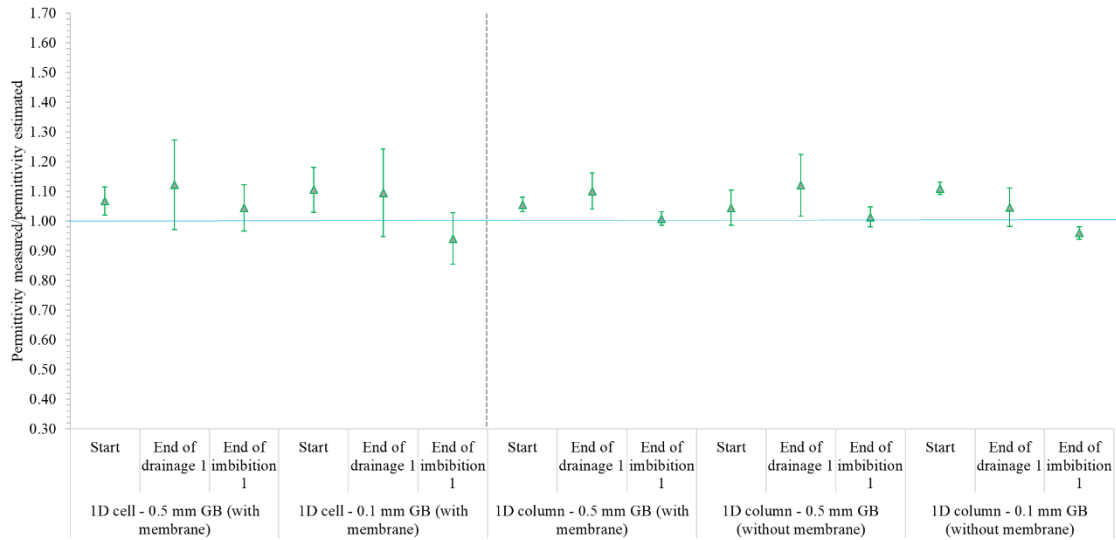


Figure 172: Measured permittivity/estimated permittivity ratios as a function of drainage-imbibition cycle for 0.5 and 0.1 mm GB in 1D cells and 1D columns (without enhancement)

As shown in Figure 172, the measured permittivity/estimated permittivity ratios were similar for the 1D cells and 1D columns. For the 0.5 mm GB these ratios varied between 1.04 and 1.07 for $S_w=100\%$ (start), 1.10 and 1.12 at the end of the drainage, and 1.01 and 1.04 at the end of the imbibition. For the 0.1 mm GB, these ratios were 1.10 and 1.11 at the start, 1.05 and 1.08 at the end of the drainage, and 0.94 and 0.96 at the end of imbibition.

5.3.1.3 Electrical resistivity monitoring

The resistivities were monitored via six unpolarizable potential electrodes (PE 1 to PE 6) (Figure 173). The measured resistivity comes from the measurements of juxtaposed potential electrodes (separated by 2.7 cm). The resistivity measurement zones inside the column were labeled as follows (from bottom to top): R1 (PE1-PE2), R2 (PE2-PE3), R3 (PE3-PE4), R4 (PE4-PE5), R5 (PE5-PE6). Therefore, these values incorporate the five juxtaposed column heights (R1 to R5). The measurement zone called R6, unlike the other measurement points (R1 to R5), incorporates a longer column height (2.7×3 i.e. 8.1 cm) since it results from the measurements of potential electrodes PE2-PE5.

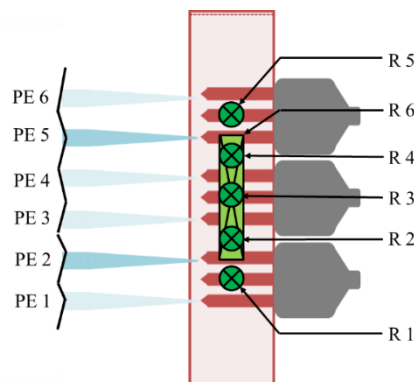


Figure 173: Position of the unpolarizable potential electrodes of 1D column

a) Drainage-imbibition with 0.5 mm GB

Figure 174 shows changes in ρ_c and in S_w (estimated from volume balances) as a function of time during a drainage-imbibition experiment conducted with 0.5 mm GB.

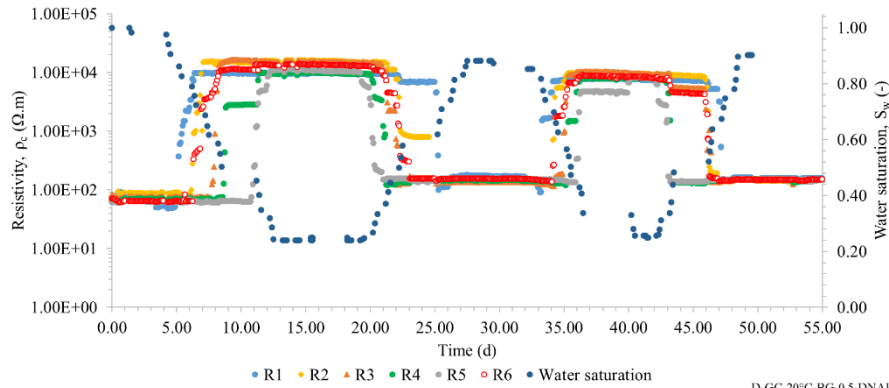


Figure 174: Evolution of water saturation and resistivity as a function of time in 1D column (example of a drainage-imbibition experiment with 0.5 mm GB)

The expected resistivity changes respectively for R1 to R6 (positioned from bottom to top) during drainage (and the reverse during imbibition). The data collected for resistivity show greater variability than for permittivity. Therefore, in the example shown in the Figure 174, the resistivities at the end of drainage 1 and imbibition 1 were in average $12\,603 \pm 2\,731 \, \Omega.m$ and $153 \pm 13 \, \Omega.m$, respectively.

b) Drainage-imbibition with 0.1 mm GB

Figure 175 shows changes in ρ_c and in S_w as a function of time during a drainage-imbibition experiment conducted with 0.1 mm GB.

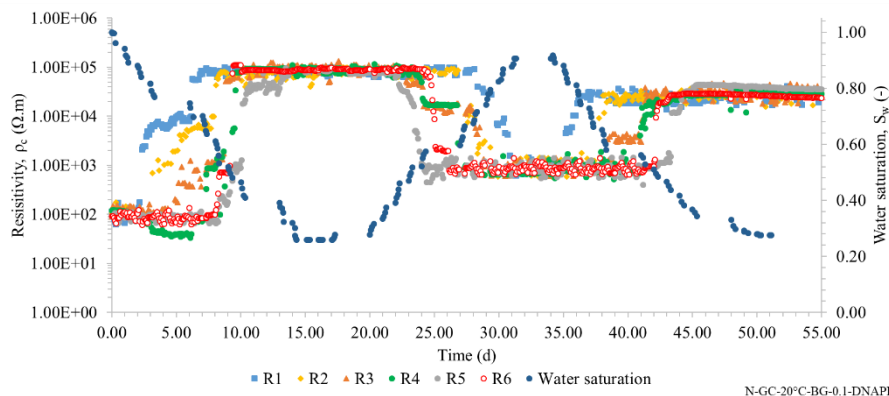


Figure 175: Evolution of water saturation and resistivity as a function of time in 1D column (example of a drainage-imbibition experiment with 0.1 mm GB)

The migration front was indeed detected successively by the electrodes. During the transition phases (*i.e.* between the variations of S_m to S_{rw}), the resistivities show even higher variability for the 0.1 mm GB than for the 0.5 mm GB. Overall, during the end of drainage and imbibition phases, the results display acceptable variabilities. For example, the resistivities at the end of drainage 1 and imbibition 1 were on average $88339 \pm 3378 \, \Omega.m$ and $934 \pm 44 \, \Omega.m$, respectively.

c) Comparison of drainage-imbibition with 0.5 and 0.1 mm GB

Figure 176 and Figure 177 compare measured and estimated resistivity, and modeled water saturation as a function of time for 0.5 and 0.1 mm GB. We examined only drainage; imbibition showed the same results. The estimated resistivity was calculated from S_w (calculated from numerical model) and Eq. 205 to Eq. 208 (Archie's law).

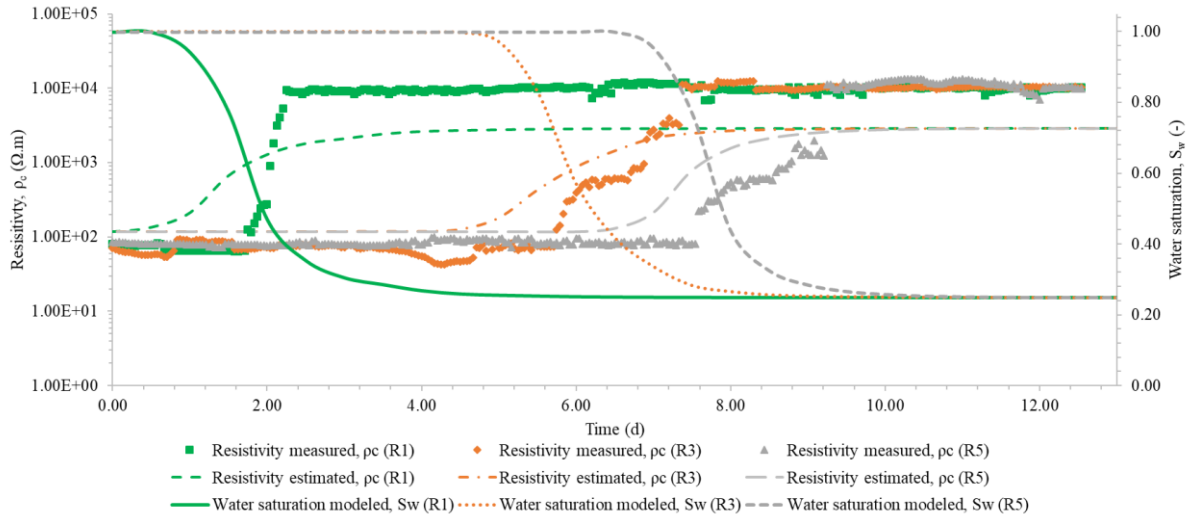


Figure 176: Comparison of measured and estimated resistivity and modeled water saturation as a function of time in 1D column (for 0.5 mm)

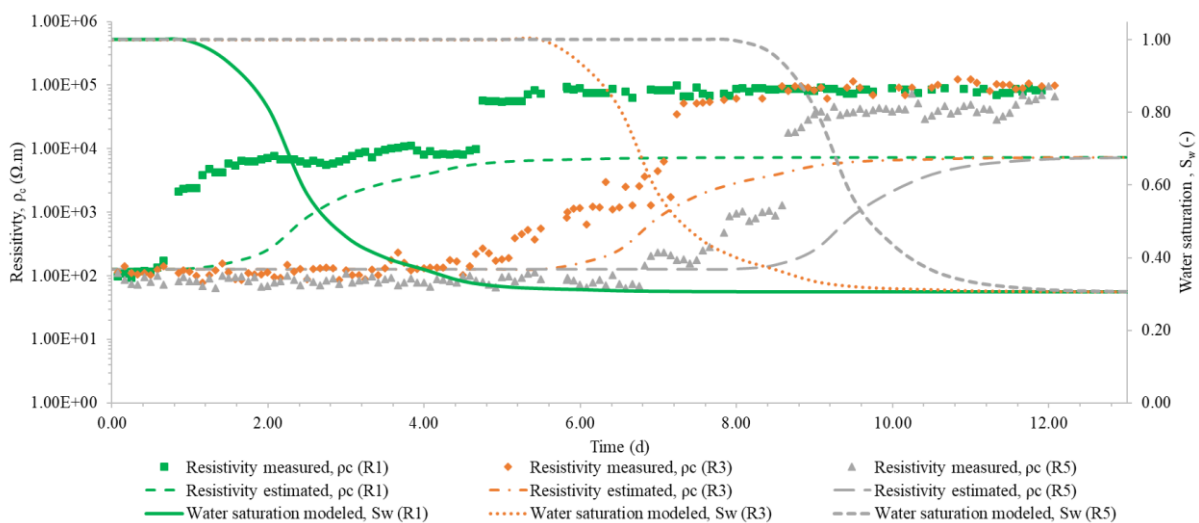


Figure 177: Comparison of measured and estimated resistivity and modeled water saturation as a function of time in 1D column (for 0.1 mm GB)

The resistivities varied earlier for the 0.1 mm GB than for the 0.5 mm GB. The increase in resistivity is slower for 0.1 mm GB, which is logical because the DNAPL-water interface is thicker. This phenomenon has already been reported for permittivities measurements.

The differences between the measured and estimated resistivities match those reported in Figure 179. Accordingly, the $\rho_{c,measured}/\rho_{c,estimated}$ ratios are 3.4 at the end of drainage with the 0.5 mm GB and 13.1 at the end of drainage with the 0.1 mm GB.

The results for water saturation and resistivity (measured and estimated) at the end of the drainages (S_{rw}) and imbibitions ($1-S_{rn}$) are shown in Figure 178.

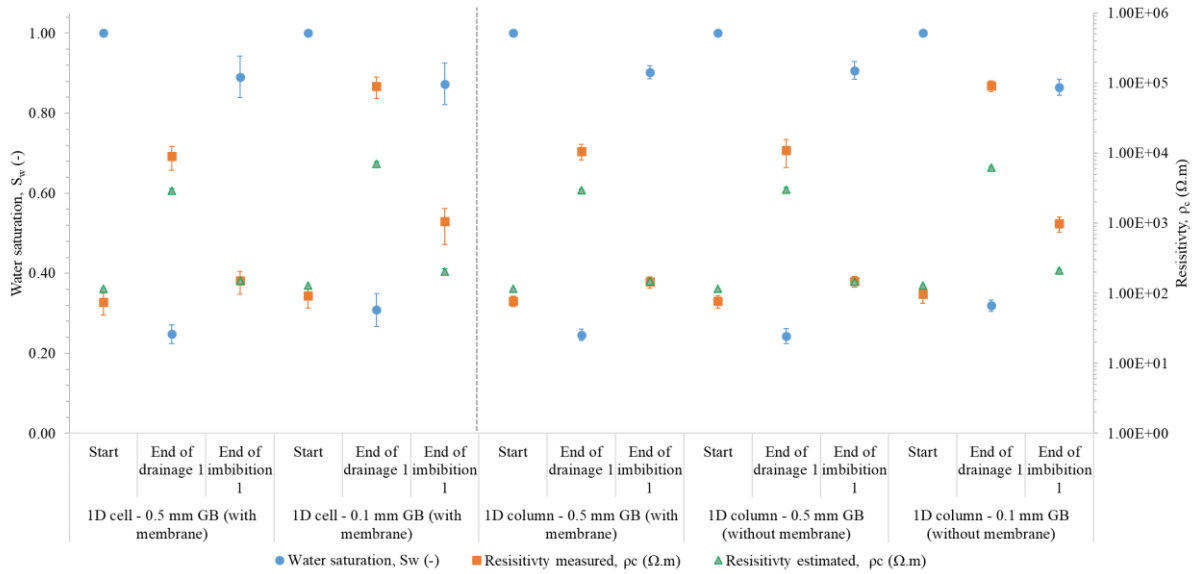


Figure 178: Change in water saturation and resistivity (measured and estimated) as a function of drainage-imbibition cycle for 0.5 and 0.1 mm GB in 1D cells and 1D columns (without enhancement)

The measured resistivities confirm the results reported for the 1D cells. Using a membrane has no influence on S_w or measured resistivity; resistivity at the end of the drainages and imbibitions for the 0.5 mm GB was respectively: $9093 \pm 3420 \Omega.m$ and $150 \pm 54 \Omega.m$ for 1D cells with membrane, $10693 \pm 2705 \Omega.m$ and $145 \pm 28 \Omega.m$ for 1D columns with membrane and, $11025 \pm 4752 \Omega.m$ and $148 \pm 25 \Omega.m$ for 1D columns without membrane.

The experimental results with the 0.1 mm GB in 1D columns matched those obtained in the 1D cells. The measured resistivities at the end of the drainages and imbibitions were respectively: $90589 \pm 30641 \Omega.m$ and $1061 \pm 563 \Omega.m$ for 1D cells with membrane and $91851 \pm 16120 \Omega.m$ and $989 \pm 243 \Omega.m$ for 1D columns without membrane.

The differences between the estimated and measured resistivity values were pretty similar to those determined for the 1D cells (Figure 179).

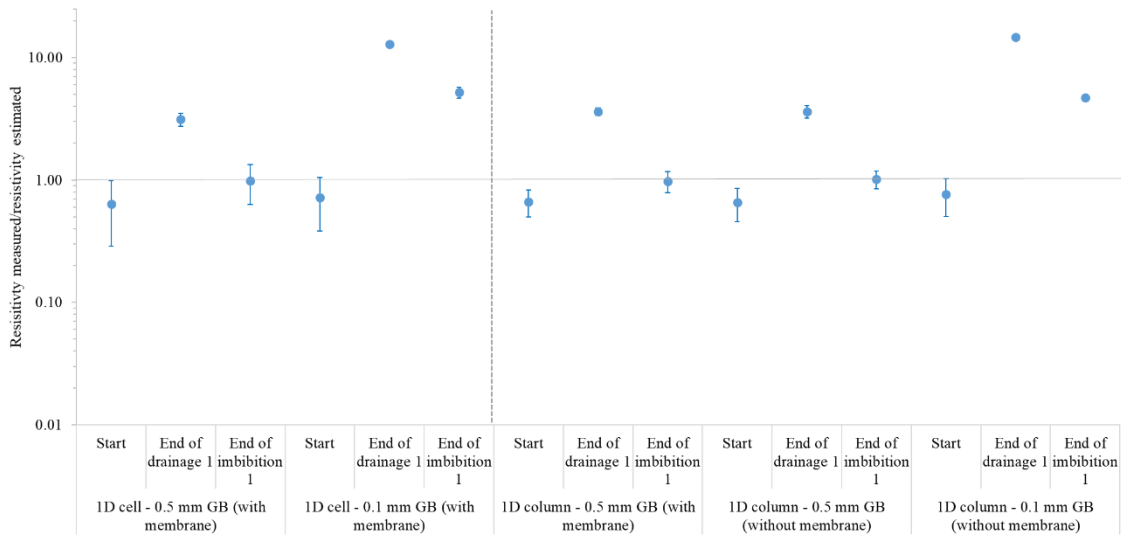


Figure 179: Measured resistivity/estimated resistivity ratios as a function of drainage-imbibition cycle for 0.5 and 0.1 mm GB in 1D cells and 1D columns (without enhancement)

For the 0.5 mm GB, the average measured resistivity/estimated resistivity ratios vary between 0.63 and 0.66 for $S_w=100\%$ (start), 3.13 and 3.63 at the end of the drainage and, 0.98 and 1.01 at the end of the imbibition. For the 0.1 mm GB, these ratios ranged between 0.72 and 0.76 at the start, 12.83 and 14.64 at the end of drainage, and 4.71 and 5.21 at the end of imbibition.

The measured resistivity/estimated resistivity were ratios were closer to 1 at the end of the imbibition than at the end of the drainage. Therefore, systematic under-estimation of estimated values at the end of drainages is reported. Since this estimation is quantified and stable for 1D cells and 1D columns, it was used to approximate S_w .

We see very good homogeneity of results for 1D cells and 1D columns. The results for S_w and $\rho_{c,measured}$ with and without membrane in the 1D columns demonstrate that it is not necessary to use membranes to approach the values determined with 1D cells with membranes.

5.3.2 Experiments in 1 D columns with chemical enhancement

In total, 6 experiments were conducted to estimate the effect of SDBS addition at the end of drainage 1:

- 3 experiments with 0.5 mm GB without membrane (the 3 experiments were monitored for permittivity and resistivity),
- 3 experiments with 0.1 mm GB without membrane (of which 2 were monitored for permittivity and resistivity).

Figure 180 shows the water saturations as a function of the drainage and imbibition cycles for 1D cells and 1D columns with chemical enhancement.

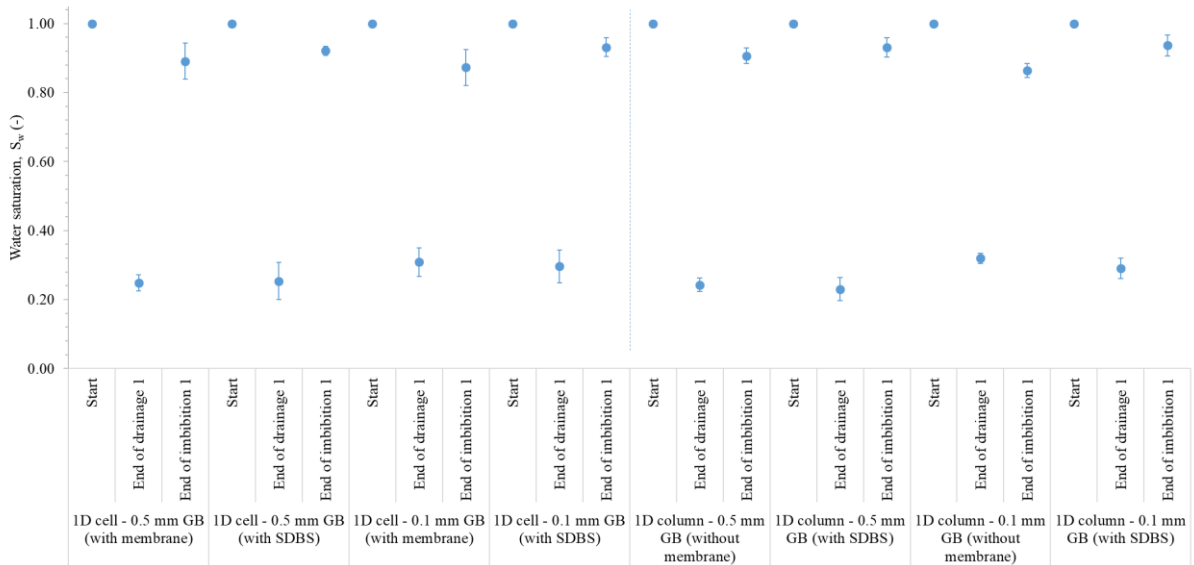


Figure 180: Change in water saturation as a function of drainage-imbibition cycle for 0.5 and 0.1 mm GB in 1D cells and 1D columns (with and without chemical enhancement)

The S_w at the end of the imbibition after SDBS addition were similar the 1D cells and 1D columns.

For the 0.5 mm GB, S_w for 1D cells and 1D columns were, respectively, 0.92 ± 0.01 and 0.93 ± 0.03 . For the 0.1 mm GB, S_w for 1D cells and 1D columns were, respectively, 0.93 ± 0.03 and 0.94 ± 0.03 . The remediation yields with chemical enhancement were of the same order of magnitude as those reported in 1D cells: 26.4% for 0.5 mm GB and 53.4% for 0.1 mm GB.

5.3.2.1 Experimental results and comparison with numerical simulation

In this section, only imbibitions were considered because SDBS was only added in the columns at the end of the drainages.

Figure 181 shows comparison of S_w measured and modeled, as well as the volume of DNAPL modeled and measured in the 1D column, during imbibition. The models were run by using the data reported in section 5.2.

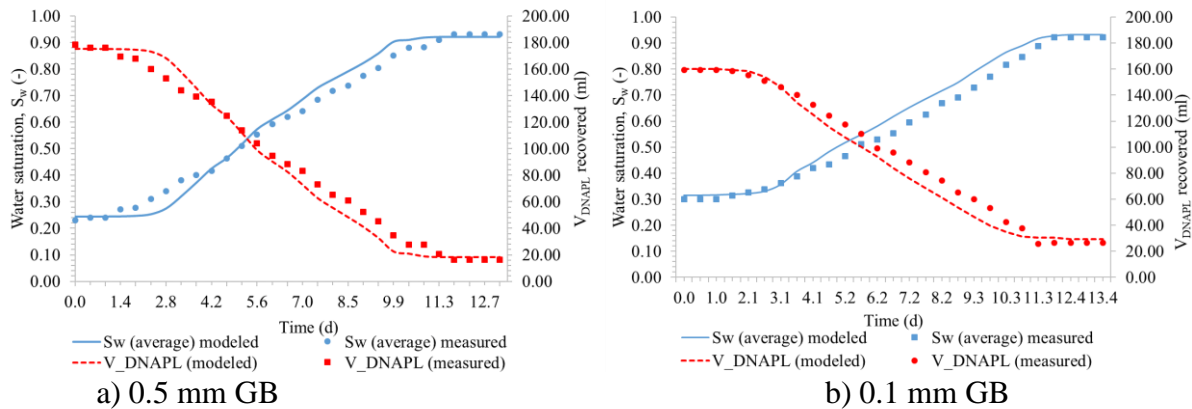


Figure 181: Comparison of drainage-imbibition experiments for a) 0.5 and b) 0.1 mm GB with chemical enhancement (DNAPL modeled volume vs DNAPL measured volume)

The two-phase flow model with chemical enhancement, like the 1D column experiments without any enhancement, allows to reproduce very well the variations of S_w and the volumes of DNAPL recovered as a function of time. The measured value/modeled values ratios are, at the end of the imbibition: 0.89 for 0.5 mm GB and 0.90 for 0.1 mm GB.

5.3.2.2 Permittivity monitoring

Figure 182 shows changes in ϵ and in S_w as a function of time during drainage-imbibition experiments conducted with 0.5 and 0.1 mm GB (with chemical enhancement).

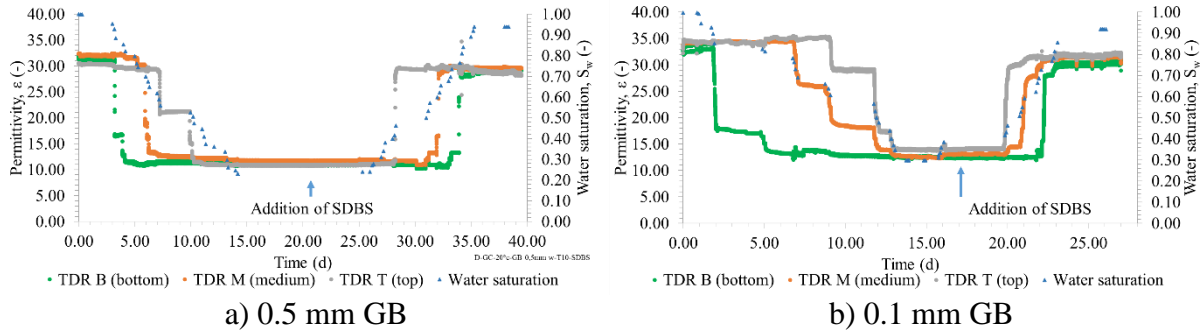


Figure 182: Evolution of water saturation and permittivity as a function of time in 1D column with chemical enhancement (example of drainage-imbibition experiments with a) 0.5 mm GB and b) 0.1 mm GB)

We see the same variations and correlations between S_w and measured permittivities as before. The permittivity variations during drainage were slower for the 0.1 mm GB than for the 0.5 mm GB (see section 5.3.1.2). Adding SDBS at the end of drainage caused faster variations in ϵ (the $\epsilon=f(t)$ slopes are steeper). The stepped curves were related to the steady-state conditions of h_{pn} and h_{pw} . The results for water saturation and permittivities (measured and estimated) at the end of the drainages (S_{rw}) and imbibitions ($1-S_m$) are displayed in Figure 183.

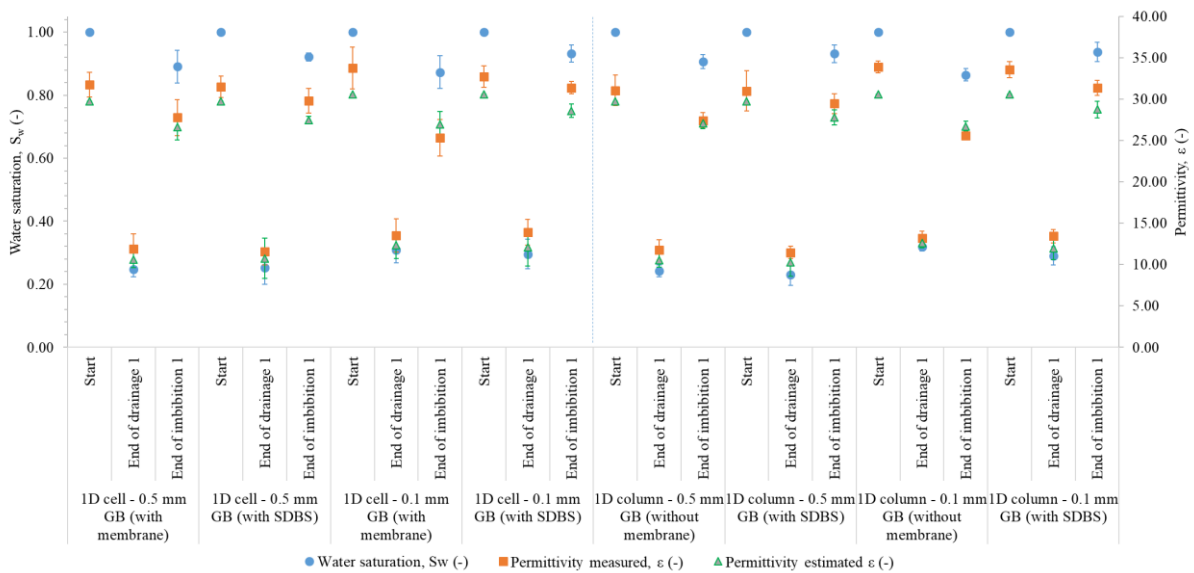


Figure 183: Change in water saturation and permittivity (measured and estimated) as a function of drainage-imbibition cycle for 0.5 and 0.1 mm GB in 1D cells and 1D columns (with and without chemical enhancement)

The measured permittivities match the measured S_w (and more specifically the reductions in S_m with chemical enhancement). At the end of imbibition, the average measured permittivities for the 0.5 mm GB with SDBS were 29.80 ± 1.46 for 1D cells and 29.46 ± 1.21 for 1D columns whereas it was 27.77 ± 2.17 for 1D cells and 27.42 ± 0.92 for 1D columns without surfactants.

For the 0.1 mm GB, the reductions in S_m with chemical enhancement were also clear. The average measured permittivities with SDBS were 32.13 ± 0.38 for 1D cells and 31.33 ± 0.91 for 1D columns and were 25.32 ± 2.19 for 1D cells and 25.58 ± 0.55 for 1D columns without surfactants.

The measured permittivity/estimated permittivity ratios with chemical enhancement matched the ratios shown without chemical enhancement (Figure 184).

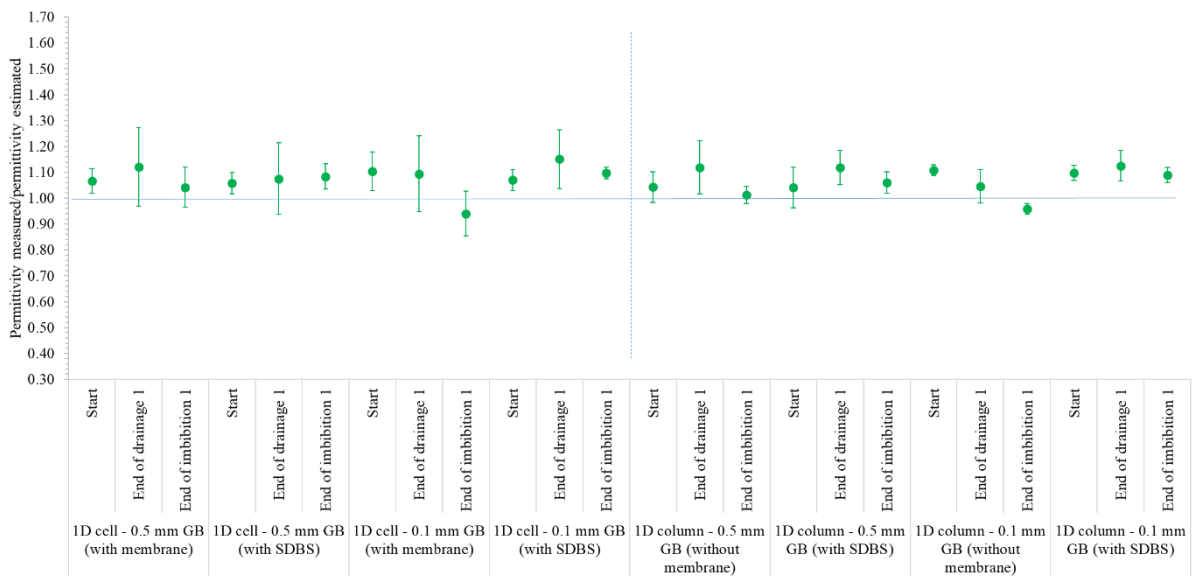


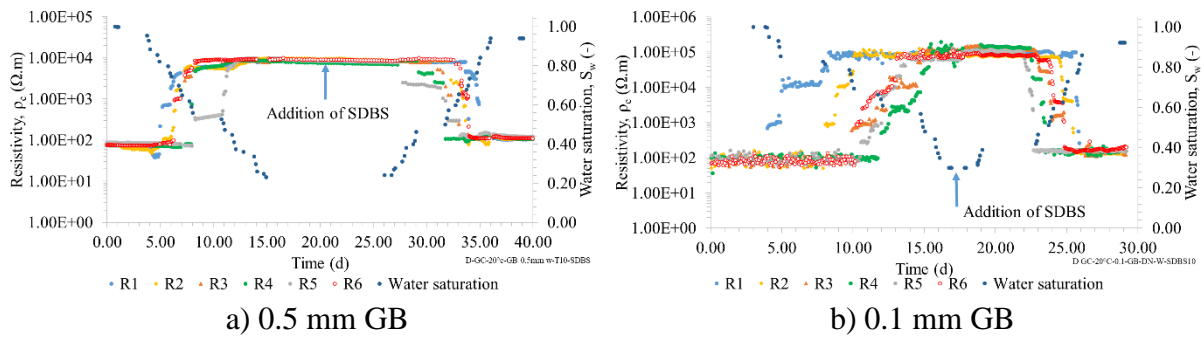
Figure 184: Measured permittivity/estimated permittivity ratios as a function of drainage-imbibition cycle for 0.5 and 0.1 mm GB in 1D cells and 1D columns (with and without chemical enhancement)

The measured permittivity/estimated permittivity ratios were very similar for the 1D cells and 1D columns. At the end of imbibition, these ratios varied between 1.01 and 1.08 for the 0.5 mm GB, and between 0.94 and 1.12 for the 0.1 mm GB.

These results confirmed that surfactants, used at the CMC, do not influence permittivity measurements. This confirms that we can estimate S_m using the TDR probes.

5.3.2.3 Electrical resistivity monitoring

Figure 185 shows changes in resistivities and in S_w as a function of time during a drainage-imbibition experiment conducted with 0.5 and 0.1 mm GB (with chemical enhancement).



a) 0.5 mm GB **b) 0.1 mm GB**
 Figure 185: Evolution of water saturation and resistivity as a function of time in 1D column with chemical enhancement (example of drainage-imbibition experiments with a) 0.5 mm GB and b) 0.1 mm GB)

Variations during drainages for 0.5 mm GB and 0.1 mm GB presented the same characteristics as previously, *i.e.* lower $\rho_c=f(t)$ slopes for 0.1 mm GB, which means a less sharp DNAPL-water interface. During imbibition, after the addition of SDBS, we see that: i. resistivity variations were minimized (lower saltatory effects) and ii., the slopes were steeper. This shows that the capillary effects were reduced and that it is easier to displace the DNAPL-water interface.

The results for water saturation and resistivity (measured and estimated) at the end of the drainages (S_{rw}) and imbibitions ($1-S_m$) are shown in Figure 186.

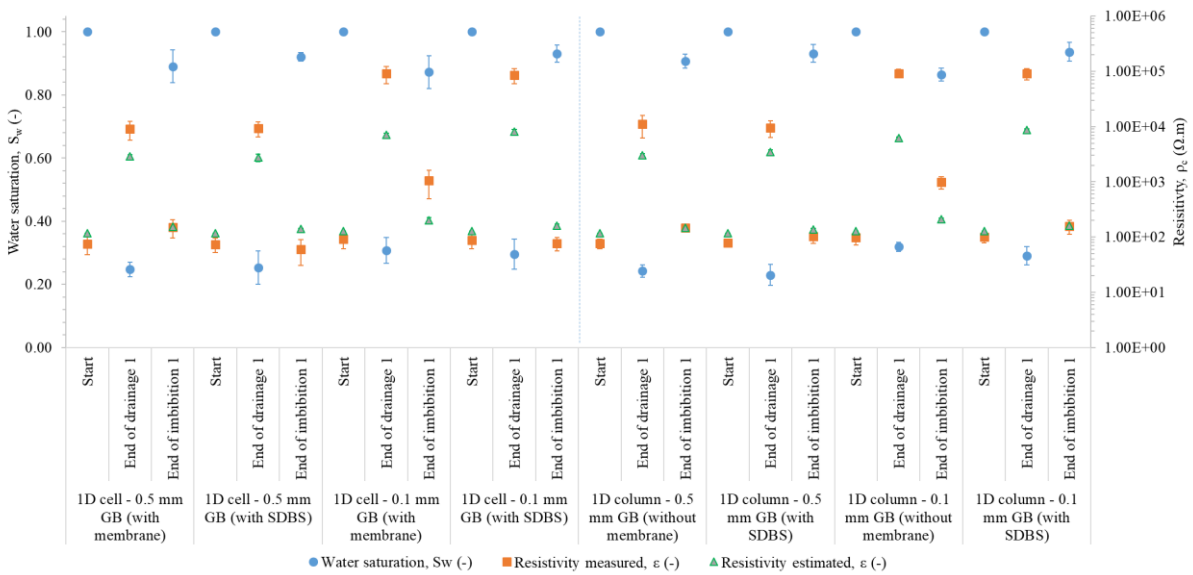


Figure 186: Change in water saturation and resistivity (measured and estimated) as a function of drainage-imbibition cycle for 0.5 and 0.1 mm GB in 1D cells and 1D columns (with and without chemical enhancement)

We can see that the measured resistivities agree with how S_w changes as a function of the drainages and imbibitions (with and without surfactants). Therefore, for 0.5 mm GB in 1D columns, the average resistivities at the end of imbibition were respectively $148 \pm 25 \Omega.m$ without SDBS and $102 \pm 26 \Omega.m$ with SDBS (for respective S_w of 0.91 and 0.93). For 0.1 mm GB in 1D columns, the average resistivities at the end of imbibition were respectively $989 \pm 243 \Omega.m$ without SDBS and $156 \pm 45 \Omega.m$ with SDBS (for respective S_w of 0.87 and 0.93). These results agree with the resistivities measured in the 1D cells.

Figure 187 shows how measured resistivity/estimated resistivity ratios vary as a function of drainage-imbibition cycle.

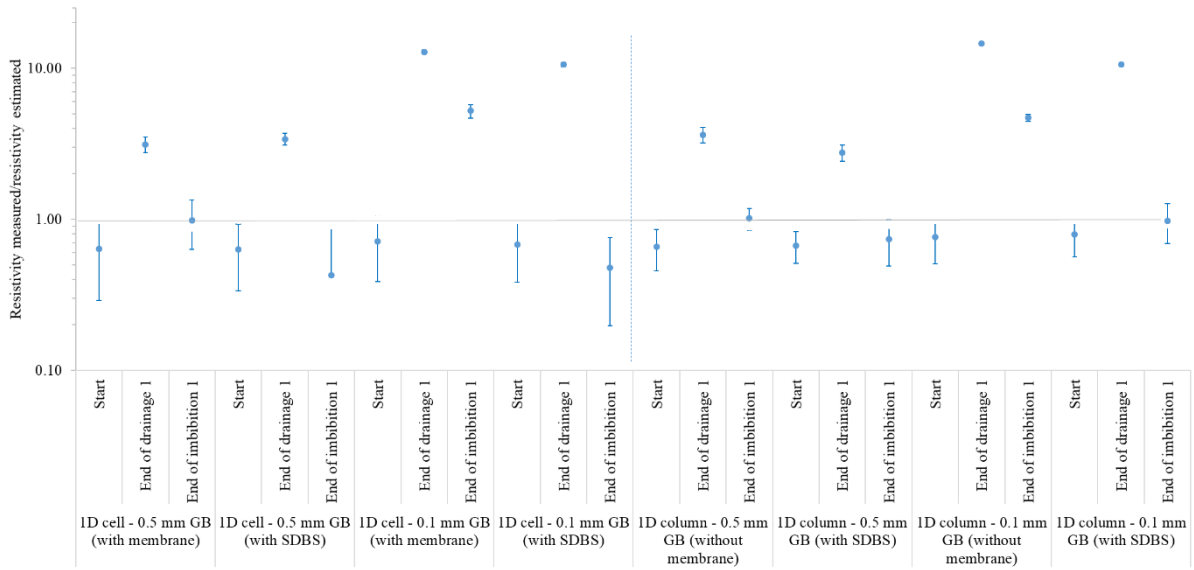


Figure 187: Measured resistivity/estimated resistivity ratios as a function of drainage-imbibition cycle for 0.5 and 0.1 mm GB in 1D cells and 1D columns (with and without chemical enhancement)

The measured resistivity/estimated resistivity ratios for 1D columns agreed with those for the 1D cells. Here also, the estimated resistivity values were underestimated at the end of the drainages. The measured resistivity/estimated resistivity ratios were close to those for the 1D cell experiments. For the 1D columns, these ratios at the end of imbibition after addition of SDBS (which are more important for estimating S_{rn}) are measured to be: 0.74 for 0.5 mm GB (vs 0.43 for 1D cells) and 0.98 for 0.1 mm GB (vs 0.47 for 1D cells).

5.3.3 Experiments in 1 D columns with thermal enhancement

In total, 6 experiments were conducted to estimate the effect of thermal enhancement at the end of drainage 1:

- 3 experiments with 0.5 mm GB without membrane (of which was one monitored with permittivity and resistivity),
- 3 experiments with 0.1 mm GB without membrane (of which was one monitored with permittivity and resistivity).

Figure 188 shows how water saturations changed as a function of the drainage and imbibition cycles for 1D cells and 1D columns with thermal enhancement.

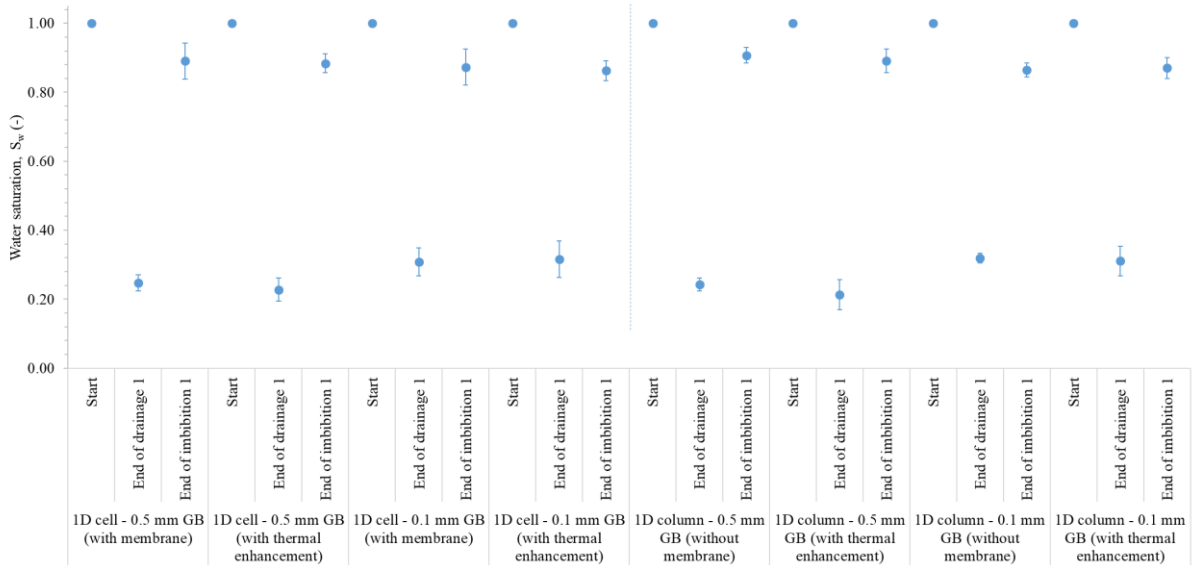


Figure 188: Change in water saturation as a function of drainage-imbibition cycle for 0.5 and 0.1 mm GB in 1D cells and 1D columns (with and without thermal enhancement)

As shown in the previous experiments (without enhancement and with chemical enhancement), the S_{rn} and S_{rw} with thermal enhancement were very similar for the 1D cells and 1D columns. For example, for the 0.5 mm GB, the S_w at the end of imbibition were, 0.88 ± 0.03 and 0.89 ± 0.03 for the 1D cells and 1D columns, respectively. In the same way, for the 0.1 mm GB, the S_w at the end of imbibition were 0.86 ± 0.03 and 0.87 ± 0.03 for the 1D cells and 1D columns, respectively.

The S_{rn} with thermal enhancement were very similar to those we determined without enhancement; therefore, thermal enhancement did not influence recovery yields.

5.3.3.1 Experimental results and comparison with numerical simulation

Only imbibitions were considered, given that the columns were only heated at the end of the drainage to see the effects of thermal enhancement on S_{rn} . Figure 189 compares measured and modeled S_w , as well as the modeled and measured volume of DNAPL in the 1D column, during imbibition.

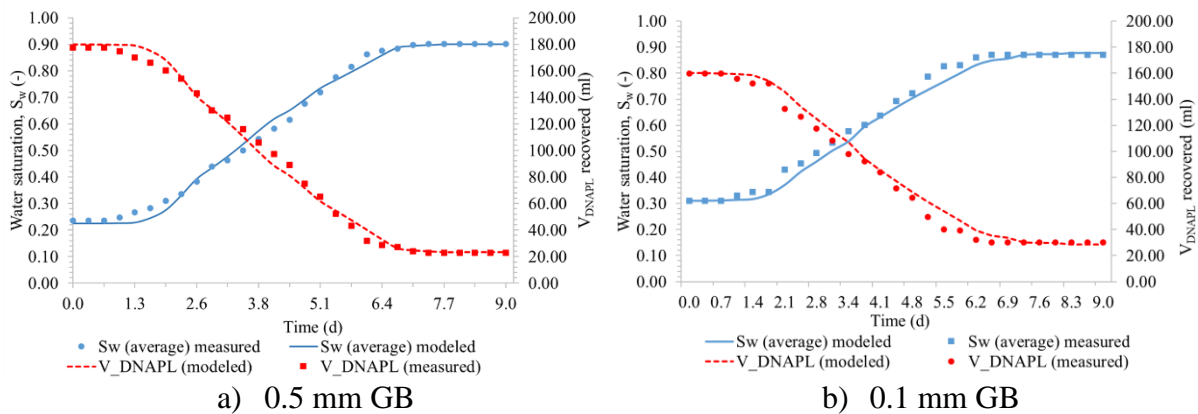


Figure 189: Comparison of drainage-imbibition experiments for a) 0.5 and b) 0.1 mm GB with thermal enhancement (DNAPL modeled volume vs DNAPL measured volume)

The two-phase model with thermal enhancement simulates the S_w variations and the DNAPL volumes recovered as a function of time very well. At the end of the imbibition, the measured value/modelled value ratios were 0.97 for 0.5 mm GB and 1.05 for 0.1 mm GB.

5.3.3.2 Permittivity monitoring

Figure 190 shows changes in ϵ and in S_w (estimated from volume balance) as a function of time during drainage-imbibition experiments conducted with 0.5 mm GB and 0.1 mm GB.

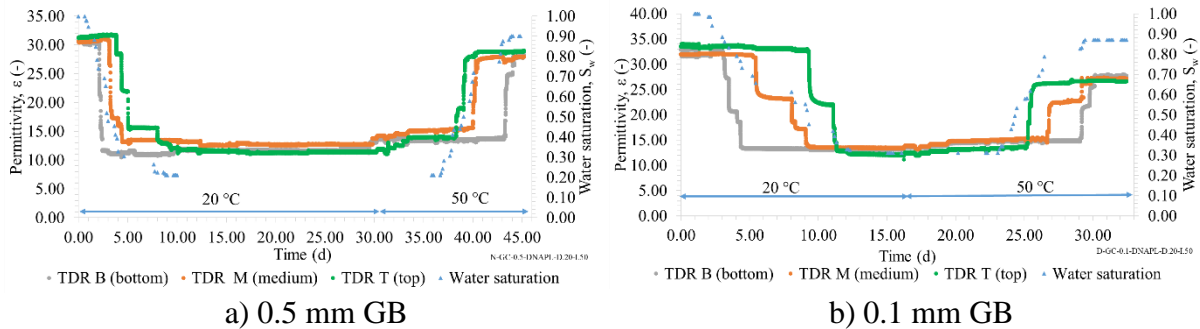


Figure 190: Evolution of water saturation and permittivity as a function of time in 1D column with thermal enhancement (example of drainage-imbibition experiments with a) 0.5 mm GB and b) 0.1 mm GB)

Just as for drainages-imbibitions without enhancement and with chemical enhancement, we observed good correlation between $\epsilon_{\text{measured}}$ variations and S_w . It is interesting to note the detected increase temperature by increasing permittivity at the end of drainage (at $t=31$ d for 0.5 mm GB and at $t=17$ d for 0.1 mm GB). This increase, about 10%, was essentially related to the high DNAPL saturation. Next, when the S_w increased, this overestimation fell, which is logical since the overestimation for $\epsilon_{\text{water+GB}}$ was 2.2%. At the end of imbibition, this overestimation was of the order of 2 to 3%. This corresponds to the estimated values (the $\epsilon_{\text{measured}}/\epsilon_{\text{estimated}}$ ratios were of the same order of magnitude).

The slopes of the $\epsilon=f(t)$ lines were steeper overall with thermal enhancement than without it, which is logical because the viscosity of the DNAPL was higher, so its mobility was too.

Figure 191 shows water saturations, measured and estimated permittivities at the start and the end of drainage and at the end of imbibition.

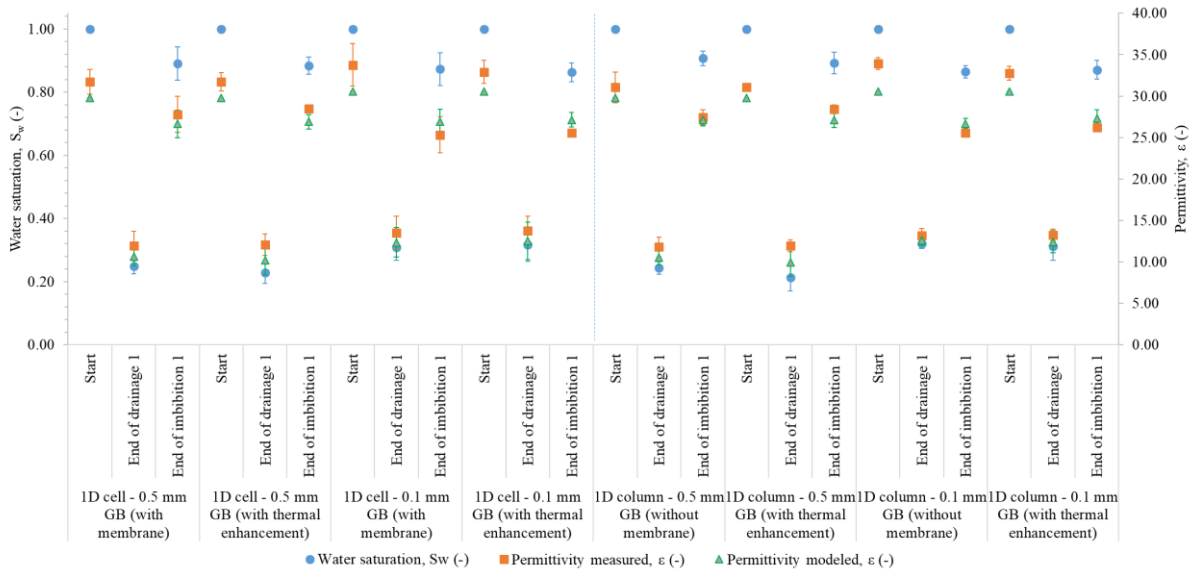


Figure 191: Change in water saturation and permittivity (measured and estimated) as a function of drainage-imbibition cycle for 0.5 and 0.1 mm GB in 1D cells and 1D columns (with and without thermal enhancement)

It has been demonstrated that increasing the temperature (from 20 to 50 °C) slightly increased permittivities (*i.e.* the increase in $\epsilon_{\text{DNAPL+GB}}$ and $\epsilon_{\text{water+GB}}$ was respectively 19.1 and 2.2%, see section 4.2.5.2). Considering that the majority of measured permittivity is essentially related to water, the increase in permittivity due to the temperature increase can be considered as negligible.

The figure leads to the following analysis. For the 0.5 mm GB with thermal enhancement, the permittivities at the end of imbibition were on average 28.50 ± 0.21 and 28.39 ± 0.51 , respectively, for the 1D cells and 1D columns, whereas without thermal enhancement they were 27.77 ± 2.17 and 27.42 ± 0.92 for 1D cells and 1D columns, respectively. Therefore, slight overestimation of $\epsilon_{\text{measured}}$ with thermal enhancement (on average, of the order of 3% for equivalent S_w) was observed.

Regarding the 0.1 mm GB with thermal enhancement, permittivities at the end of imbibition were on average 25.58 ± 0.01 and 26.22 ± 0.52 , respectively, for the 1D cells and 1D columns; whereas, without thermal enhancement they were 25.32 ± 2.19 and 25.59 ± 0.55 , respectively, for the 1D cells and 1D columns. Therefore, here also a slight overestimation in $\epsilon_{\text{measured}}$ with thermal enhancement (which represents an average of the order of 2% here as well for equivalent S_w) is observed.

It is interesting to note that the standard deviations were globally lower with thermal enhancement. This may be related to the lower viscosity (due to thermal enhancement) increasing DNAPL mobility.

The $\epsilon_{\text{measured}}/\epsilon_{\text{estimated}}$ ratios as a function of the drainage and imbibition cycles are shown in Figure 192.

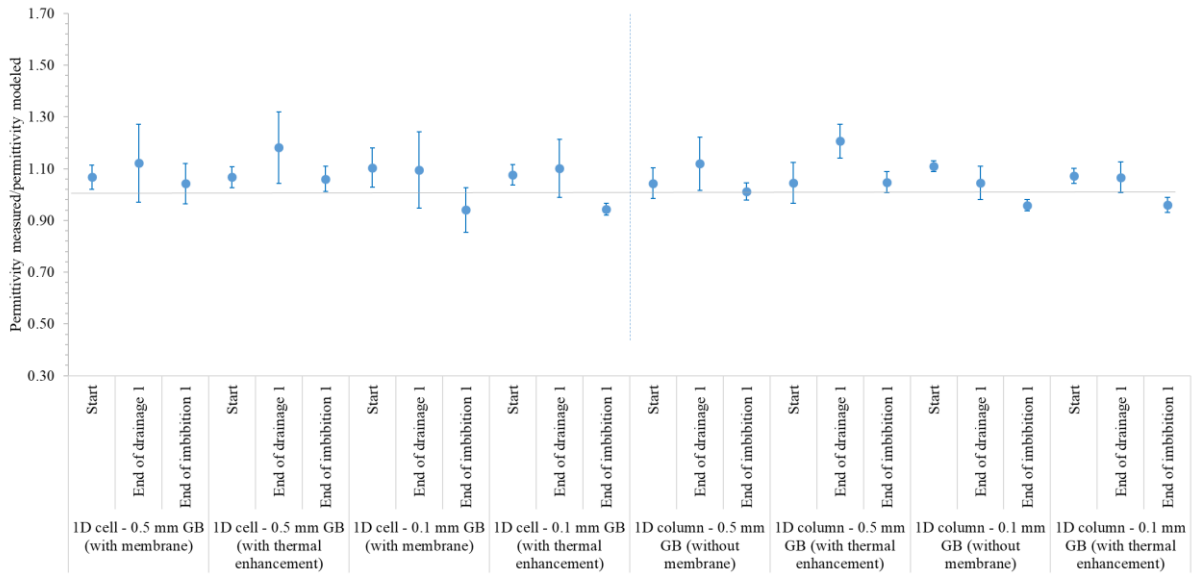


Figure 192: Measured permittivity/estimated permittivity ratios as a function of drainage-imbibition cycle for 0.5 and 0.1 mm GB in 1D cells and 1D columns (with and without thermal enhancement)

For imbibitions, the models consider changes in ϵ_{DNAPL} and ϵ_{water} as a function of temperature. As reported before, we saw good correlations between the measured and estimated permittivity values. As regards thermal enhancement, the $\epsilon_{\text{measured}}/\epsilon_{\text{estimated}}$ ratios vary between 1.05 and 1.06 for the 0.5 mm GB and 0.94 and 0.96 for the 0.1 mm GB.

5.3.3.3 Electrical resistivity monitoring

Figure 193 shows changes in resistivities and in S_w as a function of time during a drainage-imbibition experiment conducted with 0.5 and 0.1 mm GB (with thermal enhancement).

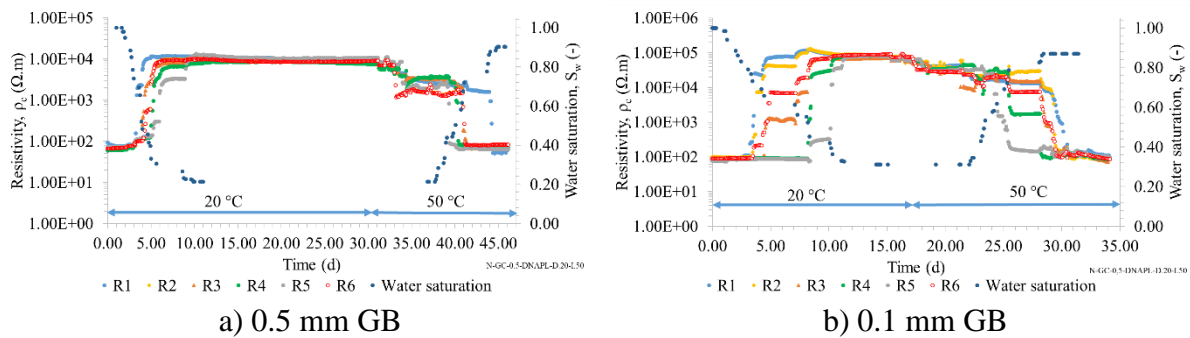


Figure 193: Evolution of water saturation and resistivity as a function of time in 1D column with thermal enhancement (example of drainage-imbibition experiments with a) 0.5 mm GB and b) 0.1 mm GB)

We saw the same variations in resistivity as a function of water saturation as before, and more specifically flatter $\rho_c=f(t)$ curves for the 0.1 mm GB. The reductions in measured resistivities are clear at $t=31$ d for 0.5 mm GB and at $t=17$ d for 0.1 mm GB.

Figure 194 shows water saturations, measured and estimated resistivities at the start and the end of drainage as well as at the end of imbibition.

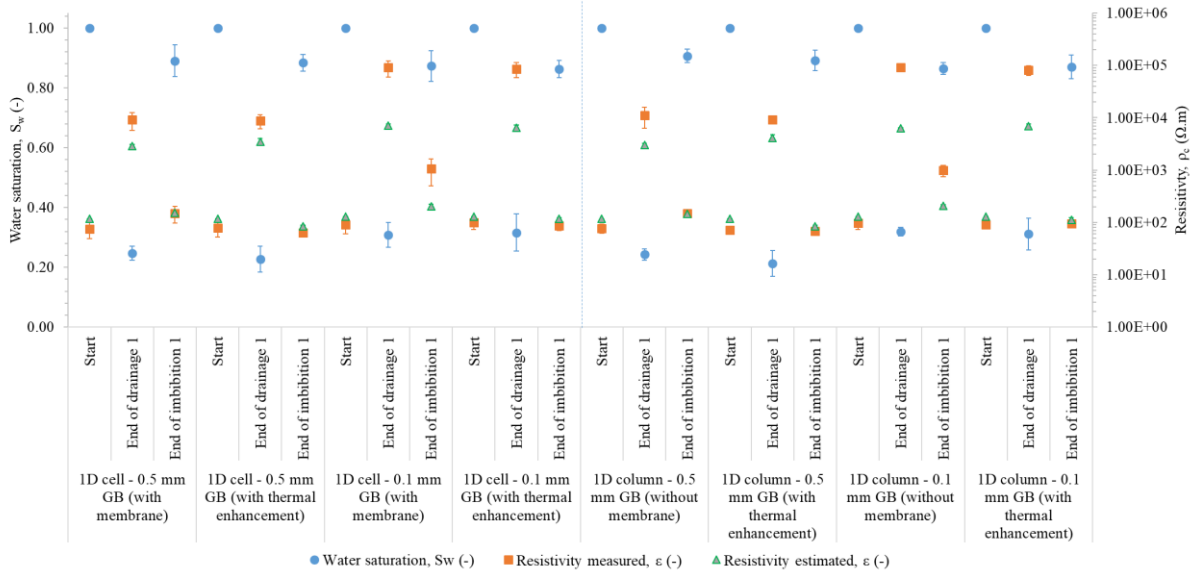


Figure 194: Change in water saturation and resistivity (measured and estimated) as a function of drainage-imbibition cycle for 0.5 and 0.1 mm GB in 1D cells and 1D columns (with and without thermal enhancement)

The resistivities measured with thermal enhancement were influenced by the temperature increase. As reported in section 4.2.5.3, $\rho_{c, \text{DNAPL}+\text{GB}}$ and $\rho_{c, \text{water}+\text{GB}}$ at 50 °C represented respectively 30.3% and 39.6% of the resistivity at 20 °C.

For equivalent S_w , $\rho_{c, \text{measured}}$ at the end of imbibition with thermal enhancement were close for the 1D cells and 1D columns. Therefore, for the 0.5 mm GB, these resistivities were 63 ± 11 and $69 \pm 8 \Omega.m$ respectively for the 1D cells and 1D columns. For the 0.1 mm GB, these resistivities were 87 ± 17 and $96 \pm 12 \Omega.m$, respectively, for the 1D cells and 1D columns.

The values measured with and without thermal enhancement, for equivalent S_w at the end of imbibition, were on average less than a ratio of 2.25 for 0.5 mm GB and 11.17 for the 0.1 mm GB.

Figure 195 shows how measured resistivity/estimated resistivity ratios vary as a function of drainage-imbibition cycle.

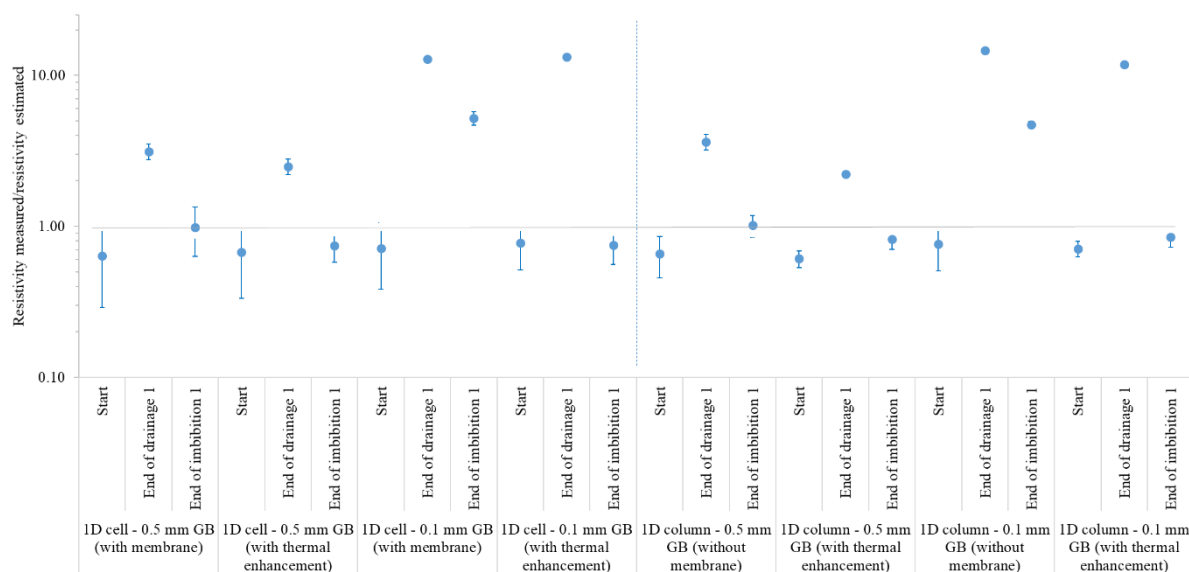


Figure 195: Measured resistivity/estimated resistivity ratios as a function of drainage-imbibition cycle for 0.5 and 0.1 mm GB in 1D cells and 1D columns (with and without thermal enhancement)

The $\rho_{c,measured}/\rho_{c,estimated}$ ratios for thermal enhancement (taking into account for the models of $\rho_{c,DNAPL}$ and $\rho_{c,water}$ at 50 °C) were similar for the 1D cells and 1D columns. Trends highlighted without enhancement and with enhancement are confirmed. Therefore, $\rho_{c,measured}$ were clearly higher than the estimated values at the end of drainage: the ratios varied from 2.22 to 3.62 for the 0.5 mm GB and from 11.83 to 14.64 for the 0.1 mm GB. The ratios at the end of imbibition (corresponding to the determination of S_m) were lower: they varied from 0.74 to 0.82 for the 0.5 mm GB and from 0.75 to 0.85 for the 0.1 mm GB.

5.4 Conclusions

The drainage-imbibition experiments were carried out in 1D columns: i. To characterize the displacement of the DNAPL-water interface according to the applied pressures; ii. To validate the two-phase flow model; iii. To compare the modeled water saturations with the permittivity and resistivity measurements along the column over time; iv. To assess how chemical and thermal enhancements affect recovery yields.

The experiments were conducted with packed column with 0.5 and 0.1 mm glass beads.

A two-phase flow model was developed and run using generalized Darcy's law (pressure-pressure formulation). In this case, the capillary pressure and relative permeability functions used were based on VGM equations. The difference between the measured DNAPL volumes in the 1D columns (by volume balance) and the modeled volumes were very low (less than 5% on average). Moreover, the S_w profile across the column during drainage-imbibition (for 0.5 and 0.1 mm GB) shows that the capillary fringe is sharper for the 0.5 mm GB than for the 0.1 mm GB. In addition, the displacement of the DNAPL-water interface modeled corresponds to what was measured visually within the 1D columns.

From permittivity monitoring, we found that, it is possible to monitor accurately the DNAPL-water interface migration front, as well as estimating how S_w changes over time and in space.

Indeed, the correlations obtained with the CRIM model in 1D cells have been confirmed: the $\epsilon_{\text{measured}}/\epsilon_{\text{estimated}}$ ratios vary between 0.92 and 1.12.

Archie's Law, used to estimate variations in resistivity as a function of S_w , correlates less well with these measurements than for permittivity. The measured resistivity/estimated resistivity ratios were closer to 1 at the end of the imbibition than at the end of the drainage; these ratios at the end of imbibition were 0.98 and 1.01 for the 0.5 mm GB and 4.71 and 5.21 for the 0.1 mm GB. The obtained correlation underestimates the water saturation at the end of drainages. However, since these under- or over-estimations are quantified and relatively stable for 1D cells and 1D columns, we could use them to approximate S_{rn} . Since the standard deviations for the results were relatively high (of the order of 30%), we should: i. use these results with caution; ii. conduct sufficient experiments; iii. correlate the results with permittivities (for which the results were more accurate).

The chemical enhancement experiments were conducted with the addition of SDBS (at the CMC concentration) at the end of drainage. The remediation yields with chemical enhancement were of the same order of magnitude as those reported in 1D cells: 26.4% for 0.5 mm GB and 53.4% for 0.1 mm GB.

We also conducted experiments with thermal enhancement at 50 °C but saw no significant improvement in the remediation yield.

Variations in S_w during the experiments with chemical and thermal enhancement were monitored alongside permittivity and resistivity. The results agreed with those reported without enhancements and with 1D cells.

The results of permittivity and resistivity for 1D cells are coherent with those for 1D columns. The results for S_w , $\epsilon_{\text{measured}}$, $\rho_{\text{c,measured}}$ with and without membrane in the 1D columns demonstrate that it is not necessary to use membranes to approach the water saturation determined with 1D cells with membranes.

Regardless of whether permittivity or resistivity is used, we can monitor saturation variations and quantify residual saturations considering the correction factors (*i.e.* measured values/estimated values) that were quantified as a function of water saturation.

6. EXPERIMENTS IN THE 2D TANK

6. EXPERIMENTS IN THE 2D TANK

The goal of DNAPL pumping experiments in the 2D tank was: i. To validate the two-phase flow model in a dynamic situation during pumping operations and, in particular to assess how the DNAPL-water interface was displaced according to the flow rates applied; ii. To compare the estimated water saturations with the permittivity and resistivity measurements as well as the optical densities during the pumping test (at different flow rates) over time; iii. To assess how chemical and thermal enhancements affect recovery yields. The experiments were performed with two types of glass beads, at different flow rates, without enhancement and with chemical and/or thermal enhancements.

The chapter is completed by a technical and economical analysis of free product recovery with and/or without enhancements.

6.1 Materials and methods

6.1.1 Drainage-imbibition experiments

6.1.1.1 *Experimental set-up*

The 2D tank is made of PVDF and was manufactured by SCODIP in Orléans (France). The main tank is composed of a reservoir for the porous medium and two counter-channels (cavities) on both sides for static level regulation. Counter-channels are connected with the central reservoir through a metallic grid that lets fluids pass through but constrains the glass beads inside the central reservoir.

The 2D tank is thermo-regulated using an internal double-wall ducts inside and between the two glasses. A “LAUDA” water bath (model ECO RE 420) was used for circulating water inside this double-wall duct. It was filled with thermo-regulated water bath via a closed system which makes the water circulate from the LAUDA to the internal tank, from the internal tank to the double-glazing, and finally back to the LAUDA (Figure 196 and Figure 197).

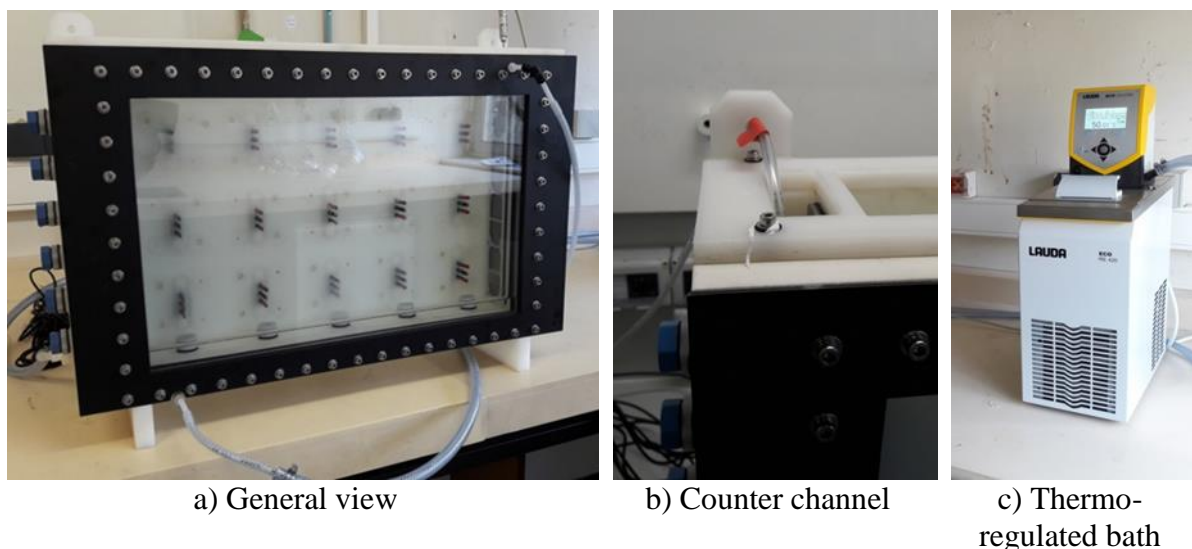


Figure 196: Photograph of the 2D tank (a) general view, b) counter channel, c) thermo-regulated bath)

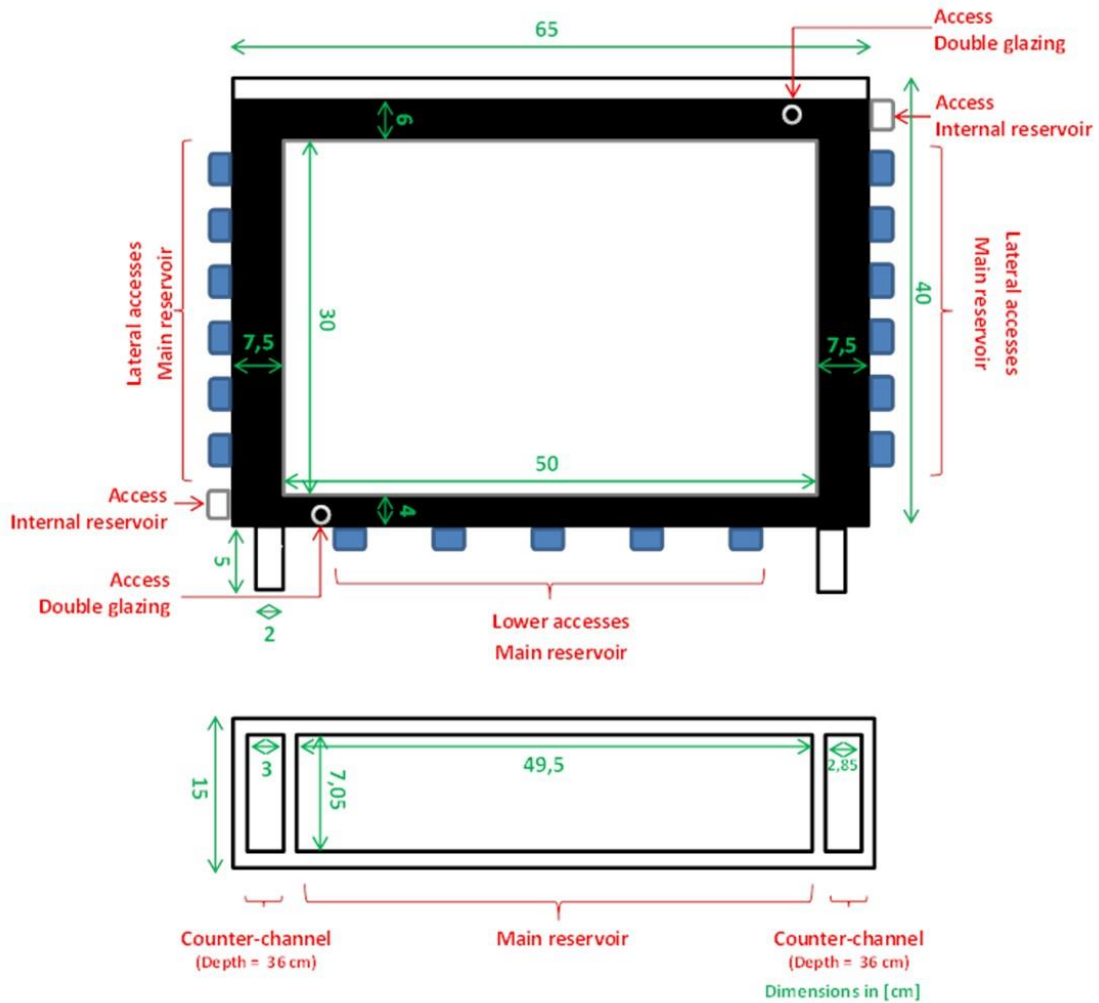


Figure 197: Main dimensions of the 2D tank

The front part of this 2D tank was made of glass in order to photograph the two-phase flow. The back part was made with PVDF in order to plug in a network of geophysical measurement tools (Figure 198 and Figure 199): 15 TDR probes to measure permittivity and 60 geophysics electrodes (30 metallic rod current electrodes for emission and 30 unpolarizable potential electrodes for reception) to measure resistivity in the porous medium. A TDR probe positioned between two currents electrodes and two potential electrodes make a unit of measurement.

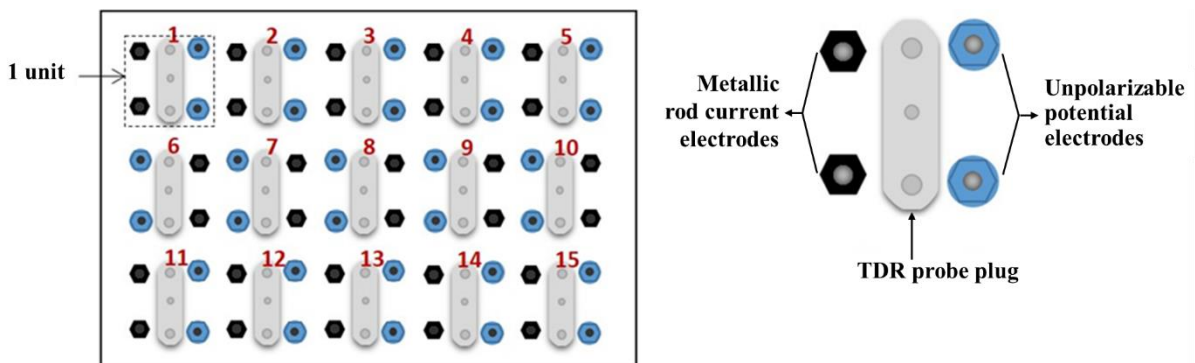


Figure 198: Permittivity and resistivity monitoring probes on the back of the 2D tank



Figure 199: Photograph of the geophysics measurement (TDR and resistivity) tools network on the back of the 2D tank

To allow fluid circulation, the tank also includes lateral access holes (6 on each side and 5 on the bottom as displayed in Figure 197). With the addition of silicone sealant and sealing rings, the tank was considered to be completely sealed and was not expected to have any fluids leaking from any of the possible exits described (geophysics probes, lateral exits, *etc.*).

6.1.1.2 Experimental procedure

a) Drainage-imbibition: liquids pumping and injection system

Before beginning to pack the tank with glass beads, it had to be properly installed. It was connected to peristaltic pumps in order to inject and pump water and DNAPL. The liquids were pumped or injected into graduated cylinders. Two types of peristaltic pumps were used (Watson Marlow 205 and Watson Marlow 530U) (Figure 200).



Figure 200: Photograph of the pumping and injection system for the 2D tank

TYGON 1/4 and 1/8 tubes were used to make all connections. A specific configuration was respected. Figure 201 shows how the pipes were plugged to the tank. It basically consisted of three systems:

- Bottom accesses (plugs): the two on the extremities were used to initially saturate the porous medium with water (at a low flow rate to avoid air bubbles formation). The three

central ones were used to inject or pump the DNAPL during the drainage-imbibition experiment and the downwelling (DNAPL pumping). Most of the time, only the central one was used.

- Static level regulation: Two rods were inserted inside each counter-channel. One of the rods, the upper one, regulated the water static level. The lower one, regulated the DNAPL static level. Two TYGON tubes were fixed to each rod, one for pumping and one for injection 1 centimeter below.
- Central Pump (10 centimeters inside the porous medium): not used until the end to achieve the upwelling (water pumping resulting in the upwelling of the DNAPL surface level).

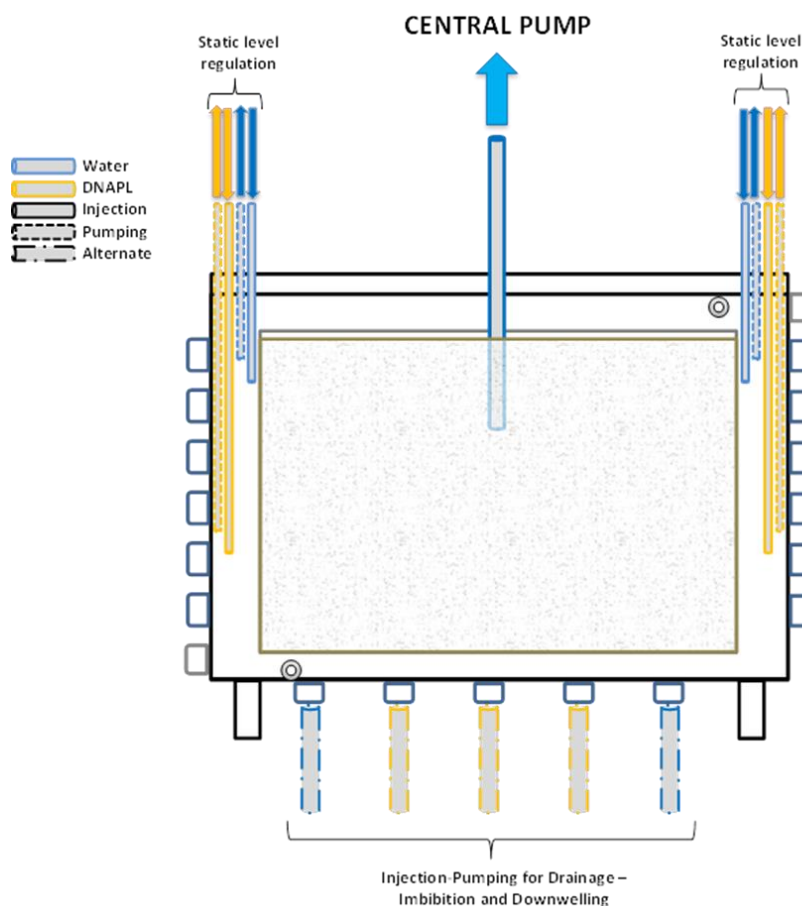


Figure 201: Principle of the injection and pumping device for water and DNAPL

b) Drainage-imbibition and downwelling

Once the set-up was completed, the tank was filled step by step with first 5 cm of glass beads and water injected from the bottom at a low flow rate (to avoid air bubble formation). From that point on, each pumped or injected (possibly evaporated or leaked) volume was precisely noted. Once the tank was full (around 1 centimeter below the top of the glass) and the porous medium was saturated, the DNAPL was injected alternatively through the lower plugs and the static level regulation system, to obtain homogeneous DNAPL penetration inside the system. The injection was stopped when the DNAPL reached half the height of the porous medium (approximately 15.00 cm). Then the pumping experiments at different flow rates could begin (Figure 202).

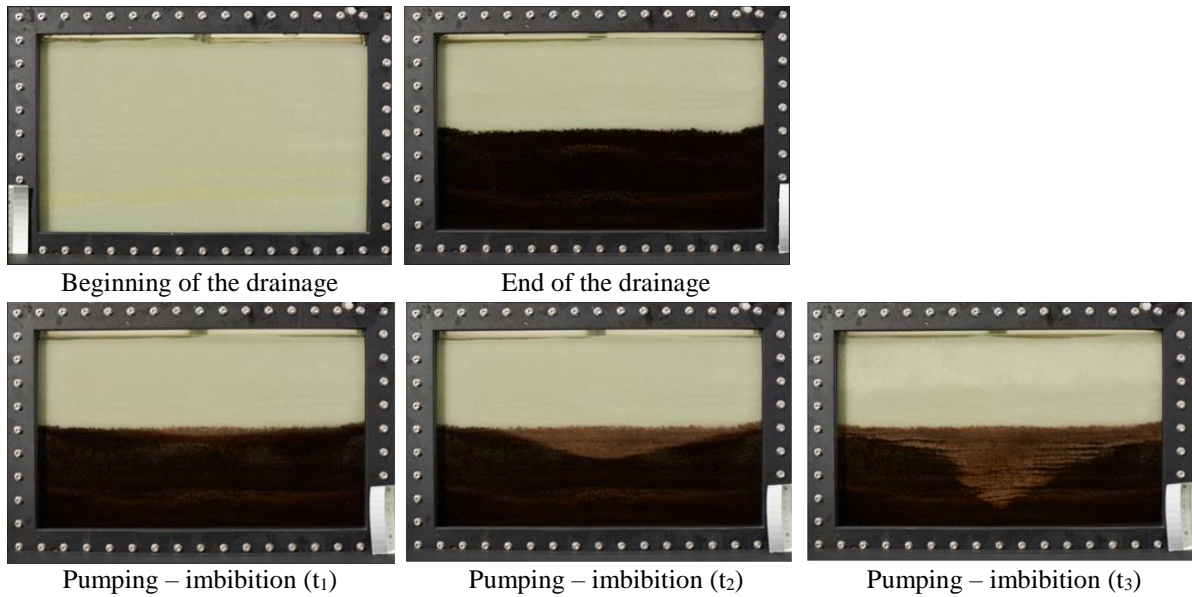


Figure 202: Photograph of the drainage and pumping in the 2D tank

The experiments were carried out with different glass beads (0.1 and 0.5 mm) at different flow rates (50, 150, 220 mL \cdot min $^{-1}$), at two different temperatures (20 and 50 °C), with or without surfactant (SDBS). The DNAPL was pumped by a hole in the bottom central part of the 2D tank. The diameter of the hole was 3.125 cm.

6.1.2 Drainage-imbibition experiments with permittivity and electrical resistivity monitoring

6.1.2.1 Permittivity monitoring

Permittivity was monitored in the same way as described in section 4.1.3.1. The arrangement of the TDR probes, unpolarizable potential electrodes and metallic rod current electrodes is shown in Figure 203. In total, 15 TDR probes were arranged in the 2D tank.

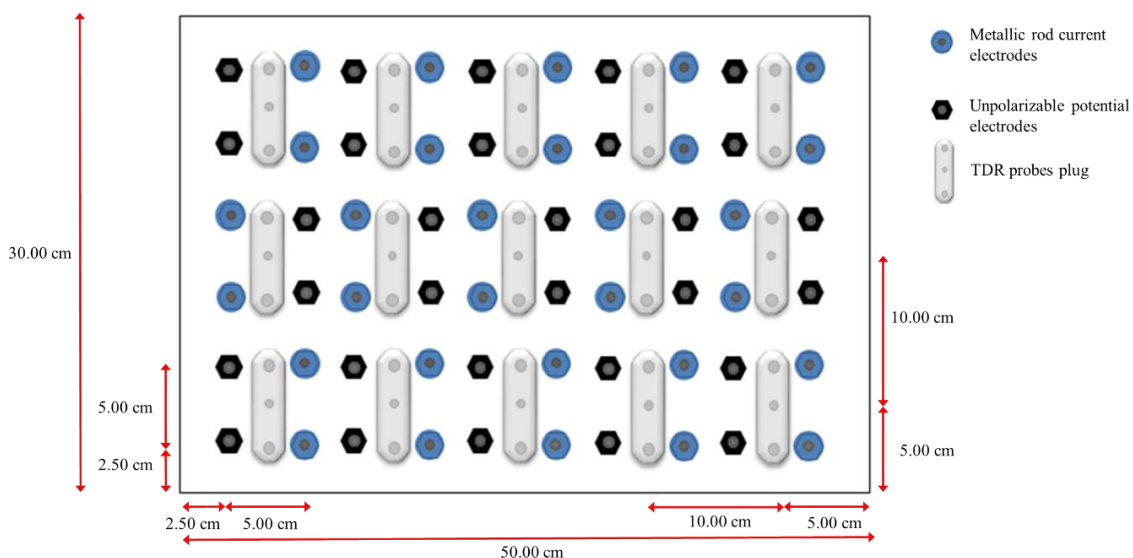


Figure 203: Position of TDR probes, unpolarizable potential electrodes and metallic rod current electrodes in the 2D tank

On the basis of the experiments conducted in 1D cells and 1D columns, the detection zone for the TDR probes is estimated at around 2 mm of said TDR (Figure 204).

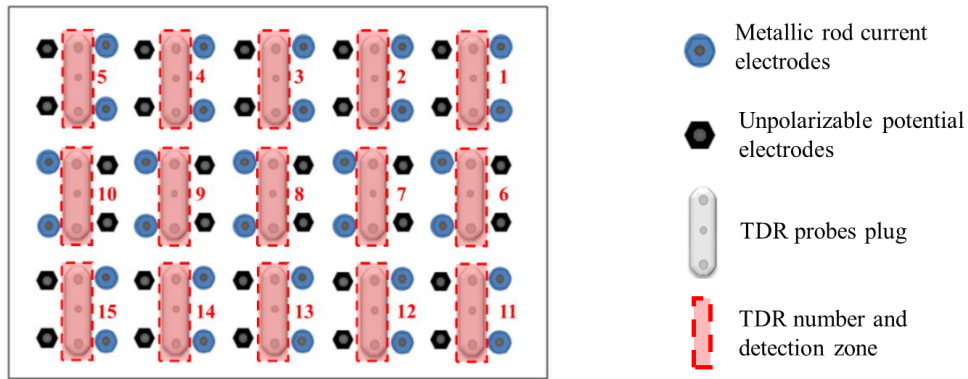


Figure 204: Position of TDR probes with associated detection zones for DNAPL

Permittivity measurements in these detection zones were compared with multiphase flow modeling and image interpretations.

6.1.2.2 Electrical resistivity monitoring

Resistivity was monitored in the same way as described in section 4.1.3.2. The arrangement of the unpolarizable potential electrodes and metallic rod current electrodes is shown in Figure 203. In total, 30 unpolarizable potential electrodes and 30 metallic rod current electrodes were arranged on the back of the 2D tank. On the basis of experiments conducted in 1D cells and 1D columns, the detection zone for resistivity was estimated at around 2.50 mm around those electrodes (Figure 205). Two dipole-dipole injection and reception configurations were programmed (vertical and crossed).

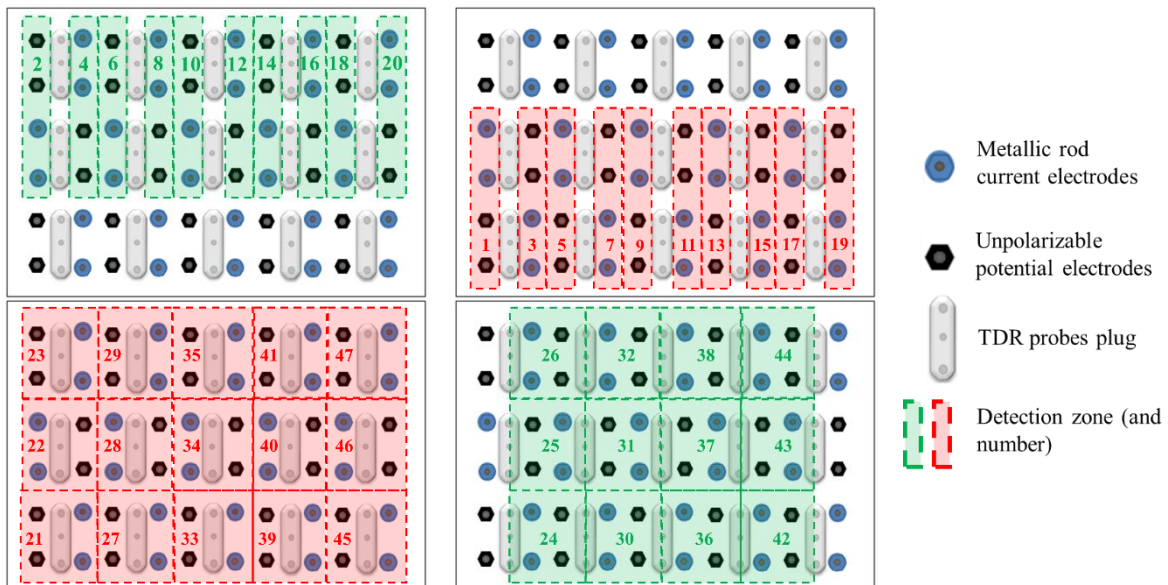


Figure 205: Position of unpolarizable potential and current electrodes with associated estimated detection zones for DNAPL

In all, there were 47 resistivity monitoring zones. The electrode configurations were Wenner for the rectangular vertical detection areas and equatorial dipole-dipole the square detection areas.

6.1.3 Monitoring of the drainage-imbibition experiments with image interpretation

6.1.3.1 Camera set-up

A camera was used to monitor the experiments. Its purpose was to capture changes in the two-phase flow over time inside the porous medium and to estimate DNAPL saturation.

The digital camera used in this study was the Nikon® D810 with NIKKOR LENS 105 (Nikon®). This digital camera has a high resolution of 34 Mega Pixels (7360×4912). Such resolution provides with an optimal image resolution, the highest applied for multiphase flow monitoring. The camera had the following set up: Aperture = 1/200 s, ISO = 100 and the shutter = f/8.

Those particular settings remained the same throughout all experiments. To avoid any reflections and to optimize the contrast that is required for the interpretation, black and white reflectors were set up at precise locations in the laboratory (also determined by the photographer). Moreover, two spotlights were used and set on a precise position and with specific light intensity and orientation. Finally, the camera had to be placed at a specific location and height. The same configuration was used for all experiments.



Figure 206: Photographical set-up with black and white reflectors

Pictures were captured via the software Capture One® which takes photographs without having to touch the camera (the camera should not be moved whatsoever during the whole procedure). All images were acquired on RAW format (.nef) to keep all the information (other formats, like JPEG, lose data).

6.1.3.2 Image interpretation

The image interpretation process is performed as follows:

1. Acquisition of the raw photographs (.nef),
2. Light intensities rectification,
3. Convert the image into 8-bit format to obtain 256 shades of grey,
4. Scaling and orthogonalization of the images,
5. Estimate total residual saturations (whole AOI),
6. Detect the DNAPL-water interface by contrast light intensity,
7. Estimate the shape of the cone of depression,
8. Measure height and radius of cone of depression, thanks to equation of the cone of depression (obtained from point 6),
9. Estimate residual saturations inside the cone of depression,
10. Estimate fingerings (from interface detected in point 5).

First of all, we had to ensure that the images had the same light intensities and the same contrasts at each place on the photograph (and therefore that the settings for the light spots produced uniform light). To achieve this, before processing each image, the color scale (always at the same place, Figure 207) ensures that minor differences in the experimental lighting setup can be corrected.

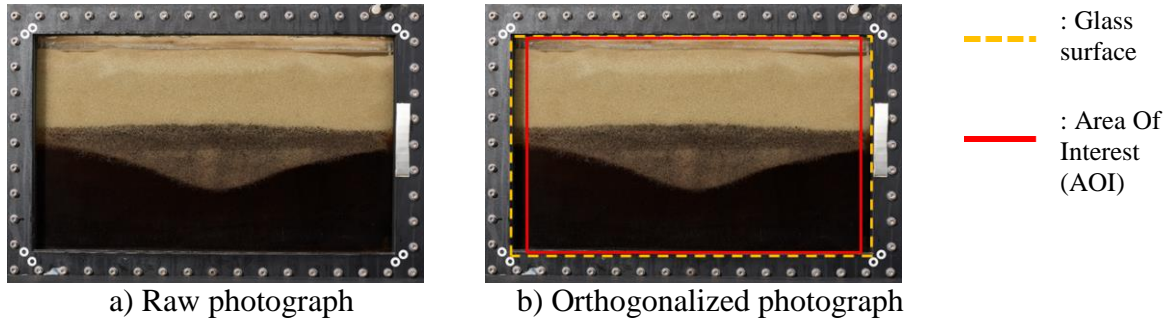


Figure 207: Scaling and orthogonalization

The photographs are converted into 8-bit format to obtain 256 shades of grey according to the procedure described in section 4.1.4.2. Next, the contrast to optimize the black pixels was set-up.

Orthogonalization is achieved using a pair of white eyelets placed at each of the tank’s four corners (Figure 207). The position of these eyelets is set on the 2D tank for all images. These eyelets helps our photograph interpretation system to determine the localization of each border of the grey external metal surface (and the glass surface located behind): centers of each couple of opposite eyelets are aligned with a border. As the internal metal rectangle is a perfect rectangle, each image can be orthogonalized to give the same dimensions and horizontality (even if the takes vary slightly). An Area Of Interest (AOI), smaller than the glass surface, is finally deducted after removal of shadows that appear near the edges of frames (which can alter the quality of the interpretation of images).

These rectification and orthogonalization steps based on the color scale mean that the images processed have the same dimensions (in terms of pixels) and light characteristics.

Total S_n (in the AOI) was determined with Fiji based on optical density and the calibration curve determined in section 4.2.3.5 (Figure 208).

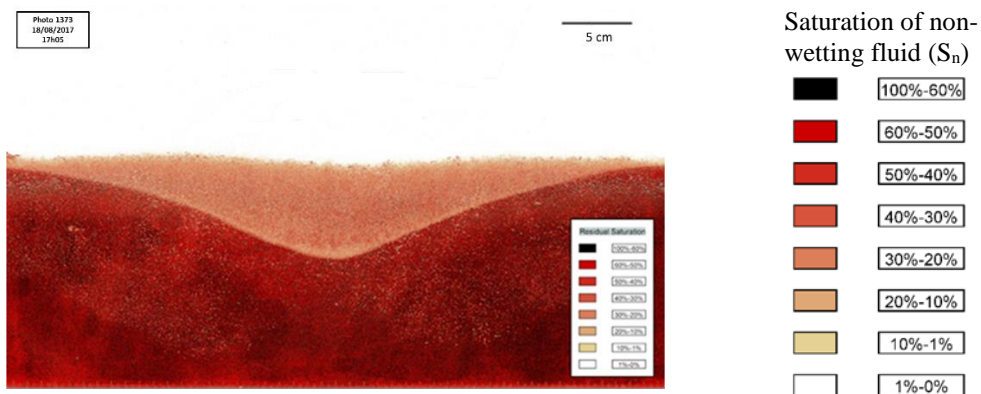


Figure 208: Estimation of the total S_n in the AOI

The interface was detected based on the difference in shades of grey between S_{rw} and S_{rn} . The interface was manually fixed by iteration using expert judgment to best fit the cone of depression visible on the photograph. This operation used Fiji. Figure 209 shows how the cone of depression and DNAPL-water interface (in blue) displacement change.

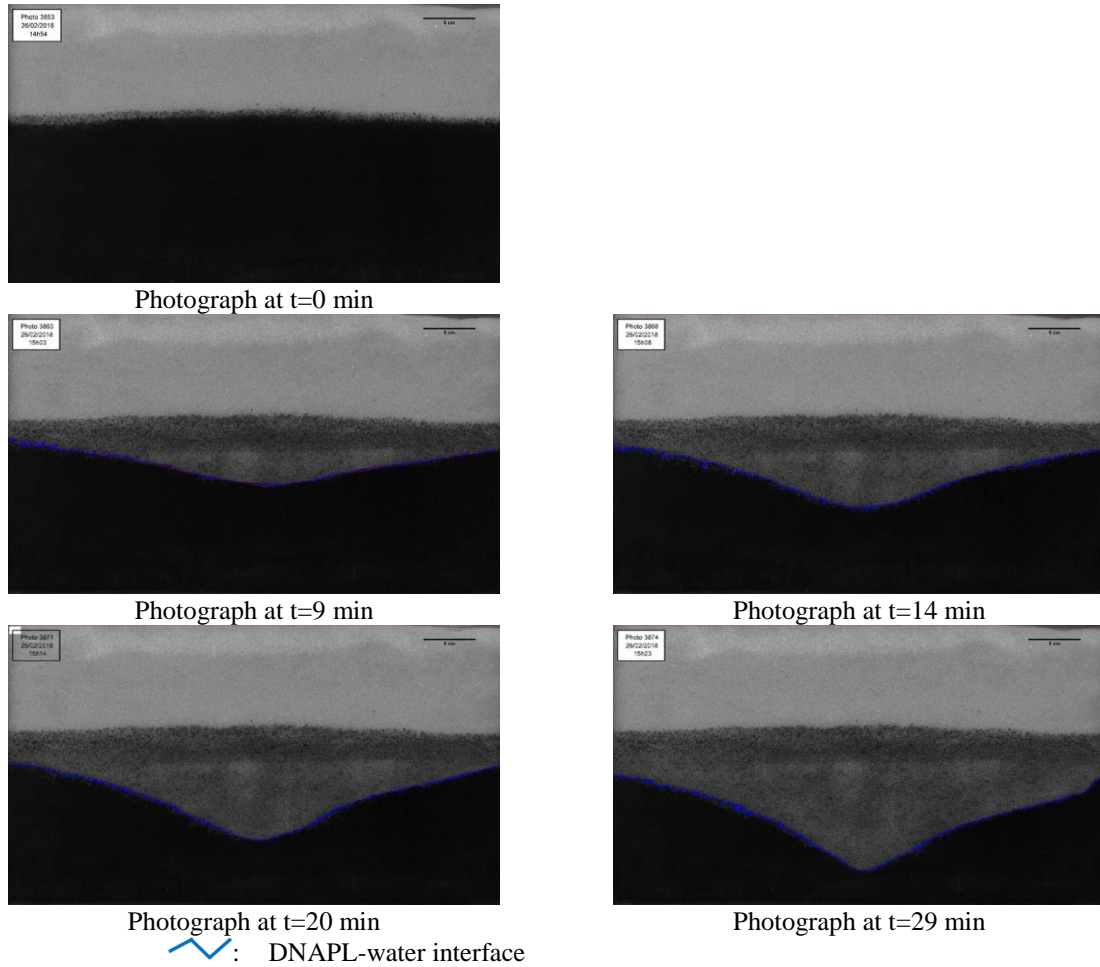


Figure 209: Change in the cone of depression and DNAPL-water interface displacement during pumping test

The interface obtained is constituted of a multitude of points whose coordinates were extracted in Excel. The shape of the cone of depression can be estimated using Hill's slope, Four Parameters Logistic Regression (Eq. 214).

$$y = d \frac{a - d}{1 + \left(\frac{x}{c}\right)^b} \quad \text{Eq. 214}$$

where:

- a: minimum value that can be obtained
- d: the maximum value that can be obtained
- c: the point of inflection
- b: Hill's slope of the curve

Figure 210 presents DNAPL-water interface and fitting with Rodbar equation.

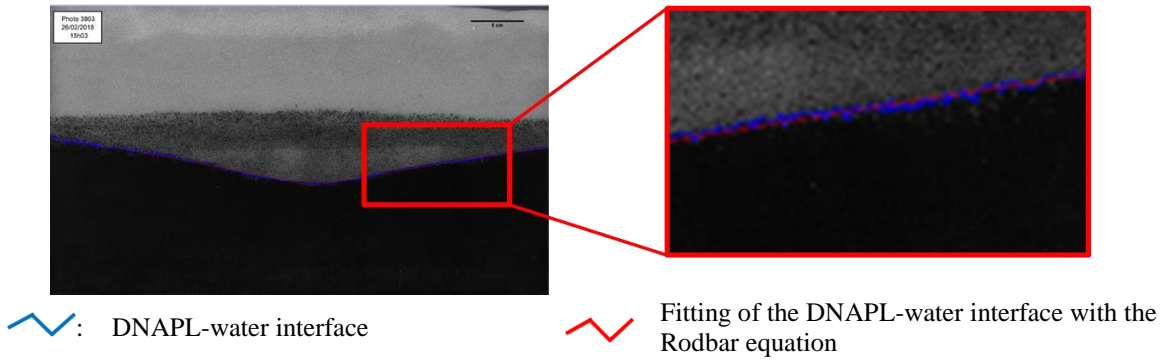


Figure 210: DNAPL-water interface and fitting with the Rodbar equation

The height and radius of the cone of depression in each photograph were automatically calculated from the equation determined in the previous step (Figure 211). The areas of the cone of depression were also determined in each photograph.

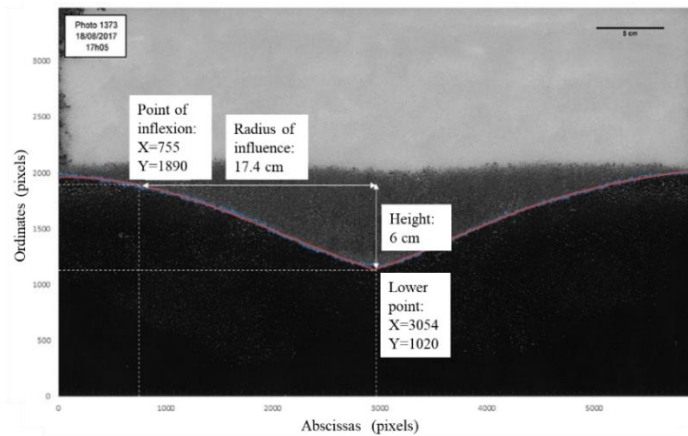


Figure 211: Measuring height and radius of the cone of depression

Next, S_n was estimated inside the cones of depression (Figure 212). We took this approach because sometimes it was difficult to maintain the pressure heads on the edges of the 2D tank. That displaced the DNAPL-water interface (upwards or downwards), and consequently changed the global S_n .

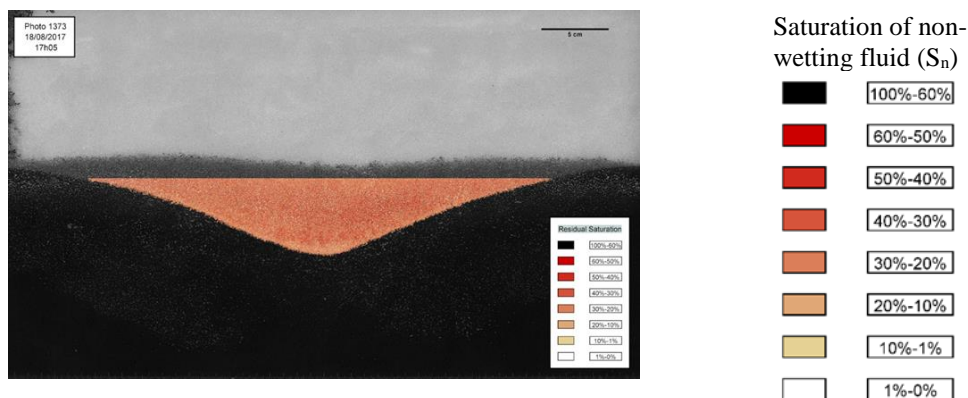


Figure 212: Estimation of S_n in the cone of depression

We took two approaches to incorporate the optical densities: “counting box” and “layers” (see section 2.7.2.2 for more details). The counting box consists in determining the optical densities in a square of 50×50 pixels then to consider the average of the optical densities measured for

the whole square. The square size was chosen to ensure the best compromise between measurement accuracy and the time calculation. By adding these averages we determined the volume of DNAPL, using Eq. 189.

The other approach was to determine which areas in the AOI had optical density within a determined interval. This interval is called layers. By adding these layers, we determined the volume of DNAPL, using Eq. 189.

The preliminary results showed that the approach using layers gave us an estimate of the DNAPL volumes pumped (as a function of time) with better accuracy than the counting box method. This is related to the fact that during pumping, the squares along the DNAPL-water interface correspond in part to an area to the S_m and in part to an area relative to the S_{rw} . The binary approach, corresponding to setting an average per square, was not therefore suitable; it generated less useful results than the layers approach. In this study, only the layers approach was therefore considered.

Next, fingerings were estimated to characterize more precisely the DNAPL-water interface displacements. To achieve this, the shape of the cone of depression was estimated based on Eq. 214; and it was compared to the actual interface between the DNAPL and water. The estimated interface and the actual interface were then flattened using Fiji (transposing the fitting curve into a horizontal axis, y) (Figure 213). This flattening is necessary for the statistical study of the fluctuation height interface.

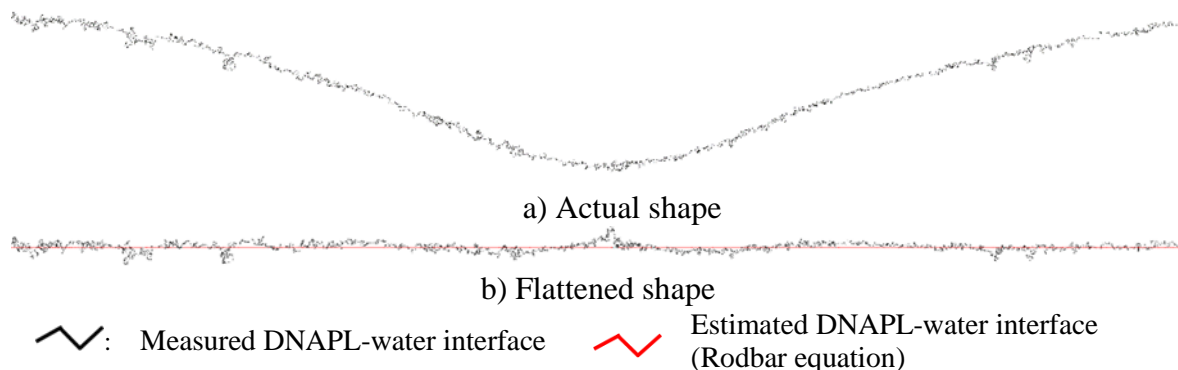


Figure 213: Comparison of the estimated and measured DNAPL-water interfaces with the Rodbar equation (a) actual shape and b) flattened shape)

Statistical comparison using XLSTAT then showed the differences between the estimated and measured DNAPL-water (standard deviation, percentile, etc.). XLSTAT is a user-friendly statistical software for Microsoft® Excel.

First, all the previous detailed operations were done manually. Next, these time consuming tasks were automated using several scripts, using VBA programming language for Excel and ImageJ Macro programming language for ImageJ [Schindelin *et al.* (2012); Rueden *et al.* (2017)]. Some other specific plugins used were as follows:

- Find eyelets [Tseng (2011)],
- Find the blank on the color scale [Herbert *et al.* (2014)],
- Orthogonalization [Schlüter (2008)].

In parallel with the global monitoring of change in optical density in the entire AOI and in the cone of depression, we also monitored how the mean optical density changed in the TDR (15 areas) and geophysical electrodes (47 zones) detection areas (Figure 204 and Figure 205).

6.2 Numerical and mathematical modeling

All numerical studies were performed using COMSOL Multiphysics®. The results presented in this chapter only relate to modeling with pressure-pressure formulations that displayed better results (Table 46: Eq. 61 to Eq. 64, Eq. 85, Eq. 110 to Eq. 112, Eq. 114, Eq. 212).

6.2.1 Design of the model

As the 1D column modeling, the capillary pressure and relative permeability functions are related to water saturation based on VGM relationships obtained from small cell experiments.

The experimental results considered for the modeling were based on:

- the drainage-imbibition experiments for 0.5 and 0.1 mm GB (α , n , S_m and S_{rw}): without enhancement (Table 40, p. 133), with SDBS (Table 43, p. 154) and with thermal enhancement (Table 45, p. 165),
- the measured rheological parameters:
 - dynamic viscosity (Figure 49, p. 100),
 - density (Figure 58, p. 109).

6.2.2 Initial values and boundary conditions

A screen shot of the geometry and meshes of the 2D tank is presented in Figure 214. There are 3965 triangular meshes.

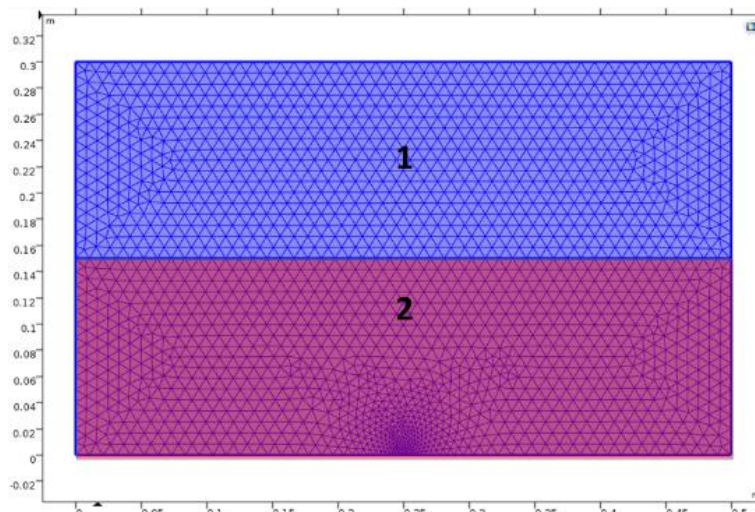


Figure 214: Mesh scale and geometry of the 2D tank

In COMSOL Multiphysics®, two subdomains with different storage models were built. The upper zone (zone 1), which is only concerned with single water phase flow neglecting the capillary effect in this zone; the lower zone (zone 2), which is concerned with two-phase flow of water and DNAPL.

6.2.2.1 Initial values

The pumping (imbibition) began once drainage had finished. The DNAPL was injected from the bottom of the 2D tank up to a height of 15.00 cm. The initial conditions were therefore the following:

- $P_w = \rho_w g(0.3-y)$,
- $P_n = 2300 + \rho_n g(0.15-y)$ for 0.1 mm GB and $P_n = 1700 + \rho_n g(0.15-y)$ for 0.5 mm GB

The values 0.3 and 0.15 cm are the heights of the air-water interface and the DNAPL-water interface in the 2D tank, respectively. The values 1700 and 2300 Pa mean additional DNAPL pressure to support DNAPL at height of 0.15 m and keep the saturation of water close to the S_{rw} for $t=0$.

6.2.2.2 Boundary conditions

Figure 215 shows the boundary conditions for imbibition in the 2D tank experiments.



2, 6, 7: no flow

4: not applicable

1, 3, 5, 8 and 9: $P_w = \rho_w g(0.3-y)$

2, 4, 7: no flow

1 and 8: $P_n = 2300 + \rho_n g(0.15-y)$ for 0.1 mm GB*

1 and 8: $P_n = 1700 + \rho_n g(0.15-y)$ for 0.5 mm GB*

6: pumping flow rate of the DNAPL

*: 1700 and 2300 [Pa] mean additional DNAPL pressure to support DNAPL at height of 0.15m and keep the saturation of water close to the S_{rw} for $t=0$

Figure 215: Boundary conditions for imbibition in the 2D tank

6.3 Results and discussion

6.3.1 Experiments in the 2D tank without enhancement

The pumping experiments (imbibition) were conducted with 0.5 and 0.1 mm GB without enhancement. We modeled imbibition and monitored variations in optical density, permittivity and electrical resistivity. Appendix 8 shows the results for the 2D tank experiments without enhancement.

6.3.1.1 Experimental results: comparison of numerical simulation with optical density monitoring

Several imbibition experiments were performed with the 2D tank (all the experiments were monitored with optical density, permittivity and resistivity):

- 3 experiments with 0.5 mm GB at three different pump flow rates: 50, 150 and 220 mL.min⁻¹,
- 3 experiments with 0.1 mm GB at three different pump flow rates: 50, 150 and 220 mL.min⁻¹.

We compared modeling with optical density monitoring in several steps: presentation of the modeling results, estimation of the volume of DNAPL recovered, estimation of the DNAPL-water interface displacement, comparison of DNAPL volumes recovered estimated by modeling and by image interpretation, change in fingerings of the DNAPL-water interface, and parametric study of the model.

a) Modeling results

Figure 216 shows the results of S_w modeling over time during DNAPL pumping with 0.5 and 0.1 mm GB.

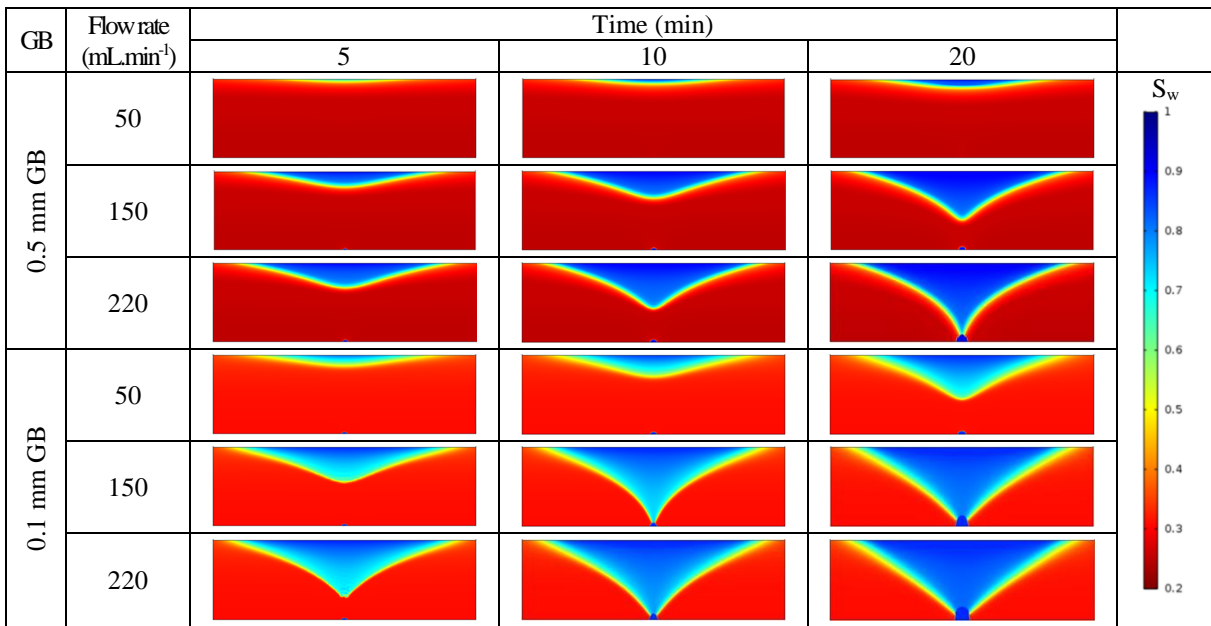


Figure 216: Water saturation modeling over time during DNAPL pumping with 0.5 and 0.1 mm GB (without enhancement)

As expected, we see that the capillary fringe was greater for the 0.1 mm GB than for the 0.5 mm GB (for further details, see Figure 218). For similar flow rates, the cone of depression was higher for the 0.1 mm GB than for the 0.5 mm GB. Figure 217 shows measured and modeled volumes of DNAPL as a function of time.

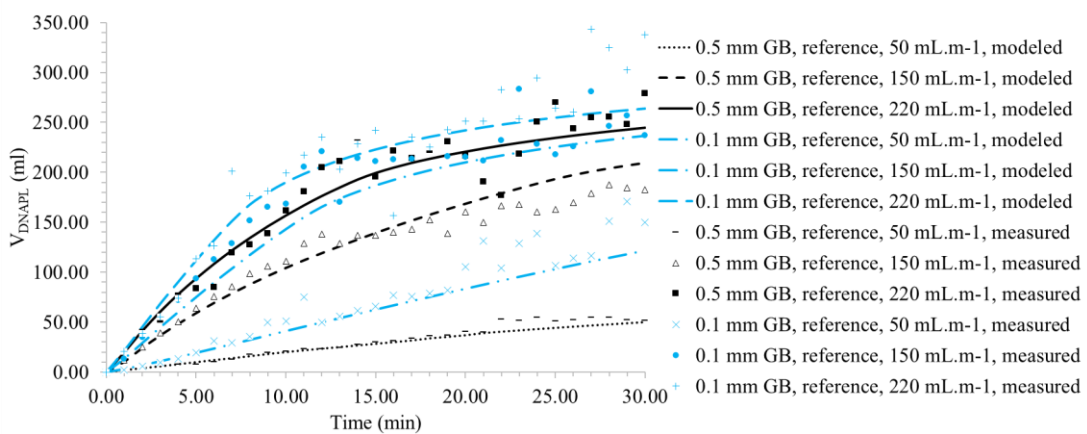


Figure 217: Evolution of measured and modeled volumes of DNAPL recovered for different flow rates with 0.5 and 0.1 mm GB (without enhancement)

Figure 217 shows that for 0.5 mm GB, at same flow rate, the depression surface area was lower. This is due to the difference in permeability making a more vertical DNAPL-water interface for 0.5 mm GB.

Figure 218 shows how S_w changed as a function of time along the horizontal and vertical profiles located at the center of the tank.

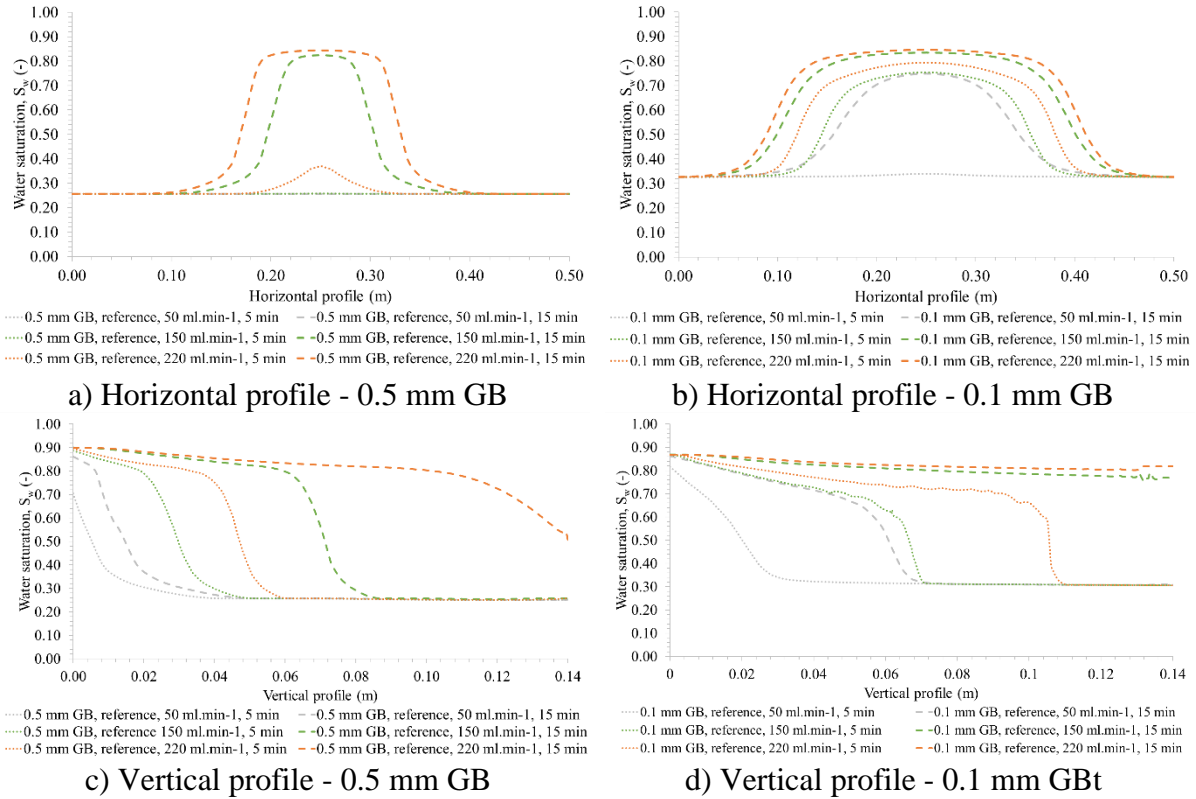


Figure 218: Evolution of the S_w along a) and b) horizontal profile and c) and d) vertical profile at the center of the 2D tank with 0.5 and 0.1 mm GB (without enhancement)

The horizontal water saturation profile shows the cone of depression radii and capillary fringes. We see that the transition zones between S_{rn} and S_{rw} are sharper for the 0.5 mm GB than for the 0.1 mm GB. This is in agreement with what Figure 164 shows. For example, this transition zone was 0.08 and 0.14 m for a flow rate of $150 \text{ mL}\cdot\text{min}^{-1}$ at 15 min, respectively for the 0.5 mm GB and the 0.1 mm GB. Moreover, the radius of the cone of depression was higher for the 0.1 mm GB than for the 0.5 mm GB. For example, it can be estimated (by measuring the length of the curve's top plateau as a first approach) at 0.05 and 0.14 m respectively for the 0.5 and 0.01 mm GB (for a flow rate of $150 \text{ mL}\cdot\text{min}^{-1}$ at 15 min).

From the vertical saturation profile we can also estimate the height of the cone of depression. For a flow rate of $150 \text{ mL}\cdot\text{min}^{-1}$ at 5 min, the height was 0.05 and 0.07 m respectively for the 0.5 mm and 0.1 mm GB. The graphs show a sharper capillary fringe for the 0.5 mm GB than the 0.1 mm GB. The DNAPL-water transition zone was smaller when the flow rates were higher.

b) Volume of DNAPL recovered

Figure 219 shows the measured and modeled volumes of DNAPL recovered during experiments.

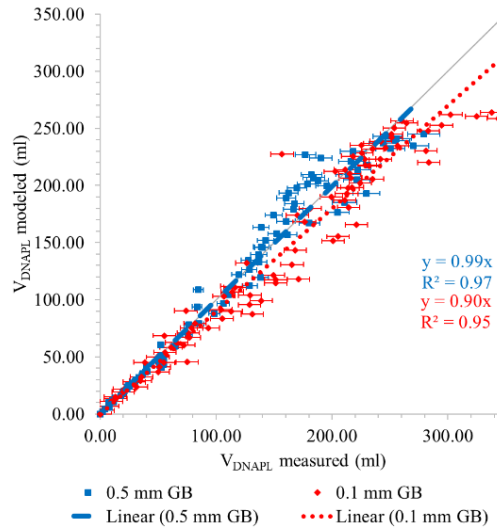


Figure 219: Comparison of measured and modeled volumes of the DNAPL recovered in the 2D tank with 0.5 and 0.1 mm GB (without enhancement)

Figure 219 shows that the experimental and modeled volumes of DNAPL recovered were very similar. The $V_{\text{DNAPL measured}}/V_{\text{DNAPL modeled}}$ ratios vary between 0.75 and 1.3 for 0.5 mm GB and between 0.69 and 1.65 for 0.1 mm GB. The linear regression curve gradients are very close to 1: 0.99 for 0.5 mm GB and 0.90 for 0.1 mm GB. The coefficients of determination were closer to 1 for the 0.5 mm GB ($R^2=0.97$) than for 0.1 mm GB ($R^2=0.95$), which obviously shows more highly dispersed data for the 0.1 than for 0.5 mm GB.

c) DNAPL-water interface displacement

The modeled DNAPL-water interfaces displacement were compared with the interfaces from image interpretation. Figure 220 shows examples of these comparisons.

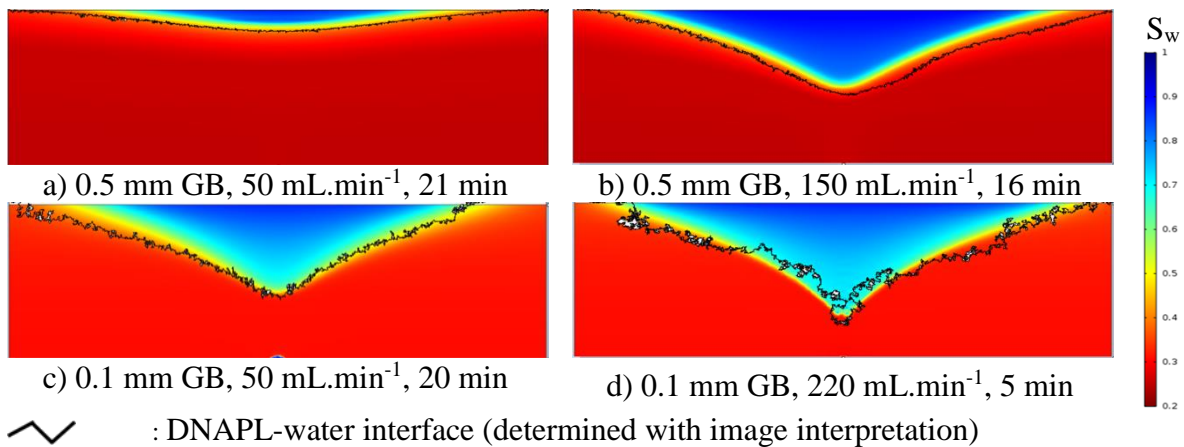


Figure 220: Comparison of measured and modeled DNAPL-water interface in the 2D tank at different times with a) and b) 0.5 mm GB and c) and d) 0.1 mm GB (without enhancement)

Figure 220 shows how the modeled DNAPL-water interface changes can be superimposed correctly with the experimental change by determined from image interpretation. We see that the interface was much tortuous for the 0.1 mm GB than for the 0.5 mm GB.

Figure 221 compares measured and modeled radius and height of the cone of depression with 0.5 mm GB and 0.1 mm GB.

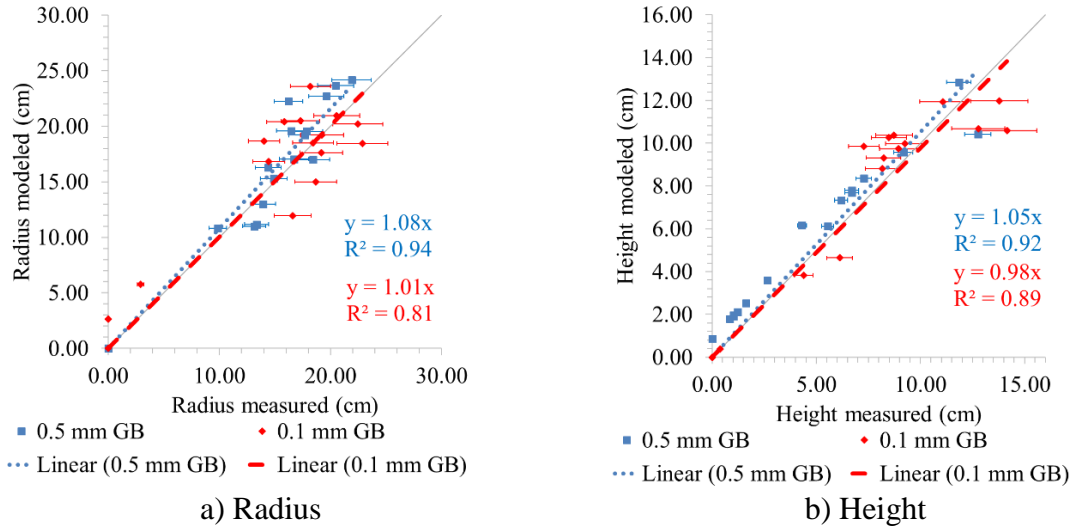


Figure 221: Comparison of measured and modeled a) radius and b) height of the cone of depression with 0.5 and 0.1 mm GB (without enhancement)

By comparing the radii and cone of depression heights we can better assess how the model fits the experimental results. Generally, the proposed model reproduces the shape of the cone of depression well. Therefore, for the modeled and measured radii, the linear regression curve gradients were 1.08 ($R^2=0.94$) and 1.01 ($R^2=0.81$) respectively for the 0.5 mm and 0.1 mm GB. For the cone of depression heights, linear regressions confirm that the model is valid: the curves were respectively 1.05 ($R^2=0.92$) and 0.98 ($R^2=0.89$).

The modeling of the experimental data was less accurate for the 0.1 mm GB than for the 0.5 mm GB. This is because the fingerings and preferential pathways were more important for the 0.1 mm GB, which affects the experimental repeatability.

d) Comparison of estimated recovered DNAPL volumes by modeling and image interpretation

From the variations in S_n , calculated from optical densities, we can estimate how the DNAPL volumes vary over time (using Eq. 189). We considered these estimations for determining the areas of the cones of depression. However, the volumes calculated by image interpretation cannot be compared directly with the volumes estimated previously in Figure 217. In fact, we must look at the difference between the total recovered DNAPL volumes and the volumes of DNAPL that come from lateral inflows. Figure 222 shows the Darcy velocity fields for wetting and non-wetting fluids for 0.5 mm GB with a flow rate of $150 \text{ mL}\cdot\text{min}^{-1}$.

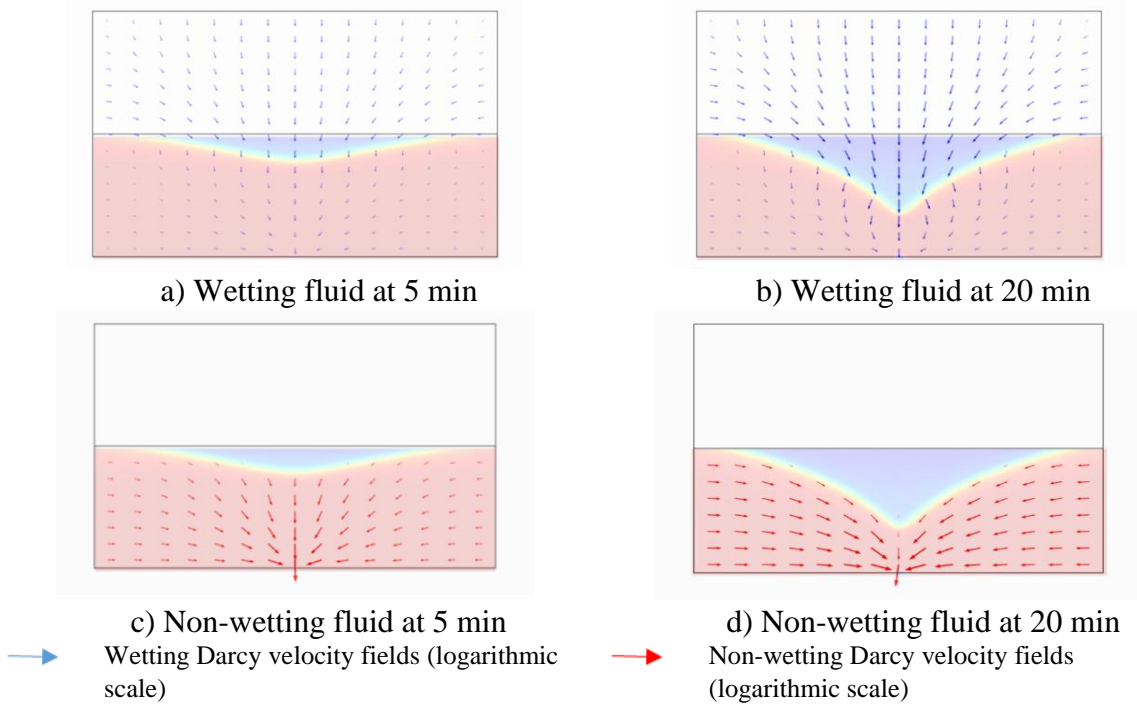


Figure 222: Darcy velocity fields for a) and b) wetting and c) and d) non-wetting fluids for 0.5 mm GB with a flow rate of 150 mL.min⁻¹ (without enhancement)

This figure shows that the lateral DNAPL flow rates became higher as the experiment advanced. Figure 223 shows the results of modeling for $V_{DNAPL\ pumped}/V_{DNAPL\ lateral}$ ratios as a function of time at different flow rates.

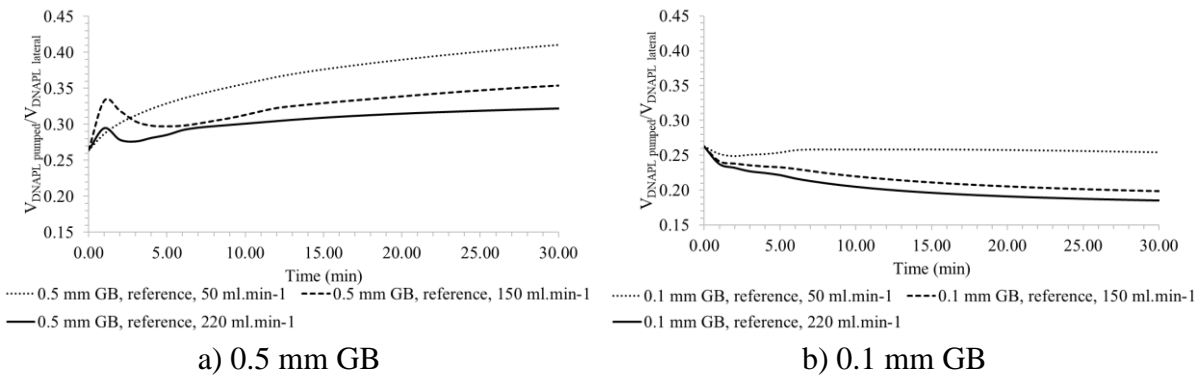


Figure 223: Evolution of the modeled $V_{DNAPL\ pumped}/V_{DNAPL\ lateral}$ ratios for different flow rates with a) 0.5 mm GB and b) 0.1 mm GB (without enhancement)

For 0.5 mm GB, the lateral flow portion varied between 0.26 and 0.41. For low flow rates, the cone of depression heights were smaller and the lateral V_{DNAPL} were higher. Therefore, for 50 mL.min⁻¹, the $V_{DNAPL\ pumped}/V_{DNAPL\ lateral}$ ratios varied between 0.26 and 0.41 whereas for 220 mL.min⁻¹, the ratios varied between 0.26 and 0.32. Finally, we see that these ratios increased as the experiment advanced; the increases were respectively 1.55, 1.33 and 1.21 for flow rates of 50, 150 and 220 mL.min⁻¹. Therefore, the lateral V_{DNAPL} are not negligible.

Conversely, for 0.1 mm GB, the $V_{DNAPL\ pumped}/V_{DNAPL\ lateral}$ ratios fall during the experiment. These ratios were lower than those estimated with 0.5 mm GB. They varied between 0.19 and 0.26. The lateral V_{DNAPL} were higher for lower flow rates than for higher ones, which is logical.

Therefore, the $V_{\text{DNAPL pumped}}/V_{\text{DNAPL lateral}}$ ratios varied for $50 \text{ mL}\cdot\text{min}^{-1}$ between 0.25 and 0.27, whereas they varied between 0.19 and 0.26 for $220 \text{ mL}\cdot\text{min}^{-1}$.

Figure 224 compares estimated DNAPL volumes recovered experimentally (with image interpretation) and by modeling (after lateral V_{DNAPL} deduction).

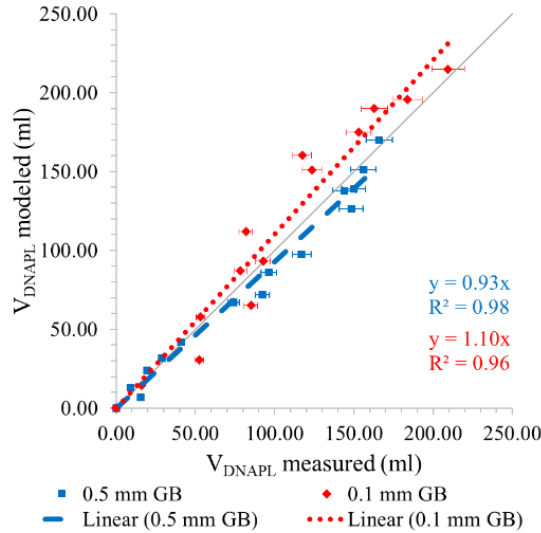


Figure 224: Comparison of estimated DNAPL volumes recovered experimentally (with image interpretation) and by modeling (after lateral V_{DNAPL} deduction) with 0.5 and 0.1 mm GB (without enhancement)

One sees that the slopes were close to 1 (0.93 for the 0.5 mm GB and 1.10 for the 0.1 mm GB). The R^2 coefficients are also close to 1 (respectively 0.98 and 0.96 for the 0.5 and 0.1 mm GB). Therefore, we can consider that measurements of saturation by image interpretation match well the simulated saturation.

e) Fingering effect at the DNAPL-water interface

All of the statistical data for fingerings in the DNAPL-water interface are reported in Appendix 8.1. Figure 225 shows some illustrations of the flattened DNAPL-water interface.

0.5 mm GB, $50 \text{ mL}\cdot\text{min}^{-1}$, 42 min

0.5 mm GB, $150 \text{ mL}\cdot\text{min}^{-1}$, 25 min

0.5 mm GB, $220 \text{ mL}\cdot\text{min}^{-1}$, 7 min

0.1 mm GB, $50 \text{ mL}\cdot\text{min}^{-1}$, 28 min

0.1 mm GB, $150 \text{ mL}\cdot\text{min}^{-1}$, 18 min

0.1 mm GB, $220 \text{ mL}\cdot\text{min}^{-1}$, 30 min

Scale: 8% of the real scale

Figure 225: DNAPL-water interface flattened (without enhancement)

We see that the DNAPL-water interfaces were more tortuous for the 0.1 mm GB than for the 0.5 mm GB. Figure 226 shows the statistical study for DNAPL-water interface shapes.

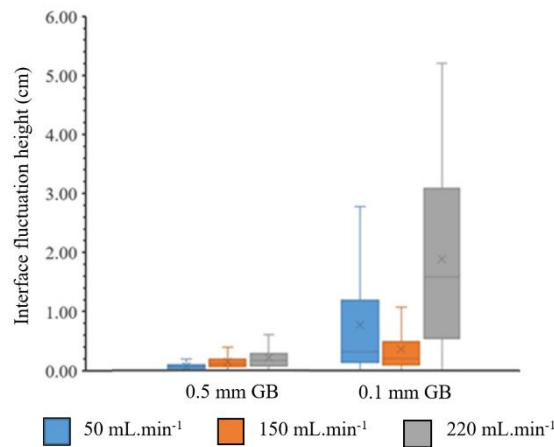


Figure 226: Statistical representation of fingerings of the DNAPL-water interface with 0.5 and 0.1 mm GB (without enhancement)

The DNAPL-water interface shapes were less irregular for the 0.5 mm GB than for the 0.1 mm GB. Generally, the higher the pump flow rate, the more irregularities there are at the interface (see section 6.3.6 for more details).

Regarding the 0.5 mm GB, the average value varies from 0.06 to 0.22 cm for flow rates from 50 to 220 mL.min⁻¹ (with respective standard deviations of 0.05 to 0.21). Regarding the 0.1 mm GB, the values were higher: for flow rates of 50 to 220 mL.min⁻¹, the average values were respectively from 0.62 to 1.61 cm (with respective standard deviations of 0.42 and 1.14).

f) Parametrical study of the model

The parametrical study was based on comparison with a reference scenario (reference: 0.1 mm GB, without enhancement, 150 mL.min⁻¹). Variations in the following parameters have been considered: permeability ($k \times 0.1$ and $k \times 10$), number of meshes ($\times 10$), porosity ($\theta \times 0.3$). Figure 227 shows the results of the parametrical study of the model.

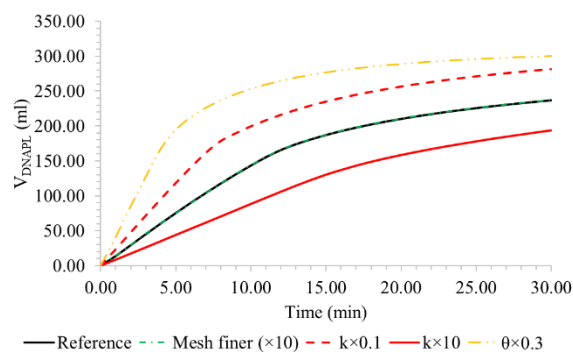


Figure 227: Parametrical study of the model (without enhancement)

The changed number of meshes ($\times 10$) did not influence the final result (+0.8%), which means that the number of meshes used in the model is sufficient.

The permeability variations ($k \times 0.1$ and $k \times 10$) reach respective differences for V_{DNAPL} recovered at 30 min of +19% and -20% relative to the base scenario. The increase in these volumes with lower permeability (without changed curves $P_c=f(S_w)$) matches the differences observed between the 0.5 and 0.1 mm GB.

The reduced porosity ($\theta \times 0.3$) increased the recovered V_{DNAPL} by 27% at 30 min.

6.3.1.2 Permittivity monitoring

Figure 228 shows changes in permittivity, ϵ (corrected relative to the reference value of air and water measured at the beginning of the experiment, see Eq. 186) as a function of time during pumping experiment conducted with 0.5 mm GB (the location of the TDR is shown in Figure 198).

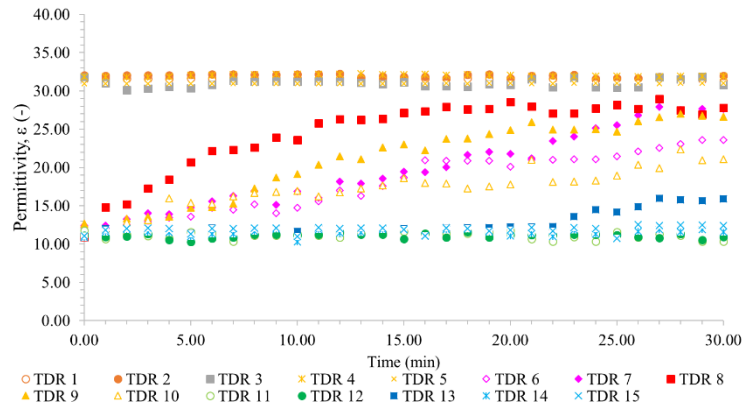


Figure 228: Evolution of the permittivity in the 2D tank with 0.5 mm GB with a flow rate of $150 \text{ mL} \cdot \text{min}^{-1}$ (without enhancement)

TDR 1 to 5 located in the upper part of the 2D tank were only surrounded by water ($S_w=1$). On average, they had the same values as those in the cells and columns when the experiments began (31.49 ± 0.51).

TDR 11 to 15 were in the lower portion of the 2D tank. As pumping began, the water contents were equivalent to S_{rw} . The monitored permittivities agreed with those measured in the cells and columns: 11.39 ± 0.39 . As pumping ended, we saw that TDR 13, in the lower central position, detected the arrival of the cone of depression (at $t=23$ min).

TDR 6 to 10 were in the middle of the 2D tank. Logically TDR 8, located in the tank's center, was the first to measure the permittivity increase; then as pumping continues, we saw TDR 7 and 9 on either side of this central position show increased permittivity (and therefore falling DNAPL content). As pumping ended, $\epsilon_{\text{measured}}$ at TDR 7 to 9 were on average 27.27 ± 1.10 , which matches what was measured at the end of imbibition in 1D cells and 1D columns. The $\epsilon_{\text{measured}}$ at TDR 6 and 10 (located at the cone of depression) were respectively 23.41 ± 0.29 and 21.46 ± 0.77 .

Figure 229 shows variations in water saturation, measured permittivity and estimated permittivity during the pumping experiment. The water saturation was calculated from image interpretation (*i.e.* from optical densities). The permittivity estimate was calculated from S_w and Eq. 197 for 0.5 mm GB, and Eq. 198 for 0.1 mm GB (CRIM model).

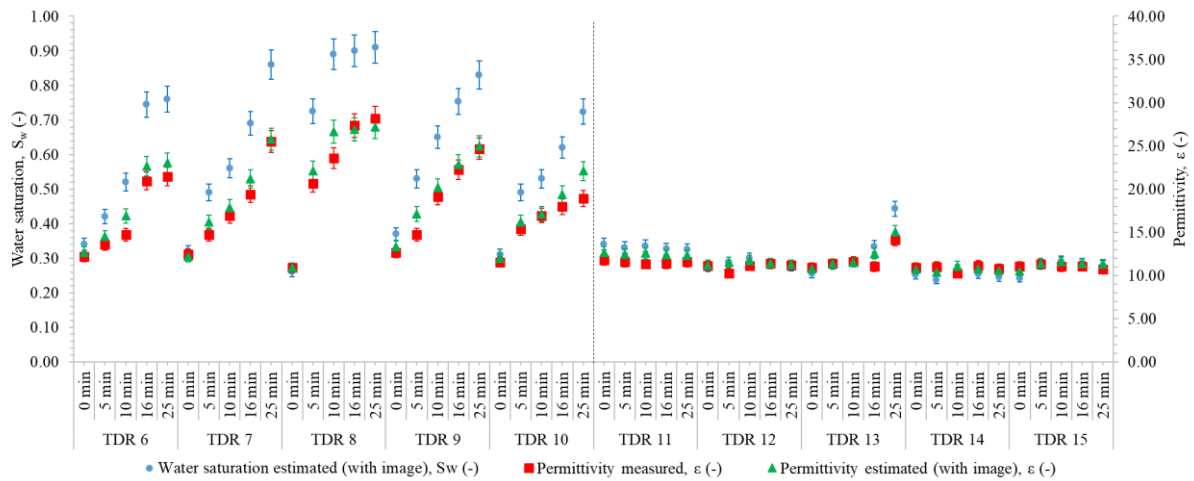


Figure 229: Average water saturation, measured and estimated permittivity during the pumping experiment in the 2D tank with 0.5 mm GB with a flow rate of $150 \text{ mL}\cdot\text{min}^{-1}$ (without enhancement)

The $\epsilon_{\text{estimated}}$ (from image interpretations) were very similar to the $\epsilon_{\text{measured}}$ at the start and end of pumping. When the migration front moved to the TDR's detection area, the $\epsilon_{\text{measured}}$ were systematically lower than the $\epsilon_{\text{estimated}}$. The value assigned to S_w is the average of the S_w at the detection area. This value is transformed into permittivity according to the CRIM model. This model is only valid in homogeneous media. When the detection zone is crossed by the migration front, the zone contains both contents similar to S_m and contents similar to S_{rw} . Therefore, for two heterogeneous zones, the weight of the portion similar to S_{rw} impacts global $\epsilon_{\text{measured}}$ more than the portion similar to S_m . Eq. 158, combined with the permittivity values for DNAPL and water ($\epsilon_n = 3.11$ and $\epsilon_w = 80$), shows that the propagation velocity function is 6 times faster for DNAPL than for water. It is therefore logical that, when the TDR detection zone is crossed by the migration front, $\epsilon_{\text{measured}}$ is systematically lower than $\epsilon_{\text{estimated}}$.

As discussed in section 4.2.3.3, this shift between the estimated and measured permittivities in the transition zones was studied for soils in the unsaturated zone (system soil-air-water):

- Some authors have shown that the CRIM model (based on the relative permittivity of free water, air and solids) may not be suitable in all situations, especially in the transition phases (when S_w are between S_m and S_{rw}). These authors have proposed to consider a 4th constituent, the bound water (whose dielectric constant is very different from free water) [Dasberg and Hopmans (1992); Capparelli *et al.* (2018)]. An equation derived from the CRIM model incorporating the bound water has been proposed [Dobson *et al.* (1985); Dirksen and Dasberg (1993)].
- Capparelli *et al.* (2018) carried out monitoring of S_w variations with TDR probes in unsaturated soils. The experimental results were compared to the classical CRIM model but also to the four-phase dielectric mixing model (with bound water), and the classical CRIM model with a variable exponent. The best results were obtained with the three-phase dielectric mixing model with a variable exponent (α_ϵ) [Capparelli *et al.* (2018)].

In this study, we did not quantify the bound water.

Figure 230 shows changes in permittivity, as a function of time during pumping experiment conducted with 0.1 mm GB.

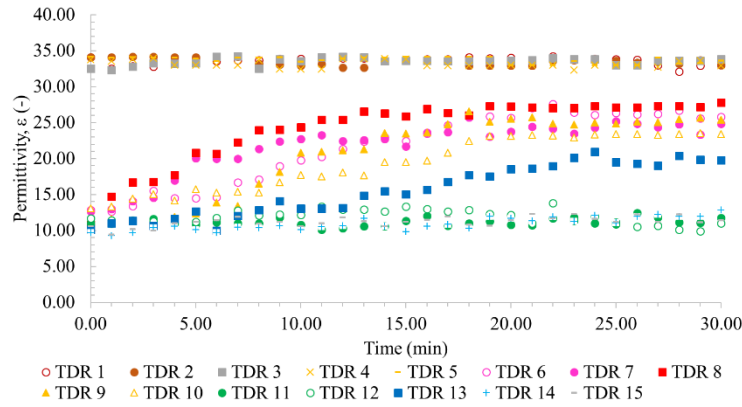


Figure 230: Evolution of the permittivity in the 2D tank with 0.1 mm GB with a flow rate of $150 \text{ mL}\cdot\text{min}^{-1}$ (without enhancement)

Globally, we observe the same trends as those shown Figure 228. However, though displacement of the migration front must be faster with the 0.1 mm GB (for the same flow rate), permittivity increases were slower than for the 0.5 mm GB. This is because the migration front was less sharp (and therefore DNAPL reduction is slower). As pumping ended, $\epsilon_{\text{measured}}$ at TDR 7 to 9 were on average 25.59 ± 1.30 , which matches what was measured at the end of imbibition in 1D cells and 1D columns.

Figure 231 shows variations in water saturation, measured and estimated permittivity during the pumping experiment.

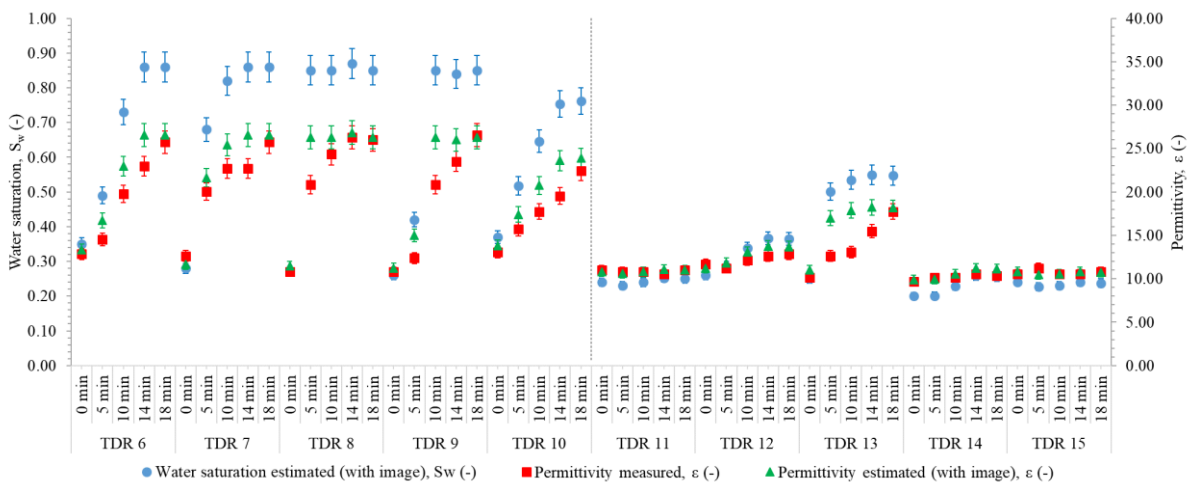


Figure 231: Average water saturation, measured and estimated permittivity during the pumping experiment in the 2D tank with 0.1 mm GB with a flow rate of $150 \text{ mL}\cdot\text{min}^{-1}$ (without enhancement)

We see the same trends as in Figure 229. We note that during transition phases the difference between $\epsilon_{\text{estimated}}$ and $\epsilon_{\text{measured}}$ is higher than for 0.5 mm GB. Moreover, in comparison with 0.5 mm GB, note that TDR 7 and TDR 9 had higher $\epsilon_{\text{estimated}}$ and $\epsilon_{\text{measured}}$, which agrees with the modeling results (the radius of action was higher). In the same way of course, TDR 13 detected the arrival of the DNAPL-water interface earlier (detection at $t = 5 \text{ min}$).

Figure 232 compares measured and estimated permittivity (with image interpretation) in the 2D tank for 0.5 and 0.1 mm GB for without enhancement case.

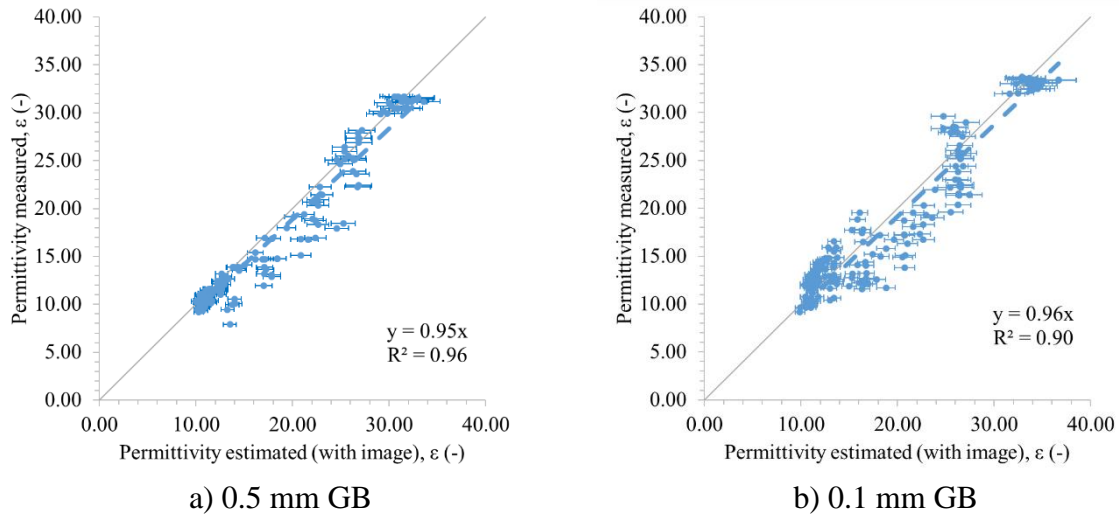


Figure 232: Comparison of measured and estimated permittivity (with image interpretation) in the 2D tank for a) 0.5 and b) 0.1 mm GB (without enhancement)

The slopes were close to 1 (0.95 for 0.5 mm GB and 0.96 for 0.1 mm GB), which shows that the measured permittivities agreed with the image interpretation. As expected, we see that R^2 for the 0.5 mm GB was higher than for the 0.1 mm GB (0.96 vs 0.90), which shows better correlation of values for 0.5 mm GB. In both cases, we saw four distinct zones:

- S_{rw} zone: this zone corresponds to ϵ around 10.50 to 12.00 for the 0.5 mm GB and 12.50 to 13.50 for the 0.1 mm GB (start of pumping)
- Transition zone: this zone corresponds to values between the S_{rw} zone and the S_{rn} zone; here the majority of points were below the linear regression line ($\epsilon_{measured}$ are below $\epsilon_{estimated}$),
- S_{rn} zone: this zone corresponds to ϵ around 27.00 to 28.00 for the 0.5 mm GB and 25.00 to 26.00 for the 0.1 mm GB (end of pumping),
- Water zone: this zone corresponds to $\epsilon_{measured}$ at TDR 1 to 5 (corresponding to $S_w=1$), *i.e.* 31.00 to 32.00 for 0.5 mm GB and 32.00 to 33.00 for 0.1 mm GB.

Figure 233 displays a surface plot of the permittivity measured on an image at the end of pumping experiment. The permittivity values were calculated using an interpolation technique (Kriging or Gaussian process regression) with Surfer software.

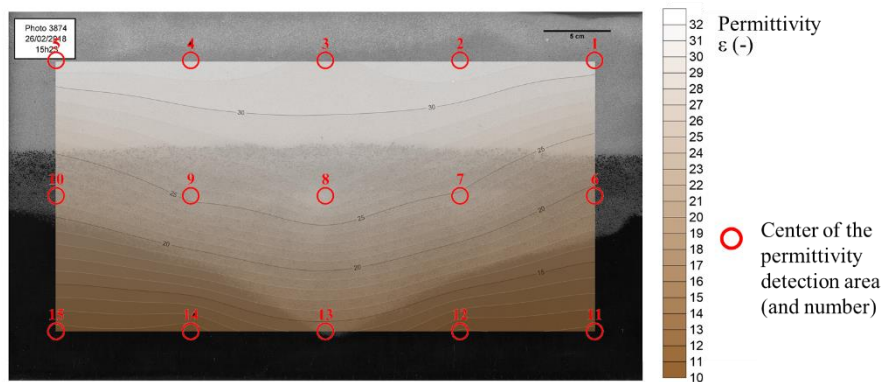
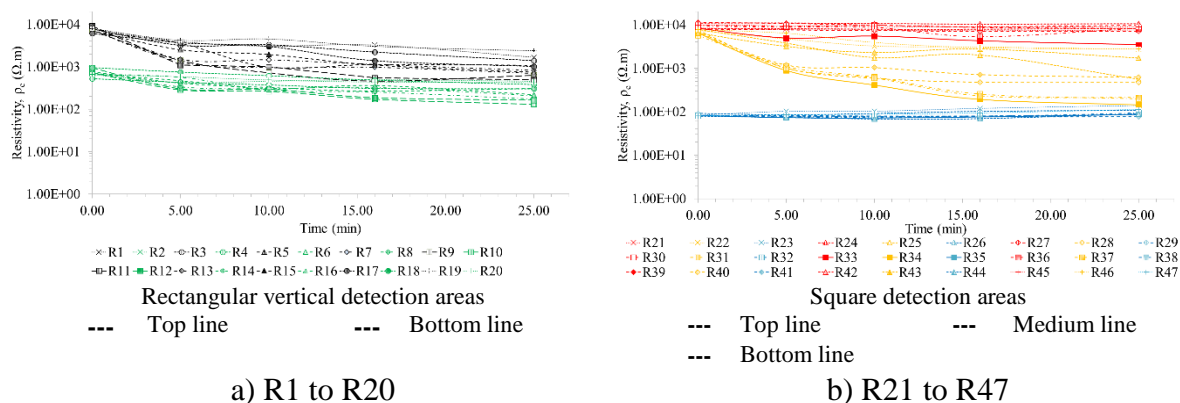


Figure 233: Surface plot of measured permittivity within an image with 0.5 mm GB with a flow rate of $150 \text{ mL} \cdot \text{min}^{-1}$ (without enhancement) at $t = 18 \text{ min}$

We note that the permittivity and the S_n do not overlap completely. This is explained by two phenomena: i. the kriging method (under Surfer) is only based on 15 points; ii. the transition zones cause an offset for the measurements. However, this does show that the cone of depression can be determined by permittivity monitoring.

6.3.1.3 Electrical resistivity monitoring

Figure 234 shows changes in resistivity as a function of time during pumping experiment conducted with 0.5 mm GB. The resistivity values were obtained from Eq. 187 and conductivity measurements for the white test (reference) as each experiment began.



a) R1 to R20
b) R21 to R47
Figure 234: Evolution of the resistivity in the 2D tank with 0.5 mm GB with a flow rate of $150 \text{ mL}\cdot\text{min}^{-1}$ (without enhancement) – a) R1 to R20 and b) R21 to R47

Detection areas R1 to R20 were vertical rectangles. R with an even number (R2 to R20) group detection areas in the upper section; they were two thirds of the upper portion of the 2D tank. At the start of the experiment, they were therefore submerged by more than one third in the DNAPL (at a content corresponding to S_{rw}) and by a little less than two thirds in water ($S_w=1$). From the start of pumping we saw that the resistivity values (ρ_c) fell for R10 and R12, located in the central section of the cone of depression. ρ_c fell in the first 5 minutes by 726 ± 208 to $286 \pm 76 \text{ }\Omega\cdot\text{m}$ for R10 and by 951 ± 205 to $304 \pm 91 \text{ }\Omega\cdot\text{m}$ for R12, respectively. Logically the other detection areas located in more lateral positions of the cone of depression had smaller and delayed reductions.

We saw the same phenomena for the vertical rectangular detection areas in the lower section (odd numbers between R1 and R19). ρ_c fell in the first 5 minutes of pumping by 7174 ± 1952 to $1409 \pm 422 \text{ }\Omega\cdot\text{m}$ for R9 and by 9162 ± 2048 to $1095 \pm 298 \text{ }\Omega\cdot\text{m}$ for R11, respectively.

The square detection areas were arranged along three horizontal lines: the top line only in contact with water, the medium line at the upper portion of the DNAPL, the bottom line at the lower portion of the DNAPL. The resistivities measured in the top line were of the same order of magnitude as those measured in the 1D cells and 1D columns: $86 \pm 11 \text{ }\Omega\cdot\text{m}$.

The mean resistivities at the start of the experiment were $7106 \pm 1406 \text{ }\Omega\cdot\text{m}$ for the medium line and $9367 \pm 1074 \text{ }\Omega\cdot\text{m}$ for the bottom line. These values show that the S_n was higher at the bottom of the DNAPL (this could be related to density effects). These data match those gathered in the 1D cells and 1D columns.

As for the medium line, the resistivities at R34 (located at the center of the 2D tank) decreased faster. At the end of pumping, this area was completely filled by values around S_m (according to the image interpretations). Logically, the $\rho_{c,measured}$ was $144 \pm 22 \Omega.m$, which was very similar to the values at the end of imbibition in the 1D experiments.

Finally, regarding the bottom line, the resistivities at R33 (located in the center of the 2D tank) fell slightly, which shows that the cone of depression partially reached this area, with resistivity at $3466 \pm 640 \Omega.m$.

Figure 235 shows how water saturation, measured and estimated resistivity varied during the pumping experiment. Transforming optical density into S_w allows a mean S_w value to be assigned by detection area. This value is transformed into resistivity according to Eq. 205 for 0.5 mm GB and Eq. 206 for 0.1 mm GB (Archie's law). A correction factor was used so as to approach the values shown in the 1D cells and 1D columns as closely as possible (Eq. 207 and Eq. 208).

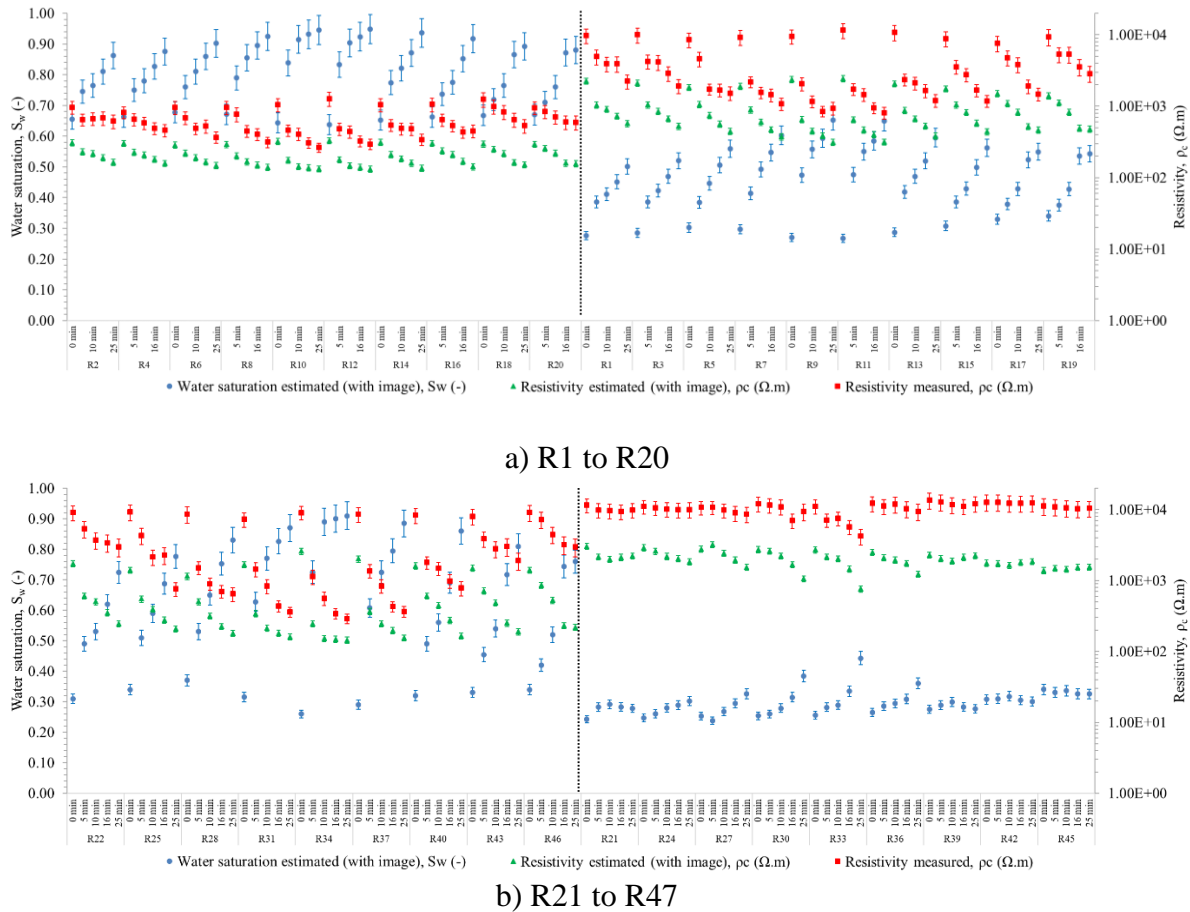


Figure 235: Average water saturation, measured and estimated resistivity during the pumping experiment in the 2D tank with 0.5 mm GB with a flow rate of $150 mL.min^{-1}$ (without enhancement) – a) R1 to R20 and b) R21 to R47

Globally, we see that the variations in $\rho_{c,measured}$ match the variations in $\rho_{c,estimated}$. However, these variations show that the differences between the $\rho_{c,measured}$ and $\rho_{c,estimated}$ are not constant. The fitting for the experiments with Archie's law (during the experiments in 1D cells and 1D columns) is not as good as for the permittivities. The $\rho_{c,measured}/\rho_{c,estimated}$ ratios increase as the resistivity values increase (and do so in spite of the fact that we have taken into account the

correction factors). This will be described in more detail with Figure 238 which compares $\rho_{c,measured}$ and $\rho_{c,estimated}$.

As discussed in section 4.2.3.4, the differences between the estimated and measured resistivities may have several causes:

- In a porous medium with water and gas, taking into account a suitable cementation factor that considers the saturation condition, would allow better estimation of resistivity with Archie's law [Byun *et al.* (2019)].
- At a pore scale, the resistivity indexes did not generally obey Archie's Law in the non-homogeneous zones (for example with a transition zone constituted of values close to S_{rn} and S_{rw}). The water films play a role not only on the pore space connectivity but also on resistivity; therefore, we can over or underestimate resistivity depending on the thickness of these water films around grains of sand or glass beads [Bernabé *et al.* (2011); Li *et al.* (2015); Bernabé *et al.* (2016)].
- Many other parameters could be considered at different scales in electrical conductivity models in porous media: tortuosity, pore size distribution, pore-conductance distributions, interconnectivity and universal power law of percolation [Glover (2010); Cai *et al.* (2017); Ghanbarian and Sahimi (2017)].

These parameters have not been considered in our experiments. However, as we see below, it is possible, as a first approach, to establish correlations between $\rho_{c,measured}$ and $\rho_{c,estimated}$.

Figure 236 shows changes in resistivity, as a function of time during pumping experiment conducted with 0.1 mm GB.

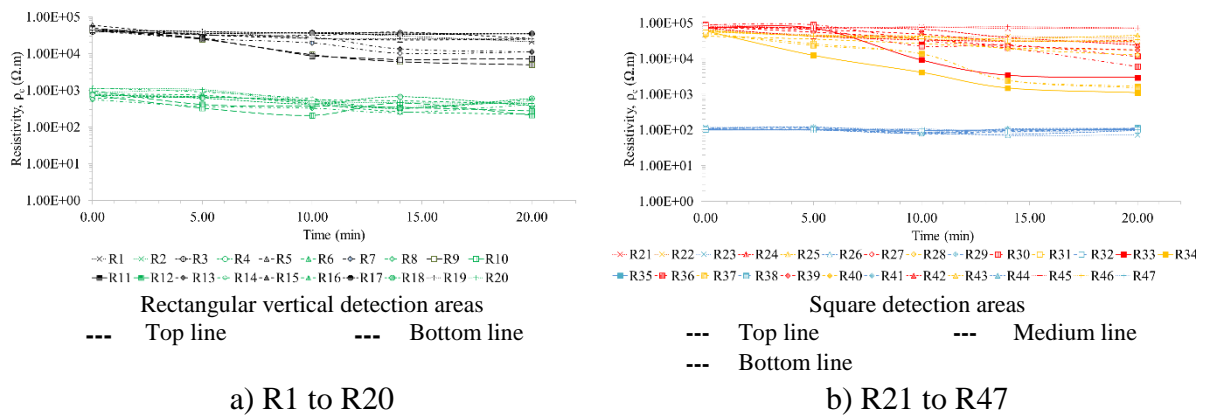


Figure 236: Evolution of the resistivity in the 2D tank with 0.1 mm GB with a flow rate of $150 \text{ mL}\cdot\text{min}^{-1}$ (without enhancement) – a) R1 to R20 and b) R21 to R47

Like with the 1D experiments, we see that resistivities were higher for 0.1 mm GB than for 0.5 mm GB (for the same S_w). Since the materials and methods are identical in every way for the 0.5 mm GB, this difference is probably due to the connectedness of the pores [Glover (2010); Cai *et al.* (2017); Ghanbarian and Sahimi (2017)].

Globally, we observe the same trends as those shown in Figure 234. The resistivities measured in the middle portion of the 2D tank fell faster and more sharply than at the sides.

The resistivities measured in the top line were of the same order of magnitude as those measured in the 1D experiments: $100 \pm 12 \text{ }\Omega\cdot\text{m}$. The mean resistivities at the start of the experiment were

$56716 \pm 6037 \Omega.m$ for the medium line and $78447 \pm 7393 \Omega.m$ for the bottom line, which also agreed with the 1D experiments.

At the end of the experiment, the resistivity at R34, totally affected by values close to S_{rn} , was $1110 \pm 313 \Omega.m$. R33 had values close to both S_m and S_{rw} , with resistivity at $2955 \pm 886 \Omega.m$. These data agree with the results of the 1D experiments.

Figure 237 shows the variations in water saturation, measured and estimated resistivity during the pumping experiment.

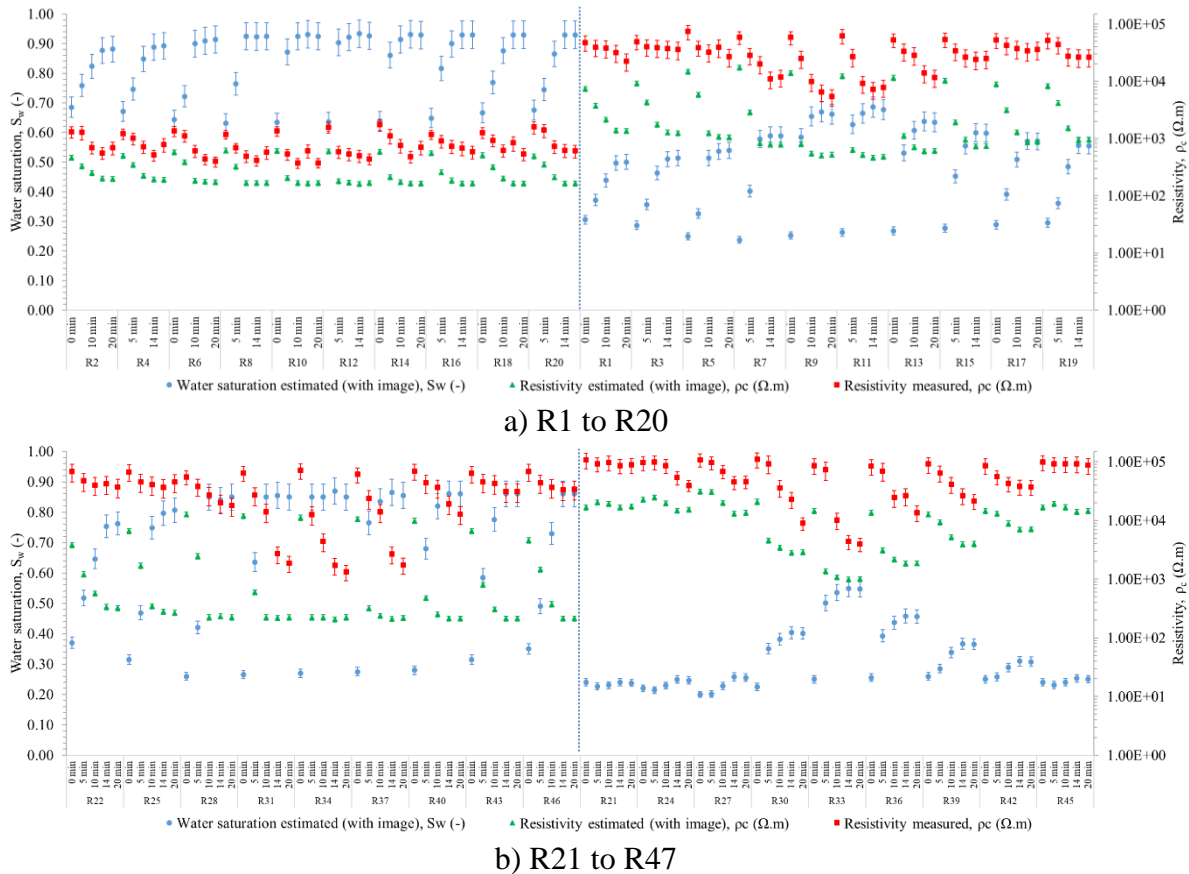


Figure 237: Average water saturation, measured and estimated resistivity during the pumping experiment in the 2D tank with 0.1 mm GB with a flow rate of $150 mL.min^{-1}$ (without enhancement) – a) R1 to R20 and b) R21 to R47

The variations in $\rho_{c,measured}$ agree with the variations in $\rho_{c,estimated}$. However, like with the 0.5 mm GB, the $\rho_{c,measured}/\rho_{c,estimated}$ ratios increased as the resistivity values increased.

As for the bottom line, we saw lower resistivities in the five areas of detection in the central position. For the 0.5 mm GB, the reduction in resistivities was only observed in the three central detection areas. The resistivities therefore showed that the cone of depression was higher than for the 0.5 mm GB.

Figure 238 compares the measured and estimated resistivity (with image interpretation) in the 2D tank for 0.5 and 0.1 mm GB.

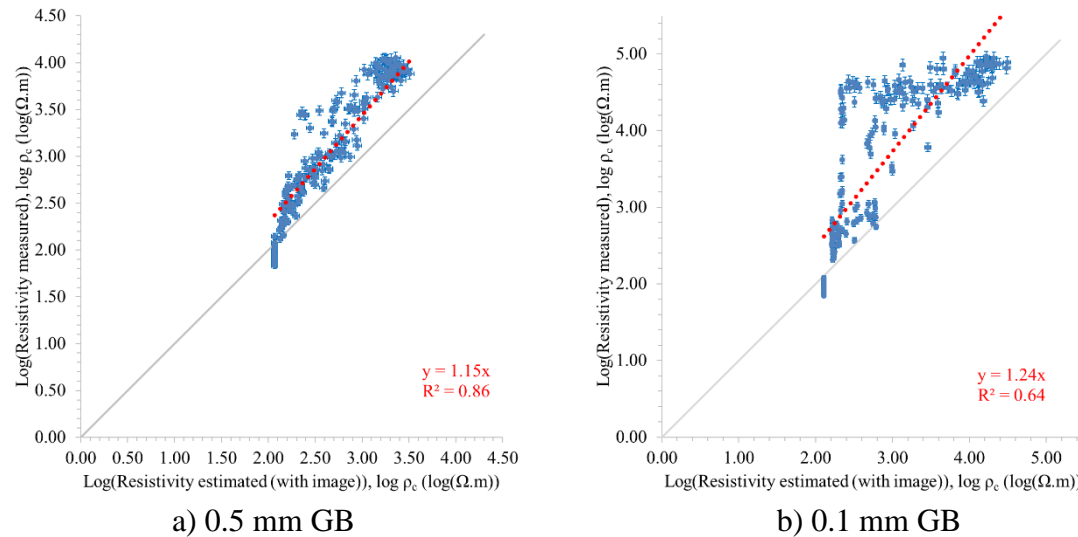


Figure 238: Comparison of measured and estimated resistivity (with image interpretation) in the 2D tank for a) 0.5 and b) 0.1 mm GB with a flow rate of $150 \text{ mL}\cdot\text{min}^{-1}$ (without enhancement)

The slopes of the curves $\log(\rho_{c,\text{measured}})=f(\log(\rho_{c,\text{estimated}}))$ were respectively 1.15 and 1.24 for 0.5 and 0.1 mm GB. Moreover, the coefficient of determination was higher for the 0.5 mm GB ($R^2=0.86$) than for the 0.1 mm GB ($R^2=0.64$). The dispersivities were quite high, in particular for the 0.1 mm GB for which the fingerings and heterogeneities in DNAPL distribution were clearly visible.

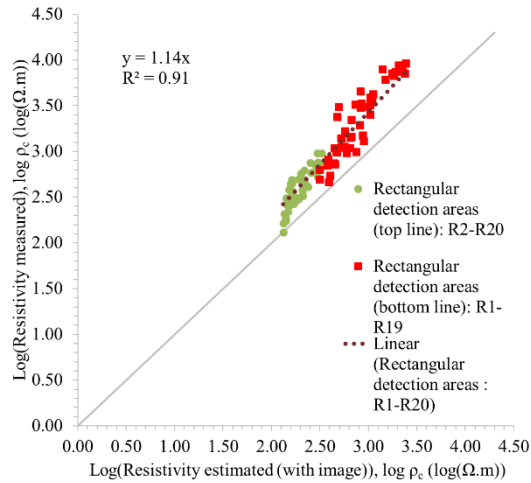
For values corresponding to zones close to the S_{rw} (*i.e.* when all of the detection area had values close to the S_{rw}), the $\rho_{c,\text{measured}}/\rho_{c,\text{estimated}}$ ratios were close to those determined during the 1D cell and 1D column experiments; these ratios were on average 2.97 for 0.5 mm GB and 4.32 for 0.1 mm GB (taking into account the correction factors). In large part, these ratios explain the slopes of above one.

For values close to the S_m (when all of the detection area has values close to the S_m), the $\rho_{c,\text{measured}}/\rho_{c,\text{estimated}}$ ratios were close to those determined during the 1D cell and 1D column experiments; these ratios were on average 1.05 for 0.5 mm GB et 2.3 and 0.1 mm GB (taking into account the correction factors).

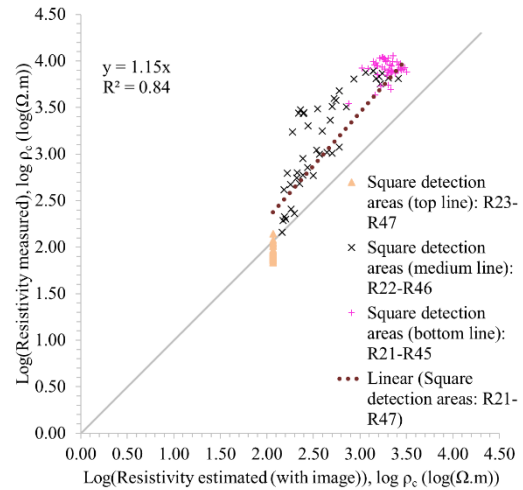
A transition zone was visible between the two previously mentioned zones. These were the detection areas for the DNAPL-water interface (and therefore, the values close to both S_{rw} and S_m). In this zone, the $\rho_{c,\text{measured}}/\rho_{c,\text{estimated}}$ ratio was variable but globally higher than those determined for the zone relative to S_m . These ratios are the second explanation for the slopes of the curves.

Therefore, we can distinguish, just like for permittivity, four distinct zones (Figure 239):

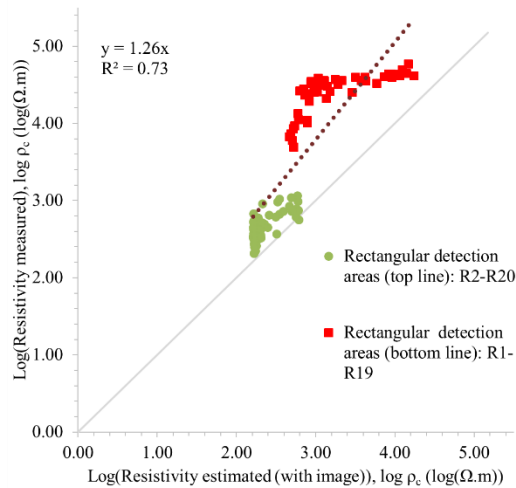
- S_{rw} zone: start of pumping
- Transition zone: this zone corresponds to values between the S_{rw} zone and the S_m zone; here, the majority of points were above the linear regression line ($\rho_{c,\text{measured}}$ are above $\rho_{c,\text{estimated}}$),
- S_m zone: end of pumping,
- Water zone: this zone corresponds to the detection areas situated in the upper zone of the 2D tank.



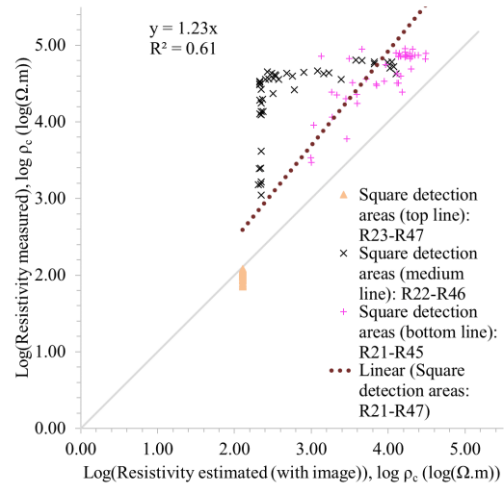
a) 0.5 mm GB-rectangular detection areas



b) 0.5 mm GB-square detection areas



c) 0.1 mm GB-rectangular detection areas



d) 0.1 mm GB-square detection areas

Figure 239: Comparison of measured and estimated resistivity (with image interpretation) in the 2D tank with a flow rate of $150 \text{ mL} \cdot \text{min}^{-1}$ for a) 0.5 mm GB-rectangular detection areas, b) 0.5 mm GB-square detection areas, c) 0.1 mm GB-rectangular detection areas, d) 0.1 mm GB-square detection areas (without enhancement)

The rectangular distinction areas all correspond to the transition zone. The areas of the bottom line (red dots) are the furthest from the linear regression. The areas of the top line (green dots), filled largely by water, are of course closer to the linear regression line (the calibrations are better for low resistivities).

As for the square detection areas, the top line measurements (brown dots), corresponding to $S_w = 1$, agree with the estimation perfectly. The bottom-line measurements (pink dots) corresponding to S_{rw} , are overestimated by the factors previously described. The points outside the group of dots correspond to the arrival of the cone of depression. In that case, the dots get further from the linear regression line (this is the transition zone). Finally, the measurements at the medium line (black dots) correspond in large part to the transition zone and are further from the linear regression line.

For lower resistivity values (corresponding to the areas of detection entirely concerned with S_{rm}) and for the highest resistivity values (corresponding to zones entirely concerned with S_{rw}), we see that the points of course fall closer to the linear regression line.

Figure 240 shows a surface plot of the resistivity measured on an image at the end of pumping experiment.

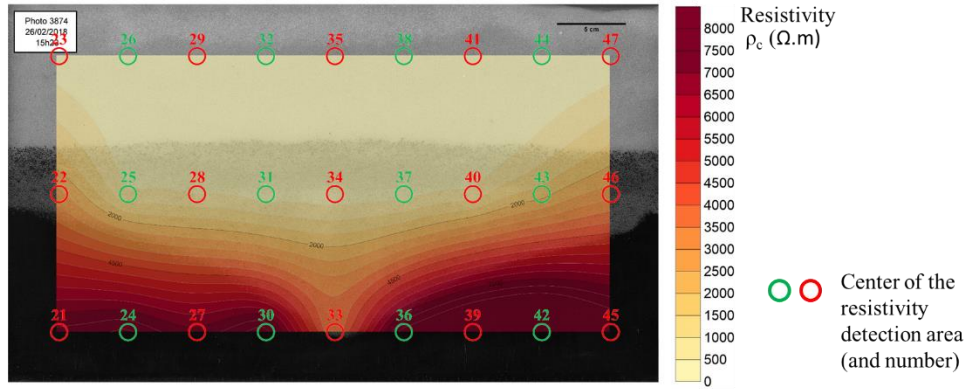


Figure 240: Surface plot of measured resistivity with an image with 0.5 mm GB with a flow rate of $150 \text{ mL}\cdot\text{min}^{-1}$ (without enhancement) at $t = 18 \text{ min}$

This image was made using Surfer software with kriging method only with the square detection areas (R21 to R47). We see that although they are not perfectly superimposed, the resistivity measurements do show the cone of depression.

6.3.2 Experiments in the 2D tank with chemical enhancement

The pumping experiments (imbibition) were conducted with 0.5 and 0.1 mm GB with chemical enhancement. Appendix 9 shows the results for the 2D tank experiments with chemical enhancement.

6.3.2.1 Experimental results: comparison of numerical simulation with optical density monitoring

a) Modeling results

Figure 241 and Figure 242 show measured and modeled volumes of DNAPL as a function of time.

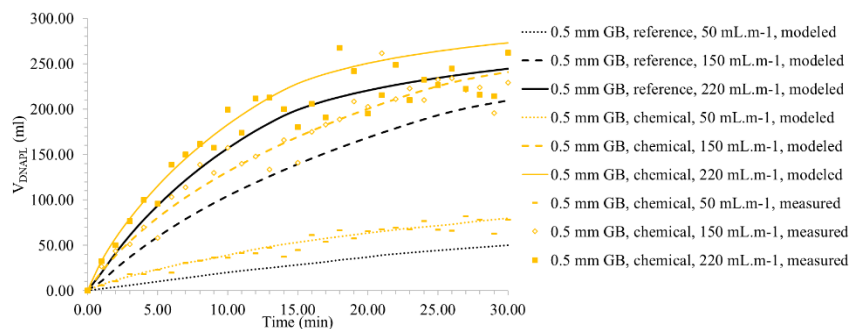


Figure 241: Evolution of measured and modeled volumes of DNAPL recovered for different flow rates with 0.5 mm GB (with chemical enhancement)

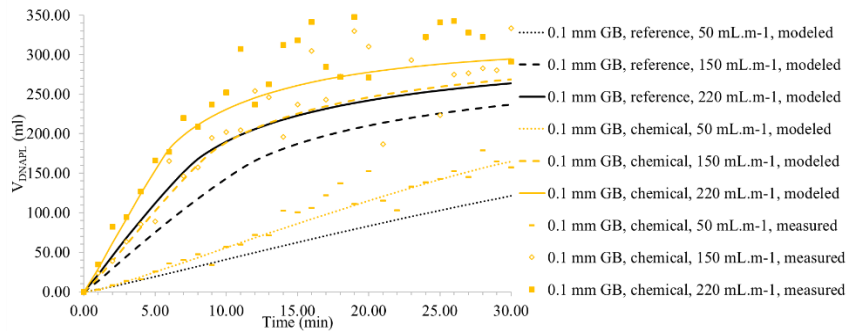


Figure 242: Evolution of measured and modeled volumes of DNAPL recovered for different flow rates with 0.1 mm GB (with chemical enhancement)

The chemical enhancement increases the DNAPL recovered with the same flow rates when compared to the test performed without enhancement. The recovery yields are higher for low DNAPL flow rates. Figure 243, showing $V_{DNAPL, chemical}/V_{DNAPL, reference}$ as a function of time, help us assess recovery yields.

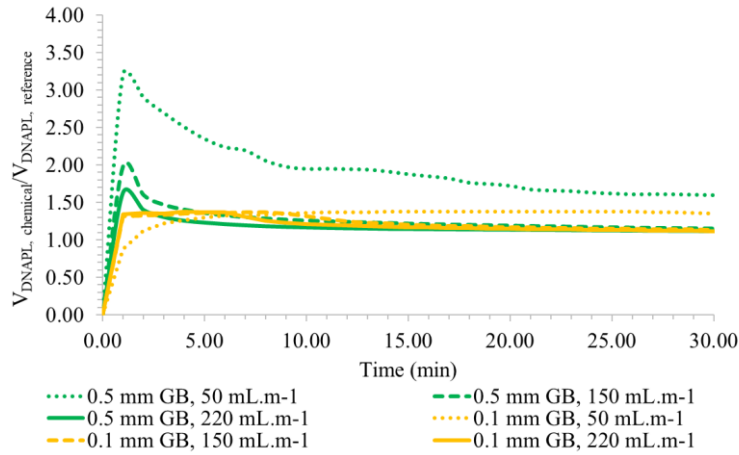


Figure 243: Modeled $V_{DNAPL, chemical}/V_{DNAPL, reference}$ ratios as a function of time with 0.5 and 0.1 mm GB

For the 0.1 mm GB the $V_{DNAPL, chemical}/V_{DNAPL, reference}$ ratios were relatively stable over time and were higher for lower flow rates than for higher flow rates (with the exception of the very start of the experiment). Also, these ratios were on average (between 5 min and 30 min) 1.37, 1.22 and 1.18 respectively for 50, 150 and 220 mL.min⁻¹. For the 0.5 mm GB, the ratios were much higher at the start of the experiment. Therefore, these ratios were at 2 min, 2.90, 1.60 and 1.40 respectively for 50, 150 and 220 mL.min⁻¹. For the rest of the experiment, the ratios were lower. For example, they were between 5 min and 30 min, on average 1.82, 1.21 and 1.14, respectively for 50, 150 and 220 mL.min⁻¹.

The use of chemical enhancement was proportionally more advantageous for lower flow rates than for higher flow rates.

Figure 244 shows how S_w changed over time along the horizontal and vertical profiles at the center of the 2D tank.

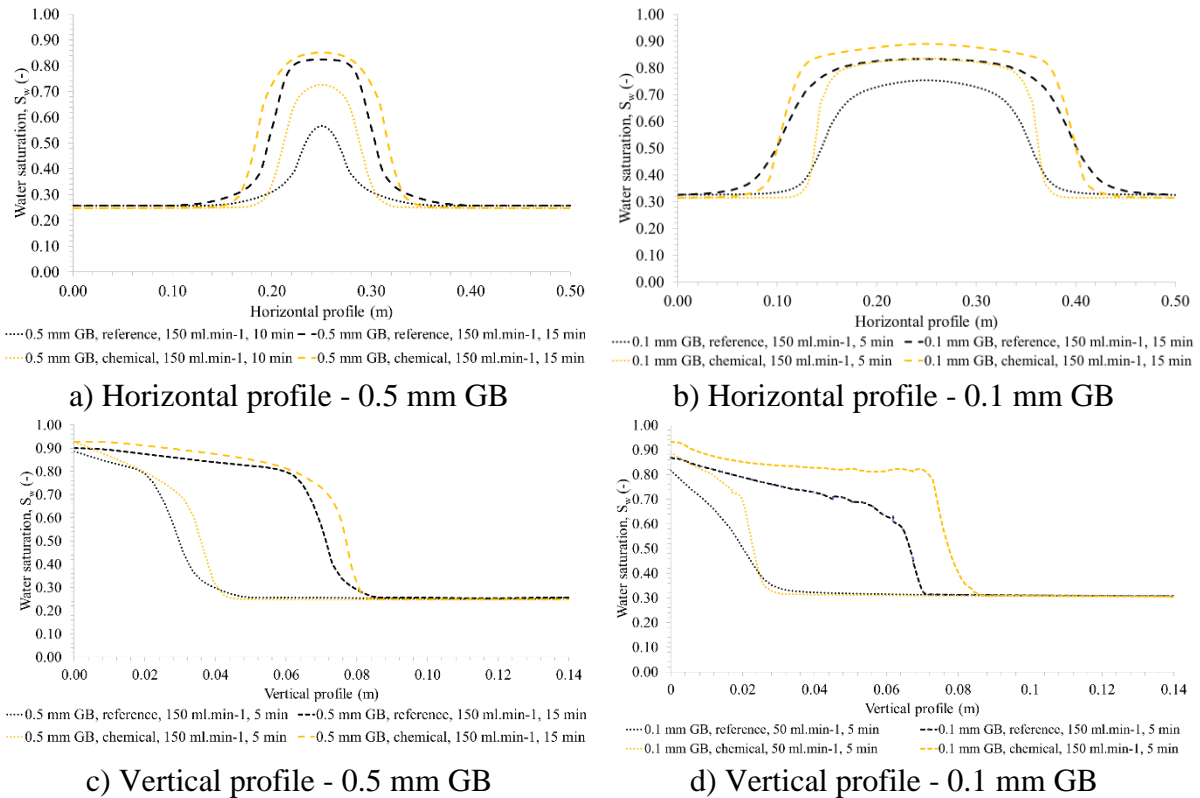


Figure 244: Evolution of the S_w along a) and b) horizontal profile and c) and d) vertical profile at the center of the 2D tank with 0.5 and 0.1 mm GB (with chemical enhancement)

The horizontal water saturation profile demonstrates how effective the chemical enhancement is. For example, regarding 0.5 mm GB at 0.25 m, S_w was 0.72 at $t=10$ min with chemical enhancement but only 0.55 without enhancement. Regarding 0.1 mm GB, S_w was 0.83 at 0.25 m at $t=5$ min with chemical enhancement but only 0.75 without enhancement.

The vertical water saturation profiles show that chemical enhancement increases the displacement of the two-phase front by more than 10% for the 0.5 mm GB and by 15% for the 0.1 mm GB (for $S_w=0.6$ for $t=15$ min).

b) Volume of DNAPL recovered

Figure 245 shows the measured and modeled volumes of DNAPL recovered during experiments.

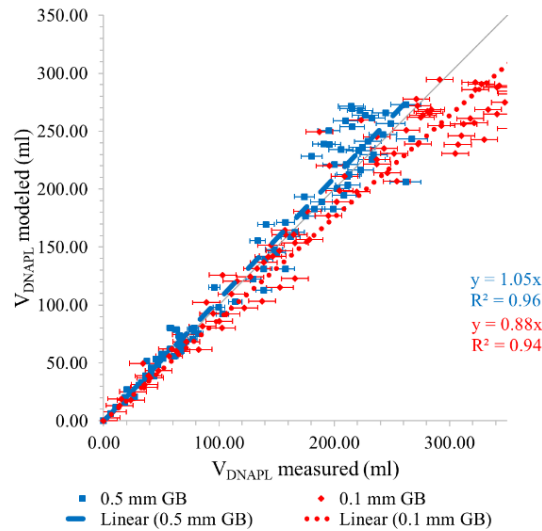


Figure 245: Comparison of measured and modeled volumes of the DNAPL recovered in the 2D tank with 0.5 and 0.1 mm GB (with chemical enhancement)

The modeled V_{DNAPL} recovered matched the measured V_{DNAPL} recovered during the experiment. The slopes of V_{DNAPL} recovered modeled = $f(V_{DNAPL}$ recovered measured) were close to 1 (1.05 and 0.88 respectively for 0.5 and 0.1 mm GB with R^2 of 0.96 and 0.94). The standard deviation was logically lower for the 0.1 mm GB.

c) DNAPL-water interface displacement

Figure 246 compares measured and modeled radius and height of the cone of depression with 0.5 mm GB and 0.1 mm GB.

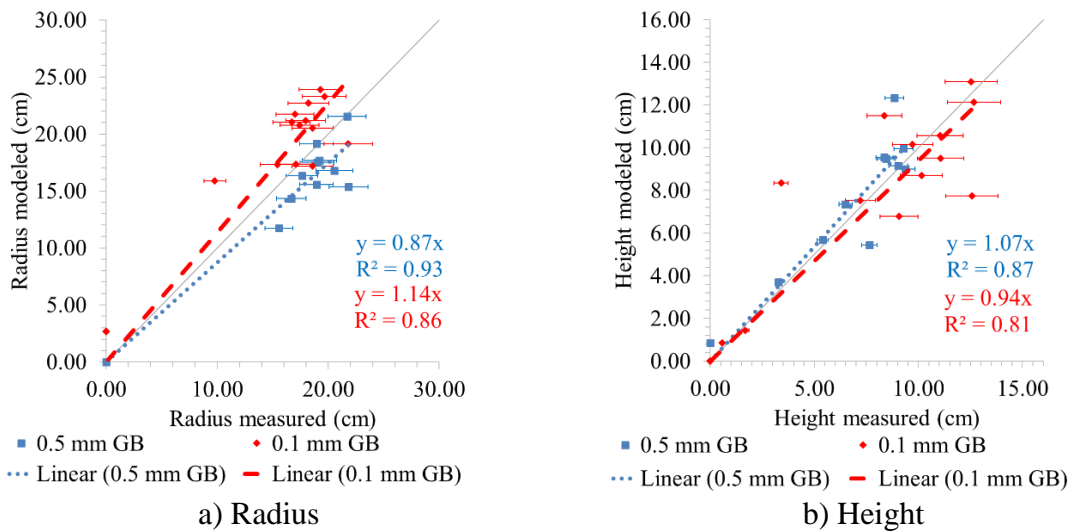


Figure 246: Comparison of measured and modeled a) radius and b) height of the cone of depression with 0.5 and 0.1 mm GB (with chemical enhancement)

The linear regression $radius_{modeled} = f(radius_{measured})$ were 0.87 and 1.14, respectively for 0.5 and 0.1 mm GB (with R^2 of 0.93 and 0.86). Moreover, the linear regression $height_{modeled} = f(height_{measured})$ were respectively 1.07 and 0.94 (with $R^2 = 0.87$ and 0.81).

Therefore, the model fits the image interpretation data well.

d) Comparison of estimated recovered DNAPL volumes by modeling and image interpretation

Figure 247 compares the estimated DNAPL volumes recovered experimentally (with image interpretation) and the one calculated by modeling (after lateral V_{DNAPL} deduction).

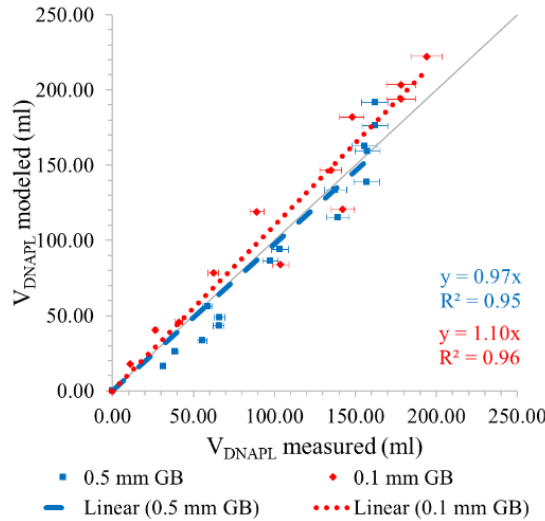


Figure 247: Comparison of estimated DNAPL volumes recovered experimentally (with image interpretation) and by modeling (after lateral V_{DNAPL} deduction) with 0.5 and 0.1 mm GB (with chemical enhancement)

Figure 247 shows that the modeling matched the image interpretations: the linear regression curve gradients were respectively 0.97 and 1.10 for the 0.5 and 0.1 mm GB. The R^2 were correct (respectively 0.95 and 0.96 for the 0.5 and 0.1 mm GB).

e) Fingerings effect at the DNAPL-water interface

Figure 248 shows the average values and standard deviations of the DNAPL-water interfaces for with chemical enhancement case.

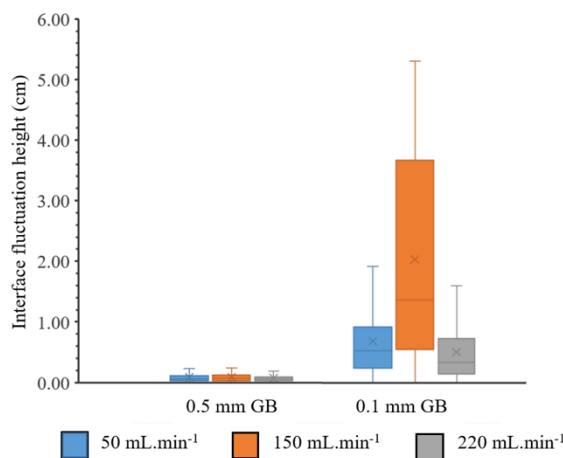


Figure 248: Statistical representation of fingerings of the DNAPL-water interface with 0.5 and 0.1 mm GB (with chemical enhancement)

We see that fingering is more important for the 0.1 mm GB than for the 0.5 mm GB: the average interface heights fluctuations were respectively 0.08 and 1.03 cm (with average standard deviations of 0.07 and 0.82). There was no notable difference between the values observed without enhancement and with chemical enhancement (see section 6.3.6 for more details). However, we can underline that increasing the flow rate had limited influence on fingering (with the exception of the 0.1 mm GB experiment at 150 mL.min⁻¹, showing anomalous results).

6.3.2.2 Permittivity monitoring

Figure 249 shows changes in permittivity as a function of time during pumping experiments conducted with 0.5 mm GB.

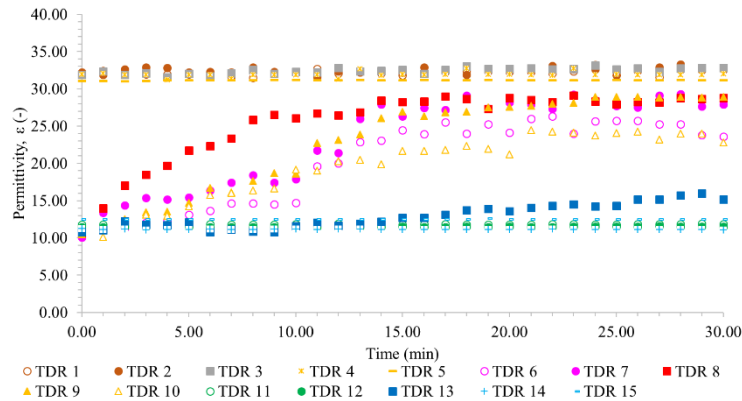


Figure 249: Evolution of the permittivity in the 2D tank with 0.5 mm GB with a flow rate of 150 mL.min⁻¹ (with chemical enhancement)

For the same flow rates, permittivity variations came earlier with chemical enhancement than without enhancement (see section 6.3.4 for more details). For TDR 8, the permittivity plateau was reached at 8 min (vs. 12 min). The final permittivities for TDR 7 to 9 were higher (28.41 ± 0.56), which confirms a lower S_{m} . These values agree with those measured at the end of imbibition with 1D cells and 1D columns. TDR 13 also detected the arrival of the cone of depression earlier (t = 15 min vs. t = 23 min). Figure 250 shows variations in water saturation, measured and estimated permittivity during the pumping experiment for 0.5 mm GB.

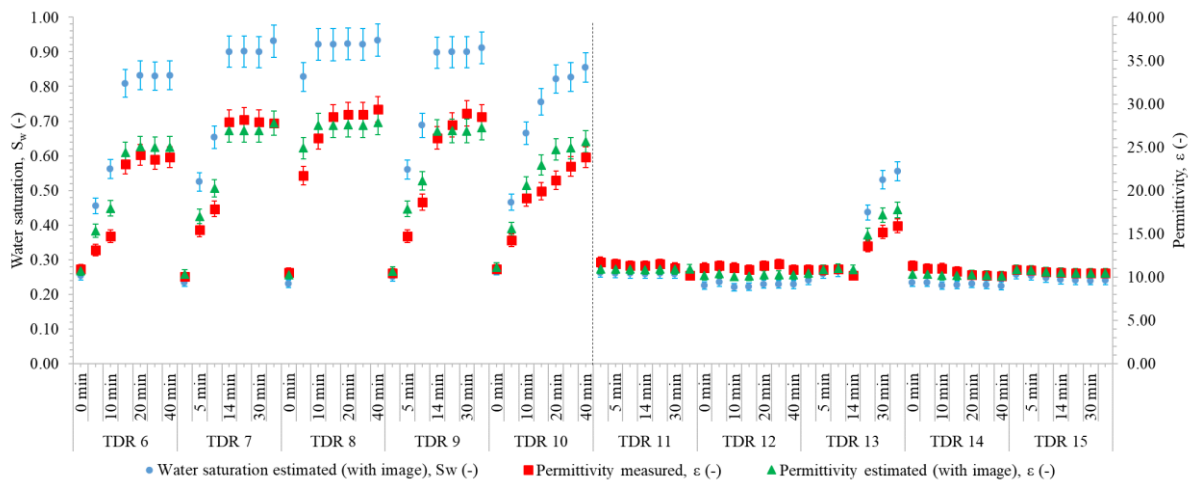


Figure 250: Average water saturation, measured and estimated permittivity during the pumping experiment in the 2D tank with 0.5 mm GB with a flow rate of 150 mL.min⁻¹ (with chemical enhancement)

We see that the $\epsilon_{\text{estimated}}$ are very close to the $\epsilon_{\text{measured}}$ for values around S_{rn} and S_{rw} . For transition phases, like in section 6.3.1.2, we see that $\epsilon_{\text{measured}}$ were always lower than $\epsilon_{\text{estimated}}$. Reduced permittivities at TDR 6 and 9 show that the radius of cone of depression is higher with chemical enhancement.

Figure 251 shows changes in permittivity as a function of time during the pumping experiment conducted with 0.1 mm GB.

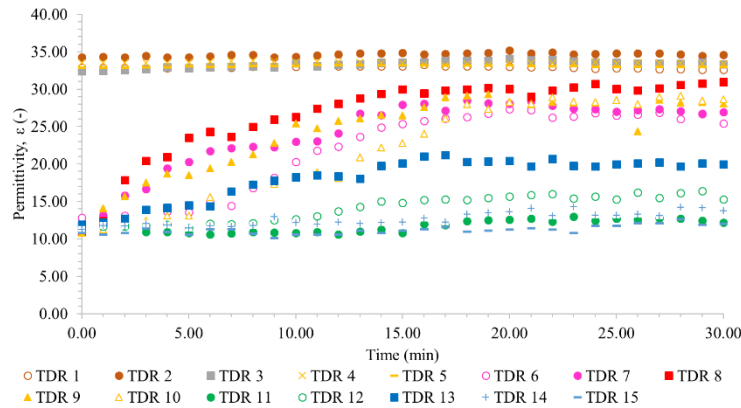


Figure 251: Evolution of the permittivity in the 2D tank with 0.1 mm GB with a flow rate of $150 \text{ mL} \cdot \text{min}^{-1}$ (with chemical enhancement)

If we compare Figure 230 (0.1 mm GB without enhancement) with Figure 251, we see that the displacement of cone of depression was faster (see also section 6.3.4 for more details). As pumping ended, $\epsilon_{\text{measured}}$ at TDR 8 was on average 30.42 ± 0.42 , which matches what was measured at the end of imbibition in 1D cells and 1D columns.

Figure 252 shows variations in water saturation, measured and estimated permittivity during the pumping experiment for 0.1 mm GB.

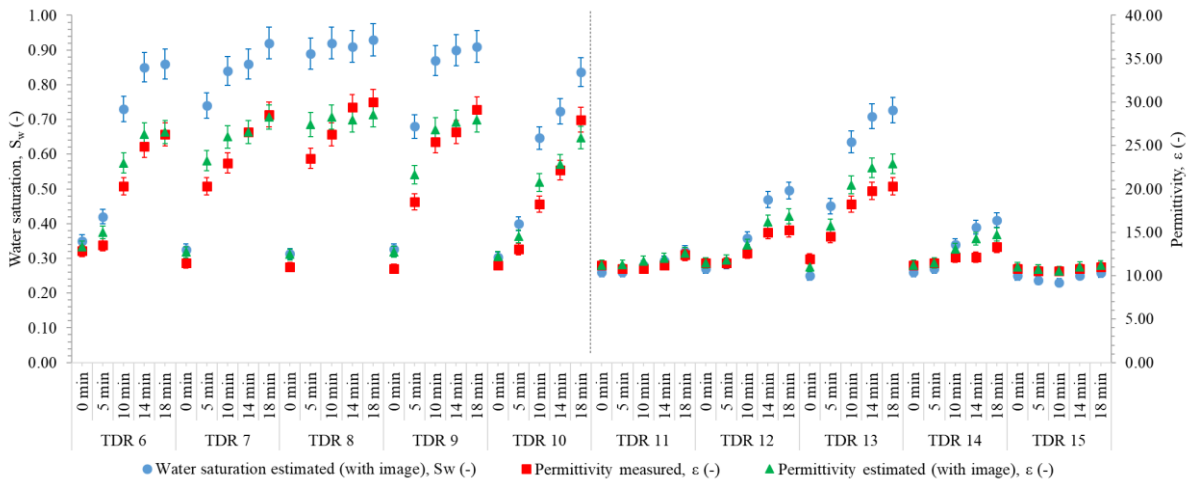


Figure 252: Average water saturation, measured and estimated permittivity during the pumping experiment in the 2D tank with 0.1 mm GB with a flow rate of $150 \text{ mL} \cdot \text{min}^{-1}$ (with chemical enhancement)

We see that the $\epsilon_{\text{estimated}}$ were very close to the $\epsilon_{\text{measured}}$ for values around S_{rn} and S_{rw} . Differences between $\epsilon_{\text{estimated}}$ and $\epsilon_{\text{measured}}$ were also very obvious for values between S_{rn} and S_{rw} . The

increased radius of action relative to the experiments without enhancement was demonstrated by $\epsilon_{\text{measured}}$ at TDR 6 and 9. Moreover, the displacement of the migration front was detected by TDR 13 and also by TDR12 and 14 (which was not the case for experiments without enhancement).

Figure 253 compares measured and estimated permittivity (with image interpretation) in the 2D tank for 0.5 and 0.1 mm GB for with enhancement case.

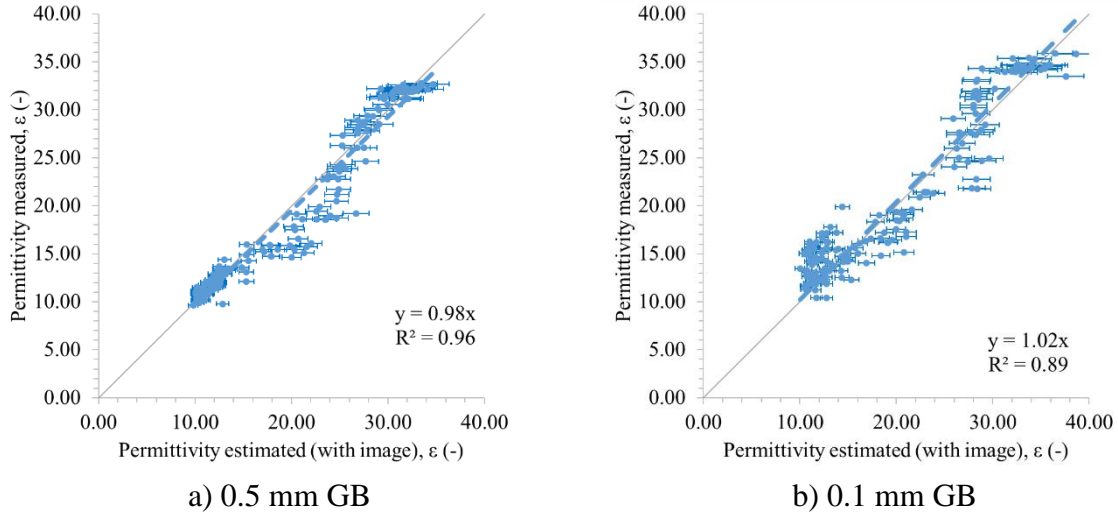


Figure 253: Comparison of measured and estimated permittivity (with image interpretation) in the 2D tank for a) 0.5 and b) 0.1 mm GB (with chemical enhancement)

The lines' slopes are close to 1: 0.98 for 0.5 mm GB and 1.02 for 0.1 mm GB. The R^2 for the 0.5 mm GB is logically higher than for the 0.1 mm GB (0.96 vs 0.89).

Four distinct zones are clearly distinguished: S_{rw} zone, transition zone, S_{m} zone and water zone. As stated above, in the transition zone the majority of the $\epsilon_{\text{measured}}$ were below $\epsilon_{\text{estimated}}$.

6.3.2.3 Electrical resistivity monitoring

Figure 254 shows changes in resistivity, as a function of time during pumping experiment conducted with 0.5 mm GB.

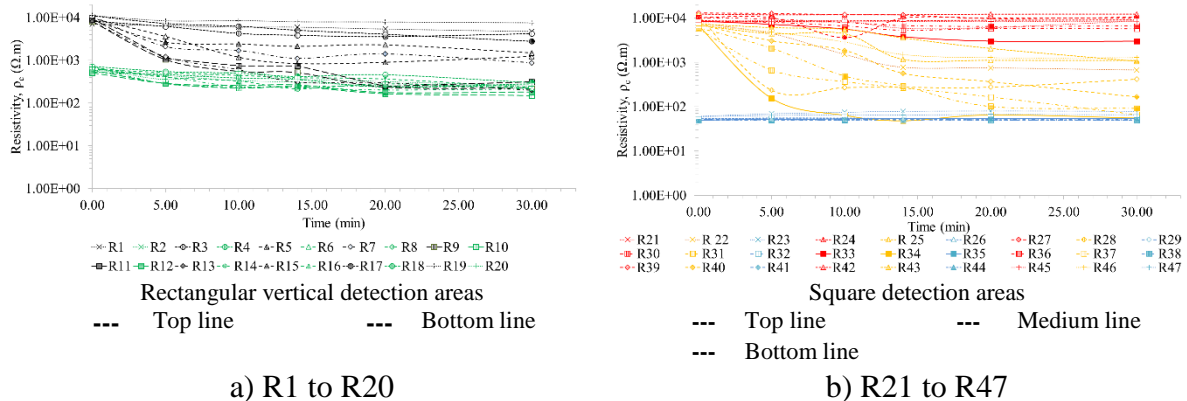


Figure 254: Evolution of the resistivity in the 2D tank with 0.5 mm GB with a flow rate of $150 \text{ mL}\cdot\text{min}^{-1}$ (with chemical enhancement) – a) R1 to R20 and b) R21 to R47

In this case, the resistivities at the start of pumping were close to the values obtained in the other experiments in the 2D tank and in the 1D experiments. We observed the same trends as those shown in Figure 234 and Figure 236 (2D tank experiment without enhancement). The resistivities measured in the middle portion of the 2D tank fell faster and more sharply than at the sides.

If we compare the resistivities with and without chemical enhancement, we see that reductions in the cone of depression were faster and higher (see section 6.3.5 for more details). Accordingly, the resistivities at R34 were, at $t=5$ min, $155 \pm 43 \Omega.m$ (vs $893 \pm 268 \Omega.m$) and, at the end of the experiment, $65 \pm 20 \Omega.m$ at $t = 20$ min (vs $144 \pm 22 \Omega.m$ at $t=25$ min). Moreover, the resistivities at R33 were, at the end of the experiment, $2999 \pm 1685 \Omega.m$ at $t = 20$ min (vs $3466 \pm 640 \Omega.m$ at $t=25$ min).

Figure 255 shows how water saturation, measured and estimated resistivity varied during the pumping experiment for 0.5 mm GB.

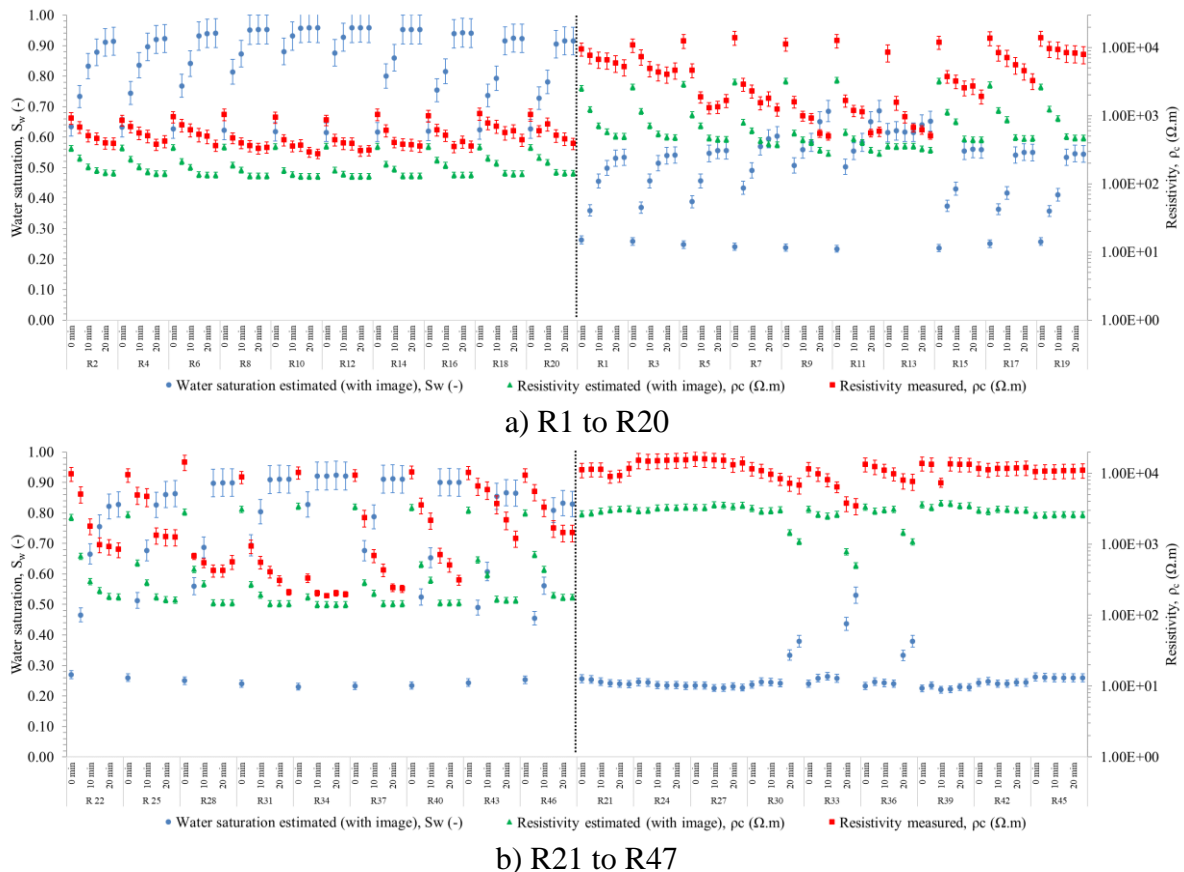


Figure 255: Average water saturation, measured and estimated resistivity during the pumping experiment in the 2D tank with 0.5 mm GB with a flow rate of $150 \text{ mL} \cdot \text{min}^{-1}$ (with chemical enhancement) – a) R1 to R20 and b) R21 to R47

The changes in S_w , $\rho_{c,\text{measured}}$ and $\rho_{c,\text{estimated}}$ agreed with each other. The differences between $\rho_{c,\text{measured}}$ and $\rho_{c,\text{estimated}}$ rose as resistivity values rose. Regarding the square detection areas of the medium line, resistivities at the central position fell faster and more sharply with chemical enhancement than without enhancement (R31, R34 and R37). In addition, the areas at the lateral position also showed greater variations. Accordingly, the resistivities at R28 were: at $t=5$ min, $236 \pm 71 \Omega.m$ (vs $1018 \pm 230 \Omega.m$). Regarding the square detection areas at the bottom line,

we saw that the reductions were greater and relate to more detection areas with chemical enhancement (R27 and R29 were impacted).

Figure 256 shows changes in resistivity as a function of time during the pumping experiment conducted with 0.1 mm GB. Figure 257 shows how water saturation, measured and estimated resistivity varied during the pumping experiment (for 0.1 mm GB).

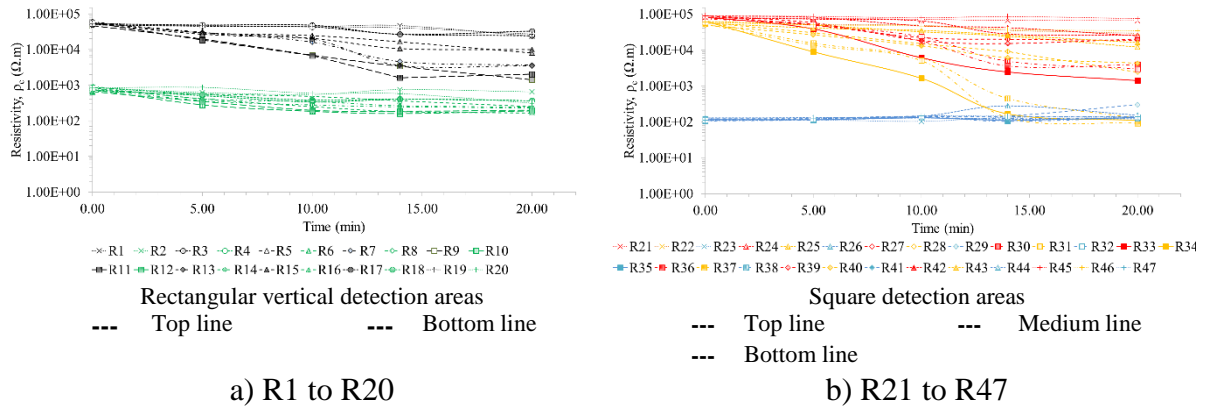


Figure 256: Evolution of the resistivity in the 2D tank with 0.1 mm GB with a flow rate of $150 \text{ mL}\cdot\text{min}^{-1}$ (with chemical enhancement) – a) R1 to R20 and b) R21 to R47

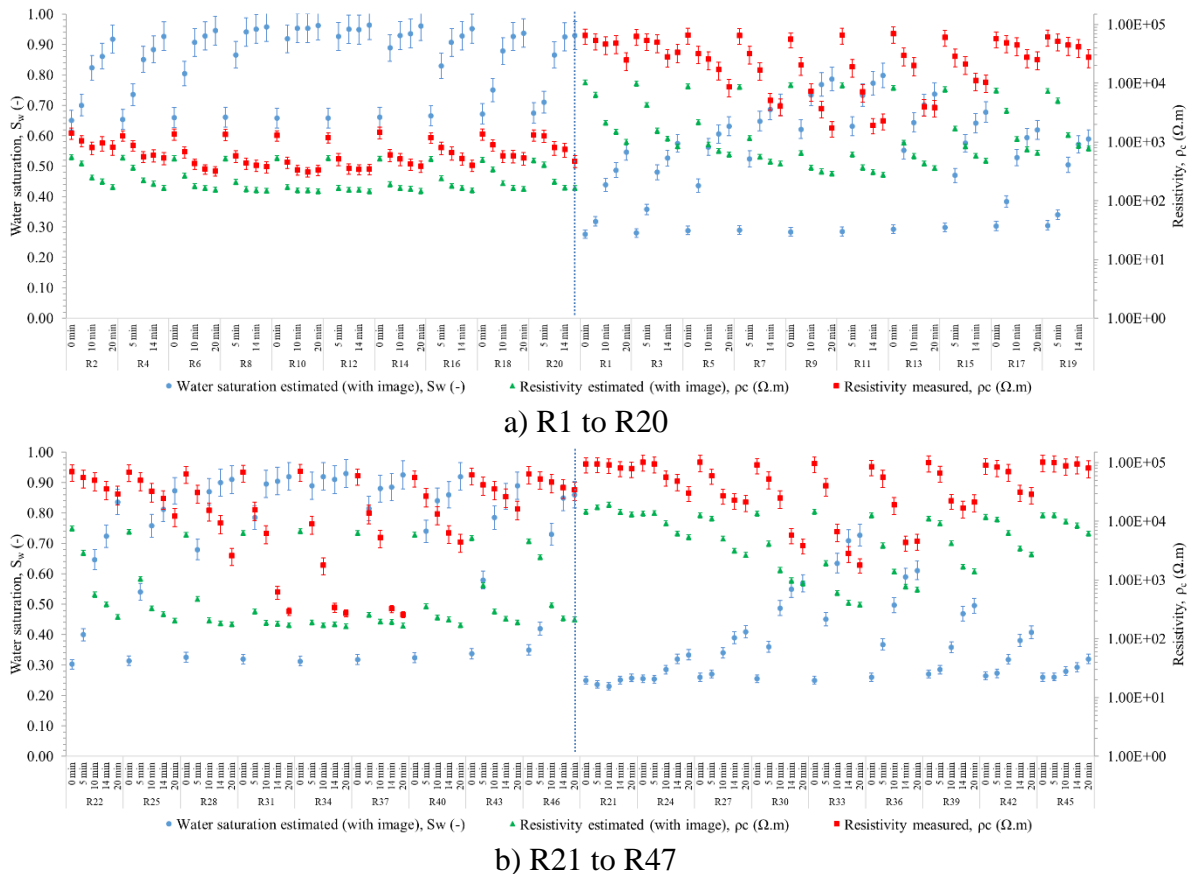


Figure 257: Average water saturation, measured and estimated resistivity during the pumping experiment in the 2D tank with 0.1 mm GB with a flow rate of $150 \text{ mL}\cdot\text{min}^{-1}$ (with chemical enhancement) – a) R1 to R20 and b) R21 to R47

The resistivities at the start of pumping agreed with the other experiments. If we compare the data for experiments with and without enhancements (Figure 235 and Figure 237, see also section 6.3.5 for more details), the beneficial effect of the chemical enhancement on residual saturation is clear from the resistivities. The resistivity at R34 at $t=20$ min was $109 \pm 33 \Omega.m$ (vs $1110 \pm 313 \Omega.m$ without enhancement). At R33, the resistivity at $t=20$ min was $1411 \pm 423 \Omega.m$ (vs $2955 \pm 886 \Omega.m$ without enhancement).

At the edge zone of the cone of depression, the resistivities were lower with chemical enhancement; at R28, the resistivity at $t=20$ min was $2426 \pm 728 \Omega.m$ (vs $17599 \pm 4280 \Omega.m$ without enhancement).

Figure 258 compares the measured and estimated resistivity (with image interpretation) in the 2D tank for 0.5 and 0.1 mm GB.

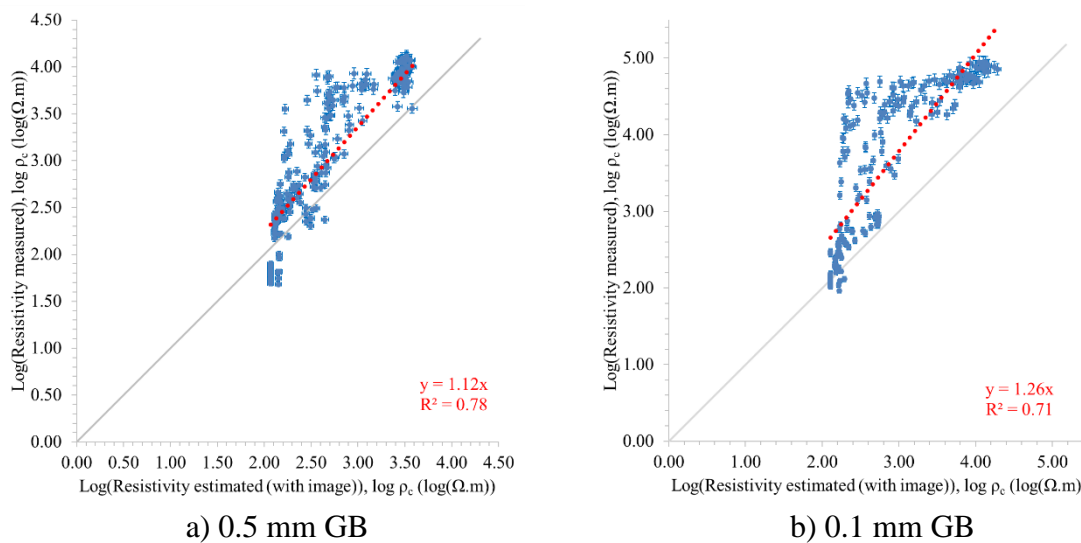


Figure 258: Comparison of measured and estimated resistivity (with image interpretation) in the 2D tank for a) 0.5 and b) 0.1 mm GB with a flow rate of $150 \text{ mL} \cdot \text{min}^{-1}$ (with chemical enhancement)

The slopes of the $\log(\rho_{c,\text{measured}})=f(\log(\rho_{c,\text{estimated}}))$ curves were respectively 1.12 and 1.26 for 0.5 and 0.1 mm GB. Moreover, the coefficient of determination was higher for the 0.5 mm GB ($R^2=0.78$) than for the 0.1 mm GB ($R^2=0.71$), which means that the data dispersivity is higher with the 0.1 mm GB.

The slopes were far from 1 were due to the $\rho_{c,\text{measured}}/\rho_{c,\text{estimated}}$ ratios for values close to S_{rw} being high: 3.20 and 5.99 for 0.5 and 0.1 mm GB, respectively.

Four distinct zones were also distinguished there: S_{rw} zone, transit ion zone, S_{rn} zone, water zone.

6.3.3 Experiments in the 2D tank with thermal enhancement

The pumping experiments (imbibition) were conducted with 0.5 and 0.1 mm GB with thermal enhancement.

Appendix 10 shows the results for the 2D tank experiments with thermal enhancement.

6.3.3.1 Experimental results: comparison of numerical simulation with optical density monitoring

a) Modeling results

Figure 259 and Figure 260 show measured and modeled volumes of DNAPL as a function of time.

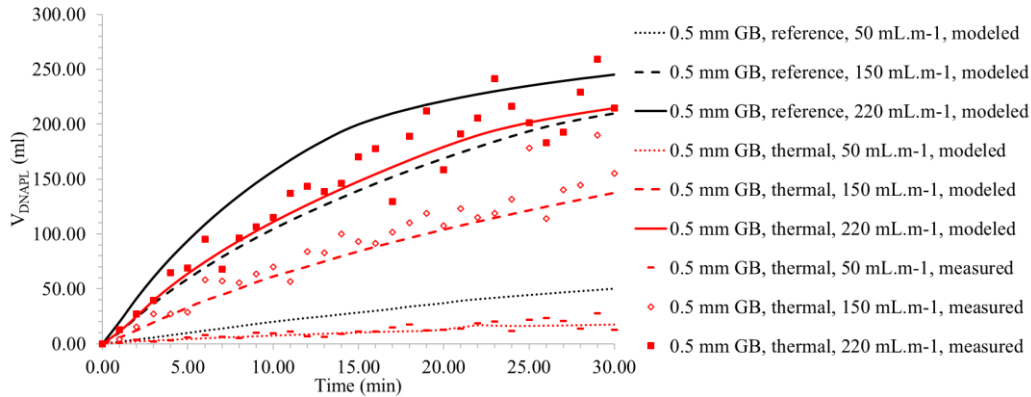


Figure 259: Evolution of measured and modeled volumes of DNAPL recovered for different flow rates with 0.5 mm GB (with thermal enhancement)

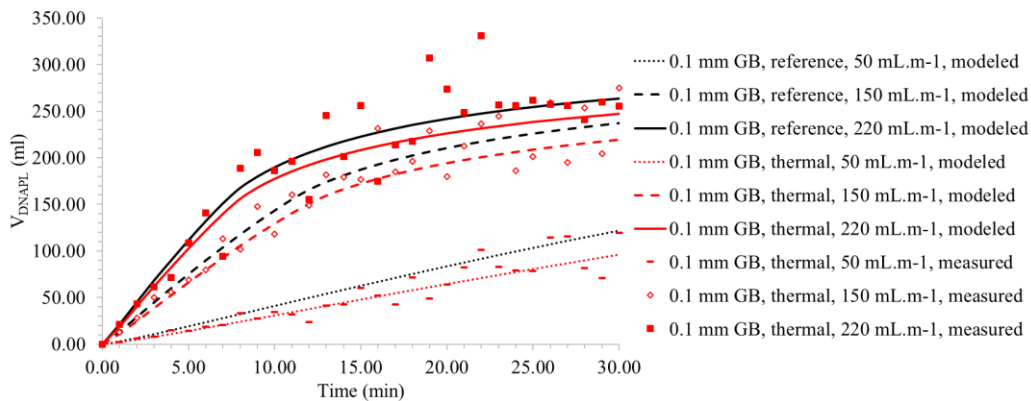


Figure 260: Evolution of measured and modeled volumes of DNAPL recovered for different flow rates with 0.1 mm GB (with thermal enhancement)

Thermal enhancement did not have any beneficial effect on recovery yield. The $V_{\text{DNAPL recovered}}$ with thermal enhancement represented on average 40, 60 and 76% of the $V_{\text{DNAPL recovered}}$ without enhancement for 0.5 mm GB (respectively for 50, 150 and 220 mL.min⁻¹). For the 0.1 mm GB, these recovery yields were between 77, 91 and 93%.

This was related to the reductions in viscosity (μ_w/μ_{nw}) and density (ρ_w/ρ_{nw}) ratios with temperature increase not being sufficient to improve recovery rates and yields.

Figure 261 shows how S_w changed over time along the horizontal profile and along a vertical profile at the center of the 2D tank.

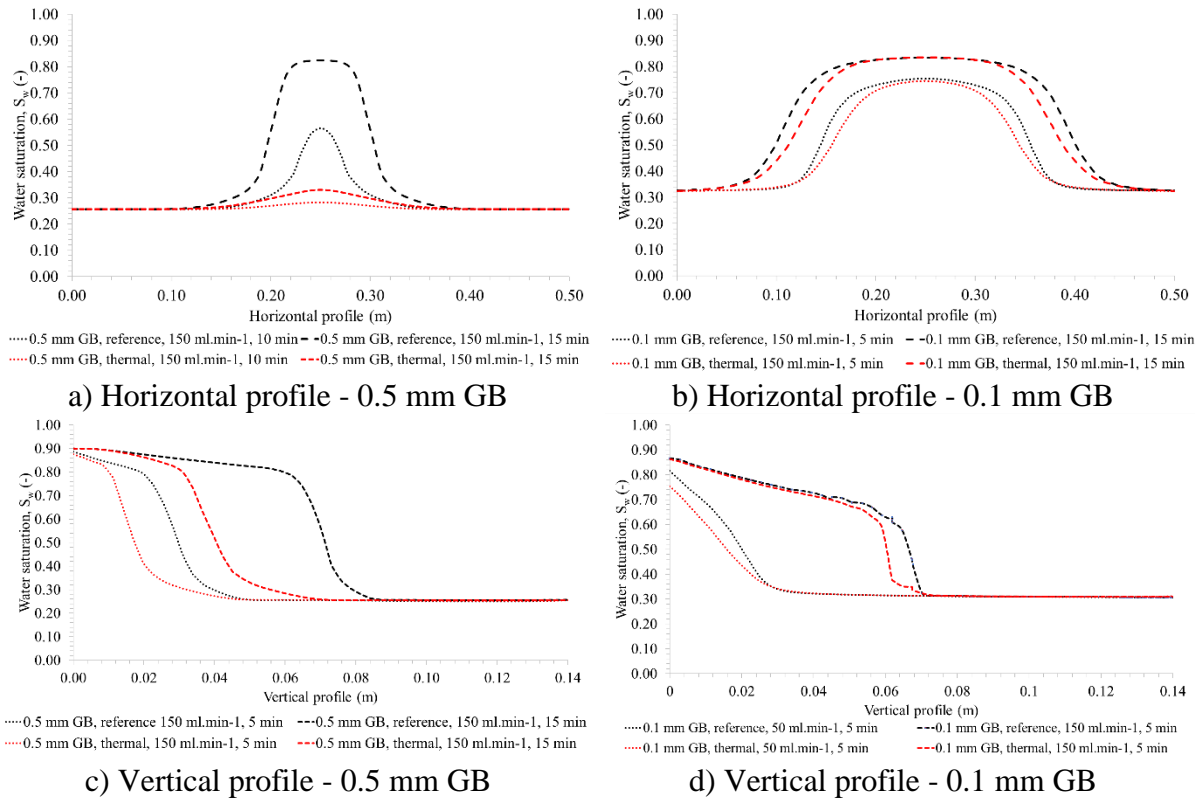


Figure 261: Evolution of the S_w along a) and b) horizontal profile and c) and d) vertical profile at the center of the 2D tank with 0.5 and 0.1 mm GB (with thermal enhancement)

The horizontal water saturation profile demonstrates that thermal enhancement was not effective. For example, regarding 0.5 mm GB at 0.25 m, S_w was 0.33 at $t=10$ min with thermal enhancement but 0.56 without enhancement. For the 0.1 mm GB, S_w at 0.17 m were 0.67 and 0.56 respectively for experiments without and with thermal enhancement (for $t=10$ min).

The vertical water saturation profile shows that thermal enhancement has a negative effect on the displacement of the migration front. We see that it reduced the displacement of the migration front by about 50% for the 0.5 mm GB and 20% for the 0.1 mm GB (for $S_w=0.5$ at $t=15$ min).

b) Volume of DNAPL recovered

Figure 262 shows modeled and measured V_{DNAPL} recovered.

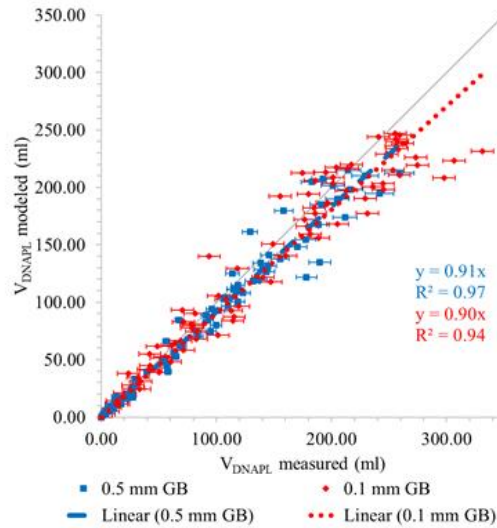


Figure 262: Comparison of measured and modeled volumes of the DNAPL recovered in the 2D tank with 0.5 and 0.1 mm GB (with thermal enhancement)

The slopes of $V_{\text{DNAPL recovered modeled}}=f(V_{\text{DNAPL recovered measured}})$ were, like for the previous experiments (without enhancement and with chemical enhancement), close to 1 (0.91 and 0.90 respectively for 0.5 and 0.1 mm GB with R^2 of 0.97 and 0.94). Again, as expected, the standard deviation was lower for the 0.1 mm GB.

c) DNAPL-water interface displacement

Figure 263 compares experimental and modeled radius and height of the cone of depression with 0.5 mm GB and 0.1 mm GB.

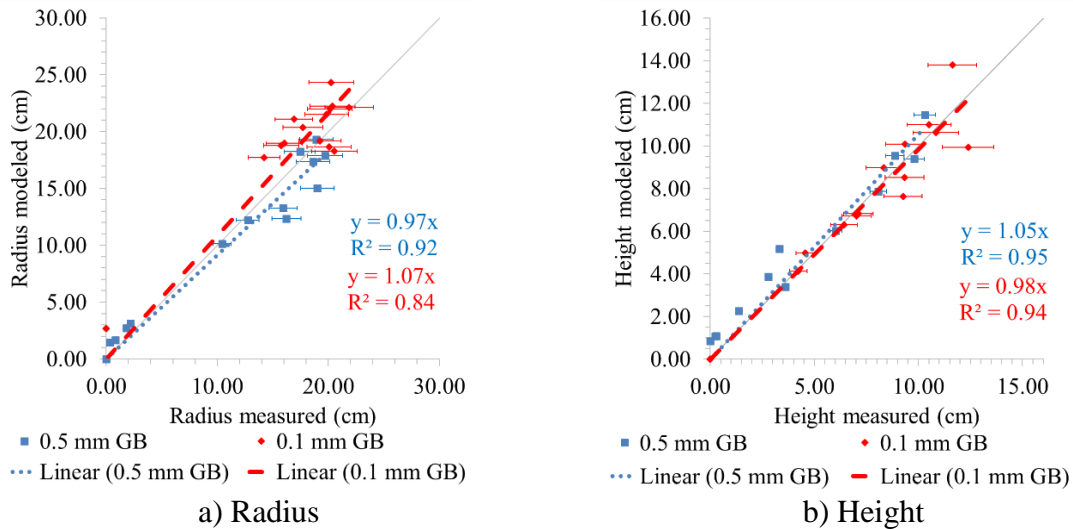


Figure 263: Comparison of measured and modeled a) radius and b) height of the cone of depression with 0.5 and 0.1 mm GB (with thermal enhancement)

The slopes of $\text{radius}_{\text{modeled}}=f(\text{radius}_{\text{measured}})$ were close to 1: 0.97 and 1.07 respectively for the 0.5 and 0.1 mm GB (with R^2 of 0.92 and 0.84). Moreover, the slopes of $\text{height}_{\text{modeled}}=f(\text{height}_{\text{measured}})$ were respectively 1.05 and 0.98 (with $R^2=0.95$ and 0.94).

d) Comparison of estimated recovered DNAPL volumes by modeling and image interpretation

Figure 264 compares estimated DNAPL volumes recovered experimentally (with image interpretation) and by modeling (after lateral V_{DNAPL} deduction).

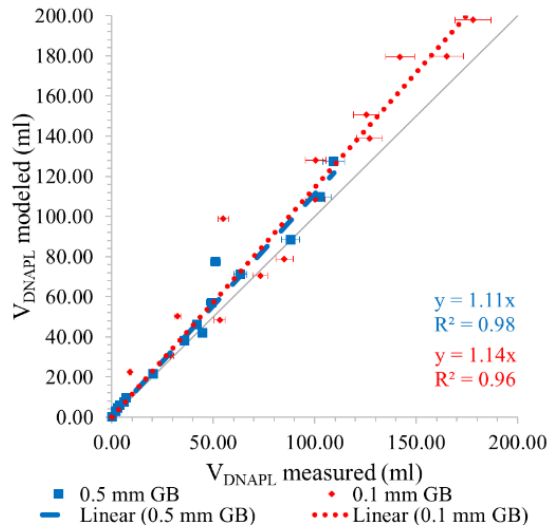


Figure 264: Comparison of estimated DNAPL volumes recovered experimentally (with image interpretation) and by modeling (after lateral V_{DNAPL} deduction) with 0.5 and 0.1 mm GB (with thermal enhancement)

The pumping experiments interpreted by image matched the modeling results. The linear regression curve gradients were respectively 1.11 and 1.14 for the 0.5 and 0.1 mm GB (with R^2 of 0.98 and 0.96).

e) Fingering effect at the DNAPL-water interface

Figure 265 shows the average values and standard deviations of the DNAPL-water interfaces for thermal enhancement case.

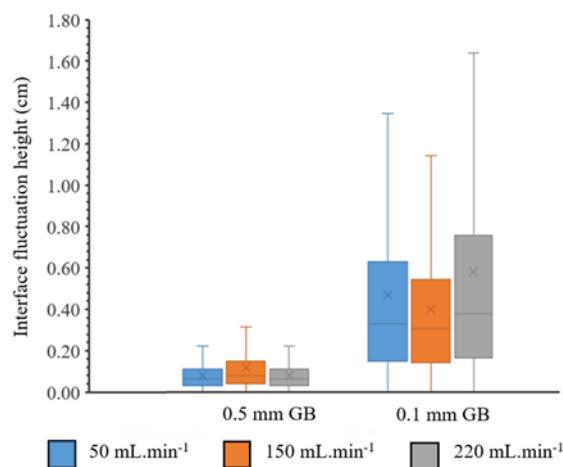
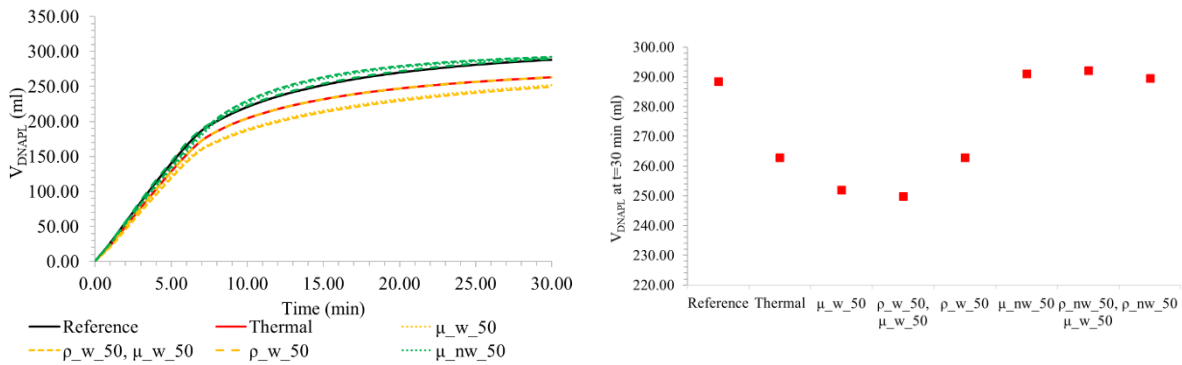


Figure 265: Statistical representation of fingerings of the DNAPL-water interface with 0.5 and 0.1 mm GB (with thermal enhancement)

Since the μ_w/μ_{nw} ratios were lower, it explains why the fingerings were globally lower for thermal enhancement than without enhancement (see section 6.3.6 for more details). The differences in fingering between the 0.5 and 0.1 mm GB were lower than for the reference (without enhancement). Therefore, the average interface heights were respectively 0.09 and 0.46 cm for the 0.5 and 0.1 mm GB (with standard deviations of 0.07 and 0.38). The flow rate had little influence on fingerings; the differences in interface height between 50 and 220 mL.min⁻¹ were 10 and 9% (respectively, for 0.5 and 0.1 mm GB).

f) Parametric study of the model

Figure 266 shows the results of the parametric study of the model.



a) V_{DNAPL} recovered as a function of time

b) Final V_{DNAPL} at $t=30$ min

Figure 266: Parametric study of the model (with thermal enhancement): a) V_{DNAPL} recovered as a function of time and b) Final V_{DNAPL} at $t=30$ min

The results demonstrate that the thermal enhancement was not effective.

The parametric study was based on comparison with a base scenario (reference: 0.1 mm GB, without enhancement, 150 mL.min⁻¹). The viscosity and density values for water and DNAPL at 50 °C were changed independently to confirm the weight of these parameters in the final modeling results.

If we keep the rheological properties of DNAPL (at 20 °C) and change the water’s properties (at 50 °C), the final V_{DNAPL} recovered falls (V_{DNAPL} between 249.79 and 262.92 mL).

Conversely, if we keep the rheological properties of the water at 20 °C and change the DNAPL’s properties to 50 °C the final V_{DNAPL} rises (V_{DNAPL} between 289.55 and 292.06 mL). Changing the viscosity has slightly more impact than changing the density (respective final V_{DNAPL} of 290.99 vs 289.55 mL). Considering both parameters (ρ and μ) at 50 °C is the best approach ($V_{DNAPL}= 292.06$ mL).

From these results, we can conclude that when the ratios μ_{nw}/μ_w and ρ_{nw}/ρ_w goes to one, the better the DNAPL recovery is achieved.

6.3.3.2 Permittivity monitoring

Figure 267 shows changes in permittivity as a function of time during pumping experiment conducted with 0.5 mm GB.

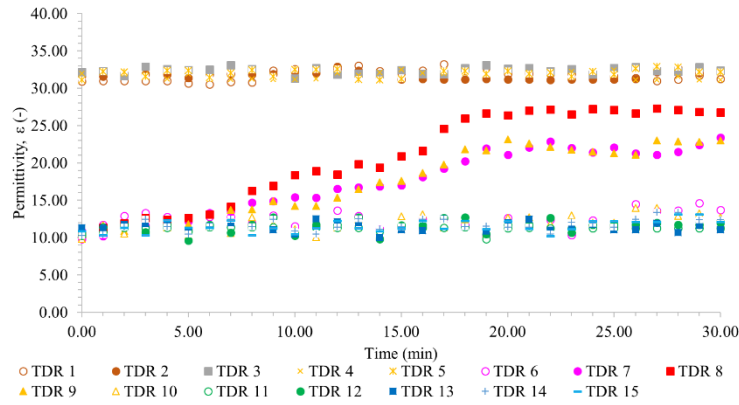


Figure 267: Evolution of the permittivity in the 2D tank with 0.5 mm GB with a flow rate of $150 \text{ mL}\cdot\text{min}^{-1}$ (with thermal enhancement)

If we compare the results with experiments in the 2D tank without enhancement, we see that the migration front is displaced more slowly (see section 6.3.4 for more details). For TDR 8, the permittivity plateau was reached at 16 min (vs. 12 min without enhancement).

Only TDR 8 had permittivity values corresponding to S_m (27.00 ± 0.25). TDR 13 was not impacted by pumping. These two points show that the radius and height of the cone of depression were lower with thermal enhancement than without.

Figure 268 shows variations in water saturation, measured and estimated permittivity during the pumping experiment for 0.5 mm GB.

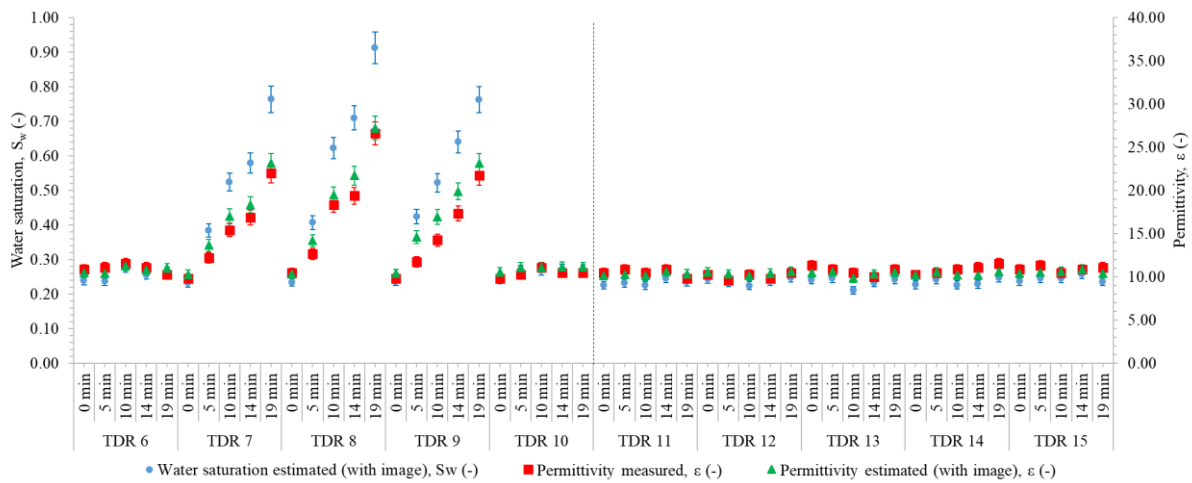


Figure 268: Average water saturation, measured and estimated permittivity during the pumping experiment in the 2D tank with 0.5 mm GB with a flow rate of $150 \text{ mL}\cdot\text{min}^{-1}$ (with thermal enhancement)

Here again, we see that the $\epsilon_{\text{estimated}}$ are very close to the $\epsilon_{\text{measured}}$ for values around S_m and S_{rw} . We see that reduced permittivities were only detected by TDR 7 to 9, which shows that the radius of the cone of depression was much lower than for experiments without enhancement.

Figure 269 shows changes in permittivity as a function of time during pumping experiment conducted with 0.1 mm GB.

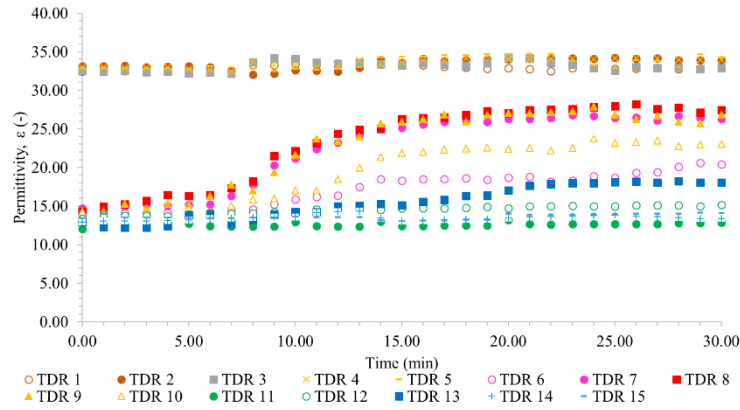


Figure 269: Evolution of the permittivity in the 2D tank with 0.1 mm GB with a flow rate of $150 \text{ mL}\cdot\text{min}^{-1}$ (with thermal enhancement)

The plateau for $\epsilon_{\text{measured}}$ at TDR 8 was only reached at $t=20$ min whereas without thermal enhancement, it was reached at $t=10$ min. $\epsilon_{\text{measured}}$ at the end of pumping (26.95 ± 0.74) agreed with the experiments done using the 1D cells and 1D columns.

Figure 270 shows variations in water saturation, measured and estimated permittivity during the pumping experiment for 0.1 mm GB.

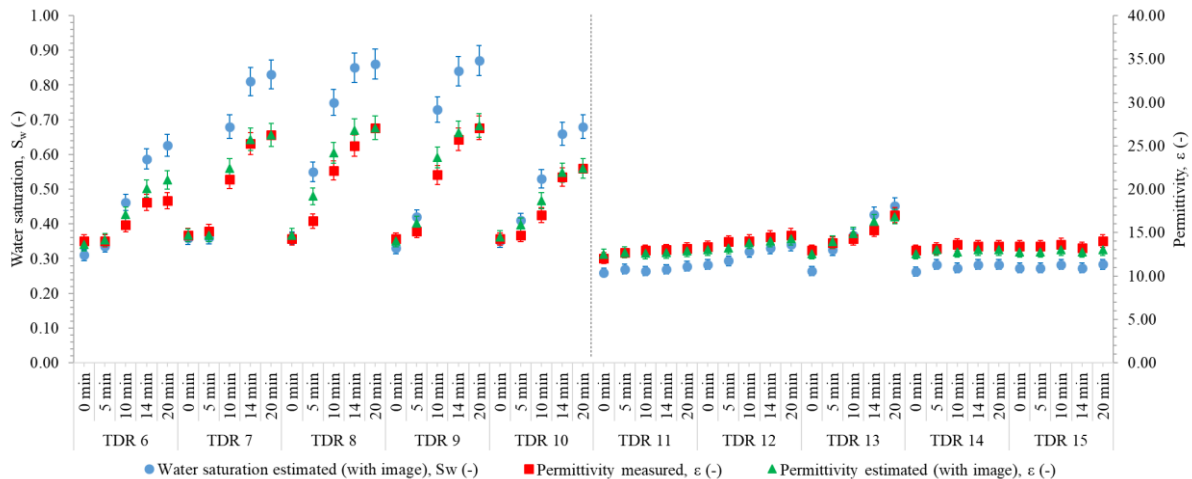


Figure 270: Average water saturation, measured and estimated permittivity during the pumping experiment in the 2D tank with 0.1 mm GB with a flow rate of $150 \text{ mL}\cdot\text{min}^{-1}$ (with thermal enhancement)

The difference between $\epsilon_{\text{estimated}}$ and $\epsilon_{\text{measured}}$ was also shown during the transition phase. In comparison with the experiments conducted without enhancement (see Figure 231), we see that permittivities fell faster and more substantially for TDR 7 to 9 but also for TDR 6 to 10. This demonstrates that the radius and height of cone of depression were higher without thermal enhancement than with it.

Figure 271 compares measured and estimated permittivity (with image interpretation) in the 2D tank for 0.5 and 0.1 mm GB for thermal enhancement case.

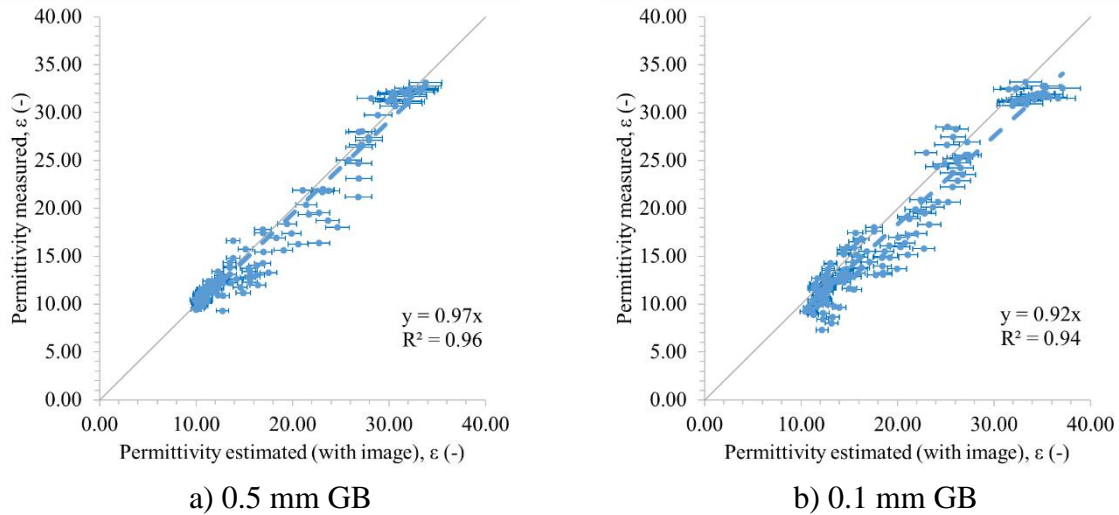


Figure 271: Comparison of measured and estimated permittivity (with image interpretation) in the 2D tank for a) 0.5 and b) 0.1 mm GB (with thermal enhancement)

As shown in these figures, the slopes are 0.97 and 0.92 respectively for 0.5 and 0.1 mm GB. The R^2 for the 0.5 mm GB is logically higher than for the 0.1 mm GB (0.96 vs 0.94). Four distinct zones are clearly distinguished: as stated above, in the transition zone the majority of the $\epsilon_{\text{measured}}$ were below $\epsilon_{\text{estimated}}$.

6.3.3.3 Electrical resistivity monitoring

Figure 272 shows changes in resistivity, as a function of time during pumping experiment conducted with 0.5 mm GB.

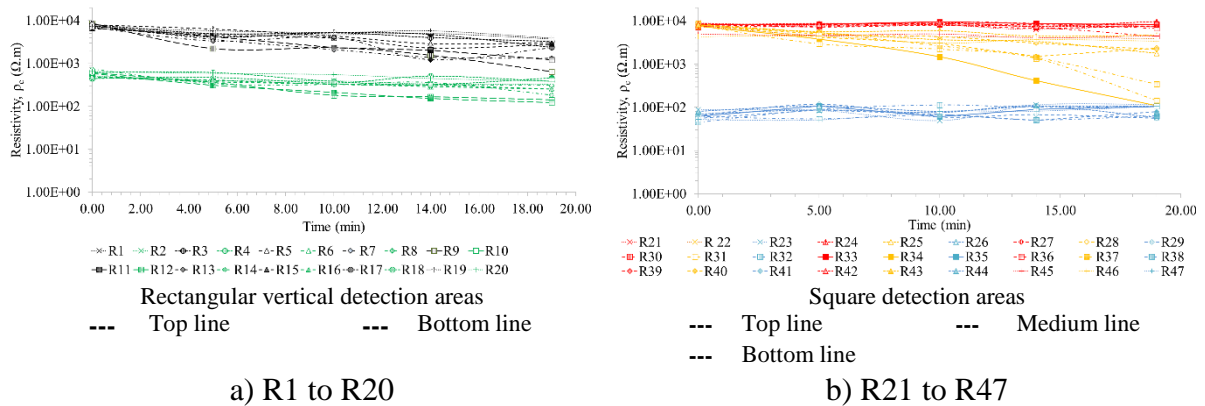


Figure 272: Evolution of the resistivity in the 2D tank with 0.5 mm GB with a flow rate of $150 \text{ mL} \cdot \text{min}^{-1}$ (with thermal enhancement) – a) R1 to R20 and b) R21 to R47

The conditions at the end of drainage were identical to those reported for the other 2D tank experiments. The resistivities measured at the start of the experiment were also similar. As we stated, in this case, the thermal enhancement has no beneficial effect on recovery yield or recovery rate.

If we compare the resistivities with thermal enhancement to resistivities without enhancement, we see that the reductions in the cone of depression were slowed and less sharp (Figure 272 and Figure 273). The resistivities at R34 were, at $t=5 \text{ min}$, $3772 \pm 1031 \text{ } \Omega \cdot \text{m}$ (vs $893 \pm 268 \text{ } \Omega \cdot \text{m}$). At the end of the experiment, the resistivities at R33 were $8188 \pm 2456 \text{ } \Omega \cdot \text{m}$ at $t = 19 \text{ min}$ (vs

3466 ± 640 Ω.m at t=25 min); the variation of resistivity is therefore very moderate. The resistivities at R28, at a side position, at t=5 min were 4168 ± 1250 Ω.m (vs 1017.51 ± 230 Ω.m). The differences between $\rho_{c,measured}$ and $\rho_{c,estimated}$ rose as resistivity values rose (Figure 273).

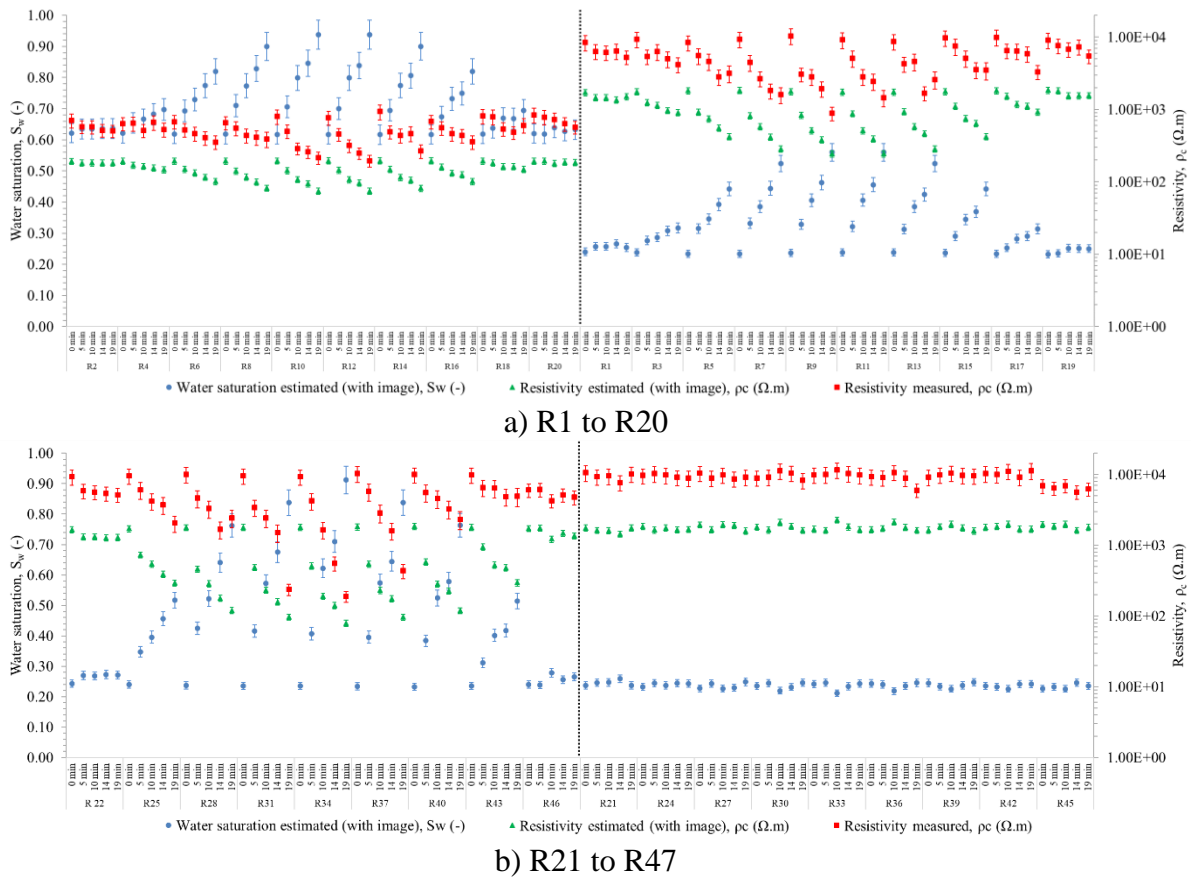


Figure 273: Average water saturation, resistivity measured and estimated during the pumping experiment in the 2D tank with 0.5 mm GB with a flow rate of 150 mL.min⁻¹ (with thermal enhancement) – a) R1 to R20 and b) R21 to R47

Figure 274 shows changes in resistivity, as a function of time during pumping experiments conducted with 0.1 mm GB.

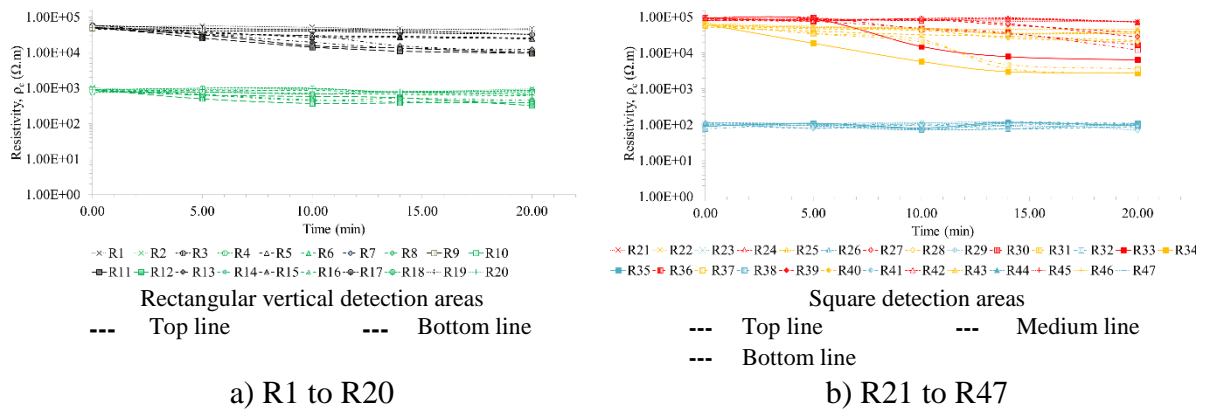


Figure 274: Evolution of the resistivity in the 2D tank with 0.1 mm GB with a flow rate of 150 mL.min⁻¹ (with thermal enhancement) – a) R1 to R20 and b) R21 to R47

The observations can be made for the 2D tank experiments with 0.1 mm GB: the monitored resistivities showed that thermal enhancement was not effective for free product recovery: the resistivity falls in the cone of depression were lower and slower.

The resistivity at R34 at t=20 min was $2818 \pm 645 \text{ } \Omega.m$ (vs $1100 \pm 313 \text{ } \Omega.m$ without enhancement). At R33, the resistivity at t=20 min was $6354 \pm 1906 \text{ } \Omega.m$ (vs $2955 \pm 886 \text{ } \Omega.m$ without enhancement).

At the edge zone of the cone of depression, the resistivities were lower with thermal enhancement; at R28, the resistivity at t=20 min was $22113 \pm 6634 \text{ } \Omega.m$ (vs $17599 \pm 4280 \text{ } \Omega.m$ without enhancement) (Figure 275).

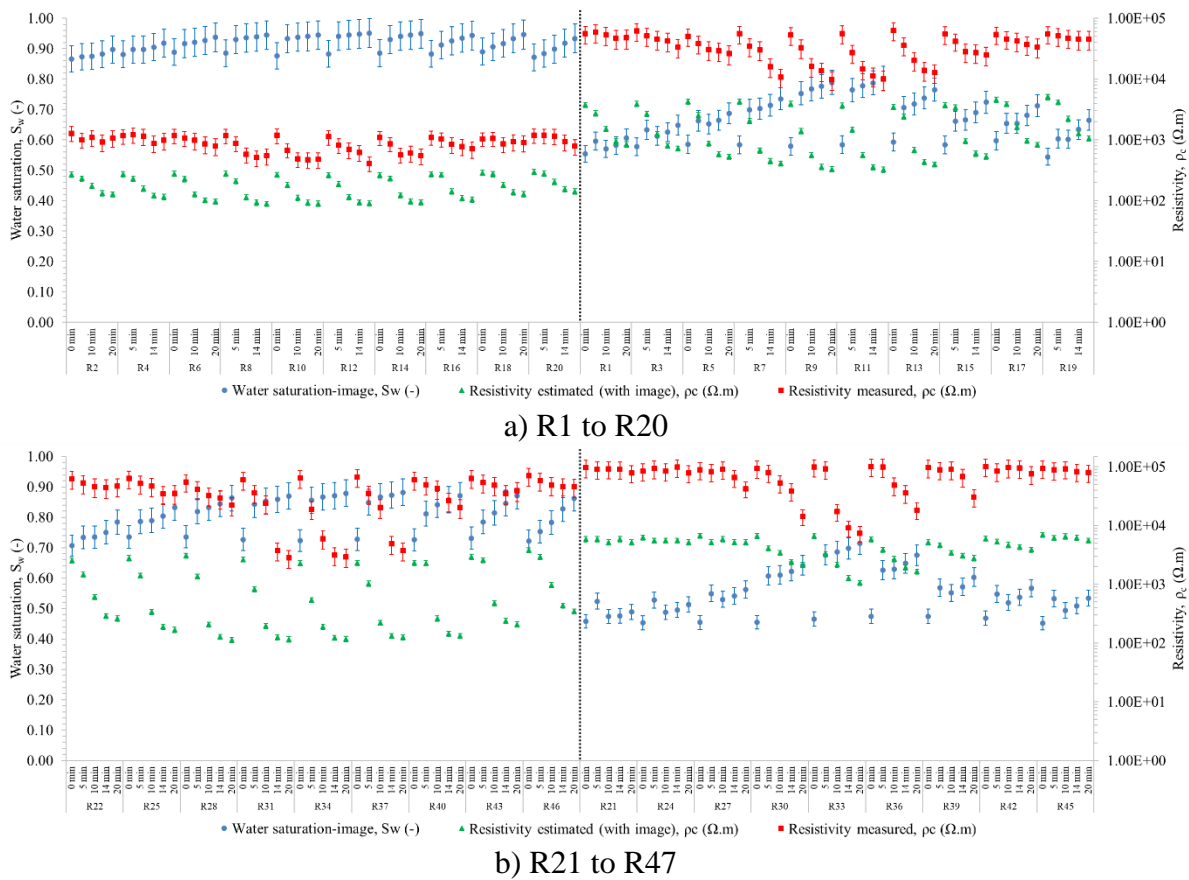


Figure 275: Average water saturation, resistivity measured and estimated during the pumping experiment in the 2D tank with 0.1 mm GB with a flow rate of $150 \text{ mL} \cdot \text{min}^{-1}$ (with thermal enhancement) – a) R1 to R20 and b) R21 to R47

Figure 276 compares the measured and estimated resistivity (with image interpretation) in the 2D tank for 0.5 and 0.1 mm GB.

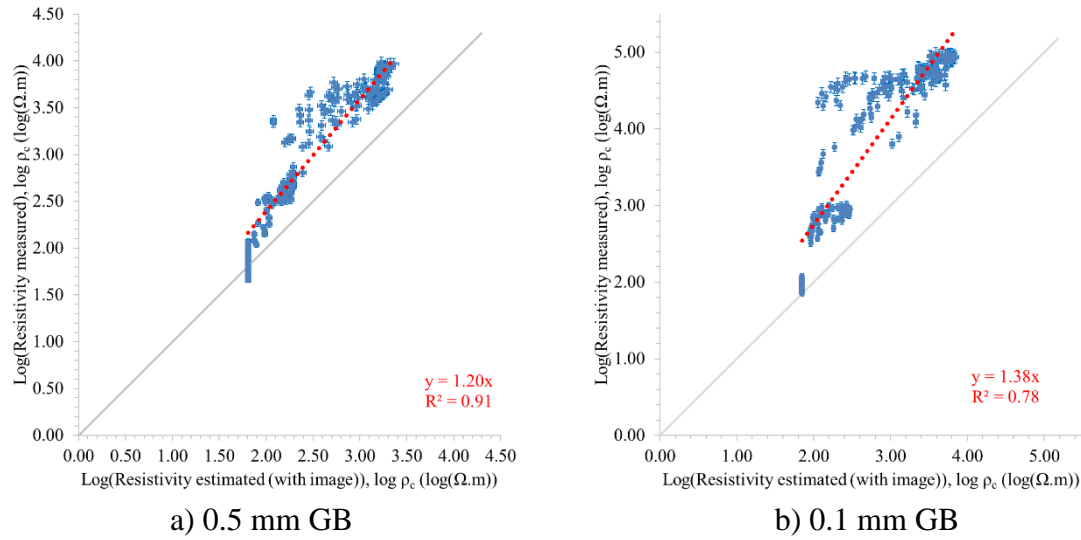


Figure 276: Comparison of measured and estimated resistivity (with image interpretation) in the 2D tank for a) 0.5 and b) 0.1 mm GB with a flow rate of $150 \text{ mL}\cdot\text{min}^{-1}$ (with thermal enhancement)

The slopes of the $\log(\rho_{c,\text{measured}})=f(\log(\rho_{c,\text{estimated}}))$ curves were respectively 1.20 and 1.37 for 0.5 and 0.1 mm GB. The dispersivity was higher with the 0.1 mm GB than the 0.5 mm GB ($R^2=0.78$ for 0.1 mm GB vs $R^2=0.91$ for 0.5 mm GB). Here also, we note that the curve slopes that were far from 1 were due to the $\rho_{c,\text{measured}}/\rho_{c,\text{estimated}}$ ratios for values close to S_{rw} being high: 4.46 and 9.37 for 0.5 and 0.1 mm GB, respectively. Finally, we also distinguished four zones: S_{rw} zone, transition zone, S_m zone, water zone.

6.3.4 Comparison of permittivities without enhancement, with chemical and thermal enhancements

Figure 277 and Figure 278 show a comparison of measured permittivity in the 2D tank (with and without enhancements) for 0.5 and 0.1 mm GB, respectively.

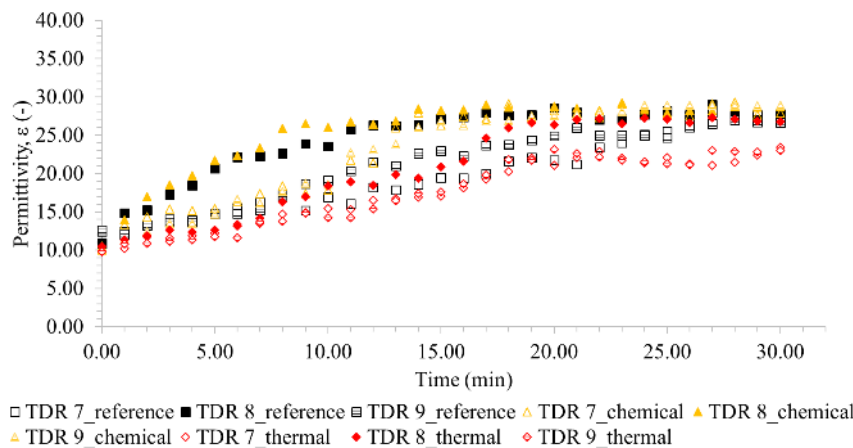


Figure 277: Comparison of measured permittivity in the 2D tank for 0.5 mm GB with a flow rate of $150 \text{ mL}\cdot\text{min}^{-1}$ (with and without enhancements)

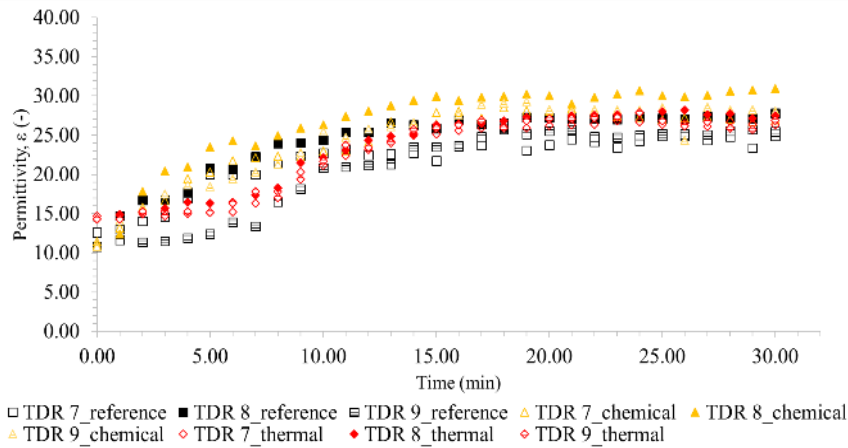


Figure 278: Comparison of measured permittivity in the 2D tank for 0.1 mm GB with a flow rate of $150 \text{ mL}\cdot\text{min}^{-1}$ (with and without enhancements)

Figure 278 shows that by using TDR it is possible to assess the differences in remediation yields and rates between recovery of free product without enhancement, with chemical enhancement and with thermal enhancement. The TDR located at the heart of the cone of depression globally showed faster and larger variations in permittivities for chemical enhancement (this is more visible for the 0.1 GB than for the 0.5 mm GB). From TDR monitoring data, we can affirm that with chemical enhancement the radius of the cone of depression of action is higher, the S_n are lower and the S_n fall faster. Moreover, since the coefficients of determination (calculated on the basis of graphs $\epsilon_{\text{measured}}=f(\epsilon_{\text{estimated}})$) are correct, the S_n can be quantified from the TDR probes.

6.3.5 Comparison of resistivities without enhancement, with chemical and thermal enhancements

Figure 279 and Figure 280 show a comparison of measured resistivity in the 2D tank (with and without enhancements) for 0.5 and 0.1 mm GB, respectively.

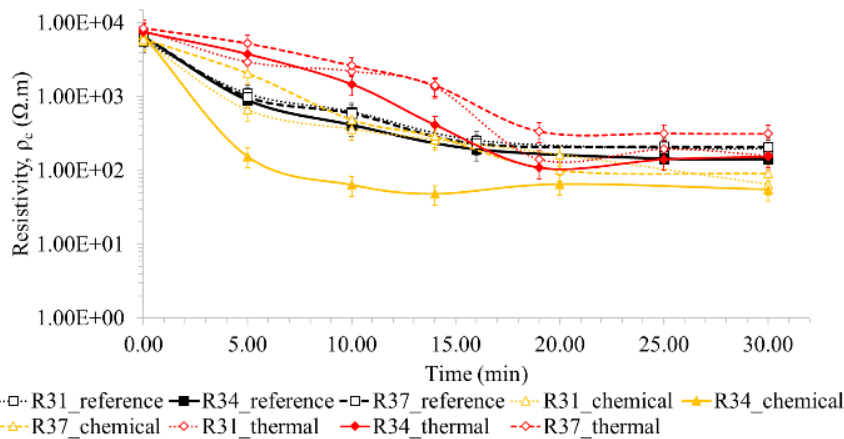


Figure 279: Comparison of measured resistivity in the 2D tank for 0.5 mm GB with a flow rate of $150 \text{ mL}\cdot\text{min}^{-1}$ (with and without enhancements)

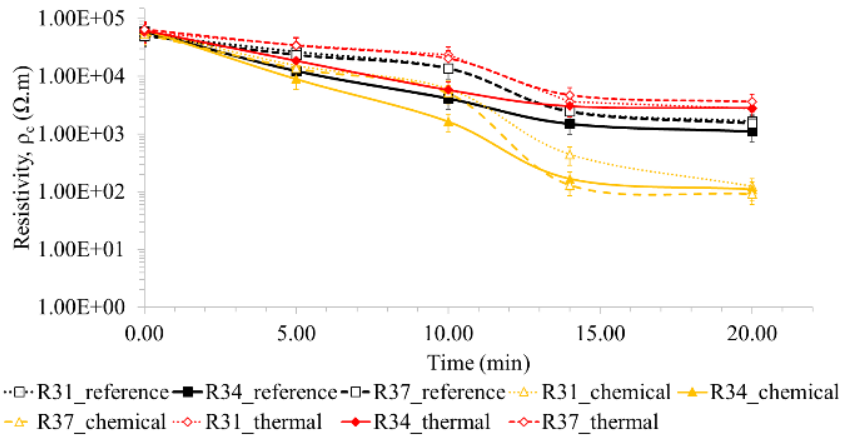


Figure 280: Comparison of measured resistivity in the 2D tank for 0.1 mm GB with a flow rate of 150 mL.min⁻¹ (with and without enhancements)

The electrical resistivity monitoring had higher standard deviations (often of the order of 30%). Therefore, we cannot closely estimate the residual saturations from electrical resistivity alone. However, the precision was sufficient (especially, for values close to the S_m) to show differences between the three treatment technologies. Figure 279 and Figure 280 show that chemical enhancement has higher remediation yields and rates: the radius of action was higher, the S_n were lower and S_n fell more quickly. We also see clearly that thermal enhancement was less effective: resistivity drops were lower and slower.

The combination of electrical resistivity monitoring (which gives an integrative view of the cone of depression) with TDR (which give precise but spatially limited data) allows to better quantify the remediation rates and yields.

6.3.6 Comparison of fingerings effect at the DNAPL-water interface without enhancement, with chemical and thermal enhancements

Figure 281 shows the experimental results on the phase-diagram of multiphase domain displacement (Figure 28). The capillary number (N_{ca}) and the mobility ratio (m_r) are calculated using Eq. 86 and Eq. 89, respectively.

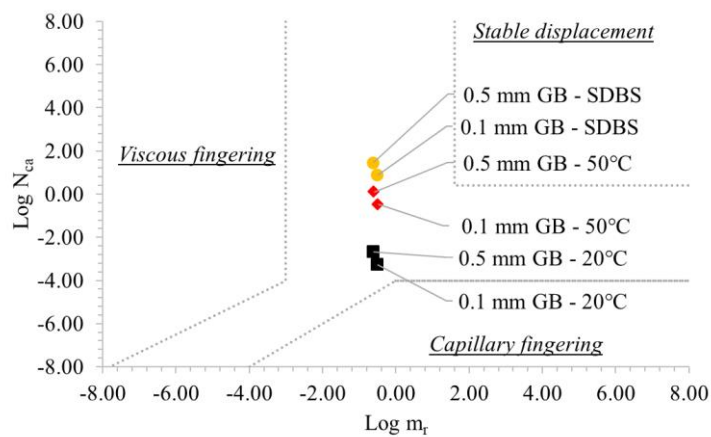


Figure 281: Representation of experimental results on the phase-diagram of multiphase domain displacement (adapted from [Lenormand et al. (1988)])

Figure 226, Figure 248 and Figure 265 highlight that fingerings were more important for 0.1 mm GB than for 0.5 mm GB. It is expected because the capillary effects are more important for 0.1 mm GB. Figure 281 shows that the dots relating to the 0.1 mm GB are always closer to the capillary fingering zone than the dots relating to 0.5 mm GB (N_{ca} are smaller). If we compare pumping without enhancement with pumping with enhancement, we note that for 0.5 and 0.1 mm GB, the dots are much closer to the capillary fingering area. The thermal and chemical enhancement makes it possible to get closer to the stable displacement zone (by reducing the interfacial tensions and dynamic viscosities). These results agree with the experimental results relating to the measurements of DNAPL-water interface fluctuation heights.

6.4 Technical and economical analysis

A technical and economic analysis of DNAPL free product recovery with and without enhancement was carried out within the SILPHES project [Colombano *et al.* (2018)]. The analysis was carried out on the basis of a fictitious case typical of contamination with chlorinated compounds: height 15.00 × width 15.00 × depth 13.00 m. Two hypotheses were considered: gravelly sand (hypothesis 1) and silty sand (hypothesis 2). The treatment of pumped water was also taken into account. Several case studies were considered: injection of surfactant, surfactant foam and several chemical reducers. Figure 282 presents the technical and economical comparison of free product recovery with and without chemical enhancement.

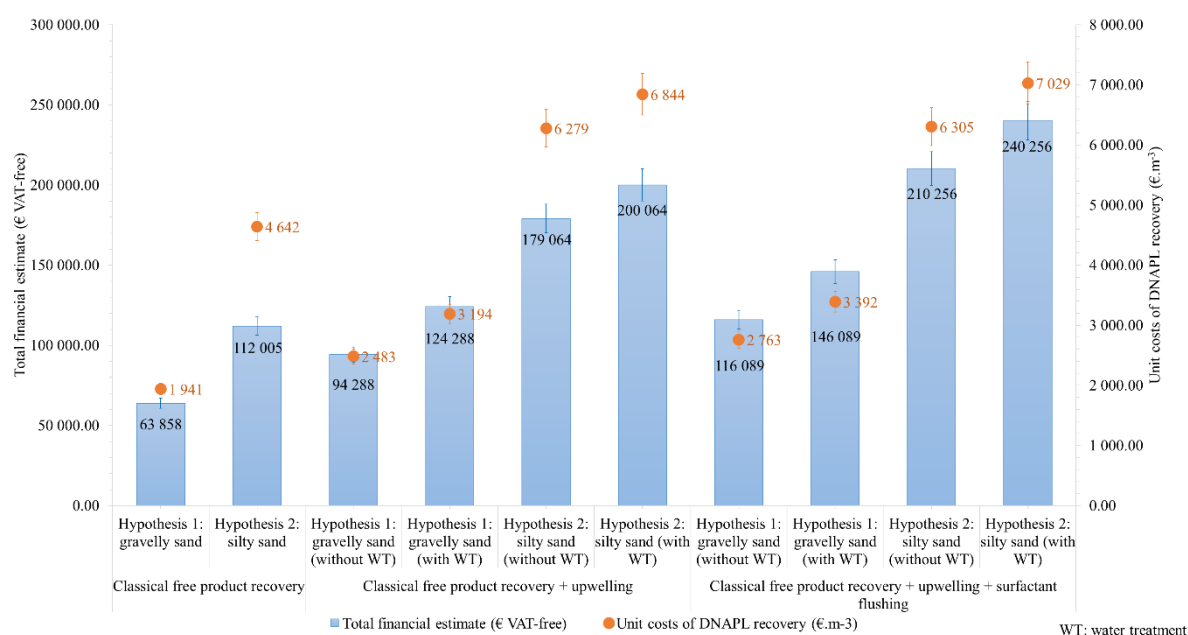


Figure 282: Total financial estimate and unit costs of DNAPL free product recovery (with and without chemical enhancement) [Colombano *et al.* (2018)]

The S_m used for the unit costs are based on the SILPHES project field scale data and on the usual treatment costs in France. Therefore, the respective S_m after classical free product recovery, classical free product recovery + upwelling and classical free product recovery + upwelling + surfactant flushing are respectively: 0.35, 0.25 and 0.17 for gravelly sand and, 0.45, 0.35 and 0.24 for silty sand. Remediation duration and ROI were not changed for the comparison between classical pumping and pumping with chemical enhancement (major assumption). The only assumption changes between the scenarios are the remediation yields.

Treatment of pumped water has also been considered. The treatment of this dissolved phase only concerns 1% of the mass balance.

Hydraulic and chemical enhancement methods greatly reduce residual saturation. Therefore, the residual masses can be reduced by a factor of two. Assisted pumping techniques generate extra costs by a factor of 1.5 to 1.9 for pumping and upwelling; and 1.8 to 2.3 for pumping, upwelling, and surfactant. However, the unit treatment costs (€·m⁻³ recovered) are of the same order of magnitude as the base scenario (between 35% and 75% extra cost).

The additional costs of using surfactants compared to upwelling are only 17 and 24%. This is because surfactants are used at low concentrations (below CMC), and also because radii and heights of cone of depression are more important.

The technical and economic analysis shows that the techniques developed and compared to conventional pumping techniques are both affordable and accessible. If there is a need to reduce residual saturations, a graduated approach with hydraulic and chemical enhancement is possible in view of the remediation goals being considered.

This technical and economic analysis demonstrated that the use of surfactant foams (as a complementary treatment to surfactant and finishing treatment) was very advantageous.

According to literature review, the duration and flow rate of pollution source released are proportional to the quantity of DNAPL remaining in the soils. These release flow rates generate water (and sometimes gases), which incur additional monitoring costs over several years. These costs can amount to tens of thousands of euros per year, and span over decades. These monitoring costs should be considered when selecting the treatment methods used to improve purification yields.

6.5 Conclusions

The goal of DNAPL pumping experiments in the 2D tank was: i. To validate the two-phase flow model ; ii. To compare the modeled water saturations with the permittivity and resistivity measurements as well as the optical densities during the pumping test (at different flow rates) over time; iii. To determine how chemical and thermal enhancements affect DNAPL recovery yields.

The experiments were conducted with 0.5 and 0.1 mm GB. Three different pump flow rates were studied for both GB sizes: 50, 150 and 220 mL·min⁻¹. The experiments were conducted without enhancement (reference), with chemical enhancement and with thermal enhancement.

The two-phase flow model was conducted with the pressure-pressure formulation. The capillary pressure function and relative permeability function used were based on VGM equations.

Numerical modelings were compared with image interpretation. Comparing experimental and modeled recovered DNAPL volumes shows that the model fits well with the experiments (whose results were treated with image interpretation). For example, for experiments without enhancement, the linear regression curves $V_{\text{DNAPL modeled}}=f(V_{\text{DNAPL measured}})$ were 0.99 ($R^2=0.97$) for 0.5 mm GB and 1.10 ($R^2=0.95$) for 0.1 mm GB. Moreover, comparing experimental and modeled radius and height of the cone of depression showed that the model was valid. Accordingly, for experiments without enhancement, the linear regression curves

$V_{\text{radii modeled}}=f(V_{\text{radii measured}})$ were 1.08 ($R^2=0.94$) and 1.003 ($R^2=0.81$) respectively for the 0.5 mm and 0.1 mm GB. For the cone of depression heights, linear regressions confirm that the model is valid: the curves were respectively 1.05 ($R^2=0.92$) and 0.98 ($R^2=0.89$).

We also compared numerical model results with experimental results successfully for chemical enhancement and thermal enhancement.

The results of modeling and experiments show that chemical enhancement has a beneficial effect on recovered DNAPL volumes. The use of chemical enhancement was proportionally more advantageous for lower flow rates than for higher flow rates. For the 0.1 mm GB the $V_{\text{DNAPL, chemical}}/V_{\text{DNAPL, reference}}$ ratios were relatively stable over time and were higher for lower flow rates than for higher flow rates. Also, these ratios were on average 1.37, 1.22 and 1.18 respectively for 50, 150 and 220 mL.min⁻¹. For the 0.5 mm GB, the ratios were much higher at the start of the experiment (the ratios were at 2 min, 2.90, 1.60 and 1.40 respectively for 50, 150 and 220 mL.min⁻¹). The cone of depression radius and height increased with added surfactant.

Thermal enhancement had no beneficial effect on DNAPL recovery rate or yield. Heating the porous media had a negative effect on cone of depression radius and height.

For experiments without enhancement, the DNAPL-water interface shapes were less irregular for the 0.5 mm GB than for the 0.1 mm GB. Obviously, the higher the pumping flow rate, the more irregularities there are at the interface. For experiments with chemical enhancement, the order of magnitude of irregularities in the DNAPL-water interface shapes is similar to that without enhancement. However, we should underline that increasing the flow rate had limited influence on fingering. Finally, for experiments with thermal enhancement, fingerings were globally lower than without enhancement or with chemical enhancement. This makes sense since the μ_w/μ_{nw} ratios were lower.

We also compared image interpretation results with measured permittivities. To do this, the average optical densities (corresponding to the area of detection for the TDR) were determined throughout the experiments. These optical densities were transformed by water saturation then into permittivities using the CRIM model (whose parameters were validated during 1D cell and 1D column experiments). The results of comparing $\epsilon_{\text{measured}}$ and $\epsilon_{\text{estimated with image}}$ are compelling for experiments without enhancement, with chemical enhancement and with thermal enhancement. For example, the slopes of linear regressions ($\epsilon_{\text{measured}} = f(\epsilon_{\text{estimated with image}})$) were close to 1 (0.95 for 0.5 mm GB and 0.96 for 0.1 mm GB), which shows that the measured permittivities agreed well with the image interpretation. As expected, we see that R^2 for the 0.5 mm GB was higher than for the 0.1 mm GB (0.96 vs 0.90), which shows better correlation of values for 0.5 mm GB.

For all experiments we clearly distinguish four distinct zones: S_{rw} zone (start of pumping), S_m zone (end of pumping), water zone (corresponding to $S_w=1$), and transition zone (this zone corresponds to values between the S_{rw} and S_m zones). The correlations are very good for the first three zones.

For the transition zone, we see that the majority of $\epsilon_{\text{measured}}$ were lower than $\epsilon_{\text{estimated}}$. This is because when the detection zone is crossed by the migration front, the zone displays both S_m and S_{rw} areas. So for two heterogeneous zones, the weight of the portion similar to S_{rw} impacts global $\epsilon_{\text{measured}}$ more than the portion similar to S_m . This shows that the CRIM model is only

valid for homogeneous media. It will be necessary to quantify this transition zone using mixing models.

However, if we consider all points (*i.e.* all four zones), the linear regressions are good for experiments without enhancement, with chemical enhancement and with thermal enhancement. For example, for experiments without enhancement, the slopes were 0.95 for 0.5 mm GB and 0.96 for 0.1 mm GB (with $R^2=0.96$ and 0.90 , respectively).

We also compared image interpretation results with measured resistivities. The average optical densities (corresponding to the area of detection of the dipole-dipole injection and reception configurations) were determined throughout the experiments. These optical densities were transformed by water saturation into resistivity using Archie's law. The results of comparing $\rho_{c,measured}$ and $\rho_{c,estimated}$ with image were not very promising for any of the experiments, with or without enhancements. The slopes of linear regressions ($\log(\rho_{c,measured}) = f(\log(\rho_{c,estimated} \text{ with image}))$) varied between 1.12 and 1.37. The R^2 varied between 0.64 and 0.87. The standard deviations for the measurements were of the order of 30%. The slopes of the lines further from 1 are due to the fact that the $\rho_{c,measured}/\rho_{c,estimated}$ ratios were higher for low S_w (close to the S_{rw}). Note that for low resistivities (*i.e.* high S_w), the $\rho_{c,measured}-\rho_{c,estimated}$ correlations are good.

Therefore, it is not possible to quantify water saturations accurately only by measuring electrical resistivities. However, the accuracy is sufficient (especially for values close to S_w) to highlight differences between the three treatment approaches. We also distinguished 4 distinct zones: S_{rw} zone, transition zone, S_m zone, water zone. By combining electrical resistivity monitoring (which gives an integrative view of the cone of depression) with TDR (which gives precise but spatially limited data), we can better: i. closely calibrate resistivities with S_w ; ii. better quantify remediation rates and yields.

The technical and economic analysis of DNAPL free product recovery has demonstrated that the chemical enhancement used below CMC is cost-effective and could be easily implemented at field scale: the additional costs of using surfactants are between 17 and 24%. If there is a need to reduce residual saturations, a graduated approach with hydraulic and chemical enhancement is possible in view of the remediation goals being considered.

7. CONCLUSIONS AND PERSPECTIVES

7. CONCLUSIONS AND PERSPECTIVES

The work presented in this thesis contributes as a whole to improve knowledge in the area of polluted site remediation. It demonstrates that DNAPL recovery as free product can be increased by implementing chemical enhancement. It has also been demonstrated that experiments in 1D cells and 1D columns produce robust parameters that can be used to accurately model the behavior of DNAPL/water in a 2D tank. Finally, the monitoring of experiments with image interpretation, permittivity and electrical resistivity allows accurate quantification of DNAPL saturation in the laboratory. These experiments and monitoring at the laboratory scale, combined with multiphase flow modeling, open up perspectives for full-scale applications.

Regarding the experimental section, we have designed and built all the 1D cells, 1D columns and the 2D tank used in this thesis. A patent filing is also in progress. A two-phase flow model was also built using COMSOL Multiphysics®.

Rheological and chemical parameters were measured (interfacial tensions, contact angles, viscosity, density, concentrations in the aqueous phase). The addition of surfactant has a beneficial effect on capillary forces (decrease in interfacial tensions and contact angles) while heating has an effect on the dynamic viscosity. From measurements of interfacial tensions and COCs in the aqueous phase we determined the Critical Micelle Concentration (CMC).

Drainage-imbibition experiments were performed in 1D cells in a saturated porous media (with 0.5 and 0.1 mm Glass Beads-GB). The experimental data fit the van Genuchten – Mualem (VGM) capillary pressure-saturation function well. We acquired α and n as well as S_{rn} and S_{rw} with the aim of comparing the different experiments and using them in multiphase flow modeling.

These experiments were performed without enhancement and with enhancements. The concentrations of surfactants used were under their CMC, to avoid solubilization. **The best remediation yield was obtained with SDBS: 27.6% for 0.5 mm GB and 46.3% for 0.1 mm GB. Experiments with thermal enhancement were also conducted at 50 °C (to avoid volatilization), but no significant improvement in the remediation yield has been reported.**

Regarding the permittivity measurements, the estimation of residual saturations fits well with the CRIM model in most cases (less than 8% difference between estimations and measurements). The estimated electrical resistivity data (with the Archie's Law) correlates less with the measurements than permittivity. The $\rho_{c,measured}/\rho_{c,estimated}$ ratios were respectively 3.14 at the end of the drainage and 0.99 at the end of the imbibition for 0.5 mm GB whereas they were 12.84 at the end of drainage and 5.22 at the end of imbibition for 0.1 mm GB. The optical density experiments show that residual saturations can be estimated accurately ($R^2=0.98$).

The drainage-imbibition experiments were carried out in 1D columns to characterize two-phase flow (and in particular the displacement of the DNAPL-water interface according to the applied pressures). The two-phase flow model was conducted with the pressure-pressure formulation. The difference between the measured DNAPL volumes in the 1D columns (by volume balance) and the modeled volumes were very low (less than 5% on average). In addition, the displacement of the DNAPL-water interface modeled corresponds to what was measured visually within the 1D columns.

Measured values of S_m and S_{rw} were similar to those determined in 1D cells (without enhancement and with chemical and thermal enhancements). The remediation yields with chemical enhancement were of the same order of magnitude as those reported in 1D cells (26.4% for 0.5 mm GB and 53.4% for 0.1 mm GB). No significant improvement in the remediation yield was observed with thermal enhancement.

From permittivity monitoring, it was possible to monitor accurately the DNAPL-water interface migration front (modeled) as well as to determine the S_w . Estimated variations in resistivity as a function of S_w correlated less with these measurements than for permittivity. The results are close to those seen in the 1D cells.

For 2D tank experiments, pumping was performed at different flow rates with 0.5 mm and 0.1 mm GB. The experiments were also performed with and without enhancement.

Modelings were compared with image interpretation (based on the optical density calibration). Comparing experimental and modeled recovered DNAPL volumes shows that the model fits well with the experiments (whose results were treated with image interpretation). The slopes of $V_{DNAPL, recovered, modeled} = f(V_{DNAPL, recovered, measured})$ for all the tests were between 0.88 and 1.14 (with R^2 between 0.93 and 0.98). The comparison of radii and heights of the cone of depression, measured with image interpretation, were also very similar to those modeled.

The use of chemical enhancement was proportionally more advantageous for lower flow rates than for higher flow rates. A few minutes after the start of the experiments, the $V_{DNAPL, chemical} / V_{DNAPL, reference}$ ratios were for 50 and 220 mL.min⁻¹ on average respectively 2.90 and 1.40 for 0.5 mm GB. For 0.1 mm GB, these ratios varied on average between 1.37 and 1.18. These increases in recovery rates are related to the increase of cone of depression radius and height and, the decrease of S_m within the cone of depression. Thermal enhancement had no beneficial effect on DNAPL recovery rate or yield.

The comparison of the image interpretations (allowing to estimate S_w and therefore ϵ within the area of detection for the TDR) with measured permittivities shows good agreement. Indeed, the slopes of $\epsilon_{measured} = f(\epsilon_{estimated\ with\ image})$ vary between 0.92 and 1.02 (with R^2 between 0.89 and 0.96).

Conversely, image interpretations and measured resistivities compare less favorably. The slopes of linear regressions ($\log(\epsilon_{measured}) = f(\log(\epsilon_{estimated\ with\ image}))$) vary between 1.12 and 1.37. The R^2 varies between 0.64 and 0.87. In addition, the standard deviations of the measurements are around 30%. For low resistivities (*i.e.* high S_w), the $\rho_{c, measured} / \rho_{c, estimated}$ correlations are good.

It is therefore not possible to quantify water saturations in an accurate way with electrical resistivity monitoring only. However, the accuracy is sufficient (especially for high values of S_w) to highlight differences between the three treatment technologies. Through a combination of electrical resistivity monitoring (which gives an integrative view of the cone of depression) and TDR (which gives accurate but spatially limited information) we can: i. finely calibrate resistivities with S_w ; ii. better quantify the remediation rates and yields.

The technical and economical analysis of DNAPL free product recovery shows that the chemical enhancement used below CMC is cost-effective: the additional costs of using surfactants are only between 17 and 24%.

Future work should focus on experiments using water and porous medium (including heterogeneities) from actual polluted sites.

Concerning the experimental research, improvements can be implemented:

- Selective pressure transducers should be installed in order to measure the average pressure of each phase within the porous medium. This would make it possible to determine the capillary pressure at different flow rates in 1D cells and 1D columns,
- On the basis of these new experiments, the hysteretic dynamic effect should be integrated into the capillary pressure-saturation function for more realistic modeling,
- A 1D cell and a 1D column (with slightly curved glass on the front) should be manufactured in order to be able to measure simultaneously permittivity, resistivity, pressures and optical density,
- A new 2D tank with selective pressure transducers should be developed and built-up.

More specifically, prospective improvements in terms of modeling with COMSOL Multiphysics® are:

- The model should consider the three dimensions,
- The heterogeneities of medium permeability must be accounted for,
- Transient chemical and thermal phenomena should be integrated into the model,
- The dissolution of the pure phase towards the aqueous phase can also be studied (in order to better assess the effects of surfactants if working at concentrations greater than the surfactant the CMC),
- The variation of capillary pressure-saturation curves of drainage and imbibition could also be incorporated into the model (to take into account effects of hysteresis),
- Fingering could also be considered,
- Coupling of multiphase flow modeling with permittivity and resistivity mixing models may better estimate the measurement/model correlations; in the case of resistivity, this would help to study the phenomena of underestimation or overestimation that we highlighted.

However, COMSOL Multiphysics® is not suitable for large scale modeling. It can be used as a first approach to validate multiphase parameters and small-scale experiments. Subsequently, the data acquired with such modeling could be integrated into other models more suitable for larger scales and which better account for the multiphase phenomena (such as TMVOC and OpenFOAM® codes).

The quantification methods developed with image interpretation can be used for experiments relating to: i. multiphase flow monitoring in porous or fractured media (injection/pumping of varied viscous and thixotropic fluids); ii. dissolution monitoring; iii. oxidant and reducer injection monitoring; iv. clogging monitoring. If the optical density contrasts are not sufficient, it is possible to add colored chemical tracers.

With respect to the permittivities, the following future work could be performed:

- Other frequencies should be tested,
- The imaginary part of the resistivity needs to be processed,
- Longer waveguides could be used to have a larger area of detection in the field.

As for electrical resistivities, the future work should focus on developing a better correlation between resistivities and DNAPL saturation. The improvements must relate to the following points:

- Influence measurement zone of probes needs to be corrected,
- Other frequencies must be tested,
- The imaginary part of the conductivity needs to be processed,
- The data must be acquired so that inversions are performed before and after the pumping in order to have a better image of the cone of depression,
- Tests must be performed with other types of electrodes including polarizable electrodes (which are closer to what is in the field).

As for applications at field conditions, the prospects are interesting. Remediation monitoring by geophysical methods (including resistivities for DNAPLs) are particularly successful. These are the main methods for indirectly interpolating data between boreholes (with soil analysis), piezometers (with water analysis) and soil-gas wells (with gas analysis). However, quantifying the S_n remains difficult. The main monitoring approach is based on differences in resistivities before, during and after treatment. Monitoring the permittivities continuously at the field would contribute to better quantify the S_n locally and to calibrate resistivity measures on these points. This permittivity/resistivity coupling, with multiphase modeling, would: i. better quantify S_n (during the diagnostic and remediation phases); ii. limit field investigations by direct measurements (boreholes, soil-gas wells and piezometers); iii. improve remediation operations (by optimizing pumping flow rates and radii of cone of depression as a function of the flows and pressures applied).

Finally, the experiments developed throughout this thesis (associated with the SILPHES project) have already generated **beneficial impacts on other on-going or future (soon to start) research projects:**

- The image interpretation, permittivity and resistivity monitoring developed for this thesis was used later in two theses in progress in relation with the BIOXYVAL project.
- This monitoring can also be used to study surfactant foam injections. A new 2D tank was built on this same principle as part of the FAMOUS project. Pressure sensors have been integrated. The foam (as blocking agent or as mobility control agent) can be studied on the basis of the contrasts of optical densities, permittivities and resistivities. It is planned to use these 2D tanks (as well as 1D cells and 1D columns) as part of the new project PAPIRUS (kick-off coming soon) dedicated to foam injection.
- In addition, another 2D tank has also been built to take into account back-diffusion (based on the same image interpretation technique). In this case, a colored chemical tracer was added to quantify the solubilization and diffusion of pollutants from the aquitard to the aquifer (internal projects BRGM Bisotope and TraMoIs).

8. REFERENCES

8. REFERENCES

- [Abdallah *et al.* (2007)] Abdallah, W., Buckley, J., Carnegie, A., Edwards, J., Fordham, E., Graue, A., Habashy, T., Seleznev, N., Signer, C., Hussain, H., Montaron, B. and Ziauddin, M.: 2007, Fundamentals of Wettability, *Oil Review Summer 2007*, 44–61.
- [Abriola *et al.* (2005)] Abriola, L., Drummond, C., Hahn, E., Hayes, K., Kibbey, T., Lemke, L., Pennell, K., Petrovskis, E., Ramsburg, C. and Rathfelder, K.: 2005, Pilot-scale demonstration of surfactant-enhanced PCE solubilization at the bachman road site. 1. Site characterization and test design, *Environmental Science & Technology* **39**(6), 1778–1790.
- [Acher *et al.* (1989)] Acher, A., Boderie, P. and Yanon, B.: 1989, Soil pollution by petroleum products, I: Multiphase migration of kerosene components in soil columns, *Journal of Contaminant Hydrology* **4**(4), 333–345.
- [Adamskii *et al.* (2003)] Adamskii, M., Kremesec, V. and Charbeneau, R.: 2003, Residual Saturation: What is it? How is it measured? How should we use it?, in 20th Conference and exposition (eds), *Proceedings of the Petroleum Hydrocarbons and Organic Chemicals in Ground Water: Prevention, Assessment, and Remediation*, Costa mesa, CA, USA.
- [Adamson and Gast (1997)] Adamson, A. and Gast, A.: 1997, *Physical Chemistry of Surfaces*, number 0-471-14873-3, 5th edn, Wiley-Interscience, New York, NY, USA. 755 p.
- [ADEME (2009)] ADEME: 2009, *Traitabilité des sols pollués - Guide méthodologique pour la sélection des techniques et l'évaluation de leurs performances - Cahier des charges*, ADEME edn, Agence de l'Environnement et de la Maîtrise de l'Energie, Agence de l'Environnement et de la Maîtrise de l'Energie - 20, avenue du Grésillé – BP 90406 – 49004 Angers Cedex 01. 246 p.
- [ADEME *et al.* (2007)] ADEME, Burgéap, Institut Français du Pétrole, Institut de Mécanique des Fluides de Toulouse and Institut de Mécanique des Fluides de Strasbourg – IFARE-DFIUIFARE-DFIU: 2007, *Modélisation du devenir des composés organo-chlorés aliphatiques dans les aquifères : Guide méthodologique - Rapport final ADEME - Programme R&D MACAOH (Modélisation, Atténuation, Caractérisation dans les Aquifères des Organo-Halogènes)*, ADEME. 192 p.
- [ADEME and Ernst & Young (2014)] ADEME and Ernst & Young: 2014, *Taux d'utilisation et coûts des différentes techniques et filières de traitement des sols et des eaux souterraines polluées en France – Synthèse des données 2012*, ADEME edn, Agence de l'Environnement et de la Maîtrise de l'Energie, Agence de l'Environnement et de la Maîtrise de l'Energie - 20, avenue du Grésillé – BP 90406 – 49004 Angers Cedex 01. 148 p.
- [ADEME *et al.* (2018)] ADEME, Provademse, Ginger/Burgeap, Enoveo and Suez: 2018, *ESTRAPOL - Essais de Traitabilité de la Pollution des sites, sols et des eaux souterraines*, Intersol, Paris, France.
- [Ajo-Franklin *et al.* (2004)] Ajo-Franklin, J., Geller, J. and Harris, J.: 2004, The dielectric properties of granular media saturated with DNAPL/water mixtures, *Geophysical Research Letters* **31**(L17501), 1–4.
- [Ajo-Franklin *et al.* (2006)] Ajo-Franklin, J., Geller, J. and Harris, J.: 2006, A survey of the geophysical properties of chlorinated DNAPLs, *Journal of Applied Geophysics* **59**, 177–189.
- [Alazaiza *et al.* (2016)] Alazaiza, M., Nigien, S., Ishak, W. and Kamaruddin, S.: 2016, A review of light reflection and transmission methods in monitoring non-aqueous phase liquid migration in porous media, *Journal of Engineering and Applied Sciences* **11**(4), 2319–2326.
- [Alexandra *et al.* (2012)] Alexandra, R., Gerhard, J. and Kueper, B.: 2012, Hydraulic Displacement of Dense Nonaqueous Phase Liquids for Source Zone Stabilization, *Groundwater* **50**, 765–774.

- [Alharti *et al.* (1986)] Alharti, A., Lange, J. and Whitaker, E.: 1986, Immiscible fluid flow in porous media: Dielectric properties, *Journal of Contaminant Hydrology* **1**(1), 107–118.
- [Amirpour *et al.* (2015)] Amirpour, M., Shadizadeh, S., Esfandyari, H. and Ahmadi, S.: 2015, Experimental investigation of wettability alteration on residual oil saturation using nonionic surfactants: Capillary pressure measurement, *Petroleum* **1**(4), 289–299.
- [Anderson (1988)] Anderson, M.: 1988, *The dissolution and transport of dense non-aqueous phase liquids in saturated porous media*, PhD thesis, Oregon Graduate Center, Beaverton, Or., USA. 260 p.
- [Anderson (1986)] Anderson, W.: 1986, Wettability literature survey Part 1: Rock/oil/brine interactions and the effects of core handling on wettability, *Journal of Petroleum Technology* **38**, 1125–1144.
- [Anderson (1987)] Anderson, W.: 1987, Wettability literature survey–part 6: The effects of wettability on waterflooding, *Journal of Petroleum Technology* **39**(12), 1605–1622.
- [Andersson *et al.* (2014)] Andersson, M., Bennetzen, M., Klamt, A. and Stipp, S.: 2014, First-Principles Prediction of Liquid/Liquid Interfacial Tension, *Journal of Chemical Theory and Computation* **10**, 3401–3408.
- [Antontsev (1972)] Antontsev, S.: 1972, On the solvability of boundary value problems for degenerate two-phase porous flow equations, *Dinamika sploshnoy sredy* **10**, 28–53.
- [Archie (1942)] Archie, G.: 1942, The electrical resistivity log as an aid in determining some reservoir characteristics, *Petroleum Transactions of AIME* **146**(1), 54–62.
- [Arrhenius (1887)] Arrhenius, S.: 1887, Uber die Dissociation der in Wasser gelosten Stoffe, *The journal of Physical Chemistry* **1**, 31–48.
- [Ataie-Ashtiani and Raesi-Ardekani (2010)] Ataie-Ashtiani, B. and Raesi-Ardekani, D.: 2010, Comparison of Numerical Formulations for Two-phase Flow in Porous Media, *Geotechnical and Geological Engineering* **28**(4), 373–389.
- [Atteia *et al.* (2013)] Atteia, O., Del Campo Estrada, E. and Bertin, H.: 2013, Soil flushing: a review of the origin of efficiency variability, *Reviews in Environmental Science and Bio/Technology* **12**, 379–389.
- [Bachmann *et al.* (2002)] Bachmann, J., Horton, R., Grant, S. and van der Ploeg, R.: 2002, Temperature dependence of water retention curves for wettable and water-repellent soils, *Soil Science Society of America Journal* **66**(1), 44–52.
- [Baehr and Corapcioglu (1987)] Baehr, A. and Corapcioglu, M.: 1987, A compositional multiphase model for groundwater contamination by petroleum products, 2. numerical solution., *Water Resources Research* **23**(1), 201–214.
- [Baird (1989)] Baird, C.: 1989, Guide to petroleum product blending, *Technical Report 27924886*, HPI Consultants, Austin, TX, USA. 125 p.
- [Baker *et al.* (2006)] Baker, R., LaChance, J. and Heron, G.: 2006, In-pile thermal desorption of PAHs, PCBs and dioxins/furans in soil and sediment, *Land Contamination & Reclamation* **14**, 620–624.
- [Banerjee (1984)] Banerjee, S.: 1984, Solubility of organic mixtures in water, *Environmental Science & Technology* **18**(8), 587–591.
- [Bastian (1999)] Bastian, P.: 1999, *Numerical Computation of Multiphase Flows in Porous Media*, PhD thesis, Technischen Fakultät der Christian–Albrechts–Universität Kiel, Kiel, Germany. 222 p.
- [Bear (1972)] Bear, J.: 1972, *Dynamics of Fluids in Porous Media*, number 9780486656755, Dover Publications, New York, NY, USA. 800 p.
- [Bear (1979)] Bear, J.: 1979, *Hydraulics of Groundwater*, number 978-0486453552, McGraw-Hill, New York, NY, USA. 569 p.
- [Bear and Cheng (2010)] Bear, J. and Cheng, A.: 2010, *Modeling Groundwater Flow and Contaminant Transport*, number 978-1-4020-6682-5, Springer, New York, NY, USA. 834 p.

- [Beliaev and Hassanizadeh (2001)] Beliaev, A. and Hassanizadeh, S.: 2001, A theoretical model of hysteresis and dynamic effects in the capillary relation for two-phase flow in porous media, *Transport in Porous Media* **43**, 487–510.
- [Benremita (2002)] Benremita, H.: 2002, *Approche expérimentale et simulation numérique du transfert de solvants chlorés en aquifère alluvial contrôlé*, PhD thesis, Université Louis Pasteur de Strasbourg, Strasbourg, France. 282 p.
- [Berglund and Cvetkovic (1995)] Berglund, S. and Cvetkovic, V.: 1995, Pump-and-Treat Remediation of Heterogeneous Aquifers: Effects of Rate-Limited Mass Transfer, *Groundwater* **33**, 675–685.
- [Bernabé *et al.* (2016)] Bernabé, Y., Li, M., Tang, Y. and Evans, B.: 2016, Pore space connectivity and the transport properties of rocks, *Oil & Gas Science and Technology* **71**(4), 1–17.
- [Bernabé *et al.* (2011)] Bernabé, Y., Zamora, M., Li, M., Mainault, A. and Tang, Y.: 2011, Pore connectivity, permeability, and electrical formation factor: A new model and comparison to experimental data, *Journal of Geophysical Research* **116**(B11204), 1–15.
- [Bertin *et al.* (1998)] Bertin, H., Apaydin, O., Castanier, L. and Kovscek, A.: 1998, Foam flow in heterogeneous porous media: effect of crossflow, *Society of Petroleum Engineers* **2**(4), 75–82.
- [Bingham (1914)] Bingham, E.: 1914, The viscosity of binary mixtures, *The journal of Physical Chemistry* **18**, 57–65.
- [Birak and Miller (2009)] Birak, P. and Miller, C.: 2009, Dense non-aqueous phase liquids at former manufactured gas plants: Challenges to modeling and remediation, *Journal of Contaminant Hydrology* **105**, 81–98.
- [Birchak *et al.* (1974)] Birchak, J., Gardner, C., Hipp, J. and Victor, J.: 1974, High dielectric constant microwave probes for sensing soil moisture, *Proceedings of the Institute of Electrical and Electronics Engineers* **62**(1), 93–98.
- [Bjørnarå and Aker (2008)] Bjørnarå, T. and Aker, E.: 2008, Comparing Equations for Two-Phase Fluid Flow in Porous Media, *COMSOL Conference 2008 Hannover*.
- [Bob *et al.* (2008)] Bob, M., Brooks, M., Mravik, S. and Wood, A.: 2008, A modified light transmission visualization method for DNAPL saturation measurements in 2-D models, *Advances in Water Resources* **31**(5), 727–742.
- [Boley and Overcamp (1998)] Boley, T. and Overcamp, T.: 1998, Displacement of Non-wetting Liquids From Unsaturated Sands by Water Infiltration, *Groundwater* **36**(5), 810–814.
- [Bradford and Leij (1996)] Bradford, S. and Leij, F.: 1996, Predicting Two- and Three-Fluid Capillary Pressure-Saturation Relationships of Porous Media With Fractional Wettability, *Water Resources Research* **32**(2), 251–259.
- [Braun and Holland (1994)] Braun, E. and Holland, R.: 1994, Relative permeability hysteresis: Laboratory measurement and conceptual model, *SPE 69th Annual Technical Conference and Exhibition*.
- [Brewster *et al.* (1995)] Brewster, M., Annan, A., Greenhouse, J., Kueper, B., Olhoeft, G., Redman, J. and Sander, K.: 1995, Observed migration of a controlled DNAPL release by geophysical methods, *Ground Water* **33**, 987–997.
- [Brooks *et al.* (2004)] Brooks, M., Annable, M., Rao, P., Hatfield, K., Jawitz, J., Wise, W., Wood, A. and Enfield, C.: 2004, Controlled release, blind test of DNAPL remediation by ethanol flushing, *Journal of Contaminant Hydrology* **69**(3-4), 281–297.
- [Brooks and Corey (1964)] Brooks, R. and Corey, A.: 1964, Hydraulic Properties of Porous Media, *Hydrology Paper 3, Civil Engineering Department, Colorado State University, Fort Collins*.

- [Brovelli and Cassiani (2010)] Brovelli, A. and Cassiani, G.: 2010, A combination of the hashin-shtrikman bounds aimed at modelling electrical conductivity and permittivity of variably saturated porous media, *Geophysical Journal International* **180**, 225–237.
- [Brown (2001)] Brown, A.: 2001, A step-by-step guide to non-linear regression analysis of experimental data using a Microsoft Excel spreadsheet, *Computer methods and programs in biomedicine* **65**(3), 191–200.
- [Brown *et al.* (2006)] Brown, D., Gupta, L., Kim, T.-H., Keith Moo-Young, H. and Coleman, A.: 2006, Comparative assessment of coal tars obtained from 10 former manufactured gas plant sites in the Eastern United States, *Chemosphere* (65), 1562–1569.
- [Brown *et al.* (2003)] Brown, S., Lesmes, D., Fourkas, G. and Sorenson, J.: 2003, Complex Electrical Resistivity for Monitoring DNAPL Contamination - Final Technical Report, *Technical Report 70012*, U.S. Department of Energy. 31 p.
- [Brown *et al.* (2004)] Brown, S., Sorenson, J. and Brown, T.: 2004, A laboratory study of the complex electrical resistivity response of soils, *In Symposium on the Application of Geophysics to Engineering and Environmental Problems 2004*, Society of Exploration Geophysicists, pp. 528–539.
- [Brusseu (1991)] Brusseu, M.: 1991, Transport of organic chemicals by gas advection in structured or heterogeneous porous media: Development of a model and application of column experiments, *Water Resources Research* **27**(12), 3189–3199.
- [Brusseu *et al.* (2008)] Brusseu, M., DiFilippo, E., Marble, J. and Oostrom, M.: 2008, Mass-removal and mass-flux-reduction behavior for idealized source zones with hydraulically poorly-accessible immiscible liquid, *Chemosphere* **71**(8), 1511 – 1521.
- [Brusseu *et al.* (1992)] Brusseu, M., Jessup, R. and Rao, P.: 1992, Modeling solute transport influenced by multi-process nonequilibrium and transformation reactions, *Water Resources Research* **28**, 175–182.
- [Brusseu *et al.* (2000)] Brusseu, M., Nelson, N., Ostrom, M., Zhang, Z., Johnson, G. and Wiestma, T.: 2000, Influence of Heterogeneity and Sampling Method on Aqueous Concentrations Associated with NAPL Dissolution, *Environmental Science & Technology* **34**(17), 3657–3664.
- [Brutsaert (1967)] Brutsaert, W.: 1967, Some methods of calculating unsaturated permeability, *Transactions of the ASABE* **10**, 400–404.
- [Burdine (1953)] Burdine, N.: 1953, Relative permeability calculations from pore size distribution data, *Petroleum Transactions, AIME* **198**, 71–78.
- [Burger *et al.* (1984)] Burger, J., Sourieau, P., Combarous, M. in collaboration with Bia, P. and Sahuquet, B.: 1984, *Récupération assistée du pétrole - Les méthodes thermiques*, number 2710804506, Publications de l'Institut Français du Pétrole, Paris, France. 416 p.
- [Byun *et al.* (2019)] Byun, Y., Hong, W. and Yoon, H.: 2019, Characterization of cementation factor of unconsolidated granular materials through time domain reflectometry with variable saturated conditions, *Materials* **12**(8), 1340–1354.
- [Cai *et al.* (2017)] Cai, J., Wei, W., Hu, X. and Wood, D.: 2017, Electrical conductivity models in saturated porous media: A review, *Earth-Science Reviews* **171**, 419–433.
- [Cao *et al.* (2018)] Cao, J., Jung, J., Song, X. and Bate, B.: 2018, On the soil water characteristic curves of poorly graded granular materials in aqueous polymer solutions, *Acta Geotechnica* **13**, 103–116.
- [Capparelli *et al.* (2018)] Capparelli, G., Spolverino, G. and Greco, R.: 2018, Experimental Determination of TDR Calibration Relationship for Pyroclastic Ashes of Campania (Italy), *Sensors* **18**(3727), 1–14.
- [Caprihan and Fukushima (1990)] Caprihan, A. and Fukushima, E.: 1990, Flow measurements by NMR, *Physics Reports* **198**(4), 195–235.

- [Carey and McBean (2010a)] Carey, G. and McBean, E.: 2010a, A mass balance Approach for estimating DNAPL Source remediation timeframe, *Proceedings of the 2010 RPIC Federal Contaminated Sites National Workshop*, Montréal, Québec, Canada.
- [Carey and McBean (2010b)] Carey, G. and McBean, E.: 2010b, Back-diffusion and discount rate implications for DNAPL Remediation Strategies, *Proceedings of the 2010 RPIC Federal Contaminated Sites National Workshop*, Montréal, Québec, Canada.
- [Cazaux *et al.* (2014)] Cazaux, D., Colombano, S., Joubert, A., Dumestre, A. and Lecuelle, G.: 2014, Optimized physical recovery of DNAPL using upwelling technique and geostatistical analysis at large field scale, *Ninth International Conference on Remediation of Chlorinated and Recalcitrant Compounds*, number A1, Battelle Press, Columbus, OH, USA, Monterey, CA, USA, p. 5.
- [Centeno *et al.* (2011)] Centeno, G., Sánchez-Reyna, G., Ancheyta, J., Muñoz, J. and Cardona, N.: 2011, Testing various mixing rules for calculation of viscosity of petroleum blends, *Fuel* **90**(12), 3561–3570.
- [Chambers *et al.* (2004)] Chambers, J., Loke, M., Ogilvy, R. and Meldrum, P.: 2004, Noninvasive monitoring of DNAPL migration through a saturated porous medium using electrical impedance tomography, *Journal of Contaminant Hydrology* **68**(1–2), 1–22.
- [Chapuis *et al.* (2015)] Chapuis, R., Weber, S. and Duhaime, F.: 2015, Permeability test results with packed spheres and non-plastic soils, *Geotechnical Testing Journal* **38**(6), 950–964.
- [Chatzis *et al.* (1988)] Chatzis, I., Kuntamukklua, M. and Morrow, N.: 1988, Effect of capillary number on the microstructure of residual oil in strongly water-wet sandstones, *SPE Reservoir Engineering* **3**(3), 902–912.
- [Chatzis *et al.* (1983)] Chatzis, I., Morrow, N. and Lim, H.: 1983, Magnitude and detailed structure of residual oil saturation, *Society of Petroleum Engineers Journal* **23**(02), 311–326.
- [Chavent and Jaffre (1986)] Chavent, G. and Jaffre, J.: 1986, *Mathematical Models and Finite Elements for Reservoir Simulation - Single Phase, Multiphase and Multicomponent Flows through Porous Media*, Vol. 17, North-Holland, Amsterdam, Netherlands. 375 p.
- [Chen *et al.* (2012)] Chen, F., Freedman, D., Falta, R. and Murdoch, L.: 2012, Henry's law constants of chlorinated solvents at elevated temperatures, *Chemosphere* **86**(2).
- [Chen *et al.* (1999)] Chen, J., Hopmans, J. and Grismer, M.: 1999, Parameter estimation of two-fluid capillary pressure - saturation and permeability functions, *Advances in Water Resources* **22**(5), 479 – 493.
- [Chen and Ewing (1997)] Chen, Z. and Ewing, R.: 1997, Fully Discrete Finite Element Analysis of Multiphase Flow in Groundwater Hydrology, *SIAM Journal on Numerical Analysis* **34**(6), 2228–2253.
- [Chen *et al.* (2006)] Chen, Z., Huan, G. and Ma, Y.: 2006, *Computational methods for multiphase flows in porous media*, number 978-0-898716-06-1, Philadelphia, PA , USA. 531 p.
- [Chevalier and Fonte (2000)] Chevalier, L. and Fonte, J.: 2000, Correlation model to predict residual immiscible organic contaminants in sandy soils, *Journal of Hazardous Materials* **72**(1), 39–52.
- [Chiapponi (2017)] Chiapponi, L.: 2017, Water retention curves of multicomponent mixtures of spherical particles, *Powder Technology* **320**, 646–655.
- [Childs *et al.* (2006)] Childs, J., Acosta, E., Annable, M., Brooks, M., Enfield, C., Harwell, J., Hasegawa, M., Knox, R., Rao, P., Sabatini, D., Shiau, B., Szekeres, E. and Wood, A.: 2006, Field demonstration of surfactant-enhanced solubilization of DNAPL at Dover Air Force Base, Delaware, *Journal of Contaminant Hydrology* **82**(1-2), 1–22.

- [Childs *et al.* (2004)] Childs, J., Acosta, E., Knox, R., Harwell, J. and Sabatini, D.: 2004, Improving the extraction of tetrachloroethylene from soil columns using surfactant gradient systems, *Journal of Contaminant Hydrology* **71**(1-4), 27–45.
- [Cho and Park (2006)] Cho, H. and Park, J.: 2006, Sorption and reduction of tetrachloroethylene with zero valent iron and amphiphilic molecules, *Chemosphere* **64**(6), 1047–1052.
- [Chu *et al.* (2004)] Chu, Y., Werth, C., Valocchi, A., Yoon, H. and Webb, A.: 2004, Magnetic resonance imaging of nonaqueous phase liquid during soil vapor extraction in heterogeneous porous media, *Journal of Contaminant Hydrology* **73**(1-4), 15–37.
- [Cohen and Mercer (1993)] Cohen, R. and Mercer, J.: 1993, DNAPL Site Evaluation, *Technical Report EPA/600/R-93/022*, Edited by USEPA Office of Research and Development. 369 p.
- [Colombano *et al.* (2019)] Colombano S., Davarzani H., van Hullebusch E.D., Huguenot D., Guyonnet D., Deparis J., Ignatiadis I.: 2019, Thermal and chemical enhanced recovery of heavy chlorinated organic compounds in saturated porous media: 1D cell drainage-imbibition experiments, *Science of the Total Environment*, article in press.
- [Colombano *et al.* (2018)] Colombano, S., Joubert, A., Cazaux, D., Maire, J., Fatin-Rouge, N., Invernizzi, T., Marion, C., Kaifas, D., Klein, P., Triger, A., Dumestre, A., Giraud, Q., Paris, B., Deparis, J. and Baillieux, P.: 2018, Le projet SILPHES - Solutions Innovantes de Lutte contre les Produits Halogénés dans les Eaux Souterraines :1) Quid de l'amélioration de la récupération physique d'un produit pur en aquifère alluvial ? *Les rendez-vous du réseau ESSORT - Solutions de traitement des sites et sols pollués*, ADEME, UPDS, and ESSORT network members, Paris, France.
- [Colombano *et al.* (2010)] Colombano, S., Saada, A., Guerin, V., Bataillard, P., Bellenfant, G., Beranger, S., Hubé, D., Blanc, C., Zornig, C. and Girardeau, I.: 2010, Quelles techniques pour quels traitements - Analyse coût-bénéfices, *Technical Report BRGM/RP - 58609 - FR*, BRGM - French Geological Survey, 3, avenue Claude Guillemin, 45 060 - Orléans Cedex 2, France. 403 p.
- [Comegna *et al.* (2013)] Comegna, A., Coppola, A., Dragonetti, G. and Sommella, A.: 2013, Dielectric Response of a Variable Saturated Soil Contaminated by Non-Aqueous Phase Liquids (NAPLs), *Procedia Environmental Sciences* **19**, 701–710.
- [Comparon (2005)] Comparon, L.: 2005, *Etude expérimentale des propriétés électriques et diélectriques des matériaux argileux consolidés*, PhD thesis, Institut de Physique du Globe de Paris, Paris, France. 399 p.
- [COMSOL Multiphysics (2012)] COMSOL Multiphysics: 2012, *Two-phase flow*, v. 4.3a edn, Comsol.
- [Connor *et al.* (1989)] Connor, J., Newell, C. and Wilson, D.: 1989, Assessment, Field Testing, Conceptual Design for Managing Dense Nonaqueous Phase Liquids (DNAPL) at a Superfund Site, *Proceedings of Petroleum Hydrocarbons and Organic Chemicals in Ground Water: Prevention, Detection, and Restoration*, Vol. 1, A Conference and Exposition, The Westin Galleria, Houston, TX, USA, pp. 519–533.
- [Constable and Srnka (2007)] Constable, S. and Srnka, L.: 2007, An introduction to marine controlled-source electromagnetic methods for hydrocarbon exploration, *Geophysics* **72**(2), WA3–WA12.
- [Coppola *et al.* (2013)] Coppola, A., Dragonetti, G., Comegna, A., Lamaddalena, N., Caushi, B., Haikal, M. and Basile, A.: 2013, Measuring and modeling water content in stony soils, *Soil and Tillage Research* **128**, 9–22.
- [Cornhill *et al.* (1990)] Cornhill, J., Herderick, E. and Stary, H.: 1990, Topography of human aortic sudanophilic lesions, *Monographs on Atherosclerosis* **15**, 13–19.

- [Corradini *et al.* (1996)] Corradini, F., Marchetti, A., Tagliazucchi, M. and Tassi, L.: 1996, Static dielectric constants of 1,2-dichloroethane + 2-methoxyethanol + 1,2-dimethoxyethane ternary liquid mixtures from 10 to 80 °C, *Fluid Phase Equilibria* **124**(1-2), 209– 220.
- [Cragoe (1933)] Cragoe, C.: 1933, Changes in the viscosity of liquids with temperature, pressure and composition, *Proceedings of the 1st World Petroleum Congress*, number WPC-201, World Petroleum Congress, London, UK, pp. 529–541.
- [Craig (1971)] Craig, F.: 1971, *The Reservoir Engineering Aspects of Waterflooding*, number 978-0-89520-202-4, Society of Petroleum Engineers of AIME, New York, NY, USA. 142 p.
- [Crichlow (1977)] Crichlow, H.: 1977, *Modern Reservoir Engineering - A Simulation Approach*, number 0135974682, Prentice Hall, Englewood Cliffs, NJ, USA. 354 p.
- [Daïan (2013)] Daïan, J.-F.: 2013, *Équilibre et transferts en milieux poreux*, Université Joseph Fourier - Laboratoire d'Étude des Transferts en Hydrologie et Environnement, Grenoble, France. 642 p.
- [Dahlin (2000)] Dahlin, T.: 2000, Short note on electrode charge-up effects in dc resistivity data acquisition using multielectrode arrays, *Geophysical Prospecting* **48**(1), 181–187.
- [Dakhnov (1962)] Dakhnov, V.: 1962, *Geophysical well logging*, number 57-2, Q. Colorado School of Mines. 445 p.
- [Dalton *et al.* (1984)] Dalton, F., Herkelrath, W., Rawlins, D. and Rhoades, J.: 1984, Time-domain reflectometry: Simultaneous measurements of soil water content and electrical conductivity with a single probe, *Science* **224**, 989– 990.
- [Darnault *et al.* (1998)] Darnault, C., Throop, J., DiCarlo, D., Rimmer, A., Steenhuis, T. and Parlange, J.: 1998, Visualization by light transmission of oil and water contents in transient two-phase flow fields, *Journal of Contaminant Hydrology* **31**(3-4), 337–348.
- [Dasberg and Hopmans (1992)] Dasberg, S. and Hopmans, J.: 1992, Time domain reflectometry calibration for uniformly and nonuniformly wetted sandy and clayey loam soils, *Soil Science Society of America Journal* **56**(5), 1341–1345.
- [Dash *et al.* (1997)] Dash, Z., Robinson, B. and Zyvoloski, G.: 1997, *Software Requirements, Design and Verification for the FEHM Application. A Finite Element Heat and Mass Transfer Code*, number LA-13305-MS, Los Alamos National Laboratory, Los Alamos, NM, USA. 206 p.
- [Davarzani *et al.* (2014)] Davarzani, H., Smits, K., Tolene, R. and Illangasekare, T.: 2014, Study of the effect of wind speed on evaporation from soil through integrated modeling of the atmospheric boundary layer and shallow subsurface, *Water Resources Research* **50**(1), 661–680.
- [Davis (1994)] Davis, E.: 1994, Effect of temperature and pore size on the hydraulic properties and flow of a hydrocarbon oil in the subsurface, *Journal of Contaminant Hydrology* **16**(1), 55–86.
- [Davis (1997)] Davis, E.: 1997, How Heat Can Enhance In-situ Soil and Aquifer Remediation: Important Chemical Properties and Guidance on Choosing the Appropriate Technique, *Technical Report EPA/540/S-97/502*, U.S. Environmental Protection Agency, U.S. Environmental Protection Agency; Solid Waste and Emergency Response, Washington, DC, USA. 18 p.
- [de Franco *et al.* (2009)] de Franco, R., Biella, G., Tosi, L., Teatini, P., Lozej, A., Chiozzotto, B., Giada, M., Rizzetto, F., Claude, C., Mayer, A., Bassan, V. and Gasparetto-Stori, G.: 2009, Monitoring the saltwater intrusion by time lapse electrical resistivity tomography: the Chioggia test site (Venice Lagoon, Italy), *Journal of Applied Geophysics* **69**(3–4), 177–130.
- [de Lima and Sharma (1990)] de Lima, O. and Sharma, M.: 1990, A grain conductivity approach to shaly sandstones, *Geophysics* **55**(10), 1347–1356.

- [Delle Site (2001)] Delle Site, A.: 2001, Factors Affecting Sorption of Organic Compounds in Natural Sorbent/Water Systems and Sorption Coefficients for Selected Pollutants. A Review, *Journal of Physical and Chemical Reference Data* **30**(1), 187–439.
- [Delshad *et al.* (2000)] Delshad, M., Pope, G., Yeh, L. and Holzmer, F.: 2000, *Design of the surfactant flood at Camp Lejeune, in Treating Dense Nonaqueous-Phase Liquids (DNAPLs): Remediation of Chlorinated and Recalcitrant Compounds*, Battelle Press, Columbus, OH, USA. 203–210.
- [Demond and Roberts (1987)] Demond, A. and Roberts, P.: 1987, An examination of relative permeability relations for two phase flow in porous media, *Water Resources Bulletin* **23**(4), 617–628.
- [Deng *et al.* (2017)] Deng, Y., Shi, X., Xu, H., Sun, Y., Wu, J. and Revil, A.: 2017, Quantitative assessment of electrical resistivity tomography for monitoring DNAPLs migration – Comparison with high-resolution light transmission visualization in laboratory sandbox, *Journal of Hydrology* **544**, 254–266.
- [Deparis (2007)] Deparis, J.: 2007, *Etude des éboulements rocheux par méthodes géophysiques*, PhD thesis, Université Joseph Fourier, Observatoire de Grenoble, Grenoble, France. 245 p.
- [Deparis *et al.* (2019)] Deparis, J., Joubert, A., Francois, B., Nodot, E., Invernizzi, T., Irvani, A., Dumestre, A., Fatin-Rouge, N., Maire, J., Kaifas, D., Triger, A., Klein, P., Giraud, Q., Paris, B., Cazaux, D., Gourry, J., Davarzani, H. and Colombano, S.: 2019, On the use of Geophysical measurements to monitor DNAPL extraction, *AquaConSoil 2019, 15th International Conference*, Antwerp, Belgium.
- [Dijk *et al.* (1999)] Dijk, P., Berkowitz, B. and Bendel, P.: 1999, Investigation of flow in water-saturated rock fractures using nuclear magnetic resonance imaging (NMRI), *Water Resources Research* **35**(2), 347–360.
- [Dirksen and Dasberg (1993)] Dirksen, C. and Dasberg, S.: 1993, Improved calibration of time domain reflectometry soil water content measurements, *Soil Science Society of America Journal* **57**(3), 660–667.
- [Dobson *et al.* (1985)] Dobson, M., Ulaby, F., Hallikainen, M. and El-Rayes, M.: 1985, Microwave dielectric behaviour of wet soil, part ii, dielectric mixing models, *Institute of Electrical and Electronics Engineers Transactions on Geoscience and Remote Sensing* **23**, 35–46.
- [Dokla (1981)] Dokla, M.: 1981, Effect of Formation Heterogeneity and Temperature on Alkaline Waterflooding Performance, in S. of Petroleum Engineer's (ed.), *Middle East Oil Technical Conference of the Society of Petroleum Engineers*, Manama, Bahrain, p. 9646.
- [Douroumis and Fahr (2013)] Douroumis, D. and Fahr, A.: 2013, *Drug Delivery Strategies for Poorly Water-soluble Drugs*, number 978-0-470-71197-2, John Wiley & Sons, Ltd., Chichester, England, United Kingdom. 626 p.
- [Dubey and Doe (1993)] Dubey, S. and Doe, P.: 1993, Base number and wetting properties of crude oils, *Society of Petroleum Engineering, Reservoir Engineering* **9**, 195–200.
- [Dullien (1992)] Dullien, F.: 1992, *Porous Media: Fluid Transport and Pore Structure*, number 978-0-12-223651-8, 2nd edn, Academic Press, San Diego, CA, USA. 574 p.
- [Dupuy *et al.* (2011)] Dupuy, A., Athes, V., Schenk, J., Jenelten, U. and Souchon, I.: 2011, Experimental and theoretical considerations on breakthrough pressure in membrane-based solvent extraction: Focus on citrus essential oil/hydro-alcoholic solvent systems with low interfacial tension, *Journal of Membrane Science* **378**(1-2), 203–213.
- [Dwarakanath *et al.* (1999)] Dwarakanath, V., Kostarelos, K., Pope, G., Shotts, G. and Wade, W.: 1999, Anionic surfactant remediation of soil columns contaminated by nonaqueous phase liquids, *Journal of Contaminant Hydrology* **38**(4), 465–488.

- [Eckert and Drake (1987)] Eckert, E. and Drake, R.: 1987, *Analysis of Heat and Mass Transfer*, Hemisphere Publishing.
- [Edmondson (1965)] Edmondson, T.: 1965, Effect of temperature on waterflooding, *Journal of Canadian Petroleum Technology* **October–December**, 236–242.
- [Edwards *et al.* (1991)] Edwards, D., Luthy, R. and Liu, Z.: 1991, Solubilization of polycyclic aromatic hydrocarbons in micellar nonionic surfactant solutions, *Environmental Science & Technology* **25**(1), 127–133.
- [Endres and Knight (1992)] Endres, A. and Knight, R.: 1992, A theoretical treatment of the effect of microscopic fluid distribution on the dielectric properties of partially saturated rocks, *Geophysical Prospecting* **40**(3), 307–324.
- [Falls *et al.* (1989)] Falls, A., Musters, J. and Ratulowski, J.: 1989, The apparent viscosity of foams in homogeneous bead packs, *SPE Reservoir Engineering* **4**(2), 155–164.
- [Falta *et al.* (2005b)] Falta, R., Basu, N. and Rao, P.: 2005b, Assessing impacts of partial mass depletion in DNAPL source zones: II. Coupling source strength functions to plume evolution, *Journal of Contaminant Hydrology* **79**(1-2), 45–66.
- [Falta *et al.* (1989)] Falta, R., Javandel, I., Pruess, K. and Witherspoon, P.: 1989, Density-drive flow of gas in the unsaturated zone due to evaporation of volatile organic chemicals, *Water Resources Research* **25**(10), 2159–2169.
- [Falta *et al.* (1995)] Falta, R., Pruess, K., Finsterle, S. and Battistelli, A.: 1995, *T2VOC User's Guide*, number LBL-36400, Lawrence Berkeley National Laboratory, Berkeley, CA, USA. 155 p.
- [Falta *et al.* (2005a)] Falta, R., Rao, P. and Basu, N.: 2005a, Assessing the impacts of partial mass depletion in DNAPL source zones: I. Analytical modeling of source strength functions and plume response, *Journal of Contaminant Hydrology* **78**(4.), 259–280.
- [Farn (2008)] Farn, R.: 2008, *Chemistry and Technology of Surfactants*, number 1405171790, 9781405171793, John Wiley & Sons, Hoboken, NJ, USA. 336 p.
- [Feenstra and Cherry (1988)] Feenstra, S. and Cherry, J.: 1988, Subsurface contamination by dense non-aqueous phase liquids (DNAPL) chemicals, *International Groundwater Symposium, International Association of Hydrogeologists*, Halifax, Nova Scotia, Canada.
- [Feenstra *et al.* (1991)] Feenstra, S., Mackay, D. and Cherry, J.: 1991, A method for assessing residual napl based on organic chemical concentrations in soil samples, *Groundwater Monitoring Review* **11**(2), 128–136.
- [Fellner-Feldegg (1969)] Fellner-Feldegg, H.: 1969, The measurement of dielectrics in the time domain, *The Journal of Physical Chemistry* **73**(3), 616–623.
- [Ferry and Dougherty (1986)] Ferry, J. and Dougherty, P.: 1986, Occurrence and Recovery of a DNAPL in a Low-Yielding Bedrock Aquifer, in P. of the NWWA/API Conference (ed.), *Petroleum Hydrocarbons and Organic Chemicals in Ground Water - Prevention, Detection and Restoration*, Houston, TX., USA, pp. 722–733.
- [Fetter (1994)] Fetter, C.: 1994, *Contaminant Hydrogeology*, number 0130882399, Prentice-Hall, Upper Slade River, NJ, USA. 598 p.
- [Flores *et al.* (2011)] Flores, G., Katsumi, T., Inui, T. and Kamon, M.: 2011, A simplified image analysis method to study LNAPL migration in porous media, soils and foundations, *Soils and Foundations* **51**(5), 35–847.
- [Fountain *et al.* (1996)] Fountain, J., Starr, R., Middleton, T., Beikirch, M., Taylor, C. and Hodge, D.: 1996, A controlled field test of surfactant-enhanced aquifer remediation, *Groundwater* **34**(5), 910–916.
- [Fournier (1965)] Fournier, K.: 1965, A numerical method for computing recovery of oil by hot water injection in a radial system, *Society of Petroleum Engineers Journal* **5**(2.), 131–140.

- [Francisca and Montoro (2012)] Francisca, M. and Montoro, M.: 2012, Measuring the dielectric properties of soil-organic mixtures using coaxial impedance dielectric reflectometry, *Journal of Applied Geophysics* **80**(101-109).
- [Fredenslund *et al.* (1975)] Fredenslund, A., Jones, R. and Prausnitz, J.: 1975, Group-contribution estimation of activity coefficients in nonideal liquid mixtures, *American Institute of Chemical Engineers Journal* **21**(6), 1086–1099.
- [Freeze and McWhorter (1997)] Freeze, A. and McWhorter, D.: 1997, A Framework for Assessing Risk Reduction Due to DNAPL Mass Removal from Low-Permeability Soils, *Groundwater* **35**(1), 111–123.
- [Fulton *et al.* (1991)] Fulton, D., Reuter, G. and Buscheck, T.: 1991, Hot water enhanced recovery of phase separated lubricating oil, in N. G. Association (ed.), *Proceedings of the Petroleum Hydrocarbons and Organic Chemicals in Ground Water: Prevention, Detection, and Restoration Conference and Exposition*, Dublin, Ireland, p. 143–156.
- [Gardner (1958)] Gardner, W.: 1958, Some steady state solutions of unsaturated moisture flow equations with application to evaporation from water table, *Soil Science* **85**(4), 228–232.
- [Gaudin and Decker (1967)] Gaudin, A. and Decker, T.: 1967, Contact angles and adsorption in the system quartz-water-dodecane modified by dodecyl ammonium chloride, *Journal of Colloid Interface Science* **24**, 151–158.
- [Geller and Hunt (1993)] Geller, J. and Hunt, J.: 1993, Mass transfer from nonaqueous phase organic liquids in water-saturated porous media, *Water Resources Research* **29**(4), 833–845. Doi: 10.1029/92WR02581
- [Gerhard (2002)] Gerhard, J.: 2002, *DNAPL infiltration, redistribution, and immobilization in porous media*, PhD thesis, Queen’s University, Kingston, Ontario, Canada. 380 p.
- [Gerhard and Kueper (2003a)] Gerhard, J. and Kueper, B.: 2003a, Capillary pressure characteristics necessary for simulating DNAPL infiltration, redistribution, and immobilization in saturated porous media, *Water Resources Research* **39**(8), 1–17.
- [Gerhard and Kueper (2003b)] Gerhard, J. and Kueper, B.: 2003b, Relative permeability characteristics necessary for simulating DNAPL infiltration, redistribution, and immobilization in saturated porous media, *Water Resources Research* **39**(8), 1–16.
- [Gerhard *et al.* (2001)] Gerhard, J., Kueper, B., Hecox, G. and Schwarz., E.: 2001, Site-specific design for dual phase recovery and stabilization of pooled DNAPL, *Groundwater Monitoring and Remediation* **21**(2), 71–88.
- [Ghanbarian and Sahimi (2017)] Ghanbarian, B. and Sahimi, M.: 2017, Electrical conductivity of partially saturated packings of particles, *Transport in Porous Media* **118**(1), 1–16.
- [Giannis *et al.* (2007)] Giannis, A., Gidakos, E. and Skouta, A.: 2007, Application of sodium dodecyl sulfate and humic acid as surfactants on electrokinetic remediation of cadmium-contaminated soil, *Desalination* **211**(1-3), 249–260.
- [Giese and Powers (2002)] Giese, S. and Powers, S.: 2002, Using polymer solutions to enhance recovery of mobile coal tar and creosote DNAPLs, *Journal of Contaminant Hydrology* **58**(1-2), 147–167.
- [Glover (2010)] Glover, P.: 2010, A generalised archie’s law for n phases, *Geophysics* **6**, E247–E265.
- [Goodyear *et al.* (1996)] Goodyear, S., Reynolds, C., Townsley, P. and Woods, C.: 1996, Hot Water Flooding for High Permeability Viscous Oil Fields, in S. of Petroleum Engineer’s (ed.), *SPE/DOE Improved Oil Recovery Symposium*, Tulsa, Oklahoma, USA, p. 35376.
- [Grant (2005)] Grant, G.: 2005, *The Evolution of Complex DNAPL Releases: Rates of Migration and Dissolution*, PhD thesis, The University of Edinburgh, Edinburgh, Scotland, United Kingdom. 429 p.

- [Grant and Gerhard (2004)] Grant, G. and Gerhard, J.: 2004, The sensitivity of predicted DNAPL source zone longevity to mass transfer correlation model, *Geoenvironmental Engineering: Integrated management of groundwater and contaminated land*, Proceedings of the 4th British Geotechnical Association, Stratford-upon-Avon, UK.
- [Grant and Gerhard (2007a)] Grant, G. and Gerhard, J.: 2007a, Simulating the dissolution of a complex dense nonaqueous phase liquid source zone: 1. Model to predict interfacial area, *Water Resources Research* **43**(W12410), 1–14.
- [Grant and Gerhard (2007b)] Grant, G. and Gerhard, J.: 2007b, Simulating the dissolution of a complex dense nonaqueous phase liquid source zone: 2. Experimental validation of an interfacial area-based mass transfer model, *Water Resources Research* **43**(W12409), 1–18.
- [Grant (2003)] Grant, S.: 2003, Extension of a temperature effects model for capillary pressure saturation relations, *Water Resources Research* **39**(1), 1–10.
- [Grant and Salehzadeh (1996)] Grant, S. and Salehzadeh, A.: 1996, Calculation of Temperature Effects on Wetting Coefficients of Porous Solids and Their Capillary Pressure Functions, *Water Resources Research* **32**(2), 261–270.
- [Grellier *et al.* (2008)] Grellier, S., Guérin, R., Robain, H., Bobachev, A., Vermeersch, F. and Tabbagh, A.: 2008, Monitoring of leachate recirculation in a bioreactor landfill by 2-d electrical resistivity imaging, *Journal of Environmental and Engineering Geophysics* **13**(4), 351–359.
- [Griffin (1949)] Griffin, W.: 1949, Classification of surface-active agents by "HLB", *Journal of the Society of Cosmetic Chemists* **1**, 311–326.
- [Grunberg and Nissan (1949)] Grunberg, L. and Nissan, A.: 1949, Mixture law for viscosity, *Nature* **164**, 799–800.
- [Guarnaccia *et al.* (1997)] Guarnaccia, J., Pinder, G. and Fishman, M.: 1997, NAPL: Simulator documentation, *EPA Project Summary* (EPA/600/8R-97/102).
- [Gueguen and Palciauskas (1994)] Gueguen, Y. and Palciauskas, V.: 1994, *Introduction to the Physics of Rocks*, number 978-0691034522, Princeton University Press, Princeton, NJ, USA. 304 p.
- [Guérin *et al.* (2004)] Guérin, R., Munoz, M., Aran, C., Laperrelle, C., Hidra, M., Drouart, E. and Grellier, S.: 2004, Leachate recirculation: moisture content assessment by means of a geophysical technique, *Waste Management* **24**, 785–794.
- [Gwo *et al.* (1995)] Gwo, J., Jardine, P., Yeh, G. and Wilson, G.: 1995, *MURT User's Guide: A Hybrid Lagrangian-Eulerian Finite Element Model of Multiple Pore Region Solute Transport through Variably Saturated Subsurface Media*, number ORNL/GWPO-015, Oak Ridge National Laboratory, Oak Ridge, TN, USA. 128 p.
- [Han *et al.* (2015)] Han, T., Best, A., Sothcott, J., North, L. and MacGregor, L.: 2015, Relationships among low frequency (2 Hz) electrical resistivity, porosity, clay content and permeability in reservoir sandstones, *Journal of Applied Geophysics* **112**, 279–289.
- [Harendra and Vipulanandan (2011)] Harendra, S. and Vipulanandan, C.: 2011, Solubilization and degradation of perchloroethylene (PCE) in cationic and nonionic surfactant solutions, *Journal of Environmental Sciences* **23**(8), 1240–1248.
- [Haridy *et al.* (2004)] Haridy, S., Persson, M. and Berndtsson, R.: 2004, Estimation of Inapl saturation in fine sand using time-domain reflectometry, *Hydrological Sciences Journal* **49**(6), 987–1000.
- [Harkness and Konzuk (2014)] Harkness, M. and Konzuk, J.: 2014, *Cost analyses for remedial options*, in *Chapter 16 in Chlorinated Solvent Source Zone Remediation*, number 978-1-4614-6921-6, Springer, SERDP ESTCP Environmental Remediation Technology, New York, NY, USA. 713 p.
- [Hasegawa *et al.* (2000)] Hasegawa, M., Shau, B., Sabatini, D., Knox, R., Harwell, J., Lago, R. and Yeh, L.: 2000, *Surfactant enhanced subsurface remediation of DNAPLs at the*

- former Naval Air Station Alameda, California, in *Treating Dense Nonaqueous-phase Liquids (DNAPLs): Remediation of Chlorinated and Recalcitrant Compounds*, Battelle Press, Battelle Press, Columbus, OH, USA. 219–226.
- [Hassanizadeh and Gray (1993)] Hassanizadeh, S. and Gray, W.: 1993, Thermodynamic basis of capillary pressure in porous media, *Water Resources Research* **29**(10), 3389–3405.
- [Hayashi (2004)] Hayashi, M.: 2004, Temperature-electrical conductivity relation of water for environmental monitoring and geophysical data inversion, *Environmental Monitoring and Assessment* **96**(1-3), 119–128.
- [Hearst *et al.* (2000)] Hearst, J., Nelson, P. and Paillet, F.: 2000, *Well Logging for Physical Properties: A Handbook for Geophysicists, Geologists and Engineers*, number 978-0471963059, John Wiley and Sons Ltd, West Sussex, England. 473 p.
- [Heimovaara *et al.* (1994)] Heimovaara, T., Bouten, W. and Verstraten, J.: 1994, Frequency domain analysis of time domain reflectometry waveforms, 2, a four component complex dielectric mixing model for soils, *Water Resources Research* **30**(2), 201–210.
- [Helmig *et al.* (1994)] Helmig, R., Braun, C. and Emmert, M.: 1994, MUFTE: A Numerical Model for Simulation of Multiphase Flow Processes in Porous and Fractured Porous Media, *Technical Report Program Documentation (HG-208) - Technical Report 94/3*, Stuttgart, Germany.
- [Herbert *et al.* (2014)] Herbert, A., Carr, A. and Hoffmann, E.: 2014, Findfoci: A focus detection algorithm with automated parameter training that closely matches human assignments, reduces human inconsistencies and increases speed of analysis, *PLoS ONE* **9**(12), 1–33.
- [Heron *et al.* (2006)] Heron, G., Baker, R., Bierschenk, J. and LaChance, J.: 2006, Heat it All the Way - Mechanisms and Results Achieved using In-Situ Thermal Remediation, *Fifth International Conference, Remediation of Chlorinated and Recalcitrant Compounds*, Battelle Press, Columbus, OH, USA, Monterey, CA, USA.
- [Heron *et al.* (1998b)] Heron, G., Christensen, T. and Enfield, C.: 1998b, Henry's Law Constant for Trichloroethylene between 10 and 95 °C, *Environmental Science & Technology* **32**(10), 1433–1437.
- [Heron *et al.* (1998a)] Heron, G., van Zutphen, M., Christensen, T. and Enfield, C.: 1998a, Soil Heating for Enhanced Remediation of Chlorinated Solvents: A Laboratory Study on Resistive Heating and Vapor Extraction in a Silty, Low-Permeable Soil Contaminated with Trichloroethylene, *Environmental Science & Technology* **32**, 1474–1481.
- [Hersir and Árnason (2009)] Hersir, P. and Árnason, K.: 2009, Resistivity of rocks, *Short Course IV on Exploration for Geothermal Resources*, UNU-GTP, KenGen and GDC, Lake Naivasha, Kenya.
- [Hiemenz and Rajagopalan (1997)] Hiemenz, P. and Rajagopalan, R.: 1997, *Principles of Colloid and Surface Chemistry*, number 9780824793975, Marcel Dekker, New York, NY, USA. 672 p.
- [Hirasaki *et al.* (1997)] Hirasaki, G., Miller, C., Szafranski, R., Tanzil, D., Lawson, J., Meinardus, H., Jin, M., Londergan, J. and Jackson, R.: 1997, Field demonstration of the surfactant/foam process for aquifer remediation, *Proceedings, SPE Annual Technical Conference and Exhibition*, number 39292-MS, SPE, San Antonio, TX, USA.
- [Hoag and Marley (1986)] Hoag, G. and Marley, M.: 1986, Gasoline Residual Saturation in Unsaturated Uniform Aquifer Materials, *Journal of Environmental Engineering* **112**(3), 586–604.
- [Hofstee *et al.* (1998)] Hofstee, C., Dane, J. and Walker, R.: 1998, Infiltration and Redistribution of Perchloroethylene in Stratified Water-Saturated Porous Media, *Soil Science Society of America Journal* **62**(1), 13–22.

- [Holzmer *et al.* (2000)] Holzmer, F., Pope, G. and Yeh, L.: 2000, *Surfactant-enhanced aquifer remediation of PCE DNAPL in low-permeability sand*, in *Treating Dense Nonaqueous-Phase Liquids (DNAPLs): Remediation of Chlorinated and Recalcitrant Compounds*, Battelle Press, Columbus, OH, USA. 211–218.
- [Homsy (1987)] Homsy, G.: 1987, Viscous fingering in porous media, *Annual Review of Fluid Mechanics* **19**, 271–311.
- [Hopmans and Dane (1986)] Hopmans, J. and Dane, J.: 1986, Temperature dependence of soil water retention curves, *Soil Sci. Soc. Am. J.* **50**, 562–567.
- [Horvath (1982)] Horvath, A.: 1982, *Halogenated Hydrocarbons: Solubility-Miscibility with Water*, number ISBN 0824711661, Marcel Dekker, New York, NY, USA. 920 p.
- [Huang *et al.* (2015)] Huang, J., Christ, J., Goltz, M. and Demond, A.: 2015, Modeling NAPL dissolution from pendular rings in idealized porous media, *Water Resources Research* **51**, 8182–8197.
- [Huisman *et al.* (2003)] Huisman, J., Hubbard, S., Redman, J. and Annan, A.: 2003, Measuring soil water content with ground penetrating radar: A review, *Vadose Zone Journal* **2**, 476–491.
- [Huling and Weaver (1991)] Huling, S. and Weaver, J.: 1991, Ground Water Issue - Dense Nonaqueous Phase Liquids, *Technical Report EPA/540/4-91-002*, U.S. Environmental Protection Agency, U.S. Environmental Protection Agency, Office of Research and Development, Office of Solid Waste and Emergency Response, Washington, DC, USA. 21 p.
- [Huling and Weaver (1996)] Huling, S. and Weaver, J.: 1996, *Dense Nonaqueous Phase Liquids*, Chapter 5 in *EPA Environmental Assessment Sourcebook*, number 9781575040097, Ann Arbor Press, Inc., Chelsea, MI, USA. 400 p.
- [Hunt *et al.* (1988)] Hunt, J., Sitar, N. and Udell, K.: 1988, Nonaqueous phase liquid transport and cleanup: 1. Analysis of mechanisms, *Water Resources Research* **24**, 1247–1258.
- [Huntley and Beckett (2002)] Huntley, D. and Beckett, G.: 2002, Persistence of LNAPL sources: relationship between risk reduction and LNAPL recovery, *Journal of Contaminant Hydrology* **59**(1-2), 3–26.
- [Huyakorn *et al.* (1994)] Huyakorn, P., Panday, S. and Wu, Y.: 1994, A three dimensional multiphase flow model for assessing NAPL contamination in porous and fractured media, 1. Formulation, *Journal of Contaminant Hydrology* **16**, 109–130.
- [Huyakorn and Pinder (1983)] Huyakorn, P. and Pinder, G.: 1983, *Computational Methods in Subsurface Flow*, number 978-0-12-363480-1, Academic Press, New York, NY, USA. 473 p.
- [Hyman and Dupont (2001)] Hyman, M. and Dupont, R.: 2001, *Groundwater and Soil Remediation: Process Design and Cost Estimating of Proven Technologies*, number 978-0-7844-0427-0, American Society of Civil Engineers (ASCE) Press, 1801 Alexander Bell River, Reston, VA, USA. 534 p.
- [IARC (2018)] IARC: 2018. <https://www.iarc.fr/>
- [Illangasekare *et al.* (1995b)] Illangasekare, T., Armbruster III, E. and Yates, D.: 1995b, Non-Aqueous-Phase Fluids in Heterogeneous Aquifers Experimental Study, *Journal of Environmental Engineering* **121**(8), 571–579.
- [Illangasekare *et al.* (1995a)] Illangasekare, T., Ramsey, J., Jensen, K. and Butts, M.: 1995a, Experimental study of the movement and distribution of dense organic contaminants in heterogeneous aquifer, *Journal of Contaminant Hydrology* **20**, 1–25.
- [Imhoff *et al.* (1997)] Imhoff, P., Frizzel, A. and Miller, C.: 1997, Evaluation of Thermal Effects on the Dissolution of a Nonaqueous Phase Liquid in Porous Media, *Environmental Science & Technology* **31**(6), 1615–1622.

- [Imhoff *et al.* (1993)] Imhoff, P., Jaffé, P. and Pinder, G.: 1993, An experimental study of complete dissolution of a nonaqueous phase liquid in saturated porous media, *Water Resources Research* **30**(2), 307–320.
- [Imhoff *et al.* (1994)] Imhoff, P., Jaffé, P. and Pinder, G.: 1994, An experimental study of complete dissolution of a nonaqueous phase liquid in saturated porous media, *Water Resources Research* **30**(2), 307–320.
- [Imhoff and Miller (1996)] Imhoff, P. and Miller, C.: 1996, Dissolution fingering during the solubilization of nonaqueous phase liquids in saturated porous media. 1. model predictions, *Water Resources Research* **32**(7), 1919–1928.
- [Irvine and Sikdar (1997)] Irvine, R. and Sikdar, S.: 1997, *Bioremediation: Principles and Practice. Volume I: Fundamentals and Applications*, number ISBN 9781566763080, CRC Press., Lancaster, PA, USA. 765 p.
- [Ishikawa (1958)] Ishikawa, T.: 1958, The viscosity of ideal solutions, *Bulletin of the Chemical Society of Japan* **31**(7), 791–796.
- [ITRC (2002)] ITRC: 2002, *DNAPL Source Reduction: Facing the Challenge*, Technical/Regulatory Guidelines, Interstate Technology & Regulatory Council, Washington, DC, USA. 40 p.
- [ITRC (2004)] ITRC: 2004, *Strategies for Monitoring the Performance of DNAPL Source Zone Remedies*, Technical/Regulatory Guidelines, Interstate Technology & Regulatory Council, Washington, DC, USA. 205 p.
- [ITRC (2013)] ITRC: 2013, *Technical and Regulatory Guidance for Surfactant cosolvent Flushing of DNAPL Source Zones*, Technical/Regulatory Guidelines, Interstate Technology & Regulatory Council, Washington, DC, USA. 20 p.
- [Ivankovic and Hrenovic (2010)] Ivankovic, T. and Hrenovic, J.: 2010, Surfactants in the environment, *Archives of Industrial Hygiene and Toxicology* **61**(1), 95–110.
- [Jacobsen and Schjønning (1995)] Jacobsen, O. and Schjønning, P.: 1995, Comparison of tdr calibration functions for soil water determination, in L. Petersen and O. Jacobsen (eds), *Proceedings of the Symposium: Time-Domain Reflectometry Applications in Soil Science*, Vol. vol. 3, Danish Institute of Plant and Soil Science, Lyngby, Denmark, p. 25–33.
- [Jafvert (1994)] Jafvert, C.: 1994, Solubilization of non-polar compounds by non-ionic surfactant micelles, *Water Research* **28**(5), 1009–1017.
- [Jalbert *et al.* (2003)] Jalbert, M., Dane, J. and Bahaminyakamwe, L.: 2003, Influence of porous medium and NAPL distribution heterogeneities on partitioning inter-well tracer tests: a laboratory investigation, *Journal of Hydrology* **272**(1-4), 79–94.
- [Jawitz *et al.* (2001)] Jawitz, J., Annable, M., Rao, P. and Rhue, R.: 2001, Evaluation of remediation performance and cost for field-scale single-phase microemulsion (spme) flushing, *Journal of Environmental Science and Health* **A**(36), 1437–1450.
- [Jawitz *et al.* (2000)] Jawitz, J., Sillan, R., Annable, M., Rao, P. and Warner, K.: 2000, In situ alcohol flushing of a DNAPL source zone at a dry cleaner site, *Environmental Science & Technology* **34**, 3722–3729.
- [Jennings (1975)] Jennings, H.: 1975, A study of caustic solution-crude oil interfacial tensions, *Society of Petroleum Engineering Journal* **15**, 197–202.
- [Jeong *et al.* (2000)] Jeong, S., Corapcioglu, M. and Roosevelt, S.: 2000, Micromodel study of surfactant foam remediation of residual trichloroethylene, *Environmental Science & Technology* **34**(16), 3456–3461.
- [Johns and Gladden (1999)] Johns, M. and Gladden, L.: 1999, Magnetic Resonance Imaging Study of the Dissolution Kinetics of Octanol in Porous Media, *Journal of Colloid and Interface Science* **210**(2), 261–270.

- [Jury *et al.* (1990)] Jury, W., Russo, D., Streile, G. and El Abd, H.: 1990, Evaluation of volatilization by organic chemicals residing below the soil surface, *Water Resources Research* **26**(1), 13–20.
- [Katyal *et al.* (1991)] Katyal, A., Kaluarachchi, J. and Parker, J.: 1991, *MOFAT: a two dimensional finite element program for multiphase flow and multicomponent transport - Program Documentation and User's Guide*, number EPA/600/2-91/020., US Environmental Protection Agency, Ada, OK, USA. 121 p.
- [Kearey *et al.* (2002)] Kearey, P., Brooks, M., and Hill, I.: 2002, *An introduction to geophysical exploration*, number ISBN 0-632-04929-4, Blackwell Science, Oxford, UK. 281 p.
- [Kechavarzi *et al.* (2000)] Kechavarzi, C., Soga, K. and Wiart, P.: 2000, Multispectral image analysis method to determine dynamic fluid saturation distribution in two-dimensional three-fluid phase flow laboratory experiments, *Journal of Contaminant Hydrology* **46**(3-4), 265–293.
- [Kemna *et al.* (2012)] Kemna, A., Binley, A., Cassiani, G., Niederleithinger, E., Revil, A., Slater, L., Williams, K., Flores Orozco, A., Haegel, F.-H., Hördt, A., Kruschwitz, S., Leroux, V., Titov, K. and Zimmermann, E.: 2012, An overview of the spectral induced polarization method for near-surface applications, *Near Surface Geophysics* **10**(6), 453 – 468.
- [Kenaga and Goring (1980)] Kenaga, E. and Goring, C.: 1980, Relationship between water solubility, soil sorption, octanol-water partitioning, and concentration of chemicals in blots, aquatic toxicology, *American Society for Testing and Materials, Philadelphia, Pennsylvania* pp. 78–115.
- [Kendall and Monroe (1917)] Kendall, J. and Monroe, K.: 1917, The viscosity of liquids II. The viscosity-composition curve for ideal liquid mixtures, *American Chemical Journal* **9**, 787–802.
- [Kestin *et al.* (1978)] Kestin, J., Mordechai, S. and Wakeham, W.: 1978, Viscosity of liquid water in the Range -8°C to 150 °C, *Journal of Physical and Chemical Reference Data* **7**(3), 941–948.
- [Kilbane *et al.* (1997)] Kilbane, J., Chowdiah, P., Kayser, K., Misra, B., Jackowski, K., Srivastava, V., Sethu, G., Nikolov, A., Wasan, D. and Hayes, T.: 1997, Remediation of contaminated soils using foams, *Land Contamination and Reclamation* **5**(1), 41–54.
- [Kingston *et al.* (2014)] Kingston, J., Johnson, P., Kueper, B. and Mumford, K.: 2014, *In situ thermal treatment of chlorinated solvent source zones, Chapter 14 in Chlorinated Solvent Source Zone Remediation*, number 978-1-4614-6921-6, Springer, SERDP ESTCP Environmental Remediation Technology, New York, NY, USA. 713 p.
- [Knauss *et al.* (2000)] Knauss, K., Dibley, M., Leif, R., Mew, D. and Aines, R.: 2000, The aqueous solubility of trichloroethene (TCE) and tetrachloroethene (PCE) as a function of temperature, *Applied Geochemistry* **15**(4), 501–512.
- [Knight (2001)] Knight, R.: 2001, Ground penetrating radar for environmental applications, *Annual Review of Earth and Planetary Sciences* **29**, 229–255.
- [Knox *et al.* (1997)] Knox, R., Sabatini, D., Harwell, J., Brown, R., West, C., Blaha, F. and Griffin, C.: 1997, Surfactant remediation field demonstration using a vertical circulation well, *Groundwater* **35**, 948–953.
- [Kommalapati *et al.* (1997)] Kommalapati, R., Valsaraj, K., Constant, W. and Roy, D.: 1997, Aqueous solubility enhancement and desorption of hexachlorobenzene from soil using a plant-based surfactant, *Water Research* **31**(9), 2161–2170.
- [Kosugi (1994)] Kosugi, K.: 1994, Three-parameter lognormal distribution model for soil water retention, *Water Resources Research* **30**(4), 891–901.
- [Kosugi (1996)] Kosugi, K.: 1996, Lognormal distribution model for unsaturated soil hydraulic properties, *Water Resources Research* **32**(9), 2697–2703.

- [Kueper *et al.* (1989)] Kueper, B., Abbot, W. and Farquhar, G.: 1989, Experimental observations of multiphase flow in heterogeneous porous media, *Journal of Contaminant Hydrology* **5**, 83–95.
- [Kueper and Frind (1991a)] Kueper, B. and Frind, E.: 1991a, Two-phase flow in heterogeneous porous media: 1. model development, *Water Resources Research* **27**, 1049–1057.
- [Kueper and Frind (1991b)] Kueper, B. and Frind, E.: 1991b, Two-phase flow in heterogeneous porous media. 2. model application, *Water Resources Research* **27**, 1059–1070.
- [Kueper and Frind (1992)] Kueper, B. and Frind, E.: 1992, Numerical modelling of multiphase /multicomponent flow and transport in porous media, *Proceedings of the International Conference on Subsurface Contamination by Immiscible Fluids*.
- [Kueper and Gerhard (2014)] Kueper, B. and Gerhard, J.: 2014, *Hydraulic displacement of Dense NonAqueous Phase Liquids, Chapter 8 in Chlorinated Solvent Source Zone Remediation*, number 978-1-4614-6921-6, Springer, SERDP ESTCP Environmental Remediation Technology, New York, NY, USA. 713 p.
- [Kueper *et al.* (1993)] Kueper, B., Redman, D., Starr, R., Reitsma, S. and Mah, M.: 1993, A field experiment to study the behavior of tetrachlorethylene below the water table: Spatial distribution of residual and pooled DNAPL, *Ground Water* **31**, 756–766.
- [Kueper *et al.* (2008)] Kueper, B., Shi, J. and Gefell, M.: 2008, Hydraulic gradient magnification in NAPL pools: Implications for MGP NAPL vertical mobility, *Sixth International Conference, Remediation of Chlorinated and Recalcitrant Compounds*, number K-004, Battelle Press, Columbus, OH, USA, Monterey, CA, USA.
- [Kueper *et al.* (2003)] Kueper, B., Wealthall, G., Smith, J., Leharne, S. and Lerner, D.: 2003, *An illustrated handbook of DNAPL transport and fate in the subsurface*, number 1844320669, U.K. Environment Agency, Bristol, England, United Kingdom. 67 p.
- [Laha *et al.* (2009)] Laha, S., Tansel, B. and Ussawarujikulchaib, A.: 2009, Surfactant–soil interactions during surfactant-amended remediation of contaminated soils by hydrophobic organic compounds: A review, *Journal of Environmental Management* **90**(1), 95–100.
- [Lahvis and Baehr (1997)] Lahvis, M. and Baehr, A.: 1997, *Documentation of R-UNSAT: A Computer Model for the Simulation of Reactive, Multispecies Transport in the Unsaturated Zone*, number 97.630, U.S. Geological Survey, West Trenton, NJ, USA. 104 p.
- [Lake (1989)] Lake, L.: 1989, *Enhanced Oil Recovery*, number 0132816016 9780132816014, Prentice Hall, Old Tappan, NJ, USA. 550 p.
- [Lappala *et al.* (1987)] Lappala, E., Healy, R. and Weeks, E.: 1987, *Documentation of Computer Program VS2D to Solve the Equations of Fluid Flow in Variably Saturated Porous Media*, number 83-4099-4184. in *Water Resources Investigation*, U.S. Geological Survey, Denver, CO, USA. 193 p.
- [Larson *et al.* (1981)] Larson, R., Scriven, L. and Davis, H.: 1981, Displacement of residual non-wetting fluid from porous media, *Chemical Engineering Science* **36**, 75–85.
- [Lederer (1933)] Lederer, E.: 1933, Viscosity of mixtures with and without diluents, *Proc. World Pet. Cong. Lond.* **2**, 526–528.
- [Ledieu *et al.* (1986)] Ledieu, J., De Bidder, P., De Clerck, P. and Dautrebande, S.: 1986, A method of measuring soil moisture by time-domain reflectometry, *Journal of Hydrology* **88**(3-4), 319–328.
- [Lee *et al.* (2007)] Lee, D., Chang, H. and Kim, C.: 2007, Mixing effect of NaCl and surfactant on the remediation of TCB contaminated soil, *Geosciences Journal* **12**, 63–68.
- [Lehikoinen *et al.* (2009)] Lehikoinen, A., Finsterle, S., Voutilainen, A., Kowalsky, M. and Kaipio, J.: 2009, Dynamical inversion of geophysical ert data: state estimation in the vadose zone, *Inverse Problems in Science and Engineering* **17**(6), 715–736.

- [Lemière *et al.* (2008)] Lemière, B., Seguin, J.-J., Le Guern, C., Guyonnet, D., Baranger, P., Saada, A., Darmendrail, D., Conil, P., Bodéan, F., Fauconnier, D., Hubé, D. and Colombano, S.: 2008, Guide sur le comportement des polluants dans les sols et les nappes, *Technical Report ISBN 2-7159-0912-8*, BRGM - French Geological Survey, 3, avenue Claude Guillemin, 45 060 - Orléans Cedex 2, France. 155 p.
- [Lenhard *et al.* (1995)] Lenhard, R., Oostrom, M. and White, M.: 1995, Modeling fluid flow and transport in variably saturated porous media with the STOMP simulator: verification and validation exercises, *Advances in Water Resources* **18**(6), 365–373.
- [Lenormand *et al.* (1988)] Lenormand, R., Touboul, E. and Zarcone, C.: 1988, Numerical models and experiments on immiscible displacements in porous media, *Journal of Fluid Mechanics* **189**, 165–187.
- [Leverett (1941)] Leverett, M.: 1941, Capillary behaviour in porous solids, *Transaction of the AIME* **142**(01), 159–172.
- [Li *et al.* (2015)] Li, M., Tang, Y., Bernabé, Y., Zhao, J., Li, X., Bai, X. and Zhang, L.: 2015, Pore connectivity, electrical conductivity, and partial water saturation: Network simulations, *Journal of Geophysical Research: Solid Earth* **120**(6), 4055–4068.
- [Light *et al.* (2005)] Light, T., Licht, S., Bevilacqua, A. and Morashc, K.: 2005, The fundamental conductivity and resistivity of water, *Electrochemical and Solid-State Letters* **8**(1), E16–E19.
- [Likos and Jaafar (2013)] Likos, W. and Jaafar, R.: 2013, Pore-scale model for water retention and fluid partitioning of partially saturated granular soil, *Journal of Geotechnical and Geoenvironmental Engineering* **139**(5), 724–737.
- [Liu and Dane (1993)] Liu, H. and Dane, J.: 1993, Reconciliation between Measured and Theoretical Temperature Effects on Soil Water Retention Curves, *Soil Science Society of America Journal* **57**(5), 1202–1207.
- [Liu *et al.* (1998)] Liu, Y., Hopmans, J., Grismer, M. and Chen, J.: 1998, Direct estimation of air-oil and oil-water capillary pressure and permeability relations from multi-step outflow experiments, *Journal of Contaminant Hydrology* **32**(3-4), 223–245.
- [Lobe (1973)] Lobe, V.: 1973, *A model for the viscosity of liquid-liquid mixtures*, Master's thesis, University of Rochester, Rochester, NY, USA. 50 p.
- [Logsdon (2000)] Logsdon, S.: 2000, Effect of cable length on time domain reflectometry calibration for high surface area soils, *Soil Science Society of America Journal* **64**(1), 54–61.
- [Logsdon (2005)] Logsdon, S.: 2005, Soil dielectric spectra from vector network analyzer data, *Soil Science Society of America Journal* **69**(4), 983–989.
- [Londergan *et al.* (2001)] Londergan, J., Meinardus, H., Mariner, P., Jackson, R., Brown, C., Dwarakanath, V., Pope, G., Ginn, J. and Taffinder, S.: 2001, DNAPL removal from a heterogeneous alluvial aquifer by surfactant-enhanced aquifer remediation, *Groundwater Monitoring & Remediation* **21**(4), 57–67.
- [Longeron *et al.* (1989)] Longeron, D., Argaud, M. and Feraud, J.: 1989, Effect of overburden pressure and the nature and microscopic distribution of fluids on electrical properties of rock samples, *Society of Petroleum Engineers Format. Eval.* **4**(2), 194–202.
- [Longpré-Girard *et al.* (2016)] Longpré-Girard, M., Martel, R., Robert, T., Lefebvre, R. and Lauzon, J.-M.: 2016, 2D sandbox experiments of surfactant foams for mobility control and enhanced LNAPL recovery in layered soils, *Journal of Contaminant Hydrology* **193**, 63–73.
- [Loon *et al.* (1967)] Loon, R., Fuks, S. and Bellemans, A.: 1967, Dielectric constant of carbon tetrachloride and 1,1,1-trichloroethane mixtures, *Bulletin des Societes Chimiques Belges* **76**(3-4), 202–210.
- [Lord *et al.* (2000)] Lord, D., Demond, A. and Hayes, K.: 2000, Effects of Organic Base Chemistry on Interfacial Tension, Wettability, and Capillary Pressure in Multiphase Subsurface Waste Systems, *Transport in Porous Media* **38**(1-2), 79–92.

- [Lowe *et al.* (1999)] Lowe, D., Oubre, C. and Ward, C.: 1999, *Surfactants and Cosolvents for NAPL Remediation A Technology Practices Manual*, 1st edition edn, CRC Press, Boca Raton, FL, USA. 448 p.
- [Lowry and Miller (1995)] Lowry, M. and Miller, C.: 1995, Pore-Scale Modeling of Nonwetting-Phase Residual in Porous Media, *Water Resources Research* **31**(3), 455–473.
- [Lu and Likos (2004)] Lu, N. and Likos, W.: 2004, *Unsaturated Soil Mechanics*, number 978-0471447313, John Wiley & Sons, Ltd., Hoboken, NJ, USA. 584 p.
- [Luciano (2009)] Luciano, A.: 2009, *Studio del comportamento dei DNAPLs nel suolo e nel sottosuolo: analisi sperimentale e simulazione numerica*, PhD thesis, Università degli studi di Roma « Tor Vergata », Rome, Italy. 154 p.
- [Luciano *et al.* (2010)] Luciano, A., Viotti, P. and Papini, M. P.: 2010, Laboratory investigation of DNAPL migration in porous media, *Journal of Hazardous Materials* **176**(1-3), 1006–1017.
- [Lucius *et al.* (1992)] Lucius, J., Olhoeft, G., Hill, P. and Duke, S.: 1992, *Properties and hazards of 108 selected substances*, number 92-527, U.S. Geological Survey, Golden, CO, USA. 554 p.
- [Luckner *et al.* (1989)] Luckner, C., van Genuchten, M. and Nielsen, D.: 1989, A consistent set of parametric models for two-phase flow of immiscible fluids in the subsurface, *Water Resources Research* **25**(10), 2187–2193.
- [Lyman *et al.* (1982)] Lyman, W., Reehl, W. and Rosenblatt, D.: 1982, *Handbook of Chemical Property Estimation Methods—Environmental Behavior of Organic Compounds.*, McGraw-Hill, New York.
- [Mackay and Cherry (1989)] Mackay, D. and Cherry, J.: 1989, Groundwater contamination: pump-and-treat remediation, *Environmental Science & Technology* **23**, 630–636.
- [Mackay *et al.* (1985)] Mackay, D., Roberts, P. and Cherry, J.: 1985, Transport of organic contaminants in groundwater, *Environmental Science & Technology* **19**(5), 384–392.
- [Mackay *et al.* (1991)] Mackay, D., Shiu, W., Maijanen, A. and Feenstra, S.: 1991, Dissolution of non-aqueous phase liquids in groundwater, *Journal of Contaminant Hydrology* **8**(1), 23–42.
- [Maineult *et al.* (2004)] Maineult, A., Bernabé, Y. and Ackerer, P.: 2004, Electrical response of flow, diffusion, and advection in a laboratory sand box, *Vadose Zone Journal* **3**(4), 1180–1192.
- [Maire *et al.* (2015)] Maire, J., Coyer, A. and Fatin-Rouge, N.: 2015, Surfactant foam technology for in situ removal of heavy chlorinated compounds-DNAPLs, *Journal of Hazardous Materials* **299**, 630–638.
- [Maire *et al.* (2016)] Maire, J., Coyer, A., Fatin-Rouge, N., Colombano, S., Giraud, Q., Paris, B., Dumestre, A., Joubert, A., Klein, P.-Y., Triger, A. and Cazaux, D.: 2016, Surfactant Foam Technology for In Situ Remediation of Heavy Chlorinated-Compound DNAPLs, *Tenth International Conference on Remediation of Chlorinated and Recalcitrant Compounds*, Battelle Press, Columbus, OH, USA, Palm Springs, CA, USA.
- [Maire and Fatin-Rouge (2017)] Maire, J. and Fatin-Rouge, N.: 2017, Surfactant foam flushing for in situ removal of DNAPLs in shallow soils, *Journal of Hazardous Materials* **321**, 247–255.
- [Maire *et al.* (2018)] Maire, J., Joubert, A., Kaifas, D., Invernizzi, T., Mardue, J., Colombano, S., Cazaux, D., Marion, C., Klein, P., Dumestre, A. and Fatin-Rouge, N.: 2018, Assessment of flushing methods for the removal of heavy chlorinated compounds DNAPL in an alluvial aquifer, *Science of the Total Environment* (612), 1149–1158.
- [Mao *et al.* (2015)] Mao, X., Jiang, R., Xiao, W. and Yu, J.: 2015, Use of surfactants for the remediation of contaminated soils: a review, *Journal of Hazardous Materials* (285), 419–435.

- [Margesin and Schinner (1999)] Margesin, R. and Schinner, F.: 1999, Biodegradation of diesel oil by cold-adapted microorganisms in presence of sodium dodecyl sulfate, *Chemosphere* **38**(15), 3463–3472.
- [Martel *et al.* (1998a)] Martel, K., Martel, R., Lefebvre, R. and Gélinas, P.: 1998a, Laboratory Study of Polymer Solutions Used for Mobility Control During In Situ NAPL Recovery, *Groundwater Monitoring & Remediation* **18**(3), 103–113.
- [Martel *et al.* (1998b)] Martel, R., Gélinas, P. and Desnoyers, J.: 1998b, Aquifer washing by micellar solutions: 1 Optimization of alcohol-surfactant-solvent solutions, *Journal of Contaminant Hydrology* **29**(4), 319–346.
- [Martel *et al.* (1993)] Martel, R., Gélinas, P., Desnoyers, J. and Masson, A.: 1993, Phase diagrams to optimize surfactant solutions for oil and DNAPL recovery in aquifers, *Groundwater* **31**(5), 789–800.
- [Martel *et al.* (1998c)] Martel, R., Gélinas, P. and Saumure, L.: 1998c, Aquifer washing by micellar solutions: 3. Field test at the Thouin Sand Pit (L'Assomption, Quebec, Canada), *Journal of Contaminant Hydrology* **30**(1-2), 33–48.
- [Martel *et al.* (2004)] Martel, R., Hébert, A., Lefebvre, R., Gélinas, P. and Gabriel, U.: 2004, Displacement and sweep efficiencies in a DNAPL recovery test using micellar and polymer solutions injected in a five-spot pattern, *Journal of Contaminant Hydrology* **75**(1), 1–29.
- [Martinez and Byrnes (2001)] Martinez, A. and Byrnes, A.: 2001, Modeling dielectric-constant values of geologic materials: An aid to ground-penetrating radar data collection and interpretation, *Current Research in Earth Sciences, Kansas Geological Survey, University of Kansas* **247**(1), 1–16.
- [Mavko *et al.* (2009)] Mavko, G., Mukerji, T. and Dvorkin, J.: 2009, *The rock physics handbook: Tools for seismic analysis, in Porous Media*, number 9780511626753, 2nd edition edn, Cambridge University Press, Cambridge, UK. 511 p.
- [Maxwell (1878)] Maxwell, J.: 1878, Matter and motion, *D. Van Nostrand*.
- [McDade *et al.* (2005)] McDade, J., McGuire, T. and Newell, C.: 2005, Analysis of DNAPL source-depletion costs at 36 field sites, *Remediation Journal* **15**(2:), 9–18.
- [McGuire *et al.* (2006)] McGuire, T., McDade, J. and Newell, C.: 2006, Performance of DNAPL Source Depletion Technologies at 59 Chlorinated Solvent-Impacted Sites, *Ground Water Monitoring and Remediation* **26**(1), 73–84.
- [McLaren *et al.* (2009)] McLaren, S., Worboys, M., Speake, O. and Mantell, P.: 2009, Ex-Situ Thermally Enhanced Coal Tar Recovery – A Low Carbon Option, *Green Remediation*, Copenhagen, Denmark.
- [MEEM (2017a)] MEEM: 2017a, *Introduction à la méthodologie nationale de gestion des sites et sols pollués*, MEEM edn, Ministère de l'Environnement, de l'Énergie et de la Mer, en charge des relations internationales sur le climat, Direction Générale de la Prévention des Risques, Bureau du Sol et du Sous-Sol. 27 p.
- [MEEM (2017b)] MEEM: 2017b, *Méthodologie nationale de gestion des sites et sols pollués*, MEEM edn, Ministère de l'Environnement, de l'Énergie et de la Mer, en charge des relations internationales sur le climat, Direction Générale de la Prévention des Risques, Bureau du Sol et du Sous-Sol. 128 p.
- [MEEM (2017c)] MEEM: 2017c, *Note du 19 avril 2017 relative aux sites et sols pollués - Mise à jour des textes méthodologiques de gestion des sites et sols pollués de 2007*, meem edn, Ministère de l'Environnement, de l'Énergie et de la Mer, en charge des relations internationales sur le climat. 3 p.
- [Mehrotra (1990)] Mehrotra, A.: 1990, Development of mixing rules for predicting the viscosity of bitumen and its fractions blended with toluene, *The Canadian Journal of Chemical Engineering* **68**(October), 839–848.

- [Mehrotra (1991)] Mehrotra, A.: 1991, A generalized viscosity equation for pure heavy hydrocarbons, *Industrial & Engineering Chemistry Research* **30**(2), 420–427.
- [Mehrotra *et al.* (1996)] Mehrotra, A., Monnery, W. and Svrcek, W.: 1996, A review of practical calculation methods for the viscosity of liquid hydrocarbons and their mixtures, *Fluid Phase Equilib* **117**(1), 344–355.
- [Meinardus *et al.* (2002)] Meinardus, H., Dwarakanath, V., Ewing, J., Hirasaki, G., Jackson, R., Jin, M., Ginn, J., Londergan, J., Miller, C. and Pope, G.: 2002, Performance assessment of napl remediation in heterogeneous alluvium, *Journal of Contaminant Hydrology* **54**(3-4), 173–193.
- [Melrose and Brandner (1974)] Melrose, J. and Brandner, C.: 1974, Role of Capillary Forces In Detennining Microscopic Displacement Efficiency For Oil Recovery By Waterflooding, *Journal of Canadian Petroleum Technology* **13**(4), 54–62.
- [Mercer and Cohen (1990)] Mercer, J. and Cohen, R.: 1990, A Review of Immiscible Fluids in the Subsurface: Properties, Models, Characterization and Remediation, *Journal of Contaminant Hydrology* **6**(2), 107–163.
- [Miadonye *et al.* (2000)] Miadonye, A., Latour, N. and Puttagunta, V.: 2000, A correlation for viscosity and solvent mass fraction of bitumen-diluent mixtures, *Petroleum Science and Technology* **18**(1-2), 1–14.
- [Miller *et al.* (1998)] Miller, C., Christakos, G., Imhoff, P., McBride, J., Pedit, J. and Trangenstein, J.: 1998, Multiphase flow and transport modeling in heterogeneous porous media: challenges and approaches, *Advances in Water Resources* **21**(2), 77–120.
- [Miller *et al.* (1990)] Miller, C., Poirier-McNeill, M. and Mayer, A.: 1990, Dissolution of Trapped Nonaqueous Phase Liquids: Mass Transfer Characteristics, *Water Resources Research* **26**(11), 2783–2796.
- [Monego *et al.* (2010)] Monego, M., Cassiani, G., Deiana, R., Putti, M., Passadore, G. and Altissimo, L.: 2010, A tracer test in a shallow heterogeneous aquifer monitored via time-lapse surface electrical resistivity tomography, *Geophysics* **75**(4), WA61–WA73.
- [Morgan and Lowry (1930)] Morgan, S. and Lowry, H.: 1930, Dielectric polarization of some pure organic compounds in the dissolved, liquid, and solid states, *The Journal of Physical Chemistry* **34**(11), 2385–2432.
- [Morrow (1970)] Morrow, N.: 1970, Irreducible wetting phase saturations in porous media, *Chemical Engineering Science* **25**(11), 1799–1815.
- [Morrow (1975)] Morrow, N.: 1975, Effects of surface roughness on contact angle with special reference to petroleum recovery, *Journal of Canadian Petroleum Technology* **14**, 42–53.
- [Morrow (1976)] Morrow, N.: 1976, Capillary pressure correlations for uniformly wetted porous media, *Journal of Canadian Petroleum Technology* **15**(04), 49–69.
- [Mousset *et al.* (2014)] Mousset, E., Oturan, N., van Hullebusch, E., Guibaud, G., Esposito, G. and Oturan, M.: 2014, Influence of solubilizing agents (cyclodextrin or surfactant) on phenanthrene degradation by electro-Fenton process - Study of soil washing recycling possibilities and environmental impact, *Water Research* **48**, 306–316.
- [MTES (2018)] MTES: 2018, Base de données Basol. <https://basol.developpement-durable.gouv.fr/>
- [Mualem (1976)] Mualem, Y.: 1976, A new model for predicting the hydraulic conductivity of unsaturated porous media, *Water Resources Research* **12**(3), 513–522.
- [Mulligan and Eftekhari (2003)] Mulligan, C. and Eftekhari, F.: 2003, Remediation with surfactant foam of PCP-contaminated soil, *Engineering Geology* **70**(3–4), 269–279.
- [Munson *et al.* (2009)] Munson, B., Young, D., Okiishi, T. and Huebsch, W.: 2009, *Fundamentals of Fluid Mechanics*, number 978-0470-26284-9, John Wiley & Sons, Inc., New York, NY, USA. 783 p.

- [Muthusamy *et al.* (2008)] Muthusamy, K., Gopalakrishnan, S., Ravi, T. and Sivachidambaram, P.: 2008, Biosurfactants: Properties, commercial production and application, *Current Science* **94**(6), 736–747.
- [Myers (1999)] Myers, D.: 1999, *Surfaces, Interfaces, and Colloids: Principles and Applications*, number 978-0-471-33060-8, 2nd edition edn, Myers, D., New-York, NY, USA. 528 p.
- [Nagata *et al.* (2016)] Nagata, Y., Ohto, T., Bonn, M. and Kühne, T.: 2016, Surface tension of ab initio liquid water at the water-air interface, *The Journal of Chemical Physics* **144**(20), 204705.
- [Nambi and Powers (2003)] Nambi, I. and Powers, S.: 2003, Mass transfer correlations for nonaqueous phase liquid dissolution from regions with high initial saturations, *Water Resources Research* **39**, 1030–1040.
- [Nath (1995)] Nath, J.: 1995, Ultrasonic velocities, relative permittivities, and refractive indices for binary liquid mixtures of trichloroethylene with pyridine and quinoline, *Fluid Phase Equilibria* **109**(1), 39–51.
- [Nath and Narain (1982)] Nath, J. and Narain, B.: 1982, Binary systems of tetrachlorethylene with benzene, toluence, p-xylene, carbon tetrachloride, and cyclohexane. 1. Ultrasonic velocities and adiabatic compressibilities at 293.15 and 303.15 K, dielectric constants at 298.15 and 308.15 K, and refractive indexes at 298.15 K, *Journal of Chemical Engineering Data* **27**(3), 308–312.
- [NAVFAC (2002)] NAVFAC: 2002, Surfactant-enhanced aquifer remediation (sear) design manual, *Technical Report TR-2206-ENV*, Naval Facilities Engineering Command, Washington, DC, USA. 110 p.
- [Newell and Adamson (2005)] Newell, C. and Adamson, D.: 2005, Planning-level source decay models to evaluate impact of source depletion on remediation timeframe, *Remediation* **15**(4), 27–47.
- [Newell and Ross (1992)] Newell, C. and Ross, R.: 1992, Estimating potential for occurrence of DNAPL at Superfund sites, *USEPA Quick Reference Fact Sheet, Robert S. Kerr Environmental Research Laboratory*.
- [Ng *et al.* (1978)] Ng, K., Davis, H. and Scriven, L.: 1978, Visualization of blob mechanics in flow through porous media, *Chemical Engineering Science* **33**(8), 1009–1017.
- [Nicolini *et al.* (1998)] Nicolini, C., Chiabrera, A. and Schwan, H.: 1998, *Interactions between electromagnetic fields and cells*, Vol. 43, North Atlantic Treaty Organization edn, NATO Scientific Affairs Division and Plenum Press, New York, NY, USA.
- [NIEHS (2015)] NIEHS: 2015, Chlorinated organics – information page, website. http://tools.niehs.nih.gov/srp/research/research4_s3_s4.cfm
- [Nitao (1996)] Nitao, J.: 1996, *Reference Manual for the NUFT Flow and Transport Code*, number UCRL-ID-113520, Lawrence Livermore National Laboratory, Livermore, CA, USA. 52 p.
- [Noel (2014)] Noel, C.: 2014, *Suivi de la biodégradation des hydrocarbures par le couplage des mesures géophysiques électriques du sol (polarisation provoquée) et des analyses des gaz (concentration du CO₂ et isotopie du carbone)*, PhD thesis, Université d'Orléans, Orléans, France. 256 p.
- [Noel *et al.* (2016)] Noel, C., Gourry, J., Deparis, J., Blessing, M., Ignatiadis, I. and Guimbaud, C.: 2016, Combining geoelectrical measurements and CO₂ analyses to monitor the enhanced bioremediation of hydrocarbon-contaminated soils: a field implementation, *Applied and Environmental Soil Science* **2016**, 1–15.
- [Nsir (2009)] Nsir, K.: 2009, *Etude expérimentale et numérique de la migration de polluants non miscibles dans un milieu poreux saturé à l'échelle de Darcy*, PhD thesis, Université de Strasbourg, Strasbourg, France. 189 p.

- [Ntarlagiannis *et al.* (2016)] Ntarlagiannis, D., Robinson, J., Soupios, P. and Slater, L.: 2016, Field-scale electrical geophysics over an olive oil mill waste deposition site: evaluating the information content of resistivity versus induced polarization (ip) images for delineating the spatial extent of organic contamination, *Journal of Applied Geophysics* **135**(2016), 418–426.
- [Nyquist *et al.* (1999)] Nyquist, J., Carr, B. and Davis, R.: 1999, DC resistivity monitoring of potassium permanganate injected to oxidize TCE in situ, *Journal of Environmental and Engineering Geophysics* **4**(3), 135–147.
- [O’Carroll *et al.* (2004)] O’Carroll, D., Bradford, S. and Abriola, L.: 2004, Infiltration of PCE in a system containing spatial wettability variations, *Journal of Contaminant Hydrology* **73**(1-4), 39–63.
- [O’Carroll and Sleep (2007)] O’Carroll, D. and Sleep, B.: 2007, Hot water flushing for immiscible displacement of a viscous NAPL, *Journal of Contaminant Hydrology* **91**, 247–266.
- [Okasha *et al.* (1998)] Okasha, T., Menouar, H. and Abu-Khamsin, S.: 1998, Oil recovery from Tarmat reservoirs using hot water and solvent flooding, *Journal of Canadian Petroleum Technology* **37**(4), 33–40.
- [Oleszek-Kudlak *et al.* (2004)] Oleszek-Kudlak, S., Shibata, E. and Nakamura, T.: 2004, The effects of temperature and inorganic salts on the aqueous solubility of selected chlorobenzenes, *Journal of Chemical & Engineering Data* **49**(3), 570–575.
- [Oostrom *et al.* (1999)] Oostrom, M., Hofstee, C., Walker, R. and Dane, J.: 1999, Movement and remediation of trichloroethylene in a saturated heterogeneous porous medium: 1. Spill behavior and initial dissolution, *Journal of Contaminant Hydrology* **37**(1 -2), 159–178.
- [Orlando and Renzi (2015)] Orlando, L. and Renzi, B.: 2015, Electrical permittivity and resistivity time lapses of multiphase DNAPLs in a lab test, *Water Resources Research* **51**(1), 377–389.
- [Orozco *et al.* (2012)] Orozco, A., Kemna, A., Oberdörster, C., Zschornack, L., Leven, C., Dietrich, P. and Weiss, H.: 2012, Delineation of subsurface hydrocarbon contamination at a former hydrogenation plant using spectral induced polarization imaging, *Journal of Contaminant Hydrology* **136-137**(2012), 131–144.
- [Orphius and Kibbey (2005)] Orphius, I. and Kibbey, T.: 2005, Dissolution-Induced Contact Angle Modification in Dense Nonaqueous Phase Liquid (DNAPL)/Water Systems, *Environmental Science and Technology* **39**, 1698–1706.
- [Ouchiyama and Tanaka (1984)] Ouchiyama, N. and Tanaka, T.: 1984, Porosity estimation for random packings of spherical particles, *Industrial & Engineering Chemistry Fundamentals* **23**, 490–493.
- [Pacwa-Plociniczak *et al.* (2011)] Pacwa-Plociniczak, M., Plaza, G., Piotrowska-Seget, Z. and Cameotra, S.: 2011, Environmental applications of biosurfactants: recent advances, *International Journal of Molecular Sciences* **12**(1), 633–654.
- [Panagopoulos *et al.* (2017)] Panagopoulos, D., Jahnke, A., Kierkegaard, A. and MacLeod, M.: 2017, Temperature dependence of the organic carbon/water partition ratios (K_{oc}) of volatile methylsiloxanes, *Environmental Science & Technology Letters* **4**, 240–245.
- [Pankow and Cherry (1996)] Pankow, J. and Cherry, J.: 1996, *Dense Chlorinated Solvents and Other DNAPLs in Groundwater: History, Behavior, and Remediation*, number 978-0964801417, Waterloo Press, Portland, OR, USA. 525 p.
- [Paria (2008)] Paria, S.: 2008, Surfactant-enhanced remediation of organic contaminated soil and water, *Advances in Colloid and Interface Science* **138**(1), 24–58.
- [Pennell *et al.* (2014)] Pennell, K., Capiro, N. and Walker, D.: 2014, *Surfactant and cosolvent flushing, Chapter 11 in Chlorinated Solvent Source Zone Remediation*, number 978-1-4614-6921-6, Springer, SERDP ESTCP Environmental Remediation Technology, New York, NY, USA. 713 p.

- [Pennell *et al.* (1996)] Pennell, K., Pope, G. and Abriola, L.: 1996, Influence of viscous and buoyancy forces on the mobilization of residual tetrachloroethylene during surfactant flushing, *Environmental Science & Technology* **30**, 1328–1335.
- [Perri *et al.* (2012)] Perri, M., Cassiani, G., Gervasio, I., Deiana, R. and Binley, A.: 2012, A saline tracer test monitored via both surface and cross-borehole electrical resistivity tomography: comparison of time-lapse results, *Journal of Applied Geophysics* **79**, 6–16.
- [Persson and Berndtsson (1998)] Persson, M. and Berndtsson, R.: 1998, Texture and electrical conductivity effects on temperature dependency in time domain reflectometry, *Soil Science Society of America Journal* **62**(4), 887–893.
- [Persson and Berndtsson (2002)] Persson, M. and Berndtsson, R.: 2002, Measuring nonaqueous phase liquid saturation in soil using time domain reflectometry, *Water Resources Research* **38**(5), 22.1–22.8.
- [Peters *et al.* (1994)] Peters, R., Enzien, W., Bouillard, J., Frank, J., Srivastava, V., Kilbane, J. and Hayes, T.: 1994, Nonaqueous-Phase Liquids-Contaminated Soil/Groundwater Remediation Using Foams in the In-Situ Remediation, in G. Gee and N. Wing (eds), *Scientific Basis for Current and Future Technologies*, Columbus, Ohio, USA, p. 1067–1087.
- [Philippe *et al.* (2017)] Philippe, N., Davarzani, H., Marcoux, M., Colombano, S., Kaifas, D., Triger, A. and Klein, P.-Y.: 2017, Thermal enhancement of coal tar pumping in saturated porous media, *AquaConSoil: Sustainable Use and Management of Soil, Sediment and Water Resources - 14th International Conference*, Deltares and BRGM, Lyon, France.
- [Pickell *et al.* (1966)] Pickell, J., Swanson, B. and Hickman, W.: 1966, Application of air-mercury and oil-air capillary pressure data in the study of pore structure and fluid distribution, *Society of Petroleum Engineers Journal* **6**(1), 55–61.
- [Pinder and Abriola (1986)] Pinder, G. and Abriola, L.: 1986, On the simulation of nonaqueous phase organic compounds in the subsurface, *Water Resources Research* **22**(9), 109S–119S.
- [Pope *et al.* (1999)] Pope, G., Sepehrnoori, K., Sharma, M., McKinney, D., Speitel, G. and Jackson, R.: 1999, *Three-Dimensional NAPL Fate and Transport Model*, number EPA/600/R-99-011, U.S. Environmental Protection Agency, Cincinnati, OH, USA. 344 p.
- [Poston *et al.* (1970)] Poston, S., Ysrael, S., Hossain, A. and Montgomery III, E.: 1970, The Effect of Temperature on Irreducible Water Saturation and Relative Permeability of Unconsolidated Sands, *Society of Petroleum Engineers* **10**, 171–180.
- [Power *et al.* (2014)] Power, C., Gerhard, J., Karaoulis, M., Tsourlos, P. and Giannopoulos, A.: 2014, Evaluating four-dimensional time-lapse electrical resistivity tomography for monitoring DNAPL source zone remediation, *Journal of Contaminant Hydrology* **162**, 27–46.
- [Power *et al.* (2015)] Power, C., Gerhard, J., Tsourlos, P., Soupios, P., Simyrdanis, K. and Karaoulis, M.: 2015, Improved time-lapse electrical resistivity tomography monitoring of dense non-aqueous phase liquids with surface-to-horizontal borehole arrays, *Journal of applied geophysics* **112**, 1–13.
- [Powers *et al.* (1994b)] Powers, S., Abriola, L., Dunkin, J. and Weber, W.J., J.: 1994b, Phenomenological models for transient NAPL-water mass-transfer processes, *Journal of Contaminant Hydrology* **16**(1), 1–33.
- [Powers *et al.* (1992)] Powers, S., Abriola, L. and Weber, W.: 1992, An experimental investigation of NAPL dissolution in saturated subsurface systems: Steady state mass transfer rates, *Water Resources Research* **28**(10), 2691–2706.
- [Powers *et al.* (1994a)] Powers, S., Abriola, L. and Weber, W.: 1994a, An experimental investigation of nonaqueous phase liquid dissolution in saturated subsurface systems: Steady state mass transfer rates, *Water Resources Research* **30**(2), 321–332.
- [Powers *et al.* (1996)] Powers, S., Anckner, W. and Seacord, T.: 1996, Wettability of NAPL-Contaminated Sands, *Journal of Environmental Engineering* **122**(10), 889–896.

- [Powers *et al.* (1991)] Powers, S., Loureiro, C., Abriola, L. and Weber, W.: 1991, Theoretical study of the significance of nonequilibrium dissolution of nonaqueous phase liquids in subsurface systems, *Water Resources Research* **27**(4), 463–477.
- [Powers and Tamblin (1995)] Powers, S. and Tamblin, M.: 1995, Wettability of porous media after exposure to synthetic gasolines, *Journal of Contaminant Hydrology* **19**, 105–125.
- [Pruess (1991)] Pruess, K.: 1991, *TOUGH2: A general numerical simulator for multiphase fluid and heat flow*, number LBL-29400, Lawrence Berkeley Laboratory, Berkeley, CA, USA. 107 p.
- [Pruess *et al.* (1999)] Pruess, K., Oldenburgh, C. and Moridis, G.: 1999, *TOUGH2 User's Guide, Version 2.0*, number LBNL-43134, Lawrence Berkeley National Laboratory, Berkeley, CA, USA. 198 p.
- [Quintard *et al.* (2001)] Quintard, M., Cherblanc, F. and Whitaker, S.: 2001, Dispersion in Heterogeneous Porous Media: One-Equation Non-equilibrium Model, *Transport in Porous Media* **44**(1), 181–203.
- [Ramli (2014)] Ramli, M.: 2014, *Dynamic Effects on Migration of Light Non-Aqueous Phase Liquids in Subsurface*, PhD thesis, Kyoto University, Kyoto, Japan. 131 p.
- [Ramsburg and Pennell (2001)] Ramsburg, C. and Pennell, K.: 2001, Experimental and economic assessment of two surfactant formulations for source zone remediation at a former dry cleaning facility, **21**(4), 68–82.
- [Ramsburg *et al.* (2005)] Ramsburg, C., Pennell, K., Abriola, L., Daniels, G., Drummond, C., Gamache, M., Hsu, H.-I., Petrovskis, E., Rathfelder, K., Ryder, J. and Yavaraski, T.: 2005, Pilot-scale demonstration of surfactant-enhanced PCE solubilization at the bachman road site. 2. System operation and evaluation, *Environmental Science & Technology* **39**(6), 1791–1801.
- [Ranjan *et al.* (2006)] Ranjan, R., Qian, Y. and Krishnapillai, M.: 2006, Effects of electrokinetics and cationic surfactant cetyltrimethylammonium bromide [CTAB] on the hydrocarbon removal and retention from contaminated soils, *Environmental Technology* **27**(7), 767–776.
- [Rao *et al.* (1997)] Rao, P., Annable, M., Sillan, R., Dai, D., Hatfield, K., Graham, W., Lynn Wood, A. and Enfield, C.: 1997, Field-scale evaluation of in situ cosolvent flushing for enhanced aquifer remediation, *Water Resources Research* **33**, 2673–2686.
- [Ratcliff and Khan (1971)] Ratcliff, G. and Khan, M.: 1971, Prediction of the viscosities of liquid mixtures by a group solution model, *The Canadian Journal of Chemical Engineering* **49**, 125–129.
- [Rathfelder *et al.* (2003)] Rathfelder, K., Abriola, L., Singletary, M. and Pennell, K.: 2003, Influence of surfactant-facilitated interfacial tension reduction on chlorinated solvent migration in porous media: observations and numerical simulation, *Journal of Contaminant Hydrology* **64**(3-4), 227–252.
- [Redman and DeRyck (1994)] Redman, J. and DeRyck, S.: 1994, Monitoring non-aqueous phase liquids in the subsurface with multilevel time domain reflectometry probes, *Proceedings of the Symposium on Time Domain Reflectometry in Environmental, Infrastructure, and Mining Applications*, Spec. Publ. SP, .NTIS PB95-105789, 19-94, U.S. Bur. of Mines, Washington, D.C., USA, p. 207–215.
- [Redman *et al.* (1991)] Redman, J., Kueper, B. and Annan, A.: 1991, Dielectric stratigraphy of a DNAPL spill and implications for detection with ground penetrating radar, *Aquifer Restoration, Ground Water Monitoring and Geophysical Methods, 5th National Outdoor Action Conference*, Natl. Ground Water Assoc., Las Vegas, NV., USA.
- [Reeves and Celia (1996)] Reeves, P. and Celia, M.: 1996, A Functional Relationship Between Capillary Pressure, Saturation, and Interfacial Area as Revealed by a Pore-Scale Network Model, *Water Resources Research* **32**(8), 2345–2358.

- [Reik (1955)] Reik, H.: 1955, The relation between viscosity and vapor pressure in binary mixtures II, *Zeitschrift für Elektrochemie Angewandte Physikalische Chemie* **59**, 126–136.
- [Revil (2012)] Revil, A.: 2012, Spectral induced polarization of shaly sands: influence of the electrical double layer, *Water Resources Research* **48**(2), 1–23.
- [Revil *et al.* (1998)] Revil, A., Cathles, L., Losh, S. and Nunn, J.: 1998, Electrical conductivity in shaly sands with geophysical applications, *Journal of Geophysical Research* **03**(B10), 23.925–23.936.
- [Revil *et al.* (2011)] Revil, A., Schmutz, M. and Batzle, M.: 2011, Influence of oil wettability upon spectral induced polarization of oil-bearing sands, *Geophysics* **76**(5), A31–A36.
- [Reynolds (2011)] Reynolds, J.: 2011, *An Introduction to Applied and Environmental Geophysics*, number 978-0-471-48535-3, 2nd edition edn, Wiley-Blackwell, Chichester, UK. 710 p.
- [Riazi (2005)] Riazi, M.: 2005, *Characterization and properties of petroleum fractions*, astm manual series: mnl50 edn, 1st ed. American Society and Testing Materials, ASTM, 100 Barr Harbor, West Conshohocken, PA, U.S.A.
- [Rios *et al.* (2013)] Rios, L., David, M., Vazquez-Arenas, J. and Anderson, W.: 2013, Use of surfactants and blends to remove DDT from contaminated soils, *The Canadian Journal of Chemical Engineering* **91**(2), 238–244.
- [Árnason *et al.* (2000)] Árnason, K., Karlsdóttir, R., Eysteinnsson, H., Flóvenz, O. and Gudlaugsson, S.: 2000, The resistivity structure of high-temperature geothermal systems in iceland, *Proceedings of the World Geothermal Congress 2000*, Kyushu-Tohoku, Japan, pp. 923–928.
- [Robert *et al.* (2006)] Robert, T., Martel, R., Conrad, S., Lefebvre, R. and Gabriel, U.: 2006, Visualization of TCE recovery mechanisms using surfactant-polymer solutions in a two-dimensional heterogeneous sand model, *Journal of Contaminant Hydrology* **86**(1-2), 3–31.
- [Robinson and Friedman (2001)] Robinson, D. and Friedman, S.: 2001, Effect of particle size distribution on the effective dielectric permittivity of saturated granular media, *Water Resources Research* **37**(1), 33–40.
- [Robinson and Friedman (2002)] Robinson, D. and Friedman, S.: 2002, The effective permittivity of dense packings of glass beads, quartz sand and their mixtures immersed in different dielectric backgrounds, *Journal of Non-Crystalline Solids* **305**, 261–267.
- [Robinson *et al.* (2005)] Robinson, D., Jones, S., Blonquist, J. and Friedman, S.: 2005, A physically derived water content/permittivity calibration model for coarse-textured, layered soils, *Soil Science Society of America Journal* **69**(5), 1372.
- [Rodrigues *et al.* (2017)] Rodrigues, R., Betelu, S., Colombano, S., Masselot, G., Tzedakis, T. and Ignatiadis, I.: 2017, Influence of temperature and surfactants on the solubilization of hexachlorobutadiene and hexachloroethane, *Journal of Chemical & Engineering Data* **62**(10), 3252–3260.
- [Rogers and Stovall (2000)] Rogers, E. and Stovall, I.: 2000, Fundamentals of Chemistry: Solubility, *Department of Chemistry. University of Wisconsin* .
- [Rose and Channapragada (1960)] Rose, W. and Channapragada, R.: 1960, Microscopic aspects of capillary imbibition, in S. of Petroleum Engineers (ed.), *Fall Meeting of the Society of Petroleum Engineers of AIME*, number SPE Paper 1549G, Denver, CO, USA.
- [Rosen and Kunjappu (2012)] Rosen, M. and Kunjappu, J.: 2012, *Surfactants and Interfacial Phenomena*, number 9780470541944, 4th edn, Wiley, New York, NY, USA. 616 p.
- [Rossen (1996)] Rossen, W.: 1996, Foams in enhanced oil recovery, *Surfactant Science Serie* **57**, 413–464.
- [Rossi and Thomas (1981)] Rossi, S. and Thomas, W.: 1981, Solubility behavior of three aromatic hydrocarbons in distilled water and natural seawater, *Environmental Science and Technology* **15**(6), 715–716.

- [Roth *et al.* (1990)] Roth, K., Schulin, R., Fluhler, H. and Attinger, W.: 1990, Calibration of time domain reflectometry for water content measurements using a composite dielectric approach, *Water Resources Research* **26**, 2267–2273.
- [Rothmel *et al.* (1998)] Rothmel, R., Peters, R., St. Martin, E. and Deflaun, M.: 1998, Surfactant foam biodegradation of in situ treatment of TCE DNAPLs, *Environmental Science & Technology* **32**(11), 1667–1675.
- [Rueden *et al.* (2017)] Rueden, C., Schindelin, J., Hiner, M., DeZonia, B., Walter, A., Arena, E. and Eliceiri, K.: 2017, ImageJ2: ImageJ for the next generation of scientific image data, *BMC Bioinformatics* **18**(529), 1–26.
- [Ruffet (1993)] Ruffet, C.: 1993, *La conductivité électrique complexe dans quelques roches crustales*, PhD thesis, Université Louis Pasteur, Strasbourg, France. 229 p.
- [Sabatini *et al.* (1998)] Sabatini, D., Harwell, J., Hasegawa, M. and Knox, R.: 1998, Membrane processes and surfactant-enhanced subsurface remediation: results of a field demonstration, *Journal of Membrane Science* **151**(1), 87–98.
- [Sabatini *et al.* (2000)] Sabatini, D., Knox, R., Harwell, J. and Wu, B.: 2000, Integrated design of surfactant enhanced DNAPL remediation: Efficient supersolubilization and gradient systems, *Journal of Contaminant Hydrology* **45**(1-2), 99–121.
- [Saint-Pierre *et al.* (2004)] Saint-Pierre, C., Martel, R., Gabriel, U., Lefebvre, R., Robert, T. and Hawari, J.: 2004, TCE recovery mechanisms using micellar and alcohol solutions: phase diagrams and sand column experiments, *Journal of Contaminant Hydrology* **71**, 155–192.
- [Sale (2001)] Sale, T.: 2001, Methods for Determining Inputs to Environmental Petroleum Hydrocarbon Mobility and Recovery Models, *Technical Report API PUBLICATION 4711*, American Petroleum Institute, 1220 L Street, Northwest., Washington, DC, USA. 72 p.
- [Sale and Applegate (1997)] Sale, T. and Applegate, D.: 1997, Mobile NAPL recovery: Conceptual, field, and mathematical considerations, *Groundwater* **35**, 418–426.
- [Sale and Kuhn (1988)] Sale, T. and Kuhn, B.: 1988, Recovery of Wood-Treating Oil from an Alluvial Aquifer Using Dual Drainlines, *Petroleum Hydrocarbons and Organic Chemicals in Ground Water: Prevention, Detection, and Restoration*, Vol. 1, Houston, Texas, USA, pp. 419–442.
- [Samouëlian *et al.* (2005)] Samouëlian, A., Cousin, I., Tabbagh, A., Bruand, A. and Richard, G.: 2005, Electrical resistivity survey in soil science: a review, *Soil & Tillage Research* **83**(2), 173–193.
- [Sauck (2000)] Sauck, W.: 2000, A model for the resistivity structure of Inapl plumes and their environs in sandy sediments, *Journal of Applied Geophysics* **44**(2–3), 151–165.
- [Schincariol *et al.* (1993)] Schincariol, R., Herderick, E. and Schwartz, F.: 1993, On the application of image analysis to determine concentration distributions in laboratory experiments, *Journal of Contaminant Hydrology* **12**(3), 197–215.
- [Schincariol and Schwartz (1990)] Schincariol, R. and Schwartz, F.: 1990, An experimental investigation of variable density flow and mixing in homogeneous and heterogeneous media, *Water Resources Research* **26**(10), 2317–2329.
- [Schindelin *et al.* (2012)] Schindelin, J., Arganda-Carreras, I., Frise, E., Kaynig, V., Longair, M., Pietzsch, T., Preibisch, S., Rueden, C., Saalfeld, S., Schmid, B., Tinevez, J.-Y., White, D., Hartenstein, V., Eliceiri, K., Tomancak, P. and Cardona, A.: 2012, Fiji: an open-source platform for biological-image analysis, *Nature methods* **9**(7), 676–682.
- [Schlüter (2008)] Schlüter, M.: 2008, Geometric mappings. http://ij.ms3d.de/geometric_mappings.php
- [Schmidtke *et al.* (1992)] Schmidtke, K., McBean, E. and Rovers, F.: 1992, Evaluation of Collection-Well Parameters for DNAPL, *Journal of Environmental Engineering* **118**(2), 183–195.

- [Schmutz *et al.* (2010)] Schmutz, M., Revil, A., Vaudelet, P., Batzle, M., Femenia Viñao, P. and Werkema, D.: 2010, Influence of oil saturation upon spectral induced polarization of oil-bearing sands, *Geophysical Journal International* **183**, 211–224.
- [Schnaart and Brusseau (2005)] Schnaart, G. and Brusseau, M.: 2005, Pore-Scale Characterization of Organic Immiscible-Liquid Morphology in Natural Porous Media Using Synchrotron X-ray Microtomography, *Environmental Science & Technology* **39**(21), 8403–8410. PMID: 16294880.
- [Schowalter (1979)] Schowalter, T.: 1979, Mechanics of secondary hydrocarbon migration and entrapment, *Am.Assoc.Pet. Geol. Bull.*, **63**(5), 724–760.
- [Schramm (1994)] Schramm, L.: 1994, *Foams: Fundamentals and Applications in the Petroleum Industry*, number 978-0841227194, Advances in chemistry, Washington, DC, USA. 555 p.
- [Schwarzenbach *et al.* (2003)] Schwarzenbach, R., Gschwend, P. and Imboden, D.: 2003, *Environmental Organic Chemistry*, 2nd edition edn, John Wiley & Sons Inc.
- [Schwille (1988)] Schwille, F.: 1988, *Dense Chlorinated Solvents in Porous and Fractured Media - Model Experiments*, number 978-0873711210, Lewis Publishers, Chelsea, MI, USA. 146 p.
- [Seyfried and Grant (2007)] Seyfried, M. and Grant, L.: 2007, Temperature effects on soil dielectric properties measured at 50 mhz, *Vadose Zone Journal* **6**(4), 759–765.
- [She and Sleep (1998)] She, H. and Sleep, B.: 1998, The effect of temperature on capillary pressure-saturation relationships for air-water and perchloroethylene-water systems, *Water Resources Research* **34**(10), 2587–2597.
- [Shen *et al.* (2010)] Shen, P., Zhu, B., Li, X. and Wu, Y.: 2010, An Experimental Study of the Influence of Interfacial Tension on Water–Oil Two-Phase Relative Permeability, *Transport in Porous Media* **85**(2), 505–520.
- [Sheng (2015)] Sheng, J.: 2015, Status of surfactant EOR technology, *Petroleum* **1**, 97–105.
- [Shiau *et al.* (1994)] Shiau, B., Sabatini, D. and Harwell, J.: 1994, Solubilization and Microemulsification of Chlorinated Solvents Using Direct Food Additive (Edible) Surfactants, *Groundwater* **32**(4), 561–569.
- [Shiu *et al.* (1988)] Shiu, W., Maijanen, A., Ng, A. and Mackay, D.: 1988, Preparation of aqueous solutions of sparingly soluble organic substances, II. Multicomponent systems-Hydrocarbon mixtures and petroleum products, *Environmental Toxicology and Chemistry* (7), 125–137.
- [Shu (1984)] Shu, W.: 1984, A viscosity correlation for mixtures of heavy oil, bitumen, and petroleum fractions, *Society of Petroleum Engineers Journal* **24**(3), 277–282.
- [Simunek and van Genuchten (1994)] Simunek, J. and van Genuchten, M.: 1994, *The CHAIN_2D Code for Simulating the Two-Dimensional Movement of Water, Heat and Multiple Solutes in Variably Saturated Porous Media*, number 136, Media. U.S. Salinity Lab Research, Riverside, CA, USA. 232 p.
- [Sinnokrot *et al.* (1971)] Sinnokrot, A., Ramey, H. and Marsden, S.: 1971, Effect of Temperature Level upon Capillary Pressure Curves, *Society of Petroleum Engineers* **11**, 13–22.
- [Skoog *et al.* (2007)] Skoog, D., Holler, F. and Crouch, S.: 2007, *Principles of Instrumental Analysis*, number 978-0495012016, 6th edn, Tomsom Brooks/cole, Belmont, CA, USA. 1056 p.
- [Sleep (2003)] Sleep, B.: 2003, *Modeling Fate and Transport of Chlorinated Organic Compounds in the Subsurface, Chapter 4 in Contaminated Ground Water and Sediment - Modeling for Management and Remediation*, number 978-1-56670-667-4, CRC Press LLC, Boca Raton, FL, USA. 288 p.

- [Sleep and Ma (1997)] Sleep, B. and Ma, Y.: 1997, Thermal variation of organic fluid properties and impact on thermal remediation feasibility, *Journal of Soil Contamination* **6**(3), 281–306.
- [Sleep and McClure (2001)] Sleep, B. and McClure, P.: 2001, The effect of temperature on adsorption of organic compounds to soils, *Canadian Geotechnical Journal* **38**, 46–52.
- [Sleep and Sykes. (1989)] Sleep, B. and Sykes., J.: 1989, Modeling the transport of volatile organics in variably saturated media, *Water Resources Research* **25**(1), 81–92.
- [Sleep and Sykes (1993)] Sleep, B. and Sykes, J.: 1993, Compositional simulation of groundwater contamination by organic compounds. I. Model development and verification, *Water Resources Research* **29**(6), 1697–1708.
- [Smallwood (2012)] Smallwood, I.: 2012, *Handbook of organic solvent properties*, Butterworth-Heinemann, Oxford, UK. 306 p.
- [Soga *et al.* (2004)] Soga, K., Page, J. and Illangasekare, T.: 2004, A review of NAPL source zone remediation efficiency and the mass flux approach, *Journal of Hazardous Materials* **110**(1-3), 13–27.
- [Stephenson (1992)] Stephenson, R.: 1992, Mutual Solubilities: Water-Ketones, Water-Ethers, and Water-Gasoline-Alcohols, *Journal of chemical & engineering data* **37**(1), 80–95.
- [Strbak (2000)] Strbak, L.: 2000, In Situ Flushing with Surfactants and Cosolvents, *Technical report*, U.S. Environmental Protection Agency, Washington, DC, USA. 31 p.
- [Stroo *et al.* (2003)] Stroo, H., Unger, M., Ward, C., Kavanaugh, M., Vogel, C., Leeson, A., Marqusee, J. and Smith, B.: 2003, Peer Reviewed: Remediating Chlorinated Solvent Source Zones, A workshop lists the challenges and research needs, *Environmental Science & Technology* **37**(11), 224A–230A.
- [Stupp and Paus (1999)] Stupp, H. and Paus, L.: 1999, Migrationsverhalten organischer Grundwasser-Inhaltsstoffe und daraus resultierende Ansätze zur Beurteilung von Monitored Natural Attenuation (MNA), *TerraTech* (5).
- [Suchomel *et al.* (2014)] Suchomel, E., Kavanaugh, M., Mercer, J. and Johnson, P.: 2014, *The source zone remediation challenge, Chapter 2 in Chlorinated Solvent Source Zone Remediation*, number 978-1-4614-6921-6, Springer, SERDP ESTCP Environmental Remediation Technology, New York, NY, USA. 713 p.
- [Suchomel *et al.* (2007)] Suchomel, E., Ramsburg, C. and Pennell, K.: 2007, Evaluation of trichloroethene recovery processes in heterogeneous aquifer cells flushed with biodegradable surfactants, *Journal of Contaminant Hydrology* **94**(3-4), 195–214.
- [Sweijen *et al.* (2017)] Sweijen, T., Hamed, A. and Hassanizadeh, S.: 2017, Capillary pressure–saturation relationships for porous granular materials: Pore morphology method vs. pore unit assembly method, *Advances in Water Resources* **107**, 22–31.
- [Szafranski *et al.* (1998)] Szafranski, R., Lawson, J., Hirasaki, G., Miller, C., Akiya, N., King, S., Jackson, R., Meinardus, H. and Londergan, J.: 1998, *Surfactant/foam process for improved efficiency of aquifer remediation, in Structure, Dynamics and Properties of Disperse Colloidal Systems*, Vol. 111, Springer, Berlin, Germany. 162–167.
- [Tadros (2005)] Tadros, T.: 2005, *Applied Surfactants: Principles and Applications*, number 978-3-527-30629-9, John Wiley & Sons, New-York, NY, USA. 654 p.
- [Taylor *et al.* (2001)] Taylor, T., Pennell, K., Abriola, L. and Dane, J.: 2001, Surfactant enhanced recovery of tetrachloroethylene from a porous medium containing low permeability lenses: 1. Experimental studies, *Journal of Contaminant Hydrology* **48**(3–4), 325–350.
- [Telford *et al.* (1990)] Telford, W., Geldart, L. and Sheriff, R.: 1990, *Applied Geophysics*, number 978-0521339384, second edition edn, Cambridge University Press, New-York, NY, USA. 770 p.

- [Tidwell and Glass (1994)] Tidwell, V. and Glass, R.: 1994, X ray and visible light transmission for laboratory measurement of two-dimensional saturation fields in thin-slab systems, *Water Resources Research* **30**(11), 2873–2882.
- [Topp *et al.* (1980)] Topp, G., Davis, J. and Annan, A.: 1980, Electromagnetics determination of soil water content: Measurements in coaxial transmission lines, *Water Resources Research* **16**, 574–582.
- [Torres *et al.* (2012)] Torres, L., Ramos, F., Avila, M. and Ortiz, I.: 2012, Removal of methyl parathion by surfactant-assisted soil washing and subsequent wastewater biological treatment, *Journal of Pesticide Science* **37**(3), 240–246.
- [Travis and Doty (1990)] Travis, C. and Doty, C.: 1990, Can contaminated aquifers at Superfund sites be remediated?, *Environmental Science & Technology* **24**, 1464–1466.
- [Trellu *et al.* (2017)] Trellu, C., Oturan, N., Pechaud, Y., Van Hullebusch, E., Esposito, G. and Oturan, M.: 2017, Anodic oxidation of surfactants and organic compounds entrapped in micelles - selective degradation mechanisms and soil washing solution reuse, *Water Research* **118**, 1–11.
- [Tseng (2011)] Tseng, Q.: 2011, *Etude d'architecture multicellulaire avec le microenvironnement contrôlé*, PhD thesis, Université de Grenoble, France. 214 p.
- [Turin (1990)] Turin, J.: 1990, *VLEACH: A One-Dimensional Finite Difference Vadose Zone Leaching Model*, number USEPA Region 9, CH2M Hill, US Environmental Protection Agency, Redding, CA, USA. 291 p.
- [Twu and Bulls (1981)] Twu, C. and Bulls, J.: 1981, Viscosity blending tested, *Hydrocarbon Process* p. 3–6.
- [Ulrich and Slater (2004)] Ulrich, C. and Slater, L.: 2004, Induced polarization measurements on unsaturated, unconsolidated sands, *Geophysics* **69**(3), 762–771.
- [Unger *et al.* (1995)] Unger, A., Sudicky, E. and Forsyth, P.: 1995, Mechanisms controlling vacuum extraction coupled with air sparging for remediation of heterogeneous formations contaminated by dense nonaqueous phase liquid, *Water Resources Research* **31**(8), 1913–1925.
- [U.S. Army Corps of Engineers (2014)] U.S. Army Corps of Engineers: 2014, Environmental Quality - Design: In situ thermal remediation, *Technical Report EM 200-1-21*, Department of the Army, Washington, DC, USA. 243 p.
- [US EPA (1996a)] US EPA: 1996a, How to effectively recover Free Product at Leaking Underground Storage Tank Sites – A guide for State Regulators, *Technical Report EPA 510-R-96-001*, U.S. Environmental Protection Agency, U.S. Environmental Protection Agency, Solid Waste and Emergency Response, Washington, DC, USA. 162 p.
- [US EPA (1996b)] US EPA: 1996b, Surfactant-Enhanced DNAPL Remediation: Surfactant Selection, Hydraulic Efficiency, and Economic Factors, *Technical Report EPA/600/S-96/002*, U.S. Environmental Protection Agency, National Risk Management, Research Laboratory, Ada, OK, USA. 15 p.
- [US EPA (2000)] US EPA: 2000, Contained Recovery of Oily Wastes (CROW) Process, *Technical Report EPA/540/R-00/500*, U.S. Environmental Protection Agency, U.S. Environmental Protection Agency, Western Research Institute, Washington, DC, USA. 114 p.
- [US EPA (2003)] US EPA: 2003, The DNAPL Remediation Challenge: Is There a Case for Source Depletion?, *Technical Report EPA/600/R-03/143*, U.S. Environmental Protection Agency, U.S. Environmental Protection Agency; National Risk Management Research Laboratory, Office of Research and Development, Cincinnati, OH, USA. 129 p.
- [Van Geel and Roy (2002)] Van Geel, P. and Roy, S.: 2002, A proposed model to include a residual NAPL saturation in a hysteretic capillary pressure-saturation relationship, *Journal of contaminant hydrology* **58**(1-2), 79–110.
- [van Genuchten (1980)] van Genuchten, M.: 1980, A closed-form equation for predicting the hydraulic conductivity of unsaturated soils, *Soil Science Society of America* **44**, 892–898.

- [Villaume (1985)] Villaume, J.: 1985, Investigations at Sites Contaminated with Dense, Non-Aqueous Phase Liquids (NAPLs), *Ground Water Monitoring Review* **5**(2), 60–74.
- [Villaume *et al.* (1983)] Villaume, J., Lowe, P. and Unites, D.: 1983, Recovery of Coal Gasification Wastes: An Innovative Approach, in N. W. W. Association (ed.), *Third National Symposium on Aquifer Restoration and Ground Water Monitoring* ., Worthington, OH, USA, pp. 434–445.
- [Vinegar and Waxman (1984)] Vinegar, H. and Waxman, M.: 1984, Induced polarization of shaly sands, *Geophysics* **49**(8), 1267–1287.
- [Vishnyakov *et al.* (2013)] Vishnyakov, A., Lee, M. and Neimark, A.: 2013, Prediction of the critical micelle concentration of nonionic surfactants by dissipative particle dynamics simulations, *The Journal of Physical Chemistry Letters* **4**(5), 797–802.
- [von Hippel (1954)] von Hippel, A.: 1954, *Dielectric Materials and Applications*, Technology Press of M.I.T. and Wiley, Hoboken, N J, USA. 456 p.
- [Voss (1984)] Voss, C.: 1984, *Saturated-Unsaturated Transport (SUTRA)*, number 84.4369 in *Water Research Investigation*, U.S. Geological Survey, Denver, CO, USA.
- [Wagner *et al.* (1994)] Wagner, J., Chen, H., Brownawell, B. and Westall, J.: 1994, Use of cationic surfactants to modify soil surfaces to promote sorption and retard migration of hydrophobic organic compounds, *Environmental Science & Technology* **28**(2), 231–237.
- [Walther (1931)] Walther, C.: 1931, The evaluation of viscosity data, *Erdöl Teer* **7**, 382–384.
- [Wang and Beckermann (1993)] Wang, C.-Y. and Beckermann, C.: 1993, A two-phase mixture model of liquid-gas flow and heat transfer in capillary porous media—I. Formulation, *International Journal of Heat and Mass Transfer* **36**(11), 2747–2758.
- [Wang *et al.* (2010)] Wang, S., Lee, M., Park, M. and Kim, J.-M.: 2010, Box experiments on monitoring the co2 migration in a homogeneous medium using electrical resistivity survey, *Geosciences Journal* **14**(1), 77–85.
- [Wang and Mulligan (2004)] Wang, S. and Mulligan, C.: 2004, Rhamnolipid foam enhanced remediation of cadmium and nickel contaminated soil, *Water, Air, and Soil Pollution* **157** (1-4), 315–330.
- [Ward and Sill (1982)] Ward, S. and Sill, W.: 1982, *Resistivity, induced polarization, and self-potential methods in geothermal exploration*, number DOE/ID/12079-90; ESL-108, Utah University, Salt Lake City, UT, USA. 105 p.
- [Watson *et al.* (2019)] Watson, F., Maes, J., Geiger, S., Mackay, E., Singleton, M., McGravie, T., Anouilh, T., Jobe, T., Zhang, S., Agar, S., Ishutov, S. and Hasiuk, F.: 2019, Comparison of Flow and Transport Experiments on 3D Printed Micromodels with Direct Numerical Simulations, *Transport in Porous Media* **129**(2), 449–466.
- [Waxman and Smits (1968)] Waxman, M. and Smits, L.: 1968, Electrical conductivities in oil-bearing shaly sands, *Society of Petroleum Engineers Journal* **8**(02), 107–122.
- [Weast (1986)] Weast, R.: 1986, *CRC handbook of chemistry and physics*, 67th edition edn, CRC Press Inc, Boca Raton, FL, USA. 2424 p.
- [Werth *et al.* (2010)] Werth, C., Zhang, C., Brusseau, M., Oostrom, M. and Baumann, T.: 2010, A review of non-invasive imaging methods and applications in contaminant hydrogeology research, *Journal of Contaminant Hydrology* **113**(1-4), 1–24.
- [Whitaker (1999)] Whitaker, S.: 1999, *The Method of Volume Averaging*, Vol. 13 of *Theory and Applications of Transport in Porous Media*, 1st edn, Kluwer Academic Publishers, Dordrecht, The Netherlands. 210 p.
- [White and Oostrom (1996)] White, M. and Oostrom, M.: 1996, *STOMP Subsurface Transport over Multiple Phases: User's Guide*, number PNNL-11216 (UC-2010), Pacific Northwest National Laboratory, Richland, WA, USA. 221 p.

- [Willhite (1986)] Willhite, G.: 1986, *Waterflooding*, number 978-1-55563-005-8, The Society of Petroleum Engineers, Richardson, TX, USA. 326 p.
- [Williams and Wilder (1971)] Williams, D. and Wilder, D.: 1971, Gasoline pollution of a ground-water reservoir – A case history, *Groundwater* **9**, 50–54.
- [Williamson (2014)] Williamson, D.: 2014, *Combined remedies, Chapter 15 in Chlorinated Solvent Source Zone Remediation*, number 978-1-4614-6921-6, Springer, SERDP ESTCP Environmental Remediation Technology, New York, NY, USA. 713 p.
- [Wilson (1988)] Wilson, A.: 1988, What color is color ?, *The Electronic System Design Magazine* **January**, 38–44.
- [Wilson *et al.* (1990)] Wilson, J., Conrad, S., Mason, W., Peplinski, W. and Hagan, E.: 1990, *Laboratory investigation of residual liquid organics from spills, leaks, and the disposal of hazardous wastes in groundwater*, number 600/6-90/004, US Environmental Protection Agency, Ada, OK, USA. 287 p.
- [Wisniewski *et al.* (1985)] Wisniewski, G., Lennon, G., Villaume, J. and Young, C.: 1985, Response of a Dense Fluid Under Pumping Stress, in L. University (ed.), *Proceedings of the 17th Mid-Atlantic Industrial Waste Conference*, Lehigh University, Bethlehem, PA, USA, pp. 226–237.
- [Wraith and Or (1998)] Wraith, J. and Or, D.: 1998, Nonlinear parameter estimation using spreadsheet software, *Journal of Natural Resources and Life Sciences Education* **27**, 13–19.
- [Wright *et al.* (1992)] Wright, D., Sandler, S. and DeVoll, D.: 1992, Infinite dilution activity coefficients and solubilities of halogenated hydrocarbons in water at ambient temperatures, *Environmental Science & Technology* **26**(9), 1828–1831.
- [Yaws (2015)] Yaws, C.: 2015, *The Yaws Handbook of Physical Properties for Hydrocarbons and Chemicals*, 2nd edn, Gulf Professional Publishing - Elsevier, Houston, Tex., USA. 832 p.
- [Yeh *et al.* (1998)] Yeh, G., Salvage, K., Gwo, J., Zachara, J. and Szecsody, J.: 1998, *HYDROBIOGEOCHEM: A Coupled Model of Hydrologic Transport and Mixed Biogeochemical Kinetic/Equilibrium reactions in Saturated-Unsaturated*, number ORNL/TM-13668, Oak Ridge National Laboratory, Oak Ridge, TN, USA. 311 p.
- [Yuan and Lee (2013)] Yuan, Y. and Lee, T.: 2013, *Contact Angle and Wetting Properties, Chapter 1 in Surface Science Techniques*, number 978-3-642-34242-4, Springer, New York, NY, USA. 663 p.
- [Zhang *et al.* (2007)] Zhang, C., Werth, C. and Webb, A.: 2007, Characterization of NAPL source zone architecture and dissolution kinetics in heterogeneous porous media using magnetic resonance imaging, *Environmental Science & Technology* **41**(10), 3672–3678.
- [Zhang *et al.* (2011)] Zhang, M., He, F., Zhao, D. and Hao, X.: 2011, Degradation of soil-sorbed trichloroethylene by stabilized zero valent iron nanoparticles: Effects of sorption, surfactants, and natural organic matter, *Water Research* **45**(7), 2401–2414.
- [Zhang and Miller (1992)] Zhang, Y. and Miller, R.: 1992, Enhanced octadecane dispersion and biodegradation by a pseudomonas rhamnolipid surfactant (biosurfactant), *Applied and Environmental Microbiology* **58**(10), 3276–3282.
- [Zhao *et al.* (2006)] Zhao, B., Zhu, L. and Yang, K.: 2006, Solubilization of DNAPLs by mixed surfactant: Reduction in partitioning losses of nonionic surfactant, *Chemosphere* **62**(5), 772–779.
- [Zheng *et al.* (2012)] Zheng, G., Selvam, A. and Wong, J.: 2012, Enhanced solubilization and desorption of organochlorine pesticides (OCPs) from soil by oil-swollen micelles formed with a nonionic surfactant, *Environmental Science & Technology* **46**(21), 12062–12068.
- [Zhong *et al.* (2003)] Zhong, L., Mayer, A. and Pope, G.: 2003, The effects of surfactant formulation on nonequilibrium NAPL solubilization, *Journal of Contaminant Hydrology* **60** (1-2), 55–75.

- [Zytner *et al.* (1989)] Zytner, R., Biswas, N. and Bewtra, J.: 1989, PCE volatilized from stagnant water and soil, *Journal of Environmental Engineering* **115**(6), 1199–1212.
- [Zytner *et al.* (1993)] Zytner, R., Biswas, N. and Bewtra, J.: 1993, Retention capacity of dry soils for NAPLS, *Environmental Technology* **14**, 1073–1080.
- [Zyvoloski *et al.* (1995)] Zyvoloski, G., Robinson, B., Dash, Z. and Trease, L.: 1995, *User's Guide for FEHMN - Application. Report*, number LA-UR-94-3788, Rev. 1, Los Alamos National Laboratory, Los Alamos, NM, USA. 127 p.

Appendices

Appendix 1

Characterization of the DNAPL without enhancement and with chemical/thermal enhancements

Appendix 1.1**Variation of DNAPL dynamic viscosities as a function of temperature**

Temperature (°C)	Dynamic viscosity (mPa.s)				
	Test1	Test2	Test3	Average	Standard deviation
10.00	5.20	5.40	5.90	5.50	0.36
15.00	4.80	4.90	5.10	4.93	0.15
20.00	4.60	4.50	4.30	4.47	0.15
30.00	3.70	3.70	3.80	3.73	0.06
45.00	2.80	2.80	2.90	2.83	0.06
60.00	2.42	2.36	2.24	2.34	0.09

Appendix 1.2

DNAPL-water interfacial tension with chemical enhancement

Tests	Interfacial tension (mN.m-1)												
Triton X-100													
	CMC/8	CMC/4	CMC/2	CMC	CMC× 2	CMC×4	CMC× 8	CMC× 16	CMC× 32	CMC× 64			
Test 1	9.01	8.21	7.44	6.53	5.75	4.62	3.15	1.96	0.38	0.38			
Test 2	9.17	8.50	7.21	6.28	5.48	4.50	3.26	1.73	0.77	0.50			
Test 3	9.23	8.47	7.18	6.49	5.36	4.28	2.89	2.00	0.56	0.56			
Average	9.14	8.39	7.28	6.43	5.53	4.47	3.10	1.89	0.57	0.48			
Stand. deviat.	0.09	0.13	0.12	0.11	0.16	0.14	0.16	0.12	0.16	0.09			
Tween 80													
	CMC/8	CMC/4	CMC/2	CMC	CMC× 2	CMC×4	CMC× 8	CMC× 16	CMC× 32	CMC× 64			
Test 1	9.69	9.53	9.45	9.24	9.38	9.23	8.73	7.52	6.42	5.3			
Test 2	9.91	9.61	9.26	9.33	9.21	9.04	8.65	7.33	6.32	5.15			
Test 3	9.83	9.33	9.46	9.41	9.24	9.13	8.52	7.50	6.26	5.39			
Average	9.81	9.49	9.39	9.33	9.28	9.13	8.64	7.45	6.33	5.28			
Stand. deviat.	0.09	0.12	0.09	0.07	0.08	0.08	0.09	0.09	0.06	0.12			
Aerosol MA-80													
	CMC/6	CMC/4	CMC/2	CMC/ 1,5	CMC	CMC× 1,5	CMC× 3	CMC×4	CMC×6	CMC×8	CMC× 16	CMC× 32	CMC× 64
Test 1	10.14	10.01	9.69	9.53	9.18	9.09	8.22	8.11	6.88	6.13	3.34	1.63	1.15
Test 2	10.05	9.96	9.72	9.37	9.07	9.18	8.40	7.95	6.96	6.16	3.21	1.53	1.05
Test 3	10.26	9.74	9.53	9.51	9.13	8.99	8.30	8.06	7.04	6.00	3.40	1.70	1.09
Average	10.15	9.90	9.65	9.47	9.12	9.09	8.31	8.04	6.96	6.10	3.32	1.62	1.10
Stand. deviat.	0.08	0.12	0.09	0.07	0.05	0.08	0.07	0.07	0.06	0.07	0.08	0.07	0.05
SDBS													
	CMC/ 128	CMC/ 64	CMC/ 32	CMC/ 16	CMC/ 8	CMC/4	CMC/2	CMC					
Test 1	7.87	6.20	4.08	1.10	0.60	0.45	0.19	0.06					
Test 2	7.61	6.34	4.12	0.89	0.60	0.34	0.09	0.08					
Test 3	7.58	6.48	3.86	1.15	0.48	0.41	0.11	0.16					
Average	7.69	6.34	4.02	1.05	0.56	0.40	0.13	0.10					
Stand. deviat.	0.13	0.12	0.12	0.11	0.06	0.05	0.04	0.04					

Appendix 1.3**DNAPL-water interfacial tension with thermal enhancement**

Temperature (°C)	Interfacial tension (mN.m ⁻¹)				
	Test1	Test2	Test3	Average	Standard deviation
10.00	12.11	12.23	12.18	12.17	0.06
15.00	11.22	11.11	11.13	11.15	0.06
20.00	10.99	10.90	11.00	10.96	0.05
30.00	11.10	11.27	11.30	11.22	0.11
45.00	12.29	12.12	12.10	12.17	0.10
60.00	11.94	11.88	11.85	11.89	0.05

Appendix 1.4
Contact angle DNAPL/water/glass with chemical enhancement

Tests	Contact angle (°)													
Triton X-100														
	CMC /8	CMC/ 4	CMC/ 2	CMC	CMC ×2	CMC ×4	CMC× 8	CMC× 16	CMC× 32	CMC× 64				
Test 1	125.00	126.50	121.20	120.80	124.00	121.00	122.00	117.50	112.00	111.50				
Test 2	130.00	123.00	124.20	124.00	123.30	127.00	125.00	114.80	115.50	111.60				
Test 3	132.00	124.20	126.80	122.00	120.50	123.50	119.00	113.60	113.20	115.00				
Average	129.00	124.57	124.07	122.27	122.60	123.83	122.00	115.30	113.57	112.70				
Stand. deviat.	3.61	1.78	2.80	1.62	1.85	3.01	3.00	2.00	1.78	1.99				
Tween 80														
	CMC /8	CMC/ 4	CMC/ 2	CMC	CMC ×2	CMC ×4	CMC× 8	CMC× 16	CMC× 32	CMC× 64				
Test 1	127.50	126.00	124.00	127.50	122.00	122.00	127.00	124.00	116.00	113.50				
Test 2	129.00	127.00	126.00	124.00	125.00	125.50	121.00	118.00	113.00	111.50				
Test 3	128.00	129.00	128.50	128.00	127.00	126.00	125.00	121.00	118.00	115.50				
Average	128.17	127.33	126.17	126.50	124.67	124.50	124.33	121.00	115.67	113.50				
Stand. deviat.	0.76	1.53	2.25	2.18	2.52	2.18	3.06	3.00	2.52	2.00				
Aerosol MA-80														
	CMC /8	CMC/ 6	CMC/ 4	CMC/ 2	CMC/ 1,5	CMC	CMC× 1,5	CMC× 3	CMC× 4	CMC× 6	CMC ×8	CMC× 16	CMC× 32	CMC× 64
Test 1	114.00	111.00	108.00	109.00	114.00	113.00	105.00	106.00	105.00	100.00	96.00	90.00	88.00	87.00
Test 2	120.00	117.00	116.00	118.00	115.00	105.00	112.00	104.00	109.00	98.00	90.00	89.00	90.00	89.00
Test 3	118.00	120.00	118.00	113.00	111.00	110.00	109.00	109.00	102.00	101.00	98.00	95.00	89.00	88.00
Average	117.33	116.00	114.00	113.33	113.33	109.33	108.67	106.33	105.33	99.67	94.67	91.33	89.00	88.00
Stand. deviat.	3.06	4.58	5.29	4.51	2.08	4.04	3.51	2.52	3.51	1.53	4.16	3.21	1.00	1.00
SDBS														
	CMC / 128	CMC/ 64	CMC/ 32	CMC/ 16	CMC/ 8	CMC/ 4								
Test 1	118.00	121.00	120.50	95.00	31.00	32.00								
Test 2	123.00	116.00	118.00	90.00	34.00	31.00								
Test 3	120.00	118.00	121.00	92.00	28.00	28.00								
Average	120.33	118.33	119.83	92.33	31.00	30.33								
Stand. deviat.	2.52	2.52	1.61	2.52	3.00	2.08								

Appendix 1.5**Contact angle DNAPL/water/glass with thermal enhancement**

Temperature (°C)	Contact angle (°)				
	Test1	Test2	Test3	Average	Standard deviation
10.00	131.00	122.00	126.00	126.33	4.51
20.00	124.00	116.00	118.00	119.33	4.16
30.00	115.00	119.00	110.00	114.67	4.51
40.00	113.00	108.00	106.00	109.00	3.61
50.00	108.00	110.00	105.00	107.67	2.52
60.00	105.00	111.00	108.00	108.00	3.00

Appendix 1.6
Contact angle DNAPL/water/glass beads with chemical enhancement

Tests	Contact angle (°)													
Triton X-100														
	CMC /8	CMC/ 4	CMC/ 2	CMC	CMC ×2	CMC ×4	CMC ×8	CMC× 16	CMC× 32	CMC× 64				
Test 1	130.00	127.00	124.00	128.10	128.00	130.50	129.50	122.00	120.10	118.50				
Test 2	133.00	132.00	125.00	126.00	129.00	125.40	123.50	121.00	122.20	122.00				
Test 3	135.00	125.00	130.00	127.80	124.50	128.80	126.60	118.00	118.40	118.00				
Average	132.67	128.00	126.33	127.30	127.17	128.23	126.53	120.33	120.23	119.50				
Stand. deviat.	2.52	3.61	3.21	1.14	2.36	2.60	3.00	2.08	1.90	2.18				
Tween 80														
	CMC /8	CMC/ 4	CMC/ 2	CMC	CMC ×2	CMC ×4	CMC ×8	CMC× 16	CMC× 32	CMC× 64				
Test 1	135.00	130.50	128.00	128.50	131.00	130.00	128.00	127.50	124.00	122.00				
Test 2	130.00	132.00	125.00	129.00	130.00	128.00	125.50	125.00	122.00	118.50				
Test 3	133.00	128.00	130.00	128.00	128.50	131.00	130.50	124.00	126.00	126.00				
Average	132.67	130.17	127.67	128.50	129.83	129.67	128.00	125.50	124.00	122.17				
Stand. deviat.	2.52	2.02	2.52	0.50	1.26	1.53	2.50	1.80	2.00	3.75				
Aerosol MA-80														
	CMC 8	CMC/ 6	CMC/ 4	CMC/ 2	CMC/ 1,5	CMC	CMC ×1,5	CMC× 3	CMC× 4	CMC× 6	CMC ×8	CMC× 16	CMC× 32	CMC× 64
Test 1	139.00	128.00	125.00	122.00	122.00	115.00	112.00	112.00	110.00	112.50	116.00	112.00	100.00	97.00
Test 2	130.00	131.00	132.00	132.00	115.00	118.00	114.00	118.00	115.00	116.80	110.00	108.00	105.00	105.00
Test 3	129.00	126.00	126.00	124.00	119.00	122.00	120.00	111.00	113.50	110.50	109.00	111.00	99.00	97.50
Average	132.67	128.33	127.67	126.00	118.67	118.33	115.33	113.67	112.83	113.27	111.67	110.33	101.33	99.83
Stand. deviat.	5.51	2.52	3.79	5.29	3.51	3.51	4.16	3.79	2.57	3.22	3.79	2.08	3.21	4.48
SDBS														
	CMC /128	CMC/ 64	CMC/ 32	CMC/ 16	CMC/ 8	CMC/ 4	CMC/ 2							
Test 1	129.00	126.00	126.00	110.00	83.00	81.00	78.00							
Test 2	123.00	122.00	122.50	102.00	86.00	80.00	75.00							
Test 3	125.50	128.00	128.00	106.00	80.00	82.00	72.00							
Average	125.83	125.33	125.50	106.00	83.00	81.00	75.00							
Stand. deviat.	3.01	3.06	2.78	4.00	3.00	1.00	3.00							

Appendix 1.7**Contact angle DNAPL/water/glass beads with thermal enhancement**

Temperature (°C)	Contact angle (°)				
	Test1	Test2	Test3	Average	Standard deviation
10.00	130.00	135.00	139.00	134.67	4.51
15.00	134.00	130.00	128.00	130.67	3.06
20.00	124.00	116.00	120.00	120.00	4.00
30.00	117.00	120.00	113.00	116.67	3.51
45.00	110.00	116.00	107.00	111.00	4.58
60.00	108.00	110.00	104.00	107.33	3.06

Appendix 1.8
DNAPL density with thermal enhancement

Temperature (°C)	Density (kg.m ⁻³)				
	Test1	Test2	Test3	Average	Standard deviation
10.00	1670.00	1679.00	1676.00	1675.00	4.58
15.00	1662.00	1670.00	1668.00	1666.67	4.16
20.00	1654.00	1664.00	1661.00	1659.67	5.13
30.00	1639.00	1653.00	1646.00	1646.00	7.00
45.00	1626.00	1630.00	1627.00	1627.67	2.08
60.00	1620.50	1630.00	1620.00	1623.50	5.63

Appendix 1.9
Concentrations of COCs with chemical enhancement

Appendix 1

Nom de l'échantillon	Unité	111TCETHANE	BENZENE	CLM4	120C3PROPANE+20C3PROPENE1	TRICHLOROETHYLENE	1127CETHANE-INC	120C4BUTANE	PERCHLOROETHYLENE	11127CETHANE+CBENZENE	1127CETHANE-INC	122C3PROPANE	130C6BENZENE-EDA	140C6BENZENE	120C6BENZENE	HCETHANE	124C6BENZENE	1237C6BENZENE	HCBUTADIENE13	Somme des POC quantifiés	Somme estimée des POC
SDBS concentration 1 (a)	mg/l	0.04	<0.03	0.12	<0.03	0.1	<0.03	<0.03	0.67	0.04	<0.1	<0.1	<0.1	<0.1	<0.1	0.1	<0.1	<0.1	0.1	1.1	1.6
SDBS concentration 1 (b)	mg/l	0.03	<0.03	0.11	<0.03	0.09	<0.03	<0.03	0.74	0.04	<0.1	<0.1	<0.1	<0.1	<0.1	0.2	<0.1	<0.1	0.2	1.3	1.8
SDBS concentration 1 (c)	mg/l	0.03	<0.03	0.08	<0.03	0.08	<0.03	<0.03	0.57	0.04	<0.1	<0.1	<0.1	<0.1	<0.1	0.1	<0.1	<0.1	0.1	1	1.5
Moyenne		0.03333333	#DIV/0!	0.10333333	#DIV/0!	0.09	#DIV/0!	#DIV/0!	0.66	0.04	#DIV/0!	#DIV/0!	#DIV/0!	#DIV/0!	#DIV/0!	0.13333333	#DIV/0!	#DIV/0!	0.13333333	1.13333333	1.63333333
Facteur dilution	25																				
Moyenne (mg/L)		0.83333333	#DIV/0!	2.58333333	#DIV/0!	2.25	#DIV/0!	#DIV/0!	16.5	1	#DIV/0!	#DIV/0!	#DIV/0!	#DIV/0!	#DIV/0!	3.33333333	#DIV/0!	#DIV/0!	3.33333333	28.33333333	40.83333333
Ecart-type		0.14433757	#DIV/0!	0.5204165	#DIV/0!	0.25	#DIV/0!	#DIV/0!	2.13600094	0	#DIV/0!	#DIV/0!	#DIV/0!	#DIV/0!	#DIV/0!	1.44337567	#DIV/0!	#DIV/0!	1.44337567	3.81881308	3.81881308
SDBS concentration 2 (a)	mg/l	<0.03	<0.03	0.08	<0.03	0.07	<0.03	<0.03	0.68	0.04	<0.1	<0.1	<0.1	<0.1	<0.1	0.2	<0.1	<0.1	0.3	1.4	1.9
SDBS concentration 2 (b)	mg/l	0.03	<0.03	0.09	<0.03	0.07	<0.03	<0.03	0.61	0.03	<0.1	<0.1	<0.1	<0.1	<0.1	0.2	<0.1	<0.1	0.5	1.5	2
SDBS concentration 2 (c)	mg/l	0.04	<0.03	0.12	<0.03	0.1	<0.03	<0.03	0.73	0.04	<0.1	<0.1	<0.1	<0.1	<0.1	0.2	<0.1	<0.1	0.2	1.3	1.8
Moyenne		0.035	#DIV/0!	0.09666667	#DIV/0!	0.08	#DIV/0!	#DIV/0!	0.67333333	0.03666667	#DIV/0!	#DIV/0!	#DIV/0!	#DIV/0!	#DIV/0!	0.2	#DIV/0!	#DIV/0!	0.33333333	1.4	1.9
Facteur dilution	25																				
Moyenne (mg/L)		0.875	#DIV/0!	2.41666667	#DIV/0!	2	#DIV/0!	#DIV/0!	16.83333333	0.91666667	#DIV/0!	#DIV/0!	#DIV/0!	#DIV/0!	#DIV/0!	5	#DIV/0!	#DIV/0!	8.33333333	35	47.5
Ecart-type		0.1767767	#DIV/0!	0.5204165	#DIV/0!	0.4330127	#DIV/0!	#DIV/0!	1.50692844	0.14433757	#DIV/0!	#DIV/0!	#DIV/0!	#DIV/0!	#DIV/0!	8.4984E-16	#DIV/0!	#DIV/0!	3.81881308	2.5	2.5
SDBS concentration 3 (a)	mg/l	<0.03	<0.03	<0.03	<0.03	<0.03	<0.03	<0.03	0.13	<0.03	<0.1	<0.1	<0.1	<0.1	<0.1	<0.1	<0.1	<0.1	0.1	<0.4	0.8
SDBS concentration 3 (b)	mg/l	<0.03	<0.03	0.05	<0.03	0.04	<0.03	<0.03	0.25	<0.03	<0.1	<0.1	<0.1	<0.1	<0.1	0.1	<0.1	<0.1	0.2	0.7	1.2
SDBS concentration 3 (c)	mg/l	<0.03	<0.03	0.05	<0.03	0.05	<0.03	<0.03	0.24	<0.03	<0.1	<0.1	<0.1	<0.1	<0.1	0.1	<0.1	<0.1	0.2	0.7	1.2
Moyenne		#DIV/0!	#DIV/0!	0.05	#DIV/0!	0.045	#DIV/0!	#DIV/0!	0.20666667	#DIV/0!	#DIV/0!	#DIV/0!	#DIV/0!	#DIV/0!	#DIV/0!	0.1	#DIV/0!	#DIV/0!	0.16666667	0.46666667	1.06666667
Facteur dilution	50																				
Moyenne (mg/L)		#DIV/0!	#DIV/0!	2.5	#DIV/0!	2.25	#DIV/0!	#DIV/0!	10.33333333	#DIV/0!	#DIV/0!	#DIV/0!	#DIV/0!	#DIV/0!	#DIV/0!	5	#DIV/0!	#DIV/0!	8.33333333	23.33333333	53.33333333
Ecart-type		#DIV/0!	#DIV/0!	0	#DIV/0!	0.35355339	#DIV/0!	#DIV/0!	3.32916406	#DIV/0!	#DIV/0!	#DIV/0!	#DIV/0!	#DIV/0!	#DIV/0!	0	#DIV/0!	#DIV/0!	2.88675135	5	11.5470054
SDBS concentration 4 (a)	mg/l	<0.03	<0.03	0.05	<0.03	0.05	<0.03	<0.03	0.21	<0.03	<0.1	<0.1	<0.1	<0.1	<0.1	<0.1	<0.1	<0.1	0.1	0.5	1
SDBS concentration 4 (b)	mg/l	<0.03	<0.03	0.05	<0.03	0.05	<0.03	<0.03	0.27	<0.03	<0.1	<0.1	<0.1	<0.1	<0.1	0.1	<0.1	<0.1	0.1	0.7	1.2
SDBS concentration 4 (c)	mg/l	<0.03	<0.03	0.05	<0.03	0.04	<0.03	<0.03	0.3	<0.03	<0.1	<0.1	<0.1	<0.1	<0.1	0.1	<0.1	<0.1	0.1	0.6	1.1
Moyenne		#DIV/0!	#DIV/0!	0.05333333	#DIV/0!	0.04666667	#DIV/0!	#DIV/0!	0.26	#DIV/0!	#DIV/0!	#DIV/0!	#DIV/0!	#DIV/0!	#DIV/0!	0.26	#DIV/0!	#DIV/0!	0.1	0.6	1.1
Facteur dilution	50																				
Moyenne (mg/L)		#DIV/0!	#DIV/0!	2.66666667	#DIV/0!	2.33333333	#DIV/0!	#DIV/0!	13	#DIV/0!	#DIV/0!	#DIV/0!	#DIV/0!	#DIV/0!	#DIV/0!	5	#DIV/0!	#DIV/0!	5	30	55
Ecart-type		#DIV/0!	#DIV/0!	0.28867513	#DIV/0!	0.28867513	#DIV/0!	#DIV/0!	2.29128785	#DIV/0!	#DIV/0!	#DIV/0!	#DIV/0!	#DIV/0!	#DIV/0!	0	#DIV/0!	#DIV/0!	8.4984E-16	5	5

Appendix 1

Nom de l'échantillon	Unité	111TCETHANE	BENZENE	CLM4	12DCPROPANE+2DCPROPENE1	TRICHLOROETHYLENE	112TCETHANE+1NC	12DCBUTANE	PERCHLOROETHYLENE	1112TCETHANE+CBENZENE	1122TCETHANE+1NC	123TOPROPANE	13DCBENZENE+EDIA	14DCBENZENE	12DCBENZENE	HCETHANE	124TCBENZENE	123TCBENZENE	HCBUTADIENE13	Somme des POC quantifiés	Somme estimée des POC
TX-100 concentration 1 (a)	mg/l	0.05	<0.03	0.12	<0.03	0.14	<0.03	<0.03	1.37	0.06	<0.1	<0.1	<0.1	<0.1	<0.1	1.1	<0.1	<0.1	10.2	13	13.5
TX-100 concentration 1 (b)	mg/l	0.06	<0.03	0.15	<0.03	0.09	<0.03	<0.03	1.53	0.06	<0.1	<0.1	<0.1	<0.1	<0.1	1.1	<0.1	<0.1	10.8	13.8	14.3
TX-100 concentration 1 (c)	mg/l	<0.03	<0.03	0.08	<0.03	0.03	<0.03	<0.03	0.15	0.04	<0.1	<0.1	<0.1	<0.1	<0.1	0.1	<0.1	<0.1	3.8	4.1	4.6
Moyenne		0.055	#DIV/0!	0.11666667	#DIV/0!	0.085	#DIV/0!	#DIV/0!	1.01666667	0.06	#DIV/0!	#DIV/0!	#DIV/0!	#DIV/0!	#DIV/0!	1.1	#DIV/0!	#DIV/0!	8.26666667	10.3	10.8
Facteur dilution	25																				
Moyenne (mg/L)		1.375	#DIV/0!	2.91666667	#DIV/0!	2.125	#DIV/0!	#DIV/0!	25.4166667	1.5	#DIV/0!	#DIV/0!	#DIV/0!	#DIV/0!	#DIV/0!	27.5	#DIV/0!	#DIV/0!	206.666667	257.5	270
Ecart-type		0.1767767	#DIV/0!	0.87797115	#DIV/0!	1.94454365	#DIV/0!	#DIV/0!	18.8701705	0	#DIV/0!	#DIV/0!	#DIV/0!	#DIV/0!	#DIV/0!	0	#DIV/0!	#DIV/0!	96.9965635	134.605906	134.605906
TX-100 concentration 2 (a)	mg/l	0.06	<0.03	0.24	<0.03	0.16	<0.03	<0.03	2.26	0.07	<0.1	<0.1	<0.1	<0.1	<0.1	2.1	<0.1	<0.1	19.2	24.2	24.7
TX-100 concentration 2 (b)	mg/l	0.07	<0.03	0.27	<0.03	0.17	<0.03	<0.03	2.51	0.07	<0.1	<0.1	<0.1	<0.1	<0.1	2.2	<0.1	<0.1	20.1	25.5	26
TX-100 concentration 2 (c)	mg/l	0.07	<0.03	0.27	<0.03	0.18	<0.03	<0.03	2.54	0.07	<0.1	<0.1	<0.1	<0.1	<0.1	2.3	<0.1	<0.1	21.3	26.8	27.3
Moyenne		0.06666667	#DIV/0!	0.26	#DIV/0!	0.17	#DIV/0!	#DIV/0!	2.43666667	0.07	#DIV/0!	#DIV/0!	#DIV/0!	#DIV/0!	#DIV/0!	2.2	#DIV/0!	#DIV/0!	20.2	25.5	26
Facteur dilution	25																				
Moyenne (mg/L)		1.66666667	#DIV/0!	6.5	#DIV/0!	4.25	#DIV/0!	#DIV/0!	60.9166667	1.75	#DIV/0!	#DIV/0!	#DIV/0!	#DIV/0!	#DIV/0!	55	#DIV/0!	#DIV/0!	505	637.5	650
Ecart-type		0.14433757	#DIV/0!	0.4330127	#DIV/0!	0.25	#DIV/0!	#DIV/0!	3.84328419	0	#DIV/0!	#DIV/0!	#DIV/0!	#DIV/0!	#DIV/0!	2.5	#DIV/0!	#DIV/0!	26.3391344	32.5	32.5
TX-100 concentration 3 (a)	mg/l	0.03	<0.03	0.13	<0.03	0.09	<0.03	<0.03	1.25	0.04	<0.1	<0.1	<0.1	<0.1	<0.1	1.2	<0.1	<0.1	14.7	17.4	17.9
TX-100 concentration 3 (b)	mg/l	0.04	<0.03	0.14	<0.03	0.09	<0.03	<0.03	1.32	0.04	<0.1	<0.1	<0.1	<0.1	<0.1	1.3	<0.1	<0.1	14.6	17.4	17.9
TX-100 concentration 3 (c)	mg/l	0.03	<0.03	0.12	<0.03	0.09	<0.03	<0.03	1.2	0.04	<0.1	<0.1	<0.1	<0.1	<0.1	1.2	<0.1	<0.1	13	15.6	16.1
Moyenne		0.03333333	#DIV/0!	0.13	#DIV/0!	0.09	#DIV/0!	#DIV/0!	1.25666667	0.04	#DIV/0!	#DIV/0!	#DIV/0!	#DIV/0!	#DIV/0!	1.23333333	#DIV/0!	#DIV/0!	14.1	17.3	17.3
Facteur dilution	50																				
Moyenne (mg/L)		1.66666667	#DIV/0!	6.5	#DIV/0!	4.5	#DIV/0!	#DIV/0!	62.8333333	2	#DIV/0!	#DIV/0!	#DIV/0!	#DIV/0!	#DIV/0!	61.6666667	#DIV/0!	#DIV/0!	705	23.3333333	865
Ecart-type		0.28867513	#DIV/0!	0.5	#DIV/0!	8.4984E-16	#DIV/0!	#DIV/0!	3.01385689	0	#DIV/0!	#DIV/0!	#DIV/0!	#DIV/0!	#DIV/0!	2.88675135	#DIV/0!	#DIV/0!	47.6969601	-	51.9615242
TX-100 concentration 4 (a)	mg/l	0.04	<0.03	0.13	<0.03	0.08	<0.03	<0.03	1.15	0.04	<0.1	<0.1	<0.1	<0.1	<0.1	1.1	<0.1	<0.1	12.1	14.6	15.1
TX-100 concentration 4 (b)	mg/l	0.04	<0.03	0.15	<0.03	0.1	<0.03	<0.03	1.44	0.04	<0.1	<0.1	<0.1	<0.1	<0.1	1.4	<0.1	<0.1	14.4	17.5	18
TX-100 concentration 4 (c)	mg/l	0.03	<0.03	0.13	<0.03	0.08	<0.03	<0.03	1.17	0.03	<0.1	<0.1	<0.1	<0.1	<0.1	1.1	<0.1	<0.1	12.4	14.9	15.4
Moyenne		0.03666667	#DIV/0!	0.13666667	#DIV/0!	0.08666667	#DIV/0!	#DIV/0!	1.25333333	0.03666667	#DIV/0!	#DIV/0!	#DIV/0!	#DIV/0!	#DIV/0!	1.2	#DIV/0!	#DIV/0!	12.9666667	15.6666667	16.1666667
Facteur dilution	50																				
Moyenne (mg/L)		1.83333333	#DIV/0!	6.83333333	#DIV/0!	4.33333333	#DIV/0!	#DIV/0!	62.6666667	1.83333333	#DIV/0!	#DIV/0!	#DIV/0!	#DIV/0!	#DIV/0!	60	#DIV/0!	#DIV/0!	648.333333	783.333333	808.333333
Ecart-type		0.28867513	#DIV/0!	0.57735027	#DIV/0!	0.57735027	#DIV/0!	#DIV/0!	8.09835374	0.28867513	#DIV/0!	#DIV/0!	#DIV/0!	#DIV/0!	#DIV/0!	8.66025404	#DIV/0!	#DIV/0!	62.5166644	79.7391581	79.7391581

Appendix 1

Nom de l'échantillon	Unité	CLM1	VCI	CHLORURE-ETHYLE	2CPROPENE1	2CPROPANE	1CPROPENE1-CIS	VCI+1CPROPENE1-TRANS	CLM2	CAL	1CPROPANE	12DCETHYLENE-TRANS	11DCETHANE	12DCETHYLENE-CIS	CLM3	12DCETHANE
T80 concentration 1 (a)	mg/l	<0.1	<0.1	<0.1	<0.1	<0.1	<0.1	<0.1	<0.1	<0.1	<0.1	<0.1	<0.1	<0.1	0.1	<0.1
T80 concentration 1 (b)	mg/l	<0.1	<0.1	<0.1	<0.1	<0.1	<0.1	<0.1	<0.1	<0.1	<0.1	<0.1	<0.1	<0.1	0.1	<0.1
T80 concentration 1 (c)	mg/l	<0.1	<0.1	<0.1	<0.1	<0.1	<0.1	<0.1	<0.1	<0.1	<0.1	<0.1	<0.1	<0.1	0.1	<0.1
Moyenne		#DIV/0!	#DIV/0!	#DIV/0!	#DIV/0!	#DIV/0!	#DIV/0!	#DIV/0!	#DIV/0!	#DIV/0!	#DIV/0!	#DIV/0!	#DIV/0!	#DIV/0!	0.1	#DIV/0!
Facteur dilution	10															
Moyenne (mg/L)		#DIV/0!	#DIV/0!	#DIV/0!	#DIV/0!	#DIV/0!	#DIV/0!	#DIV/0!	#DIV/0!	#DIV/0!	#DIV/0!	#DIV/0!	#DIV/0!	#DIV/0!	1	#DIV/0!
Ecart-type		#DIV/0!	#DIV/0!	#DIV/0!	#DIV/0!	#DIV/0!	#DIV/0!	#DIV/0!	#DIV/0!	#DIV/0!	#DIV/0!	#DIV/0!	#DIV/0!	#DIV/0!	1.6997E-16	#DIV/0!
T80 concentration 2 (a)	mg/l	<0.1	<0.1	<0.1	<0.1	<0.1	<0.1	<0.1	<0.1	<0.1	<0.1	<0.1	<0.1	<0.1	<0.1	<0.1
T80 concentration 2 (b)	mg/l	<0.1	<0.1	<0.1	<0.1	<0.1	<0.1	<0.1	<0.1	<0.1	<0.1	<0.1	<0.1	<0.1	0.1	<0.1
T80 concentration 2 (c)	mg/l	<0.1	<0.1	<0.1	<0.1	<0.1	<0.1	<0.1	<0.1	<0.1	<0.1	<0.1	<0.1	<0.1	0.1	<0.1
Moyenne		#DIV/0!	#DIV/0!	#DIV/0!	#DIV/0!	#DIV/0!	#DIV/0!	#DIV/0!	#DIV/0!	#DIV/0!	#DIV/0!	#DIV/0!	#DIV/0!	#DIV/0!	0.1	#DIV/0!
Facteur dilution	10															
Moyenne (mg/L)		#DIV/0!	#DIV/0!	#DIV/0!	#DIV/0!	#DIV/0!	#DIV/0!	#DIV/0!	#DIV/0!	#DIV/0!	#DIV/0!	#DIV/0!	#DIV/0!	#DIV/0!	1	#DIV/0!
Ecart-type		#DIV/0!	#DIV/0!	#DIV/0!	#DIV/0!	#DIV/0!	#DIV/0!	#DIV/0!	#DIV/0!	#DIV/0!	#DIV/0!	#DIV/0!	#DIV/0!	#DIV/0!	0	#DIV/0!
T80 concentration 3 (a)	mg/l	<0.1	<0.1	<0.1	<0.1	<0.1	<0.1	<0.1	<0.1	<0.1	<0.1	<0.1	<0.1	<0.1	0.1	<0.1
T80 concentration 3 (b)	mg/l	<0.1	<0.1	<0.1	<0.1	<0.1	<0.1	<0.1	<0.1	<0.1	<0.1	<0.1	<0.1	<0.1	<0.1	<0.1
T80 concentration 3 (c)	mg/l	<0.1	<0.1	<0.1	<0.1	<0.1	<0.1	<0.1	<0.1	<0.1	<0.1	<0.1	<0.1	<0.1	0.1	<0.1
Moyenne		#DIV/0!	#DIV/0!	#DIV/0!	#DIV/0!	#DIV/0!	#DIV/0!	#DIV/0!	#DIV/0!	#DIV/0!	#DIV/0!	#DIV/0!	#DIV/0!	#DIV/0!	0.1	#DIV/0!
Facteur dilution	12.5															
Moyenne (mg/L)		#DIV/0!	#DIV/0!	#DIV/0!	#DIV/0!	#DIV/0!	#DIV/0!	#DIV/0!	#DIV/0!	#DIV/0!	#DIV/0!	#DIV/0!	#DIV/0!	#DIV/0!	1.25	#DIV/0!
Ecart-type		#DIV/0!	#DIV/0!	#DIV/0!	#DIV/0!	#DIV/0!	#DIV/0!	#DIV/0!	#DIV/0!	#DIV/0!	#DIV/0!	#DIV/0!	#DIV/0!	#DIV/0!	0	#DIV/0!
T80 concentration 4 (a)	mg/l	<0.1	<0.1	<0.1	<0.1	<0.1	<0.1	<0.1	<0.1	<0.1	<0.1	<0.1	<0.1	<0.1	0.1	<0.1
T80 concentration 4 (b)	mg/l	<0.1	<0.1	<0.1	<0.1	<0.1	<0.1	<0.1	<0.1	<0.1	<0.1	<0.1	<0.1	<0.1	0.1	<0.1
T80 concentration 4 (c)	mg/l	<0.1	<0.1	<0.1	<0.1	<0.1	<0.1	<0.1	<0.1	<0.1	<0.1	<0.1	<0.1	<0.1	<0.1	<0.1
Moyenne		#DIV/0!	#DIV/0!	#DIV/0!	#DIV/0!	#DIV/0!	#DIV/0!	#DIV/0!	#DIV/0!	#DIV/0!	#DIV/0!	#DIV/0!	#DIV/0!	#DIV/0!	0.1	#DIV/0!
Facteur dilution	16.6666667															
Moyenne (mg/L)		#DIV/0!	#DIV/0!	#DIV/0!	#DIV/0!	#DIV/0!	#DIV/0!	#DIV/0!	#DIV/0!	#DIV/0!	#DIV/0!	#DIV/0!	#DIV/0!	#DIV/0!	1.66666667	#DIV/0!
Ecart-type		#DIV/0!	#DIV/0!	#DIV/0!	#DIV/0!	#DIV/0!	#DIV/0!	#DIV/0!	#DIV/0!	#DIV/0!	#DIV/0!	#DIV/0!	#DIV/0!	#DIV/0!	0	#DIV/0!

Appendix 1

Nom de l'échantillon	Unité	111TCETHANE	BENZENE	CLIM	12DCPROPANE+23DCPROPENE1	TRICHOETHYLENE	112TCETHANE+INC	12DCBUTANE	PERCHLORETHYLENE	1112TCETHANE+CBENZENE	1122TCETHANE+INC	122TCPROPANE	13DCBENZENE+EDIA	14DCBENZENE	12DCBENZENE	HCETHANE	124TCBENZENE	122TCBENZENE	HCBUTADIENE13	Somme des POC quantifiés	Somme estimée des POC
T80 concentration 1 (a)	mg/l	0.1	<0.1	0.3	<0.1	0.2	<0.1	<0.1	2	0.1	0.1	0.1	<0.1	<0.1	<0.1	0.8	<0.1	<0.1	4.1	7.9	8.4
T80 concentration 1 (b)	mg/l	0.1	<0.1	0.3	<0.1	0.3	<0.1	<0.1	1.7	0.1	0.1	0.1	<0.1	<0.1	<0.1	0.4	<0.1	<0.1	0.7	3.9	4.4
T80 concentration 1 (c)	mg/l	0.1	<0.1	0.3	<0.1	0.2	0.1	<0.1	1.7	0.1	0.1	0.1	<0.1	<0.1	<0.1	0.4	<0.1	<0.1	0.9	4.1	4.6
Moyenne		0.1	#DIV/0!	0.3	#DIV/0!	0.23333333	0.1	#DIV/0!	1.8	0.1	0.1	0.1	#DIV/0!	#DIV/0!	#DIV/0!	0.53333333	#DIV/0!	#DIV/0!	1.9	5.3	5.8
Facteur dilution	10																				
Moyenne (mg/L)		1	#DIV/0!	3	#DIV/0!	2.33333333	1	#DIV/0!	18	1	1	1	#DIV/0!	#DIV/0!	#DIV/0!	5.33333333	#DIV/0!	#DIV/0!	19	53	58
Ecart-type		1.6997E-16	#DIV/0!	0	#DIV/0!	0.57735027	#DIV/0!	#DIV/0!	1.73205081	1.6997E-16	1.6997E-16	0	#DIV/0!	#DIV/0!	#DIV/0!	2.30940108	#DIV/0!	#DIV/0!	19.078784	22.5388553	22.5388553
T80 concentration 2 (a)	mg/l	0.1	<0.1	0.3	<0.1	0.3	<0.1	<0.1	1.9	0.1	0.1	0.1	<0.1	<0.1	<0.1	0.4	<0.1	<0.1	0.7	4	4.5
T80 concentration 2 (b)	mg/l	0.1	<0.1	0.3	<0.1	0.3	<0.1	<0.1	1.6	0.1	0.1	0.1	<0.1	<0.1	<0.1	0.4	<0.1	<0.1	0.4	3.5	4
T80 concentration 2 (c)	mg/l	0.1	<0.1	0.3	<0.1	0.2	<0.1	<0.1	1.6	0.1	0.1	0.1	<0.1	<0.1	<0.1	0.4	<0.1	<0.1	0.4	3.4	3.9
Moyenne		0.1	#DIV/0!	0.3	#DIV/0!	0.26666667	#DIV/0!	#DIV/0!	1.7	0.1	0.1	0.1	#DIV/0!	#DIV/0!	#DIV/0!	0.4	#DIV/0!	#DIV/0!	0.5	3.63333333	4.13333333
Facteur dilution	10																				
Moyenne (mg/L)		1	#DIV/0!	3	#DIV/0!	2.66666667	#DIV/0!	#DIV/0!	17	1	1	1	#DIV/0!	#DIV/0!	#DIV/0!	4	#DIV/0!	#DIV/0!	5	36.33333333	41.33333333
Ecart-type		1.6997E-16	#DIV/0!	0	#DIV/0!	0.57735027	#DIV/0!	#DIV/0!	1.73205081	1.6997E-16	1.6997E-16	1.6997E-16	#DIV/0!	#DIV/0!	#DIV/0!	6.7987E-16	#DIV/0!	#DIV/0!	1.73205081	3.21455025	3.21455025
T80 concentration 3 (a)	mg/l	0.1	<0.1	0.3	<0.1	0.2	<0.1	<0.1	1.4	0.1	0.1	<0.1	<0.1	<0.1	<0.1	0.3	<0.1	<0.1	0.4	3	3.5
T80 concentration 3 (b)	mg/l	0.1	<0.1	0.2	<0.1	0.2	<0.1	<0.1	1.4	0.1	0.1	<0.1	<0.1	<0.1	<0.1	0.3	<0.1	<0.1	0.7	3.1	3.6
T80 concentration 3 (c)	mg/l	0.1	<0.1	0.3	<0.1	0.2	<0.1	<0.1	1.4	0.1	0.1	<0.1	<0.1	<0.1	<0.1	0.3	<0.1	<0.1	0.5	3.1	3.6
Moyenne		0.1	#DIV/0!	0.26666667	#DIV/0!	0.2	#DIV/0!	#DIV/0!	1.4	0.1	0.1	#DIV/0!	#DIV/0!	#DIV/0!	#DIV/0!	0.3	#DIV/0!	#DIV/0!	0.53333333	3.06666667	3.56666667
Facteur dilution	12.5																				
Moyenne (mg/L)		1.25	#DIV/0!	3.33333333	#DIV/0!	2.5	#DIV/0!	#DIV/0!	17.5	1.25	1.25	#DIV/0!	#DIV/0!	#DIV/0!	#DIV/0!	3.75	#DIV/0!	#DIV/0!	6.66666667	38.33333333	44.58333333
Ecart-type		2.1246E-16	#DIV/0!	0.72168784	#DIV/0!	4.2492E-16	#DIV/0!	#DIV/0!	3.3993E-15	2.1246E-16	2.1246E-16	#DIV/0!	#DIV/0!	#DIV/0!	#DIV/0!	0	#DIV/0!	#DIV/0!	1.90940654	0.72168784	0.72168784
T80 concentration 4 (a)	mg/l	0.1	<0.1	0.2	<0.1	0.2	<0.1	<0.1	1.2	0.1	0.1	<0.1	<0.1	<0.1	<0.1	0.4	<0.1	<0.1	1.5	3.9	4.4
T80 concentration 4 (b)	mg/l	0.1	<0.1	0.2	<0.1	0.1	<0.1	<0.1	1	0.1	<0.1	<0.1	<0.1	<0.1	<0.1	0.3	<0.1	<0.1	0.9	2.8	3.3
T80 concentration 4 (c)	mg/l	0.1	<0.1	0.2	<0.1	0.2	<0.1	<0.1	1.1	0.1	<0.1	<0.1	<0.1	<0.1	<0.1	0.2	<0.1	<0.1	0.4	2.3	2.8
Moyenne		0.1	#DIV/0!	0.2	#DIV/0!	0.16666667	#DIV/0!	#DIV/0!	1.1	0.1	0.1	#DIV/0!	#DIV/0!	#DIV/0!	#DIV/0!	0.3	#DIV/0!	#DIV/0!	0.93333333	3	3.5
Facteur dilution	16.6666667																				
Moyenne (mg/L)		1.66666667	#DIV/0!	3.33333333	#DIV/0!	2.77777778	#DIV/0!	#DIV/0!	18.33333333	1.66666667	1.66666667	#DIV/0!	#DIV/0!	#DIV/0!	#DIV/0!	5	#DIV/0!	#DIV/0!	15.55555556	50	58.33333333
Ecart-type		2.8328E-16	#DIV/0!	5.6656E-16	#DIV/0!	0.96225045	#DIV/0!	#DIV/0!	1.66666667	2.8328E-16	#DIV/0!	#DIV/0!	#DIV/0!	#DIV/0!	#DIV/0!	1.66666667	#DIV/0!	#DIV/0!	9.17928425	13.6422546	13.6422546

Appendix 1

Nom de l'échantillon	Unité	CLM1	VC1	CHLORURE-ETHYLE	2CPROPENE1	2CPROPANE	1CPROPENE-CIS	VC2+1CPROPENE-1-TRANS	CLM2	CAL	1CPROPANE	12DCETHYLENE-TRANS	11DCETHANE	12DCETHYLENE-CIS	CLM3	12DCETHANE
Aerosol concentration 1 (a)	mg/l	<0,03	<0,03	<0,03	<0,03	<0,03	<0,03	<0,03	<0,03	<0,03	<0,03	<0,03	<0,03	<0,03	0.1	<0,03
Aerosol concentration 1 (b)	mg/l	<0,03	<0,03	<0,03	<0,03	<0,03	<0,03	<0,03	<0,03	<0,03	<0,03	<0,03	<0,03	<0,03	<0,03	<0,03
Aerosol concentration 1 (c)	mg/l	<0,03	<0,03	<0,03	<0,03	<0,03	<0,03	<0,03	<0,03	<0,03	<0,03	<0,03	<0,03	<0,03	<0,03	<0,03
Moyenne		#DIV/0!	#DIV/0!	#DIV/0!	#DIV/0!	#DIV/0!	#DIV/0!	#DIV/0!	#DIV/0!	#DIV/0!	#DIV/0!	#DIV/0!	#DIV/0!	#DIV/0!	0.1	#DIV/0!
Facteur dilution	10															
Moyenne (mg/L)		#DIV/0!	#DIV/0!	#DIV/0!	#DIV/0!	#DIV/0!	#DIV/0!	#DIV/0!	#DIV/0!	#DIV/0!	#DIV/0!	#DIV/0!	#DIV/0!	#DIV/0!	1	#DIV/0!
Ecart-type		#DIV/0!	#DIV/0!	#DIV/0!	#DIV/0!	#DIV/0!	#DIV/0!	#DIV/0!	#DIV/0!	#DIV/0!	#DIV/0!	#DIV/0!	#DIV/0!	#DIV/0!	#DIV/0!	#DIV/0!
Aerosol concentration 2 (a)	mg/l	<0,03	<0,03	<0,03	<0,03	<0,03	<0,03	<0,03	<0,03	<0,03	<0,03	<0,03	<0,03	<0,03	<0,03	<0,03
Aerosol concentration 2 (b)	mg/l	<0,03	<0,03	<0,03	<0,03	<0,03	<0,03	<0,03	<0,03	<0,03	<0,03	<0,03	<0,03	<0,03	<0,03	<0,03
Aerosol concentration 2 (c)	mg/l	<0,03	<0,03	<0,03	<0,03	<0,03	<0,03	<0,03	<0,03	<0,03	<0,03	<0,03	<0,03	0.03	0.04	<0,03
Moyenne		#DIV/0!	#DIV/0!	#DIV/0!	#DIV/0!	#DIV/0!	#DIV/0!	#DIV/0!	#DIV/0!	#DIV/0!	#DIV/0!	#DIV/0!	#DIV/0!	0.03	0.04	#DIV/0!
Facteur dilution	10															
Moyenne (mg/L)		#DIV/0!	#DIV/0!	#DIV/0!	#DIV/0!	#DIV/0!	#DIV/0!	#DIV/0!	#DIV/0!	#DIV/0!	#DIV/0!	#DIV/0!	#DIV/0!	0.3	0.4	#DIV/0!
Ecart-type		#DIV/0!	#DIV/0!	#DIV/0!	#DIV/0!	#DIV/0!	#DIV/0!	#DIV/0!	#DIV/0!	#DIV/0!	#DIV/0!	#DIV/0!	#DIV/0!	#DIV/0!	#DIV/0!	#DIV/0!
Aerosol concentration 3 (a)	mg/l	<0,03	<0,03	<0,03	<0,03	<0,03	<0,03	<0,03	<0,03	<0,03	<0,03	<0,03	<0,03	<0,03	<0,03	<0,03
Aerosol concentration 3 (b)	mg/l	<0,03	<0,03	<0,03	<0,03	<0,03	<0,03	<0,03	<0,03	<0,03	<0,03	<0,03	<0,03	<0,03	<0,03	<0,03
Aerosol concentration 3 (c)	mg/l	<0,03	<0,03	<0,03	<0,03	<0,03	<0,03	<0,03	<0,03	<0,03	<0,03	<0,03	<0,03	<0,03	<0,03	<0,03
Moyenne		#DIV/0!	#DIV/0!	#DIV/0!	#DIV/0!	#DIV/0!	#DIV/0!	#DIV/0!	#DIV/0!	#DIV/0!	#DIV/0!	#DIV/0!	#DIV/0!	#DIV/0!	#DIV/0!	#DIV/0!
Facteur dilution	16.6666667															
Moyenne (mg/L)		#DIV/0!	#DIV/0!	#DIV/0!	#DIV/0!	#DIV/0!	#DIV/0!	#DIV/0!	#DIV/0!	#DIV/0!	#DIV/0!	#DIV/0!	#DIV/0!	#DIV/0!	#DIV/0!	#DIV/0!
Ecart-type		#DIV/0!	#DIV/0!	#DIV/0!	#DIV/0!	#DIV/0!	#DIV/0!	#DIV/0!	#DIV/0!	#DIV/0!	#DIV/0!	#DIV/0!	#DIV/0!	#DIV/0!	#DIV/0!	#DIV/0!
Aerosol concentration 4 (a)	mg/l	<0,03	<0,03	<0,03	<0,03	<0,03	<0,03	<0,03	<0,03	<0,03	<0,03	<0,03	<0,03	<0,03	<0,03	<0,03
Aerosol concentration 4 (b)	mg/l	<0,03	<0,03	<0,03	<0,03	<0,03	<0,03	<0,03	<0,03	<0,03	<0,03	<0,03	<0,03	<0,03	<0,03	<0,03
Aerosol concentration 4 (c)	mg/l	<0,03	<0,03	<0,03	<0,03	<0,03	<0,03	<0,03	<0,03	<0,03	<0,03	<0,03	<0,03	<0,03	<0,03	<0,03
Moyenne		#DIV/0!	#DIV/0!	#DIV/0!	#DIV/0!	#DIV/0!	#DIV/0!	#DIV/0!	#DIV/0!	#DIV/0!	#DIV/0!	#DIV/0!	#DIV/0!	#DIV/0!	#DIV/0!	#DIV/0!
Facteur dilution	16.6666667															
Moyenne (mg/L)		#DIV/0!	#DIV/0!	#DIV/0!	#DIV/0!	#DIV/0!	#DIV/0!	#DIV/0!	#DIV/0!	#DIV/0!	#DIV/0!	#DIV/0!	#DIV/0!	#DIV/0!	#DIV/0!	#DIV/0!
Ecart-type		#DIV/0!	#DIV/0!	#DIV/0!	#DIV/0!	#DIV/0!	#DIV/0!	#DIV/0!	#DIV/0!	#DIV/0!	#DIV/0!	#DIV/0!	#DIV/0!	#DIV/0!	#DIV/0!	#DIV/0!

Appendix 1

Nom de l'échantillon	Unité	111TCETHANE	BENZENE	CLM4	12DCPROPANE/23DCPROPENE1	TRICHOLORETHYLENE	112TCETHANE+1NC	12DCBUTANE	PERCHLORETHYLENE	1112TCETHANE+CBENZENE	1122TCETHANE+1NC	123TCPROPANE	13DCBENZENE+EDA	14DCBENZENE	12DCBENZENE	14CETHANE	124TCBENZENE	123TCBENZENE	14CBUTADIENE13	Somme des POC quantifiés	Somme des limite des POC
Aerosol concentration 1 (a)	mg/l	0.09	<0,03	0.25	<0,03	0.2	<0,03	<0,03	1.31	0.11	0.1	0.1	<0,1	<0,1	<0,1	0.3	<0,1	<0,1	0.2	2.7	3.2
Aerosol concentration 1 (b)	mg/l	0.13	<0,03	0.32	0.03	0.24	<0,03	<0,03	1.44	0.11	0.1	<0,1	<0,1	<0,1	<0,1	0.3	<0,1	<0,1	0.3	2.8	3.3
Aerosol concentration 1 (c)	mg/l	0.09	<0,03	0.29	<0,03	0.2	<0,03	<0,03	1.33	0.1	0.1	0.1	<0,1	<0,1	<0,1	0.3	<0,1	<0,1	0.3	2.8	3.3
Moyenne		0.09666667	#DIV/0!	0.28666667	0.03	0.21333333	#DIV/0!	#DIV/0!	1.36	0.10666667	0.1	0.1	#DIV/0!	#DIV/0!	#DIV/0!	0.3	#DIV/0!	#DIV/0!	0.26666667	2.76666667	3.26666667
Facteur dilution	10																				
Moyenne (mg/L)		0.96666667	#DIV/0!	2.86666667	0.3	2.13333333	#DIV/0!	#DIV/0!	13.6	1.06666667	1	1	#DIV/0!	#DIV/0!	#DIV/0!	3	#DIV/0!	#DIV/0!	2.66666667	27.66666667	32.66666667
Ecart-type		0.11547005	#DIV/0!	0.35118846	#DIV/0!	0.23094011	#DIV/0!	#DIV/0!	0.7	0.05773503	1.6997E-16	0	#DIV/0!	#DIV/0!	#DIV/0!	0	#DIV/0!	#DIV/0!	0.57735027	0.57735027	0.57735027
Aerosol concentration 2 (a)	mg/l	0.13	<0,03	0.33	0.03	0.24	<0,03	<0,03	1.72	0.11	0.1	0.1	<0,1	<0,1	<0,1	0.4	<0,1	<0,1	0.5	3.5	4
Aerosol concentration 2 (b)	mg/l	0.13	<0,03	0.39	0.03	0.26	<0,03	<0,03	1.8	0.11	0.1	0.1	<0,1	<0,1	<0,1	0.4	<0,1	<0,1	0.5	3.8	4.3
Aerosol concentration 2 (c)	mg/l	0.2	<0,03	0.55	0.06	0.43	<0,03	<0,03	2.19	0.17	0.2	0.1	<0,1	<0,1	<0,1	0.4	<0,1	<0,1	0.5	4.9	5.4
Moyenne		0.14666667	#DIV/0!	0.42333333	0.04	0.31	#DIV/0!	#DIV/0!	1.90333333	0.13	0.13333333	0.1	#DIV/0!	#DIV/0!	#DIV/0!	0.4	#DIV/0!	#DIV/0!	0.5	4.06666667	4.56666667
Facteur dilution	10																				
Moyenne (mg/L)		1.46666667	#DIV/0!	4.23333333	0.4	3.1	#DIV/0!	#DIV/0!	19.03333333	1.3	1.33333333	1	#DIV/0!	#DIV/0!	#DIV/0!	4	#DIV/0!	#DIV/0!	5	40.66666667	45.66666667
Ecart-type		0.47258156	#DIV/0!	1.13724814	0.17320508	1.04403065	#DIV/0!	#DIV/0!	2.5146239	0.34641016	0.57735027	1.6997E-16	#DIV/0!	#DIV/0!	#DIV/0!	6.7987E-16	#DIV/0!	#DIV/0!	0	7.3711148	7.3711148
Aerosol concentration 3 (a)	mg/l	0.1	<0,03	0.4	<0,03	0.21	<0,03	<0,03	3.5	0.12	0.2	<0,1	<0,1	<0,1	<0,1	3.7	<0,1	<0,1	36.8	45.4	45.9
Aerosol concentration 3 (b)	mg/l	0.1	<0,03	0.39	<0,03	0.21	<0,03	<0,03	3.82	0.11	0.2	0.1	<0,1	<0,1	<0,1	3.5	<0,1	<0,1	35	43.4	43.9
Aerosol concentration 3 (c)	mg/l	0.09	<0,03	0.36	<0,03	0.2	<0,03	<0,03	3.74	0.11	0.2	0.1	<0,1	<0,1	<0,1	3.5	<0,1	<0,1	36.4	44.7	45.2
Moyenne		0.09666667	#DIV/0!	0.38333333	#DIV/0!	0.20666667	#DIV/0!	#DIV/0!	3.82	0.11333333	0.2	0.1	#DIV/0!	#DIV/0!	#DIV/0!	3.56666667	#DIV/0!	#DIV/0!	36.06666667	44.5	45
Facteur dilution	16.6666667																				
Moyenne (mg/L)		1.61111111	#DIV/0!	6.38888889	#DIV/0!	3.44444444	#DIV/0!	#DIV/0!	63.6666667	1.88888889	3.33333333	1.66666667	#DIV/0!	#DIV/0!	#DIV/0!	59.4444444	#DIV/0!	#DIV/0!	601.111111	741.6666667	750
Ecart-type		0.09622504	#DIV/0!	0.34694433	#DIV/0!	0.09622504	#DIV/0!	#DIV/0!	1.33333333	0.09622504	5.6656E-16	0	#DIV/0!	#DIV/0!	#DIV/0!	1.9245009	#DIV/0!	#DIV/0!	15.7527188	16.9148193	16.9148193
Aerosol concentration 4 (a)	mg/l	0.09	<0,03	0.33	<0,03	0.19	<0,03	<0,03	3.58	0.1	0.3	0.1	<0,1	<0,1	<0,1	3.4	<0,1	<0,1	36.4	44.5	45
Aerosol concentration 4 (b)	mg/l	0.09	<0,03	0.37	<0,03	0.2	<0,03	<0,03	3.62	0.11	0.2	<0,1	<0,1	<0,1	<0,1	3.4	<0,1	<0,1	35.1	43.1	43.6
Aerosol concentration 4 (c)	mg/l	0.1	<0,03	0.37	<0,03	0.2	<0,03	<0,03	3.81	0.11	0.5	0.4	<0,1	<0,1	<0,1	3.4	<0,1	<0,1	33.8	42.7	43.2
Moyenne		0.09333333	#DIV/0!	0.35666667	#DIV/0!	0.19666667	#DIV/0!	#DIV/0!	3.67	0.10666667	0.33333333	0.25	#DIV/0!	#DIV/0!	#DIV/0!	3.4	#DIV/0!	#DIV/0!	35.1	43.4333333	43.9333333
Facteur dilution	16.6666667																				
Moyenne (mg/L)		1.55555556	#DIV/0!	5.94444444	#DIV/0!	3.27777778	#DIV/0!	#DIV/0!	61.1666667	1.77777778	5.55555556	4.16666667	#DIV/0!	#DIV/0!	#DIV/0!	56.6666667	#DIV/0!	#DIV/0!	595	723.888889	732.222222
Ecart-type		0.09622504	#DIV/0!	0.38490018	#DIV/0!	0.09622504	#DIV/0!	#DIV/0!	2.04803429	0.09622504	2.54587539	3.53553391	#DIV/0!	#DIV/0!	#DIV/0!	0	#DIV/0!	#DIV/0!	21.68666667	15.7527188	15.7527188

Appendix 1.10
Concentrations of COCs with thermal enhancement

Appendix 1

Nom de l'échantillon	Unité	11TCETHANE	BENZENE	CLM4	12DOPROPANE+23DOPROPENE 1	TRICHOETHYLENE	112TCETHANE+NC	12DOBUTANE	PERCHLOROETHYLENE	11212TCETHANE+OEBENZENE	1122TCETHANE+NC	122TCOPROPANE	13DOBENZENE+EDIA	14DOBENZENE	12DOBENZENE	HCEETHANE	121TCBENZENE	122TCBENZENE	HCOBUTADIENE 13	Somme des POC quantifiés	Somme estimée des POC
Solubilité bulle 12°C eau du robinet (a)	mg/l	0.03	<0.03	0.1	<0.03	0.1	<0.03	<0.03	0.66	0.04	<0.1	<0.1	<0.1	<0.1	<0.1	0.1	<0.1	<0.1	0.2	1.2	1.7
Solubilité bulle 12°C eau du robinet (b)	mg/l	0.03	<0.03	0.11	<0.03	0.12	<0.03	<0.03	0.66	0.04	<0.1	<0.1	<0.1	<0.1	<0.1	0.1	<0.1	<0.1	0.2	1.1	1.6
Solubilité bulle 12°C eau du robinet (c)	mg/l	0.04	<0.03	0.13	<0.03	0.12	<0.03	<0.03	0.75	0.04	<0.1	<0.1	<0.1	<0.1	<0.1	0.2	<0.1	<0.1	0.3	1.5	2
Moyenne		0.03333333	#DIV/0!	0.11333333	#DIV/0!	0.11333333	#DIV/0!	#DIV/0!	0.69	0.04	#DIV/0!	#DIV/0!	#DIV/0!	#DIV/0!	#DIV/0!	0.13333333	#DIV/0!	#DIV/0!	0.2	1.26666667	1.76666667
Facteur dilution	25																				
Moyenne (mg/L)		0.83333333	#DIV/0!	2.83333333	#DIV/0!	2.83333333	#DIV/0!	#DIV/0!	17.25	1	#DIV/0!	#DIV/0!	#DIV/0!	#DIV/0!	#DIV/0!	3.33333333	#DIV/0!	#DIV/0!	5	31.66666667	44.16666667
Ecart-type		0.14433757	#DIV/0!	0.38188131	#DIV/0!	0.28867513	#DIV/0!	#DIV/0!	1.29903811	0	#DIV/0!	#DIV/0!	#DIV/0!	#DIV/0!	#DIV/0!	1.44337567	#DIV/0!	#DIV/0!	2.5	5.20416499	5.204165
Solubilité bulle 20°C eau du robinet (a)	mg/l	0.03	<0.03	0.08	<0.03	0.1	<0.03	<0.03	0.45	0.04	<0.1	<0.1	<0.1	<0.1	<0.1	0.1	<0.1	<0.1	<0.1	0.8	1.3
Solubilité bulle 20°C eau du robinet (b)	mg/l	0.03	<0.03	0.11	<0.03	0.11	<0.03	<0.03	0.64	0.04	<0.1	<0.1	<0.1	<0.1	<0.1	0.1	<0.1	<0.1	0.1	1	1.5
Solubilité bulle 20°C eau du robinet (c)	mg/l	0.04	<0.03	0.14	<0.03	0.13	<0.03	<0.03	0.8	0.06	<0.1	<0.1	<0.1	<0.1	<0.1	0.2	<0.1	<0.1	0.2	1.5	2
Moyenne		0.03333333	#DIV/0!	0.11	#DIV/0!	0.11333333	#DIV/0!	#DIV/0!	0.63	0.04333333	#DIV/0!	#DIV/0!	#DIV/0!	#DIV/0!	#DIV/0!	0.13333333	#DIV/0!	#DIV/0!	0.15	1.1	1.6
Facteur dilution	25																				
Moyenne (mg/L)		0.83333333	#DIV/0!	2.75	#DIV/0!	2.83333333	#DIV/0!	#DIV/0!	15.75	1.08333333	#DIV/0!	#DIV/0!	#DIV/0!	#DIV/0!	#DIV/0!	3.33333333	#DIV/0!	#DIV/0!	3.75	27.5	40
Ecart-type		0.14433757	#DIV/0!	0.75	#DIV/0!	0.38188131	#DIV/0!	#DIV/0!	4.38035387	0.14433757	#DIV/0!	#DIV/0!	#DIV/0!	#DIV/0!	#DIV/0!	1.44337567	#DIV/0!	#DIV/0!	1.76776696	9.01387819	9.01387819
Solubilité bulle 35°C eau du robinet (a)	mg/l	<0.03	<0.03	0.05	<0.03	0.05	<0.03	<0.03	0.3	<0.03	<0.1	<0.1	<0.1	<0.1	<0.1	0.1	<0.1	<0.1	0.2	0.8	1.3
Solubilité bulle 35°C eau du robinet (b)	mg/l	<0.03	<0.03	0.06	<0.03	0.06	<0.03	<0.03	0.31	<0.03	<0.1	<0.1	<0.1	<0.1	<0.1	0.1	<0.1	<0.1	0.1	0.7	1.2
Solubilité bulle 35°C eau du robinet (c)	mg/l	<0.03	<0.03	0.05	<0.03	0.05	<0.03	<0.03	0.27	<0.03	<0.1	<0.1	<0.1	<0.1	<0.1	0.1	<0.1	<0.1	0.1	0.7	1.2
Moyenne		#DIV/0!	#DIV/0!	0.05333333	#DIV/0!	0.05333333	#DIV/0!	#DIV/0!	0.29333333	#DIV/0!	#DIV/0!	#DIV/0!	#DIV/0!	#DIV/0!	#DIV/0!	0.1	#DIV/0!	#DIV/0!	0.13333333	0.73333333	1.23333333
Facteur dilution	50																				
Moyenne (mg/L)		#DIV/0!	#DIV/0!	2.66666667	#DIV/0!	2.66666667	#DIV/0!	#DIV/0!	14.66666667	#DIV/0!	#DIV/0!	#DIV/0!	#DIV/0!	#DIV/0!	#DIV/0!	5	#DIV/0!	#DIV/0!	6.66666667	36.66666667	61.66666667
Ecart-type		#DIV/0!	#DIV/0!	0.28867513	#DIV/0!	0.28867513	#DIV/0!	#DIV/0!	1.040833	#DIV/0!	#DIV/0!	#DIV/0!	#DIV/0!	#DIV/0!	#DIV/0!	8.4984E-16	#DIV/0!	#DIV/0!	2.88675135	2.886751346	2.88675135
Solubilité bulle 45°C eau du robinet (a)	mg/l	<0.03	<0.03	0.05	<0.03	0.05	<0.03	<0.03	0.27	<0.03	<0.1	<0.1	<0.1	<0.1	<0.1	0.1	<0.1	<0.1	0.1	0.7	1.2
Solubilité bulle 45°C eau du robinet (b)	mg/l	<0.03	<0.03	0.06	<0.03	0.05	<0.03	<0.03	0.3	<0.03	<0.1	<0.1	<0.1	<0.1	<0.1	0.1	<0.1	<0.1	0.1	0.7	1.2
Solubilité bulle 45°C eau du robinet (c)	mg/l	<0.03	<0.03	0.06	<0.03	0.05	<0.03	<0.03	0.3	<0.03	<0.1	<0.1	<0.1	<0.1	<0.1	0.1	<0.1	<0.1	0.1	0.7	1.2
Moyenne		#DIV/0!	#DIV/0!	0.05666667	#DIV/0!	0.05	#DIV/0!	#DIV/0!	0.29	#DIV/0!	#DIV/0!	#DIV/0!	#DIV/0!	#DIV/0!	#DIV/0!	0.1	#DIV/0!	#DIV/0!	0.1	0.7	1.2
Facteur dilution	50																				
Moyenne (mg/L)		#DIV/0!	#DIV/0!	2.83333333	#DIV/0!	2.5	#DIV/0!	#DIV/0!	14.5	#DIV/0!	#DIV/0!	#DIV/0!	#DIV/0!	#DIV/0!	#DIV/0!	5	#DIV/0!	#DIV/0!	5	35	60
Ecart-type		#DIV/0!	#DIV/0!	0.28867513	#DIV/0!	4.2492E-16	#DIV/0!	#DIV/0!	0.8660254	#DIV/0!	#DIV/0!	#DIV/0!	#DIV/0!	#DIV/0!	#DIV/0!	8.4984E-16	#DIV/0!	#DIV/0!	8.4984E-16	6.7987E-15	0
Solubilité bulle 60°C eau du robinet (a)	mg/l	<0.03	<0.03	0.03	<0.03	0.03	<0.03	<0.03	0.18	<0.03	<0.1	<0.1	<0.1	<0.1	<0.1	0.1	<0.1	<0.1	0.2	0.5	1
Solubilité bulle 60°C eau du robinet (b)	mg/l	<0.03	<0.03	0.04	<0.03	0.04	<0.03	<0.03	0.24	<0.03	<0.1	<0.1	<0.1	<0.1	<0.1	0.1	<0.1	<0.1	0.2	0.5	1
Solubilité bulle 60°C eau du robinet (c)	mg/l	<0.03	<0.03	0.03	<0.03	0.03	<0.03	<0.03	0.2	<0.03	<0.1	<0.1	<0.1	<0.1	<0.1	0.1	<0.1	<0.1	0.2	0.5	1
Moyenne		#DIV/0!	#DIV/0!	0.03333333	#DIV/0!	0.03333333	#DIV/0!	#DIV/0!	0.20666667	#DIV/0!	#DIV/0!	#DIV/0!	#DIV/0!	#DIV/0!	#DIV/0!	0.1	#DIV/0!	#DIV/0!	0.2	0.5	1
Facteur dilution	50																				
Moyenne (mg/L)		#DIV/0!	#DIV/0!	1.66666667	#DIV/0!	1.66666667	#DIV/0!	#DIV/0!	10.33333333	#DIV/0!	#DIV/0!	#DIV/0!	#DIV/0!	#DIV/0!	#DIV/0!	5	#DIV/0!	#DIV/0!	10	25	50
Ecart-type		#DIV/0!	#DIV/0!	0.28867513	#DIV/0!	0.28867513	#DIV/0!	#DIV/0!	1.52752523	#DIV/0!	#DIV/0!	#DIV/0!	#DIV/0!	#DIV/0!	#DIV/0!	8.4984E-16	#DIV/0!	#DIV/0!	1.6997E-15	0	0
Solubilité bulle 12°C eau casier (a)	mg/l	0.25	<0.03	0.68	0.35	1.02	0.89	<0.03	2.88	0.35	0.6	0.7	<0.1	<0.1	<0.1	1.5	<0.1	<0.1	3.2	13.7	14.1
Solubilité bulle 12°C eau casier (b)	mg/l	0.25	<0.03	0.7	0.36	1.02	0.89	0.03	3	0.36	0.7	0.7	<0.1	<0.1	<0.1	1.7	<0.1	<0.1	5.1	16	16.4
Solubilité bulle 12°C eau casier (c)	mg/l	0.24	<0.03	0.65	0.34	0.98	0.86	0.03	2.64	0.34	0.6	0.7	<0.1	<0.1	<0.1	1.5	<0.1	<0.1	2.8	12.7	13.1
Moyenne		0.24666667	#DIV/0!	0.67666667	0.35	1.00666667	0.88	0.03	2.84	0.35	0.63333333	0.7	#DIV/0!	#DIV/0!	#DIV/0!	1.56666667	#DIV/0!	#DIV/0!	3.7	14.13333333	14.53333333
Facteur dilution	25																				
Moyenne (mg/L)		6.16666667	#DIV/0!	16.91666667	8.75	25.16666667	22	0.75	71	8.75	15.83333333	17.5	#DIV/0!	#DIV/0!	#DIV/0!	39.16666667	#DIV/0!	#DIV/0!	92.5	353.33333333	363.33333333
Ecart-type		0.14433757	#DIV/0!	0.62915287	0.25	0.57735027	0.4330127	0	4.58257569	0.25	1.44337567	3.3993E-15	#DIV/0!	#DIV/0!	#DIV/0!	2.88675135	#DIV/0!	#DIV/0!	30.7205143	42.30346715	42.3034672

Appendix 2

1D cells experiments without enhancement

Appendix 2.1
Permeability tests

GB 1.0 mm	GB 1.0 mm	GB 1.0 mm	GB 0.5 mm	GB 0.5 mm	GB 0.5 mm
Q/A	$\Delta H/L$	K (m/s)	Q/A	$\Delta H/L$	K (m/s)
1.99E-02	3.33E+00	5.06E-03	6.10E-03	3.33E+00	1.27E-03
8.15E-03	1.93E+00	k (m2)	2.03E-03	2.33E+00	k (m2)
4.38E-03	9.33E-01	5.16E-10	7.63E-04	1.33E+00	1.30E-10
2.02E-02	3.33E+00		4.75E-03	3.33E+00	
1.09E-02	2.20E+00		2.03E-03	2.17E+00	
5.19E-03	1.20E+00		8.14E-04	8.33E-01	
1.53E-02	3.33E+00		2.33E-04	1.67E-01	
7.28E-03	1.93E+00		3.87E-03	3.33E+00	
3.90E-03	6.00E-01		2.44E-03	2.07E+00	
1.82E-02	3.33E+00		1.16E-03	1.07E+00	
1.48E-02	2.50E+00		4.36E-04	4.00E-01	
4.26E-03	1.17E+00		4.58E-03	3.33E+00	
1.46E-02	3.33E+00		4.07E-03	2.83E+00	
7.28E-03	2.00E+00		2.71E-03	2.17E+00	
1.65E-03	6.67E-01		1.53E-03	1.50E+00	
3.31E-03	6.67E-01		3.49E-04	5.00E-01	
			4.07E-03	3.33E+00	
			3.99E-03	3.33E+00	
			2.29E-03	2.40E+00	
			2.44E-03	1.40E+00	
			2.91E-04	4.00E-01	

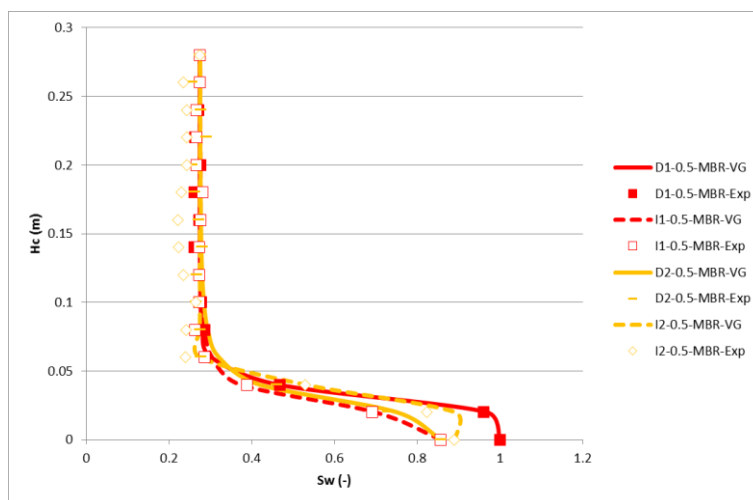
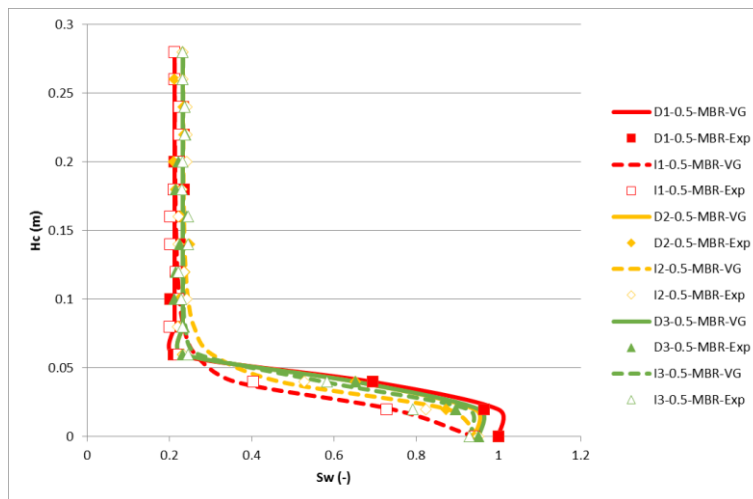
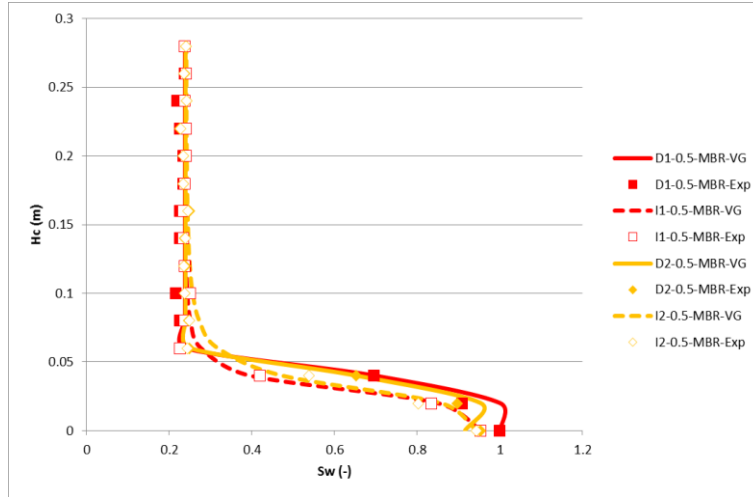
Appendix 2

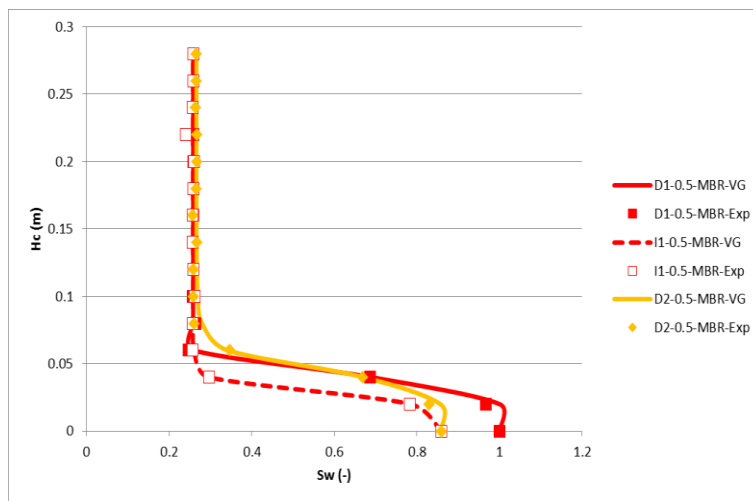
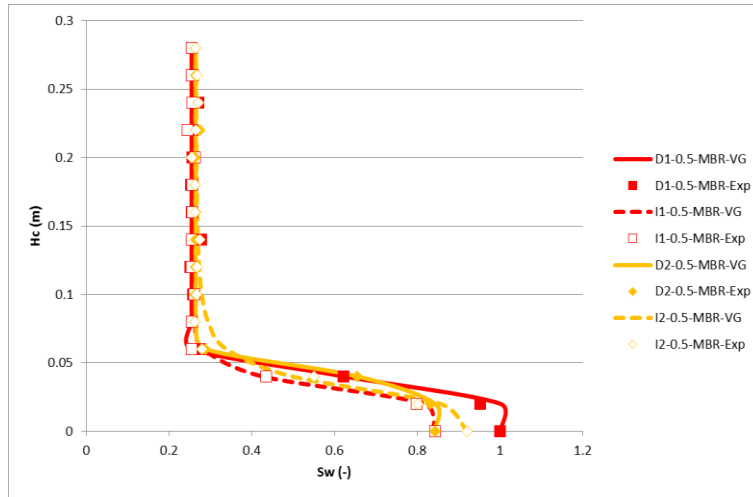
GB 0.1 mm	GB 0.1 mm	GB 0.1 mm	GB 0.1-0.2 mm	GB 0.1-0.2 mm	GB 0.1-0.2 mm	Tavaux sample	Tavaux sample	Tavaux sample
Q/A	ΔH/L	K (m/s)	Q/A	ΔH/L	K (m/s)	Q/A	ΔH/L	K (m/s)
2.43E-04	3.33E+00	6.60E-05	1.72E-03	3.33E+00	4.84E-04	1.29E-03	3.33E+00	3.51E-04
1.78E-04	2.67E+00	k (m2)	9.10E-04	2.00E+00	k (m2)	5.91E-04	1.92E+00	k (m2)
1.30E-04	2.00E+00	6.73E-12	5.20E-04	1.33E+00	4.93E-11	3.92E-04	1.32E+00	3.58E-11
7.83E-05	1.33E+00		1.65E-04	6.67E-01		1.08E-04	6.50E-01	
3.34E-05	6.67E-01		1.52E-05	0.00E+00		1.20E-05	0.00E+00	
8.31E-06	0.00E+00		1.29E-03	3.33E+00		8.49E-04	3.33E+00	
1.28E-04	3.33E+00		4.55E-04	1.07E+00		3.44E-04	1.05E+00	
2.27E-04	3.33E+00		1.46E-04	4.00E-01		9.50E-05	3.86E-01	
2.02E-04	2.83E+00		6.42E-05	6.67E-02		4.84E-05	6.50E-02	
1.27E-04	1.83E+00		2.08E-05	0.00E+00		1.59E-05	0.00E+00	
9.25E-05	1.33E+00		1.82E-03	3.33E+00		1.37E-03	3.33E+00	
5.20E-05	8.33E-01		1.21E-03	2.50E+00		7.94E-04	2.53E+00	
1.49E-05	5.00E-01		9.10E-04	1.83E+00		6.03E-04	1.89E+00	
2.31E-04	3.33E+00		5.20E-04	1.17E+00		3.34E-04	1.20E+00	
1.82E-04	2.70E+00		1.55E-04	5.00E-01		1.18E-04	5.10E-01	
1.30E-04	1.87E+00		6.28E-06	0.00E+00		4.80E-06	0.00E+00	
7.91E-05	1.37E+00		1.76E-03	3.33E+00		1.27E-03	3.33E+00	
2.67E-05	7.00E-01		9.10E-04	2.37E+00		7.67E-04	2.28E+00	
3.14E-06	3.33E-02		9.10E-04	1.70E+00		6.85E-04	1.64E+00	
2.24E-04	3.33E+00		4.04E-04	1.03E+00		3.23E-04	9.98E-01	
1.21E-04	2.10E+00		1.52E-04	3.67E-01		1.29E-04	3.58E-01	
6.39E-05	7.67E-01		1.48E-05	0.00E+00		1.28E-05	0.00E+00	
4.23E-05	4.33E-01		1.67E-03	3.33E+00		1.26E-03	3.33E+00	
2.58E-05	2.67E-01		1.21E-03	2.57E+00		8.92E-04	2.66E+00	
9.01E-06	0.00E+00		8.09E-04	1.90E+00		5.28E-04	1.89E+00	
2.91E-04	3.33E+00		6.07E-04	1.23E+00		4.79E-04	1.27E+00	
1.62E-04	2.67E+00		7.66E-05	5.67E-01		5.79E-05	5.92E-01	
1.28E-04	2.00E+00		1.64E-03	3.33E+00		1.41E-03	3.33E+00	
8.99E-05	1.33E+00		1.21E-03	2.53E+00		9.28E-04	2.52E+00	
4.28E-05	6.67E-01		1.04E-03	1.87E+00		7.96E-04	1.80E+00	
1.26E-05	3.33E-01		5.20E-04	1.20E+00		3.92E-04	1.19E+00	
0.00E+00	0.00E+00		1.69E-04	5.33E-01		1.13E-04	5.15E-01	
			2.23E-05	0.00E+00		7.43E-06	0.00E+00	
			1.74E-03	3.33E+00		1.02E-03	3.33E+00	
			1.04E-03	1.90E+00		6.92E-04	1.94E+00	
			5.60E-04	1.23E+00		3.71E-04	1.25E+00	
			2.14E-04	5.67E-01		1.42E-04	5.72E-01	
			3.93E-05	0.00E+00		2.97E-05	0.00E+00	

Appendix 2.2

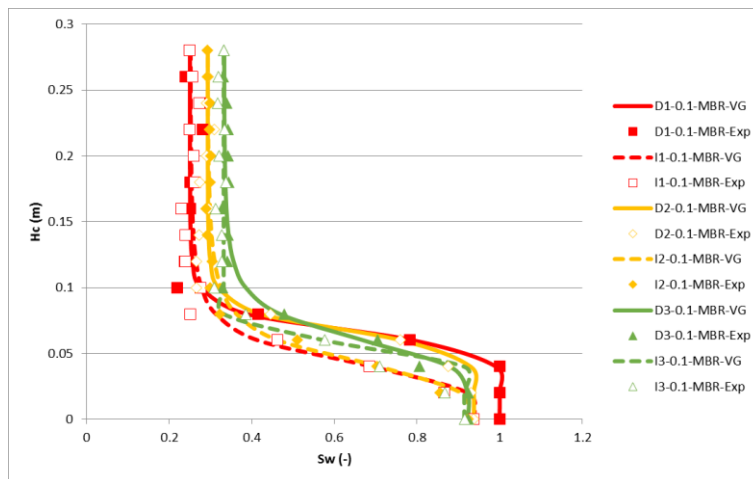
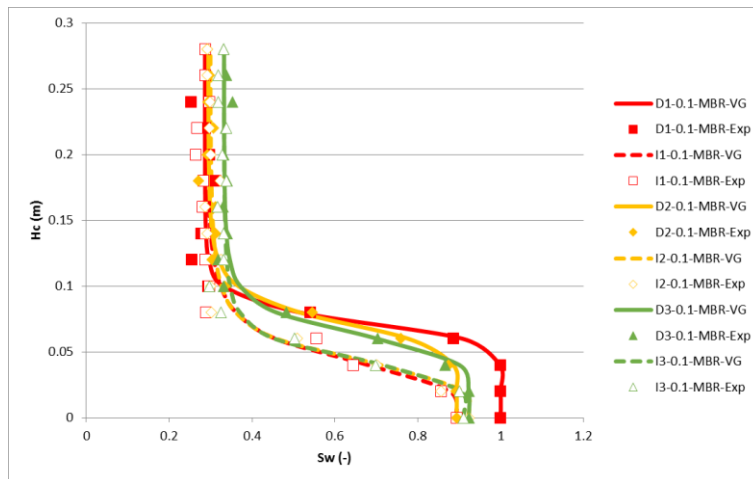
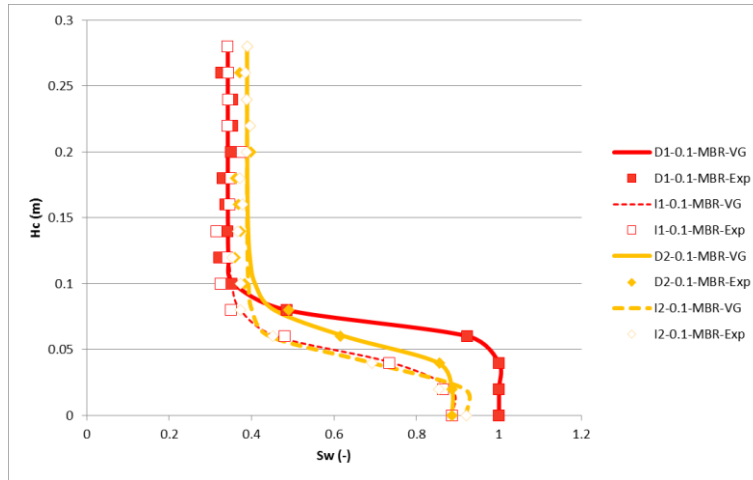
Drainage-imbibition experiments for 0.5 and 0.1 mm GB with membrane

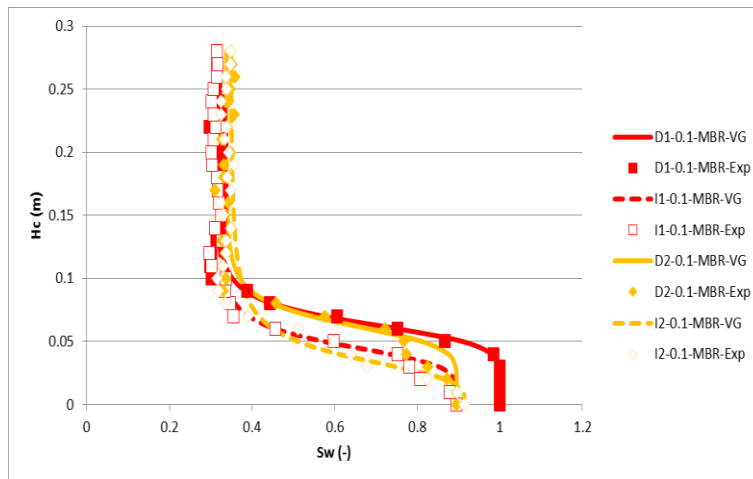
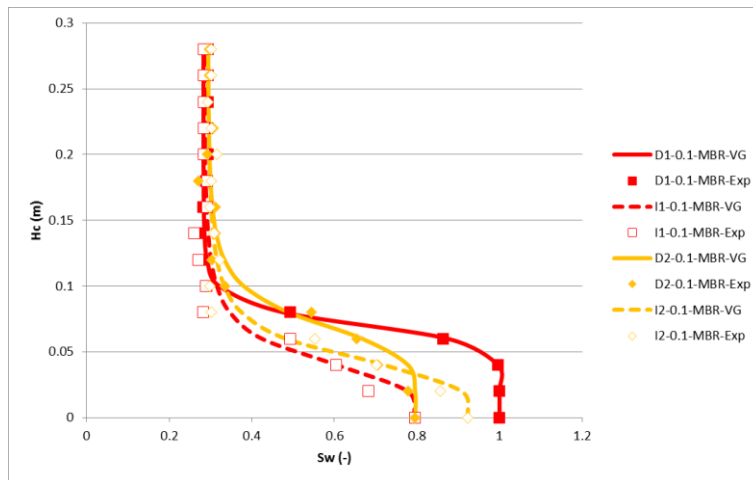
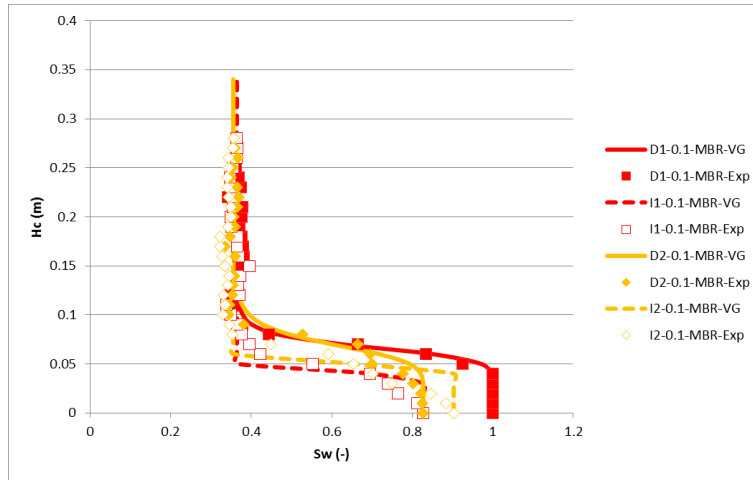
0.5 mm GB





0.1 mm GB

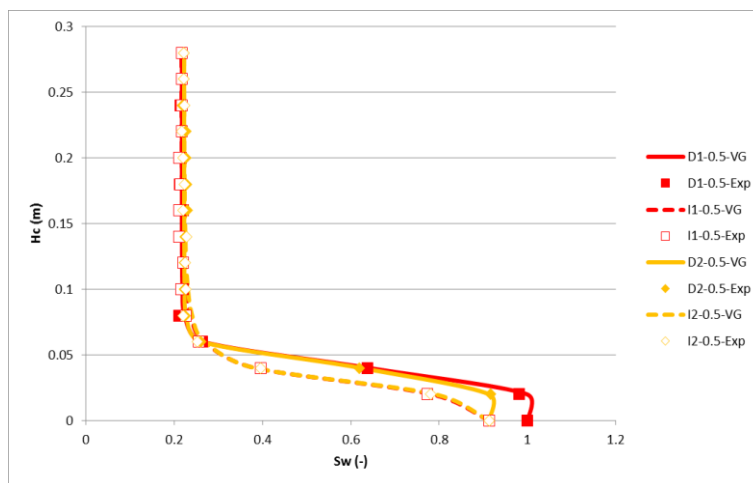
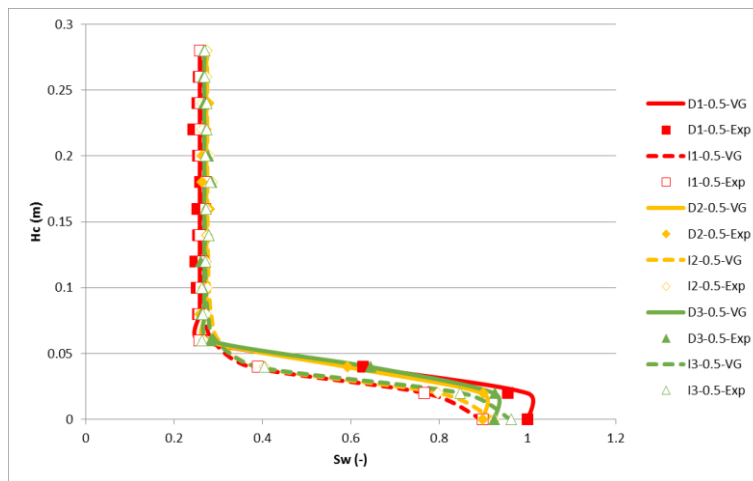
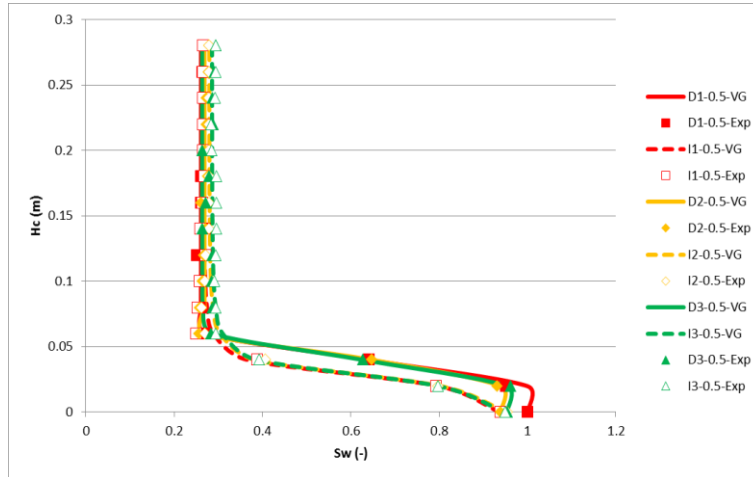


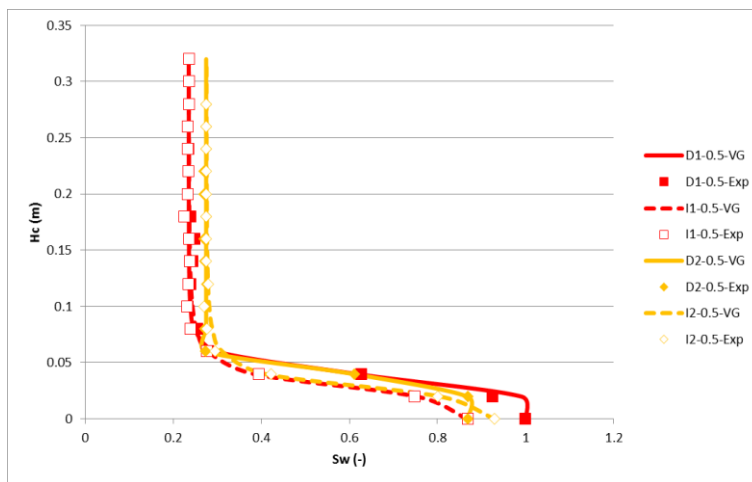
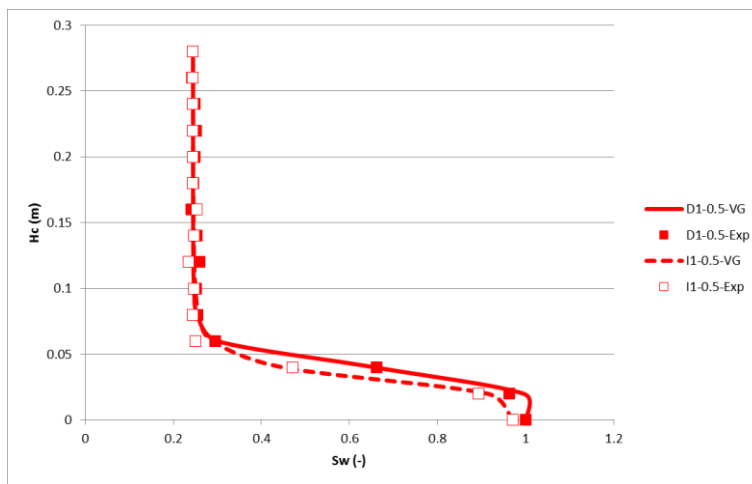
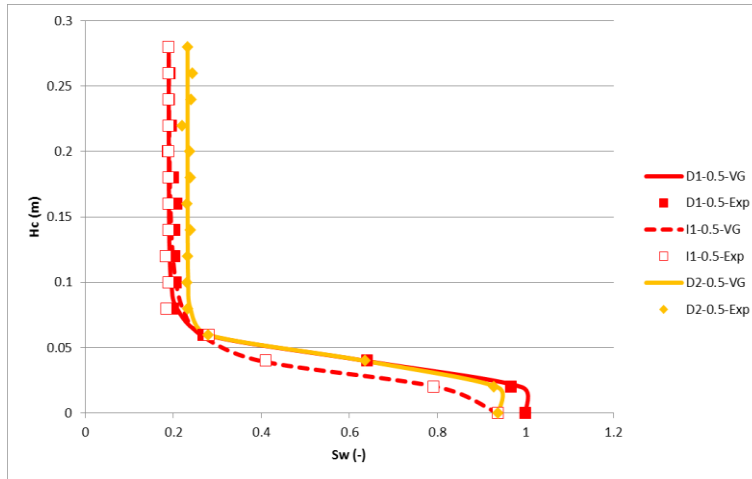


Appendix 2.3

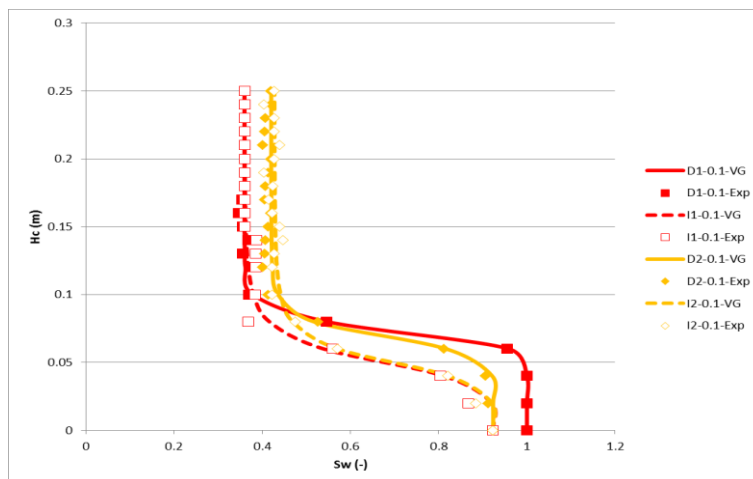
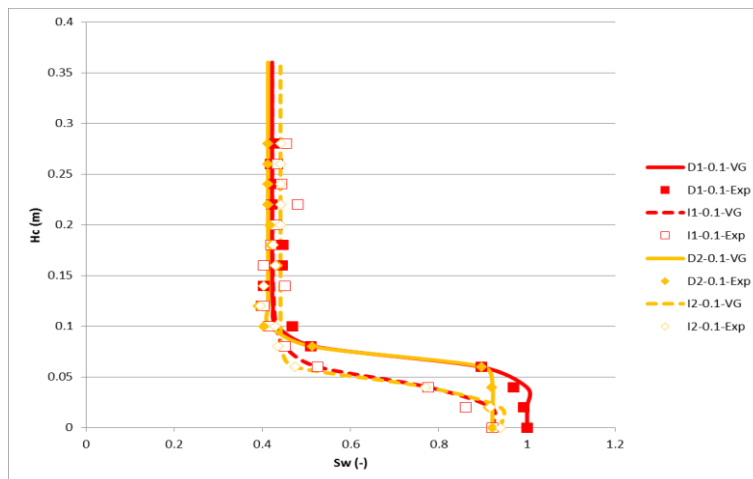
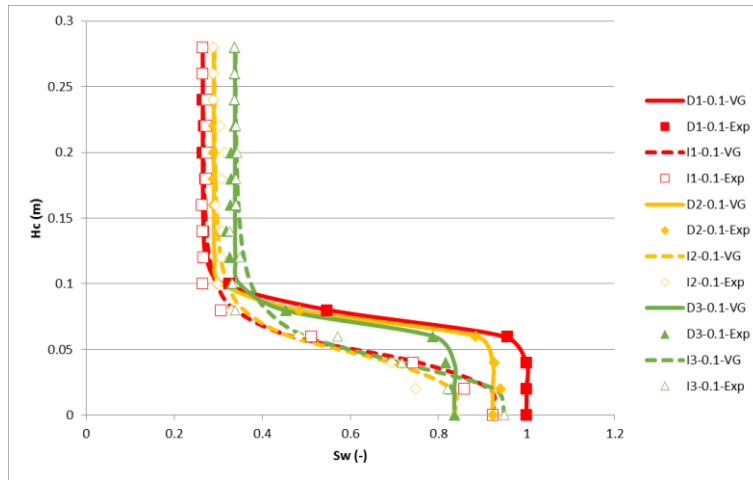
Drainage imbibition experiments for 0.5 and 0.1 mm GB without membrane

0.5 mm GB

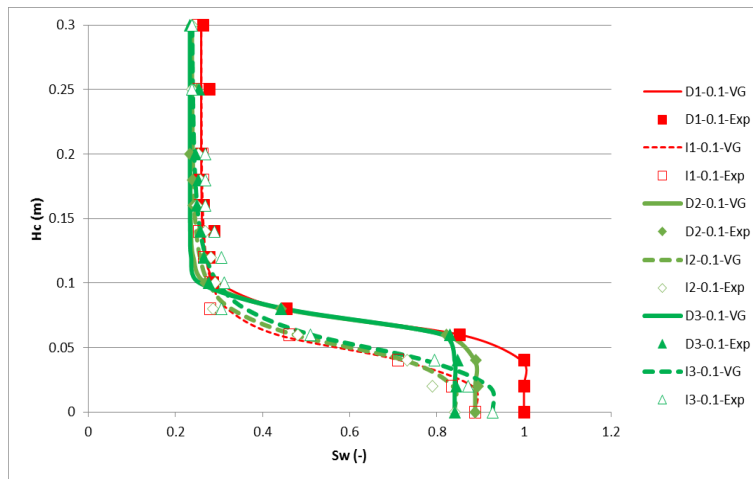
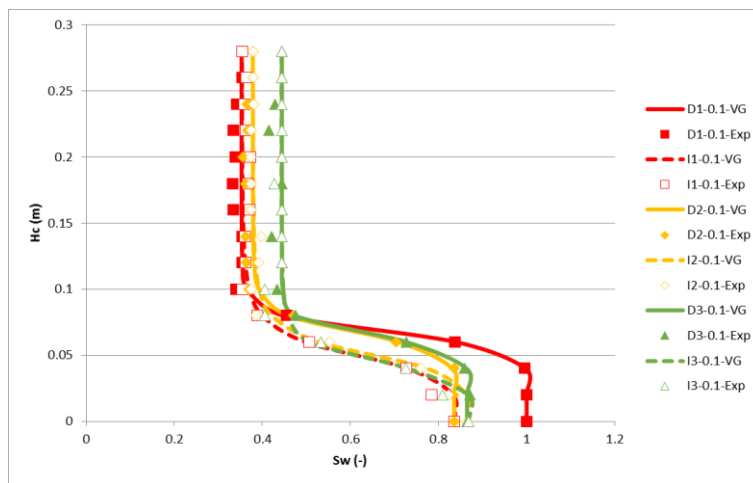
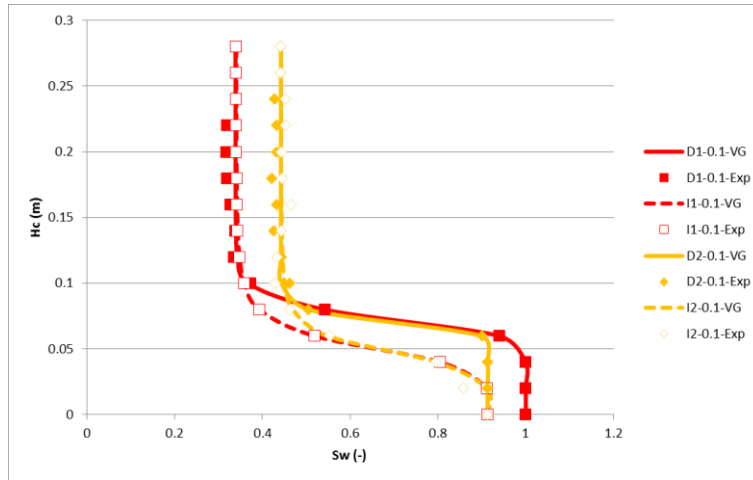


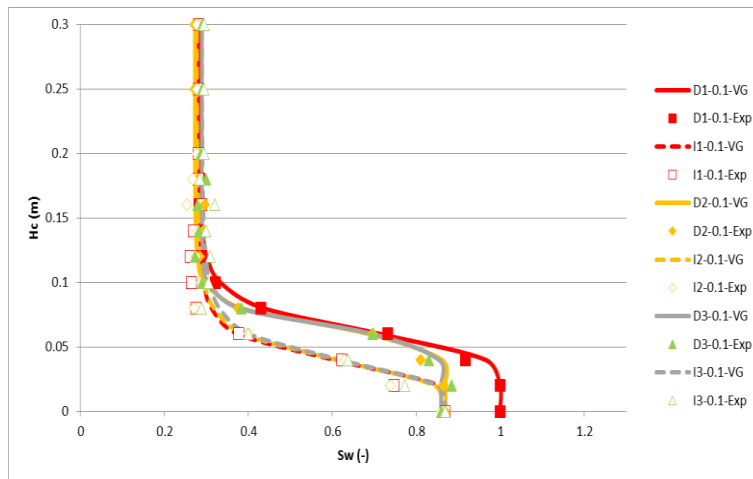
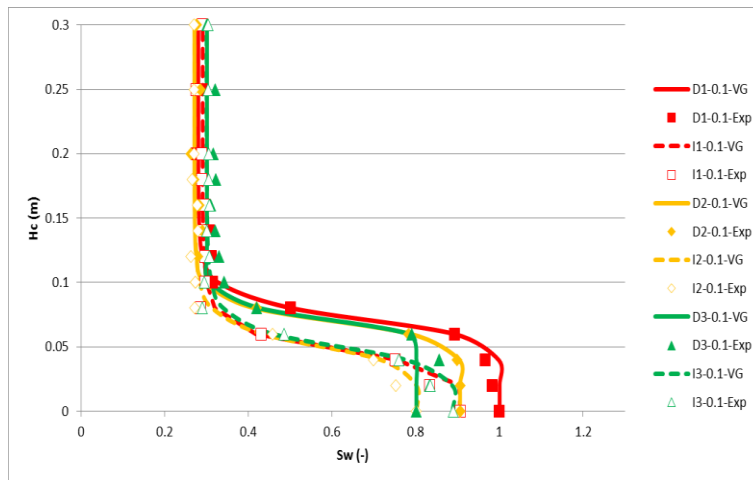
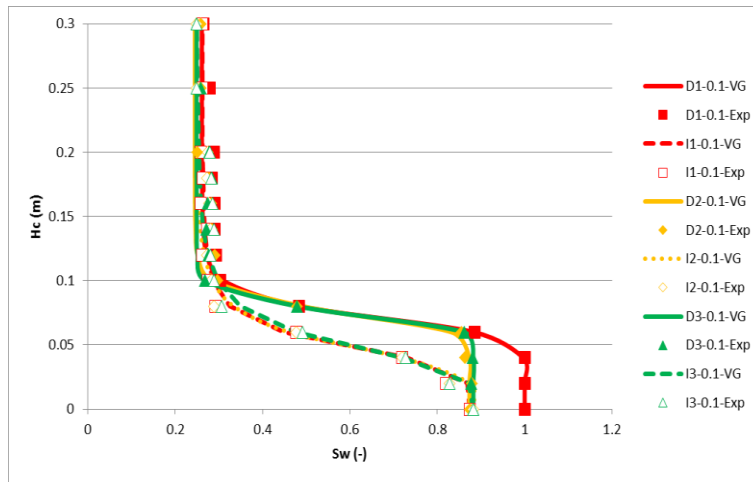


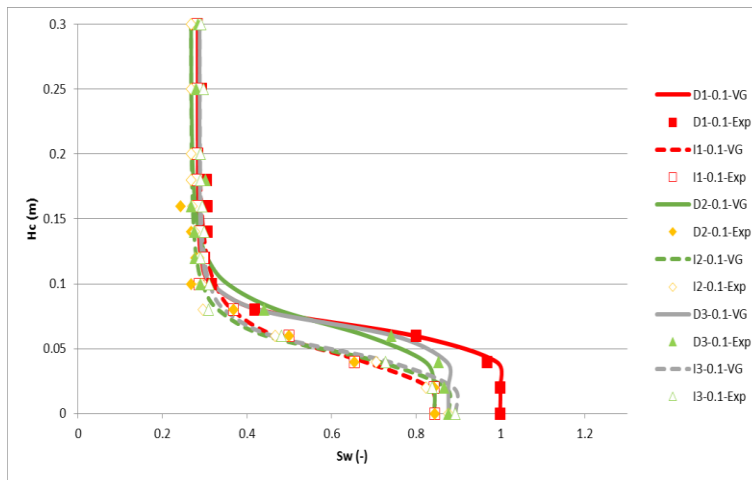
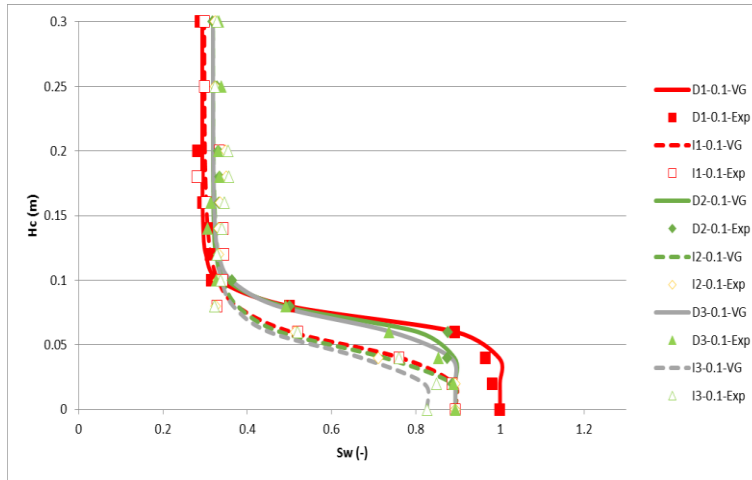
0.1 mm GB



Appendix 2





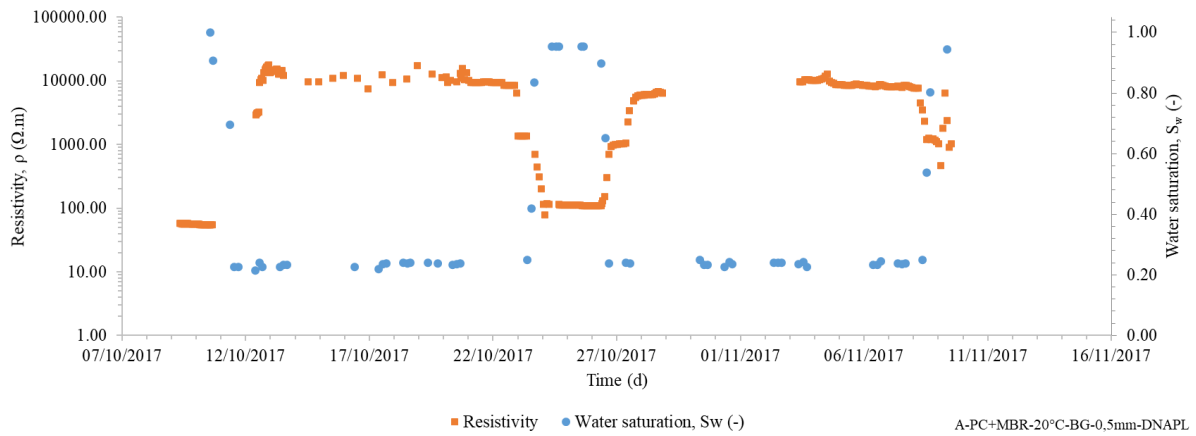
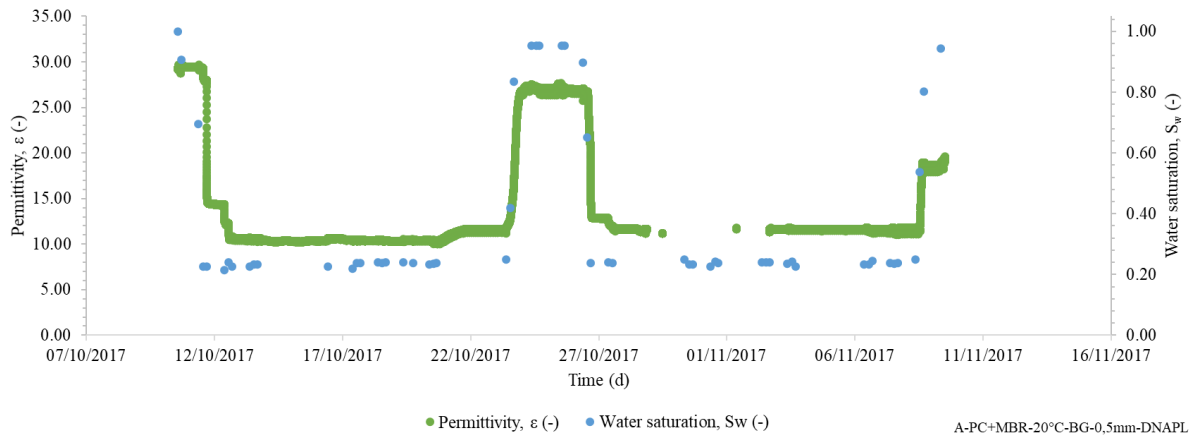


Appendix 2.4

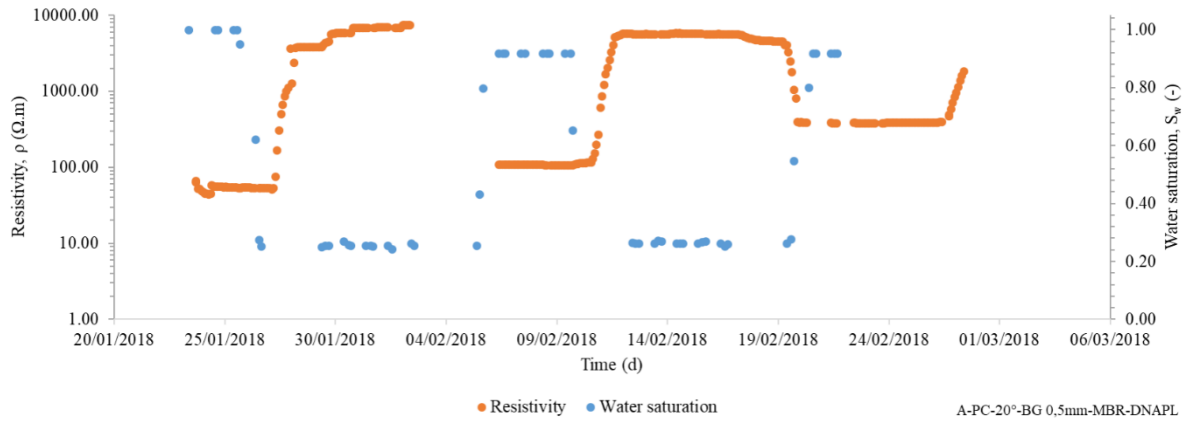
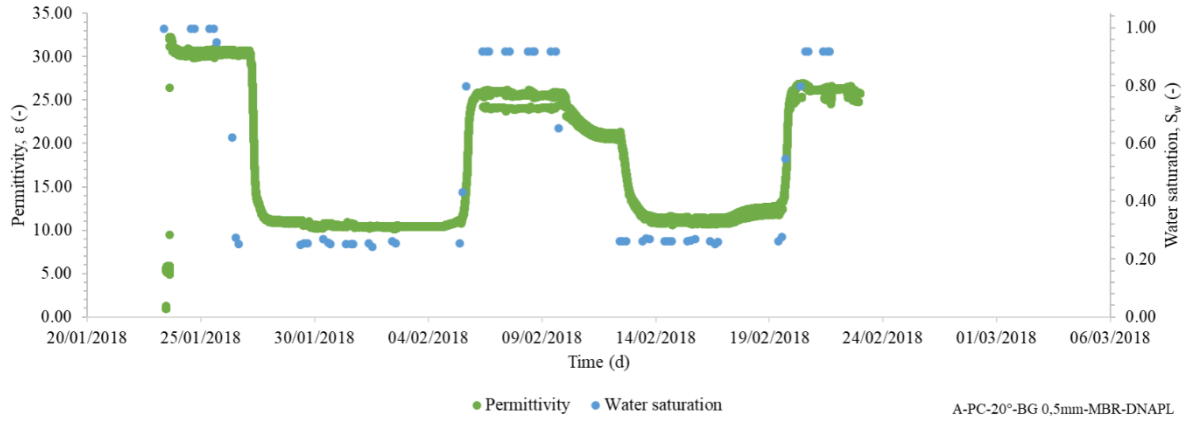
Permittivity and resistivity monitorings of the drainage-imbibition experiments with 0.5 and 0.1 mm GB with membrane

0.5 mm GB

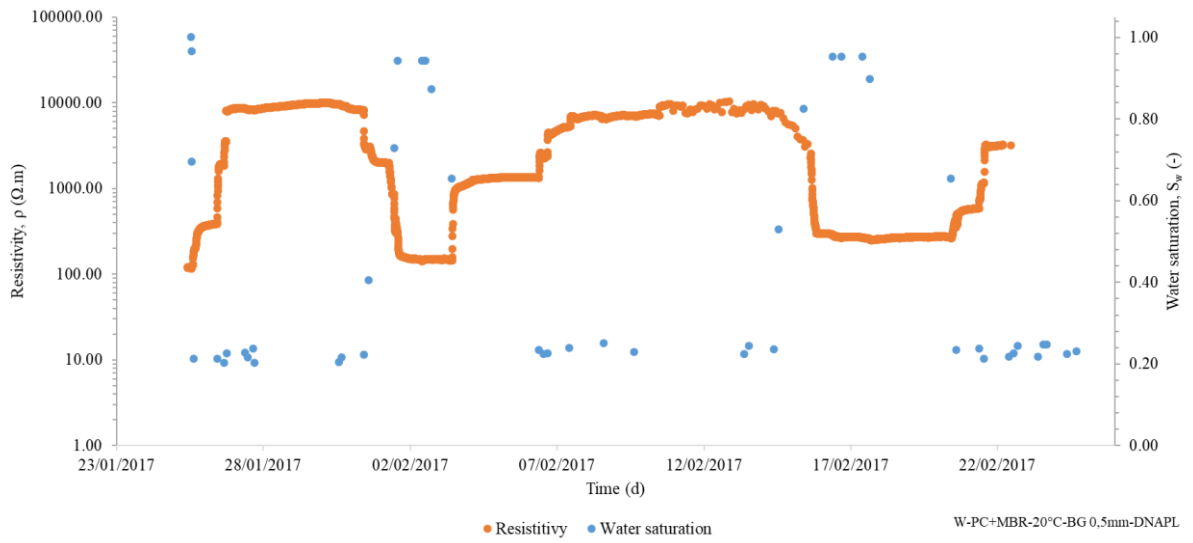
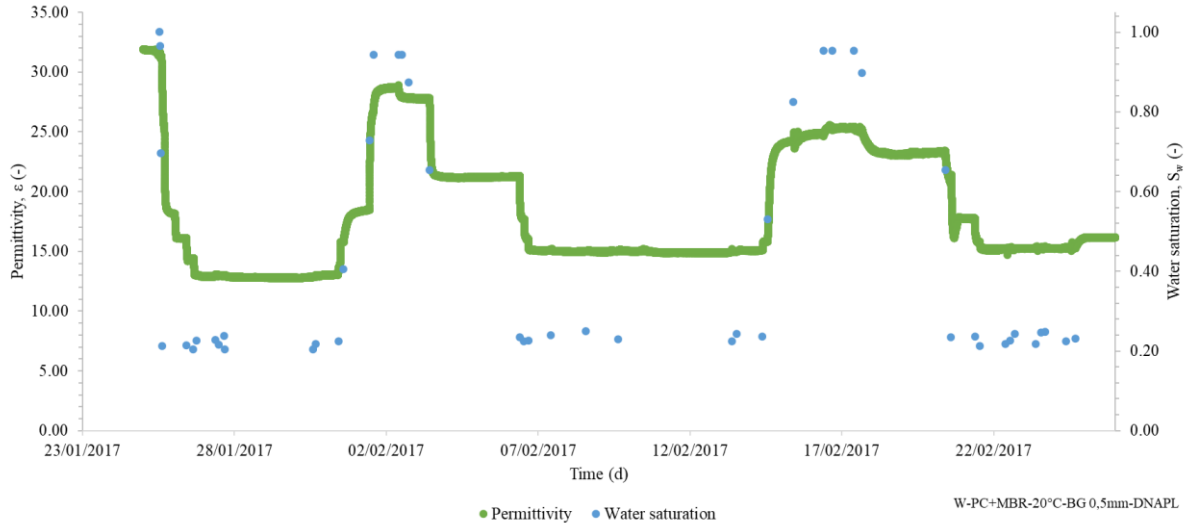
A-PC+MBR-20°C-BG-0,5mm-DNAPL



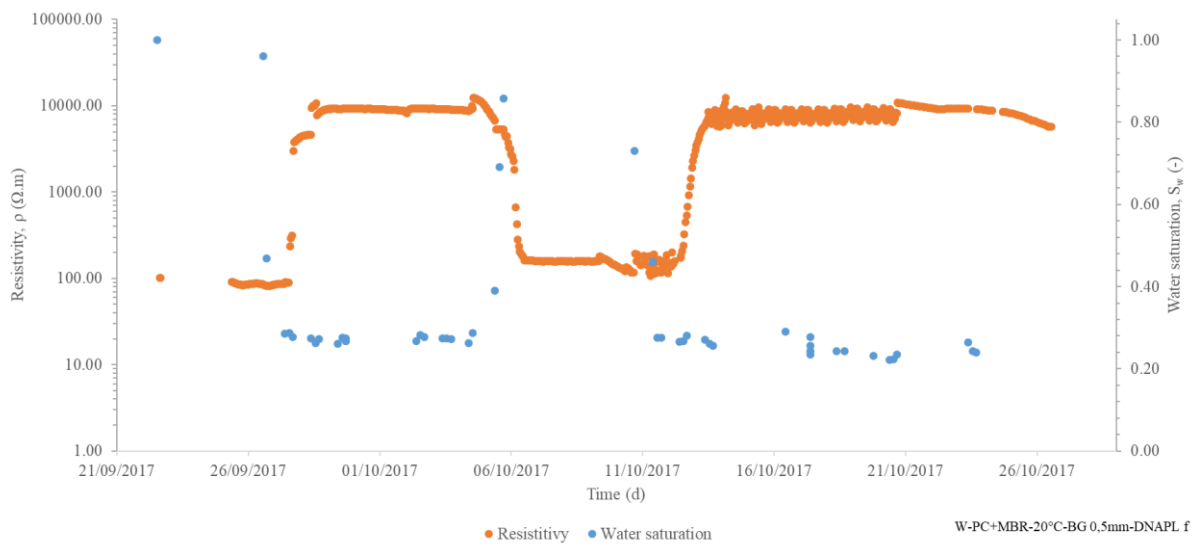
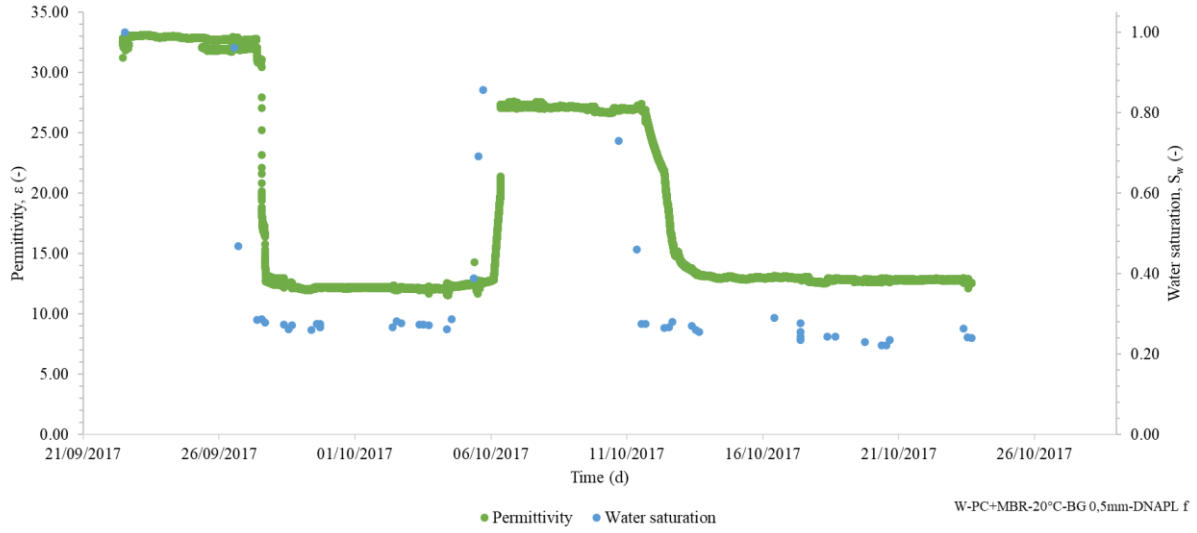
A-PC-20°-BG 0,5mm-MBR-DNAPL



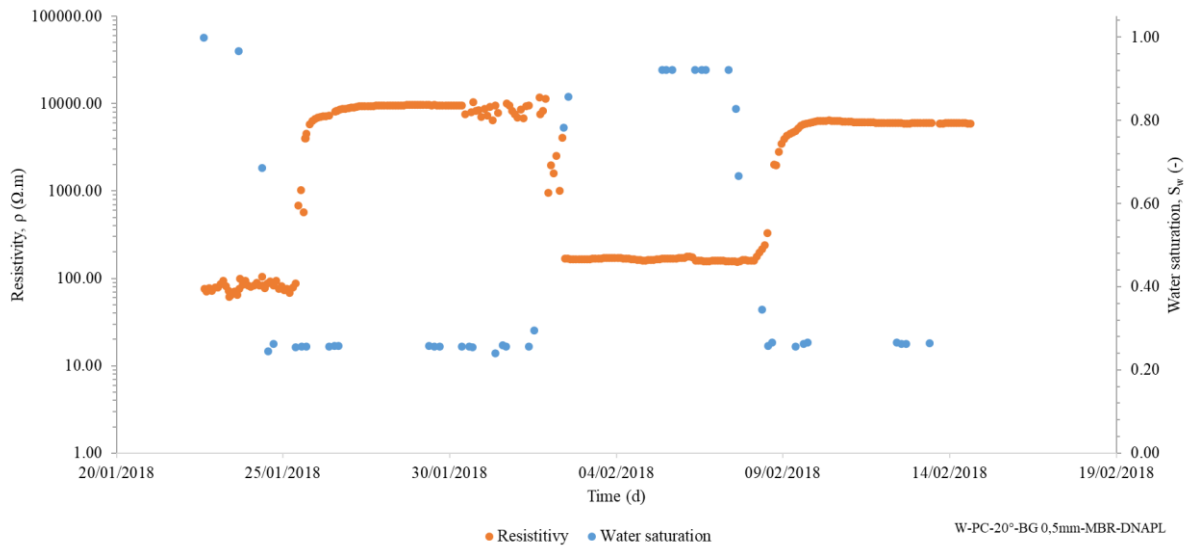
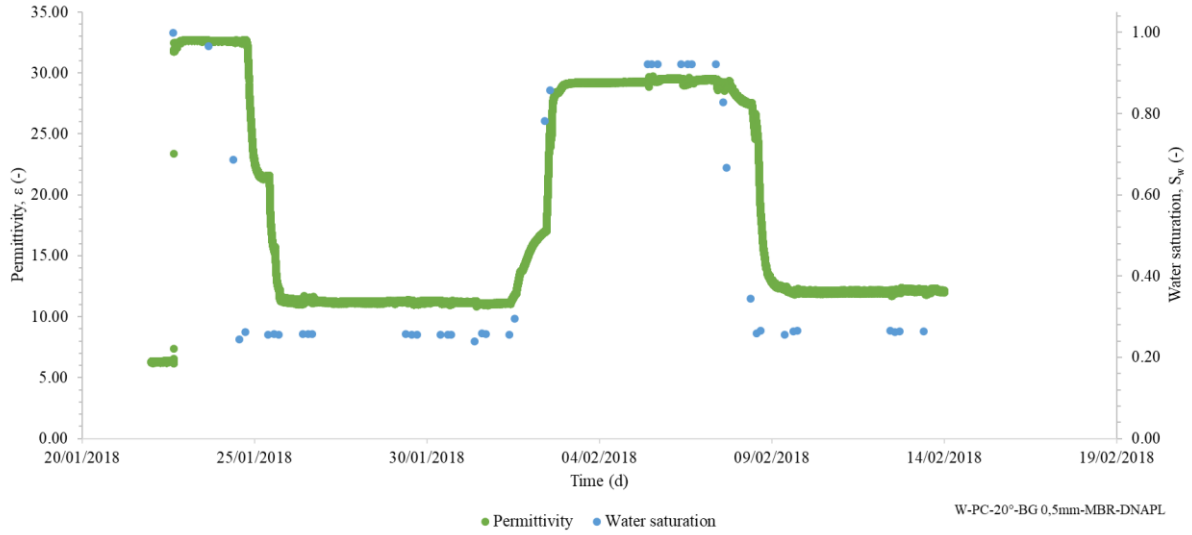
W-PC+MBR-20°C-BG 0,5mm-DNAPL



W-PC+MBR-20°C-BG 0,5mm-DNAPL f

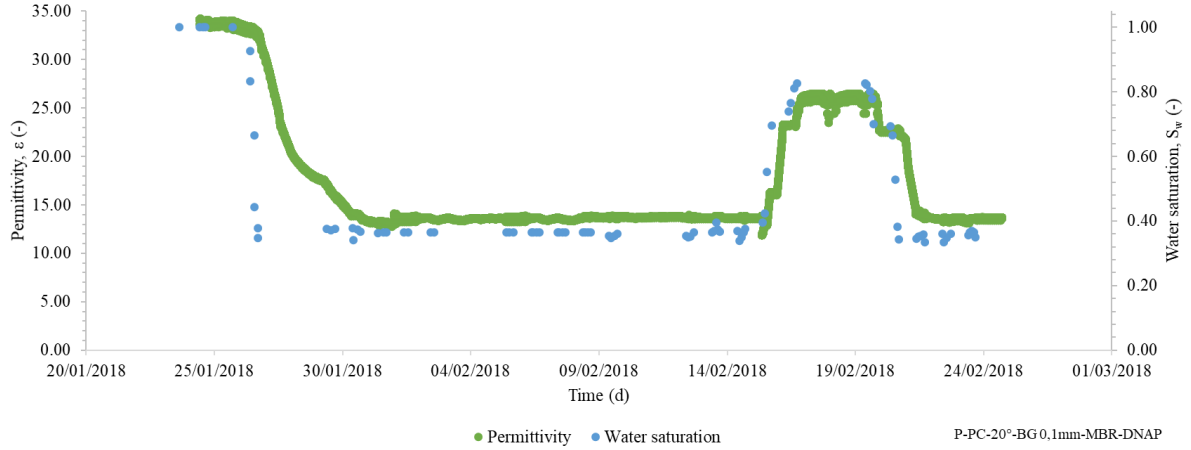


W-PC-20°-BG 0,5mm-MBR-DNAPL

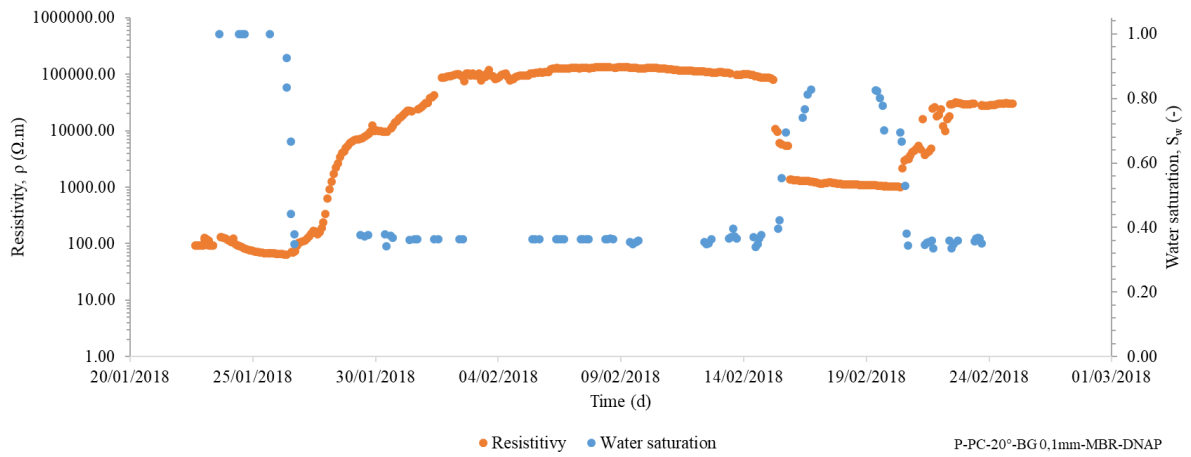


0.1 mm GB

P-PC-20°-BG 0,1mm-MBR-DNAP

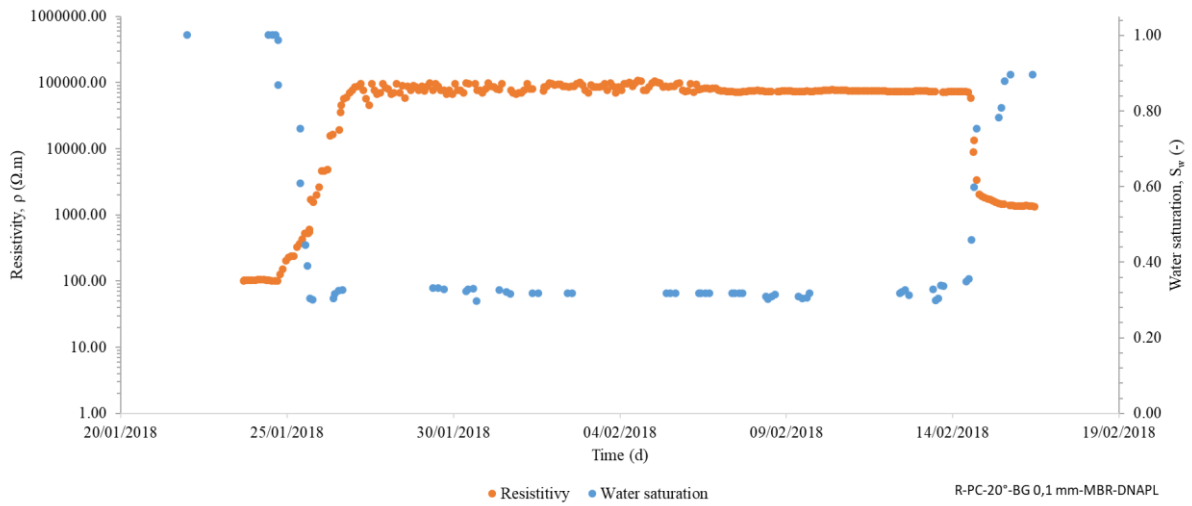
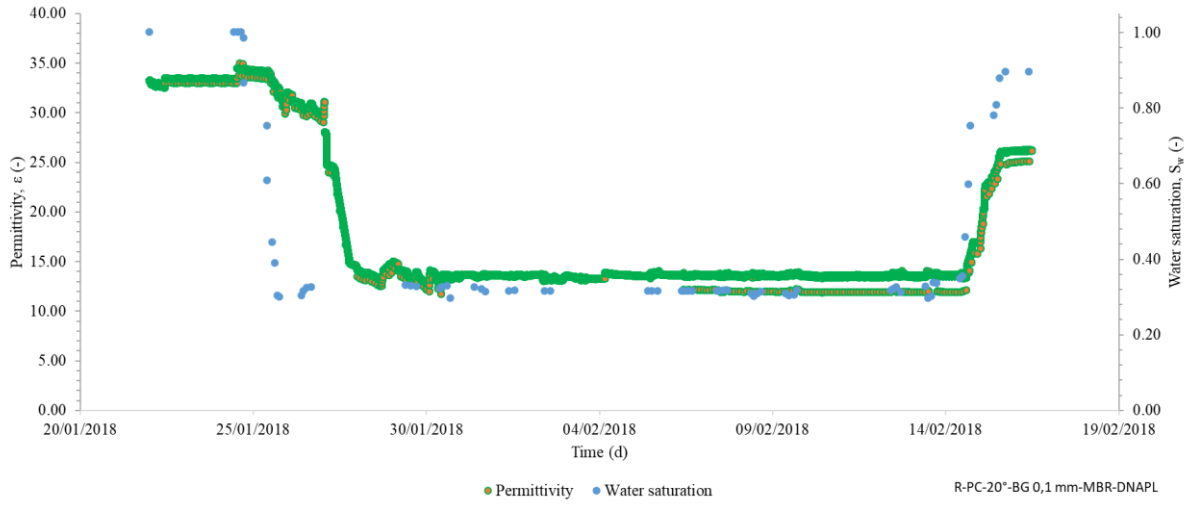


● Permittivity ● Water saturation P-PC-20°-BG 0,1mm-MBR-DNAP

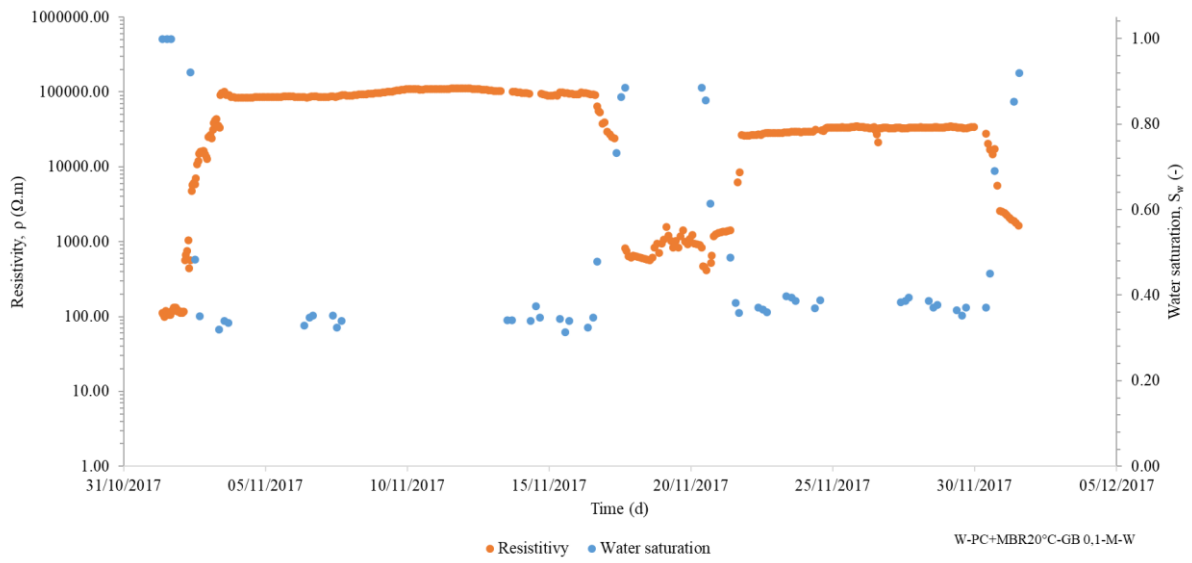
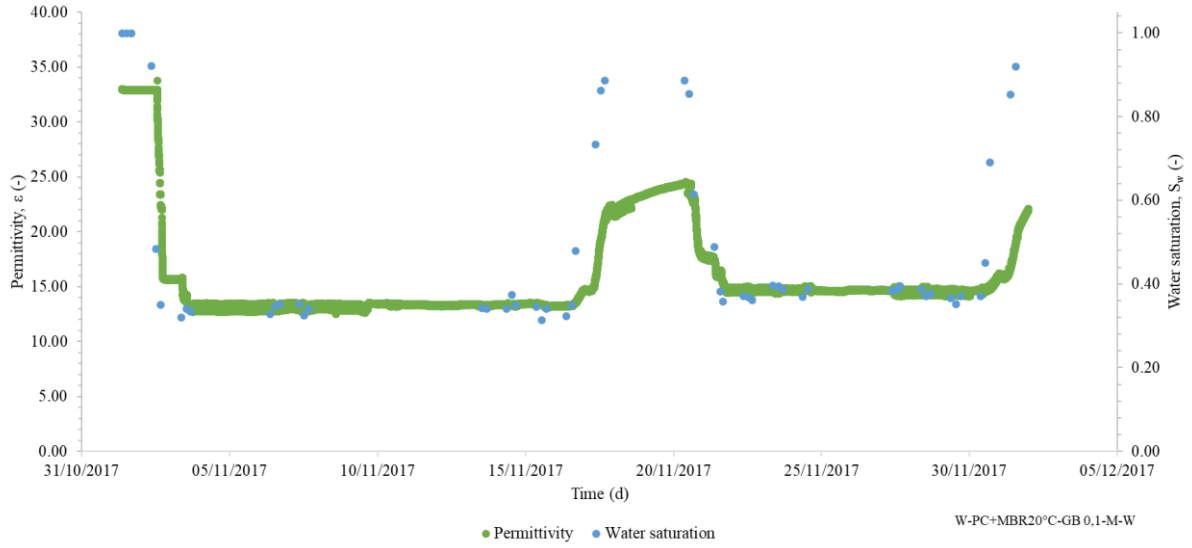


● Resistivity ● Water saturation P-PC-20°-BG 0,1mm-MBR-DNAP

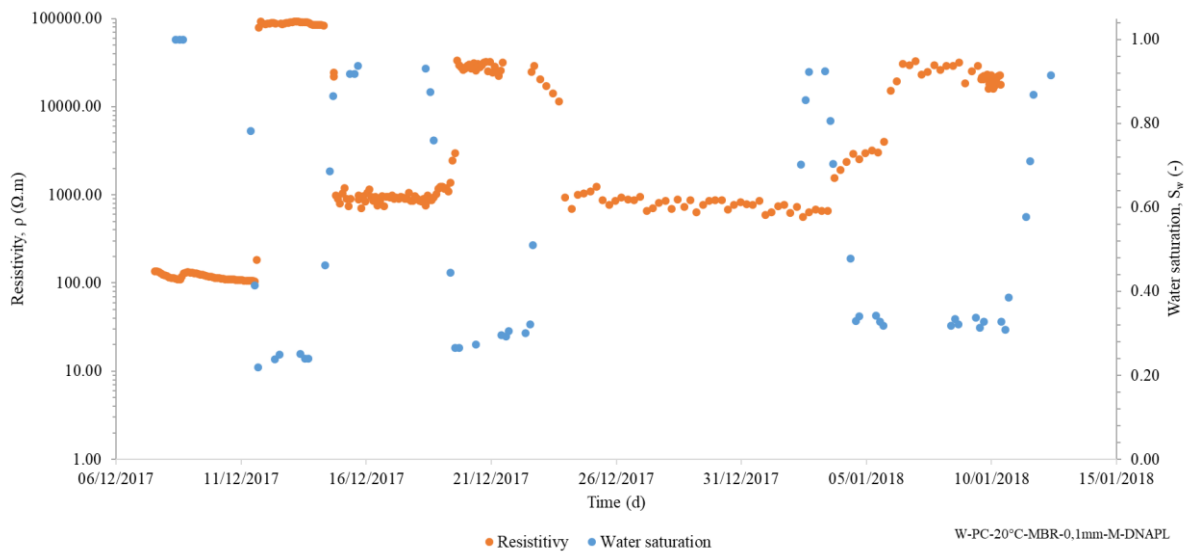
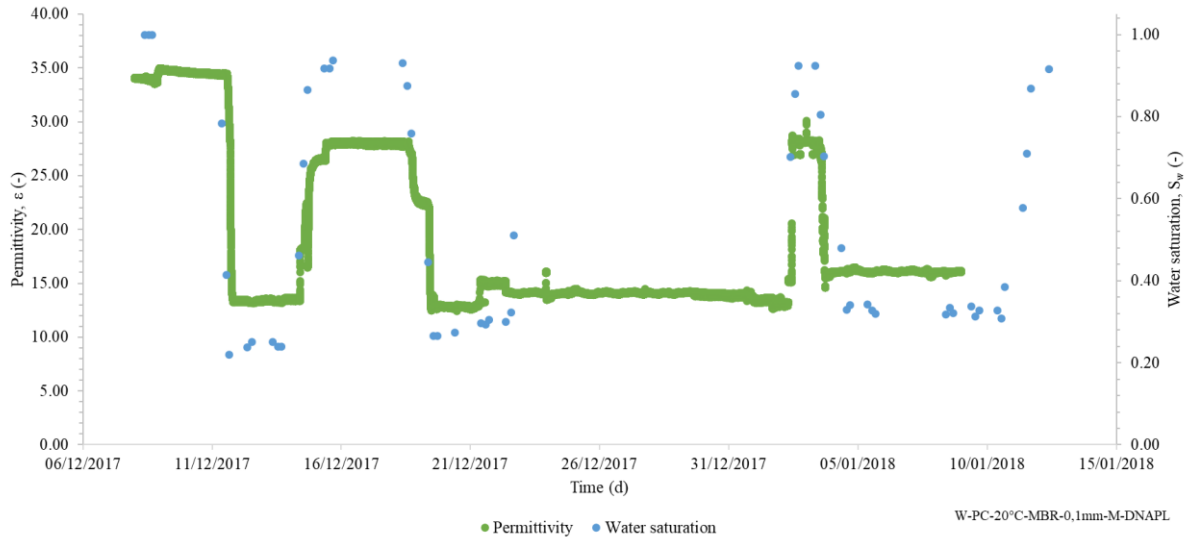
R-PC-20°-BG 0,1 mm-MBR-DNAPL



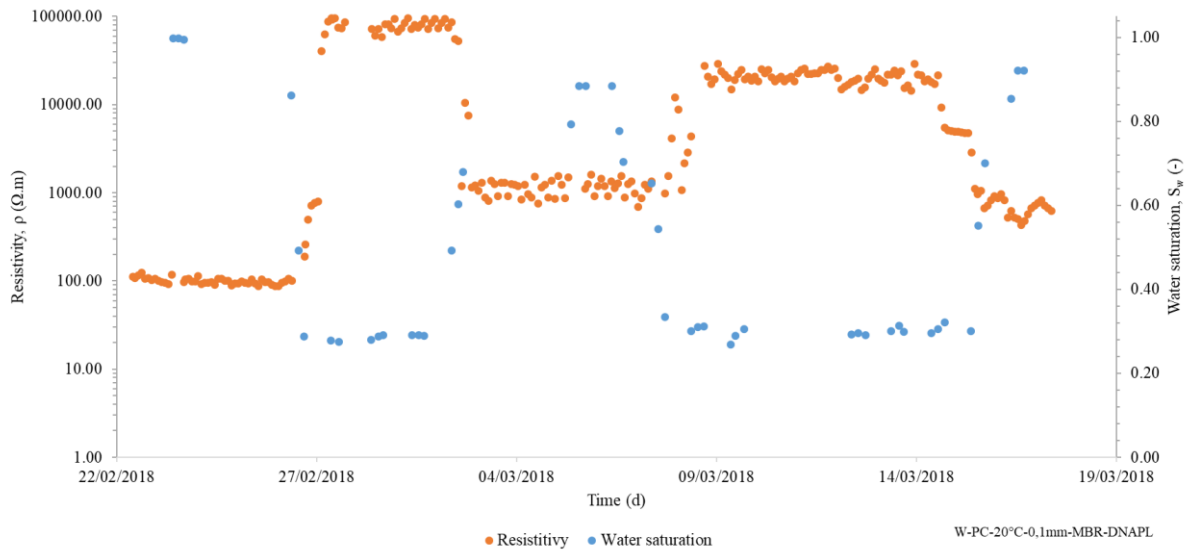
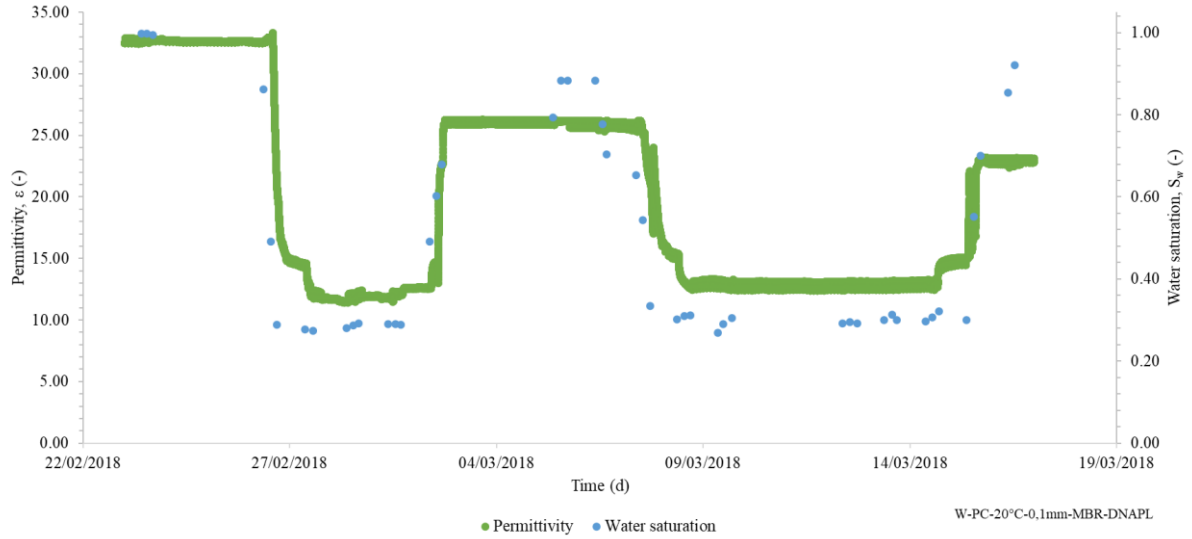
W-PC+MBR20°C-GB 0,1-M-W



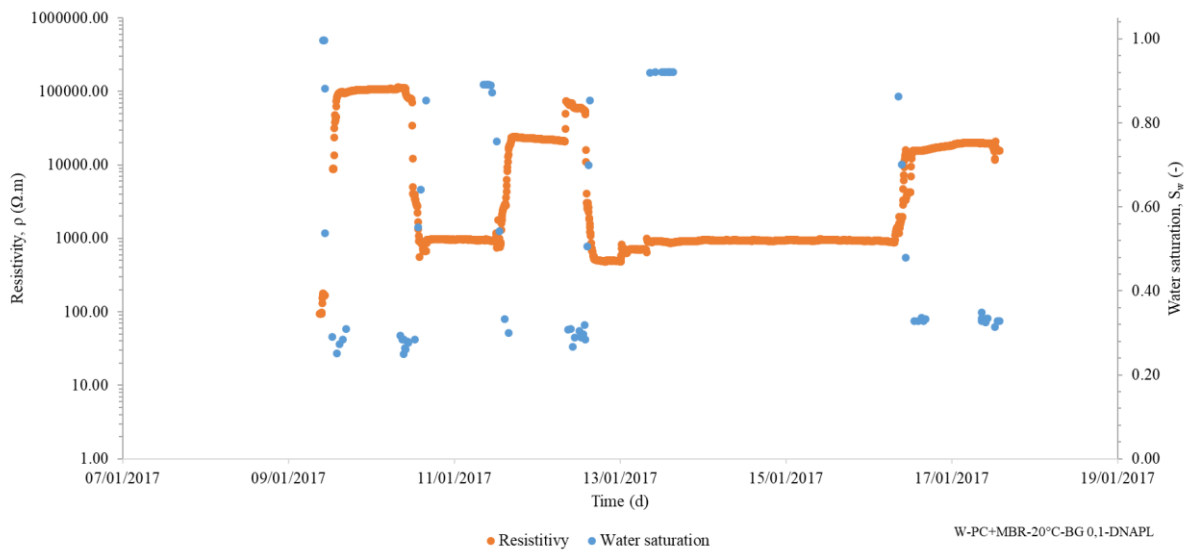
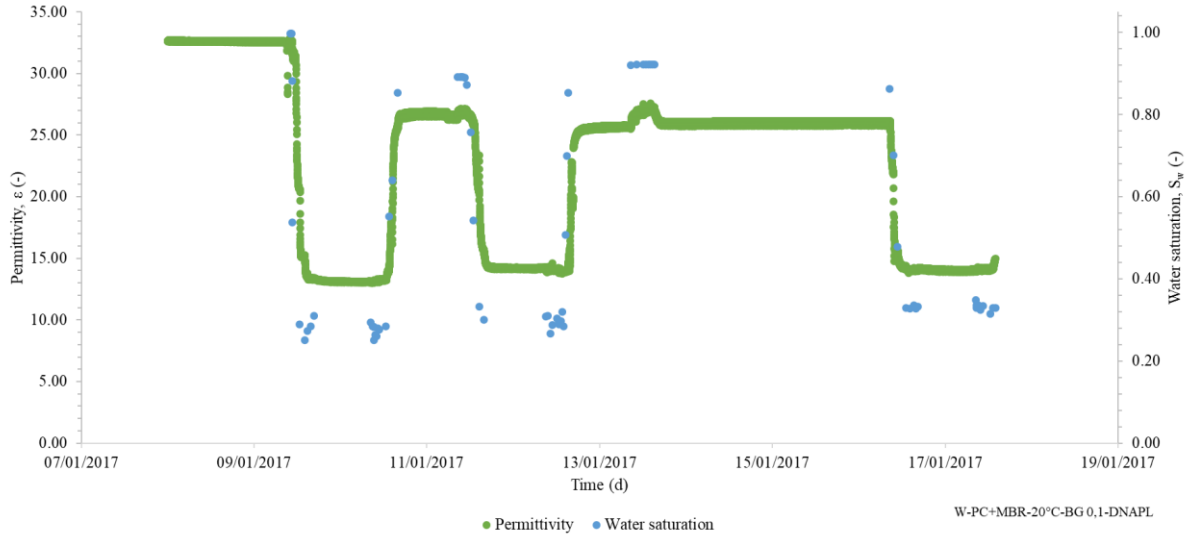
W-PC-20°C-MBR-0,1mm-M-DNAPL



W-PC-20°C-0,1mm-MBR-DNAPL



W-PC+MBR-20°C-BG 0,1DNAPL

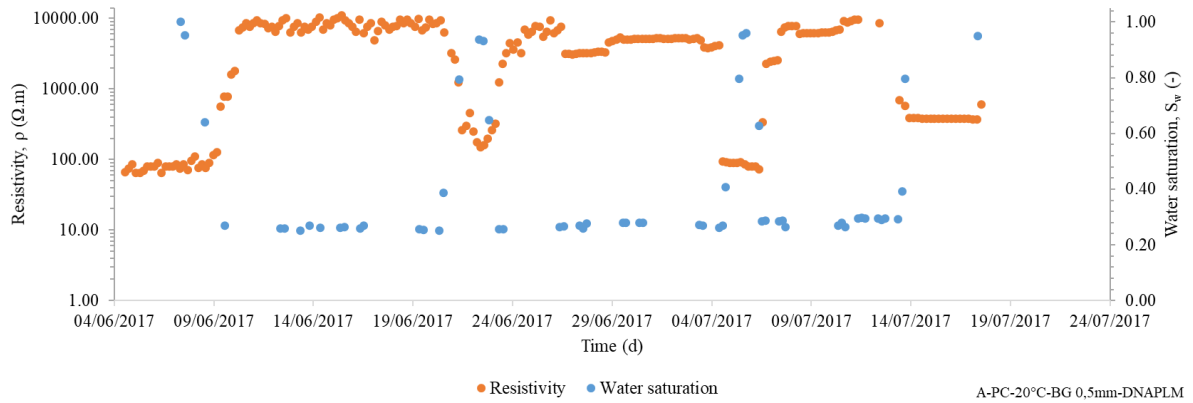
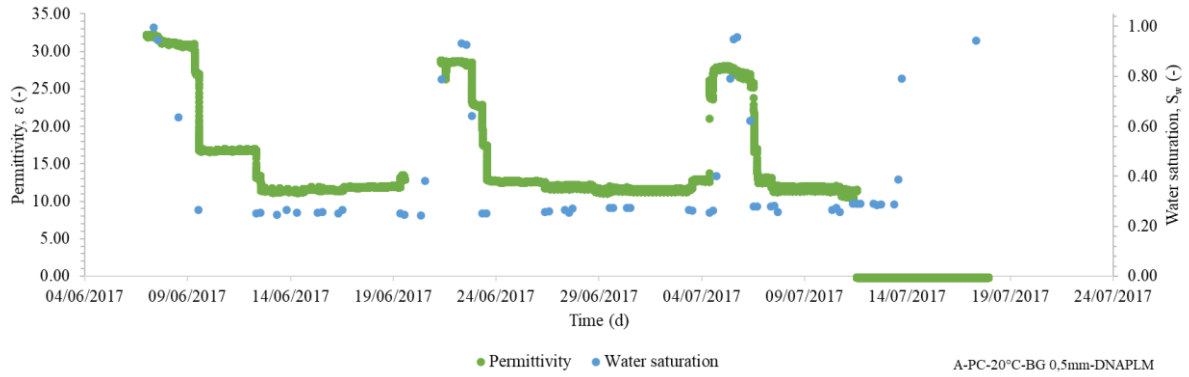


Appendix 2.5

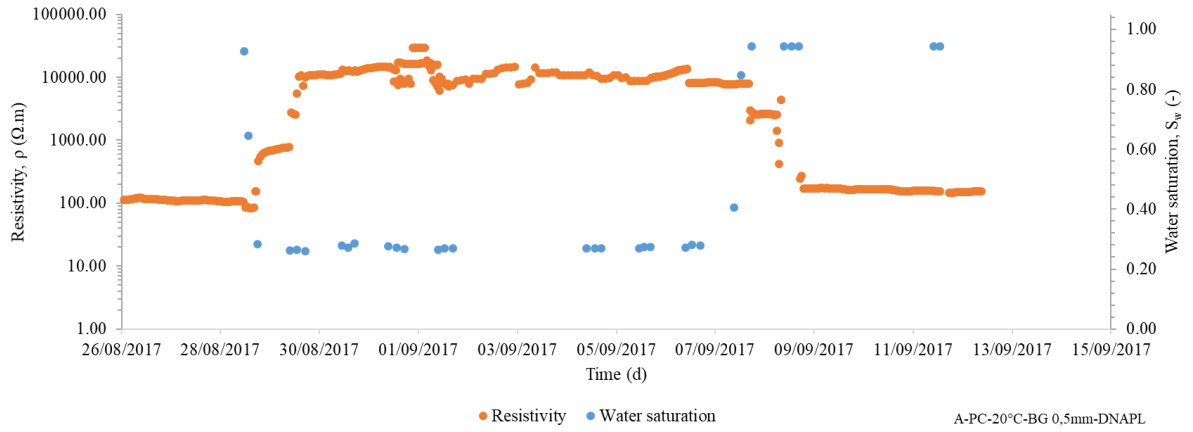
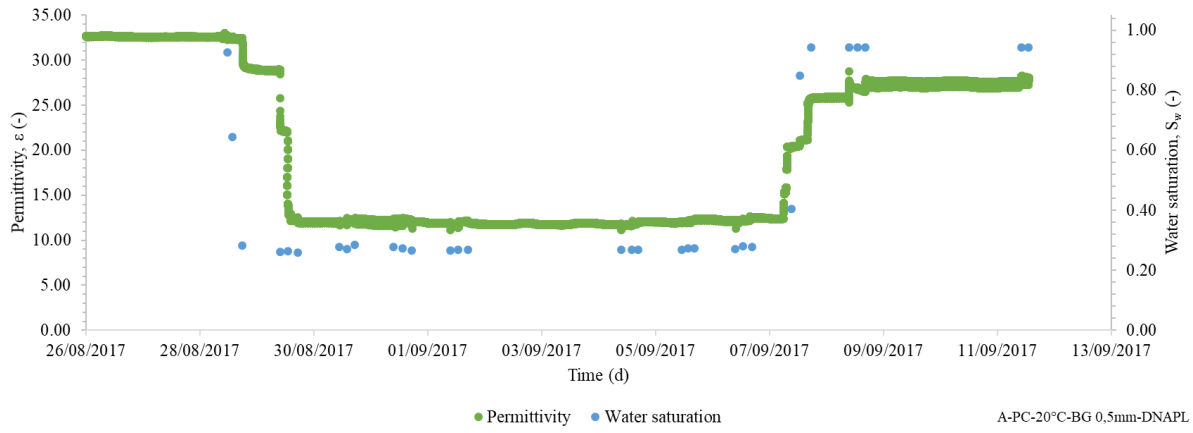
Permittivity and resistivity monitorings of the drainage-imbibition experiments with 0.5 and 0.1 mm GB without membrane

0.5 mm GB

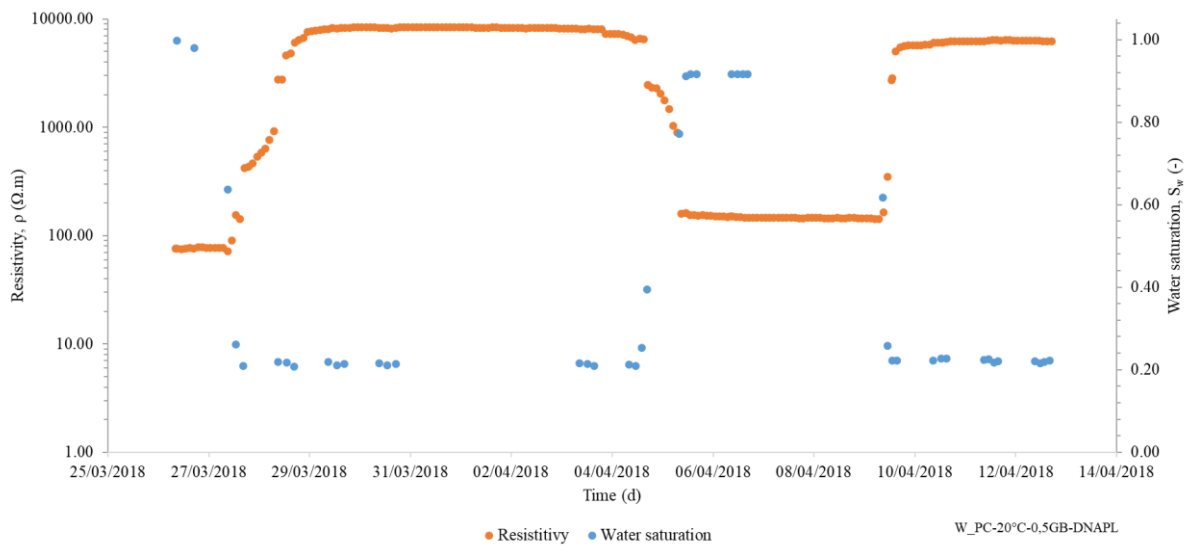
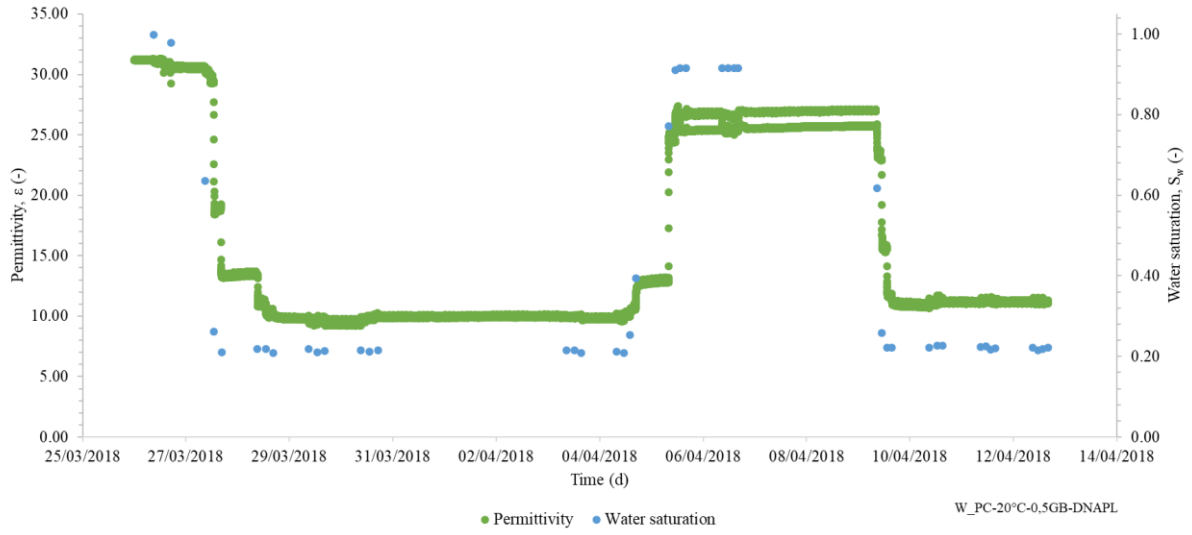
A-PC-20°C-BG 0,5mm-DNAPLM



A-PC-20°C-BG 0,5mm-DNAPL

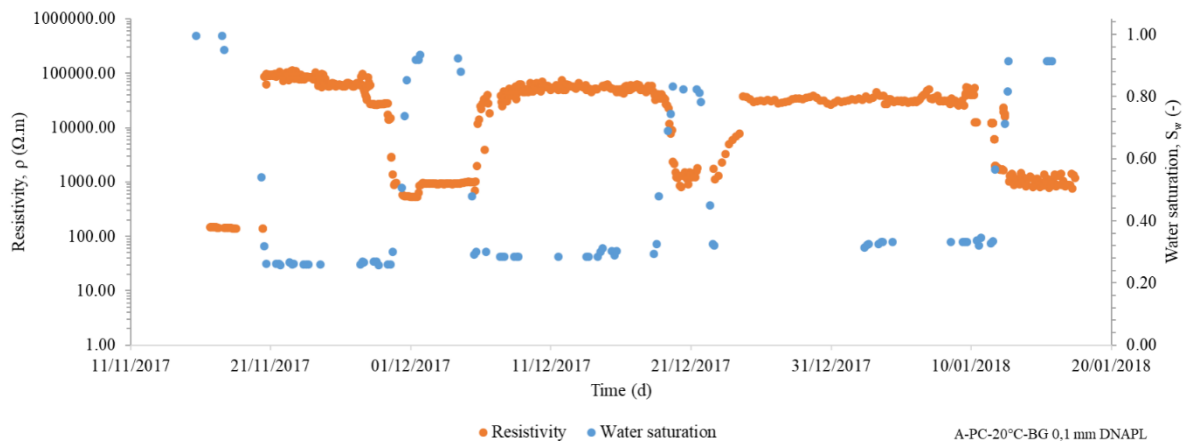
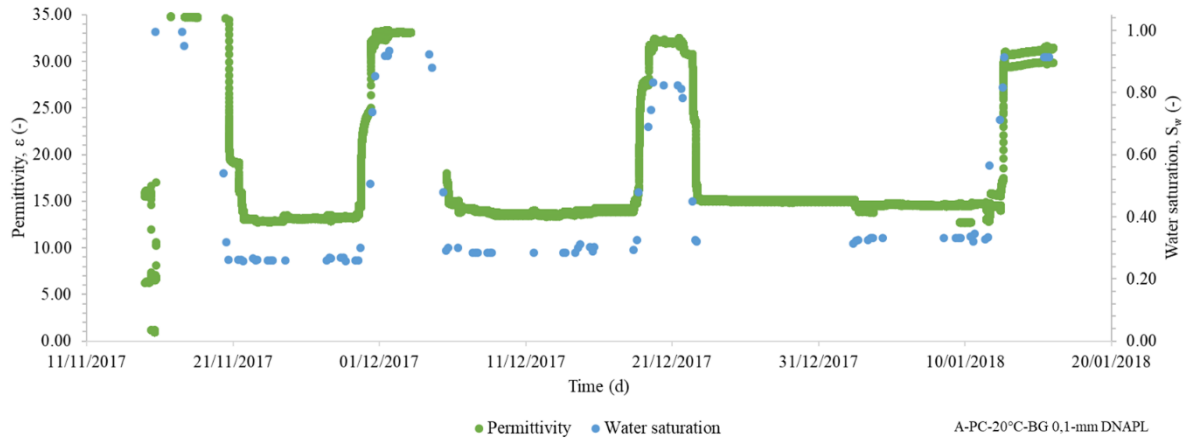


W_PC-20°C-0,5GB-DNAPL

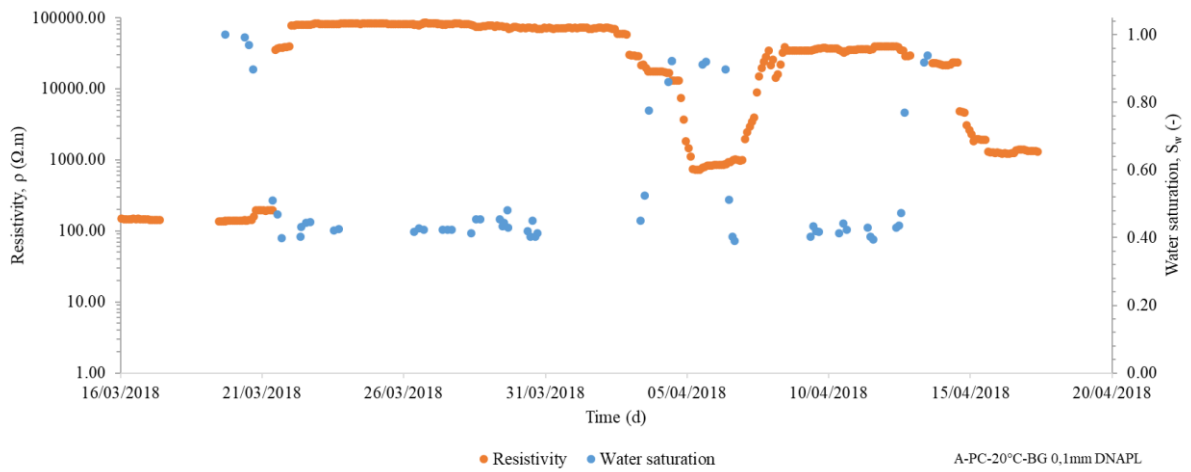
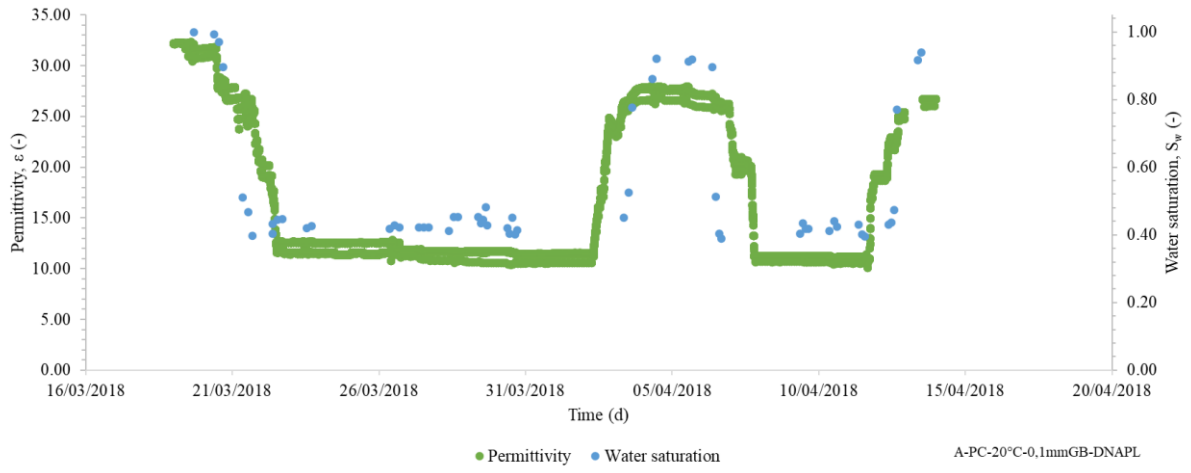


0.1 mm GB

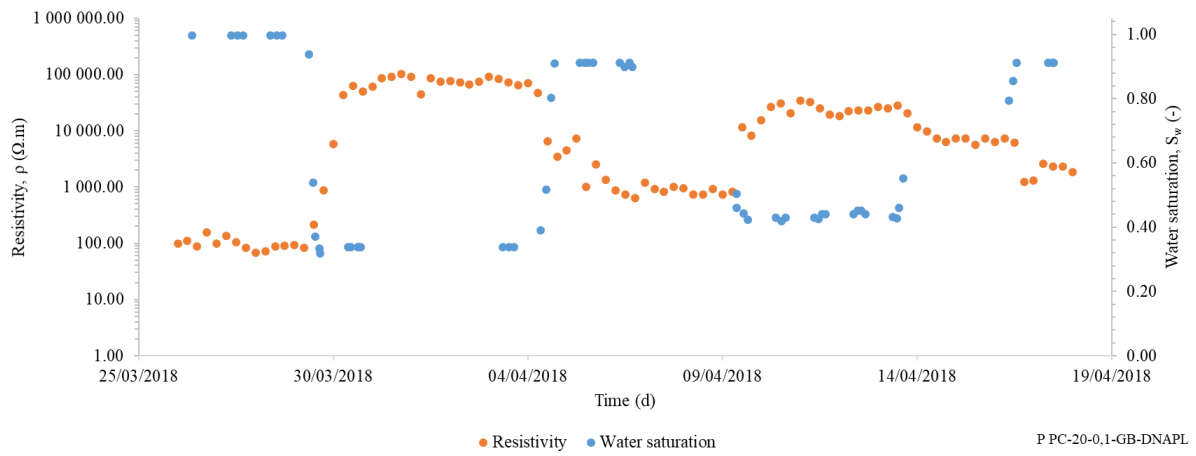
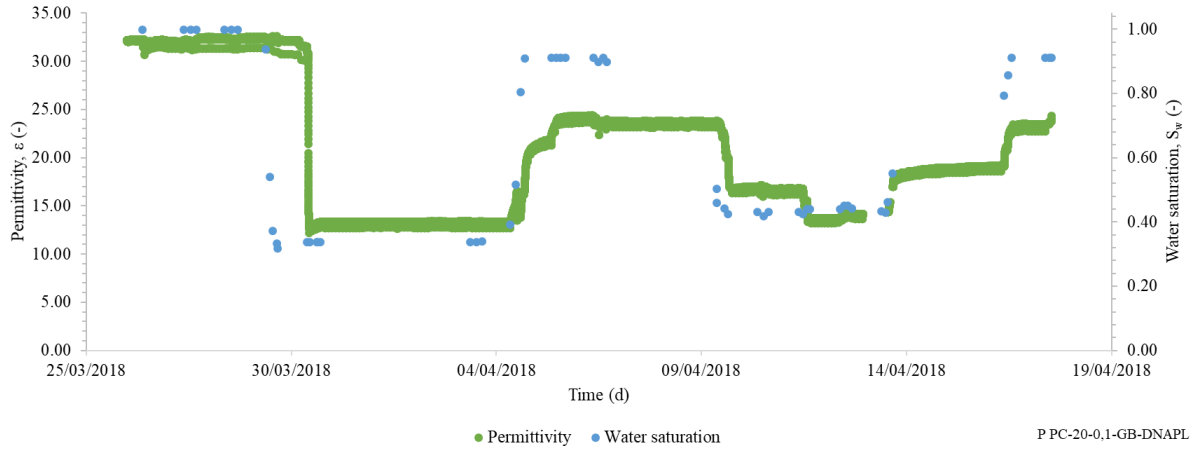
A-PC-20°C-BG 0,1mm DNAPL



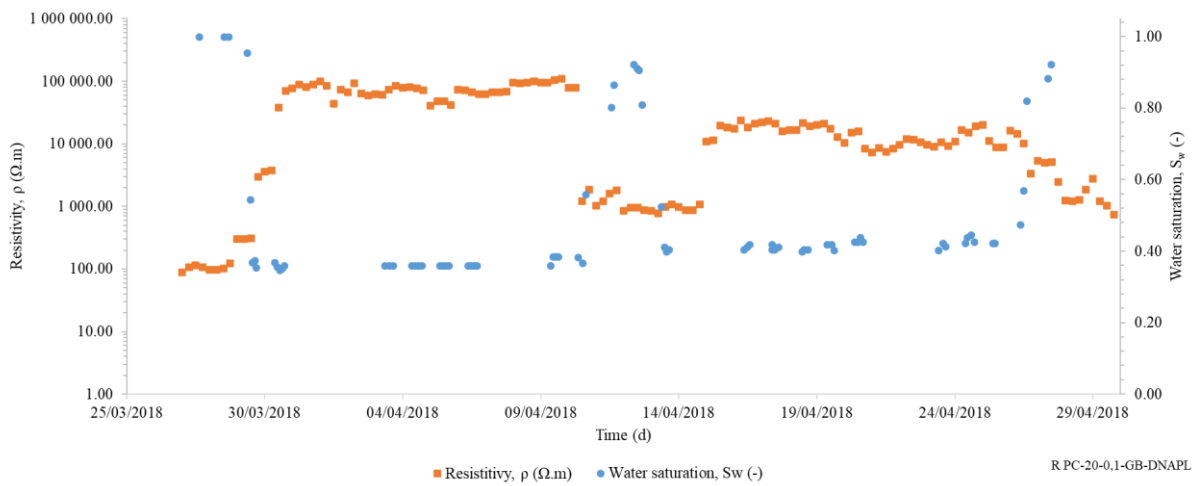
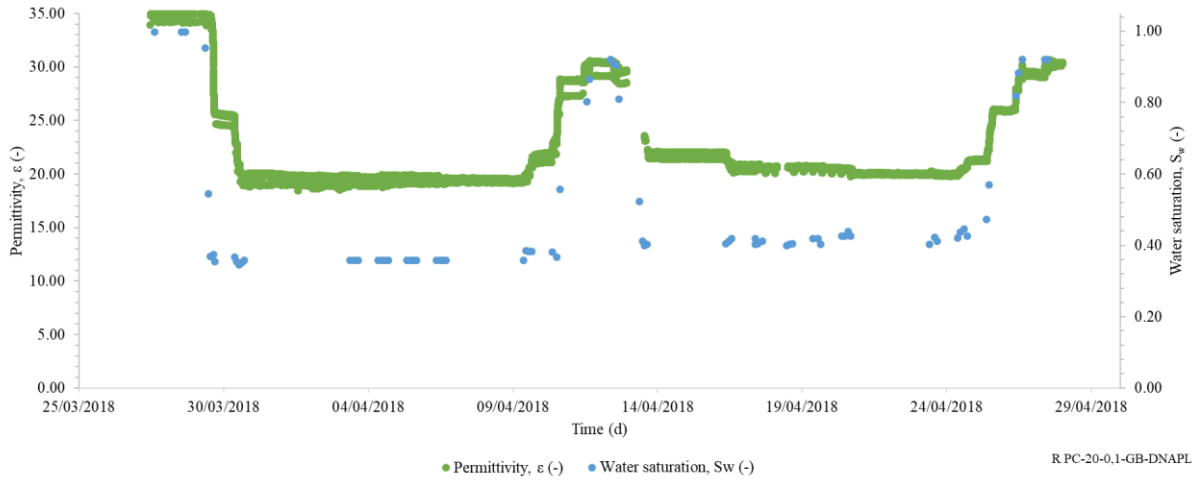
A-PC-20°C-0.1mmGB-DNAPL



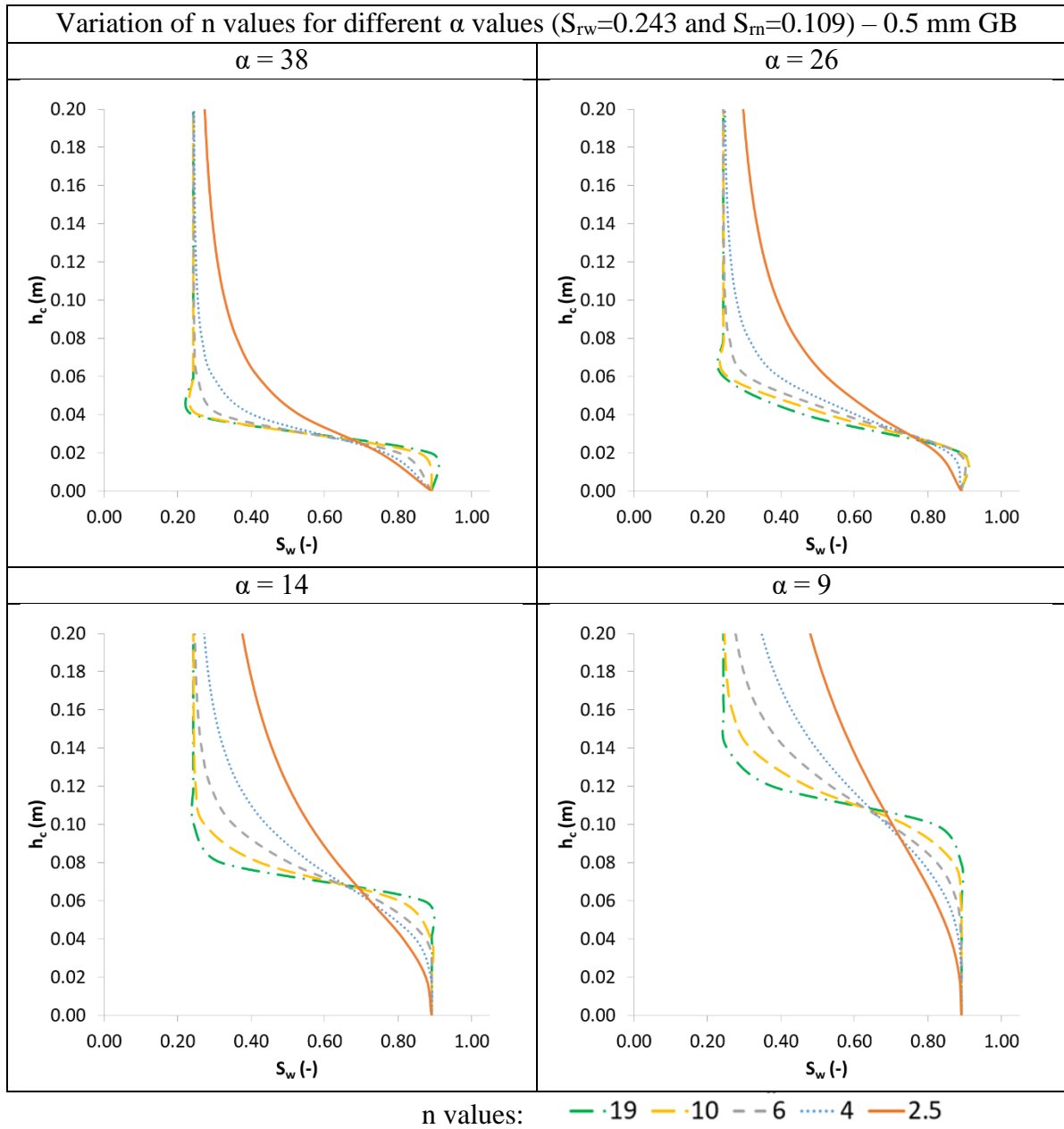
P PC-20-0,1-GB-DNAPL

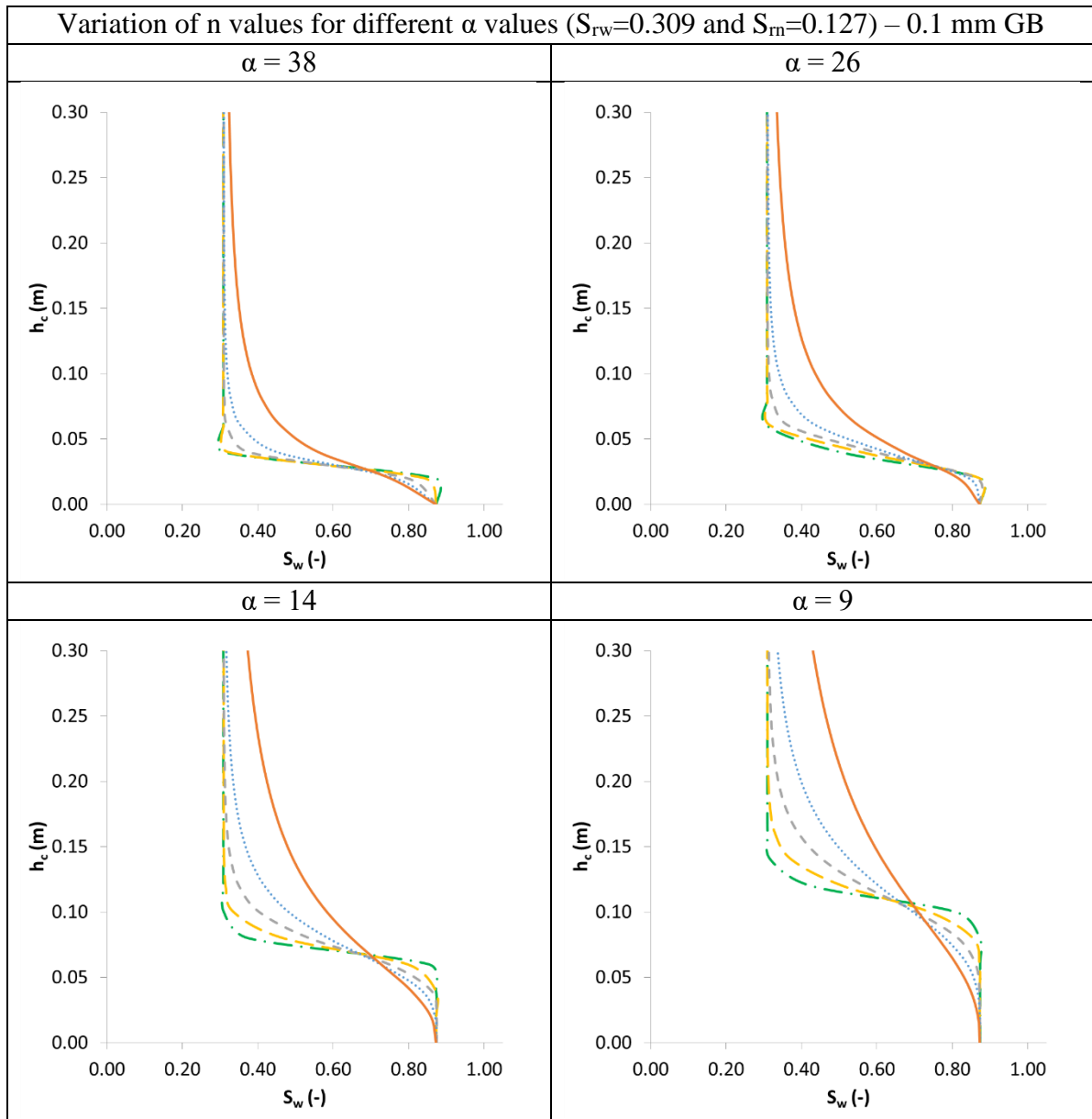


R PC-20-0,1-GB-DNAPL



Appendix 2.6
Sensitivity tests for van Genuchten-Mualem model





n values: — 19 — 10 — 6 4 — 2.5

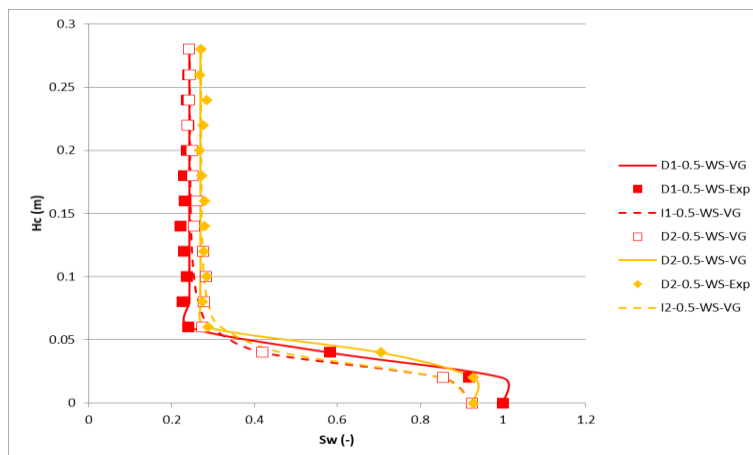
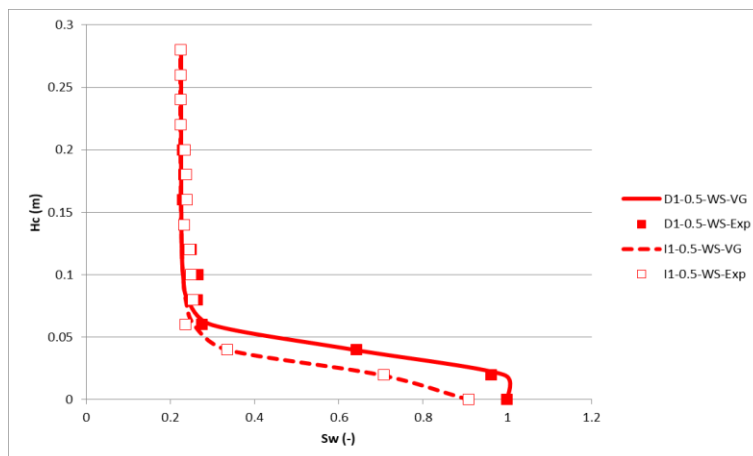
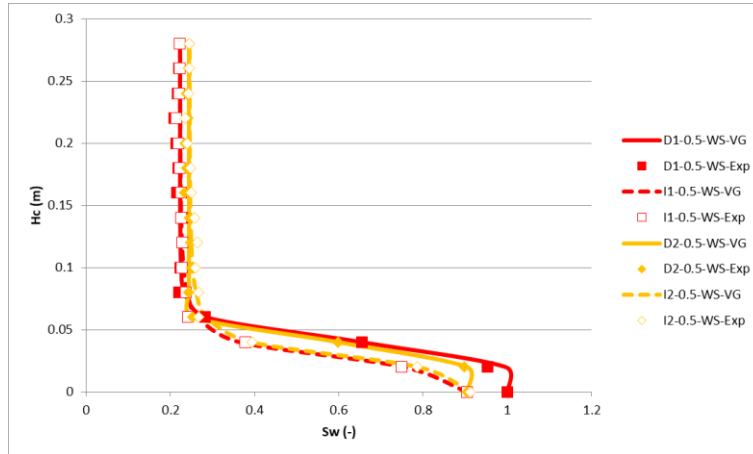
Appendix 3

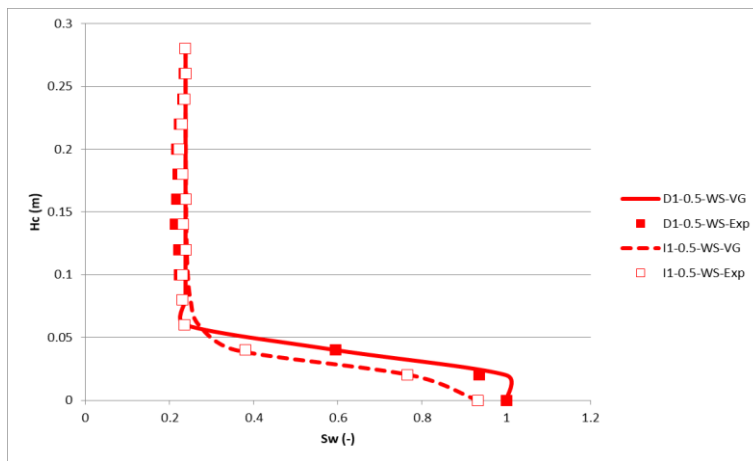
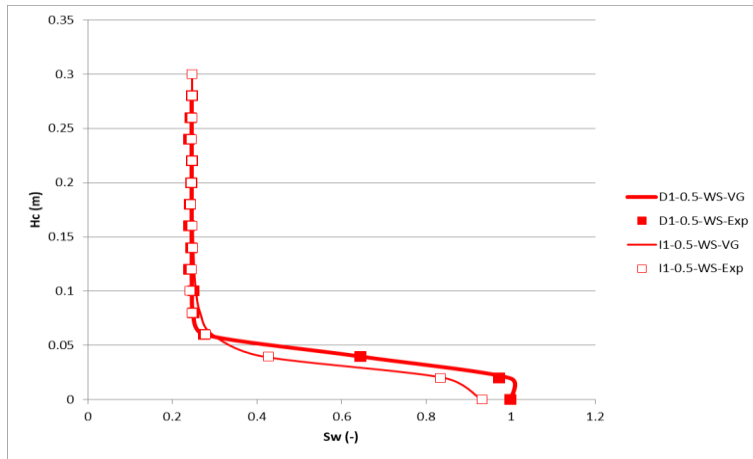
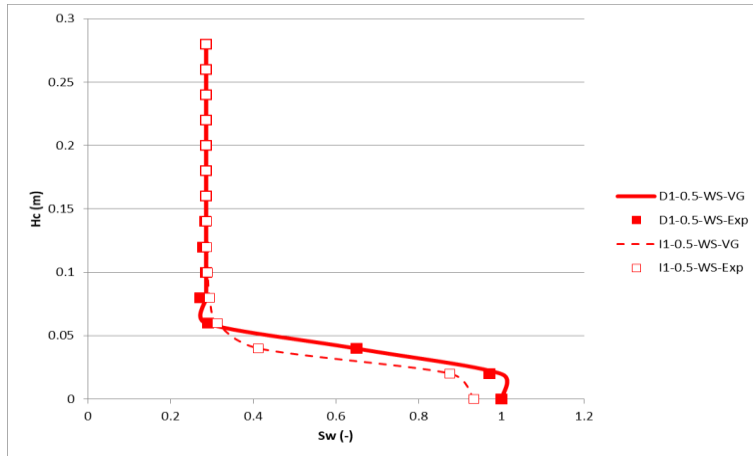
1D cells experiments with chemical enhancement

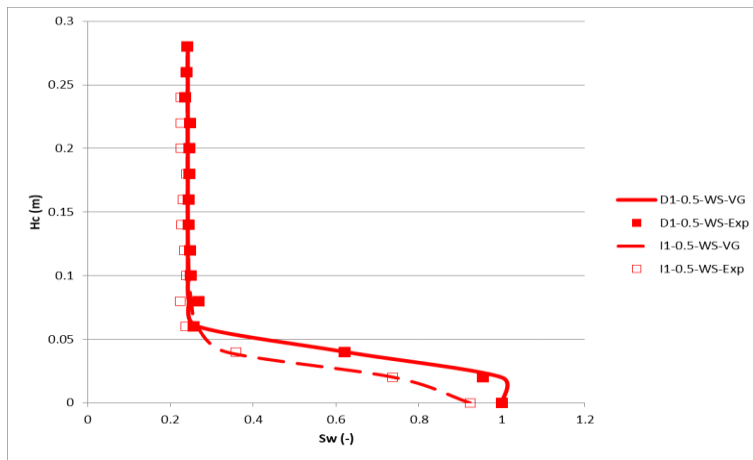
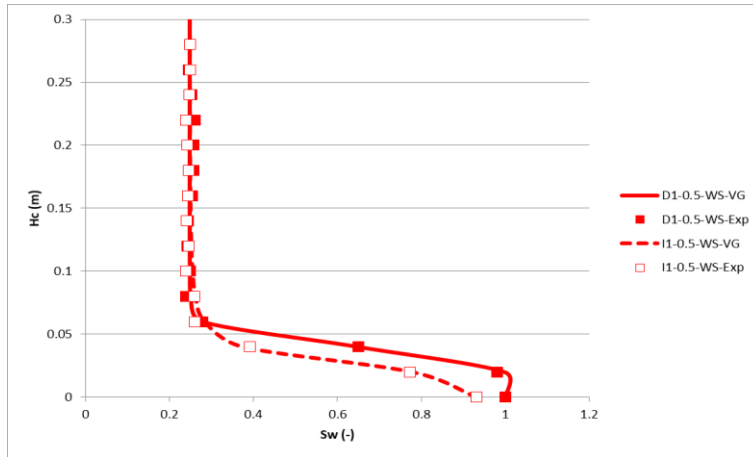
Appendix 3.1

Drainage-imbibition experiments for 0.5 and 0.1 mm GB with chemical enhancement

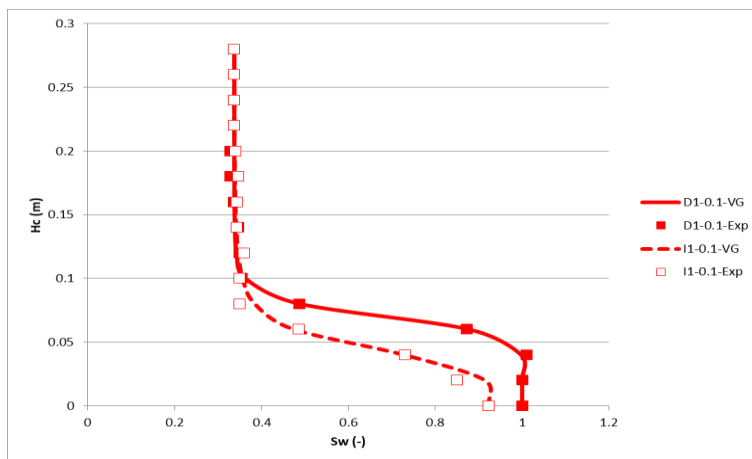
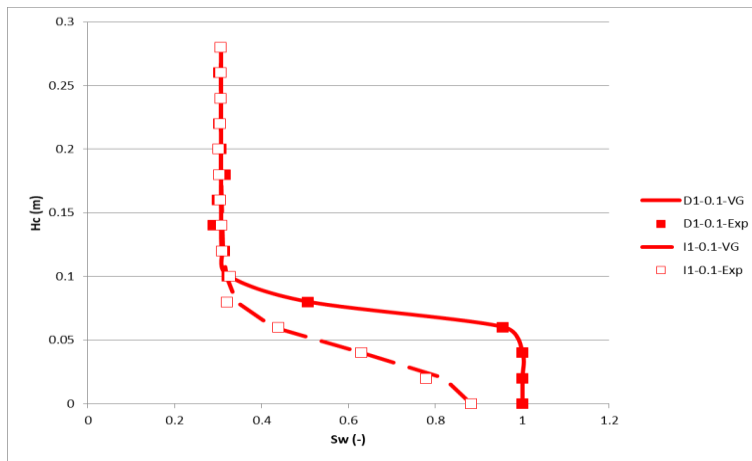
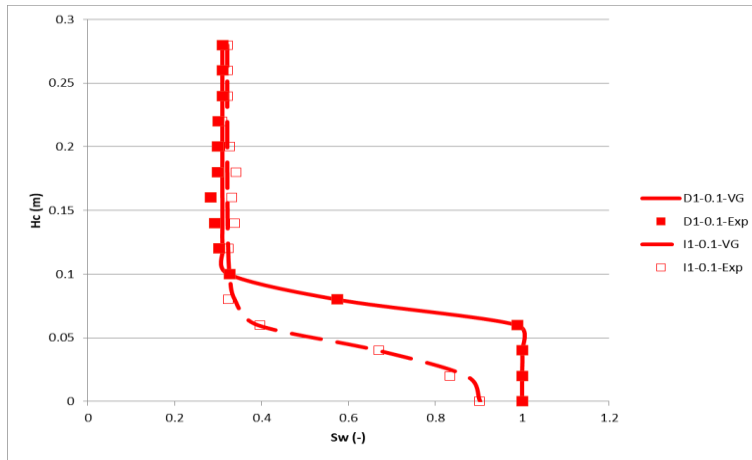
0.5 mm GB

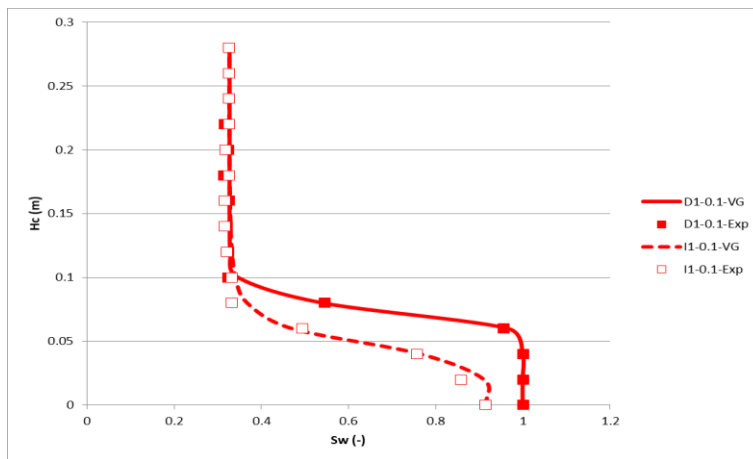
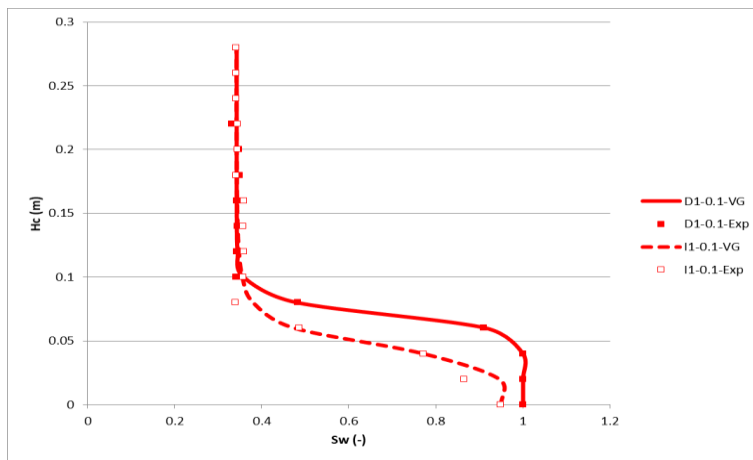
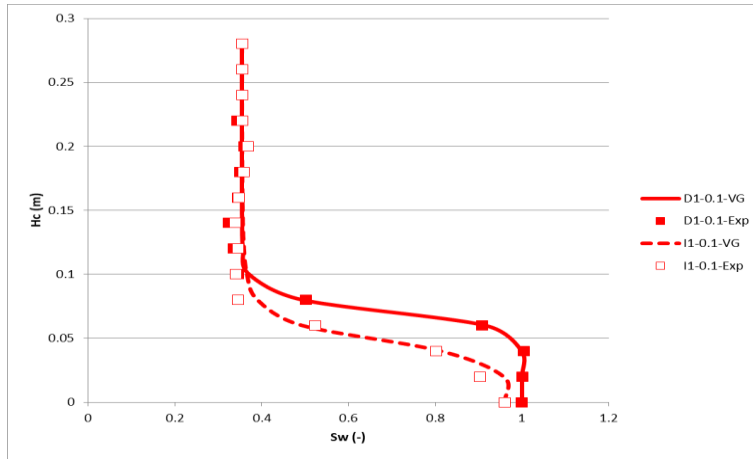






0.1 mm GB



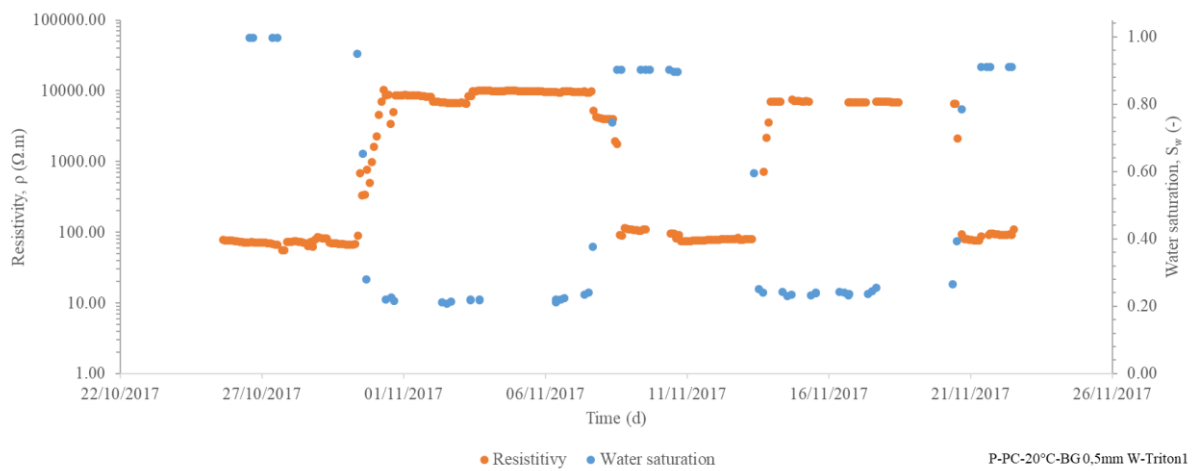
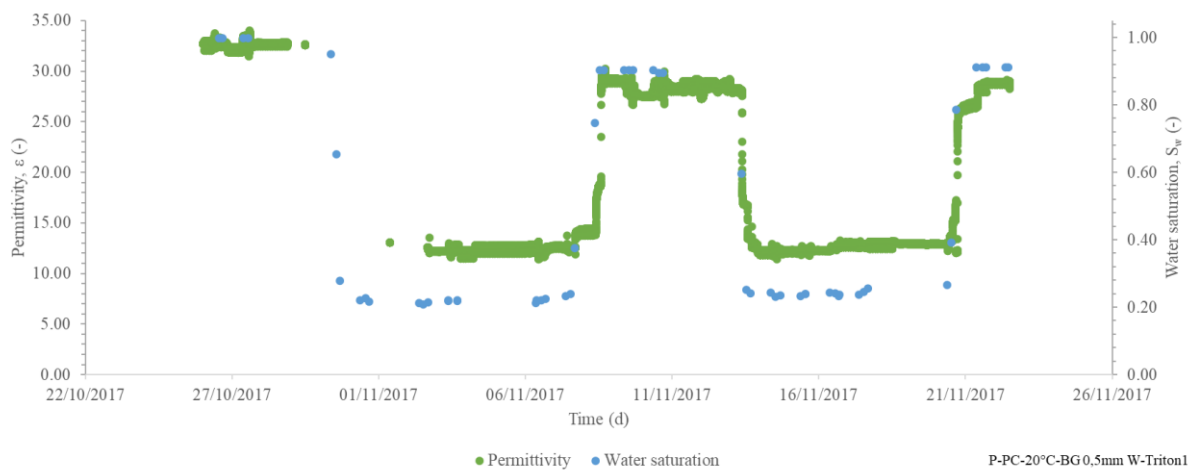


Appendix 3.2

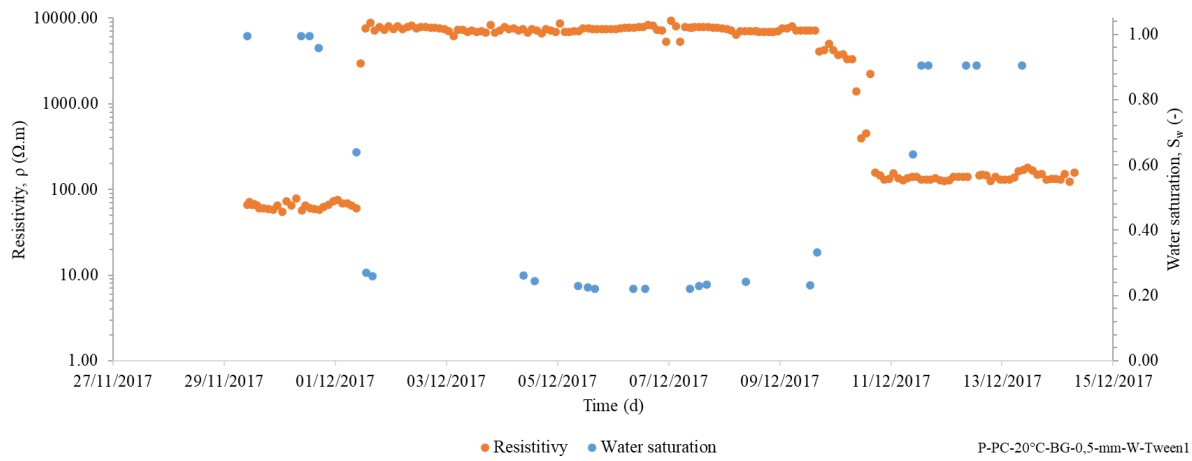
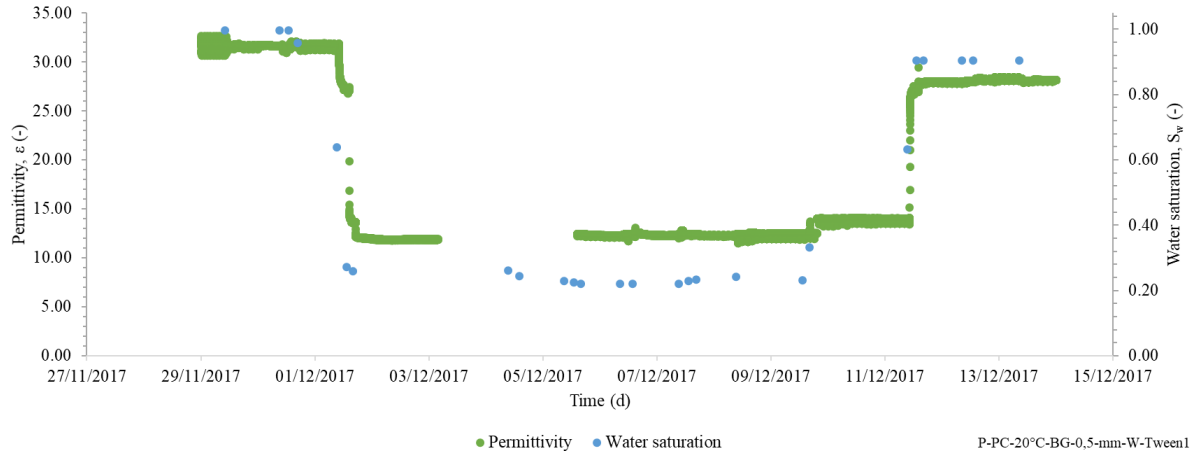
Permittivity and resistivity monitorings of the drainage-imbibition experiments with 0.5 and 0.1 mm GB with chemical enhancement

0.5 mm GB

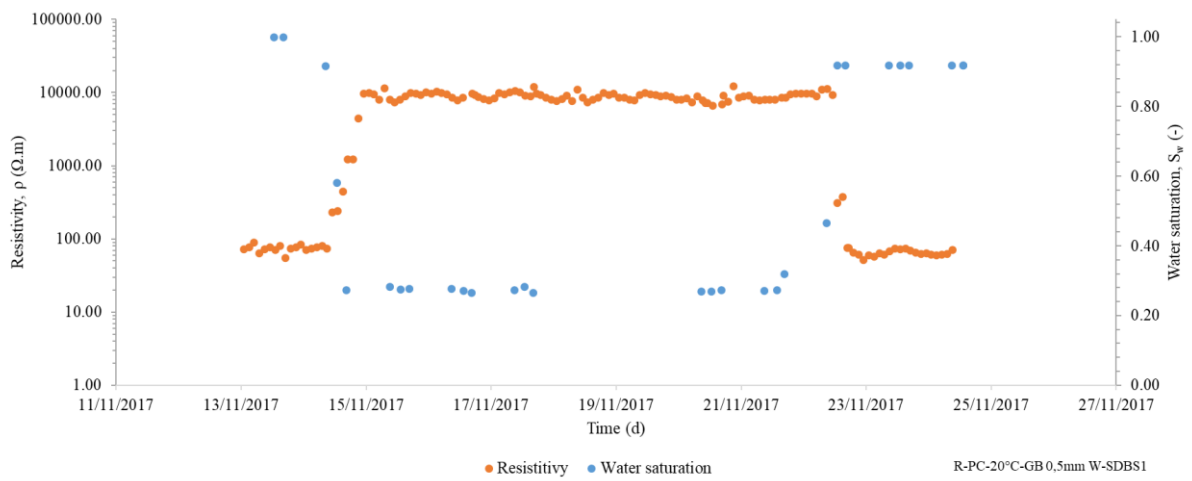
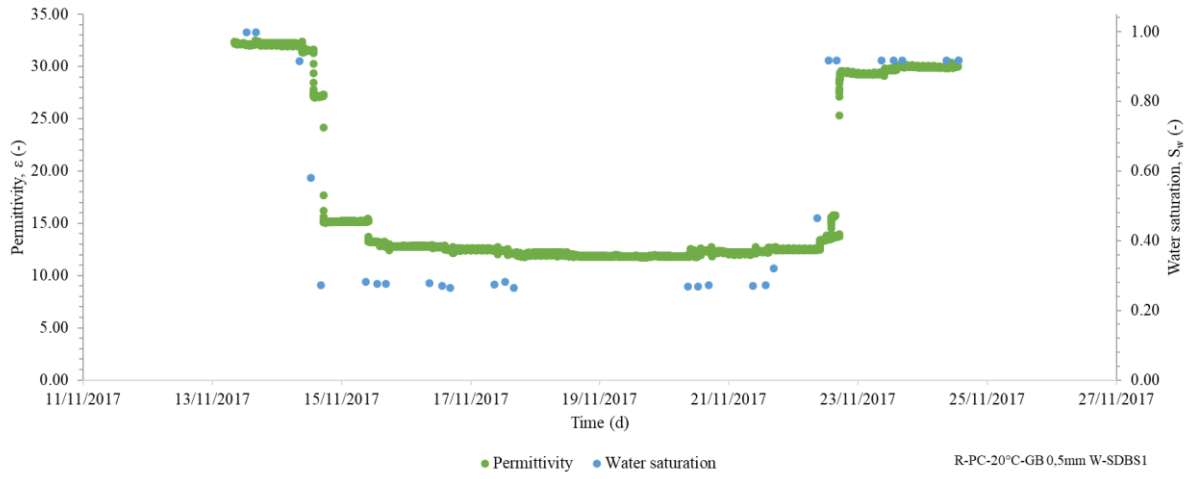
P-PC-20°C-BG 0,5mm-W-Triton1



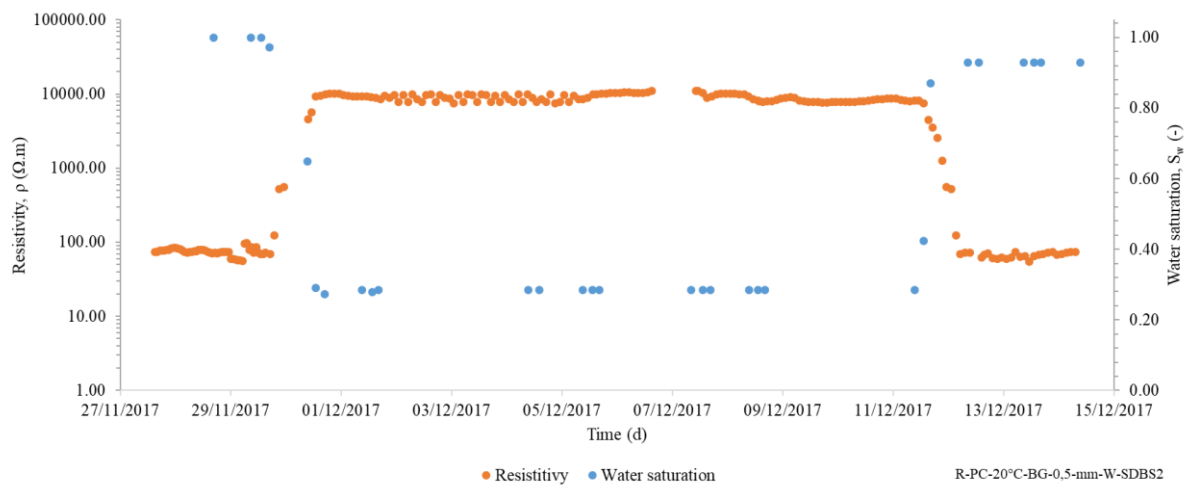
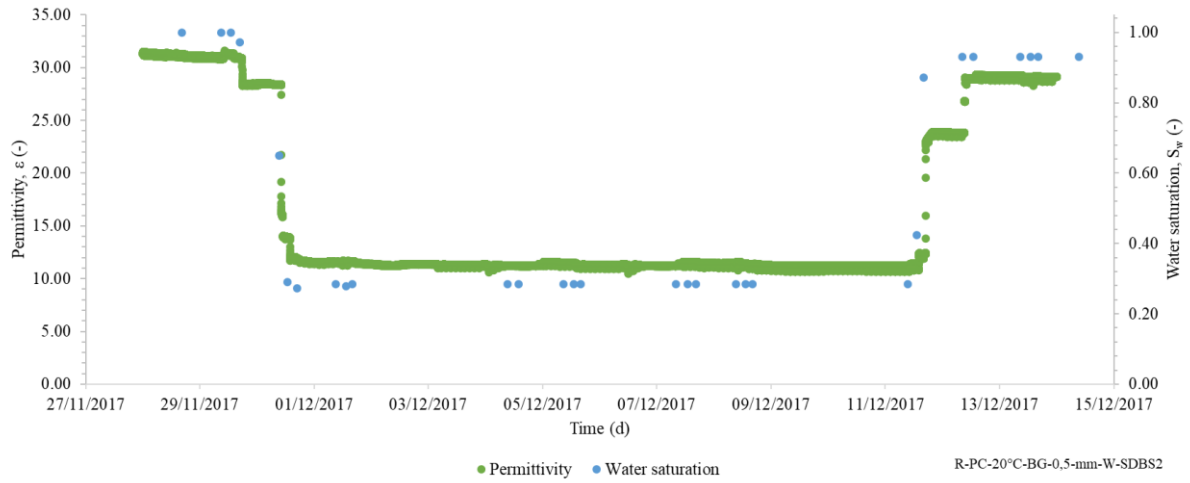
P-PC-20°C-BG-0,5-mm-W-Tween1



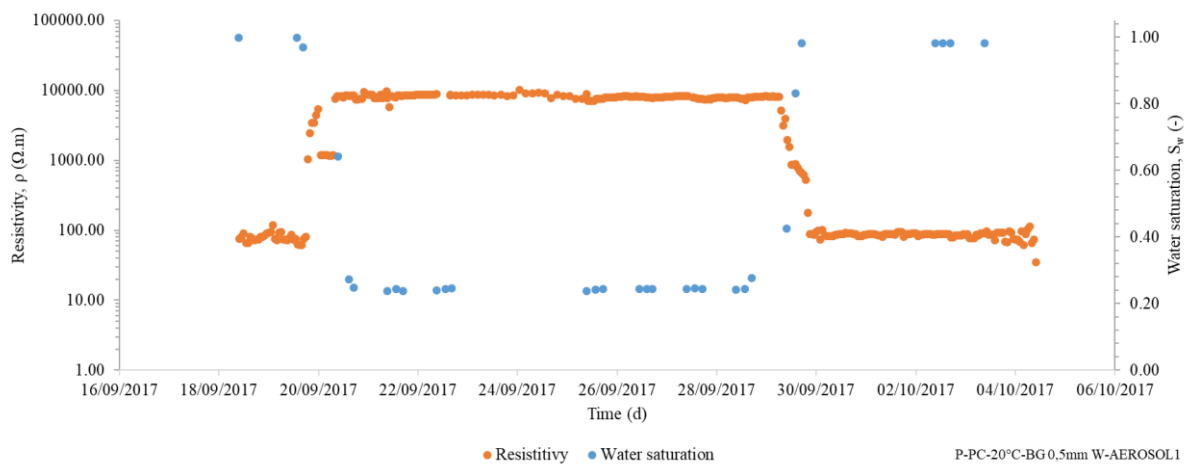
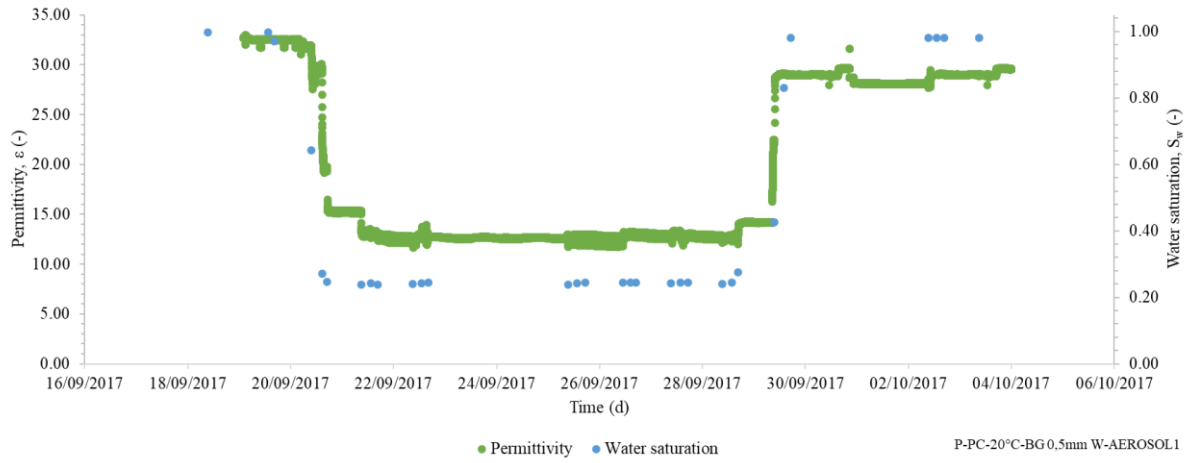
R-PC-20°C-GB 0,5mm W-SDBS1



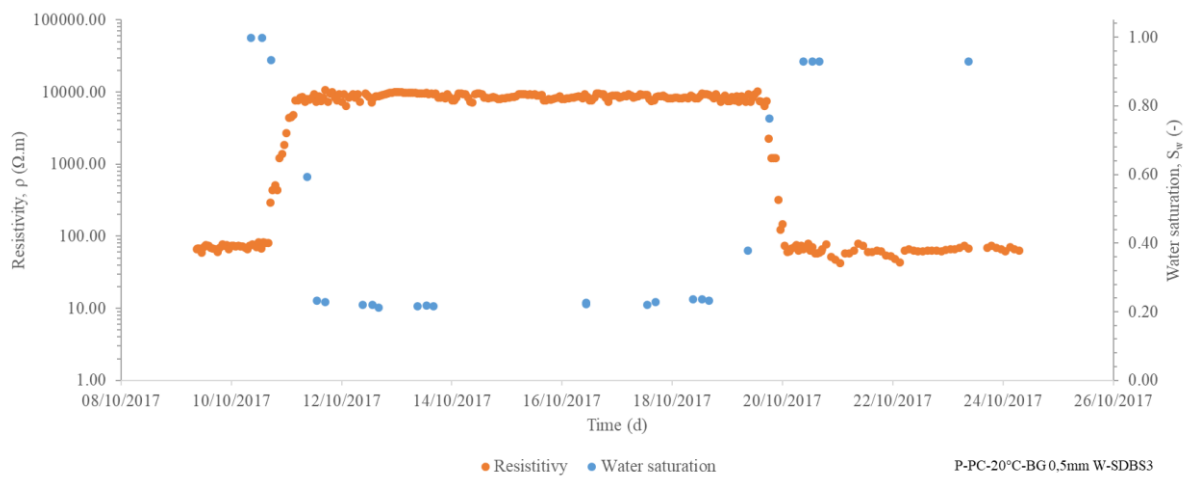
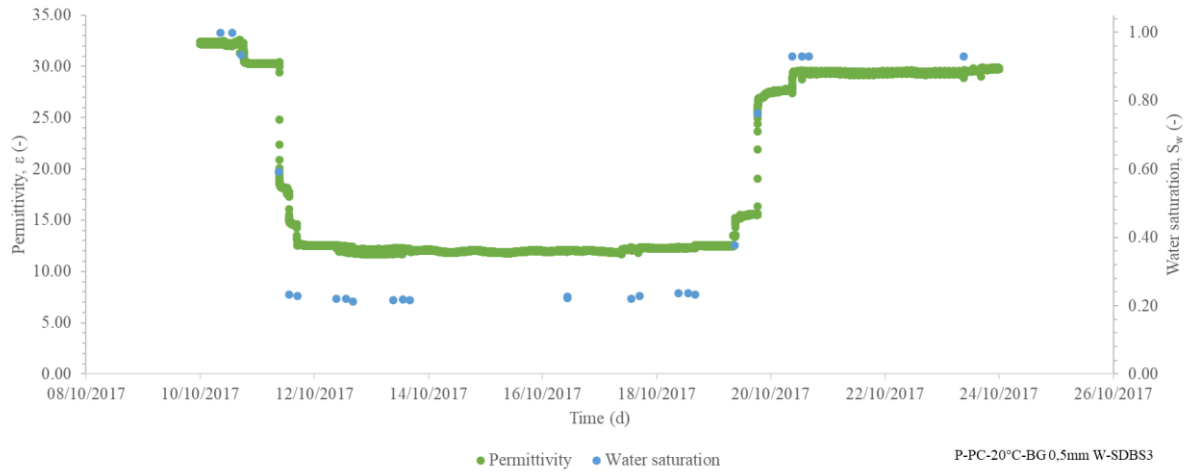
R-PC-20°C-BG-0,5-mm-W-SDBS2



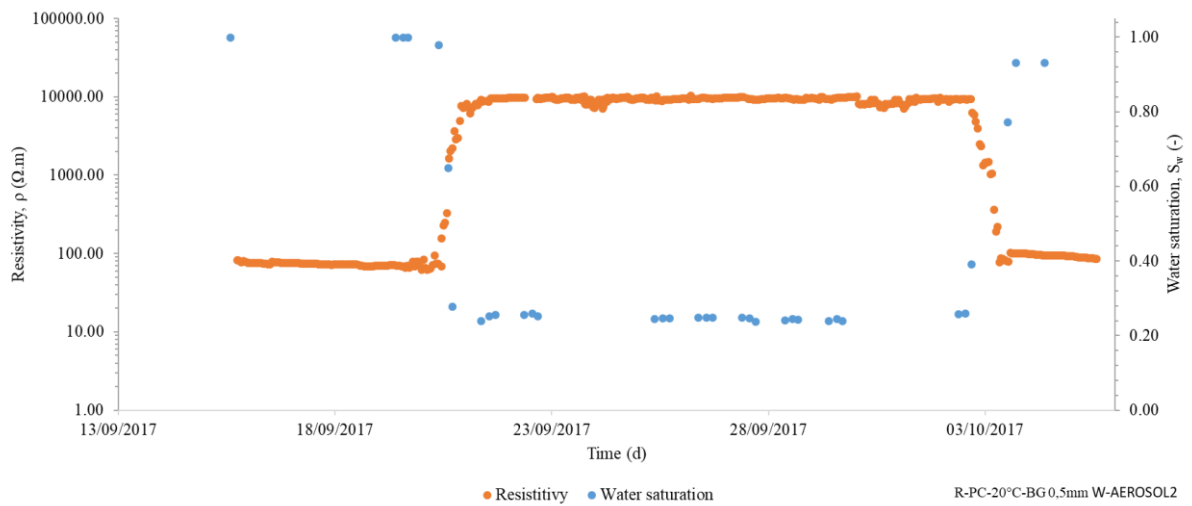
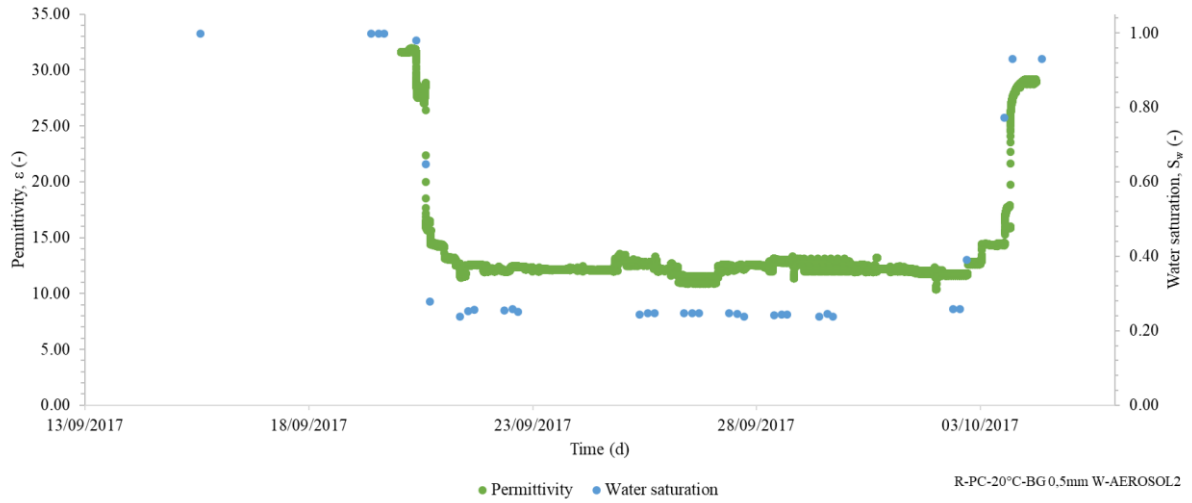
P-PC-20°C-BG 0,5mm W-AEROSOL1



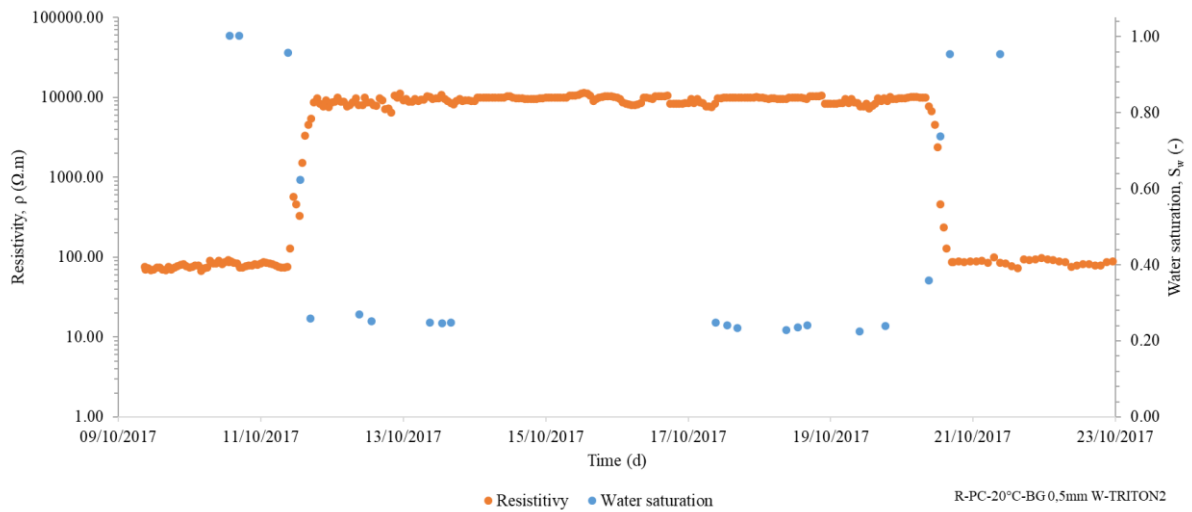
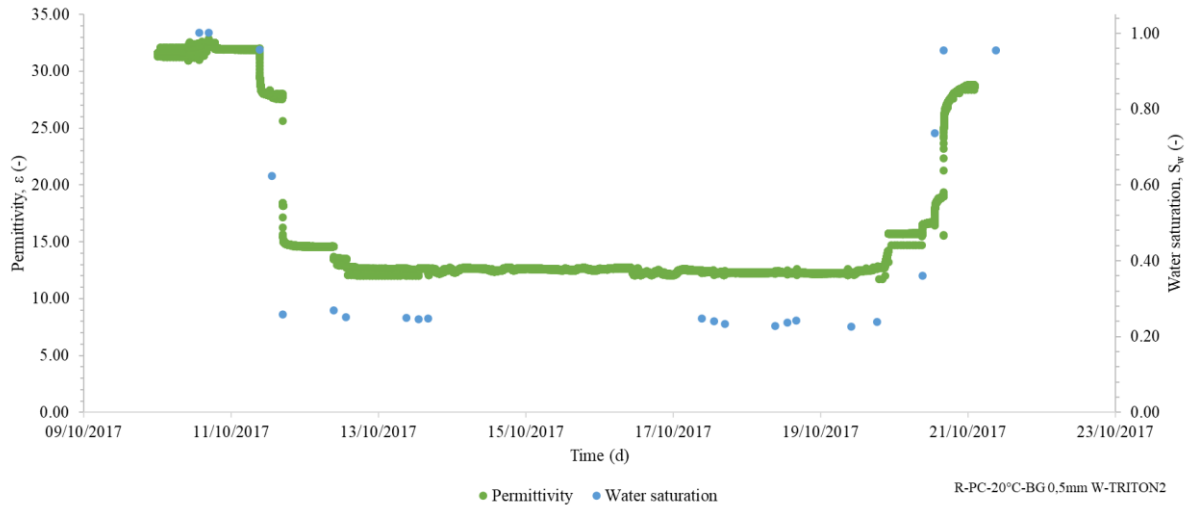
P-PC-20°C-BG 0,5mm W-SDBS3



R-PC-20°C-BG 0,5mm W-AEROSOL2

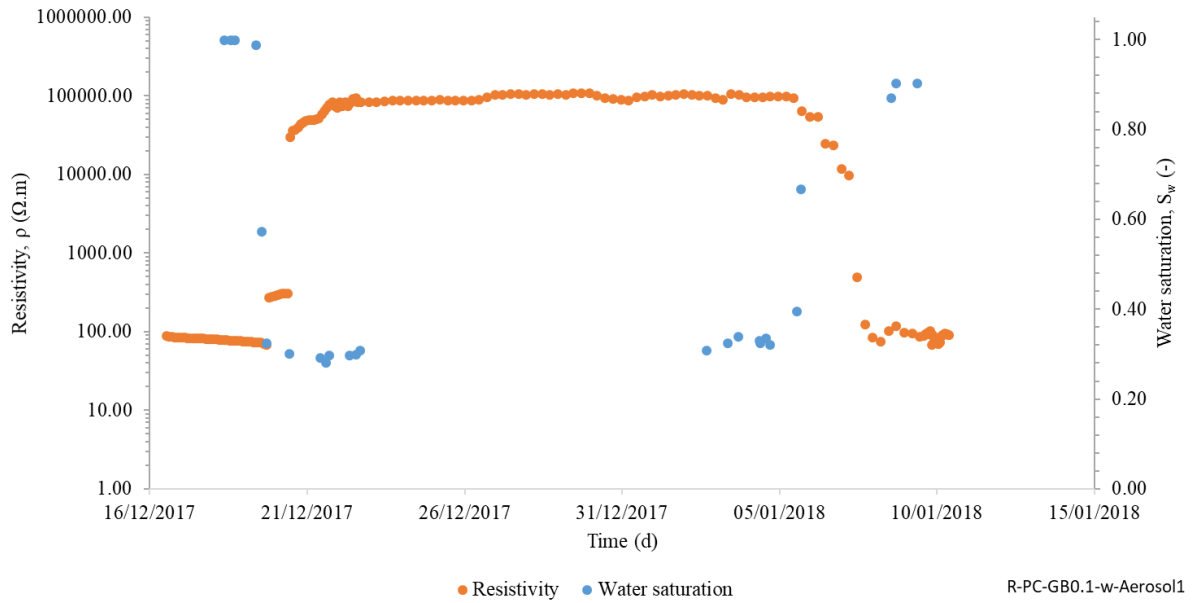
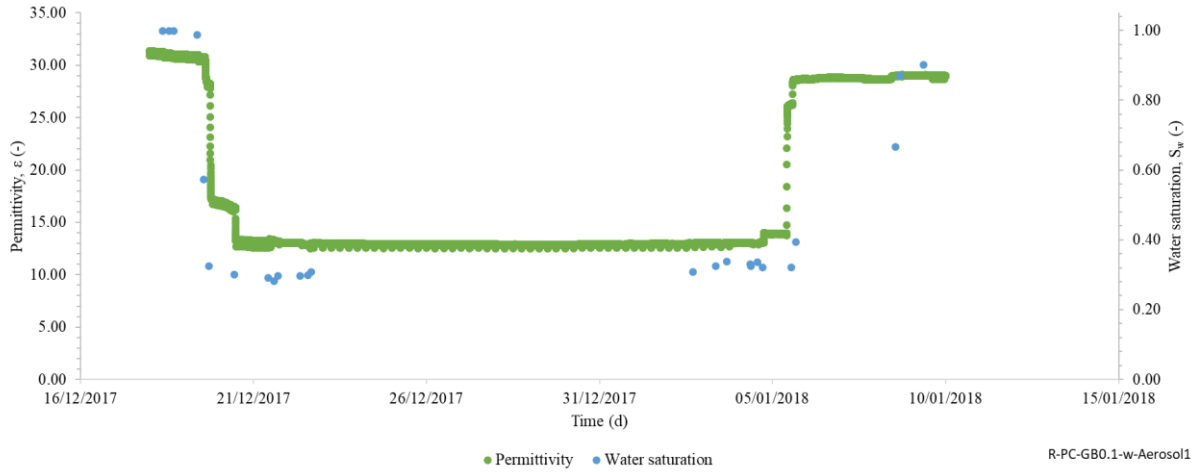


R-PC-20°C-BG 0,5mm W-TRITON2

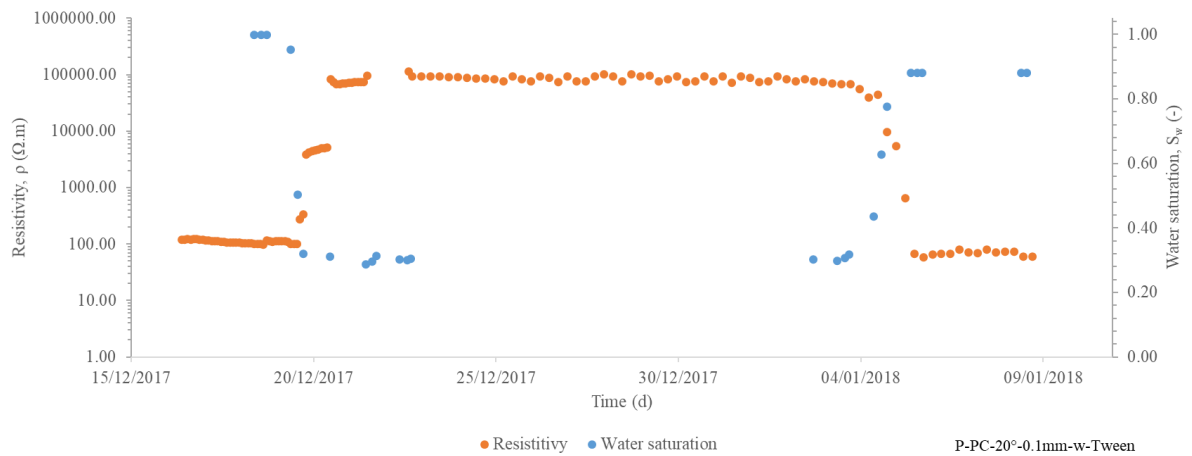
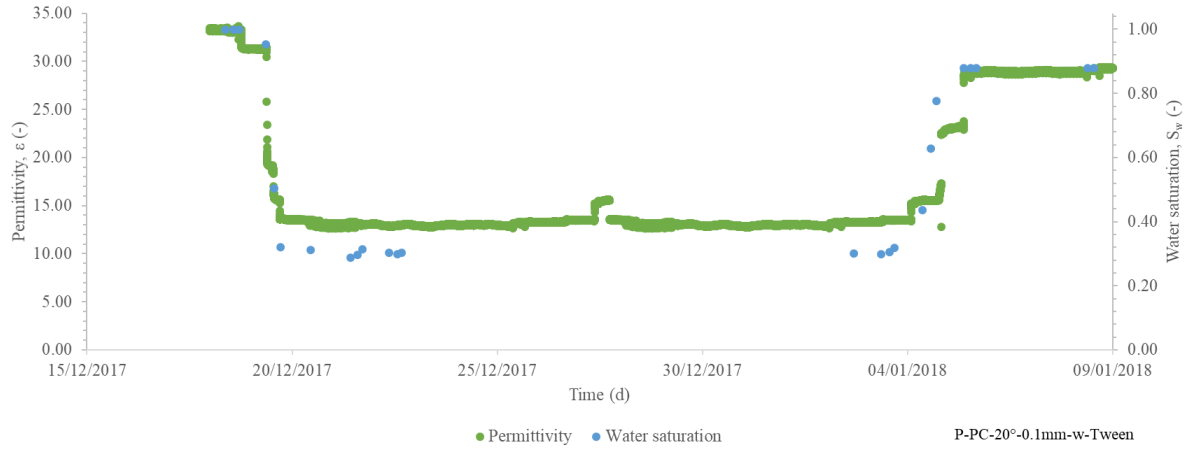


0.1 mm GB

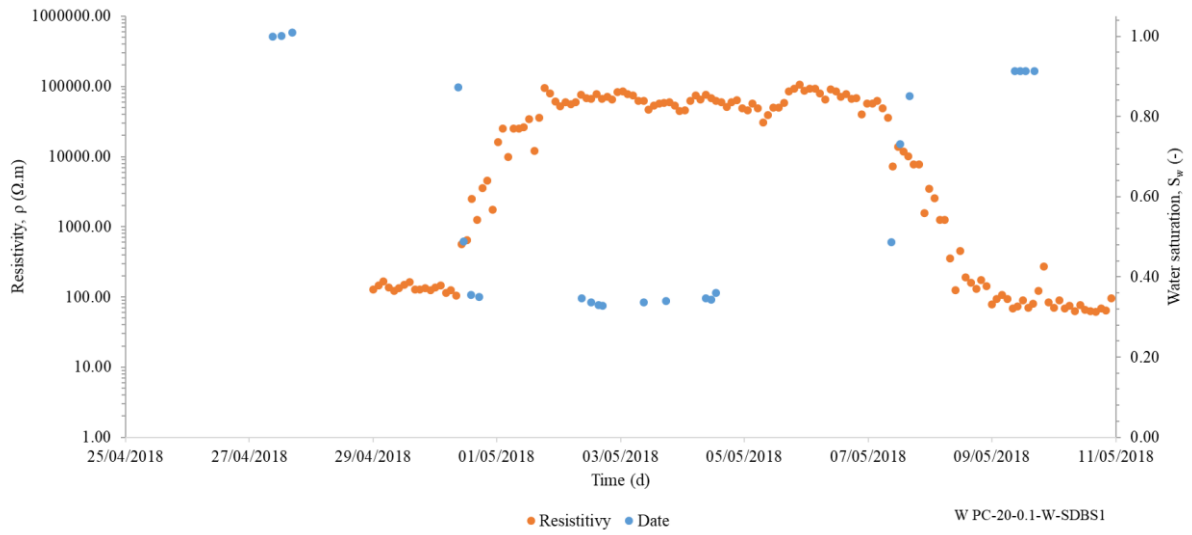
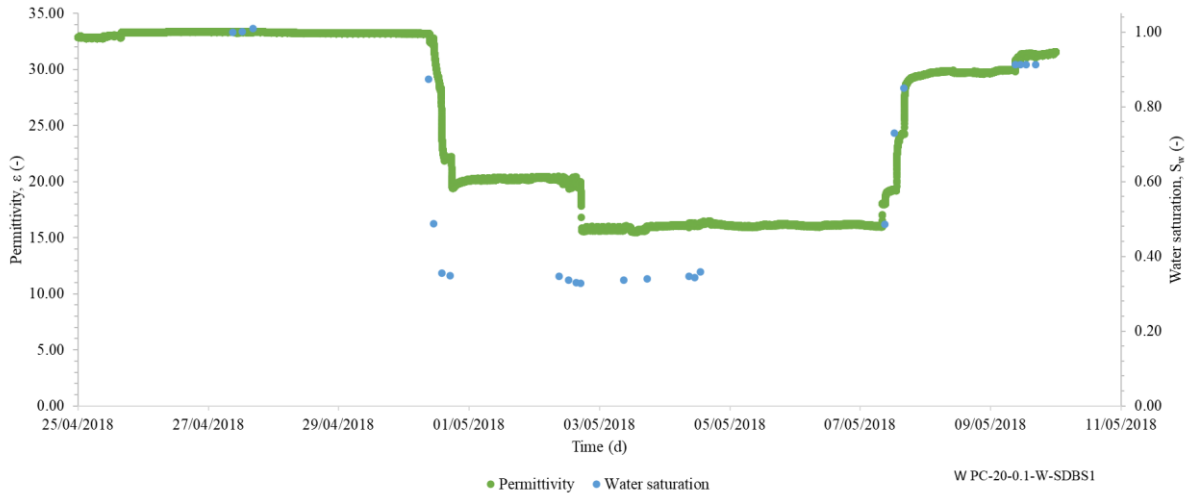
R-PC-GB0.1-w-Aerosol1



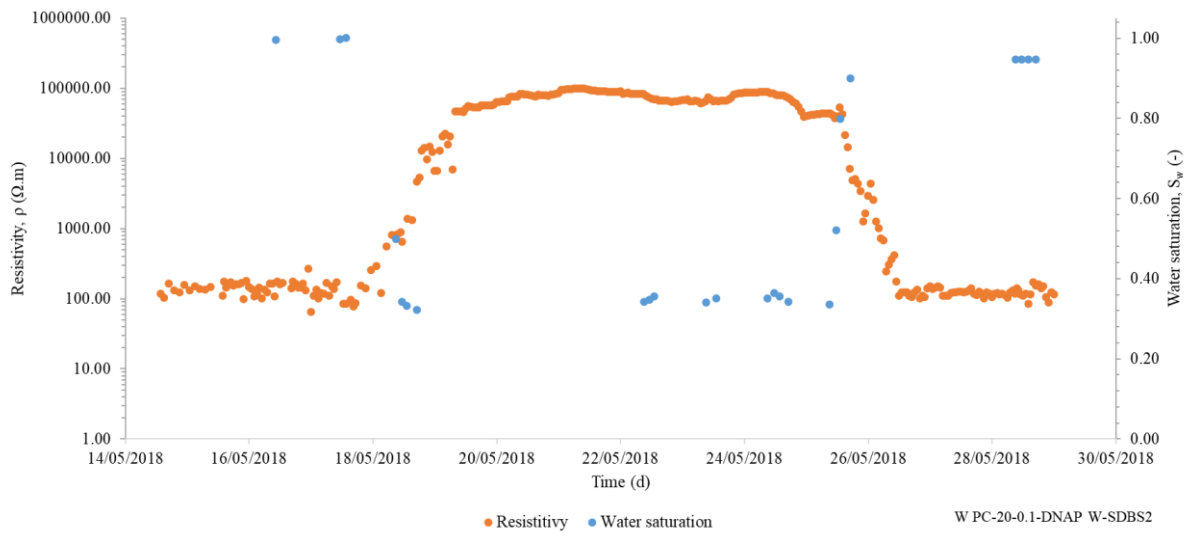
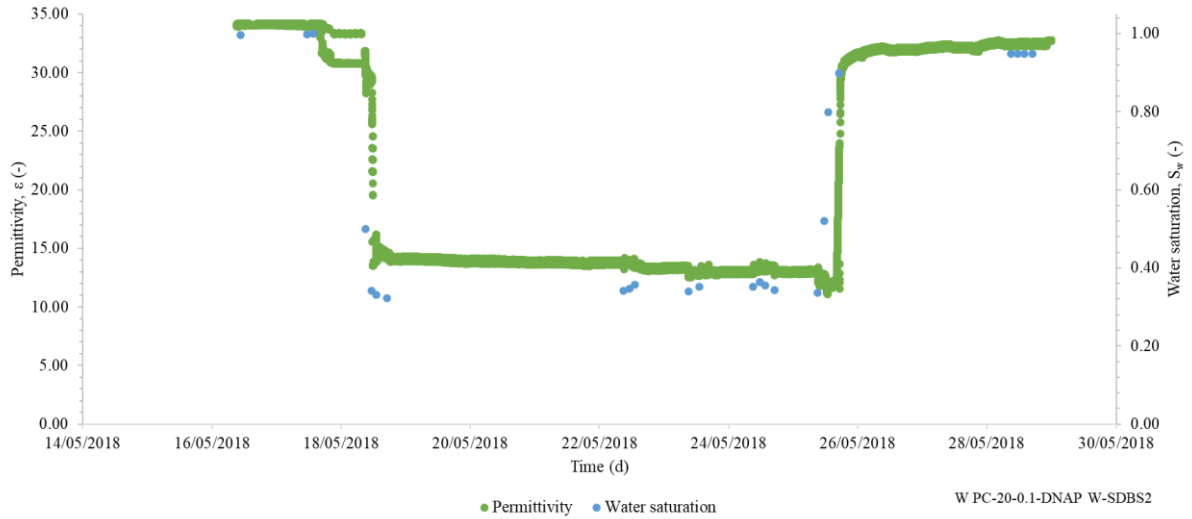
P-PC-20°-0.1mm-w-Tween



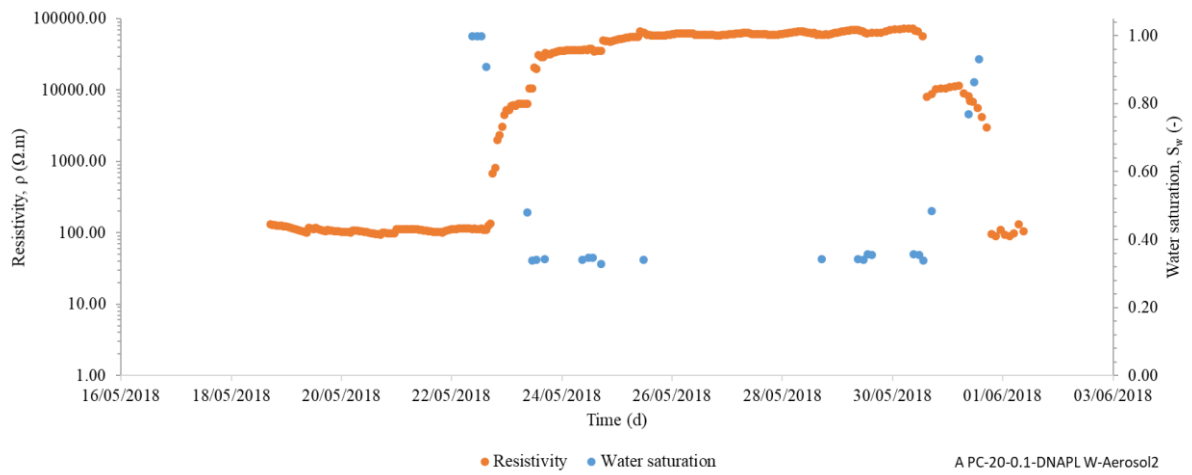
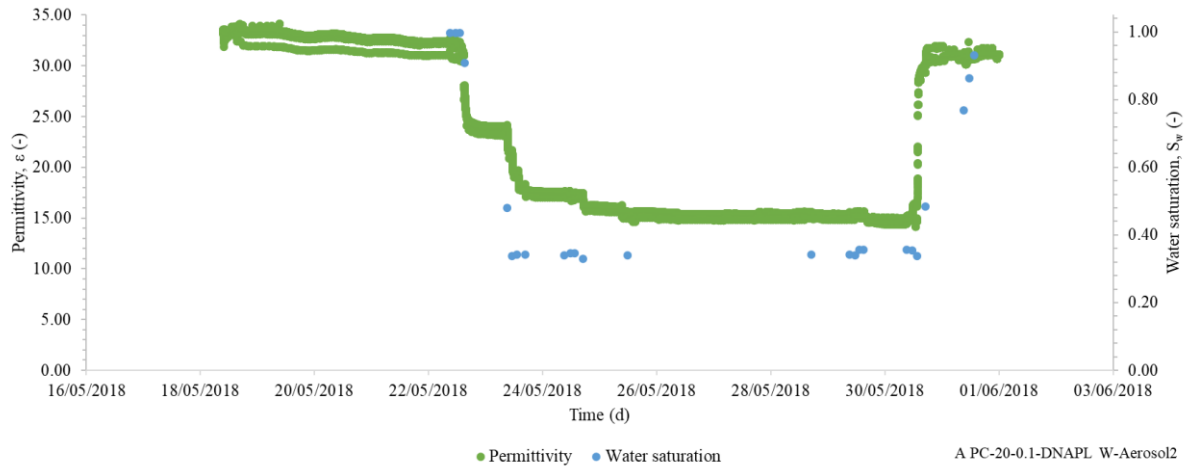
W PC-20-0.1-W-SDBS1



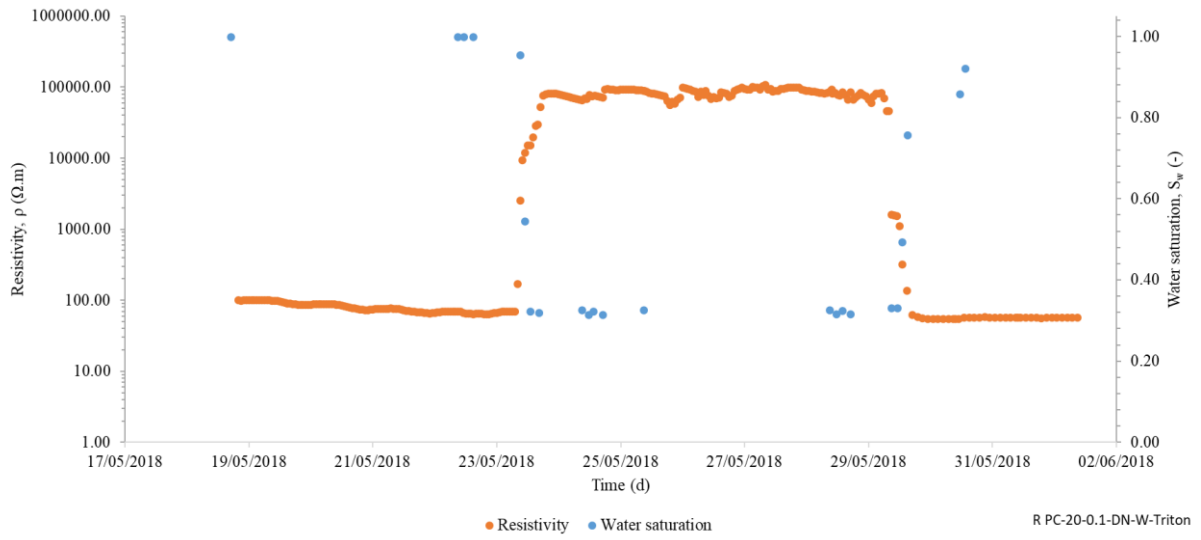
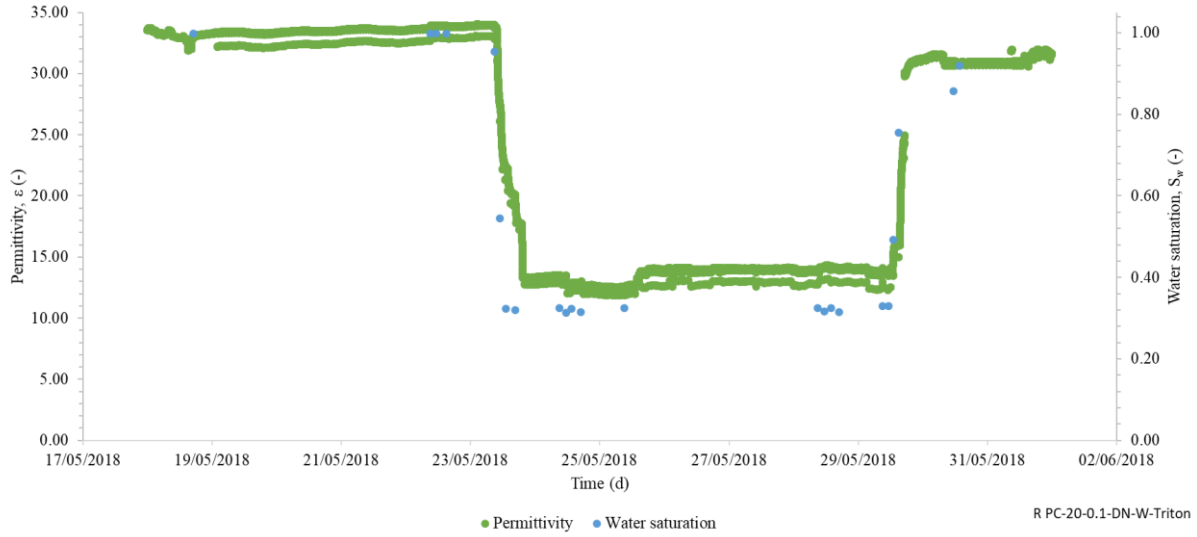
W PC-20-0.1-DNAP W-SDBS2



A PC-20-0.1-DNAPL W-Aerosol2



R PC-20-0.1-DN-W-Triton



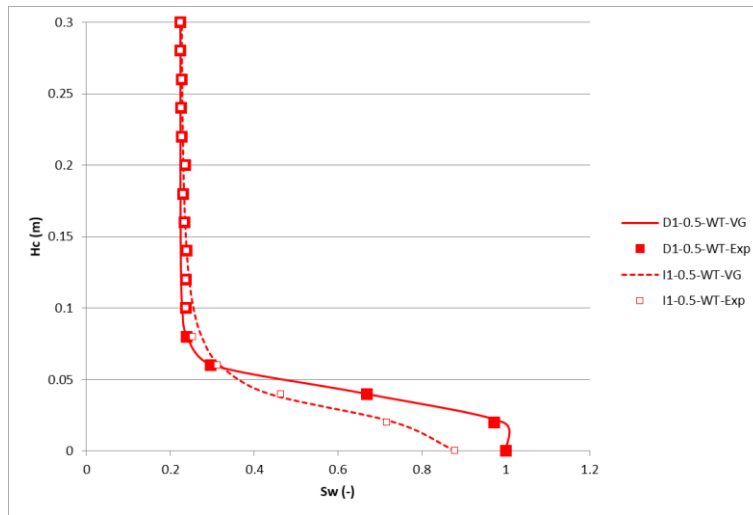
Appendix 4

1D cells experiments with thermal enhancement

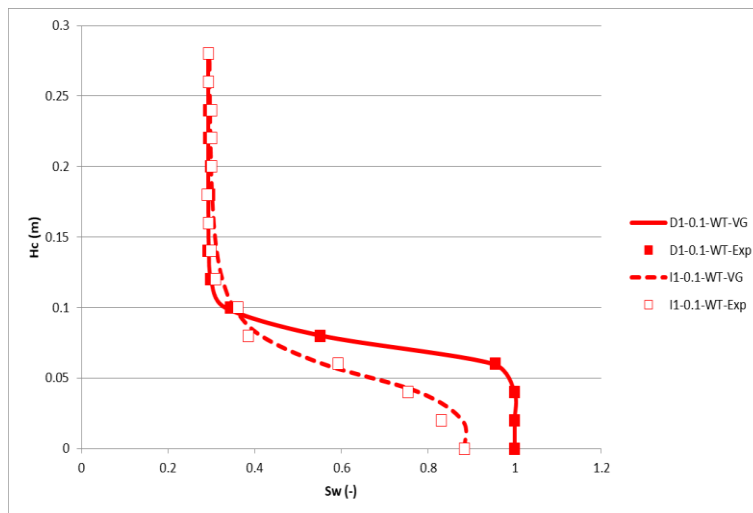
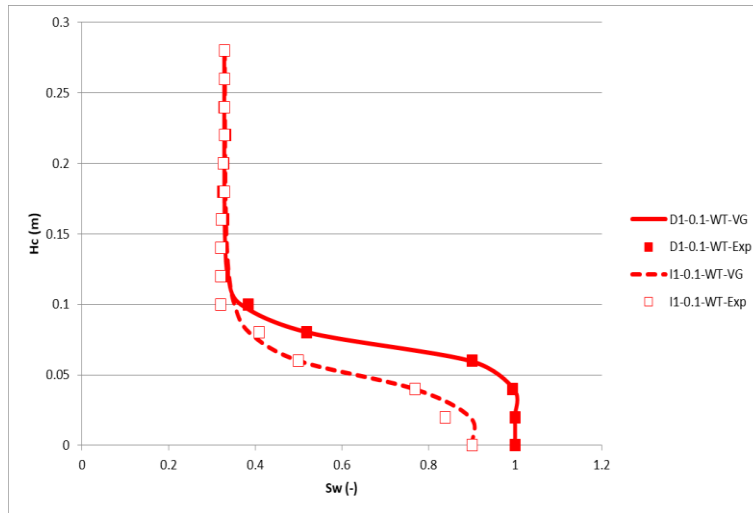
Appendix 4.1

Drainage-imbibition experiments with 0.5 and 0.1 mm GB with thermal enhancement

0.5 mm GB



0.1 mm GB

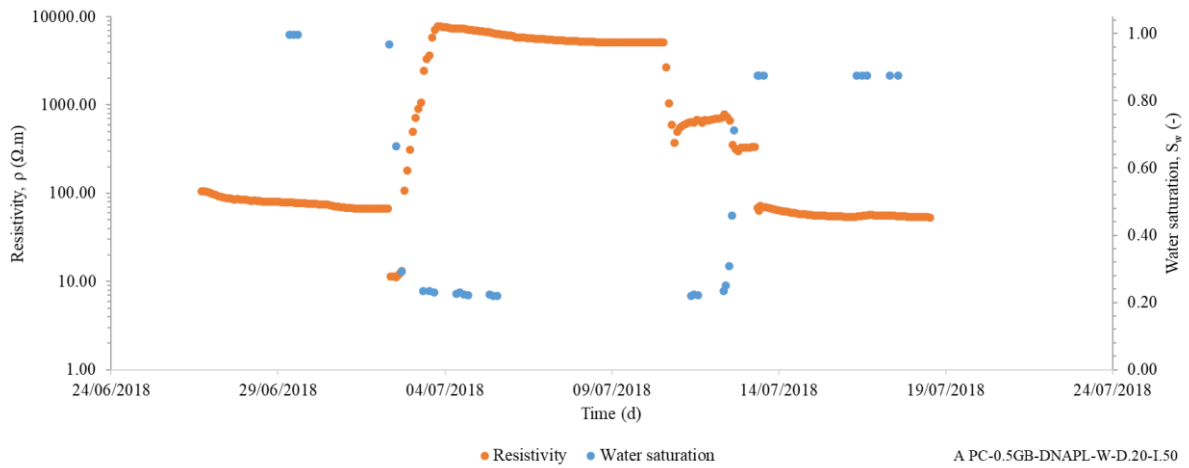
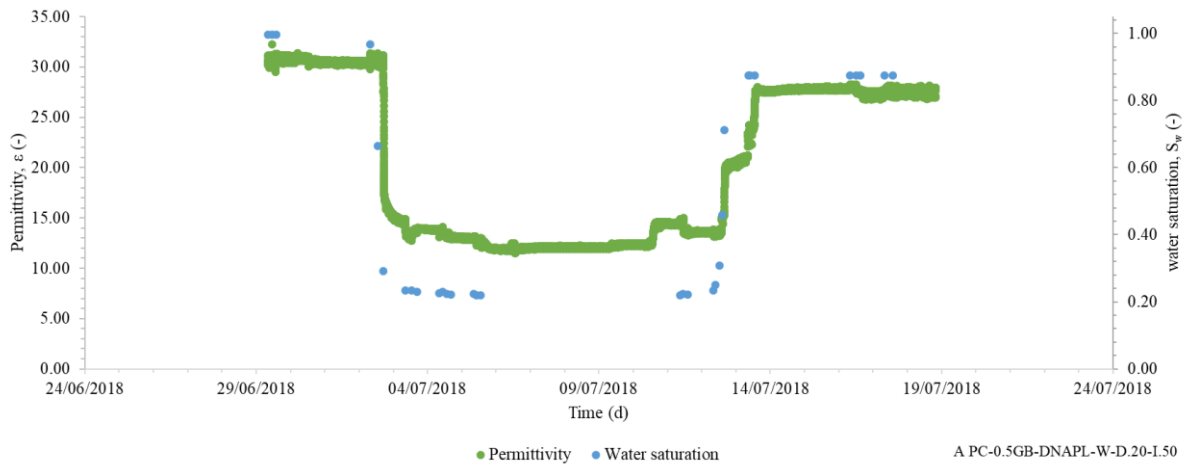


Appendix 4.2

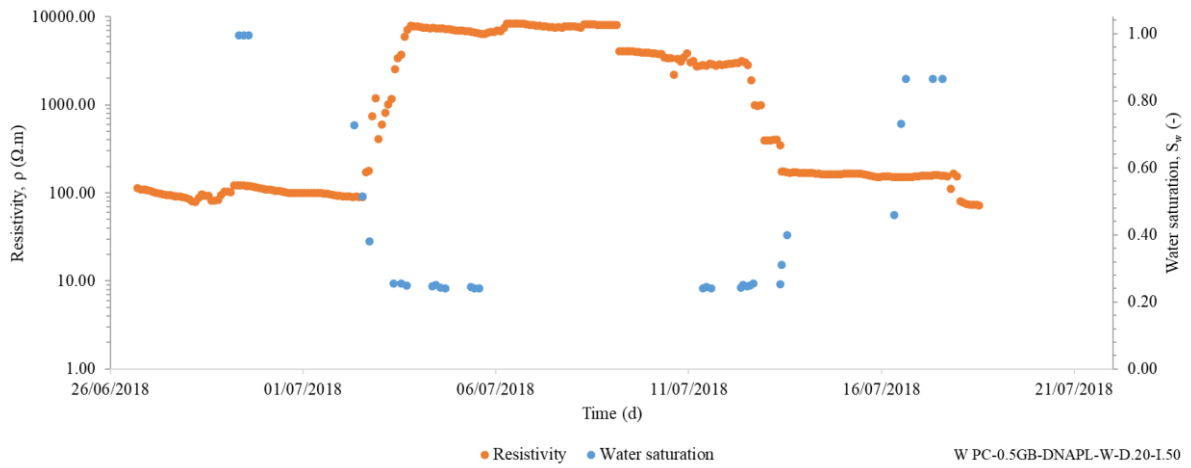
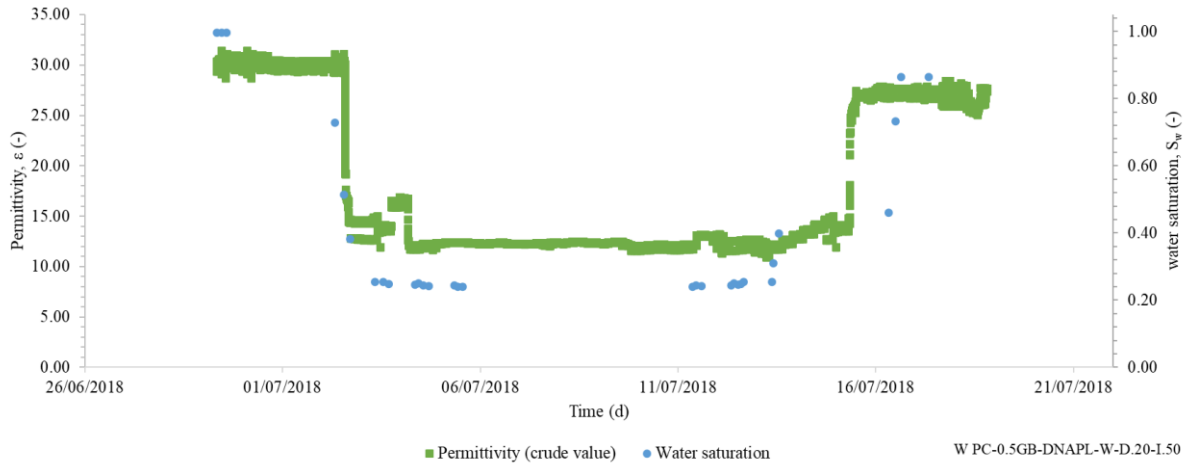
Permittivity and resistivity monitorings of the drainage-imbibition experiments with 0.5 and 0.1 mm GB with thermal enhancement

0.5 mm GB

A PC-0.5GB-DNAPL-W-D.20-I.50

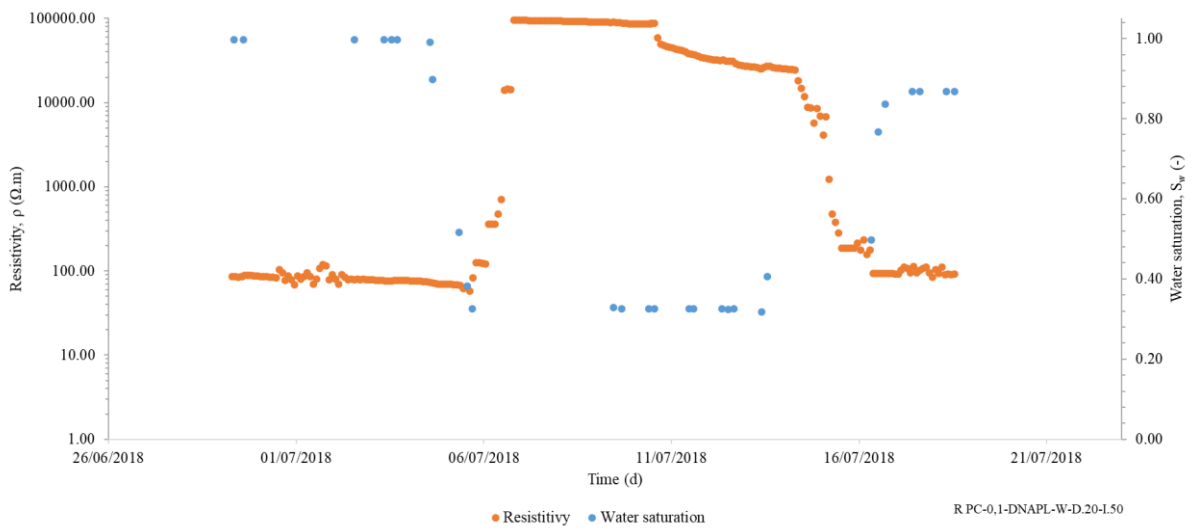
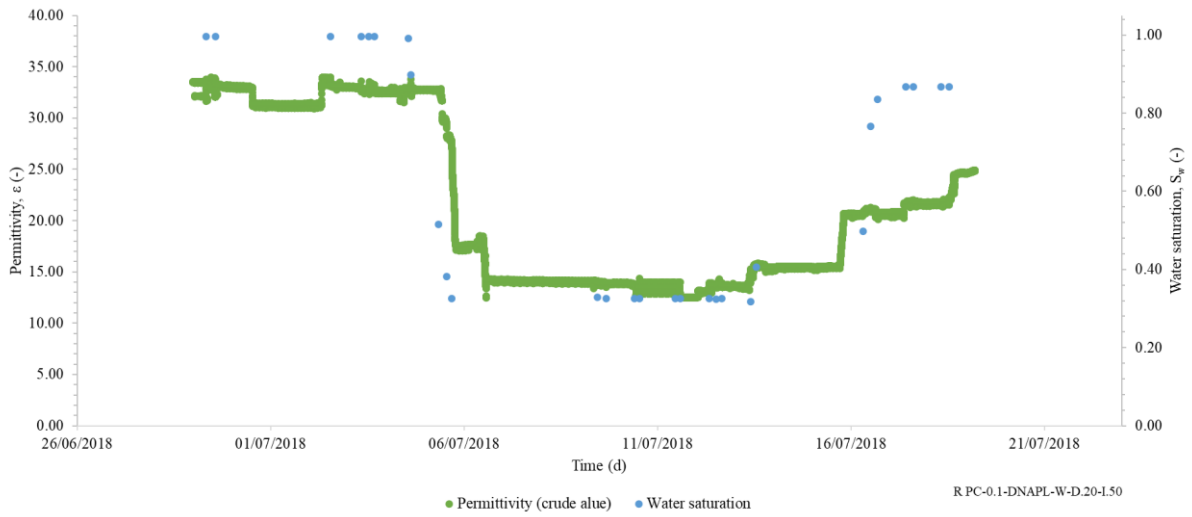


W PC-0.5GB-DNAPL-W-D.20-I.50

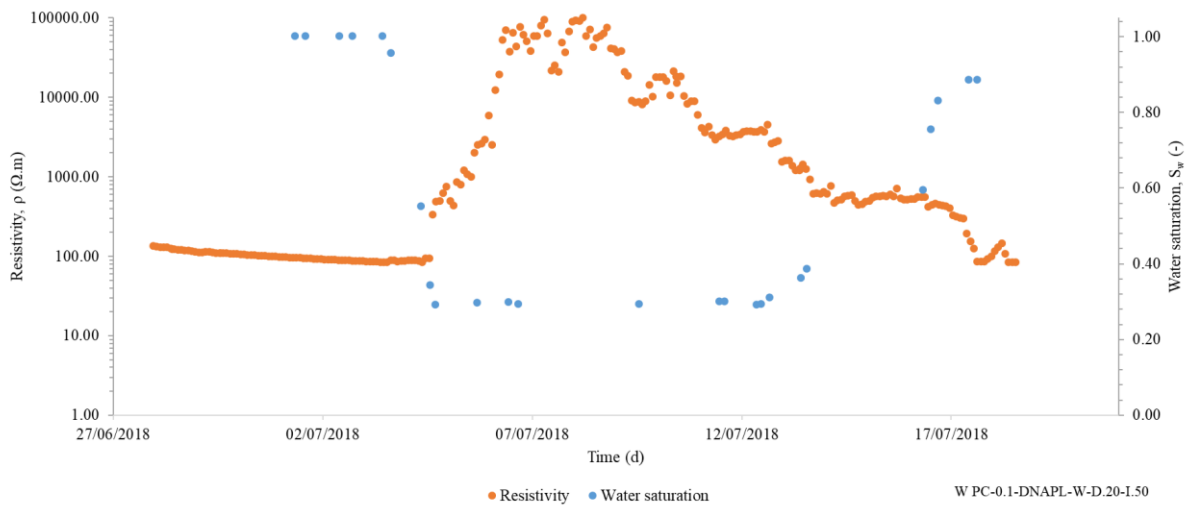
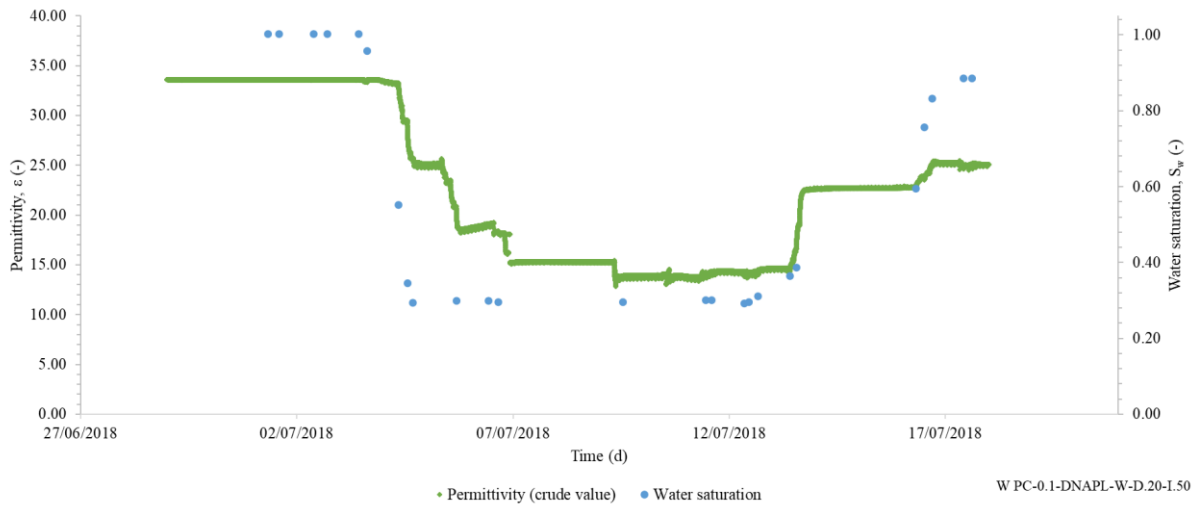


0.1 mm GB

R PC-0.1-0.2-DNAPL-W-D.20-I.50



W PC-0.1-DNAPL-W-D.20-I.50

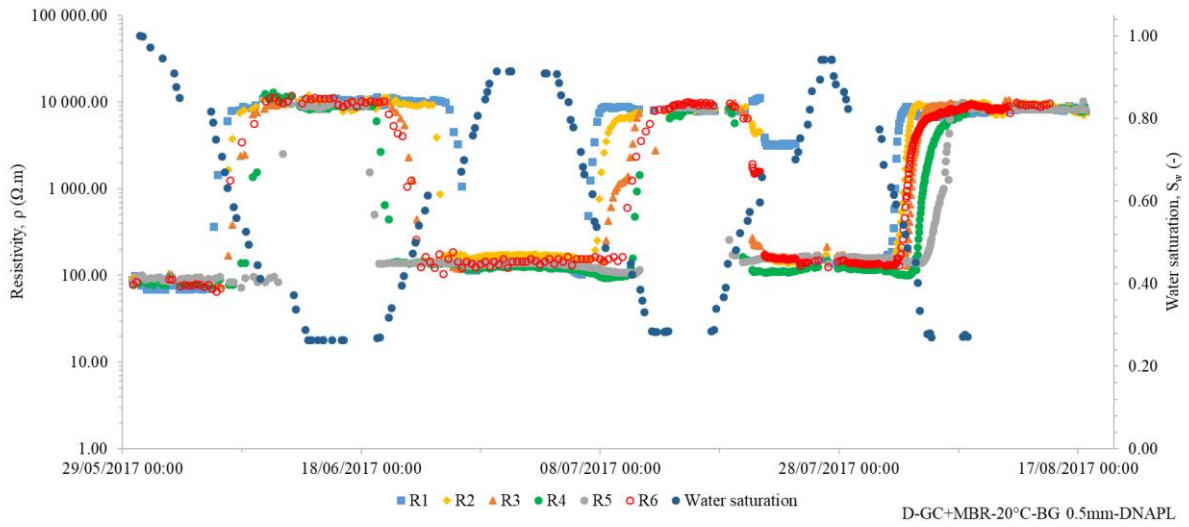
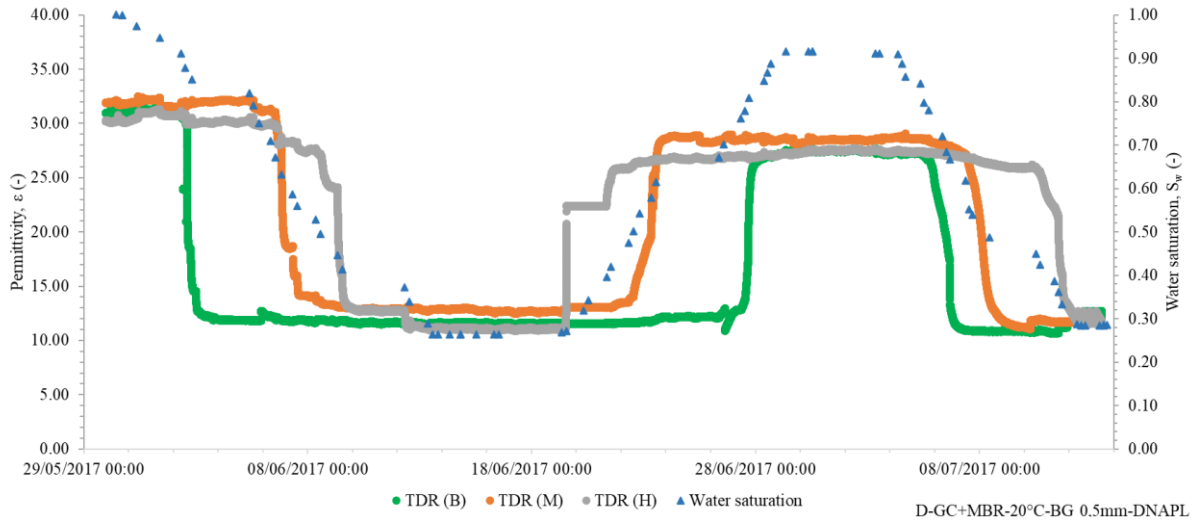


Appendix 5

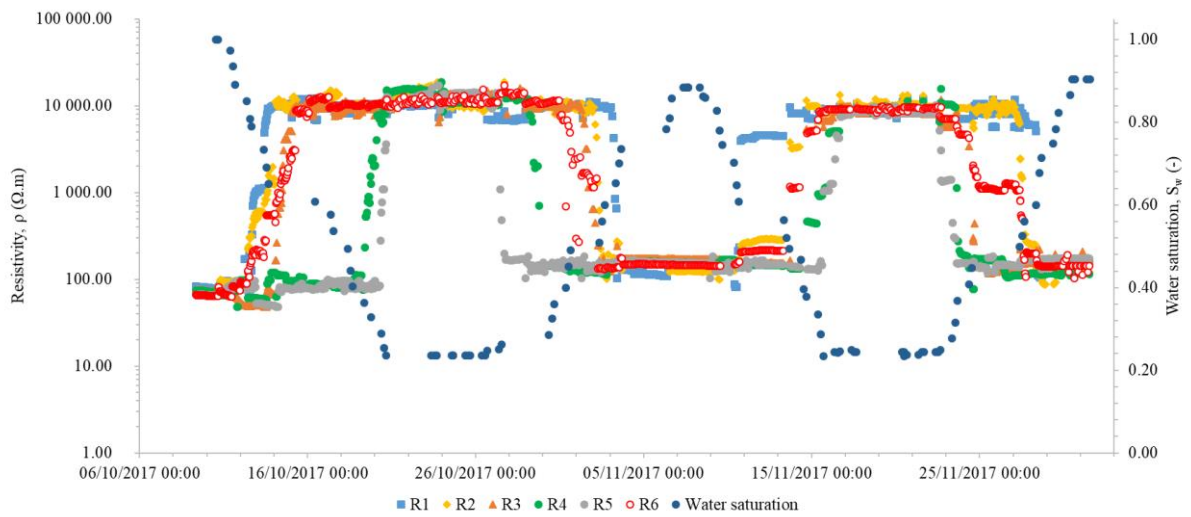
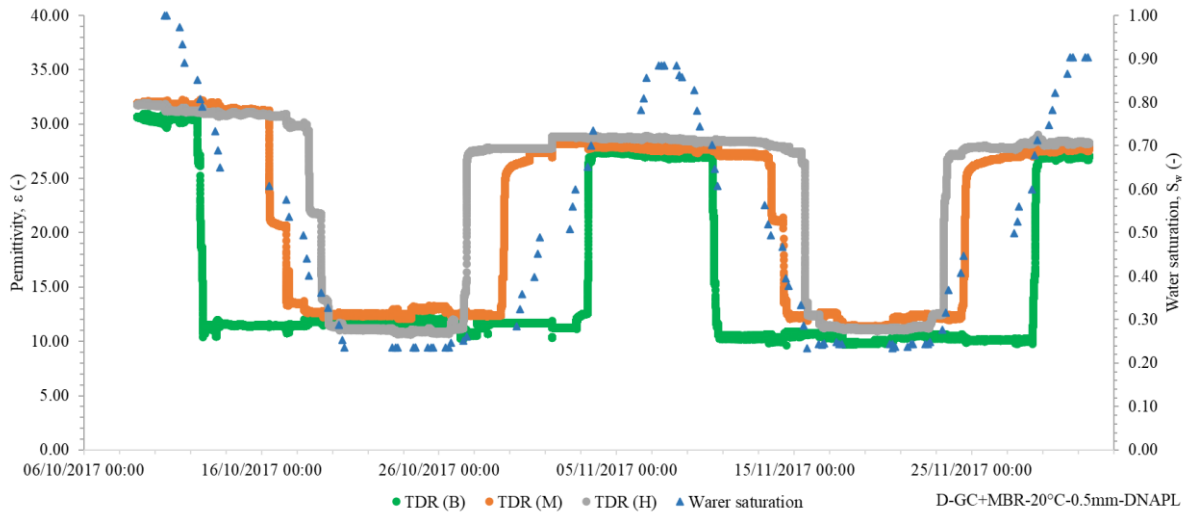
1D columns experiments without enhancement

0.5 mm GB with membrane

D-GC+MBR-20°C-BG 0.5mm-DNAPL

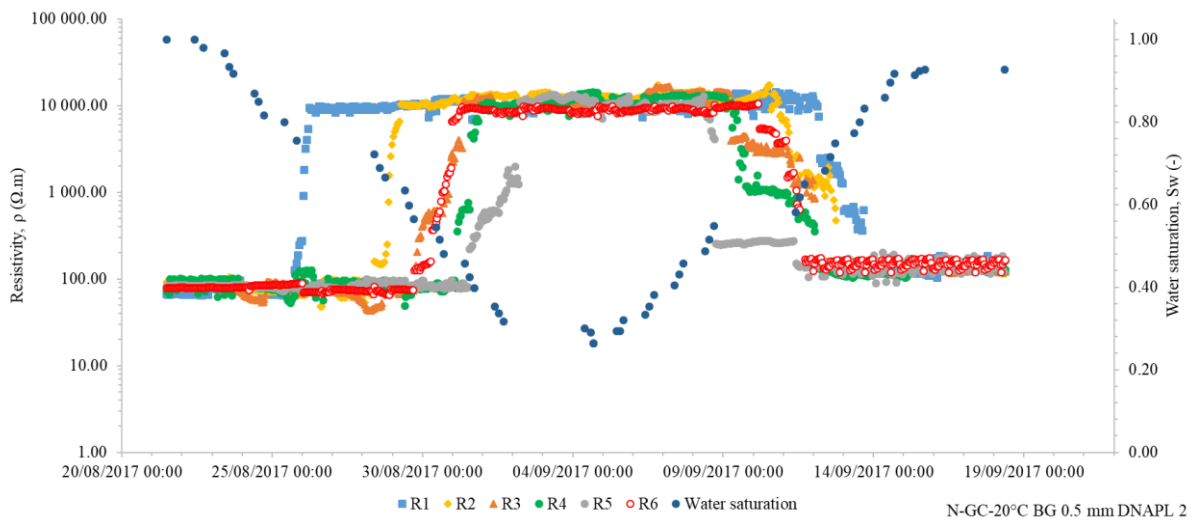
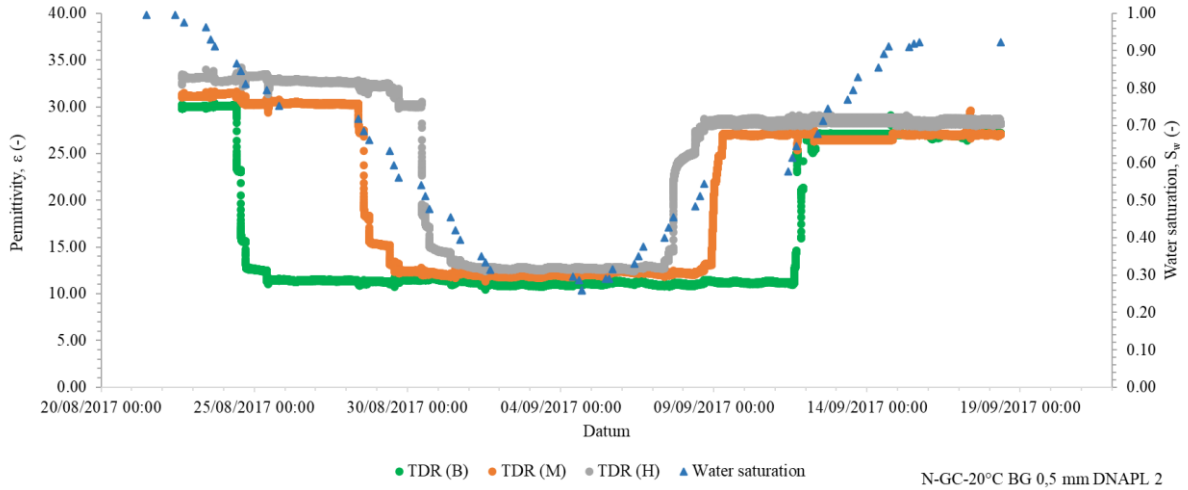


D-GC+MBR-20°C-BG 0.5mm-DNAPL

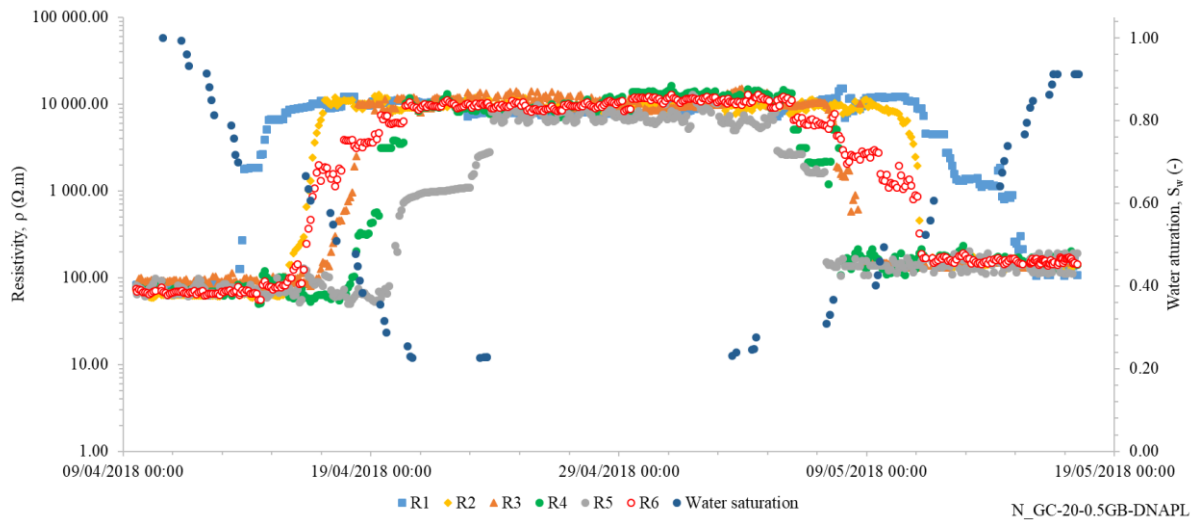
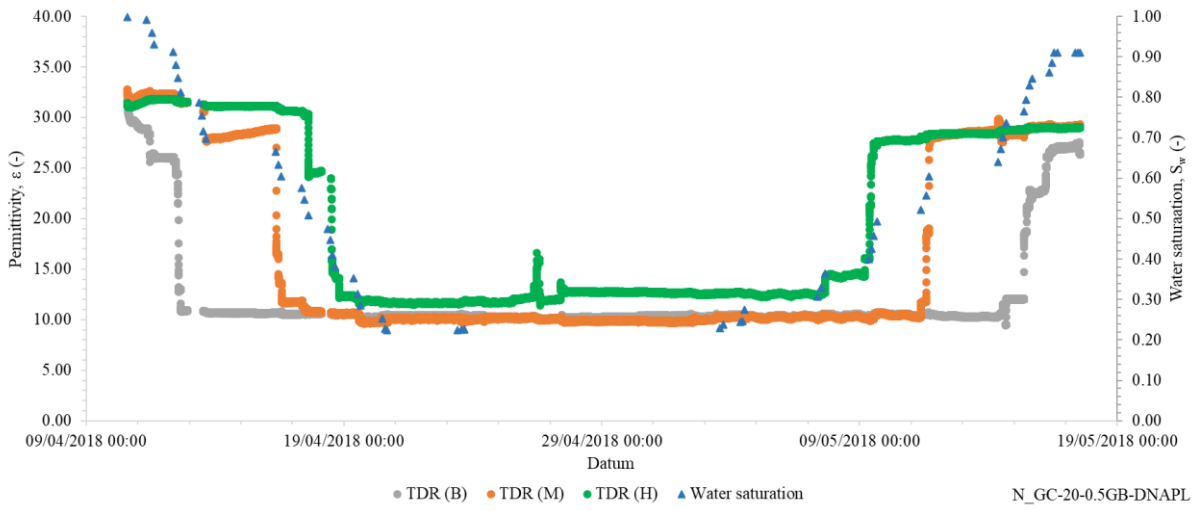


0.5 mm GB without membrane

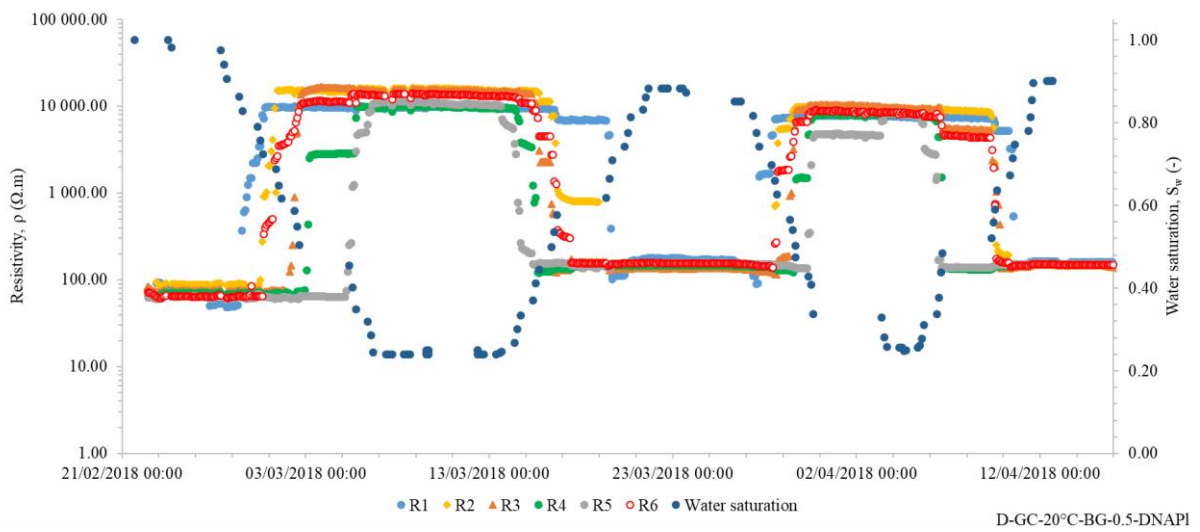
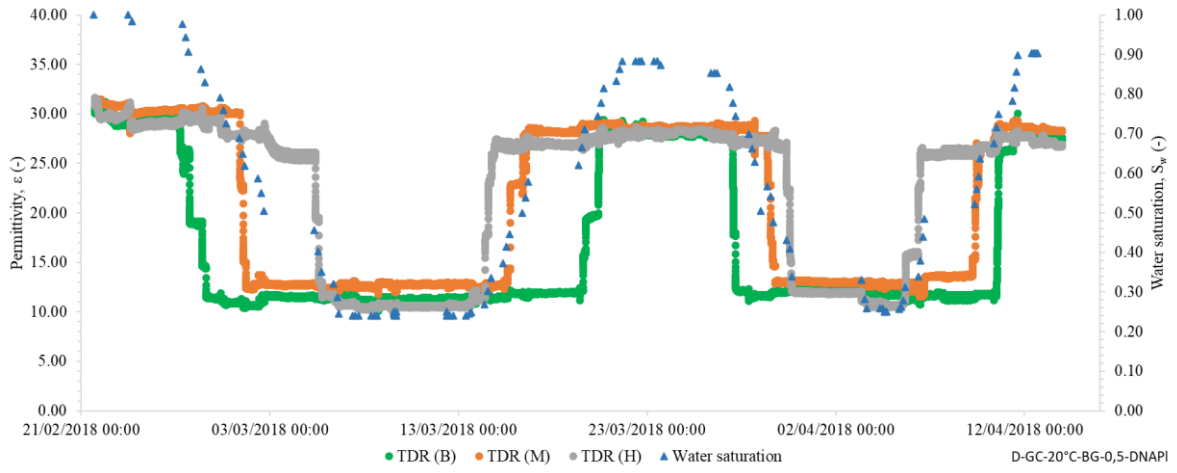
N-GC-20°C BG 0,5 mm DNAPL 2



N_GC-20-0,5GB-DNAPL

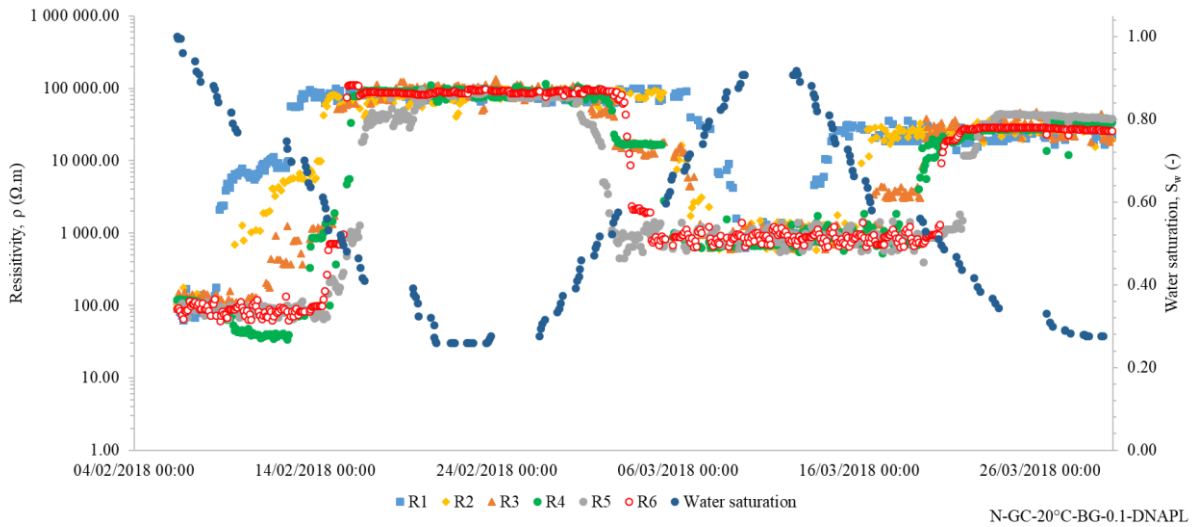
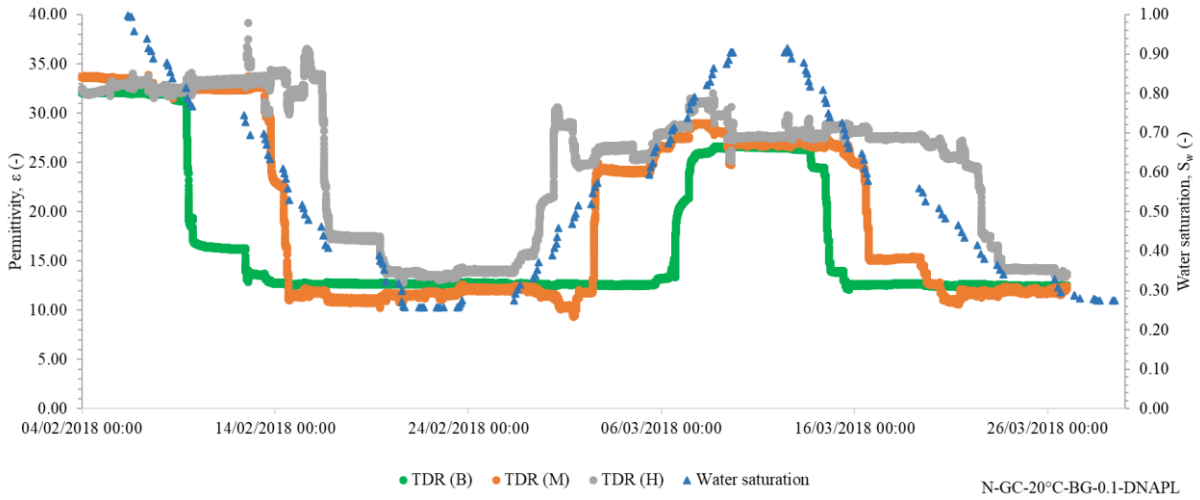


D-GC-20°C-BG-0,5-DNAPI

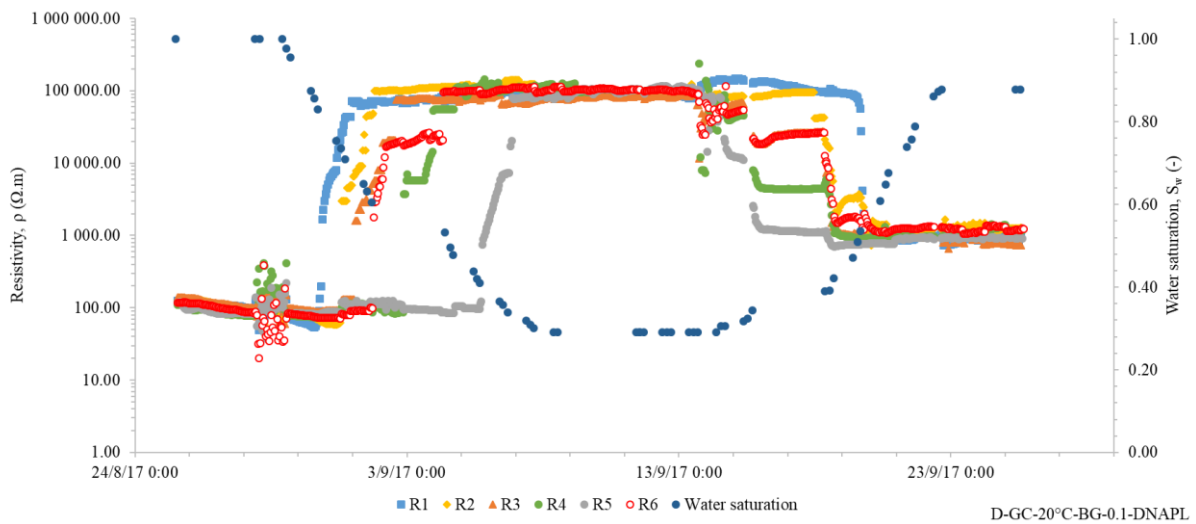
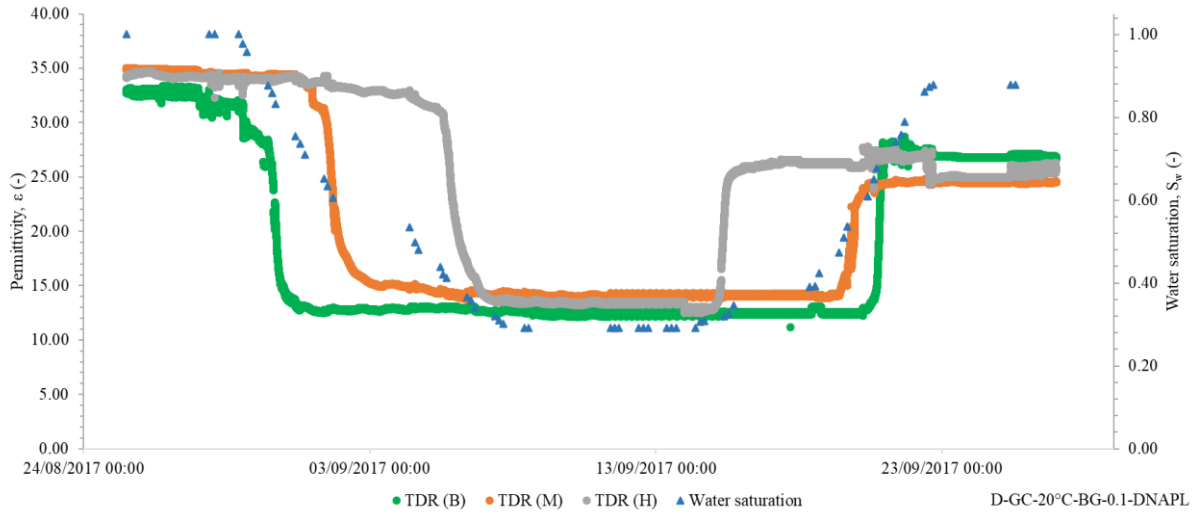


0.1 mm GB without membrane

N-GC-20°C-BG-0.1-DNAPL



D-GC-20°C-BG-0.1-DNAPL

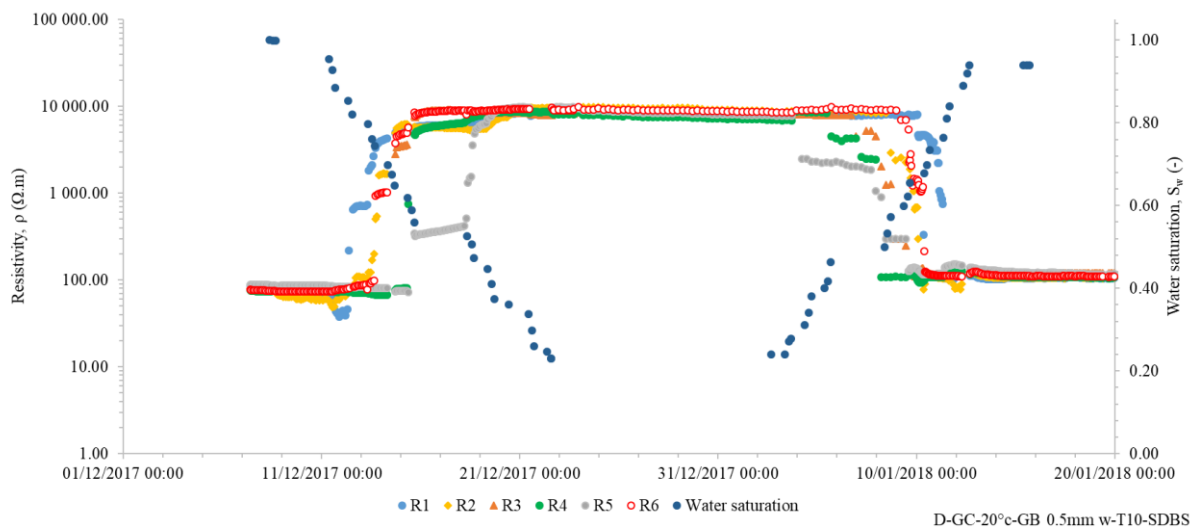
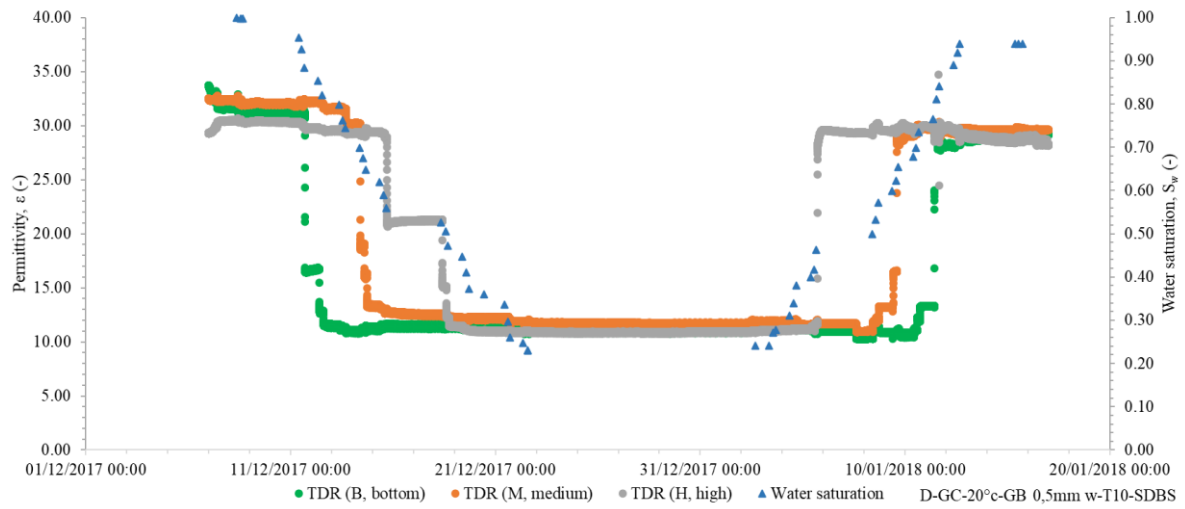


Appendix 6

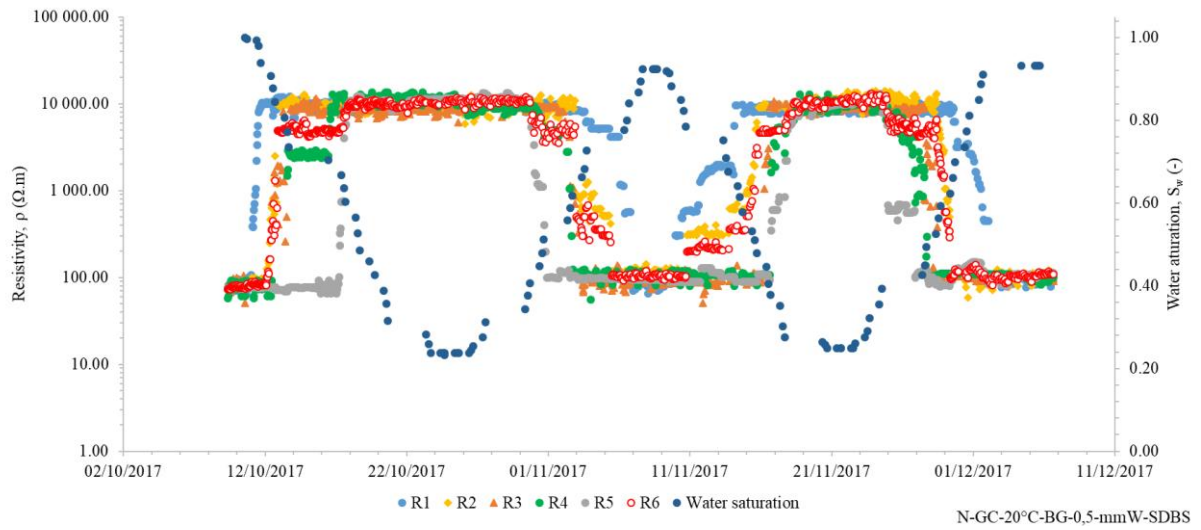
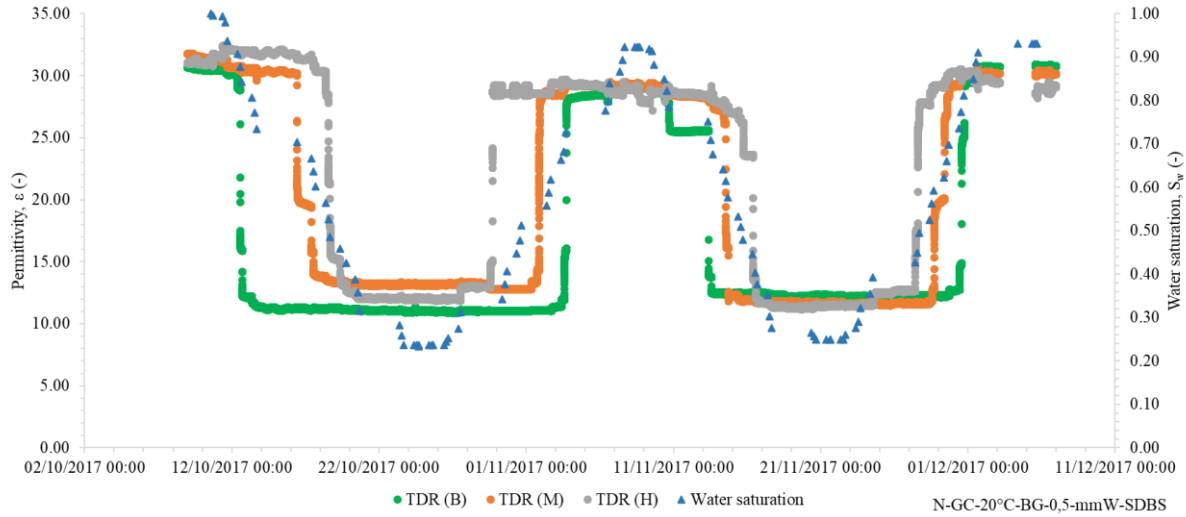
1D columns experiments with chemical enhancement

0.5 mm GB

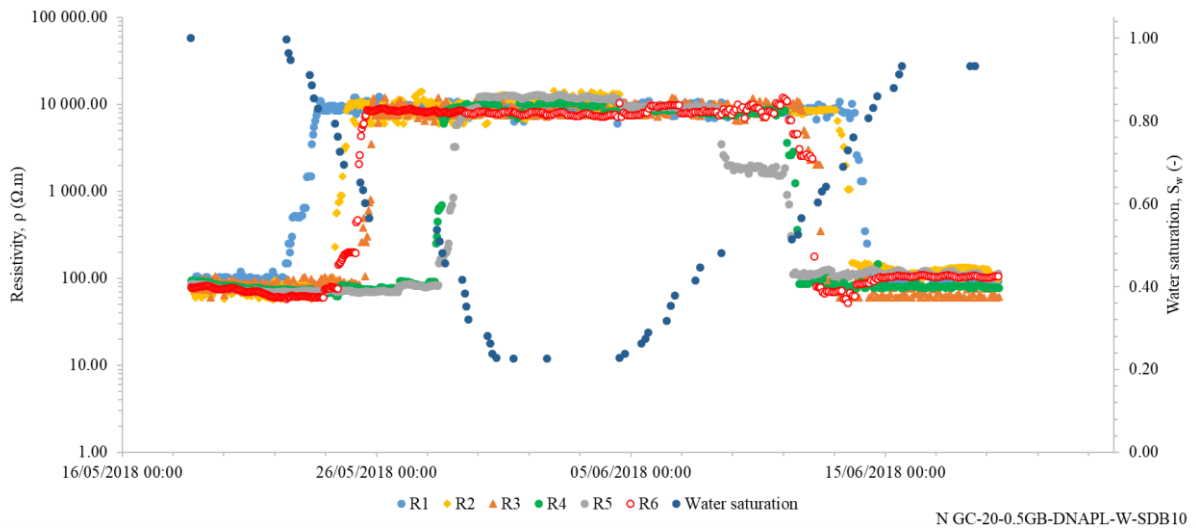
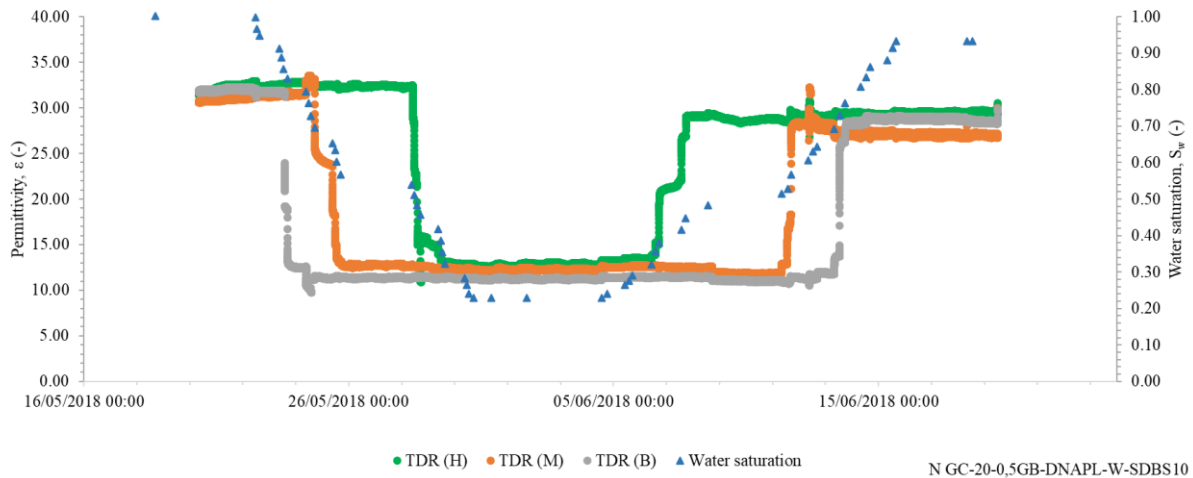
D-GC-20°C-GB 0,5mm w-SDBS



N-GC-20°C-BG-0,5-mmW-SDBS

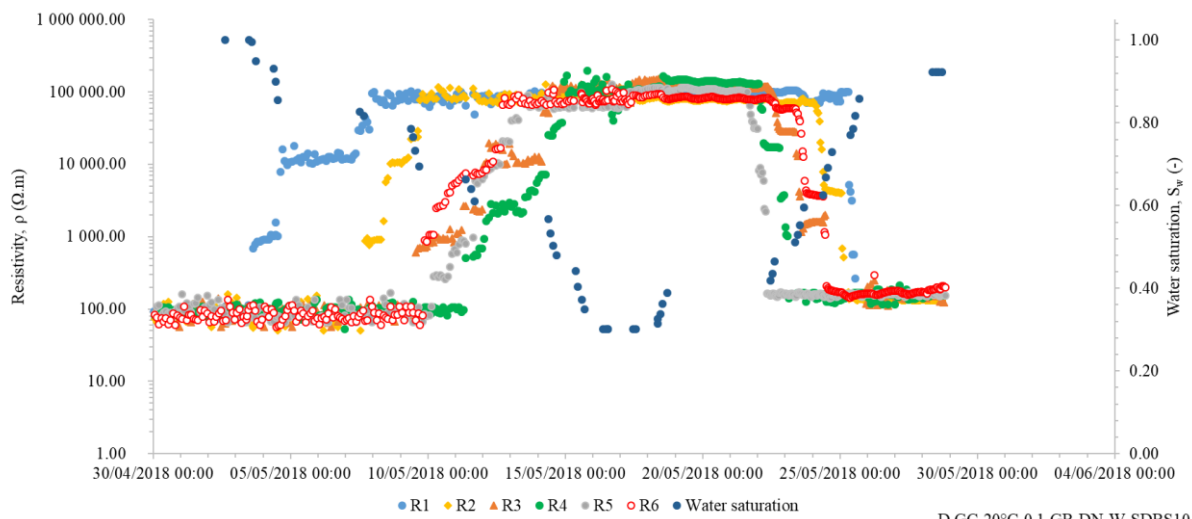
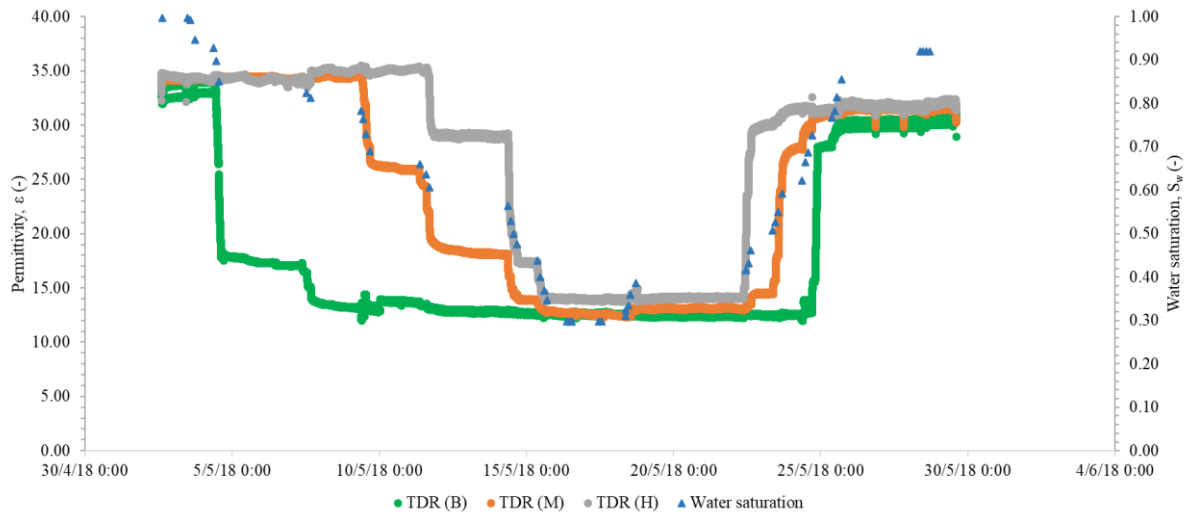


N GC-20-0,5GB-DNAPL-W-SDBS10



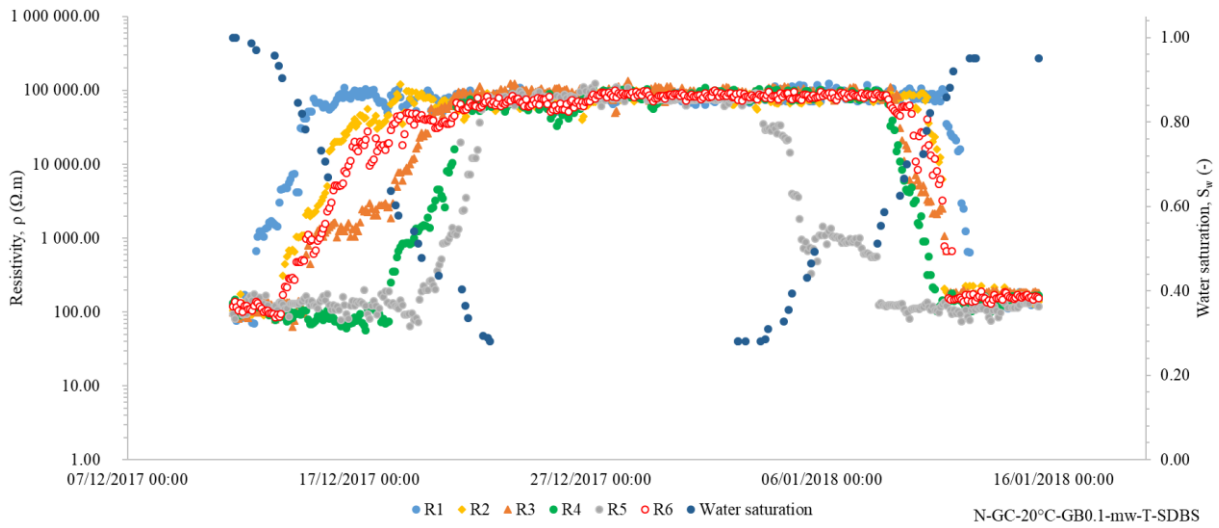
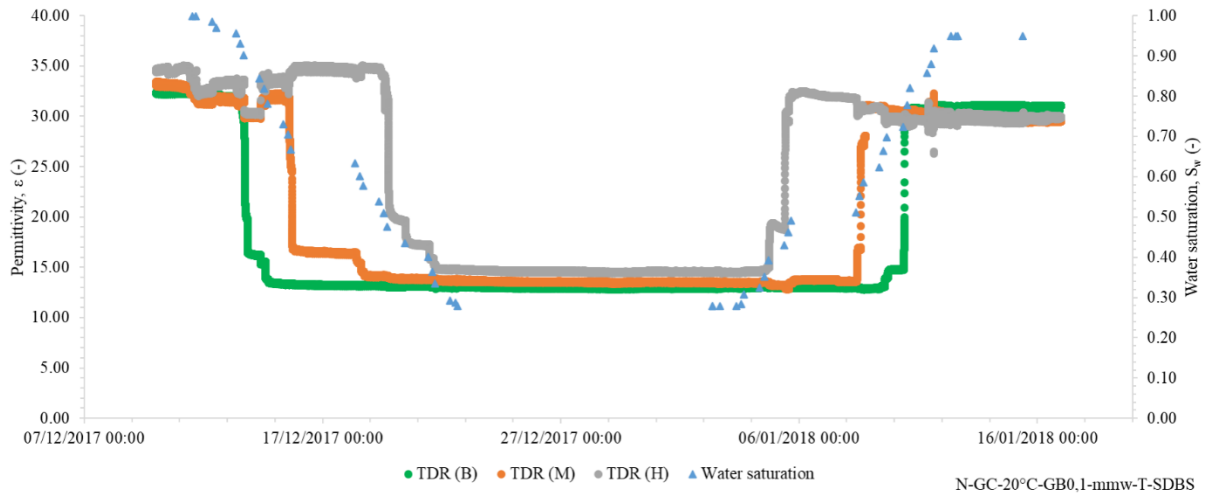
0.1 mm GB

D GC-20°C-0,1-0,2GB-DN-W-SDBS10



D GC-20°C-0.1-GB-DN-W-SDBS10

N-GC-20°C-GB0,1-0,2mw-SDBS

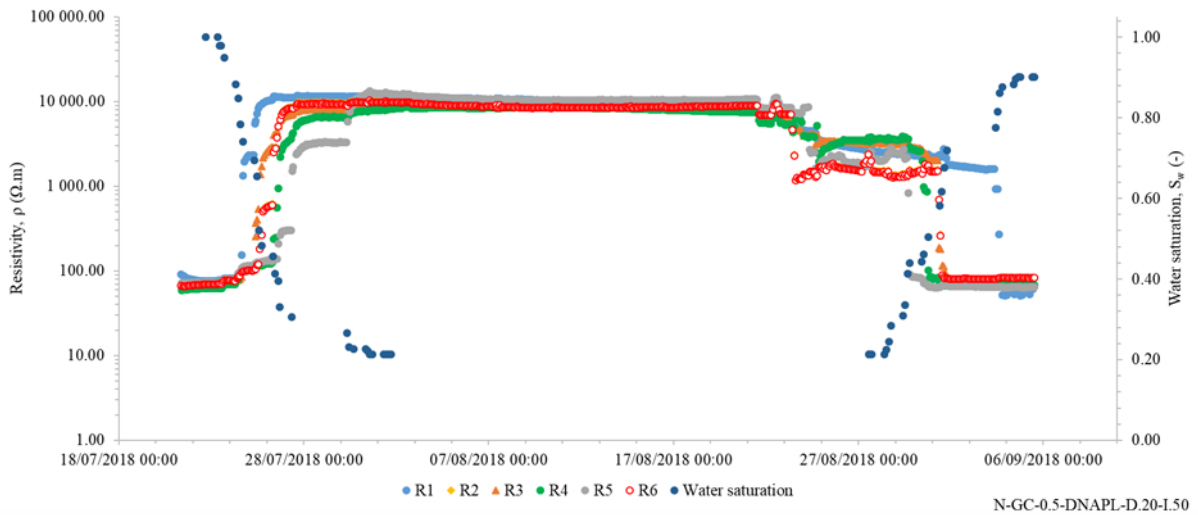
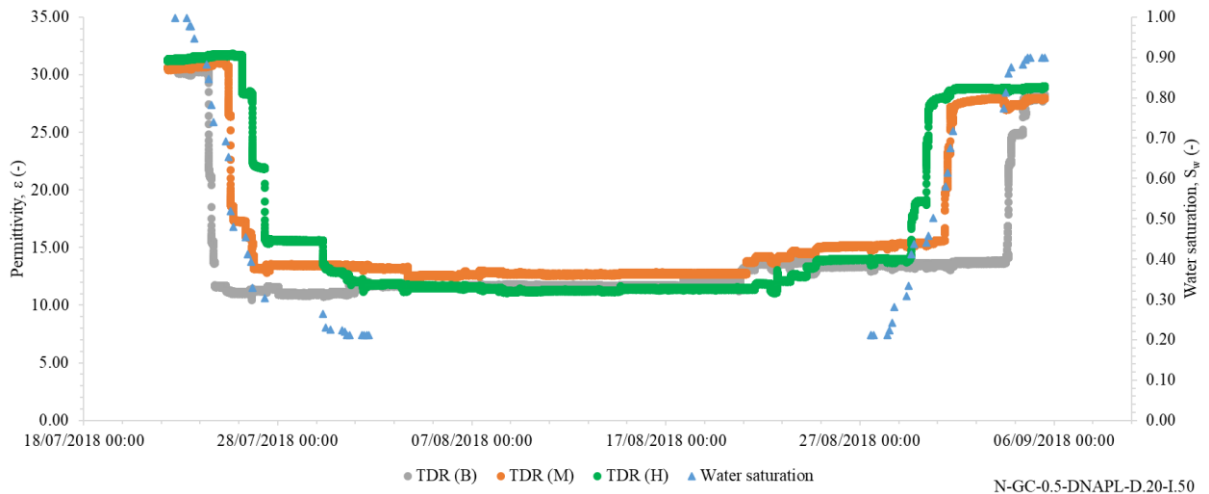


Appendix 7

1D columns experiments with thermal enhancement

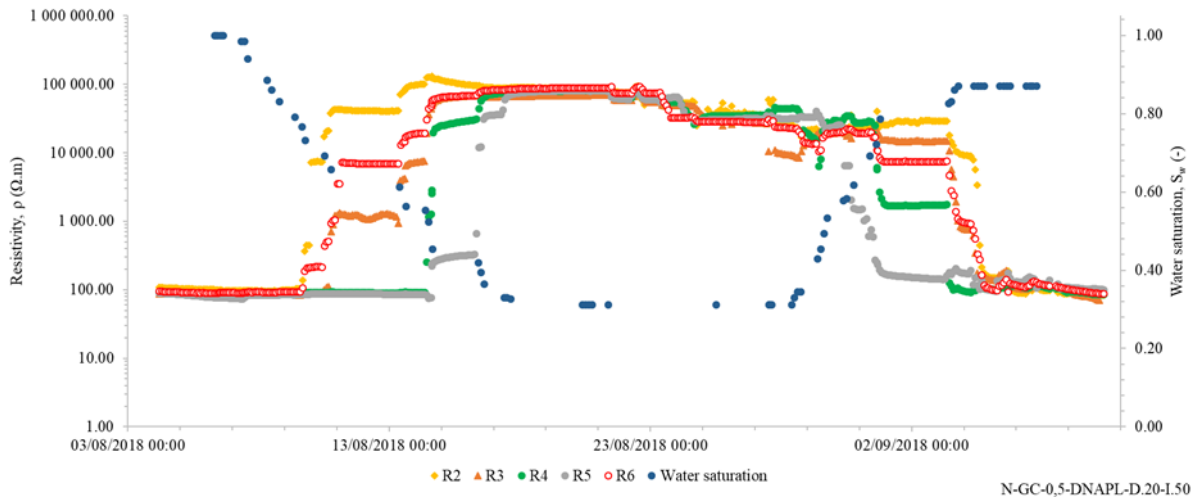
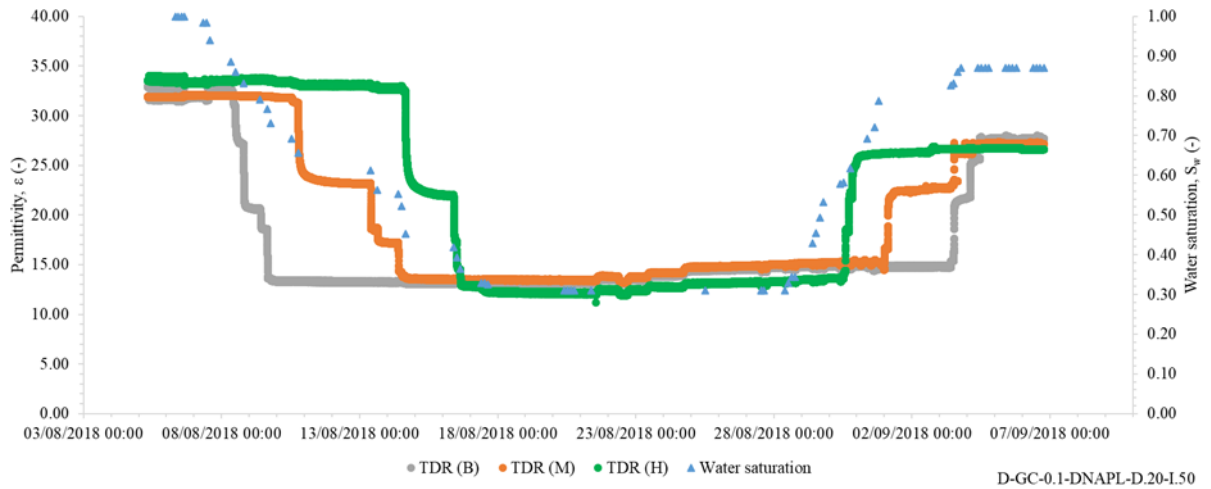
0.5 mm GB

N-GC-0.5-DNAPL-D.20-I.50



0.1 mm GB

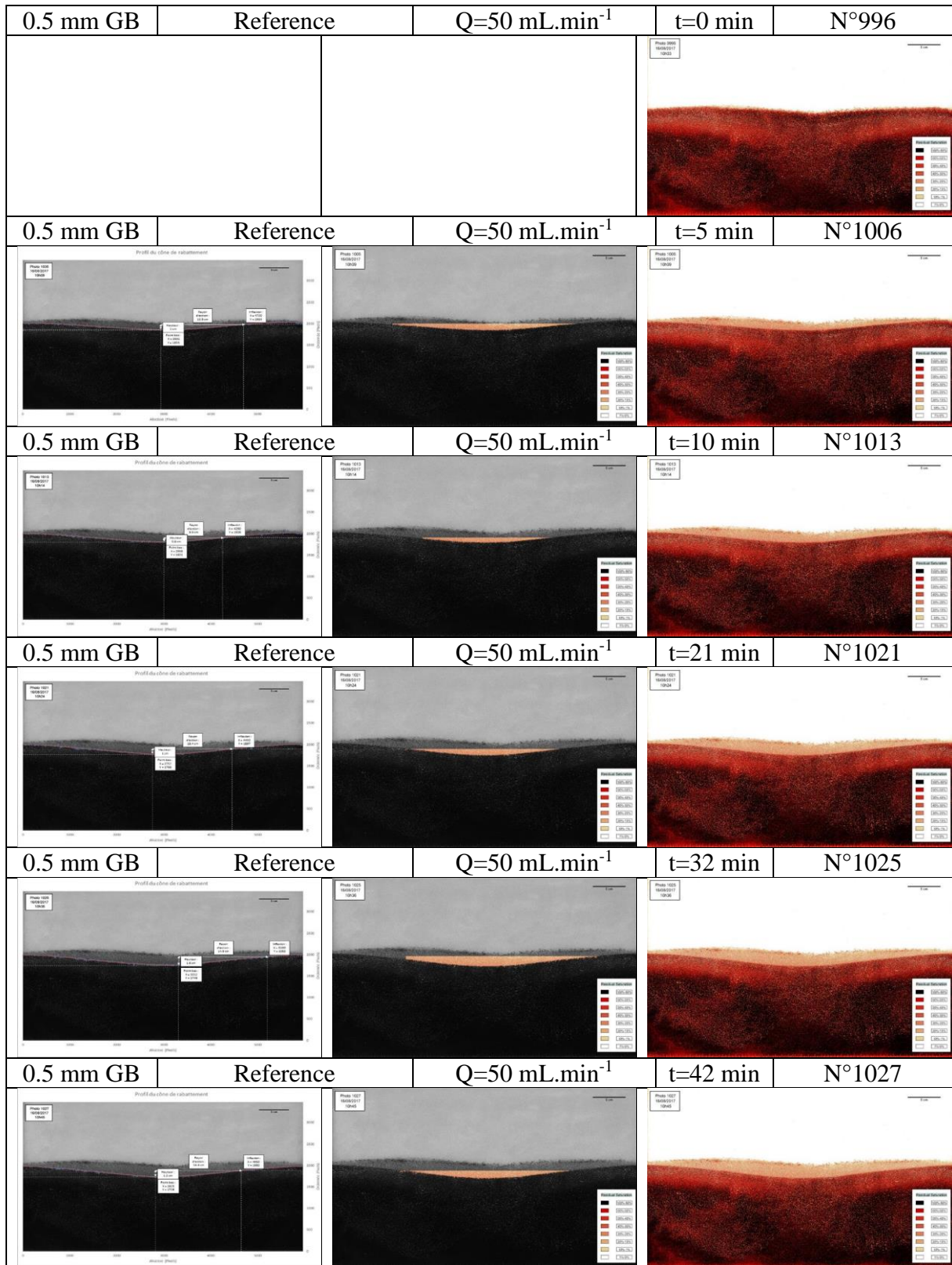
D-GC-0.1-DNAPL-D.20-I.50



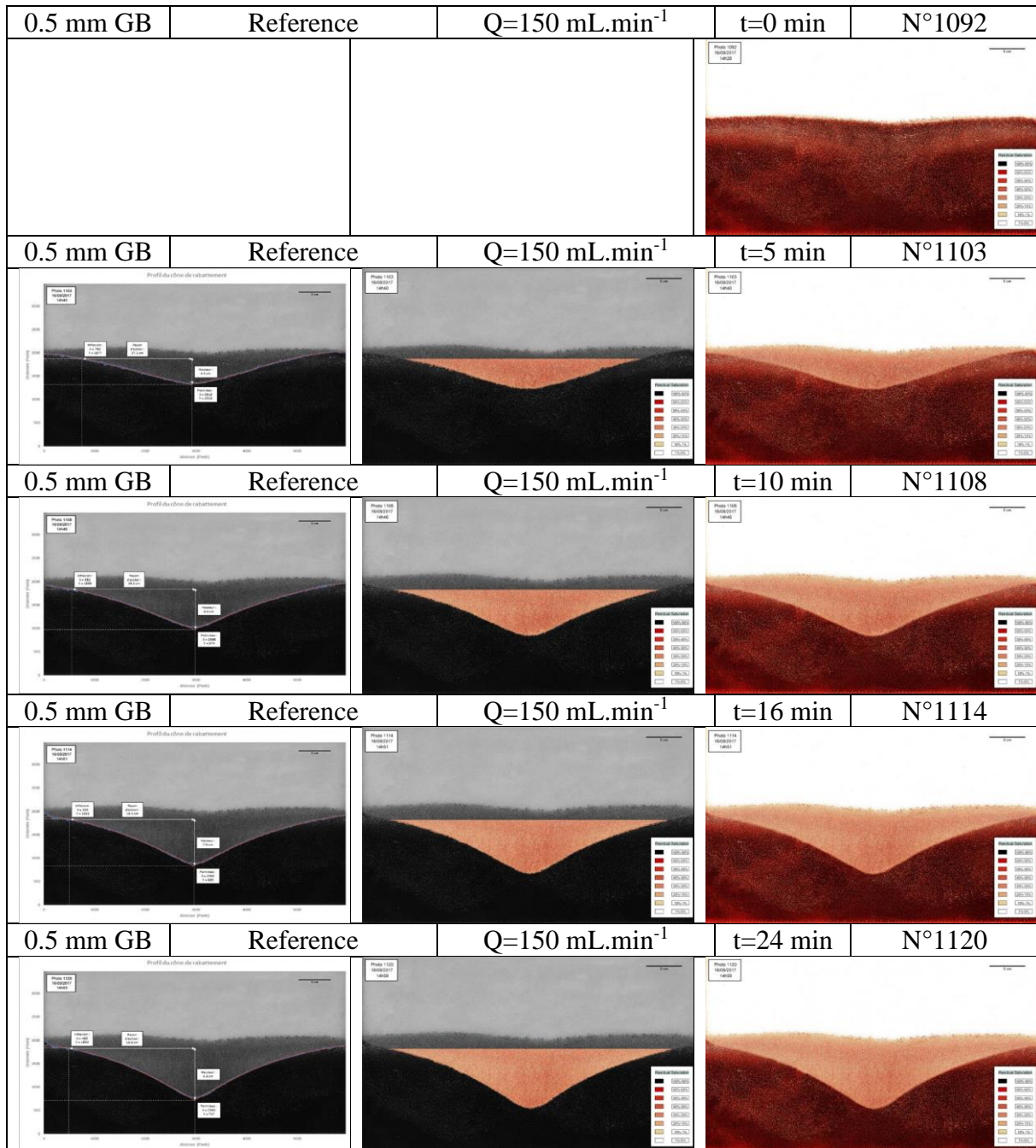
Appendix 8

2D tank experiments without enhancement

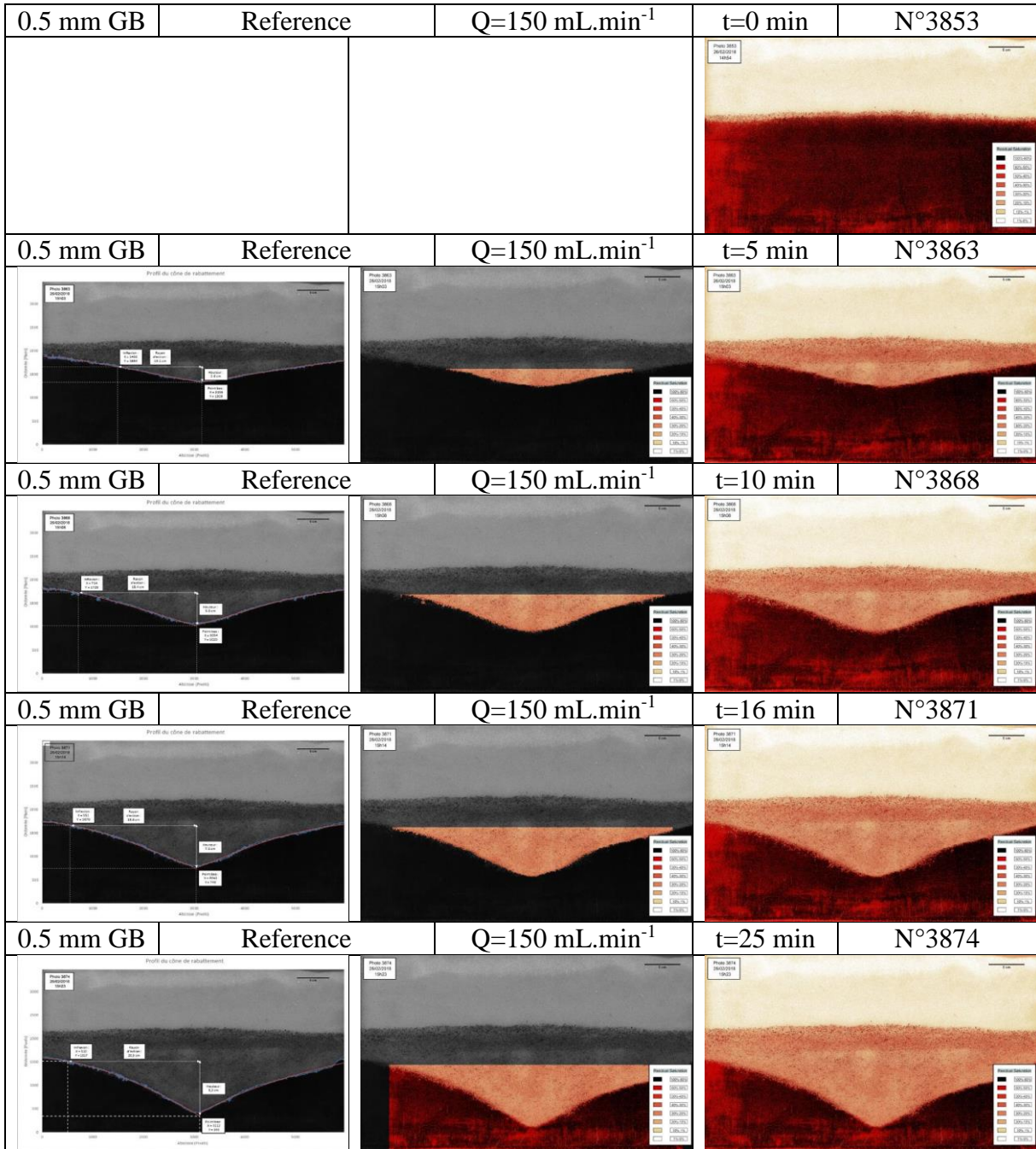
0.5 mm GB Reference $Q=50 \text{ mL}\cdot\text{min}^{-1}$



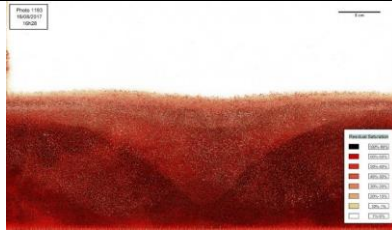
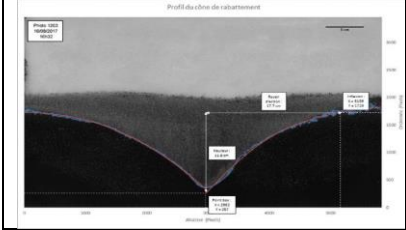
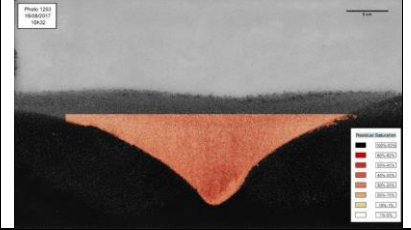
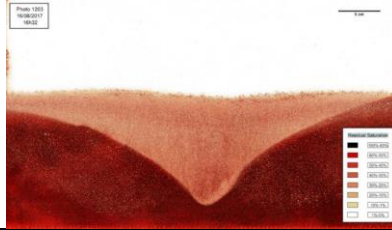
0.5 mm GB Reference $Q=150 \text{ mL}\cdot\text{min}^{-1}$



0.5 mm GB Reference $Q=150 \text{ mL}\cdot\text{min}^{-1}$

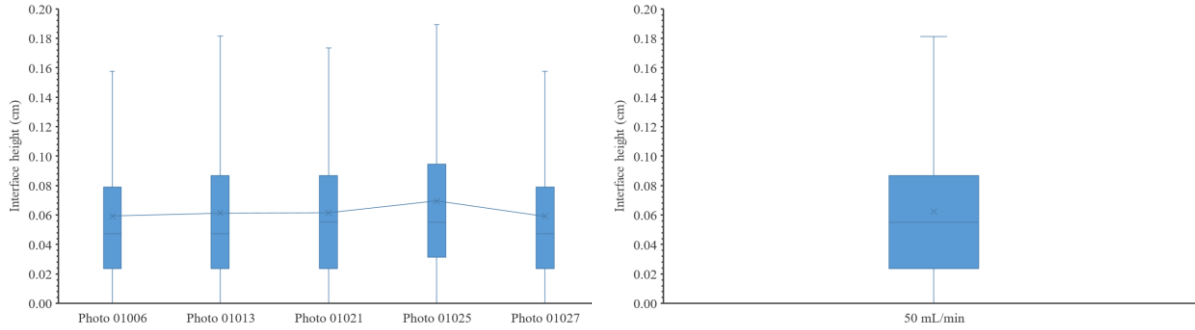


0.5 mm GB Reference $Q=220 \text{ mL}\cdot\text{min}^{-1}$

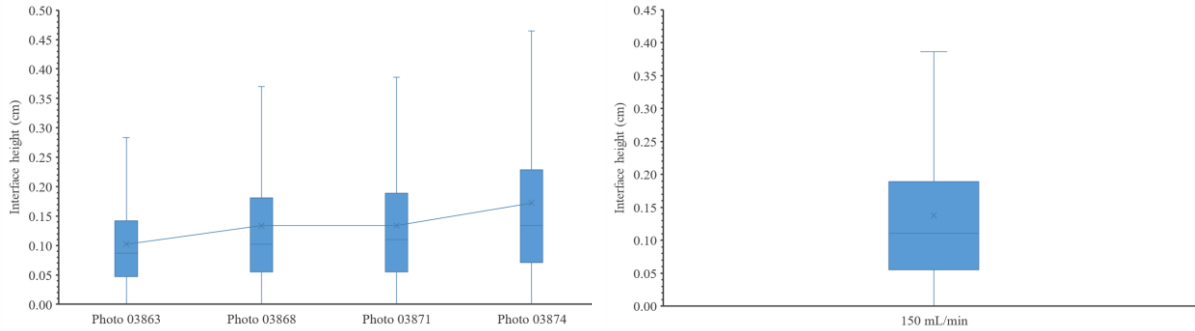
0.5 mm GB	Reference	$Q=220 \text{ mL}\cdot\text{min}^{-1}$	t=0 min	N°1193
				
0.5 mm GB	Reference	$Q=220 \text{ mL}\cdot\text{min}^{-1}$	t=5 min	N°1203
				

0.5 mm GB Reference

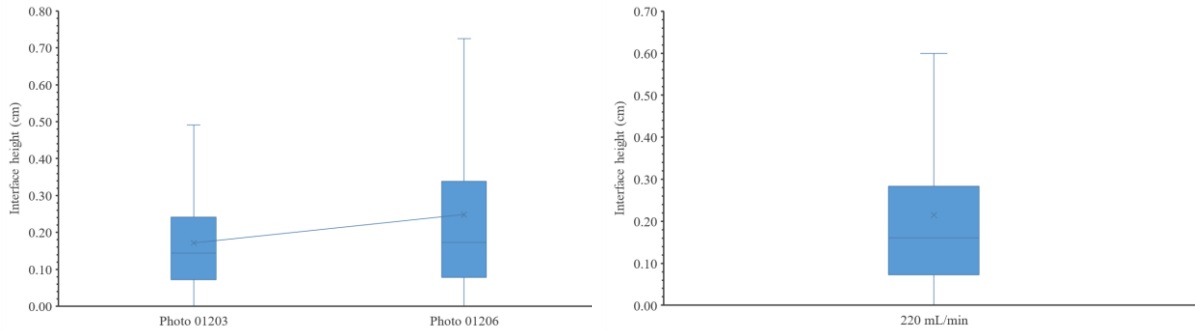
Statistical representation of fingerings of the DNAPL-water interface - 50 mL.min⁻¹



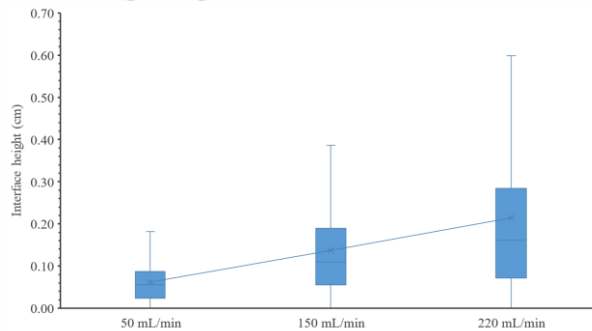
Statistical representation of fingerings of the DNAPL-water interface - 150 mL.min⁻¹



Statistical representation of fingerings of the DNAPL-water interface - 220 mL.min⁻¹



Statistical representation of fingerings of the DNAPL-water interface - Total



0.1 mm GB Reference Q=50 mL.min⁻¹

0.1 mm GB	Reference	Q=50 mL.min ⁻¹	t=0 min	N°3560
0.1 mm GB	Reference	Q=50 mL.min ⁻¹	t=5 min	N°3569
0.1 mm GB	Reference	Q=50 mL.min ⁻¹	t=10 min	N°3574
0.1 mm GB	Reference	Q=50 mL.min ⁻¹	t=14 min	N°3576
0.1 mm GB	Reference	Q=50 mL.min ⁻¹	t=20 min	N°3579
0.1 mm GB	Reference	Q=50 mL.min ⁻¹	t=28 min	N°3583

0.1 mm GB Reference Q=150 mL.min⁻¹

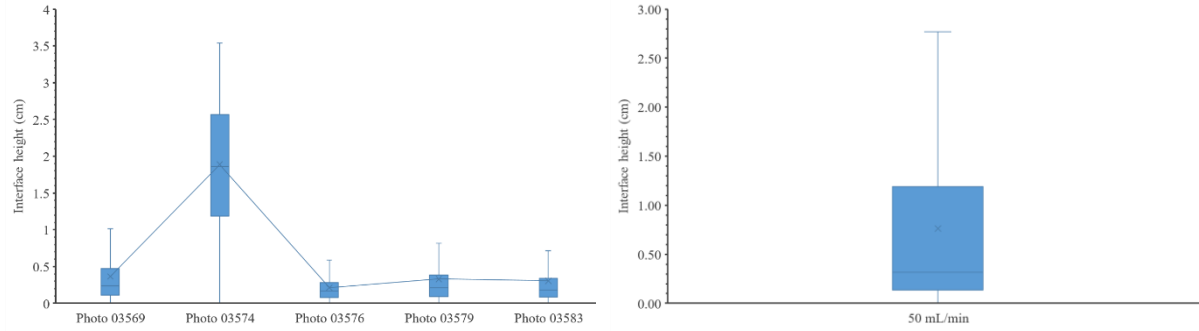
0.1 mm GB	Reference	Q=150 mL.min ⁻¹	t=0 min	N°3511
0.1 mm GB	Reference	Q=150 mL.min ⁻¹	t=5 min	N°3520
0.1 mm GB	Reference	Q=150 mL.min ⁻¹	t=10 min	N°3522
0.1 mm GB	Reference	Q=150 mL.min ⁻¹	t=14 min	N°3523
0.1 mm GB	Reference	Q=150 mL.min ⁻¹	t=18 min	N°3524

0.1 mm GB Reference $Q=220 \text{ mL}\cdot\text{min}^{-1}$

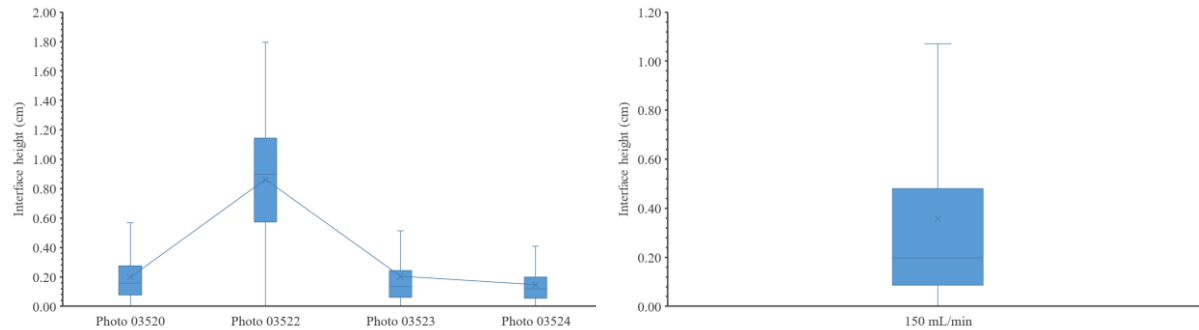
0.1 mm GB	Reference	$Q=220 \text{ mL}\cdot\text{min}^{-1}$	t=0 min	N°3637
0.1 mm GB	Reference	$Q=220 \text{ mL}\cdot\text{min}^{-1}$	t=5 min	N°3646
0.1 mm GB	Reference	$Q=220 \text{ mL}\cdot\text{min}^{-1}$	t=10 min	N°3651
0.1 mm GB	Reference	$Q=220 \text{ mL}\cdot\text{min}^{-1}$	t=14 min	N°3653
0.1 mm GB	Reference	$Q=220 \text{ mL}\cdot\text{min}^{-1}$	t=20 min	N°3656
0.1 mm GB	Reference	$Q=220 \text{ mL}\cdot\text{min}^{-1}$	t=30 min	N°3658

0.1 mm GB Reference

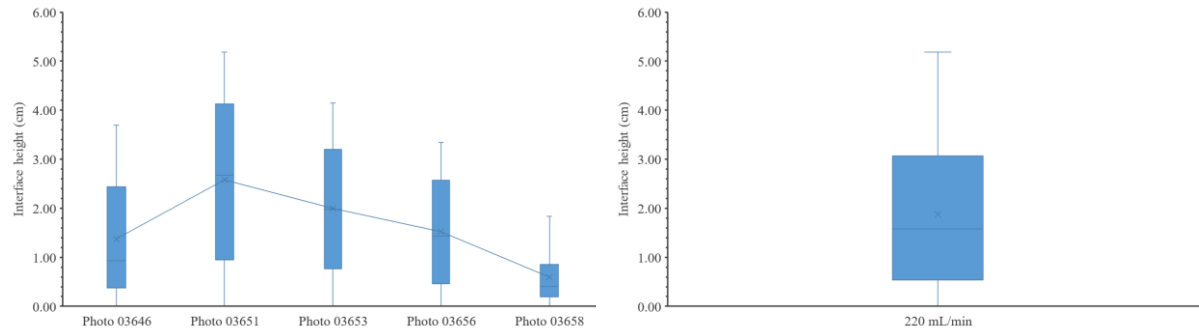
Statistical representation of fingerings of the DNAPL-water interface - 50 mL.min⁻¹



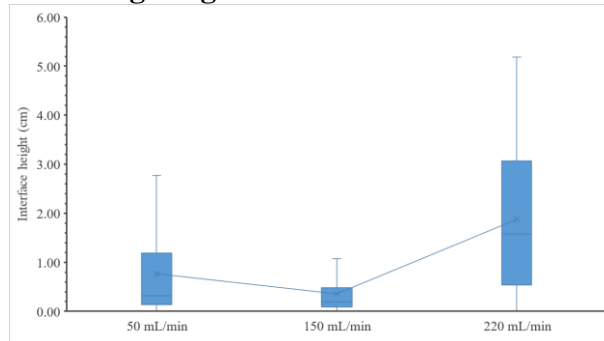
Statistical representation of fingerings of the DNAPL-water interface - 150 mL.min⁻¹



Statistical representation of fingerings of the DNAPL-water interface - 220 mL.min⁻¹



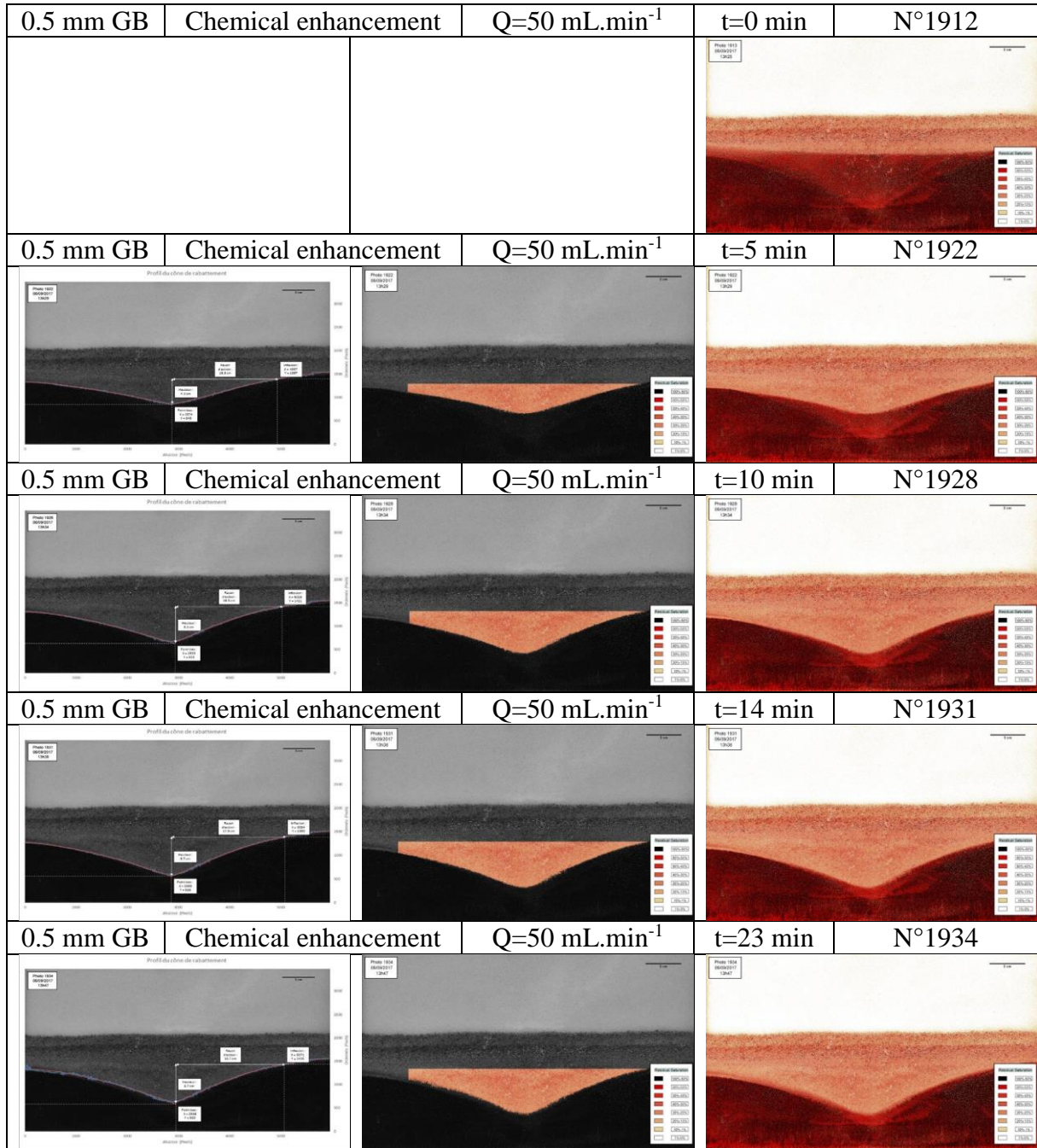
Statistical representation of fingerings of the DNAPL-water interface - Total



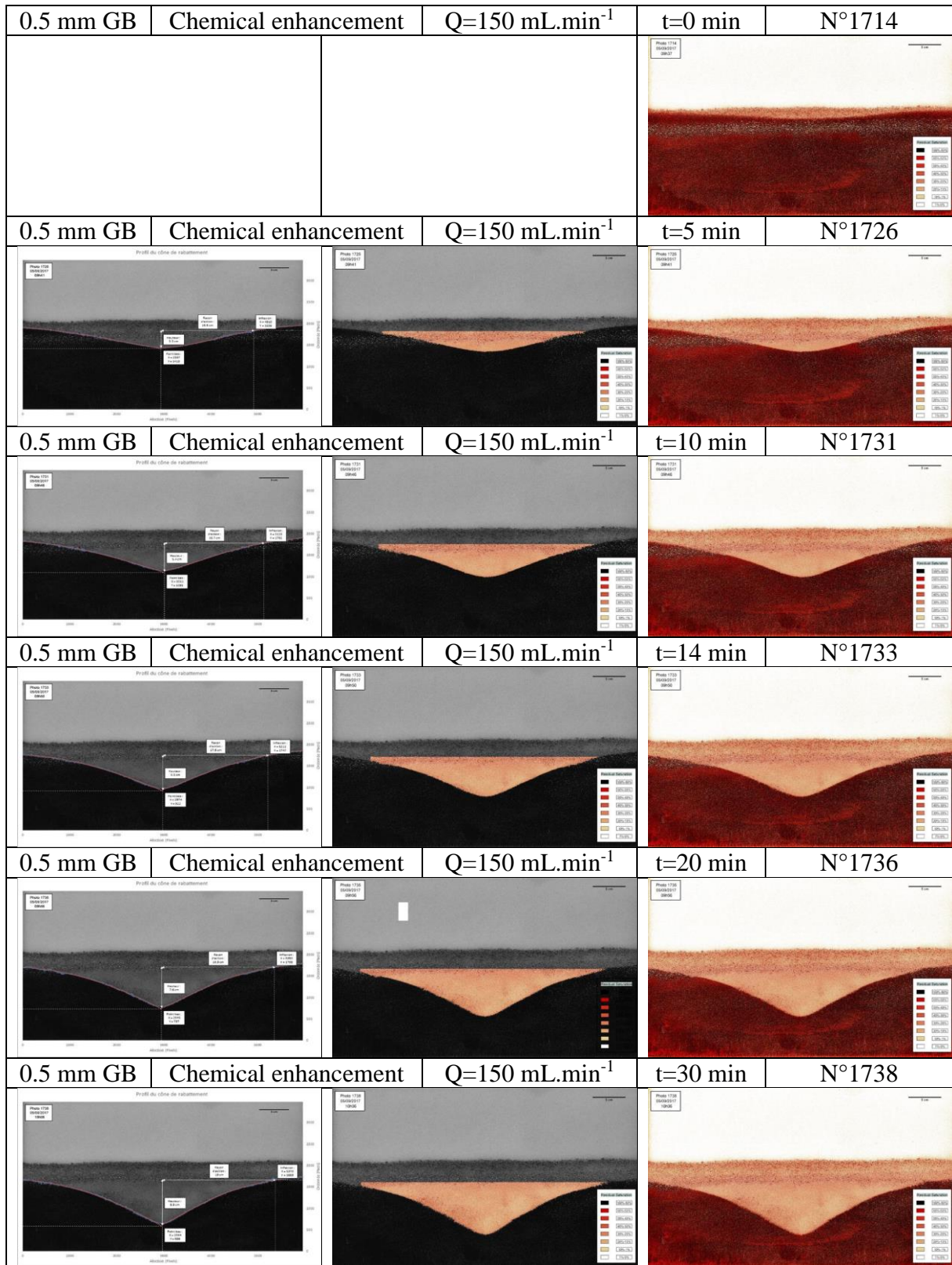
Appendix 9

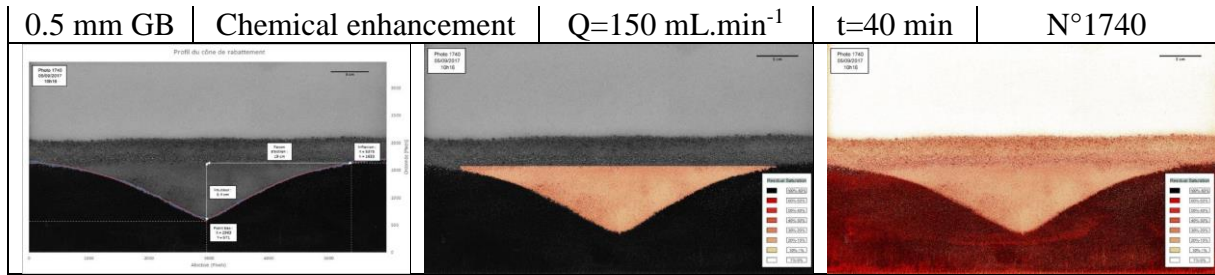
2D tank experiments with chemical enhancement

0.5 mm GB Chemical enhancement Q=50 mL.min⁻¹

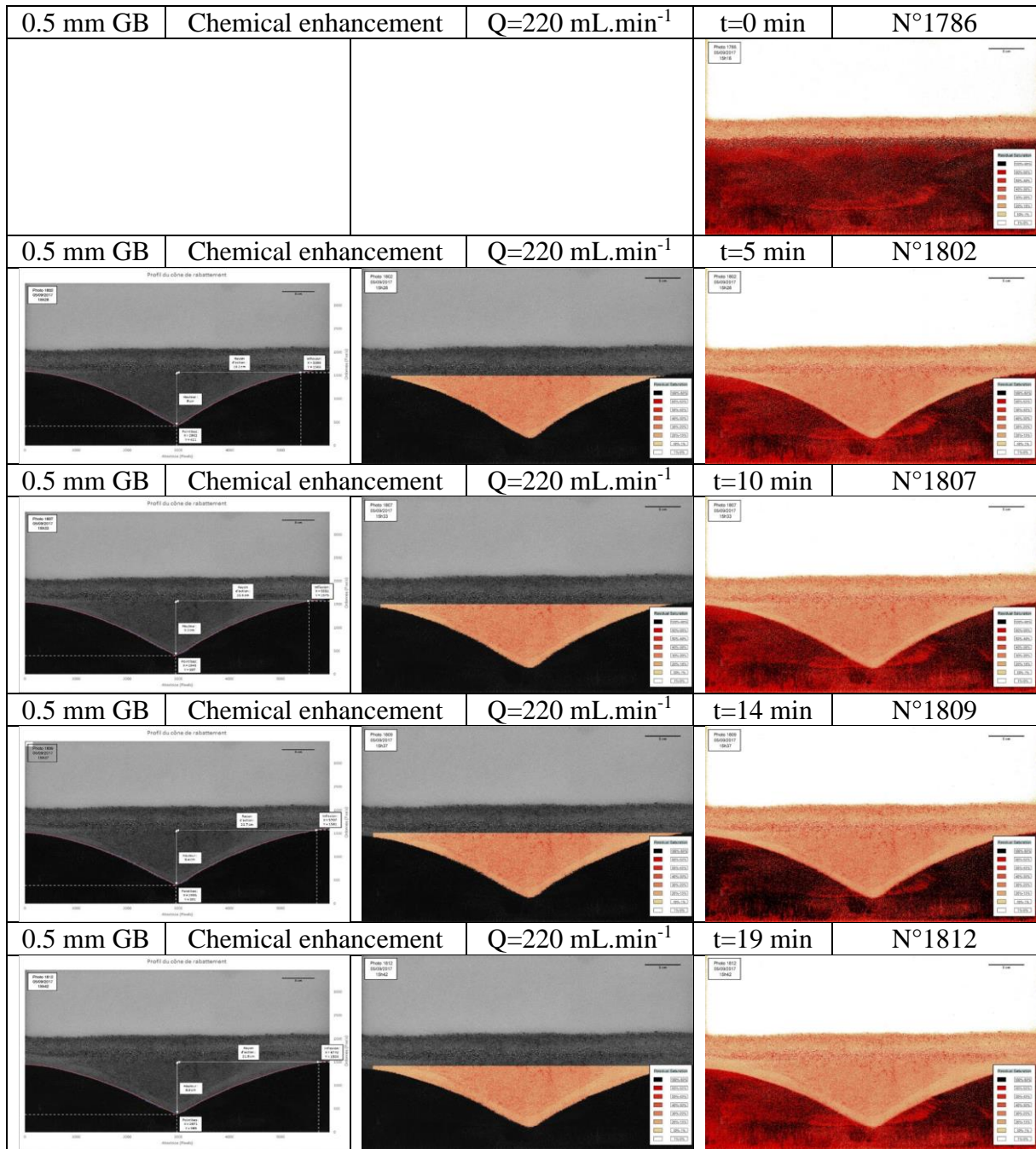


0.5 mm GB Chemical enhancement $Q=150 \text{ mL}\cdot\text{min}^{-1}$



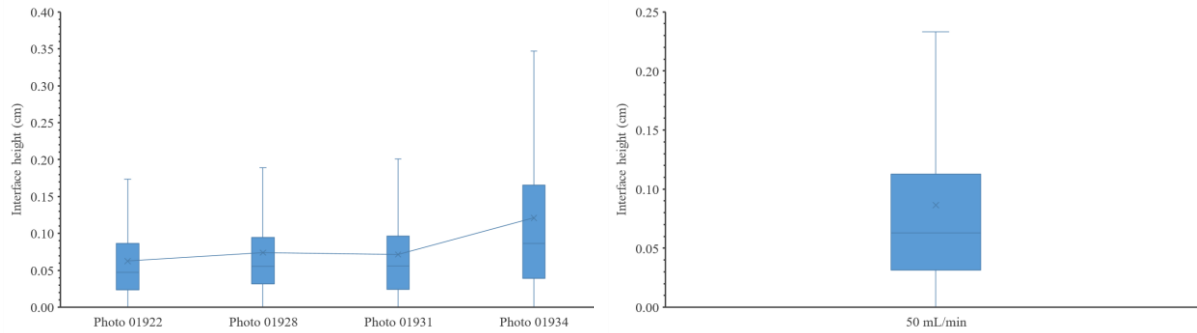


0.5 mm GB Chemical enhancement $Q=220 \text{ mL}\cdot\text{min}^{-1}$

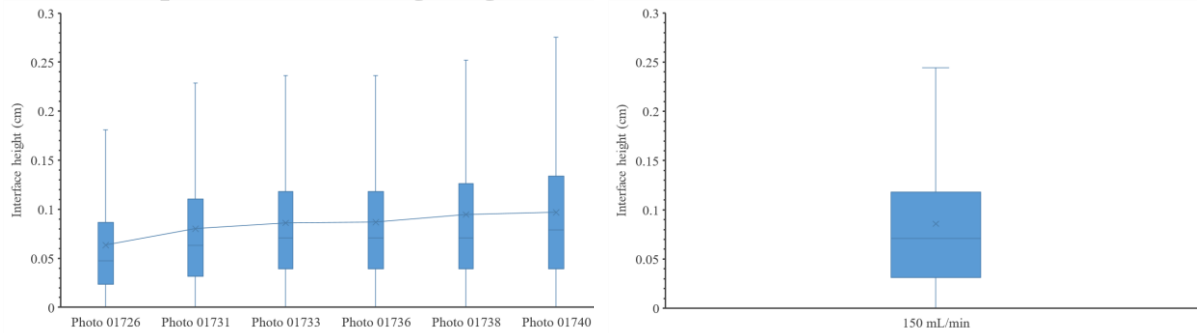


0.5 mm GB Chemical enhancement

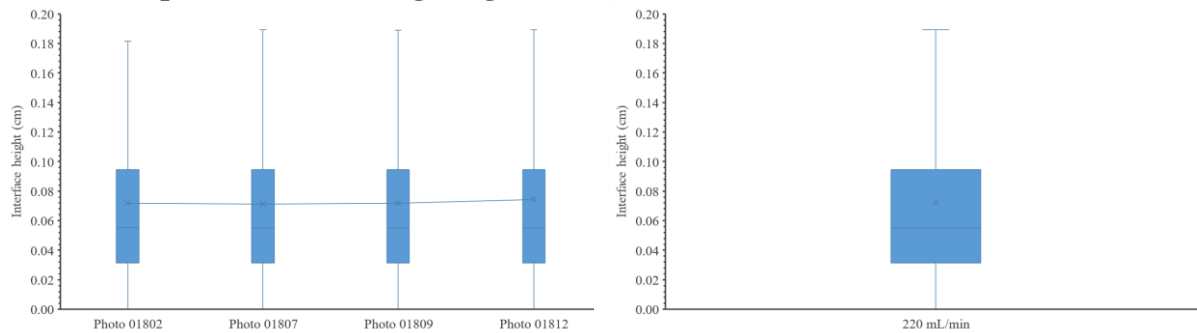
Statistical representation of fingerings of the DNAPL-water interface – 50 mL.min⁻¹



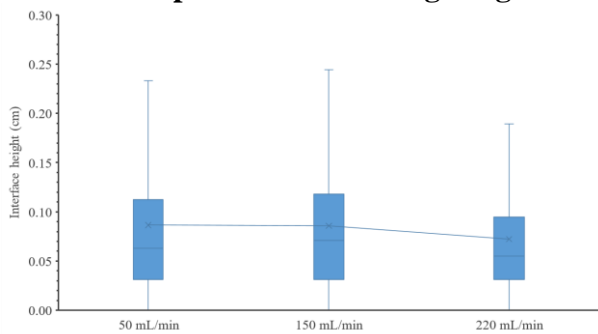
Statistical representation of fingerings of the DNAPL-water interface – 150 mL.min⁻¹



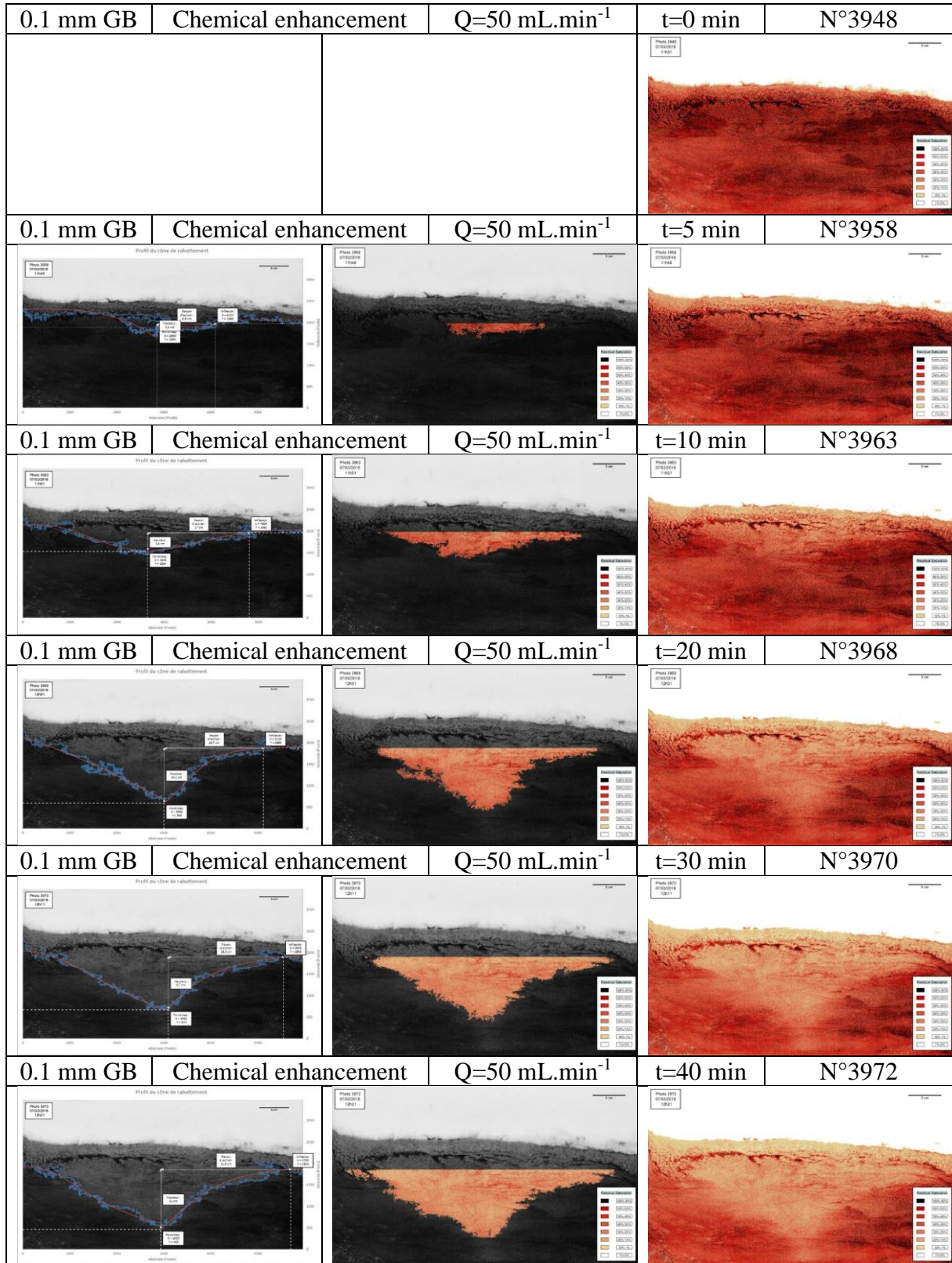
Statistical representation of fingerings of the DNAPL-water interface – 220 mL.min⁻¹



Statistical representation of fingerings of the DNAPL-water interface – Total



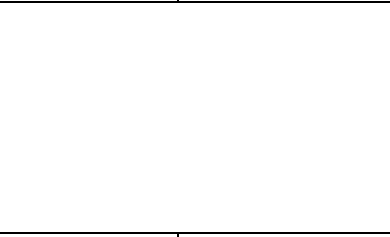
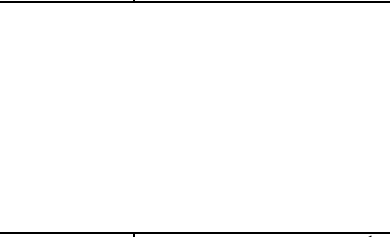
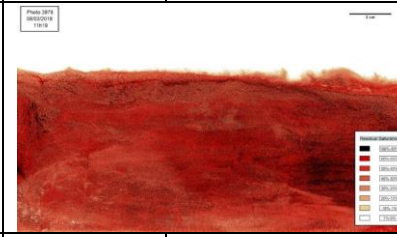
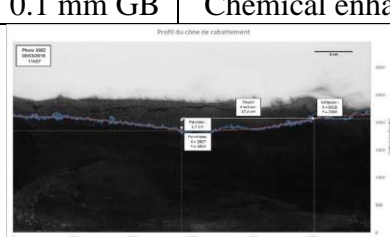
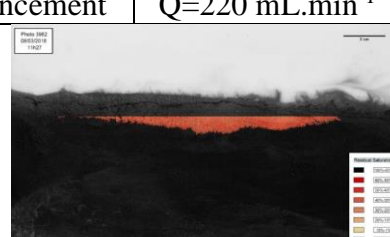
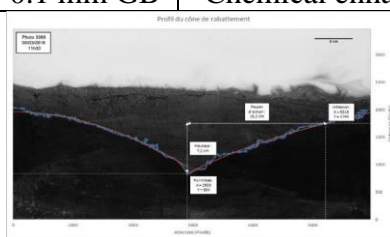
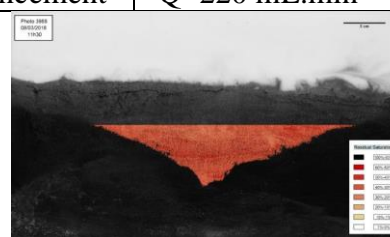
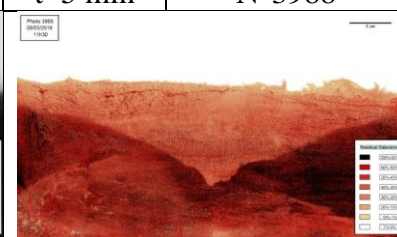
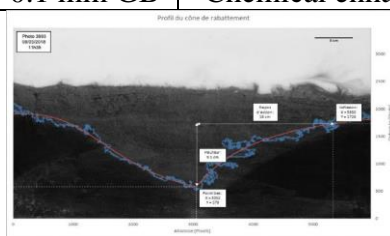
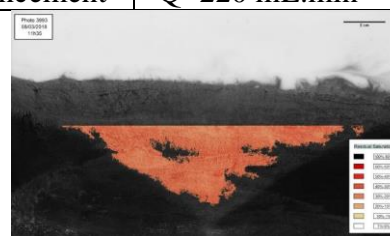
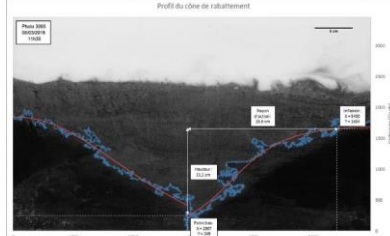

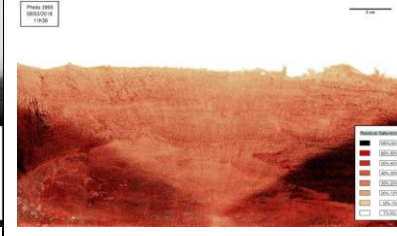





0.1 mm GB Chemical enhancement $Q=50 \text{ mL}\cdot\text{min}^{-1}$



0.1 mm GB Chemical enhancement $Q=150 \text{ mL}\cdot\text{min}^{-1}$

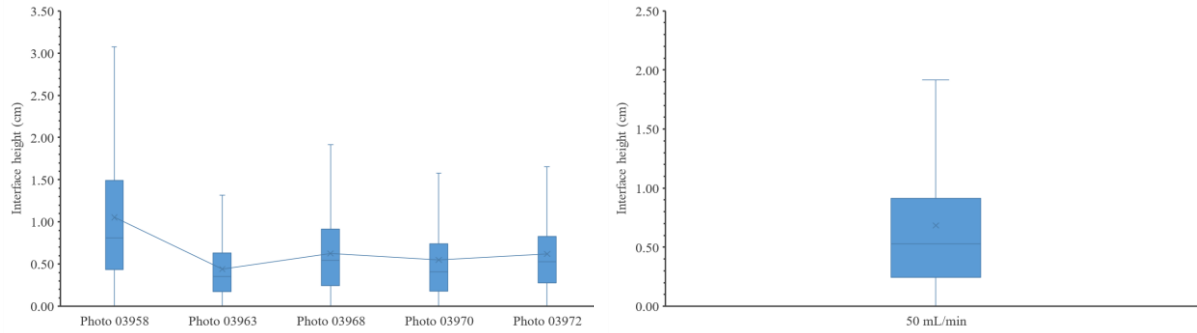
0.1 mm GB	Chemical enhancement	$Q=150 \text{ mL}\cdot\text{min}^{-1}$	t=0 min	N°3920
0.1 mm GB	Chemical enhancement	$Q=150 \text{ mL}\cdot\text{min}^{-1}$	t=5 min	N°3930
0.1 mm GB	Chemical enhancement	$Q=150 \text{ mL}\cdot\text{min}^{-1}$	t=10 min	N°3935
0.1 mm GB	Chemical enhancement	$Q=150 \text{ mL}\cdot\text{min}^{-1}$	t=14 min	N°3937
0.1 mm GB	Chemical enhancement	$Q=150 \text{ mL}\cdot\text{min}^{-1}$	t=18 min	N°3939

0.1 mm GB Chemical enhancement $Q=220 \text{ mL}\cdot\text{min}^{-1}$

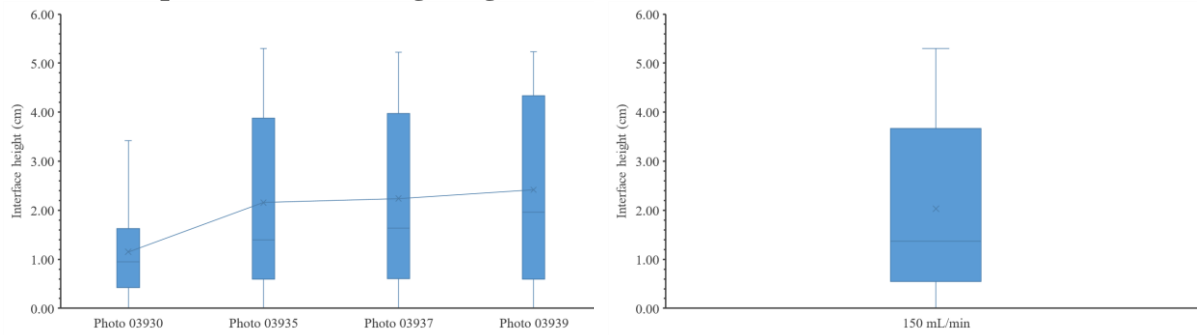
0.1 mm GB	Chemical enhancement	$Q=220 \text{ mL}\cdot\text{min}^{-1}$	t=0 min	N°3978
				
0.1 mm GB	Chemical enhancement	$Q=220 \text{ mL}\cdot\text{min}^{-1}$	t=2 min	N°3982
				
0.1 mm GB	Chemical enhancement	$Q=220 \text{ mL}\cdot\text{min}^{-1}$	t=5 min	N°3988
				
0.1 mm GB	Chemical enhancement	$Q=220 \text{ mL}\cdot\text{min}^{-1}$	t=10 min	N°3993
				
0.1 mm GB	Chemical enhancement	$Q=220 \text{ mL}\cdot\text{min}^{-1}$	t=14 min	N°3995

0.1 mm GB Chemical enhancement

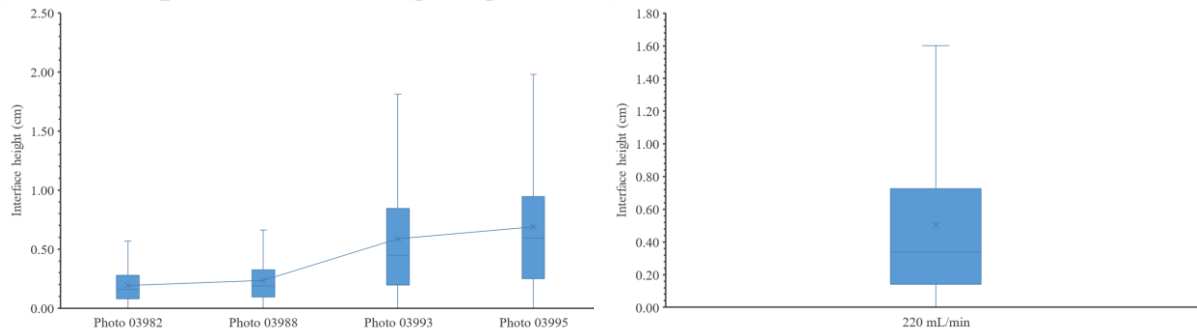
Statistical representation of fingerings of the DNAPL-water interface - 50 mL.min⁻¹



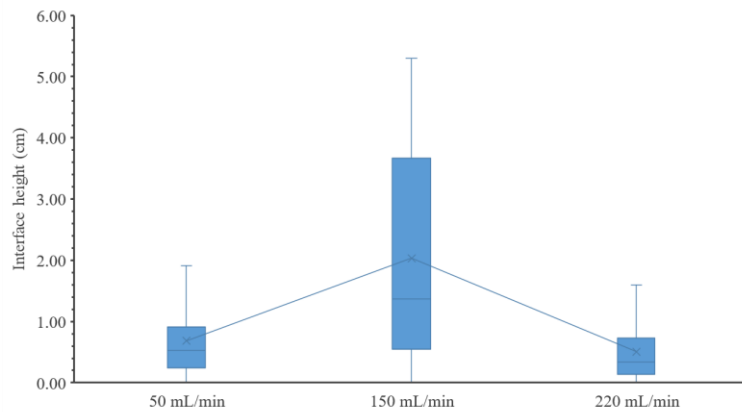
Statistical representation of fingerings of the DNAPL-water interface - 150 mL.min⁻¹



Statistical representation of fingerings of the DNAPL-water interface - 220 mL.min⁻¹



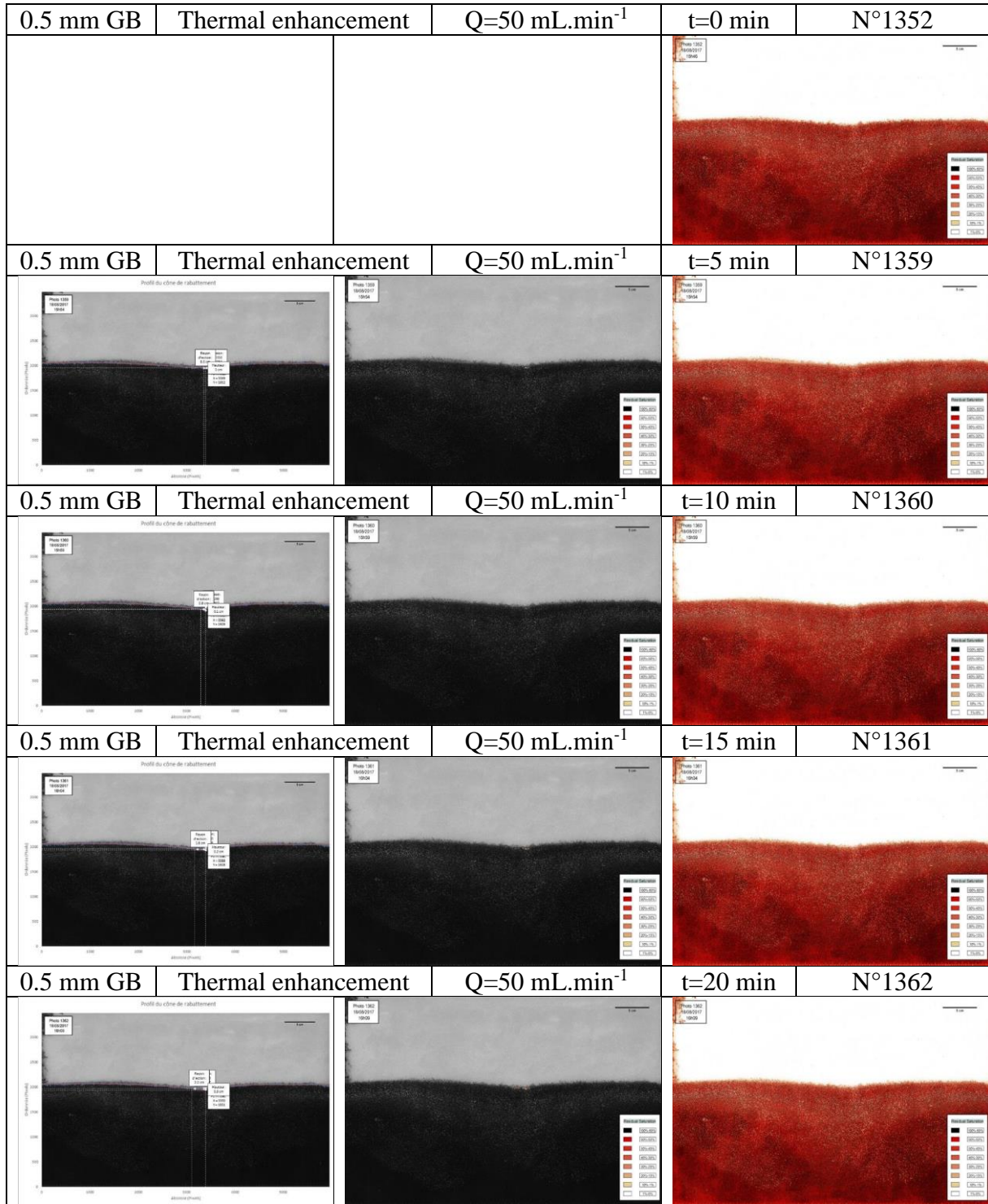
Statistical representation of fingerings of the DNAPL-water interface - Total



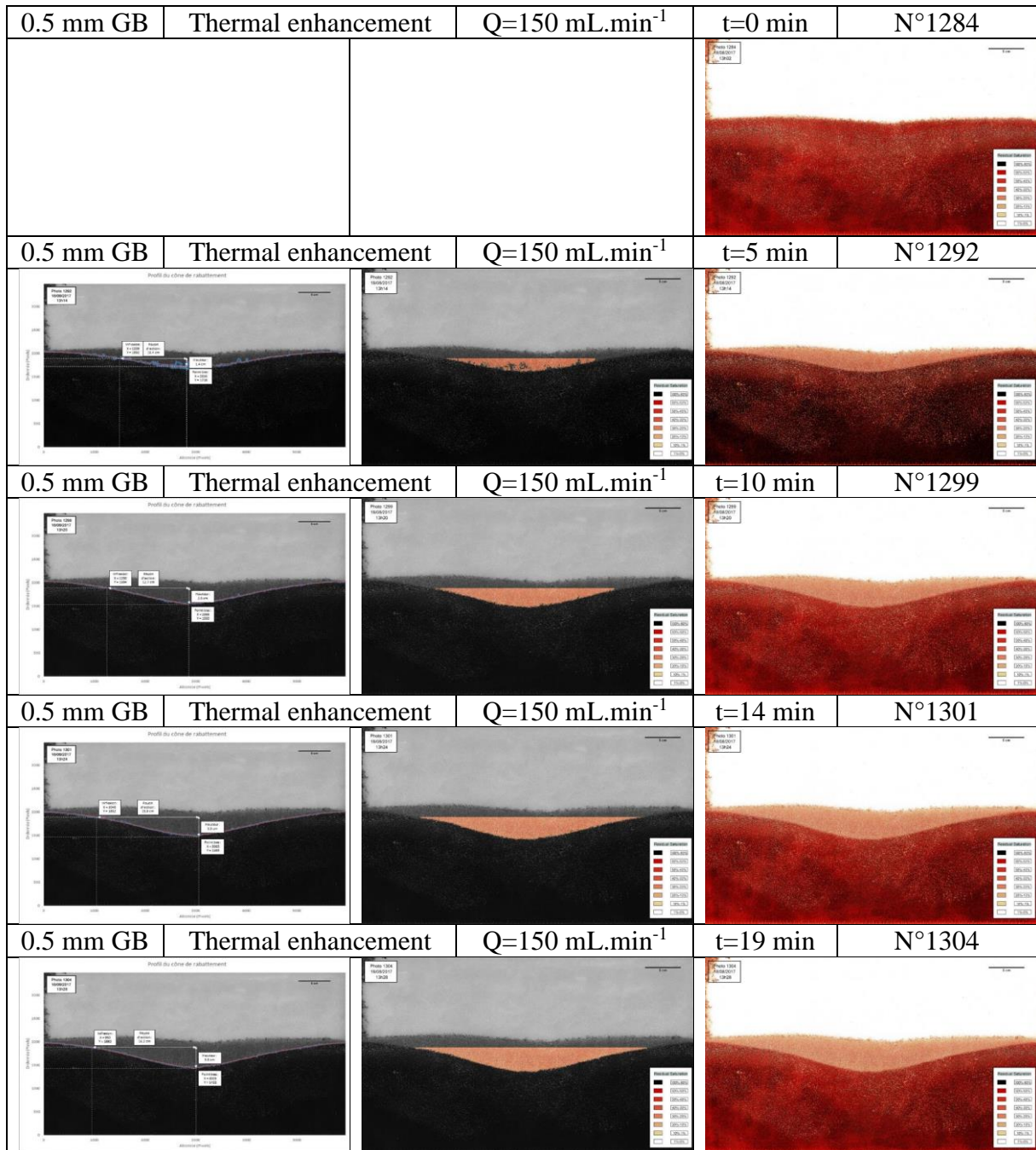
Appendix 10

2D tank experiments with thermal enhancement

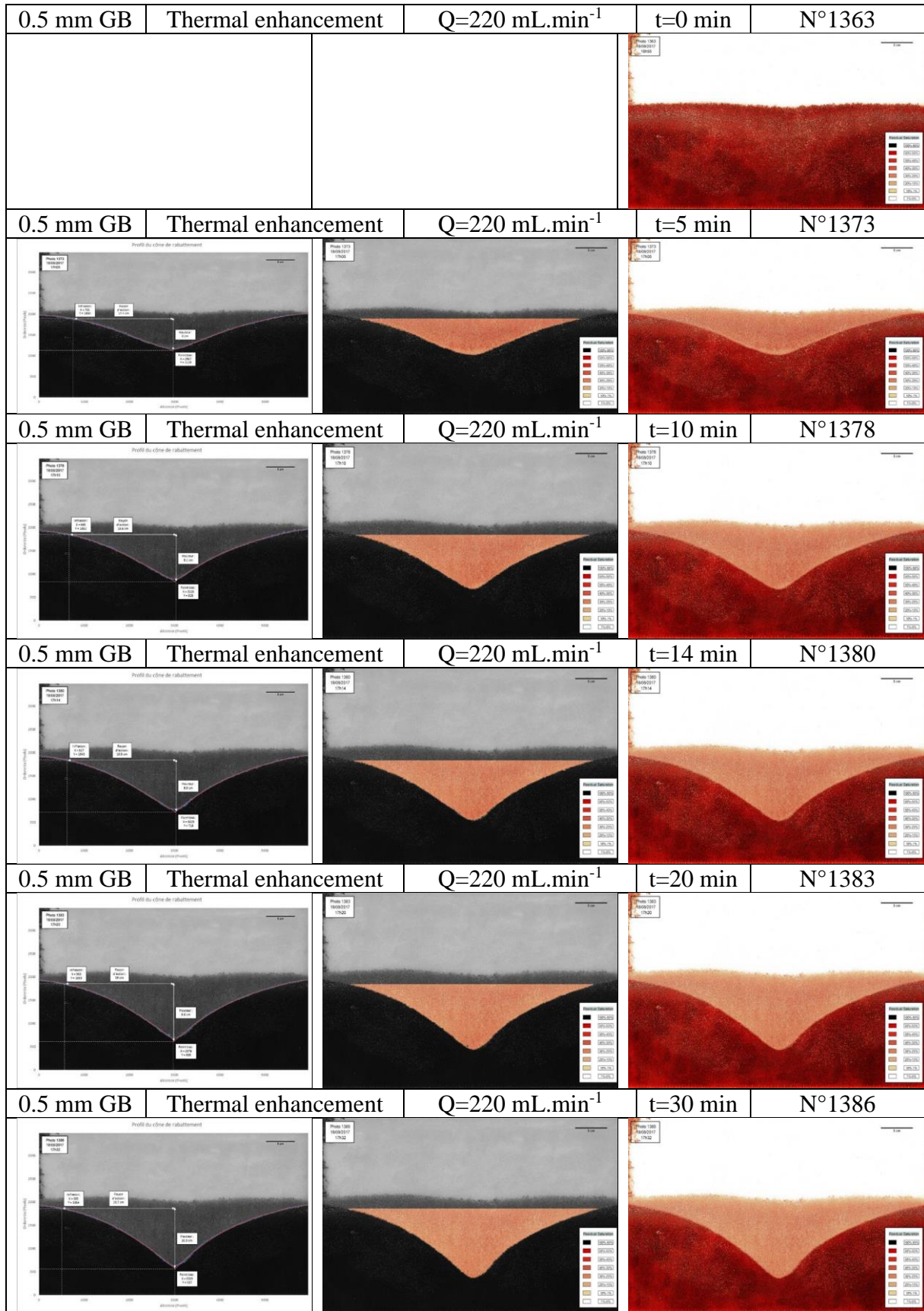
0.5 mm GB Thermal enhancement $Q=50 \text{ mL}\cdot\text{min}^{-1}$



0.5 mm GB Thermal enhancement $Q=150 \text{ mL}\cdot\text{min}^{-1}$

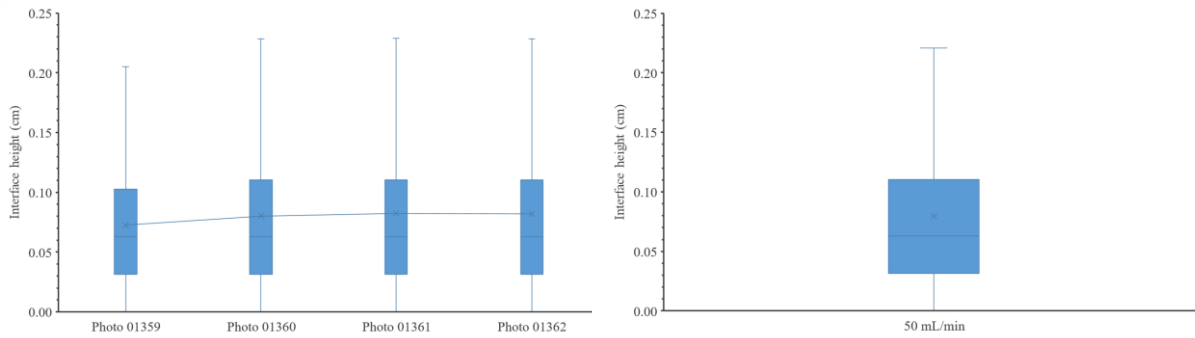


0.5 mm GB Thermal enhancement $Q=220 \text{ mL}\cdot\text{min}^{-1}$

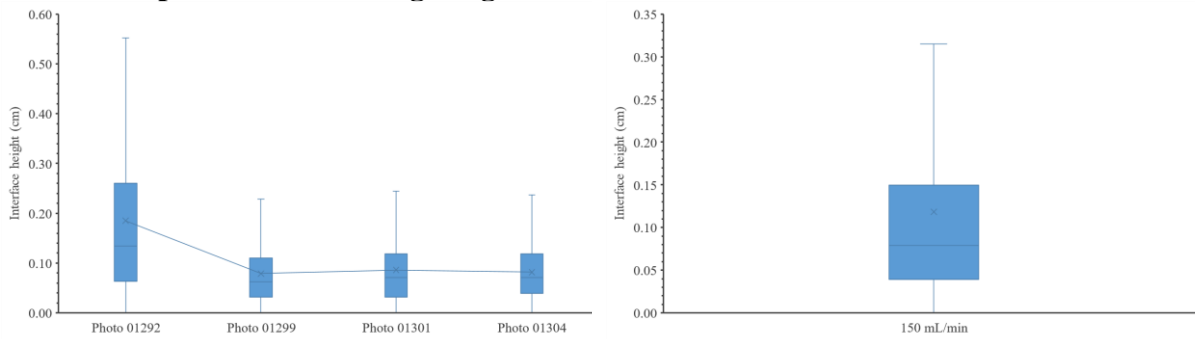


0.5 mm GB Thermal enhancement

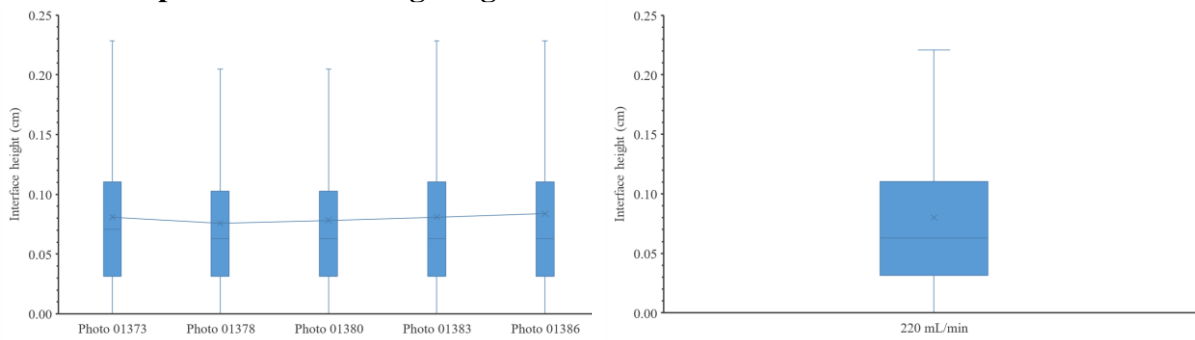
Statistical representation of fingerings of the DNAPL-water interface – 50 mL.min⁻¹



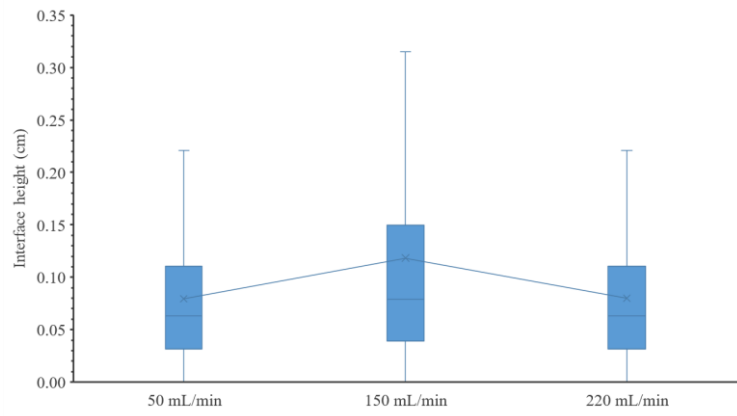
Statistical representation of fingerings of the DNAPL-water interface – 150 mL.min⁻¹



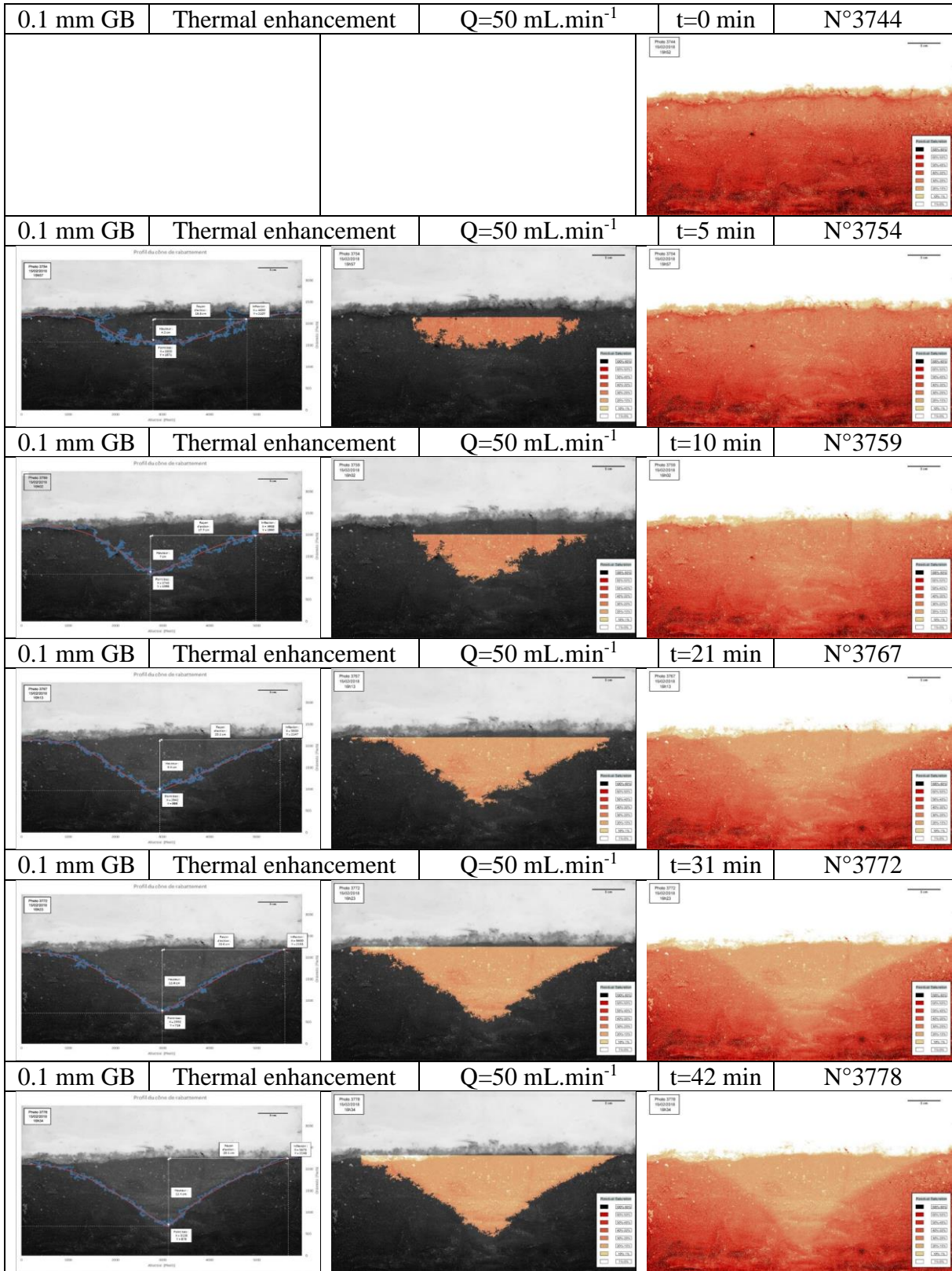
Statistical representation of fingerings of the DNAPL-water interface – 220 mL.min⁻¹




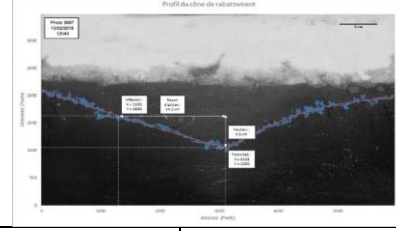

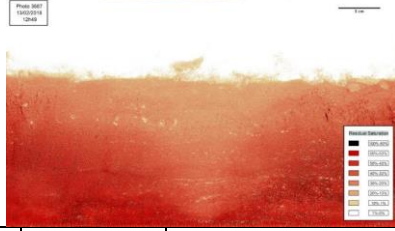
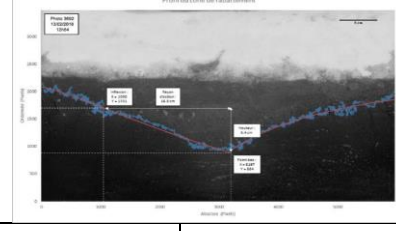


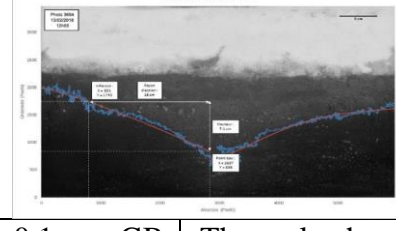
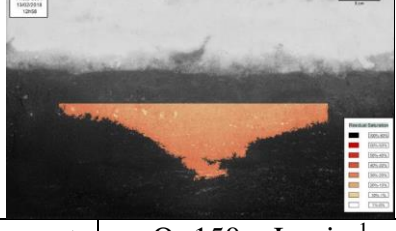
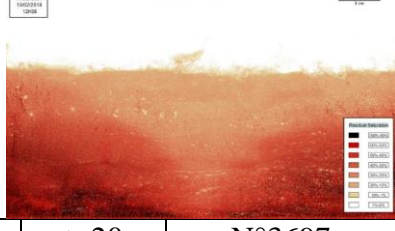
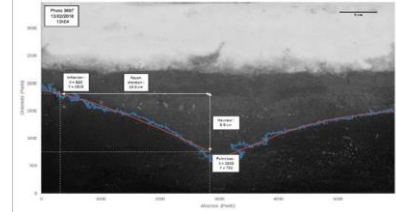


Statistical representation of fingerings of the DNAPL-water interface – Total



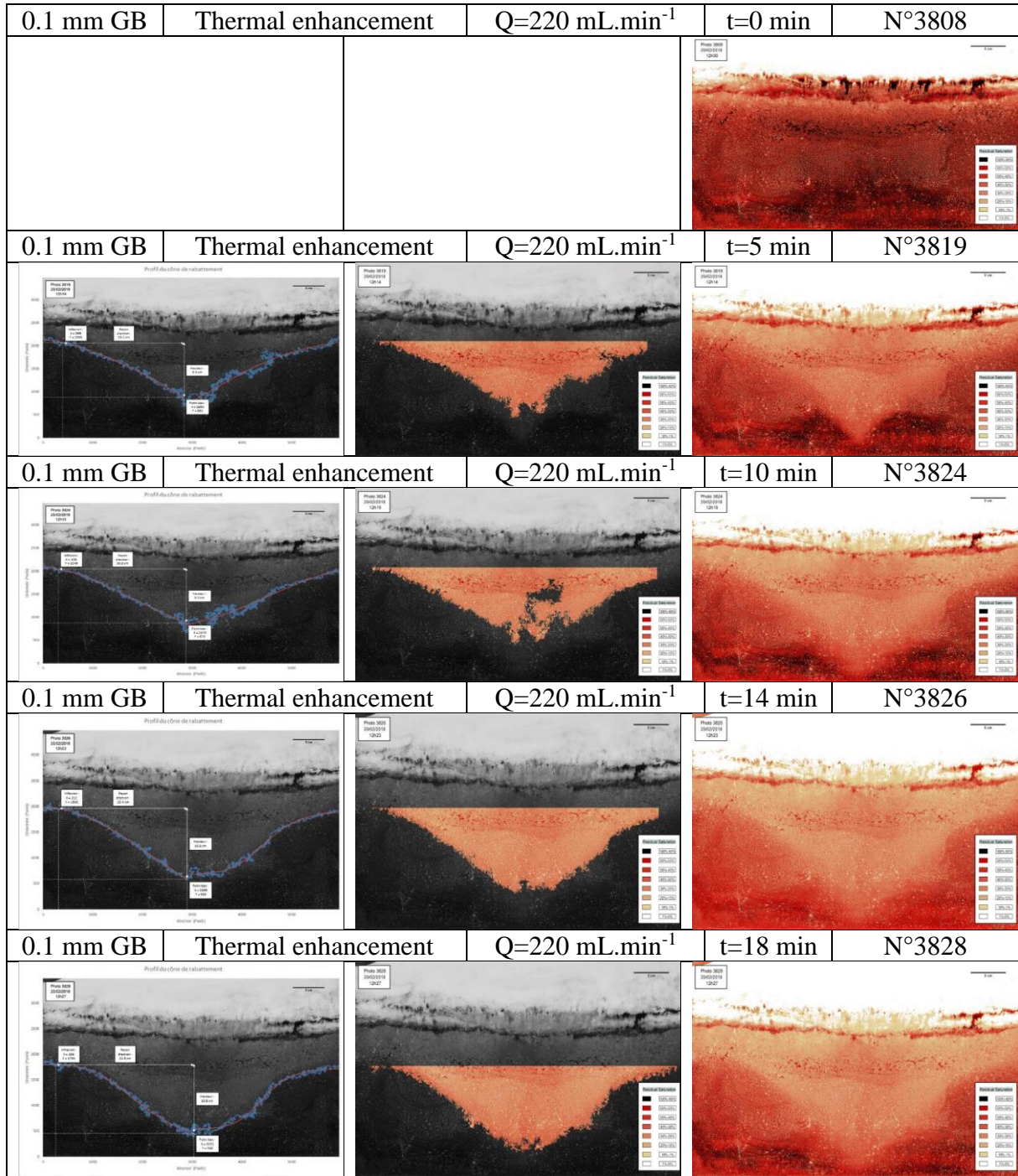
0.1 mm GB Thermal enhancement $Q=50 \text{ mL}\cdot\text{min}^{-1}$



0.1 mm GB Thermal enhancement $Q=150 \text{ mL}\cdot\text{min}^{-1}$

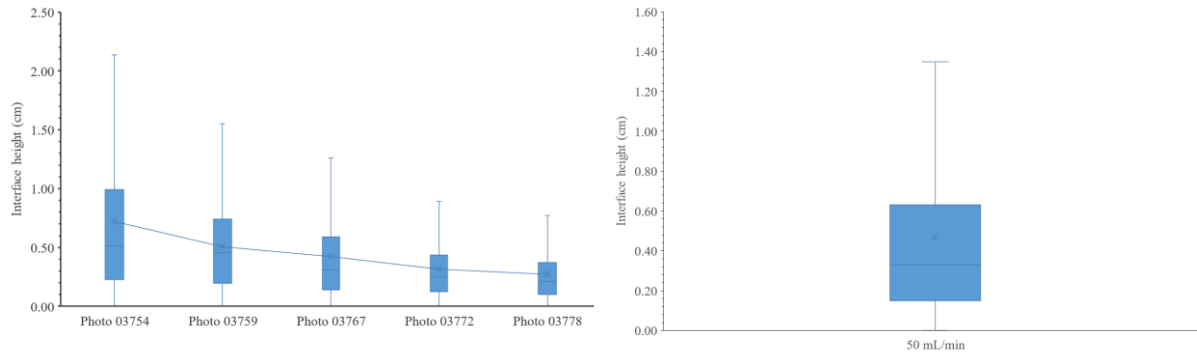
0.1 mm GB	Thermal enhancement	$Q=150 \text{ mL}\cdot\text{min}^{-1}$	t=0 min	N°3678
				
0.1 mm GB	Thermal enhancement	$Q=150 \text{ mL}\cdot\text{min}^{-1}$	t=5 min	N°3687
				
0.1 mm GB	Thermal enhancement	$Q=150 \text{ mL}\cdot\text{min}^{-1}$	t=10 min	N°3692
				
0.1 mm GB	Thermal enhancement	$Q=150 \text{ mL}\cdot\text{min}^{-1}$	t=14 min	N°3694
				
0.1 mm GB	Thermal enhancement	$Q=150 \text{ mL}\cdot\text{min}^{-1}$	t=20 min	N°3697
				

0.1 mm GB Thermal enhancement $Q=220 \text{ mL}\cdot\text{min}^{-1}$

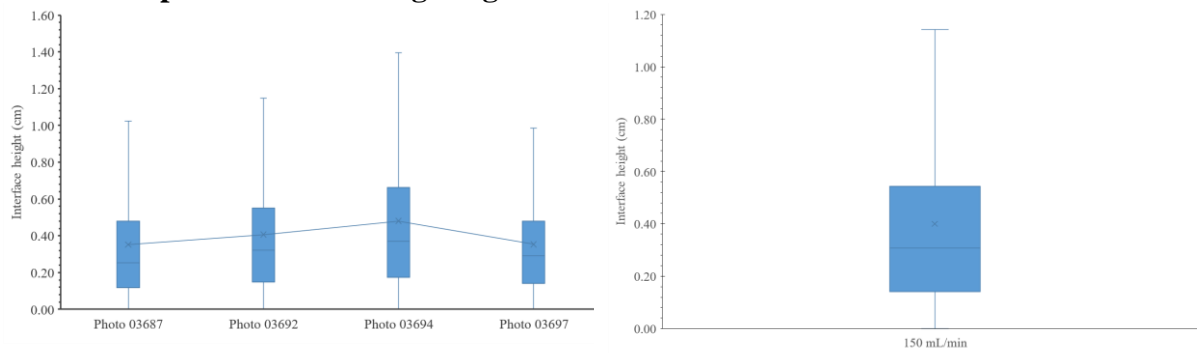


0.1 mm GB Thermal enhancement

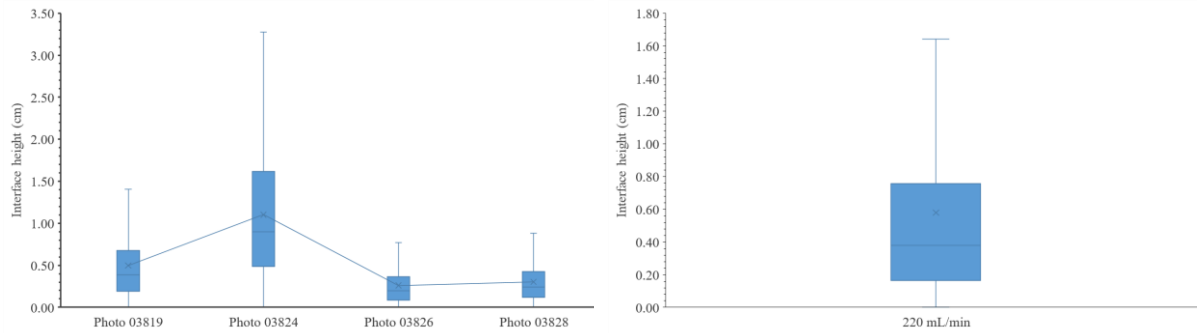
Statistical representation of fingerings of the DNAPL-water interface – 50 mL.min⁻¹



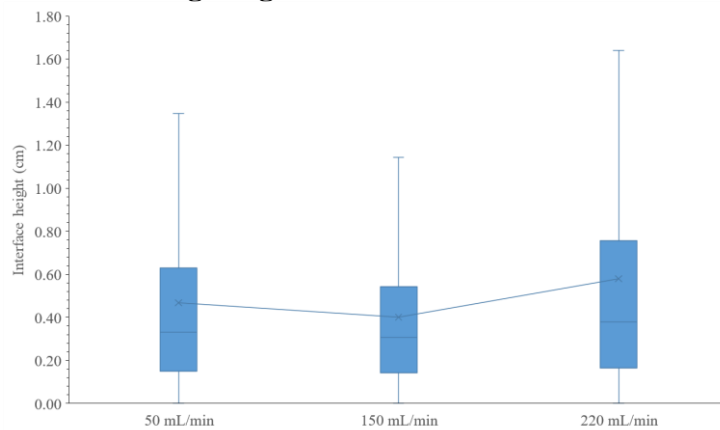
Statistical representation of fingerings of the DNAPL-water interface – 150 mL.min⁻¹



Statistical representation of fingerings of the DNAPL-water interface – 220 mL.min⁻¹



Statistical representation of fingerings of the DNAPL-water interface – Total



La pollution des eaux souterraines par des composés organochlorés constitue un problème majeur. En effet, ces polluants, particulièrement toxiques, dégradent durablement les sols et les eaux souterraines. Leur dispersion (par solubilisation et volatilisation) à partir des sources de pollution peut générer des panaches de contamination importants. La récupération de ces composés sous forme de produit pur (DNAPL) est principalement basée sur les techniques de pompage/traitement. Pour autant, cette technique est lente et ne permet pas de récupérer le DNAPL de manière efficace. Une quantité de DNAPL reste piégée dans le sol sous forme de saturation résiduelle (S_m).

L'objectif de cette thèse est d'améliorer le rendement et la vitesse de récupération du DNAPL en utilisant les soutiens chimiques et thermiques au cours du pompage. L'augmentation de la température vise à diminuer la viscosité du DNAPL (et donc à augmenter sa mobilité) alors que l'ajout de surfactant vise à diminuer les forces capillaires qui piègent le DNAPL. Des expérimentations à l'échelle du laboratoire (basées notamment sur des suivis de permittivités, résistivités électriques et densités optiques) et une modélisation multiphasique ont été réalisées afin de pouvoir quantifier les effets de ces soutiens.

Le chauffage du DNAPL, réalisé jusqu'à 50 °C (afin d'éviter la volatilisation), diminue la viscosité par un facteur 2. L'ajout d'un surfactant, le Sodium Dodecyl Benzene Sulfonate-SDBS, à sa Concentration Micellaire Critique (afin d'éviter la solubilisation du DNAPL) diminue la tension interfaciale par un facteur 12.

Les essais de drainage-imbibition ont été réalisés dans des cellules 1D afin d'obtenir les courbes de rétention du système diphasique (pression capillaire en fonction de la saturation en eau). Les diminutions des S_m obtenues avec le SDBS sont de 28% pour les billes de verre (BV) de 0,5 mm de diamètre et 46% pour les BV de 0,1 mm. Aucune amélioration significative du rendement épuratoire a été obtenue avec le chauffage. Les courbes ont été calées avec le modèle de van Genuchten - Mualem dans le but de fournir les données pour la modélisation.

Les expériences de drainage-imbibition ont été réalisées dans des colonnes 1D pour caractériser les écoulements diphasiques (notamment le déplacement de l'interface DNAPL-eau en fonction des pressions appliquées). Le modèle d'écoulement diphasique a été réalisé avec la formulation de pression-pression (à l'aide de COMSOL Multiphysics®). La modélisation des volumes récupérés et du déplacement de l'interface sont en accord avec les résultats expérimentaux. Les rendements épuratoires avec les soutiens chimiques et thermiques étaient du même ordre de grandeur que pour les cellules 1D.

Des essais de pompage ont été effectués dans un bac 2D à différents débits avec les BV de 0,5 mm et 0,1 mm. Les expériences ont également été réalisées avec et sans soutien. Les modélisations ont été comparées à l'interprétation d'images (basée sur l'étalonnage de la densité optique). Les valeurs expérimentales sont en adéquation avec les valeurs modélisées. Les rapports $V_{\text{DNAPL, chimique}}/V_{\text{DNAPL, blanc}}$ pour des débits lents et élevés, étaient en moyenne respectivement de 2,90 et 1,40 pour les BV de 0,5 mm et, de 1,37 et 1,18 pour les BV de 0,1 mm. Le chauffage n'a aucun effet bénéfique sur la récupération du DNAPL.

Les mesures indirectes des saturations en eau (S_w) pour les expériences 1D ou 2D aboutissent aux résultats suivants: i. les permittivités mesurées sont très proches des valeurs modélisées avec le modèle de CRIM; ii. les modélisations des résistivités électriques avec la loi d'Archie sont moins probantes; iii. les densités optiques permettent d'estimer S_w avec précision. A l'échelle terrain, la combinaison des suivis avec la résistivité électrique (qui permet d'avoir une vision intégrative) et la permittivité (qui fournit des données précises mais spatialement limitées), permettrait de mieux quantifier les S_m .

Groundwater pollution by chlorinated organic compounds is a major problem. Actually, these particularly toxic pollutants, permanently degrade soil and groundwater quality. Their dispersion (by solubilization and volatilization) from the pollution source zone can generate large contaminants plumes. Chlorinated organic compounds are recovered as pure product (Dense Non-Aqueous Phase Liquids-DNAPL) mainly using pump/treat technologies. However, these technologies are time-consuming and do not recover the pure product in an efficient way. A significant amount of DNAPL remains trapped in soil as residual saturation (S_m).

The objective of this PhD project was to enhance DNAPL recovery rate and yield using chemical and thermal enhancements during the pumping process. Temperature increases aimed to reduce the viscosity of DNAPL (and therefore to increase its mobility) while the addition of surfactant aimed to reduce the capillary forces that trap the DNAPL. Experiments at the laboratory scale (based on monitoring of permittivities, electrical resistivities and optical densities) and two-phase flow modeling were performed to quantify the effects of these enhancements.

Heating the DNAPL up to 50 °C (to avoid volatilization) decreases the viscosity by a factor of two. The addition of surfactant, Sodium Dodecyl Benzene Sulfonate-SDBS, at its Critical Micelle Concentration (to prevent DNAPL solubilization) decreases interfacial tensions by a factor of 12.

Drainage-imbibition experiments were carried out in 1D cells to obtain the retention curves of the two-phase system (capillary pressure as a function of water saturation). The decreases of S_m obtained with SDBS were 28% for 0.5 mm glass beads (GB) diameter and 46% for 0.1 mm GB. We reported no significant improvement in the remediation yield with thermal enhancement. The curves were fitted with the van Genuchten – Mualem model to generate data for modeling.

Drainage-imbibition experiments were carried out in 1D columns to characterize two-phase flow (and in particular the displacement of the DNAPL-water interface according to the pressures applied). The two-phase flow model used a pressure-pressure formulation (using COMSOL Multiphysics®). The modeling of recovered volumes and the displacement of the interface agreed with the experimental results. The remediation yields with chemical and thermal enhancements were of the same order of magnitude as those reported in 1D cells.

For 2D tank experiments, pumping was performed at different flow rates with 0.5 mm and 0.1 mm GB. The experiments were also performed with and without enhancement. Models were compared with image interpretation (based on the optical density calibration). Comparing experimental and modeled values shows that the model fitted well with the experiments. The $V_{\text{DNAPL, chemical}}/V_{\text{DNAPL, reference}}$ ratios were for low and high flow rates on average respectively 2.90 and 1.40 for 0.5 mm GB and 1.37 and 1.18 for 0.1 mm GB. Thermal enhancement had no beneficial effect on DNAPL recovery rate or yield.

Indirect measurements of water saturations (S_w) for 1D or 2D experiments yielded the following results: i. the measured permittivities were very similar to the values modeled with the CRIM model; ii. modeling of electrical resistivities with Archie's Law was less accurate; iii. optical densities allow accurate S_w estimation. At field scale, the combination of monitoring both electrical resistivities (which provide a global picture) and permittivities (which provide precise but spatially limited data), is expected to provide S_m data.

